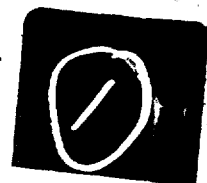


FILE COPY



AD-A209 726

AIR FORCE OFFICE OF
SCIENTIFIC RESEARCH
UNITED STATES AIR FORCE
RESEARCH INITIATION
PROGRAM
CONDUCTED BY
UNIVERSAL ENERGY SYSTEMS
U.E.S.



1987

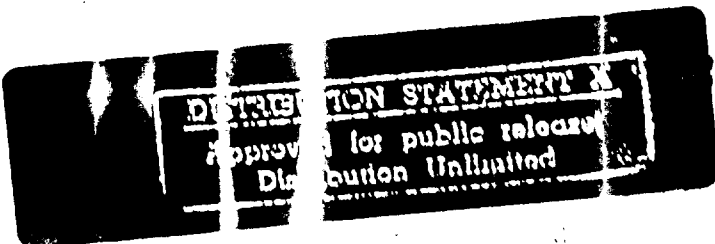
Best Available Copy

TECHNICAL REPORT
VOLUME 1 OF 4

RODNEY C. DARRAH
PROGRAM DIRECTOR, UES

SUSAN R. SPY
PROGRAM ADMINISTRATOR, UES

LT. COL. CLAUDE CAVENDER
PROGRAM MANAGER, AFOSR



Best Available Copy

Approved for public release;
distribution unlimited.

AIR FORCE OFFICE OF SCIENTIFIC RESEARCH (AFSC)
NOTICE OF TRANSMISSION TO DTIC
This technical report has been reviewed and is
approved for release to DTIC under AFOSR 190-12.
Distribution is unlimited.
MARTIN J. KETPER
Chief, Technical Information Division

INTRODUCTION

Research Initiation Program - 1987

AFOSR has provided funding for follow-on research efforts for the participants in the Summer Faculty Research Program. Initially this program was conducted by AFOSR and popularly known as the Mini-Grant Program. Since 1983 the program has been conducted by the Summer Faculty Research Program (SFRP) contractor and is now called the Research Initiation Program (RIP). Funding is provided to establish RIP awards to about half the number of participants in the SFRP.

Participants in the 1987 SFRP competed for funding under the 1987 RIP. Participants submitted cost and technical proposals to the contractor by 1 November 1987, following their participation in the 1987 SFRP.

Evaluation of these proposals was made by the contractor. Evaluation criteria consisted of:

1. Technical Excellence of the proposal
2. Continuation of the SFRP effort
3. Cost sharing by the University

The list of proposals selected for award was forwarded to AFOSR for approval of funding. Those approved by AFOSR were funded for research efforts to be completed by 31 December 1988.

The following summarizes the events for the evaluation of proposals and award of funding under the RIP.

- A. Rip proposals were submitted to the contractor by 1 November 1987. The proposals were limited to \$20,000 plus cost sharing by the universities. The universities were encouraged to cost share since this is an effort to establish a long term effort between the Air Force and the university.
- B. Proposals were evaluated on the criteria listed above and the final award approval was given by AFOSR after consultation with the Air Force Laboratories.
- C. Subcontracts were negotiated with the universities. The period of performance of the subcontract was between October 1987 and December 1988.

Copies of the Final Reports are presented in Volumes I through III of the 1987 Research Initiation Program Report. There were a total of 83 RIP awards made under the 1987 program.

UNCLASSIFIED
SECURITY CLASSIFICATION OF THIS PAGE

REPORT DOCUMENTATION PAGE

Form Approved
OMB No. 0704-0188

REPORT SECURITY CLASSIFICATION UNCLASSIFIED			1b. RESTRICTIVE MARKINGS		
2a. SECURITY CLASSIFICATION AUTHORITY			3. DISTRIBUTION/AVAILABILITY OF REPORT Approved for public release; distribution unlimited.		
2b. DECLASSIFICATION/DOWNGRADING SCHEDULE					
4. PERFORMING ORGANIZATION REPORT NUMBER(S)			5. MONITORING ORGANIZATION REPORT NUMBER(S) AFOSR-ATR-89-0329		
6a. NAME OF PERFORMING ORGANIZATION UNIVERSAL ENERGY SYSTEMS INC.		6b. OFFICE SYMBOL (If applicable)	7a. NAME OF MONITORING ORGANIZATION Air Force Office of Scientific Research/XOT		
6c. ADDRESS (City, State, and ZIP Code) 4401 Dayton Xenia Rd Dayton OH 45432			7b. ADDRESS (City, State, and ZIP Code) Building 410 Bolling AFB DC 20332		
8a. NAME OF FUNDING/SPONSORING ORGANIZATION AFOSR		8b. OFFICE SYMBOL (If applicable) XOT	9. PROCUREMENT INSTRUMENT IDENTIFICATION NUMBER F49620-85-C-0013		
8c. ADDRESS (City, State, and ZIP Code) Building 410 Bolling AFB, DC 20332			10. SOURCE OF FUNDING NUMBERS		
			PROGRAM ELEMENT NO. 61102F	PROJECT NO. 3396	TASK NO. D5
			WORK UNIT ACCESSION NO.		
11. TITLE (Include Security Classification) USAF Research Initiation Program Volume 1 of 4					
PERSONAL AUTHOR(S) Program Director Rodney C. Darrah					
13a. TYPE OF REPORT Interim		13b. TIME COVERED FROM _____ TO _____		14. DATE OF REPORT (Year, Month, Day) April - 1987	
15. PAGE COUNT					
16. SUPPLEMENTARY NOTATION					
17. COSATI CODES			18. SUBJECT TERMS (Continue on reverse if necessary and identify by block number)		
FIELD	GROUP	SUB-GROUP			
19. ABSTRACT (Continue on reverse if necessary and identify by block number) (SEE REVERSE)					
20. DISTRIBUTION/AVAILABILITY OF ABSTRACT <input checked="" type="checkbox"/> UNCLASSIFIED/UNLIMITED <input type="checkbox"/> SAME AS RPT. <input type="checkbox"/> DTIC USERS			21. ABSTRACT SECURITY CLASSIFICATION UNCLASSIFIED		
22a. NAME OF RESPONSIBLE INDIVIDUAL Lt Col Claude Guenier			22b. TELEPHONE (Include Area Code) (202) 767-4971		22c. OFFICE SYMBOL XOT

89 6 29 009

**EFFECTS OF BENDING FLEXIBILITY
ON THE AERODYNAMIC CHARACTERISTICS OF
SLENDER CYLINDERS DETERMINED FROM
FREE-FLIGHT BALLISTIC DATA**

by

Robert W. Courter and Thomas K. Harkins
Department of Mechanical Engineering
Louisiana State University

FINAL REPORT
to
Air Force Office of Scientific Research
through
Universal Energy Systems, Inc.
under contract
F49620-85-C-0013/SB5851-0360
and subcontract
S-760-7MG-018

December, 1988

UNITED STATES AIR FORCE
1987 RESEARCH INITIATION PROGRAM

Conducted by
UNIVERSAL ENERGY SYSTEMS, INC.

under
USAF Contract Number F49620-85-C-0013

RESEARCH REPORTS
VOLUME I OF IV

Submitted to
Air Force Office of Scientific Research
Bolling Air Force Base
Washington, DC

By
Universal Energy Systems, Inc.
April 1989



Accession For	
NTIS ORA-21	<input checked="" type="checkbox"/>
DTIC TAB	<input type="checkbox"/>
Unannounced	<input type="checkbox"/>
Justification	
By	
Distribution /	
Availability Codes	
Dist	Availability for Special
A-1	

TABLE OF CONTENTS

<u>SECTION</u>	<u>PAGE</u>
INTRODUCTION	i
STATISTICS	ii
PARTICIPANT LABORATORY ASSIGNMENT	vii
RESEARCH REPORTS	xvi

INTRODUCTION

Research Initiation Program - 1987

AFOSR has provided funding for follow-on research efforts for the participants in the Summer Faculty Research Program. Initially this program was conducted by AFOSR and popularly known as the Mini-Grant Program. Since 1983 the program has been conducted by the Summer Faculty Research Program (SFRP) contractor and is now called the Research Initiation Program (RIP). Funding is provided to establish RIP awards to about half the number of participants in the SFRP.

Participants in the 1987 SFRP competed for funding under the 1987 RIP. Participants submitted cost and technical proposals to the contractor by 1 November 1987, following their participation in the 1987 SFRP.

Evaluation of these proposals was made by the contractor. Evaluation criteria consisted of:

1. Technical Excellence of the proposal
2. Continuation of the SFRP effort
3. Cost sharing by the University

The list of proposals selected for award was forwarded to AFOSR for approval of funding. Those approved by AFOSR were funded for research efforts to be completed by 31 December 1988.

The following summarizes the events for the evaluation of proposals and award of funding under the RIP.

- A. Rip proposals were submitted to the contractor by 1 November 1987. The proposals were limited to \$20,000 plus cost sharing by the universities. The universities were encouraged to cost share since this is an effort to establish a long term effort between the Air Force and the university.
- B. Proposals were evaluated on the criteria listed above and the final award approval was given by AFOSR after consultation with the Air Force Laboratories.
- C. Subcontracts were negotiated with the universities. The period of performance of the subcontract was between October 1987 and December 1988.

Copies of the Final Reports are presented in Volumes I through III of the 1987 Research Initiation Program Report. There were a total of 83 RIP awards made under the 1987 program.

STATISTICS

Total SFRP Participants	159
Total RIP Proposals submitted by SFRP	117
Total RIP Proposals submitted by GSRP	7
Total RIP Proposals submitted	124
Total RIP's funded to SFRP	81
Total RIP's funded to GSRP	2
Total RIP's funded	83
Total RIP's Proposals submitted by HBCU's	11
Total RIP's Proposals funded to HBCU's	7

<u>Laboratory</u>	<u>SFRP Participants</u>	<u>RIP's Submitted</u>	<u>RIP's Funded</u>
AAMRL	13	12 (2 GSRP)	6
AFWAL/APL	8	6	4
ATL	9	8 (1 GSRP)	6
AEDC	6	4	3
AFWAL/AL	9	9 (1 GSRP)	5
LC	1	1	1
ESMC	1	0	0
ESD	1	1	0
ESC	8	8	6
AFWAL/FDL	9	8 (1 GSRP)	6 (1 GSRP)
FJSRL	9	5	5
AFGL	13	10 (1 GSRP)	7
HRL/OT	2	2	1
HRL/LR	3	3	2
HRL/MO	3	2	2
HRL/ID	0	0	0
LMC	3	1	0
AFWAL/ML	13	11 (1 GSRP)	6 (1 GSRP)
OEHL	5	3	3
AL	7	4	3
RADC	11	10	7
SAM	16	8	6
DEOMI	2	2	0
WL	7	6	4
Total	159	124	83

LIST OF UNIVERSITY THAT PARTICIPATED

Adelphi University	- 1	Meharry Medical College	- 1
Alabama, University of	- 1	Memphis State University	- 1
Alaska-Fairbanks, Univ. of	- 1	Metropolitan State College	- 1
Alfred University	- 1	Michigan State University	- 1
Arizona State University	- 1	Mississippi State University	- 4
Arkansas State University	- 1	Mississippi, University of	- 1
Arkansas, University of	- 1	Missouri-Kansas City, Univ.	- 1
Auburn University	- 1	Missouri-Rolla, Univ. of	- 3
Bishop College	- 1	Montana, University of	- 1
Capital University	- 1	Montclair State College	- 1
Catholic Univ. of America	- 1	Morehouse College	- 1
Cedarville College	- 1	Nazareth College	- 1
Central State University	- 1	Nebraska-Lincoln, Univ. of	- 2
Cincinnati, University of	- 5	New Mexico State University	- 1
Colorado, University of	- 2	New York State, Univ. of	- 3
Dayton, University of	- 7	N. Carolina A&T State Univ.	- 1
Dillard University	- 1	N. Carolina-Greensboro, Univ	- 1
Drury College	- 1	Northwestern University	- 1
Eastern Illinois University	- 1	Ohio State University	- 5
Eastern Kentucky University	- 1	Ohio University	- 2
Eastern New Mexico University	- 2	Oklahoma State University	- 1
Fairfield University	- 1	Oregon Institute of Tech.	- 1
Florida A&M University	- 1	Oregon State University	- 1
Florida, University of	- 2	Ouachita Baptist University	- 1
Fort Lewis College	- 1	Pace University	- 1
Gonzaga University	- 1	Pennsylvania State Univ.	- 1
Grambling State University	- 1	Point Loma College	- 1
Hampton University	- 1	Puerto Rico-Mayaguez, Univ.	- 1
Houston, University of	- 2	Purdue University	- 1
Howard University	- 1	Rochester Inst. of Tech.	- 1
Idaho, University of	- 1	Rose-Hulman Inst. of Tech.	- 2
Illinois-Chicago, Univ. of	- 2	Saint Paul's College	- 1
Indiana University	- 1	San Francisco State Univ.	- 1
Indiana Univ. of Pennsylvania	- 1	South Dakota State Univ.	- 1
Iowa, University of	- 1	South Florida, University of	- 2
Jackson State University	- 1	Southeastern Mass. Univ.	- 2
Jarvis Christian College	- 1	Southern Illinois University	- 2
Jesm Baromedical Res. Inst.	- 1	Southern Mississippi, Univ.	- 1
John Hopkins Evening College	- 1	Southern University	- 2
Kansas State University	- 1	St. Louis University	- 1
Kansas, University of	- 1	St. Mary's University	- 1
Kentucky, University of	- 1	Talladega College	- 1

Continued

LIST OF UNIVERSITY THAT PARTICIPATED
Continued

Lock Haven Univ. of Pennsylv.	- 1	Taylor University	- 1
Long Island University	- 1	Temple University	- 1
Louisiana State University	- 1	Tennessee Technical Univ.	- 1
Louisiana Tech. University	- 1	Tennessee, University of	- 1
Lowell, University of	- 4	Texas A&M University	- 2
Texas Southern University	- 3	Wichita State University	- 2
Texas Technical University	- 2	Wilberforce University	- 1
Texas-Austin, University of	- 1	Wisconsin-Eau Claire Univ.	- 2
Tuskegee University	- 1	Wisconsin-Madison, Univ. of	- 1
Utah State University	- 1	Wisconsin-Whitewater, Univ.	- 1
Walla Walla College	- 1	Wittenberg University	- 1
Washington State University	- 1	Worcester Polytech. Inst.	- 2
West Florida, University of	- 1	Wright State University	- 3
Western Michigan University	- 3	Xavier University	- 1

PARTICIPANTS LABORATORY ASSIGNMENT

PARTICIPANT LABORATORY ASSIGNMENT (Page 1)

AERO PROPULSION LABORATORY

(Wright-Patterson Air Force Base)

Dr. Suresh K. Aggarwal
Univ. of Illinois at Chicago
Specialty: Aerospace Engineering

Dr. Richard Tankin
Northwestern University
Specialty: Mechanical Engineering

Dr. Bryan R. Becker
Rose-Hulman Institute
Specialty: Engineering Science

Dr. Cheng-Hsiao Wu
Univ. of Missouri
Specialty: Solid State Physics

ARMAMENT LABORATORY

(Eglin Air Force Base)

Dr. Charles Bell
Arkansas State University
Specialty: Mechanical Engineering

Dr. Elmer C. Hansen
University of Florida
Specialty: Mechanical Engineering

Dr. Robert W. Courter
Louisiana State University
Specialty: Aerospace Engineering

Dr. James Hoffmaster
Gonzaga University
Specialty: Physics

Dr. Joseph J. Feeley
University of Idaho
Specialty: Electrical Engineering

Dr. James Nail
Mississippi State Univ.
Specialty: Electrical Engineering

Ms. Jennifer L. Davidson (1986), (GSRP)
University of Florida
Specialty: Mathematics

Dr. Meckinley Scott (1986)
University of Alabama
Specialty: Statistics

Dr. Mo Samimy (1986)
Ohio State University
Specialty: Mechanical Engineering

Mr. Jim S. Sirkis (1986), (GSRP)
University of Florida
Specialty: Engineering Mechanics

HARRY G. ARMSTRONG AEROSPACE MEDICAL RESEARCH LABORATORY

(Wright-Patterson Air Force Base)

Dr. Praphulla K. Bajpai
University of Dayton
Specialty: Immunology

Dr. Thomas Nygren
Ohio State University
Specialty: Psychology

Dr. Gwendolyn Howze
Texas Southern University
Specialty: Physics

Dr. Donald Robertson
Indiana University of PA
Specialty: Psychology

PARTICIPANT LABORATORY ASSIGNMENT (Page 2)

HARRY G. ARMSTRONG AEROSPACE MEDICAL RESEARCH LABORATORY
(Wright-Patterson Air Force Base)
(continued)

Dr. Noel Nussbaum
Wright State University
Specialty: Biology

Dr. John Westerkamp
University of Dayton
Specialty: Electrical Engineering

Dr. Jacqueline Paver (1986)
Duke University
Specialty: Biomechanical Engineering

ARNOLD ENGINEERING DEVELOPMENT CENTER
(Arnold Air Force Systems)

Dr. Suhrit K. Dey
Eastern Illinois University
Specialty: Aerospace Engineering

Dr. Surgounda Patil
Tennessee Technical University
Specialty: Math Statistics

Dr. William M. Grissom
Morehouse College
Specialty: Mechanical Engineering

ASTRONAUTICS LABORATORY
(Edwards Air Force Base)

Dr. Gurbux S. Alag
Western Michigan University
Specialty: Systems Engineering

Dr. Lawrence Schovanec
Texas Tech University
Specialty: Mathematics

Dr. John Kenney
Eastern New Mexico University
Specialty: Physical Chemistry

AVIONICS LABORATORY
(Wright-Patterson Air Force Base)

Dr. Vernon L. Bakke
University of Arkansas
Specialty: Mathematics

Dr. Narayan C. Halder
University of South Florida
Specialty: Physics

PARTICIPANT LABORATORY ASSIGNMENT (Page 3)

AVIONICS LABORATORY

(Wright-Patterson Air Force Base)
(continued)

Prof. William K. Curry
Rose-Hulman Inst. of Technology
Specialty: Computer Science

Dr. Verlynda S. Dobbs
Wright State University
Specialty: Computer Science

Dr. George W. Zobrist (1986)
University of Missouri-Rolla
Specialty: Electrical Engineering

Dr. Alastair McAulay
Wright State University
Specialty: Electrical Engineering

Dr. John Y. Cheung (1986)
University of Oklahoma
Specialty: Electrical Engineering

ENGINEERING AND SERVICES CENTER
(Tyndall Air Force Base)

Dr. William W. Bannister
University of Lowell
Specialty: Organic Chemistry

Dr. William M. Bass
The University of Tennessee
Specialty: Physical Anthropology

Dr. Peter Jeffers
S.U.N.Y.
Specialty: Chemistry

Dr. William T. Cooper (1986)
Florida State University
Specialty: Chemistry

Dr. William Schulz
Eastern Kentucky University
Specialty: Chemistry

Dr. Joseph Tedesco
Auburn University
Specialty: Civil Engineering

Dr. Dennis Truax
Mississippi State University
Specialty: Civil Engineering

Dr. Yong S. Kim (1986)
The Catholic Univ. of America
Specialty: Civil Engineering

FLIGHT DYNAMICS LABORATORY

(Wright-Patterson Air Force Base)

Mr. Thomas Enneking (GSRP)
University of Notre Dame
Specialty: Civil Engineering

Dr. Gary Slater
University of Cincinnati
Specialty: Aerospace Engineering

PARTICIPANT LABORATORY ASSIGNMENT (Page 4)

FLIGHT DYNAMICS LABORATORY

(Wright-Patterson Air Force Base)
(continued)

Dr. Oliver McGee
Ohio State University
Specialty: Engineering Mechanics

Dr. Forrest Thomas
University of Montana
Specialty: Chemistry

Dr. Shiva Singh
Univ. of Kentucky
Specialty: Mathematics

Dr. William Wolfe
Ohio State University
Specialty: Engineering

Dr. George R. Doyle (1986)
University of Dayton
Specialty: Mechanical Engineering

Dr. V. Dakshina Murty (1986)
University of Portland
Specialty: Engineering Mechanics

Dr. Tsun-wai G. Yip (1986)
Ohio State University
Specialty: Aeronautics-Astronautics Engineering

FRANK J. SEILER RESEARCH RESEARCH LABORATORY
(United State Air Force Academy)

Dr. Charles M. Bump
Hampton University
Specialty: Organic Chemistry

Dr. Howard Thompson
Purdue University
Specialty: Mechanical Engineering

Dr. Stephen J. Gold
South Dakota State University
Specialty: Electrical Engineering

Dr. Melvin Zandler
Wichita State Univ.
Specialty: Physical Chemistry

Dr. Henry Kurtz
Memphis State Univ.
Specialty: Chemistry

GEOPHYSICS LABORATORY

(Hanscom Air Force Base)

Dr. Lee A. Flippin
San Francisco State Univ.
Specialty: Organic Chemistry

Dr. Gandikota Rao
St. Louis University
Specialty: Meteorology

PARTICIPANT LABORATORY ASSIGNMENT (Page 5)

GEOFYSICS LABORATORY

(Hanscom Air Force Base)
(continued)

Dr. Mayer Humi
WPI
Specialty: Applied Mathematics

Dr. Steven Leon
Southeastern Massachusettes
Specialty: Mathematics

Dr. Henry Nebel
Alfred University
Specialty: Physics

Dr. Timothy Su
Southeastern Massachusetts Univ.
Specialty: Physical Chemistry

Dr. Keith Walker
Point Loma College
Specialty: Physics

HUMAN RESOURCES LABORATORY

(Brooks, Williams and Wright-Patterson Air Force Base)

Dr. Patricia A. Carlson
Rose-Hulman Inst. of Technology
Specialty: Literature/Language

Dr. Ronna E. Dillon
Southern Illinois University
Specialty: Educational Psychology

Dr. Michael Matthews
Drury College
Specialty: Psychology

Dr. Stephen Loy (1986)
Iowa State University
Specialty: Management Information Sys.

Dr. Doris Walker-Dalhouse (1986)
Jackson State University
Specialty: Reading Education

Dr. John Uhlarik
Kansas State University
Specialty: Psychology

Dr. Charles Wells
University of Dayton
Specialty: Management Science

Dr. Charles Lance (1986)
University of Georgia
Specialty: Psychology

Dr. Jorge Mendoza
Texas A&M University
Specialty: Psychology

Dr. Billy Wooten (1986)
Brown University
Specialty: Philosophy, Psychology

PARTICIPANT LABORATORY ASSIGNMENT (Page 6)

LOGISTICS COMMAND

(Wright-Patterson Air Force Base)

Dr. Howard Weiss

Specialty: Industrial Engineering

Temple University

MATERIALS LABORATORY

(Wright-Patterson Air Force Base)

Dr. Bruce A. DeVantier

S. Illinois University

Specialty: Civil Engineering

Dr. Ravinder Diwan

Southern University

Specialty: Metallurgy

Dr. Bruce A. Craver

University of Dayton

Specialty: Physics

Dr. Robert Patsiga (1986)

Indiana Univ. of Pennsylvania

Specialty: Organic Polymer Chemistry

Dr. Gopal M. Mehrotra (1986)

Wright State University

Specialty: Metallurgy

Dr. John W. Gilmer

Penn State University

Specialty: Physical Chemistry

Dr. Gordon Johnson

Walla Walla College

Specialty: Electrical Engineering

Mr. John Usher (GSRP)

Louisiana State University

Specialty: Chemical Engineering

Dr. Nisar Shaikh (1986)

University of Nebraska-Lincoln

Specialty: Applied Mathematics

OCCUPATIONAL AND ENVIRONMENT HEALTH LABORATORY

(Brooks Air Force Base)

Dr. Richard H. Brown

Ouachita Baptist University

Specialty: Physiology

Dr. Elvis E. Deal

University of Houston

Specialty: Industrial Engineering

Dr. Kiah Edwards

Texas Southern University

Specialty: Molecular Biology

Dr. Ralph J. Rascati (1986)

Kennesaw College

Specialty: Biochemistry

PARTICIPANT LABORATORY ASSIGNMENT (Page 7)

ROME AIR DEVELOPMENT CENTER
(Griffis Air Force Base)

Prof. Beryl L. Barber
Oregon Institute of Technology
Specialty: Electrical Engineering

Dr. Kevin Bowyer
University of South Florida
Specialty: Computer Science

Dr. Ronald V. Canfield
Utah State University
Specialty: Statistics

Dr. Lionel R. Friedman
Worcester Polytechnic Inst.
Specialty: Physics

Dr. John M. Jobe (1986)
Miami University of Ohio
Specialty: Statistics

Dr. Louis Johnson
Oklahoma State Univ.
Specialty: Electrical Engineering

Dr. Panapkkam Ramamoorthy
University of Cincinnati
Specialty: Electrical Engineering

Dr. David Sumberg
Rochester Institute of Tech.
Specialty: Physics

Dr. Donald Hanson (1986)
University of Mississippi
Specialty: Electrical Engineering

Dr. Stephen T. Welstead (1986)
University of Alabama in Hunts.
Specialty: Applied Mathematics

SCHOOL OF AEROSPACE MEDICINE
(Brooks Air Force Base)

Prof. Phillip A. Bishop
University of Alabama
Specialty: Exercise Physiology

Dr. Mohammed Maleque
Meharry Medical College
Specialty: Pharmacology

Dr. Kurt Oughstun
University of Wisconsin
Specialty: Optical Sciences

Dr. Hoffman H. Chen (1986)
Grambling State University
Specialty: Mechanical Engineering

Dr. Ralph Peters
Wichita State University
Specialty: Zoology

Dr. Stephen Pruett
Mississippi State University
Specialty: Immunology

Dr. Wesley Tanaka
University of Wisconsin
Specialty: Biochemistry

Dr. Vito DelVecchio (1986)
University of Scranton
Specialty: Biochemistry, Genetics

PARTICIPANT LABORATORY ASSIGNMENT (Page 8)

WEAPONS LABORATORY

(Kirtland Air Force Base)

Dr. Jerome Knopp
University of Missouri
Specialty: Electrical Engineering

Dr. Barry McConnell
Florida A&M University
Specialty: Computer Science

Dr. Martin A. Shadday, Jr. (1986)
University of South Carolina
Specialty: Mechanical Engineering

Dr. Randall Peters
Texas Tech University
Specialty: Physics

Dr. William Wheless
New Mexico State University
Specialty: Electrical Engineering

RESEARCH REPORTS

MINI-GRANT RESEARCH REPORTS
1987 RESEARCH INITIATION PROGRAM

<u>Technical Report Number</u> Volume I Armament Laboratory	<u>Title and Mini-Grant No.</u>	<u>Professor</u>
1	Report Not Available at this Time 760-7MG-025	Dr. Charles Bell
2	Effects of Bending Flexibility on the Aerodynamic Characteristics of Slender Cylinders Determined from Free-Flight Ballistic Data 760-7MG-018	Dr. Robert W. Courter
3	Image Complexity Measures and Edge Detection 760-6MG-024	Ms. Jennifer L. Davidson (1986 GSRP)
4	Report Not Available at this Time 760-7MG-070	Dr. Joesph J. Feeley
5	Advanced Gun Gas Diversion 760-7MG-012	Dr. Elmer Hansen
6	A Physical and Numerical Study of Pressure Attenuation in Solids 760-7MG-002	Dr. James Hoffmaster
7	Pyroelectric Sensing for Potential Multi-Mode Use 760-7MG-026	Dr. James Nail
8	Gaseous Fuel Injection and Mixing in a Supersonic Combustor 760-6MG-059	Dr. Mo Samimy (1986)
9	Systems Effectiveness for Targets with Repair or Replacement Facilities of Damaged Components 760-6MG-025	Dr. Meckinley Scott (1986)
10	A Pattern Recognition Application in Elastic-Plastic Boundary Element, Hybrid Stress Analysis 760-6MG-142	Mr. Jim S. Sirkis (1986 GSRP)

Arnold Engineering Development Center

- 11 → Vectorized Perturbed Functional
Iterative Scheme (VPFIS): A Large-
Scale Nonlinear System Solver,
760-7MG-037

Dr. Suhrit K. Dey

- 12 → Liquid Film Cooling in Rocket
Engines,
760-7MG-022

Dr. William M. Grissom

- 13 → Estimation of Autocorrelation and
Power Spectral Density for Randomly
Sampled Systems;
760-7MG-085

Dr. Surgounda Patil

Astronautics Laboratory

- 14 Report Not Available at this Time
760-7MG-042

Dr. Gurbux S. Alag

- 15 Report Not Available at this Time
760-7MG-019

Dr. John Kenney

- 16 → Fracture in Solid Propellant:
Damage Effects upon Crack
Propagation,
760-7MG-065

Dr. Lawrence Schovanec

- 17 → Novel Conversion of Organometallics to
Energetic Nitro Compounds
760-6MG-130

Dr. Nicholas E. Takach
(1986)

Engineering and Services Center

- 18 → Correlations of Spontaneous
Ignition Temperatures with Molecular
Structures of Flammable Compounds,
760-7MG-101

Dr. William W. Bannister

- 19 → The Estimation of Stature from
Fragments of the Femur: A
Revision of the Steele Method,
760-7MG-014

Dr. William M. Bass

- 20 → Effects of Water Solubility and
Functional Group Content on the
Interactions of Organic Solutes
with Soil Organic Matter,
760-6MG-081

Dr. William T. Cooper
(1986)

- 21 Report Not Available at this Time
760-7MG-038

Dr. Peter Jeffers

- | | | |
|----|--|------------------------|
| 22 | ➤ A Study of Semihardened Concrete Arch Structure Response Under Protective Layers ; <i>and</i>
760-6MG-004 | Dr. Yong S. Kim (1986) |
| 23 | Report Not Available at this Time
760-7MG-079 | Dr. William Schulz |
| 24 | ➤ Stress Wave Propagation in Layered Media . <i>(74d)</i> ←
760-7MG-834 | Dr. Joseph Tedesco |
| 25 | Report Not Available at this Time
760-7MG-105 | Dr. Dennis Truax |

Volume II

Frank J. Seiler Research Laboratory

- | | | |
|----|---|---------------------|
| 26 | Report Not Available at this Time
760-7MG-076 | Dr. Charles M. Bump |
| 27 | The Omnidirectional Torquer - Experimental Prototype Model I
760-7MG-123 | Dr. Stephen J. Gold |
| 28 | Calculation of Nonlinear Optical Properties
760-7MG-030 | Dr. Henry Kurtz |
| 29 | Report Not Available at this Time
760-7MG-071 | Dr. Howard Thompson |
| 30 | Report Not Available at this Time
760-7MG-092 | Dr. Melvin Zandler |

Geophysics Laboratory

- | | | |
|----|---|--------------------|
| 31 | Report Not Available at this Time
760-7MG-056 | Dr. Lee A. Flippin |
| 32 | Modelling and Prediction in a Nonlocal Turbulence Model
760-7MG-028 | Dr. Mayer Humi |
| 33 | Report Not Available at this Time
760-7MG-036 | Dr. Steven Leon |
| 34 | CO ₂ (001) Vibrational Temperatures and Limb-View Infrared Radiances Under Terminator Conditions in the 60-100 Altitude Range
760-7MG-035 | Dr. Henry Nebel |

- | | | |
|-----------------------------|--|---------------------------|
| 35 | Comparison of SSM/I Rainrates and Surface Winds with the Corresponding Conventional Data in the North West Pacific Typhoons
760-7MG-072 | Dr. Gandikota Rao |
| 36 | Report Not Available at this Time
760-7MG-040 | Dr. Timothy Su |
| 37 | Development of a System for the Measurement of Electron Excitation Cross Sections of Atoms and Molecules in the Near Infrared
760-7MG-074 | Dr. Keith Walker |
| Rome Air Development Center | | |
| 38 | Superconductor Testing
760-7MG-103 | Prof. Beryl L. Barber |
| 39 | A Form and Function Knowledge Representation for Reasoning about Classes and Instances of Objects
760-7MG-003 | Dr. Kevin Bowyer |
| 40 | Development and Evaluation of a Bayesian Test for System Testability
760-7MG-032 | Dr. Ronald V. Canfield |
| 41 | Crystalline Silicon Electro-Optic Waveguides
760-7MG-040 | Dr. Lionel R. Friedman |
| 42 | Measurements of a Slot Antenna Fed by Coplanar Waveguide and Solution of an Infinite Phased Array of Slots Fed by Coplanar Waveguide Over a Dielectric Half-Space
760-6MG-092 | Dr. Donald Hanson (1986) |
| 43 | A New Measure of Maintainability/Reliability and Its Estimation
760-6MG-019 | Dr. John M. Jobe (1986) |
| 44 | Report Not Available at this Time
760-7MG-050 | Dr. Louis Johnson |
| 45 | Signed-Digit Number System for Optical Adaptive Processing
760-7MG-015 | Dr. Panapkkam Ramamoorthy |

46	Report Not Available at this Time 760-7MG-113	Dr. David Sumberg
47	Implementation of Iterative Algorithms for an Optical Signal Processor 760-6MG-063	Dr. Stephen T. Welstead (1986)
Weapons Laboratory		
48	Experimental Evaluation of Imaging Correlography 760-7MG-109	Dr. Jerome Knopp
49	Report Not Available at this Time 760-7MG-047	Dr. Barry McConnell
50	Interaction of Lasers with Superconductors 760-7MG-008	Dr. Randall Peters
51	Three Dimensional Thermal Conduction Effects in High Power CW Laser Target Plates 760-6MG-089	Dr. Martin A. Shadday (1986)
52	Report Not Available at this Time 760-7MG-068	Dr. William Wheless
Volume III		
Air Force Wright Aeronautical Laboratories		
Aero Propulsion Laboratory		
53	Report Not Available at this Time 760-7MG-061	Dr. Suresh K. Aggerwal
54	A Numerical Study of the Flow Field and Heat Transfer in a Rectangular Passage with a Turbulator 760-7MG-066	Dr. Bryan R. Becker
55	Report Not Available at this Time 760-7MG-051	Dr. Richard Tankin
56	Report Not Available at this Time 760-7MG-093	Sr. Cheng-Hsiao Wu
Avionics Laboratory		
57	Analysis of an Algorithm for Multiple Frequency Resolution 760-7MG-090	Dr. Vernon L. Bakke

58	Signal Processing in EW Environment 760-6MG-135	Dr. John Y. Cheung (1986)
59	Report Not Available at this Time 760-7MG-081	Prof. William K. Curry
60	Implementation of Blackbroad Systems in Ada 760-7MG-010	Dr. Verlynda S. Dobbs
61	Surface States and Electron Trans- port Properties in Semi-Insulating Gallium Arsenide 760-7MG-049	Dr. Narayan C. Halder
62	Investigate Feasibility of Implemen- ting Associative Memories Using Luminescent Rebroadcasting Devices 760-7MG-029	Dr. Alastair McAulay
63	Automated Translation of Digital Logic Equations into Optimized VHDL Code 760-6MG-055	Dr. George Zobrist (1986)
Flight Dynamics Laboratory		
64	Analytical Model and Computer Program of F-16 Nose Gear and F-16 ALGS 760-6MG-006	Dr. George Doyle (1986)
65	Report Not Available at this Time 760-7MG-124	Mr. Thomas Enneking (GSRP)
66	Report Not Available at this Time 760-7MG-115	Dr. Oliver McGee
67	Development of a Technique for Pre- diction of Internal Heat Transfer in Actively Cooled Structures 760-6MG-079	Dr. V. Dakshina Murty (1986)
68	Radiation Hypersonic Aerodynamics 760-7MG-121	Dr. Shiva Singh
69	Report Not Available at this Time 760-7MG-088	Dr. Gary Slater
70	Report Not Available at this Time 760-7MG-080	Dr. Forrest Thomas

71	Report Not Available at this Time 760-7MG-102	Dr. William Wolfe
72	A Chemical Kinetics Model for Mach 5 - 14 Hypersonic Flow 760-6MG-109	Dr. Tsun-wai G. Yip (1986)
Logistics Command		
73	Development of a Microcomputer Lateral Resupply Simulation System 760-7MG-116	Dr. Howard Weiss
Materials Laboratory		
74	Development of Expert System Control of a Carbon Fiber Production Process 760-7MG-027	Dr. Bruce A. DeVantier
75	Influence of Microstructural Variations on the Thermomechanical Processing in Dynamic Material Modeling of Titanium Aluminides 760-7MG-077	Dr. Ravinder Diwan
76	Report Not Available at this Time 760-7MG-097	Dr. Bruce A. Craver
77	Report Not Available at this Time 760-7MG-013	Dr. John W. Gilmer
78	Report Not Available at this Time 760-7MG-075	Dr. Gordon Johnson
79	Studies on the Compatibility of Potential Matrix and Reinforcement Materials in Ceramic Composites for High-Temperature, Aerospace Applications 760-6MG-121	Dr. Gopal Mehrotra (1986)
80	Synthesis of Compounds Capable of Intramolecular Cyclization - Aromat- ization Reactions 760-6MG-065	Dr. Robert Patsiga (1986)
81	Leaky Rayleigh and Lamb Waves on Composites 760-6MG-007	Dr. Nisar Shaikh (1986)
82	Performance Improvement in Know- ledge-Based Process Control Systems 760-7MG-044	Mr. John Usher (GSRP)

Volume IV

Human Systems Division Laboratories

Harry G. Armstrong Aerospace Medical Research Laboratory

- | | | |
|----|--|-------------------------------|
| 83 | Development of Implantable Devices
for Sustained Delivery of Volatile
Hydrocarbons in Rats
760-7MG-098 | Dr. Praphulla K. Bajpai |
| 84 | In Situ Detection of Osteoprogenitor
Cells in an Actively Growing Bone
System
760-7MG-112 | Dr. Gwendolyn Howze |
| 85 | Trauma-Activated Periosteum Derived
Osteogenic Cells: Response to Selected
Growth Factors
760-7MG-089 | Dr. Noel Nussbaum |
| 86 | Assessing the Attributes of Expert
Judgment: Measuring Bias in Subjective
Uncertainty Estimates
760-7MG-052 | Dr. Thomas Nygren |
| 87 | Mathematical Modeling
760-6MG-020 | Dr. Jaqueline Paver
(1986) |
| 88 | Report Not Available at this Time
760-7MG-094 | Dr. Donald Robertson |
| 89 | Learning Behavior of Adaptive
Filters for Evoked Brain Potentials
760-7MG-039 | Dr. John Westerkamp |

Human Resources Laboratory

- | | | |
|----|--|--------------------------|
| 90 | The Rhetoric of Hypertext: An Exam-
ination of Document Database Concepts
and the Integrated Maintenance Infor-
mation System (IMIS)
760-7MG-021 | Dr. Patricia A. Carlson |
| 91 | Report Not Available at this Time
760-7MG-100 | Dr. Ronna E. Dillon |
| 92 | Structural Representations of Multi-
Dimensional Criterion Construct Space
760-6MG-031 | Dr. Charles Lance (1986) |
| 93 | Report Not Publishable at this Time
760-6MG-134 | Dr. Stephen Loy (1986) |

- | | | |
|---|--|-----------------------------------|
| 94 | Comparison of Supervisor's and Incumbent's Estimates of SDy
760-7MG-009 | Dr. Michael Matthews |
| 95 | Report Not Available at this Time
760-6MG-136 | Dr. Jorge Mendoza (1986) |
| 96 | The Role of Fourier Descriptions for Shape in Visual Form Perception
760-7MG-082 | Dr. John Uhlarik |
| 97 | Comprehensibility of Technical Text
760-6MG-080 | Dr. Doris Walker-Dalhousie (1986) |
| 98 | Report Not Available at this Time
760-7MG-046 | Dr. Charles Wells |
| 99 | Mechanisms of Contrast and Lightness Constancy
760-6MG-051 | Dr. Billy Wooten (1986) |
| Occupational and Environment Health Laboratory
100 | Phytotoxicity of Soil Residues of JP-4 Aviation Fuel
760-7MG-059 | Dr. Richard H. Brown |
| 101 | An Impact Study for the Contracting Out of In-House Analytical Services at the USAF Occupational & Environmental Health Laboratory - Brooks AFB, San Antonio, Texas
760-7MG-096 | Dr. Elvis E. Deal |
| 102 | Effects of Metal Mutagens on the Synthesis and Accumulation of Macromolecules
760-7MG-001 | Dr. Kiah Edwards |
| 103 | Development of a Rapid and Sensitive Assay Procedure for the Detection of the Protozoan Parasite Giardia Lamblia in Drinking Water Supplies
760-6MG-062 | Dr. Ralph J. Rascati (1986) |
| School of Aerospace Medicine
104 | Limitations to Heavy Work of Personnel Wearing at 21°C: U.S. Military Chemical Defense Ensemble
760-7MG-067 | Prof. Phillip A. Bishop |

105	Report Not Available at this Time 760-6MG-118	Dr. Hoffman Chen (1986)
106	Nucleic Acid Hybridization - Dot Blot Test for the Presence of Ureaplasma Urealyticum and Mycoplasma Hominis 760-6MG-076	Dr. Vito DelVecchio (1986)
107	Report Not Available at this Time 760-7MG-078	Dr. Mohammed Maleque
108	The Asymptotic Description of Precursor Fields in a Causally Dispersive Medium 760-7MG-033	Dr. Kurt Oughstun
109	Report Not Publishable at this Time 760-7MG-091	Dr. Ralph Peters
110	Model Systems for Assessing the Effects of Microwave Radiation on the Immune System 760-7MG-060	Dr. Stephen Pruett
111	Report Not Available at this Time 760-7MG-043	Dr. Wesley Tanaka

FINAL REPORT NUMBER 1
REPORT NOT AVAILABLE AT THIS TIME
Dr. Charles Bell
760-7MG-025

ACKNOWLEDGEMENTS

The authors would like to recognize those persons who provided support for this effort. The research topic was suggested by Mr. Gerald Winchenbach, Section Chief of the Ballistics Branch at the Air Force Armament Testing Laboratory, Eglin AFB, Florida. He and Project Engineer Gregg Abate provided significant technical guidance and support throughout the research program. Gratitude is also due to Mr. Alvin Harkins who provided expert advice in the application of parameter estimation methods. Finally, thanks is extended to Dr. Sam Lambert, Chief Scientist at AFATL, to Mr. Rodney Darrah, contract administrator for Universal Energy Systems, Inc. and to the Air Force Office of Scientific Research for arranging for the financial support of this work.

List of Symbols

A	Frontal area of projectile, expressed in square feet.
A_0	Amplitude of vibration, expressed in feet.
d	Diameter of projectile, expressed in feet.
E	Young's Modulus, expressed in pounds per square inch.
F_x	External force component in the x-body direction, expressed in pounds.
F_y	External force component in the y-body direction, expressed in pounds.
F_z	External force component in the z-body direction, expressed in pounds.
g	Gravity constant, expressed in feet per second per second.
H_{zz}	Elastic inertia term (see Nomenclature, Appendix B), expressed in slugs-square feet.
I	Area moment of inertia, expressed in feet ⁴ .
I_{xx}	Axial moment of inertia (see Nomenclature, Appendix B), expressed in slugs-square feet.
I_{yy}	Transverse moment of inertia (see Nomenclature, Appendix B), expressed in slugs-square feet.
I_{zz}	Transverse moment of inertia (see Nomenclature, Appendix B), expressed in slugs-square feet.
K_x	Elastic inertia term (see Nomenclature, Appendix B), expressed in slugs-square feet.
L_{zz}	Elastic inertia term (see Nomenclature, Appendix B), expressed in slugs-square feet.
L/D	Length over diameter ratio, dimensionless.

L	External moment component acting about the x-body axis, expressed in foot-pounds.
M	External moment component acting about the y-body axis, expressed in foot-pounds.
N	External moment component acting about the z-body axis, expressed in foot-pounds.
m	Mass of the projectile, expressed in pounds.
p	Roll rate of the projectile, expressed in radians per second.
q	Pitch rate of the projectile, expressed in radians per second.
r	Yaw rate of the projectile, expressed in radians per second.
\bar{q}	Dynamic pressure, expressed in pounds per square inch.
u	Velocity component of the projectile in the x-body direction, expressed in feet per second.
v	Velocity component of the projectile in the y-body direction, expressed in feet per second.
w	Velocity component of the projectile in the z-body direction, expressed in feet per second.
V	Total velocity of the projectile, expressed in feet per second.
α	Angle of attack of the projectile, expressed in radians.
β	Angle of sideslip of the projectile, expressed in radians.
β_1	Constant used in frequency equation.
ϕ	Euler angle relating the roll-plane to the inertial coordinate system, expressed in radians.
θ	Euler angle relating the pitch-plane to the inertial coordinate system, expressed in radians.
ψ	Euler angle relating the yaw-plane to the inertial coordinate system, expressed in radians.

ρ Density of projectile material, expressed in slugs per cubic foot.

Abstract

A mathematical model which describes the motion of a long, slender free-flight projectile in single-plane bending is developed. The model utilizes a free-free fundamental vibrational analysis to determine the natural frequency and mode shape. A simulation program employs the flexible body model as a parameter estimation function. The effect of model bending on the aerodynamic coefficients of the free-flight projectile is investigated. The approach taken is to regress on the aerodynamic coefficients at various amplitudes of deflection using a hybrid nonlinear parameter estimation technique.

The results of the analysis show that the effects of model bending are lower than the standard error of the aerodynamic coefficients within the elastic range of deflection. Thus, it is concluded that elastic bending has a negligible effect on the quality of the aerodynamic coefficients determined from free-flight ballistic tests.

Chapter I

Introduction

1.1 Aeroballistic Research Facility

Free-flight aerodynamic characteristics can be determined from several forms of data acquisition. One of these methods, the ballistic spark range, has proven to be an accurate means of obtaining aerodynamic characteristics of a flight configuration.

The ballistic spark range is instrumented with shadowgraph stations. These stations photograph the model in both the vertical and horizontal planes, thereby allowing for the measurement of the translational position and rotational orientation of the model. A timing instrument is also utilized so that dynamic data can be measured. Experimental resolution obtainable from a ballistic spark range is on the order of (Ref. 1):

- 0.2 microseconds in time
- 0.1 degree in pitch and sideslip angle
- 1.0 degree in roll angle
- 0.001 foot in x,y,z coordinates

The U. S. Air Force carries out such aerodynamic research in the Aeroballistic Research Facility (ARF) located at Eglin AFB, Florida. The ARF is a 750-foot indoor range with fifty shadowgraph stations (Ref. 2). Each station consists of two sets of sparks and cameras located in orthogonal planes in the wall and floor (pit). The sparks are triggered when infrared emitter-detectors are interrupted by the passage of the projectile. The infrared devices are interfaced with a

timing instrument to provide precise time histories of the linear and angular displacements. This data gathering technique also provides a bonus in that it makes key features of the flow field visible in the photograph.

The range is continuously calibrated through the use of catenary wires suspended in front of the wall and ceiling reflective screens. Reference beads are positioned precisely along these wires, with the position of all of the beads known to 0.0001 foot.

1.2 Data Correlation

The data gathered in the range form a trajectory which is matched with analytical predictions by appropriate estimations of the aerodynamic coefficients of the model being tested. The quality of the aerodynamic characteristics determined from such range data reduction depends heavily upon the analytical model which is used to fit the experimental model.

The experimental data reduction process consists of (Ref. 3):

1. "Reading" film exposed during the experimental flight to determine precise position and angular orientation.
2. Using the film readings to construct the experimental trajectory of the projectile.
3. Mathematically modeling the projectile's theoretical equations of motion.
4. Matching the theoretical equations of motion to the experimental trajectory.

The last two tasks are broken down into a two-step process. The first step is a linear approximation known as linear theory. Stated briefly, the method uses a closed form approximate solution to an exact set of differential equations of motion. A least squares fitting technique is used to solve for the aerodynamic parameters used in the linearized model (Refs. 4 and 5).

After linear theory is performed, a six-degree-of-freedom analysis is performed using the results from linear theory as initial approximations. In 1969, Chapman and Kirk of NASA Ames, California (Ref. 6) documented a technique which allows the nonlinear differential equations of motion to be used directly in the data correlation process. The technique eliminates the requirement for closed form approximations to the equations of motion. The method is basically a differential correction process. The aerodynamic coefficients used in the equations of motion are adjusted until the theoretical trajectory matches the experimental trajectory. Efficient coding of a computer program is of the utmost importance if a satisfactory solution is to be obtained at a reasonable cost.

The differential equations of motion currently incorporated into the parameter estimation algorithms at the ARF are six-degree-of-freedom rigid body equations with aerodynamic forcing functions tailored to the particular configuration being studied. The ARF staff has been successful in determining the aerodynamic characteristics of a wide variety of configurations with these algorithms.

1.3 Objectives of Present Research

Data from a recent test series involving high-fineness ratio penetrators have suggested that model flexibility may influence the results of free-flight range test programs. Figure 1 shows one of the penetrator designs that was flown. This particular configuration has a length over diameter ratio (L/D) of 50.

Two important factors become evident when dealing with an aerodynamically flexing object. First is the fact that an elastically flexing model will possess a time-dependent inertia distribution which could lead to dynamic coupling. Secondly, a flexing model may alter the flow field in which it flies to the extent that aerodynamic loads are affected. Since the present algorithms in the ARF parameter estimation programs do not account for either of these effects, the accuracy of aerodynamic predictions may be compromised in tests of slender, flexible configurations.

The present research effort is directed toward determining the effect of model aeroelasticity on the aerodynamic coefficients which are being fit to the range-acquired data sets. A methodology is selected which will permit an evaluation of the limitations of rigid-body theory in determining the model's aerodynamic coefficients. The study is carried out in two phases outlined below.

Phase 1: Derive the equations of motion for a flexible model in single-plane bending (torsion, shear, and axial flexibility neglected).

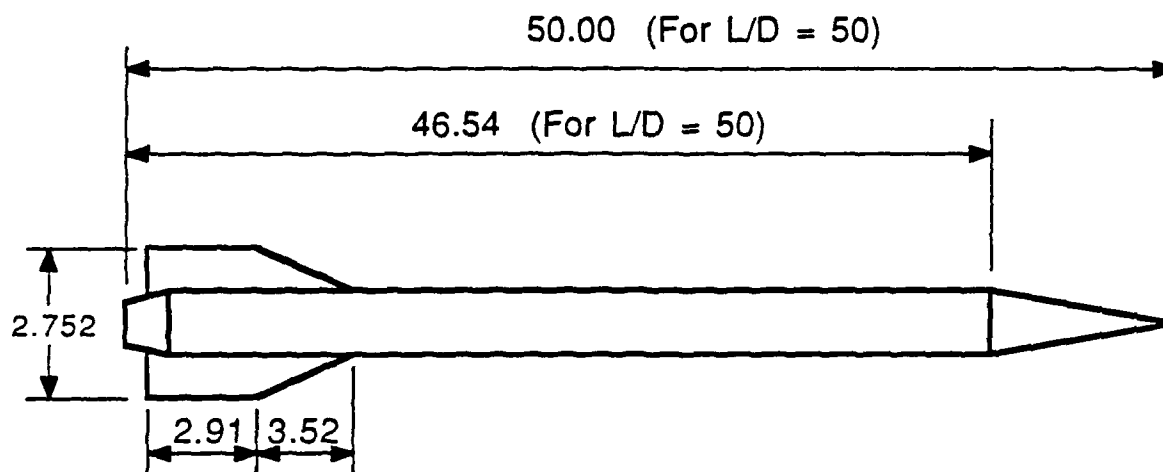
Phase 2: Regress on the aerodynamic coefficients using the flexible model as parameter function.

1.4 Survey of Previous Research and Experimental Data

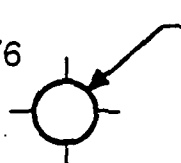
The objective of a high-fineness ratio penetrator is to strike a target in a manner in which the target can be defeated. Normal design criteria are minimum time of flight, maximum velocity when striking the target and minimum target pattern dispersion. Short time of flight improves hit probability, especially on a moving target. High velocity delivers more kinetic energy to the target, and small pattern dispersion allows a higher energy concentration. The amount of dispersion depends on the entire weapons system, but the above criteria dictate that the projectile must have low aerodynamic drag, must be stable in flight and must have geometric and mass properties which minimize target dispersion.

As a result of these criteria, modern penetrators are long and slender in shape in order to deliver a given mass with a low aerodynamic drag. This configuration requires fins for stabilization. The main disadvantage of slender-body penetrators is the increased flexibility of the projectile.

Other flight vehicles which are similar in configuration and exhibit high flexibility effects are unguided multistage launch vehicles. Although they are not free-flight projectiles, the designers of these systems must take aeroelasticity into account due to high L/D ratios and high dynamic pressures (Ref. 7). The LTV research vehicle "Scout" is a typical example of such a multi-stage system.



Fin Height = 0.876 $D = 1.00$



Cross Section

All dimensions are in body diameters.

FIGURE 1. High L/D Finned Projectile

There are several considerations that may be incorporated into a missile design to minimize the severity of the aeroelastic problem. However, these considerations will more than likely be subordinate to other design criteria. The most obvious consideration is to minimize the vehicle's length to diameter ratio. For a uniform beam, the frequency of vibration varies directly as the square of L/D , and the generalized flexibility varies directly as the square of the frequency. Thus, it is seen that the flexibility effects increase very rapidly as the vehicle becomes long and slender. For several vehicles analyzed it has been found that L/D values in excess of ten produce significant aeroelastic effects (Ref. 7).

No aeroelastic research has been performed on projectiles fired in a ballistic range to date. However, the effects of model bending have been observed in shadowgraphs of typical high L/D models. Appendix A shows a sequence of shadowgraphs of a high L/D model. The projectile model has a conical nose, a cylindrical body with Nicolaides fins at its center and a truncated conical afterbody. The model is made of aluminum. Apparently, resonance was achieved, and the model failed at the stress concentration of the Nicolaides fins.

Chapter II

Dynamics of an Elastic Body

2.1 Background

Aeroelasticity is the study of the effect of aerodynamic forces on elastic bodies. A major problem is the flutter of aerodynamic vehicles. Flutter is a self-excited oscillation of a vehicle surface or component caused and maintained by the combination of aerodynamic, elastic, and inertial forces of the system. At a given Mach number, flight at dynamic pressures below the flutter boundary will result in damped oscillations. At the flutter boundary a transition occurs such that for higher dynamic pressures, oscillations will be sustained at some limiting amplitude or will diverge until a structural failure occurs. In addition to being dependent on Mach number and aerodynamic pressure, the occurrence of flutter is dependent on such factors as structural stiffness, mass and mass distribution, stiffness changes due to steady and transient thermal inputs, control surface actuation system dynamics, misalignments, and free-play of control surfaces (Ref. 8).

The determination of the forced vibrational behavior of an elastic body requires that the forces applied to the body or the precise shape of the deflected body at maximum deflection be known. In the present case, however, the loads cannot be explicitly determined. In fact, the objective of ballistic testing is to determine the loads on the projectile from free-flight trajectory analysis. The shape of the projectile at maximum deflection cannot accurately be determined from the shadowgraphs either. Indirect methods must be used to solve for the deformation of the model (Ref. 9).

The emphasis of the present research is to determine the influence of aeroelastic vibration in the determination of aerodynamic coefficients rather than on calculating the frequency of vibration for known aerodynamics. The technique which is used is that of free-free natural vibration. The frequency chosen for analysis is the fundamental natural frequency. The fundamental mode of vibration is the dominant vibration mode that has been observed (See Appendix A).

The actual vibration of the model is a damped, forced vibration. The damping is low and the forcing function frequency is certainly close to the natural frequency of the model. This would put the actual frequency of vibration below the natural frequency. How far below the natural frequency would depend upon the relative magnitude of the damping term. For the present case of vibration in an atmospheric environment, the damping is low enough so that the assumption of the model vibrating at its natural frequency is reasonable.

The term free-free vibration pertains to the boundary conditions of the vibrating system. In other words, the system is unrestrained in that it has no external restraints or supports. The system can also move as a rigid body.

2.2 Derivation of Equations

The dynamic equations of motion of an elastically flexing body can be derived by considering a typical differential mass element positioned at an arbitrary location relative to the center of mass of the body. The body itself is translating and rotating relative to an inertial axis system (Earth axis system). A typical flexible body

configuration is shown in Figure 2. The location of the mass element with respect to the origin of the inertial axis system is the vector sum of the radius of the center of mass, \vec{R}_0 , the position of the rigid body mass element from the center of mass, $\vec{\rho}$, and the elastic displacement of the mass element from the rigid body position, $\vec{\xi}$. The vector is written as:

$$\vec{R} = \vec{R}_0 + \vec{\rho} + \vec{\xi} \quad (2.1)$$

$$\text{where } \vec{R}_0 = X_E \vec{i}_E + Y_E \vec{j}_E + Z_E \vec{k}_E \quad (2.2)$$

$$\vec{\rho} = \rho_x \vec{i}_b + \rho_y \vec{j}_b + \rho_z \vec{k}_b \quad (2.3)$$

$$\text{and } \vec{\xi} = \xi_x \vec{i}_b + \xi_y \vec{j}_b + \xi_z \vec{k}_b \quad (2.4)$$

The definition of a vector rate in a rotating reference axis system includes both the rate of change of the vector length and the rate of change of the vector direction. Taking this into account, the velocity and acceleration of the elastically displaced mass element are:

$$\dot{\vec{R}} = \dot{\vec{R}}_0 + \dot{\vec{\rho}} + \dot{\vec{\xi}} + \vec{\omega} \times \vec{\rho} + \vec{\omega} \times \vec{\xi} \quad (2.5)$$

$$\begin{aligned} \ddot{\vec{R}} = \ddot{\vec{R}}_0 + \ddot{\vec{\rho}} + \ddot{\vec{\xi}} + 2 \vec{\omega} \times \dot{\vec{\rho}} + \dot{\vec{\omega}} \times \vec{\rho} + \vec{\omega} \times \vec{\omega} \times \vec{\rho} \\ + 2 \vec{\omega} \times \dot{\vec{\xi}} + \dot{\vec{\omega}} \times \vec{\xi} + \vec{\omega} \times \vec{\omega} \times \vec{\xi} \end{aligned} \quad (2.6)$$

$$\text{where } \vec{\omega} = p \vec{i}_b + q \vec{j}_b + r \vec{k}_b \quad (2.7)$$

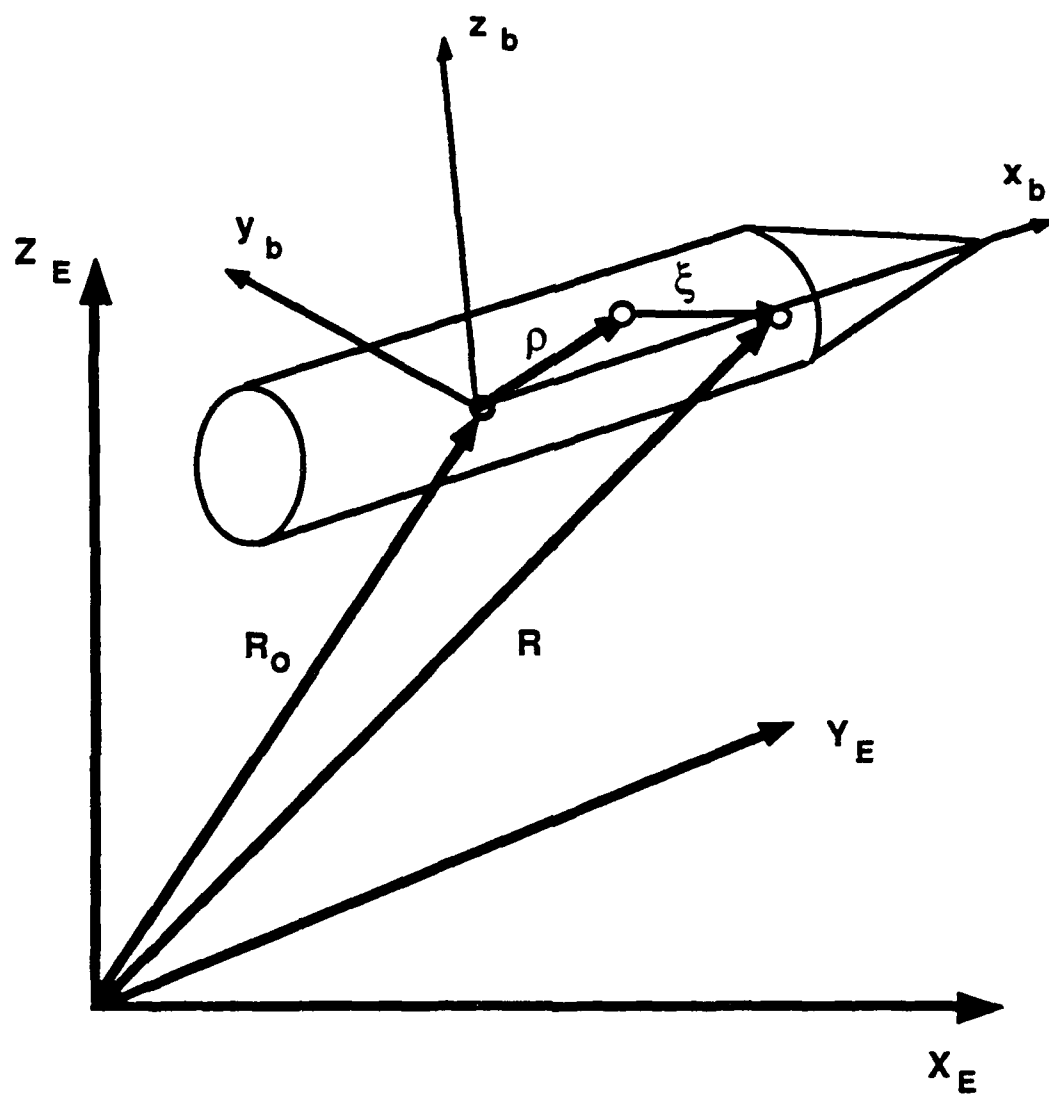


FIGURE 2. Flexible Body Configuration

It is now possible to derive the equations of motion for the system of mass elements. The internal forces and moments caused by the elastic displacement of the mass elements equate to zero when summed over the entire system. Therefore, the only forces and moments applied to the body are external forces and moments. The translational and rotational equations of motion become, respectively,

$$\int \ddot{\vec{R}} \, dm = \sum \vec{F}_{\text{ext}} \quad (2.8)$$

$$\int \vec{R}_o \times \ddot{\vec{R}} \, dm = \sum \vec{M}_{\text{ext}} \quad (2.9)$$

Equations (2.8) and (2.9) in conjunction with Equation (2.6) are general. The full scalar expansions are given in Appendix B. In order to simplify the analysis, assumptions can be made regarding the flexure properties of a high L/D slender body. It will be assumed that all terms involving the x -component of $\vec{\xi}$ are zero (no axial deformations). Furthermore, it will be assumed that the other components of $\vec{\xi}$ act independently and normal to the x -axis (torsional flexibility is neglected). It should be noted that when the elastic terms in the general equations of motion are set to zero, the equations reduce to those for a rigid body.

2.3 Flexibility Analysis

The assumption of single-plane bending can be thought of as a lateral vibration with no torsional effects. The choice of the direction of vibration is arbitrary. In other words, the vibration can be in either the y-plane of the model or the z-plane or a combination of both of these. Obviously, the direction of lateral bending must be chosen and adhered to throughout the rest of the development of the analysis. The direction of lateral bending is therefore assumed to be in the z-plane of the model.

The high L/D penetrator is shown in Figure 1. The overall length is 12.5 inches. It is basically a right circular cylinder with a conical nose and four fins for stabilization. The material of construction is steel for both the body (high strength steel; 100 kpsi yield strength) and the fins (SAE 1040). The diameter of the body is one-quarter of an inch and the thickness of the fins is ten-thousandths of an inch. The fins are soldered into milled slots on the body.

The vibration analysis can be simplified by assuming the structure of the model is a circular cylinder. This means that the stiffness effects of the fins are neglected. The conical nose is treated as a cylinder with the same volume as the cone, making the length of this cylindrical segment one-fourth of the length of the cone. The effective length, L , of the structural cylinder is 11.84 inches.

The structure can now be considered continuous beam of constant section modulus. The lateral free vibration can be described by the following differential equation:

$$\frac{\partial^2 \xi_z}{\partial t^2} = -c^2 \frac{\partial^4 \xi_z}{\partial x^4} \quad (2.10)$$

$$\text{where } c = \sqrt{\frac{EI}{\rho A}}$$

The lateral displacement is ξ_z taken along the axial position, x . The modulus of elasticity and the area moment of inertia are E and I , respectively. The unit density of the material is ρ , and the cross sectional area is A . The solution to Equation (2.10) can be found by using the method of separation of variables. By applying the boundary conditions, the fundamental mode shape is

$$\xi_z(x) = \cos \frac{\beta_1 x}{L} + \cosh \frac{\beta_1 x}{L} - 0.9825 \left(\sin \frac{\beta_1 x}{L} + \sinh \frac{\beta_1 x}{L} \right) \quad (2.11)$$

where β_1 is a dimensionless constant determined from the frequency equation and is 4.730 (Ref. 10).

The fundamental natural frequency of the beam structure is calculated by

$$\omega_1 = \beta_1^2 \sqrt{\frac{EI}{\rho A}} = (\beta_1 L)^2 \sqrt{\frac{EI}{\rho A L^4}} \quad (2.12)$$

where the natural frequency, ω_1 , is in radians per second. The fundamental natural frequency is 2023 radians per second, or 322.0 cycles per second.

The flexibility of the penetrator can now be written in terms of body position and time as

$$\xi_z(x,t) = A_0 \{\xi_z(x)\} \sin \omega t \quad (2.13)$$

During the initial phase of this research project, both the natural frequency and mode shape were determined using a finite element analysis with the model broken into twenty segments. The approach of assuming the structure as a right cylinder was assumed as before. The results from the finite element analysis match the theoretical analysis in the determination of the natural frequency precisely and mode shape in Equation (2.11) precisely. Figure 3 illustrates the normalized fundamental mode shape.

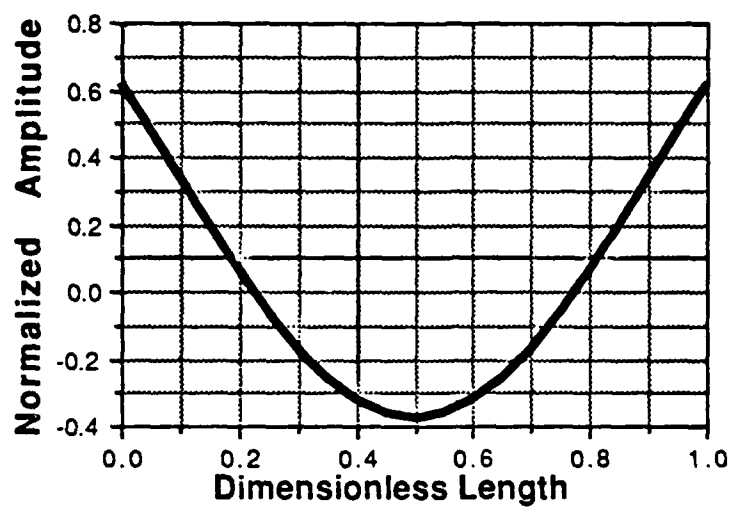


**FIGURE 3. Normalized Mode Shape
for $L/D=50$ Model**

Chapter III

Dynamic Simulation

3.1 Dynamic Simulation of a Rigid Body

The dynamic simulation of a rigid body for aeroballistic research has been performed in several different ways, ranging from simplified linear equations of motion to a full six-degree-of-freedom simulation of nonsymmetric configurations (Ref. 1). It is this latter simulation analysis which will be used as a baseline for flexible body simulations. The reason behind this is that the analysis performed by Hathaway and Whyte utilizes a body-fixed coordinate system to describe the aerodynamic forces and moments rather than a fixed-plane coordinate system. The body-fixed coordinate system is advantageous in that asymmetries of the model (both mass and aerodynamic) can be represented. The disadvantage of a body-fixed analysis is that the number of computations required to solve for the coefficients is up to 25 times greater than that for a fixed-plane analysis. In addition, the accuracy of the coefficients regressed upon by body-fixed analysis is inferior (Ref. 2). The two coordinate systems are shown in Figure 4 and 5.

In fixed-plane simulations, the body's axis system does not roll with the projectile. In other words, the model is allowed to spin in the fixed-plane coordinate system. This is the reason why only symmetrical or slightly asymmetrical bodies can be simulated using fixed-plane analysis.

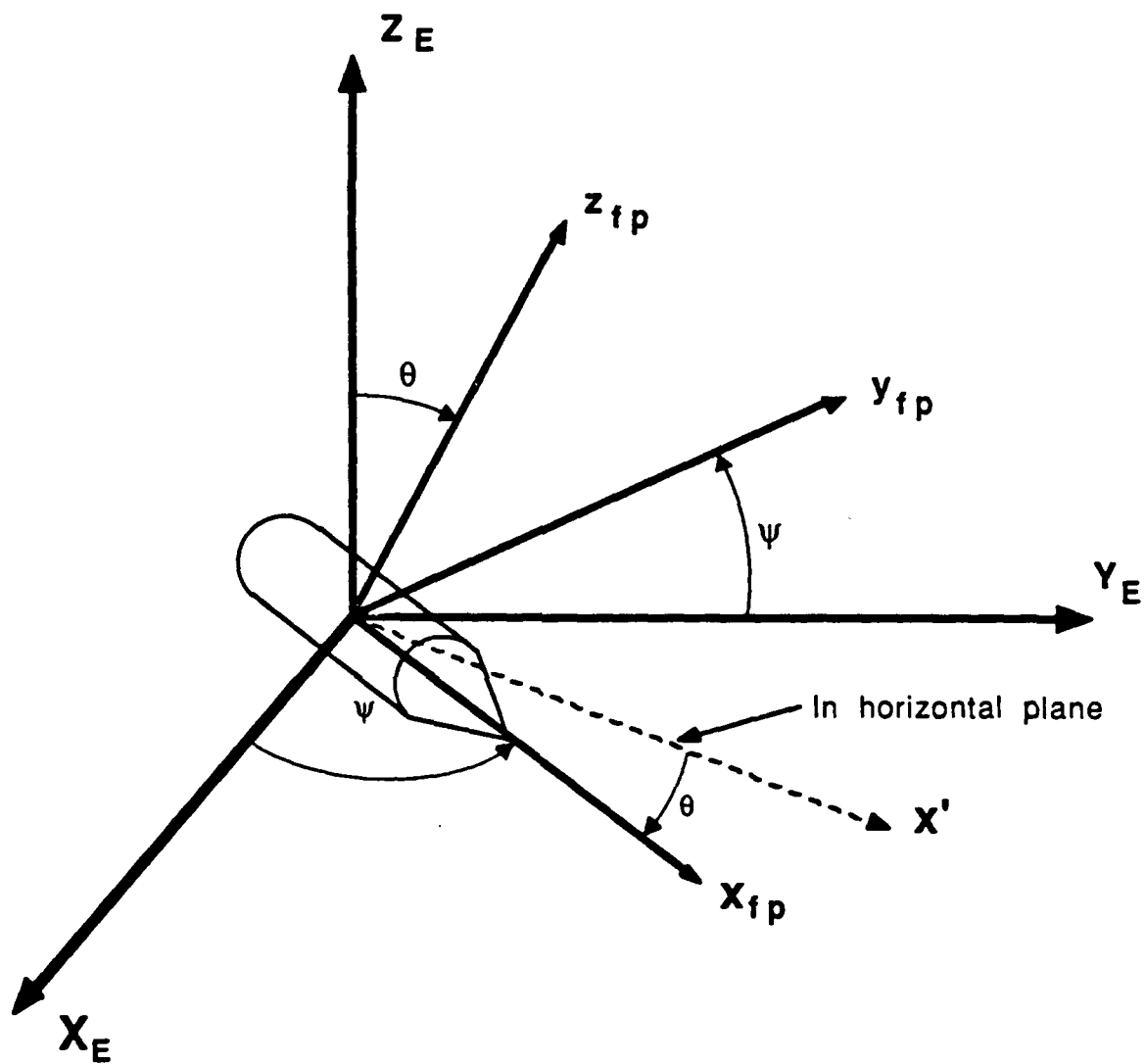


FIGURE 4. Fixed Plane Coordinate System

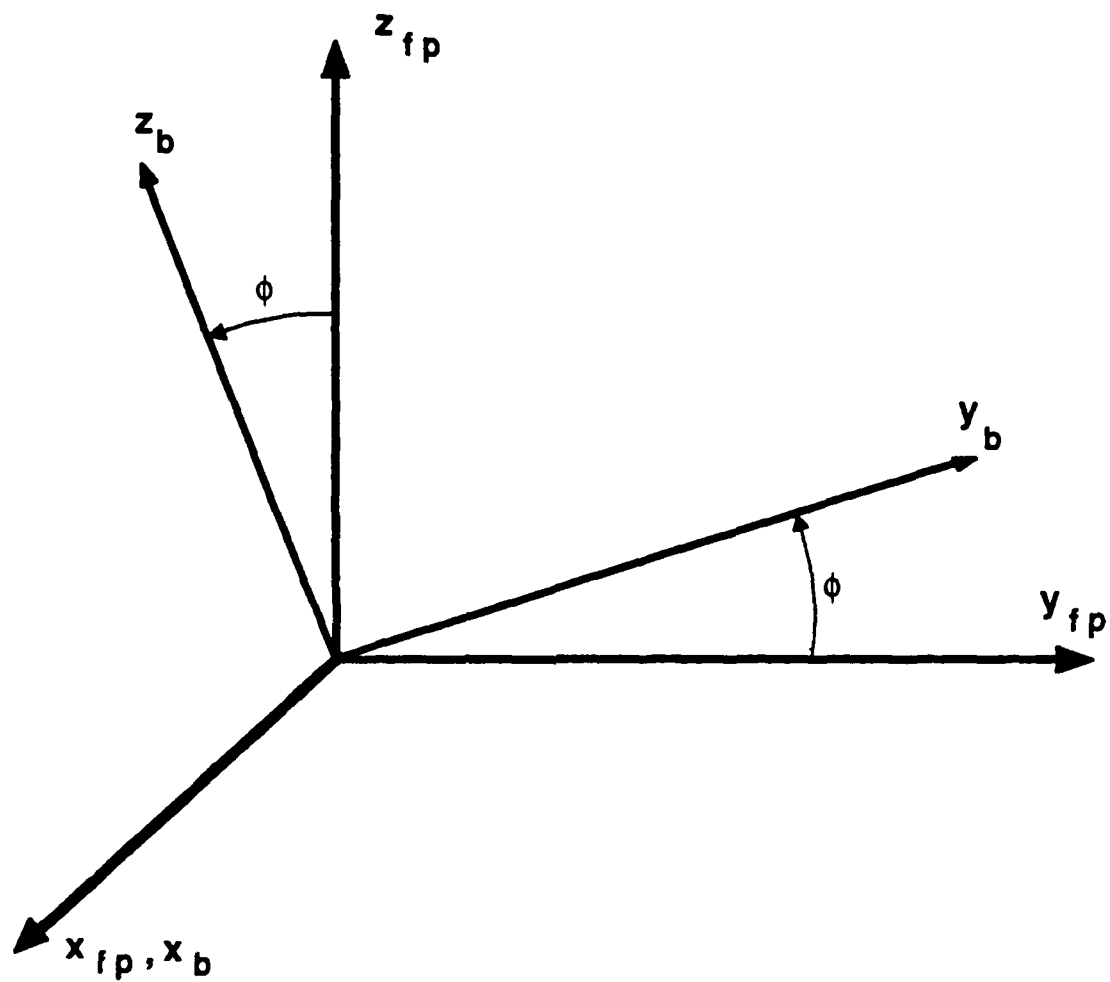


FIGURE 5. Body Fixed Coordinate System

3.2 Dynamic Simulation of a Flexible Body

In the preceding chapter, the general equations for a dynamic analysis of free-flight elastic bodies have been presented. The full scalar expansions are listed in Appendix B. The case of single-plane bending will be considered here. The equations of motion can be written in matrix form as (Ref. 9):

$$\begin{bmatrix} a_{11} & a_{12} & a_{13} & a_{14} & a_{15} & a_{16} \\ a_{21} & a_{22} & a_{23} & a_{24} & a_{25} & a_{26} \\ a_{31} & a_{32} & a_{33} & a_{34} & a_{35} & a_{36} \\ a_{41} & a_{42} & a_{43} & a_{44} & a_{45} & a_{46} \\ a_{51} & a_{52} & a_{53} & a_{54} & a_{55} & a_{56} \\ a_{61} & a_{62} & a_{63} & a_{64} & a_{65} & a_{66} \end{bmatrix} \begin{pmatrix} \dot{u} \\ \dot{v} \\ \dot{w} \\ \dot{p} \\ \dot{q} \\ \dot{r} \end{pmatrix} = \begin{pmatrix} A \\ B \\ C \\ D \\ E \\ F \end{pmatrix} \quad (3.1a-f)$$

$$\text{where } A = \frac{F_x}{m} + rv - qw$$

$$B = \frac{F_y}{m} + pw - ru$$

$$C = \frac{F_z}{m} + qu - pv$$

$$D = L + p(q K_x - 2L_{zz}) + qr(H_{zz} + I_{yy} - I_{zz})$$

$$E = M - 2q L_{zz} - (p^2 - r^2)K_x - pr(H_{zz} + I_{xx} - I_{zz})$$

$$F = N + K_x(qr + 2p) - pq(I_{xx} - I_{yy})$$

$$a_{11} = a_{22} = a_{33} = 1$$

$$a_{44} = I_{xx} + H_{zz}$$

$$a_{46} = -K_x$$

$$a_{55} = I_{yy} + H_{zz}$$

$$a_{64} = -K_x$$

$$a_{66} = I_{zz}$$

All of the other elements of the a -matrix which are not listed are zero due to the single-plane bending assumption or due to symmetry of the model in question. Specifically, a_{45} , a_{54} , a_{56} , and a_{65} are zero because the cross products of inertia are zero ($I_{xy} = I_{xz} = I_{yz} = 0$). I_{xx} is the axial moment of inertia and I_{yy} and I_{zz} are the transverse moments of inertia. The *elastic inertia* terms are defined as follows:

$$K_x = \int x_b \xi_z dm \quad (3.2)$$

$$L_{zz} = \int \dot{\xi}_z \xi_z dm \quad (3.3)$$

$$H_{zz} = \int \xi_z^2 dm \quad (3.4)$$

where the integration is performed over the entire mass of the body.

The external forces are resolved into three components, F_x , F_y , and F_z acting in the direction of the body-fixed coordinates x_b , y_b , and, z_b . Similarly, the external moments that act about the body-fixed axes are L , M , and N .

The terms u , v , and w are the velocity components in the x_b , y_b , and, z_b directions, respectively. The variables p , q , and r relate to the angular velocity of the body-fixed coordinates x_b , y_b , and, z_b . Together, the time derivatives of u , v , w , p , q , and r make up the body-fixed state variable derivative vector. This vector is solved using Equation (3.1) and the vector is integrated to obtain the body-fixed state variables.

The equations of motion have been derived in the body-fixed coordinate system for the purpose of conveniently relating the external forces and moments to the dynamics of the projectile. The integration of these equations results in the determination of the translational and rotational rates of motion of the body-fixed coordinates. The data acquired from the ballistic spark range is defined as motion relative to the earth. Therefore, in order to relate the body-fixed state variables to the earth state variables $(X, Y, Z, \phi, \theta, \psi)$, a set of transformation differential equations is used. They are written as

$$\dot{X}_E = u \cos \theta \cos \psi + v (\sin \theta \sin \phi \cos \psi - \cos \phi \sin \psi) + w (\sin \theta \cos \phi \cos \psi + \sin \phi \sin \psi) \quad (3.5)$$

$$\dot{Y}_E = u \cos \theta \sin \psi + v (\sin \theta \sin \phi \sin \psi + \cos \phi \cos \psi) + w (\sin \theta \cos \phi \sin \psi + \sin \phi \cos \psi) \quad (3.6)$$

$$\dot{Z}_E = -u \sin \theta + v \cos \theta \sin \phi + w \cos \theta \cos \phi \quad (3.7)$$

$$\dot{\phi} = p + \tan \theta (q \sin \phi + r \cos \phi) \quad (3.8)$$

$$\dot{\theta} = q \cos \phi - r \sin \phi \quad (3.9)$$

$$\dot{\psi} = (q \sin \phi + r \cos \phi) / \cos \theta \quad (3.10)$$

The transformation equations contain the earth state variables (which will now be called as just the state variables) in derivative form. These equations are integrated with respect to time in order to obtain the state variables.

It should be noted here that all integration is performed using a fourth-order Runge-Kutta method. The body-fixed differential equations and the transformation differential equations are integrated simultaneously since the method of integration is self starting and the two sets of differential equations use the same initial conditions.

3.3 Aerodynamic Forces and Moments

The aerodynamic forces and moments acting on a nonsymmetric body can be defined as a series expansion of perturbations to the steady-state flight condition. The basic definitions of the aerodynamics are based upon References 11 and 12. The forces and moments could be linear or nonlinear functions of the angle of attack, α , and angle of sideslip, β . The aerodynamic angles $\bar{\alpha}$, α , and β are defined in Figure 6. The Mach number change in a ballistic range is relatively small. Therefore, Mach number effects are neglected, except along the axial axis where the variation of drag with Mach number may be significant. The nonlinearities with flow angle are modeled as polynomial functions of the sine of the angle of attack or angle of sideslip.

The primary forces and moments acting on a body in free flight are shown in Figure 6. Aerodynamic moments which act about the projectile's center of gravity are a result of aerodynamic forces acting at the center of pressure, which is not necessarily coincident with the center of gravity. A detailed description of the primary force and moment terms is as follows (Ref. 1):

- C_x - Axial force coefficient; acts along the x-body axis
opposite to the u velocity vector
- C_z - Normal force coefficient; acts in the α -pitch plane
perpendicular to the body axis
- C_y - Normal force coefficient; acts in the β -sideslip
plane perpendicular to the body axis
- C_{zp} - Magnus force coefficient; acts perpendicular to
the β -sideslip plane
- C_{yp} - Magnus force coefficient; acts perpendicular to
the α -pitch plane
- C_l - Roll moment coefficient; acts about the x-body
axis
- C_m - Pitching moment coefficient; acts about the y-
body axis
- C_n - Yawing moment coefficient; acts about the z-body
axis
- C_{mp} - Magnus moment coefficient; acts about the y-
body axis
- C_{np} - Magnus moment coefficient; acts about the z-
body axis

The magnus forces and moments are associated with flow phenomena about a spinning body. Therefore, they are dependent upon the nondimensional spin parameter, $pd/2V$, where p is the spin rate, d is the diameter of the model, and V is the total velocity. The primary forces and moments are modeled as coefficient derivative functions of the sine of the angle of attack and angle of sideslip. The forces and moment coefficients are expanded in a Taylor series and only the terms that have been proven by past experience to

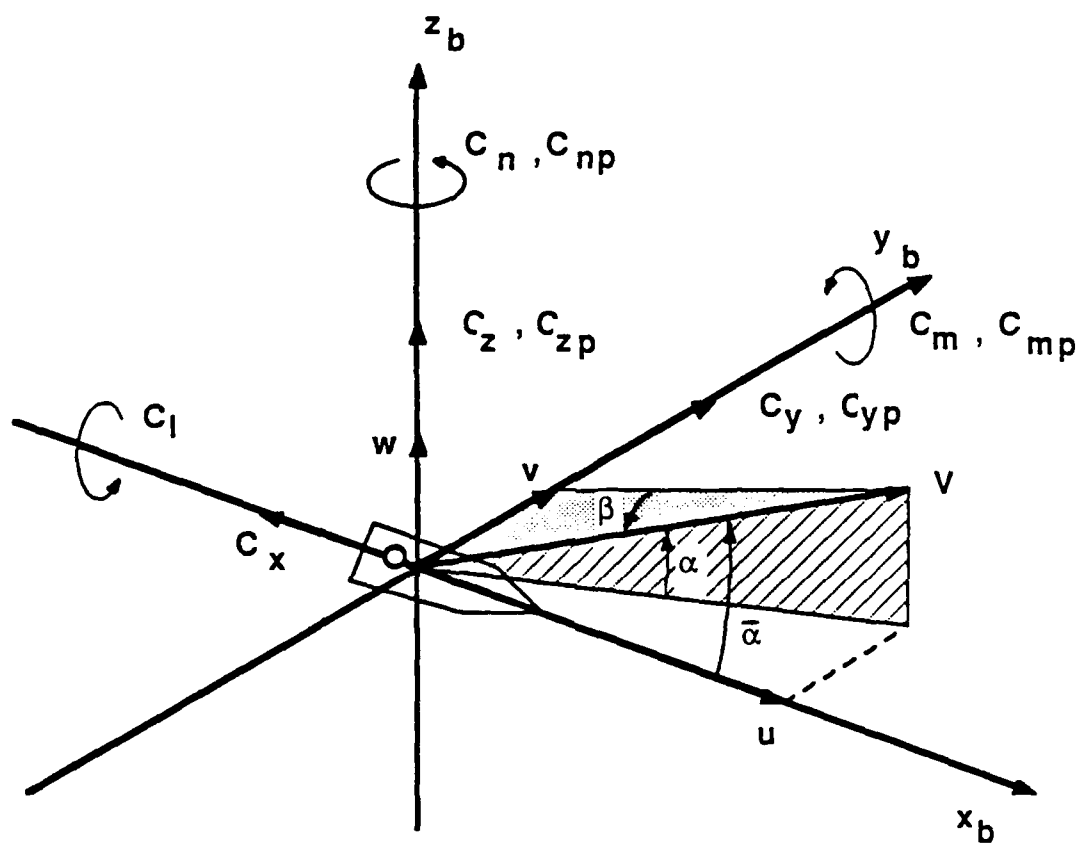


FIGURE 6. Body Fixed Coordinate System with Basic Force and Moment Definition

adequately represent a projectile such as the one studied here are retained. The sines of these angles are defined in terms of the body-fixed velocity components as

$$\sin \alpha = \frac{w}{V} \quad (3.11)$$

$$\sin \beta = \frac{v}{V} \quad (3.12)$$

Using Equations (3.11) and (3.12), the aerodynamic force and moment coefficients can be written in expanded form as:

$$C_x = C_{x0} + C_{x\alpha 2} \left(\left(\frac{w}{V} \right)^2 + \left(\frac{v}{V} \right)^2 \right) + C_{xM} (M - M_{ref}) \quad (3.13a)$$

$$C_z = C_{z\alpha} \left(\frac{w}{V} \right) + C_{z\alpha 3} \left(\frac{w}{V} \right)^3 \quad (3.13b)$$

$$C_y = C_{y\beta} \left(\frac{v}{V} \right) + C_{y\beta 3} \left(\frac{v}{V} \right)^3 \quad (3.13c)$$

$$C_{xp} = C_{xp\beta} \left(\frac{pd}{2V} \right) \left(\frac{v}{V} \right) \quad (3.13d)$$

$$C_{yp} = C_{yp\alpha} \left(\frac{pd}{2V} \right) \left(\frac{w}{V} \right) \quad (3.13e)$$

$$C_l = d \left\{ C_{l\delta} + C_{lp} \left(\frac{pd}{2V} \right) \right\} \quad (3.13f)$$

$$C_m = d \left\{ C_{m\alpha} \left(\frac{w}{V} \right) + C_{m\alpha 3} \left(\frac{w}{V} \right)^3 \right\} \quad (3.13g)$$

$$C_n = d \left\{ C_{n\beta} \left(\frac{v}{V} \right) + C_{n\beta 3} \left(\frac{v}{V} \right)^3 \right\} \quad (3.13h)$$

$$C_{mp} = d \left\{ C_{mp\beta} \left(\frac{pd}{2V} \right) \left(\frac{v}{V} \right) \right\} \quad (3.13i)$$

$$C_{np} = d \left\{ C_{np\alpha} \left(\frac{pd}{2V} \right) \left(\frac{w}{V} \right) \right\} \quad (3.13j)$$

The damping moment acts to damp out oscillations, just as the roll damping term damps out the spin rate. The damping moments are defined as acting perpendicular to the x-body axis but independent of the angle of attack or angle of sideslip planes. The moments are dependent upon the pitch and yaw angular velocities, q , and r , respectively. The damping coefficients are defined as:

$$\bar{C}_{mq} = d \left(\frac{qd}{2V} \right) \left\{ C_{mq} + C_{mq2} \left(\frac{w}{V} \right)^2 \right\} \quad (3.14a)$$

$$\bar{C}_{nr} = d \left(\frac{rd}{2V} \right) \left\{ C_{nr} + C_{nr2} \left(\frac{v}{V} \right)^2 \right\} \quad (3.14b)$$

The directions in which these coefficients act are shown in Figure 7. The bars on top of the damping moment coefficients denote that the coefficients are a summation of both the plain damping moment coefficient and the nonlinear damping term.

Asymmetrical aerodynamic forces and moments are brought about by misalignment, cant, or body and lift surface asymmetries. The asymmetrical forces and moments, also referred to as trims, cause the free-flight angular motion of the body to oscillate about an axis which is not coincident with the x-body axis. The trim forces will be defined as C_{y0} and C_{z0} . The trim moments are C_{m0} and C_{n0} . These trim coefficients are depicted in Figure 7. The trim forces act at the center of pressure causing the trim moments about the center of gravity. It should be noted that the trims along and about the x-



body axis are absorbed in the axial force coefficient [Equation (3.13a)] and roll moment coefficient [Equation (3.13f)].

The external forces and moments can now be defined using Equations (3.13) and (3.14) with the addition of the gravity vector:

$$F_x = - \bar{q} A C_x + mg \sin \theta \quad (3.15)$$

$$F_y = \bar{q} A (C_{y0} + C_y + C_{yp}) - mg \cos \theta \sin \phi \quad (3.16)$$

$$F_z = \bar{q} A (C_{z0} + C_z + C_{zp}) - mg \cos \theta \cos \phi \quad (3.17)$$

$$L = \bar{q} A C_l \quad (3.18)$$

$$M = \bar{q} A (C_{m0} + C_m + C_{mp} + \bar{C}_{mq}) \quad (3.19)$$

$$N = \bar{q} A (C_{n0} + C_n + C_{np} + \bar{C}_{nr}) \quad (3.20)$$

The negative sign in front of the drag force term is there so that the drag coefficient turns out to be positive.

Chapter IV

Parameter Estimation

4.1 Introduction

The aerodynamic coefficients which are described in Chapter III are parameters which must be estimated. The technique of the estimation process is to minimize the error between the calculated trajectory and experimental data. Most algorithms which are used for nonlinear parameter estimation employ either the Taylor series method or the gradient method. In the Taylor series method, the model is expanded as a Taylor series and corrections to the several parameter estimations are calculated at each iteration on the assumption of local linearity. The gradient method (or method of steepest-descent) simply steps off from the current trial value in the direction of the negative gradient.

Both methods can have problems of not converging to a proper solution. The Taylor series method may diverge due to the fact that the linear correction approximation may not be valid, and the gradient method has difficulty because of agonizingly slow convergence after the first few iterations.

In the present work, the aerodynamic coefficients are estimated by a modified version of the Marquardt algorithm (Ref. 13). This algorithm performs an optimum interpolation between the Taylor series method and the gradient method, the interpolation being based upon the maximum neighborhood in which the truncated Taylor series gives an adequate representation of the nonlinear mathematical model.

4.2 Statement of the Problem

The model that is to be fitted to experimental data is written as a function of the aerodynamic coefficients, C_n , where n is the number of coefficients to estimate:

$$\widehat{S}_i = f(C_k), k = 1, n \quad (4.1)$$

In this equation, \widehat{S}_i is the calculated state variable vector where the observed state variables, S_i , are $X_E, Y_E, Z_E, \phi, \theta$, and ψ . Letting m be the number of points at which the state variables are measured, a set of 6 by m weighted residuals is determined by subtracting the model predictions from the experimentally observed value of the state variable and dividing by the standard deviation for the observation as

$$R_i = \frac{S_i - \widehat{S}_i}{\sigma_i} \quad (4.2)$$

The problem is to solve for the estimates in a way to minimize the sum of the square of the residuals:

$$\Phi = \sum_{i=1}^{6m} R_i^2 \quad (4.3)$$

When f is a linear function of the parameters, C , the contours of constant Φ are ellipsoids, while if f is nonlinear, the contours are distorted, according to the severity of the nonlinearity (Ref. 13). Even with the case of nonlinear models, however, the contours are nearly elliptical in the immediate region of minimum Φ . The contour

surface of Φ is typically greatly attenuated in some directions and elongated in others so that the minimum lies at the bottom of a long, curving trough.

4.3 Taylor Series Method

The method based upon expanding the model, f , in a Taylor series is known as the Taylor series method, also referred to as the Gauss method, the Gauss-Newton method, or the least-squares differential correction method (LSDC). The truncated Taylor series is written as:

$$\langle S_i \rangle = f(C + \Delta C) = f(C) + \sum_{j=1}^n \left(\frac{\partial f_i}{\partial C_j} \right) (\delta C)_j \quad (4.4)$$

or

$$\langle S_i \rangle = f_o + [J](\delta C) \quad (4.4a)$$

The vector δC is a small correction to C . The brackets $\langle \rangle$ are used to designate that it is a *predicted* set of state variables based upon the linearized model. Thus, the predicted value of Φ is

$$\langle \Phi \rangle = \sum_{i=1}^{6m} \langle R_i \rangle^2 \quad (4.5)$$

The J-matrix is known as the sensitivity matrix, the state transformation matrix, or the state Jacobian. The vector δC appears linearly in Equation (4.4). Substituting Equation (4.4) into Equation (4.3), δC can be solved for by the standard least-squares method of

setting the partial derivative of the predicted sum of squares with respect to the estimation parameters equal to zero.

$$\frac{\partial \langle \Phi \rangle}{\partial C_j} = 0 \quad (4.6)$$

for all j . The result of Equation 4.6 can be written as

$$[J]^T [J] \delta C = -[J]^T R \quad (4.7)$$

The differential correction vector is solved for and a numerically converged solution is obtained when the size of the *predicted* sum of squares, $\langle \Phi \rangle$, reaches some limiting value. Of course, another convergence criterion would be to compare the successive values of Φ and determine when it is minimized to the accuracy required.

From a statistical standpoint, the size of the differential correction vector should not be used as the convergence check. The reason behind this is that the parameters with a large predicted change will invariably have a large probable error associated with them. Defining a precise optimum value on these parameters is a futile exercise. Conversely, parameters with a low probable error would require extremely tight tolerances on the correction step size in order to obtain a meaningful estimate. Tying the convergence criteria to a predicted change in the residual sum of squares overcomes these difficulties. The test for convergence involves a comparison of the successive values of $\langle \Phi \rangle$.

$$\frac{\langle \Phi \rangle^{(k)} - \Phi^{(k)}}{\Phi^{(k)}} \leq 10^{-3} \quad (4.8)$$

The superscripts in Equation (4.8) refer to the the iteration interval.

4.4 The Gradient Method

The method of gradients, by contrast, simply takes a step in the direction of the negative gradient of Φ . The differential correction vector is written as:

$$\delta C_g = - \left[\frac{\partial \Phi}{\partial C_1}, \frac{\partial \Phi}{\partial C_2}, \dots, \frac{\partial \Phi}{\partial C_n} \right]^T \quad (4.9)$$

where the subscript g on the correction vector denotes that it is determined by the gradient method. Various modified steepest-descent methods have been developed to compensate for the poor conditioning of the Φ surface which leads to very slow convergence of the gradient method (Ref. 13). The Marquardt algorithm uses a scaled gradient for minimization defined as:

$$\delta C_g = - \left[\frac{\sum_{i=1}^{6m} R_i \frac{\partial R_i}{\partial C_1}}{\sum_{i=1}^{6m} \left(\frac{\partial R_i}{\partial C_1} \right)^2}, \frac{\sum_{i=1}^{6m} R_i \frac{\partial R_i}{\partial C_2}}{\sum_{i=1}^{6m} \left(\frac{\partial R_i}{\partial C_2} \right)^2}, \dots, \frac{\sum_{i=1}^{6m} R_i \frac{\partial R_i}{\partial C_n}}{\sum_{i=1}^{6m} \left(\frac{\partial R_i}{\partial C_n} \right)^2} \right]^T \quad (4.9)$$

The convergence test in Equation (4.8) is also applicable to the gradient method.

4.5 The Marquardt Algorithm

The Marquardt algorithm strikes a balance between the weighted gradient and the Gauss-Newton vector by multiplying the diagonal elements of $[J]^T[J]$ by $(1+\lambda)$, where λ determines how much of the gradient method is used for the determination of the differential correction. As λ approaches zero, the Gauss-Newton correction dominates. Conversely, as λ approaches large values, small steps are made in the direction of the weighted negative gradient.

A typical initial starting value of λ is 0.01. If, upon iteration, the weighted sum of squares is reduced, then λ is decreased by dividing by v ($v=10$ gives good results). If the weighted sum of squares is not reduced, λ is multiplied by v to decrease the amount of Gauss-Newton parameter correction and to turn the correction more towards the weighted negative gradient.

4.6 The Modified Marquardt Algorithm

A variation of the Marquardt algorithm is useful when parameters are locally highly correlated. In the general nonlinear case, parameters may be highly correlated (correlation coefficient > 0.99) at one point and not as highly correlated in other regions. The variation of the Marquardt algorithm presented here will take into account the high local correlation of the parameters.

The correlation coefficients are calculated using the inverse of $[J]^T[J]$. The nondiagonals give the covariances of the estimates. By letting Q represent the elements of the inverse of $[J]^T[J]$, the

correlation function, r , of two estimation parameters is

$$r(C_i C_j) = \frac{Q_{ij}}{\sqrt{Q_{ii} Q_{jj}}} \quad (4.10)$$

The λ multiplier concept is extended to apply to individual elements of $[J]^T [J]$. In other words there is a λ_i associated with each diagonal element. The correlation coefficients of all the estimation parameters are calculated every iteration. If a pair of parameters is highly correlated, one of these parameters can be held essentially constant during a given iteration by increasing its λ_i multiplier to a suitably high value. The value of λ_i for one of the two highly correlated parameters is set to 10^{25} times the other λ_i 's associated with the other parameters. The choice of which parameter to *freeze* during the iteration is arbitrarily chosen to be the second one. The size of the remainder of the λ multipliers is determined as before.

The technique of *freezing* a parameter is particularly effective when a pair of parameters are highly correlated at a point. It permits a wider range of correction to parameters that are not highly correlated, whereas the unmodified Marquardt algorithm unnecessarily restricts all of the parameter corrections in order to overcome high correlations. In the particular problem at hand, there are a large number of local correlations that are greater than 0.97. The modified Marquardt algorithm speeds up the convergence process. The results of the Marquardt algorithm and the modified version are the same once a converged solution is obtained.

The algorithm is listed below with the convergence test included. The set of λ multipliers is written as λ_n , where n is the number of estimation parameters.

1. Denote $\lambda_n^{(k-1)}$ as λ_n of the previous iteration.
Initially, let $\lambda_n^{(0)} = 0.01$. Set $v = 10$.
2. Calculate $\Phi(\lambda_n^{(k)})$, $\Phi(\lambda^{(k-1)})$, $\Phi(\lambda_n^{(k-1)}/v)$.
 - i. If $\Phi(\lambda_n^{(k-1)}/v) \leq \Phi(\lambda_n^{(k)})$, let $\lambda^{(k)} = \frac{\lambda^{(k-1)}}{v}$.
 - ii. If $\Phi(\lambda_n^{(k)}) \geq \Phi(\lambda^{(k-1)})$, let $\lambda^k = v\lambda^{k-1}$.
3. Calculate the correlation coefficients for all of the parameters. If $|r(C_i C_j)| \geq 0.97$, set λ_j^k to $10^{25}\lambda_j^k$.
4. Calculate the corrections δC using Equation (4.7) and add them to the current estimates.
5. If $(\langle \Phi \rangle^{(k)} - \Phi^{(k)}) / \Phi^{(k)} \leq 10^{-3}$, the solution is converged. If not, repeat the process.

It should be noted that part ii in Step 2 is repeated as many times as necessary. The test for correlation is performed each iteration. If the parameters become less correlated, the condition of Step 3 is not true and the algorithm continues to Step 4.

Chapter V

Computer Program Description and Verification

5.1 Program Description

The computer program which simulates a free-flight trajectory and estimates the aerodynamic coefficients from experimental data is written in FORTRAN. The program, listed in Appendix C, is written entirely in double precision. The reason behind this is that all of the partial derivatives that make up the state Jacobian are calculated numerically using a forward difference approximation with a differential step size of 10^{-6} . A differential step size this small could not be handled with single precision numbers. A central difference technique was tried using single precision numbers with a step size of 10^{-4} , but the time to calculate the partial derivatives takes twice as long. The state Jacobian has to be calculated at every iteration, so double precision was chosen on the basis of speed. The small differential step sizes are necessary because the solution to least squares problems requires that the partial derivatives be as accurate as possible.

Integration of the differential equations described in Chapter III is done using a fourth order Runge-Kutta technique. To calculate a flexible body simulation, the derivative vector in Equation (3.1) is determined and integrated simultaneously with Equations (3.5) through (3.10). In order to start the integration, the initial position and angular orientation as well as the initial velocity and spin rate are read into the program from an input file.

The program can be configured to perform a simulation or a coefficient regression using either rigid body or flexible body equations of motion simply by setting the proper flags (see Figure 8). A branch which estimates the aerodynamic coefficients using a rigid body trajectory as *experimental data* is also included for testing of the regression algorithm. If the program is used to determine the aerodynamic coefficients, the initial conditions are also estimated from the experimental data.

5.2 Program Verification

The first phase of testing the program involves performing a rigid-body simulation using aerodynamic coefficients and initial conditions that were determined using the Air Force's ARFDAS (Aeroballistic Research Facility Data Analysis System) program and comparing the trajectories of both programs. The resulting trajectories match, and a table of the state variables as a function of time is shown in Table 3 of Appendix D. The experimental data that the ARFDAS program used to generate the aerodynamic coefficients and initial conditions are shown in Table 4 of Appendix D. Next, the flexible-body equations are used for simulation with the amplitude of vibration set to zero. This is done to check the procedure for calculating the body-fixed state variable rate vector in Equation (3.1). As expected, the trajectory matches the rigid-body trajectory.

The second phase of testing is to perform a coefficient regression. The test regression involves using the trajectory in Table 3 as experimental data. The initial estimate of the aerodynamic coefficients and initial conditions are the same as those that generated the trajectory. The results were determined in one

iteration and are identical to the initial estimates, which is expected since the data contain no noise.

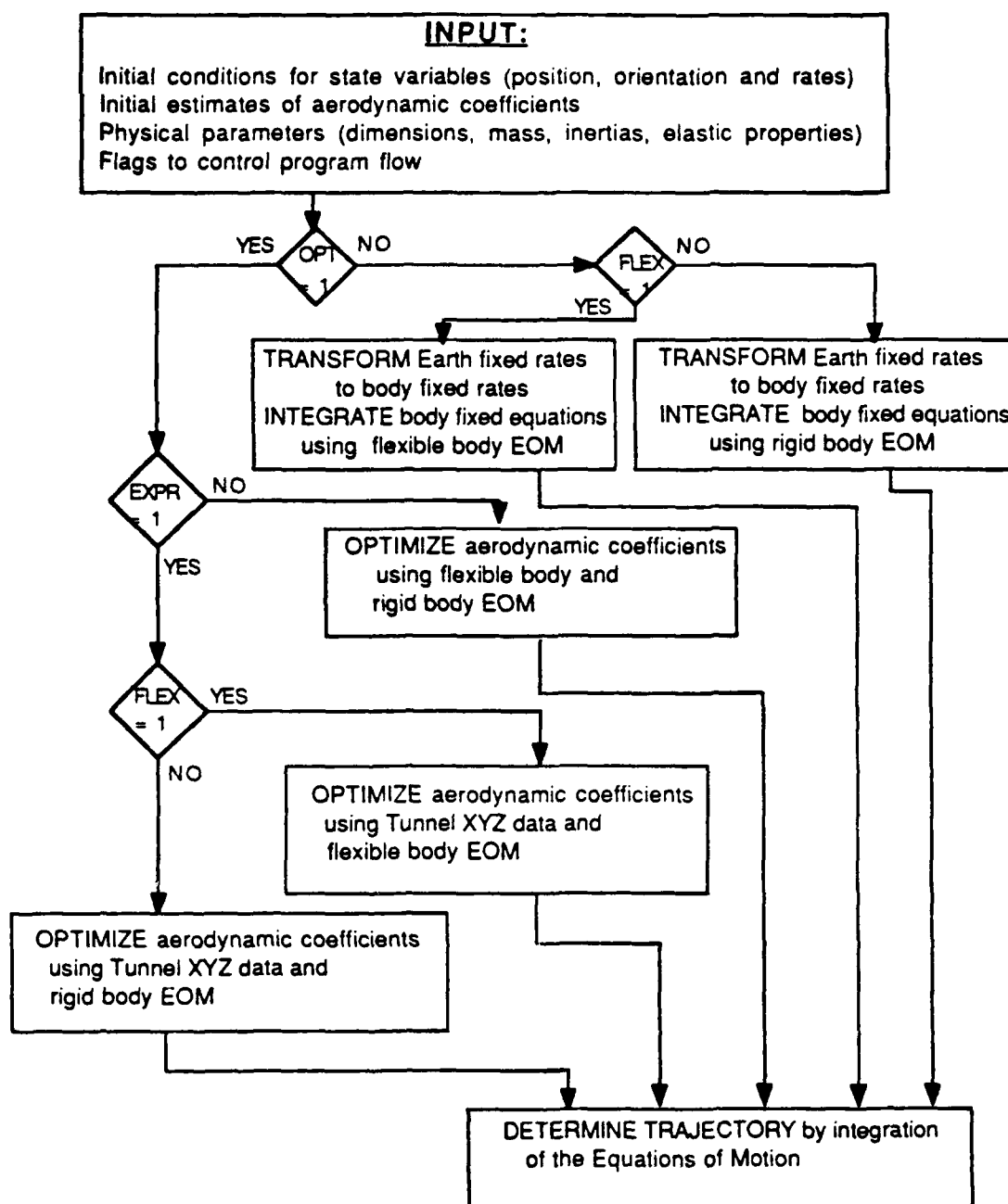


FIGURE 8. Flow Chart for Extraction Program

Chapter VI

Results

6.1 Ballistic Tests of High L/D Models

The model which is chosen for studying elastic effects is characteristic of the $L/D = 50$ models that have been tested to date; that is, the angular motion is on the order of one degree in both pitch and yaw. The ARF designates their experiments by a "shot number", and the model being studied herein is shot number BS87070976. This is the same case that is used to test the trajectory simulations in Chapter V. The ARF fires a series of shots out of a light gas gun at different Mach numbers so that the Mach number effects on the aerodynamics can be studied. The Mach number of BS87070976 is approximately 2. The shots fired at Mach 3 have poor roll data associated with them or none at all. The very nature of using a body-fixed aerodynamic analysis is to include the roll effect of an asymmetric projectile. Therefore, no shots at Mach 3 have been tested for elastic effects. The ARF is currently involved with another series of high L/D ballistic tests in order to gather more data on these projectiles.

The results from the film reading process provide the position and angular orientation of the projectile. In the film reading process, no bending of the model has been taken into account. Not all of the high L/D models exhibit flexibility of a magnitude which is noticeable from the shadowgraphs. It is believed that the minimum noticeable deflection is on the order of one degree. In terms of amplitude, this is 0.22 inches for an L/D of 50 ($L = 12.5$ inches). It is questionable whether elastic deflections can be measured in a ballistic range

unless divergence is achieved as in the shadowgraph sequence of Appendix A. In order to have success in measuring small elastic deflections, the model would have to be photographed at its maximum (or near maximum) deflection at one of the shadowgraph stations. As stated before, no attempt has been made to date to measure the elastic deflection.

6.2 Aerodynamic Coefficient Regressions

The aerodynamic coefficients of shot BS87070976 are regressed upon using rigid and flexible body equations of motion. Specifically, the amplitude of vibration used in the flexible body analysis is varied to study the elastic effects over a range of deflections. The amplitudes chosen for analysis are 0.25 and 0.5 inches. These represent dimensionless amplitudes of 0.0127 and 0.0254, respectively.

Since the data measured in a ballistic range have different accuracies associated with them (the angular motion has less accuracy than the translational motion), the data are weighted with the standard deviation as shown in Equation (4.2). The standard deviations of the state variables are shown below:

0.00851 feet in X_E

0.00631 feet in Y_E

0.00631 feet in Z_E

0.278 degrees in θ

0.278 degrees in ψ

8.65 degrees in ϕ

The coefficients that were determined from the ARFDAS program are shown in the first column of Table 1. Note that the probable errors of the damping moment coefficients, C_{mq} and C_{nr} are quite high. This is due mainly to the low angular motion of the projectile in flight. Without significant oscillations, the proportion of the measurement noise to the actual data increases. The nonlinear drag term, $C_{x\ddot{\alpha}^2}$, is not fit very accurately for the same reason.

The second column of Table 1 shows the results of a rigid body fit of the program which is listed in Appendix C. The damping moment terms of this case vary significantly from those determined by ARFDAS. The probable error is high on these coefficients just as before, but note that C_{nr} is shown to be *positive*. The only reasoning behind this is the angular motion is so small that the moment damping effects have little effect on the motion of the projectile.

Table 1: A Comparison of Aerodynamic Coefficients Determined by ARFDAS and Rigid-Body Regressions

Coeff.	ARFDAS	Rigid-Body
$C_{m\alpha}$	-238.7 ± 11.5	-229.7 ± 15.4
$C_{n\beta}$	193.3 ± 7.65	241.4 ± 14.0
C_{mq}	$-31020. \pm 5160.$	$-142600. \pm 38400.$
C_{nr}	$-1366. \pm 4150.$	$104200. \pm 33700.$
C_{x0}	0.7619 ± 0.0277	0.7388 ± 0.0351
$C_{x\ddot{\alpha}^2}$	$413.8 \pm 107.$	$414.6 \pm 112.$
$C_{y\beta}$	-18.01 ± 4.18	-6.056 ± 2.01
$C_{z\alpha}$	-23.00 ± 5.88	-4.511 ± 2.02
C_{lp}	-116.7 ± 16.1	-116.5 ± 0.900

Since the projectile is symmetric, one would expect to find symmetry in the aerodynamic coefficients as well. This is case for $C_{m\alpha}$ and $C_{n\beta}$ as well as for $C_{y\beta}$ and $C_{z\alpha}$ for both program regressions. However, the damping moment coefficients, C_{mq} and C_{nr} , do not exhibit any symmetry in the ARFDAS regression. These coefficients have relatively the same magnitude in the rigid-body branch, but the sign of C_{nr} is opposite of what is normally expected. Note that the magnitudes of $C_{y\beta}$ and $C_{z\alpha}$ vary between the two programs. This can be attributed in most part to the large variation of the damping moment coefficients. Regressions were performed holding the damping moment coefficients constant to the values obtained by ARFDAS and similar results to the ARFDAS values for $C_{y\beta}$ and $C_{z\alpha}$ were obtained.

Before a set of regressions can be made, the *elastic inertia* terms must be calculated using Equations (3.2) through (3.4). The mode shape defined by Equation (2.13) is used to calculate the integrals (See Appendix E). This procedure is performed in the main program if the FLEX flag is set (see Figure 8). The calculated *elastic inertia* terms are normalized to unity. They are multiplied by the amplitude of deflection, which is read into the program. The scalar value of the normalized elastic inertia coefficients are shown below:

$$K_x = 0$$

$$L_{zz} = 0.000110$$

$$H_{zz} = 0.000110$$

The term K_x is zero due to the symmetrical bending about the center of mass. The units on these *elastic inertia* terms are slugs-square feet.

Table 2 shows the results of the set of flexible body regressions. The elastic effects are negligible compared with the probable error of the aerodynamic coefficients. The elastic cases had a slightly better fit than the rigid body case. The deviations are within the standard error incurred in ballistics tests of this nature. The trajectories are shown in Tables 5 and 6 in Appendix D.

Table 2: A Comparison of Aerodynamic Coefficients
Determined using a Flexible Body Model

Coeff.	1/4" deflection	1/2" deflection
$C_{m\alpha}$	-230.1 ± 15.12	-230.1 ± 14.7
$C_{n\beta}$	241.7 ± 13.8	241.5 ± 13.5
C_{mq}	$-144200. \pm 37700.$	$-145100. \pm 36600.$
C_{nr}	$105600. \pm 33200$	$106200. \pm 32400.$
C_{x0}	0.7393 ± 0.0348	0.7402 ± 0.0292
$C_{x\bar{\alpha}^2}$	$410.0 \pm 111.$	$402.2 \pm 108.$
$C_{y\beta}$	-5.866 ± 1.90	-5.594 ± 1.76
$C_{z\alpha}$	-4.379 ± 1.90	-4.215 ± 1.75
C_{lp}	-116.6 ± 0.910	-119.1 ± 0.954

The results shown in Tables 1 and 2 point out that the effects of single-plane bending are negligible in comparison with the probable errors of the aerodynamic coefficients. Plots of the trajectories for the rigid-body regression and the two flexible-body regressions are identical (See Figures 9-15 and in Appendix D).

Chapter VII

Conclusion and Recommendations

7.1 Conclusion

The results of this study show that the flexing model has little effect on the aerodynamic coefficients that are determined from free-flight ballistic tests. Taking into consideration the size of the probable errors that these coefficients have, it is safe to say that the rigid-body motion assumption is valid. This does not say that the body is rigid, it just says that the aerodynamic coefficients determined from rigid-body theory are adequate.

The present research study is basically a kinematic superposition of a flexing model vibrating at its fundamental natural frequency onto the six-degree-of-freedom dynamics. Without changing the aerodynamic model that is presently in use by ARFDAS, this is all that can be done to study elastic motion. Certainly, the vibratory nature of the model itself can be modified to include more degrees of freedom (torsional and axial effects). Even higher mode shapes can easily be handled by the program that has been developed, but it is felt that even these elastic motions will show no significant effects on the coefficient regression scheme.

It is unwise to make a sweeping statement on these elastic effects based on only one set of experimental data. The ARF staff is currently performing additional tests to broaden the aerodynamic data base for high L/D projectiles. It is expected that the methods of the present study will be applied to those shots which demonstrate measureable flexibility.

In addition, the methods may be applied to data from other laboratories. Continued applications of this type will serve to establish a confidence level of the methodology.

7.2 Recommendations

The methods of analysis described herein do not involve changing the type of data which are acquired in free-flight ballistics tests. Instead, the equations of motion have been altered to include flexibility-induced dynamic terms. An alternate approach would be to use the rigid-body dynamic equations of motion together with an aerodynamic model which includes terms which account for body flexibility. Thus, present ballistic tests can be modified to include measuring an experimental deflection curve at each shadowgraph station. This experimental deflection curve would be determined by measuring the deflection at several locations along the model. The kinematic vibration of the model could be included in the dynamics as before. The difference would lie in the fact that the mode and/or frequency of vibration would now be regression parameters. Then, an aeroelastic coefficient could be included in the aerodynamic model which would be a function of this experimental deflection curve. A regression could then be made on the coefficients in hopes of iterating on a better solution (lower probable errors or a reduction in the sum of squares of the residuals). Still another approach would involve including such flexibility coefficients together with the flexible-body equations of motion.

Both of these suggested modifications could be accomplished with the computer program developed in the present study.

However, in light of the present test results, it is not recommended that the additional effort be expended until the present technique has been thoroughly tested.

References

1. Hathaway, W. H. and Whyte, R. H., "Aeroballistic Range Data Analysis for Nonsymmetric Configurations", AFATL-TR-76-109, September 1976.
2. Hathaway, W. H. and Whyte, R. H., "Aeroballistic Range Data Reduction Technique Utilizing Numerical Integration", AFATL-TR-74-41, February, 1974.
3. Hathaway, W. H., Whyte, R. H., and Burnett, J., "Aeroballistic Research Facility Data Analysis System User Manual", General Electric Company, Burlington, Vermont, February, 1982.
4. Murphy, C. H., "Free Flight Motion of Symmetric Missiles", BRL Report 1216, July, 1963.
5. Murphy, C. H., "Data Reduction for the Free Flight Spark Ranges", BRL Report 900, February, 1954.
6. Chapman, G. T. and Kirk, D. B., "A Method for Extracting Aerodynamic Coefficients from Free Flight Data", AIAA Journal, Vol. 8, No. 4, April, 1970.
7. Keith, J. S., Lincoln, J. W., and Tarnower, G., "Aeroelastic Analyses of Multistage Rocket Systems", NATO-AGARD-390, July, 1961.
8. Fung, Y. C., "An Introduction to the Theory of Aeroelasticity", John Wiley and Sons, Inc., 1955.

9. Courter, R.W., "The Effect of Model Flexibility on the Accuracy of Aerodynamic Coefficients Determined from Free-Flight Ballistic Tests", Universal Energy Systems Report, July, 1987.
10. Blevins, R. D., "Formulas for Natural Frequency and Mode Shape", Van Nostrand Reinhold Co., 1979.
11. Nicolaides, J. D., "Free Flight Dynamics", University of Notre Dame, South Bend, Indiana, 1967.
12. Brunk, J., "User's Manual: Extended Capability Magnus Rotor and Ballistic Body 6-DOF Trajectory Program", AFATL-TR-70-40, May 1970.
13. Marquardt, D. W., "An Algorithm for Least-Squares Estimation of Nonlinear Parameters", SIAM Journal, Vol. 11, No. 2., June, 1963.

Appendices can be obtained from
Universal Energy Systems, Inc.

1986 USAF-UES SFRP and MINIGRANTS PROGRAM

Sponsored by

AIR FORCE OFFICE OF SCIENTIFIC RESEARCH

Conducted by the

Universal Energy Systems, Inc.

FINAL REPORT

IMAGE COMPLEXITY MEASURES AND EDGE DETECTION

Principal Investigators	Jennifer L. Davidson University of Florida Department of Mathematics
	Dr. Gerhard X. Ritter University of Florida Department of Computer and Information Science
Date	June 23, 1988
Contract Number	F49620-85-C-0113

ABSTRACT

Edge detection is one of the first steps often used for segmentation purposes in image processing. The main goal of the research performed under this contract was to determine if image measures would aid in the selection of an optimum edge detector algorithm for a given image. A classification scheme of a family of edge detectors developed during the Graduate Student Summer Support Program, 1986, was expanded and modified, and several image measures investigated. The image algebra was used as the mathematical environment in which to develop these concepts. No correlation between edge detectors and optimality on a given image was found. However, a recent report, acquired too late for use in this research, is very applicable to this area and needs to be investigated. The report presents a background, research completed during the contract, and suggestions for further research.

1. **Introduction.** Solutions of the problem of automatic target recognition (ATR) is of obvious importance in a variety of military applications. A general approach in modeling the ATR system is to first segment the image into regions, attach previously defined labels to the regions, determine a list of relations between the regions, and deduce from that list the target or object of interest. Figure 1 gives a flowchart of this approach.

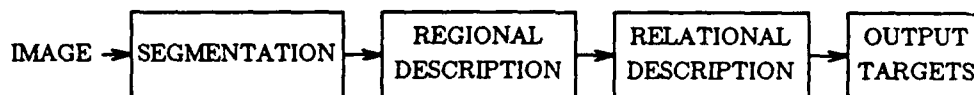


Figure 1.

Segmentation is an important first step. The information extracted here is passed on to successive steps in the processing sequence, and how much or how little gets passed on is determined by the segmentation algorithm. Many types of segmentation techniques exist, one of which is edge-based segmentation. There exist a vast variety of algorithms which detect boundaries of objects in an image. After a collection of boundary or edge points are chosen, a thinning algorithm can be applied to narrow the edge width as desired, usually to one or two pixels. Then a linking technique which links disconnected edges together is often applied. These linked edges are the output of the edge segmentation scheme. Since this is the initial stage of the processing, it is crucial that the boundaries output from the segmentation algorithm be as close as possible to the true boundaries that exist in the image, so the maximum amount of exact information is passed onto successive steps in the processing. Thus an accurate edge segmentation algorithm is an essential block of the processing scheme.

There are of course other edge segmentation techniques than the one just described [1]. There are also methods, sometimes called figure of merit ratings, which evaluate the performance of edge detectors on synthetic data smeared with various levels of white noise (for

example see [1]). Obviously, figure of merit ratings of edge detectors is not a satisfactory classification of edge detectors and their performances, as much research and discussion continues on this subject up to the present day [2,3,4].

A good edge detector reduces the need for complicated thinning and linking algorithms, so there is strong motivation to use the "best" edge detector for the job. Thus, the concept of an edge and edge detector must be made precise, and the classification of edge detectors based on the definition. The classification scheme is discussed in Section 4(III).

2. Research Objectives. In order to achieve our goal, we proposed to concentrate efforts on the following specific objectives:

1. Extend the classification scheme of edge detectors developed this past summer to encompass as many edge detector algorithms as possible.
2. Examine an upcoming ERIM (Environmental Research Institute of Michigan) report on the consolidation of several DARPA-supported contracts on image metrics; continue to survey the literature.
3. Investigate in depth surface complexity measures of differential geometry and algebraic topology and examine their applicability to digital image intensity variations.
4. Compose a list of statistical measures and explore potential interrelations between the results of 3. and the statistical measures.
5. Investigate the properties of the edge detectors as developed in the classification scheme combined with results from 4. in creating decision rules which will optimize the effect of an edge detector application to an image.

The image algebra and the Image Algebra Preprocessor were used to facilitate the algorithm development and implementation of these objectives. The image algebra is a mathematically rigorous, efficient algebraic structure that is specifically designed for image manipulation. The University of Florida was awarded a DARPA contract to develop a complete, unified algebraic structure that provides a common mathematical environment for image algorithm development, optimization, comparison, coding and performance evaluation. This structure is known as the standard **AFATL image algebra**. This algebra has been implemented in software in form of a preprocessor which translates image algebra expressions into Fortran 77. See [5] for more detailed information on the structure of image algebra.

3. Details of the Completed Research

A. The Classification of Edge Detectors. In order to define an edge detector, an edge must first be defined. Although there does not exist a standard definition of an "edge" in the literature, the basic concept of an edge which is used in design of edge detectors is fairly uniform. The purpose of an edge detector is to detect and characterize intensity variations of a significant nature in a neighborhood of a pixel p , and the discrete nature of the surface in a neighborhood of p allows such models as the step function or ramp function to be used with equivalent results.

There are different ways to characterize variations in magnitude of a collection of pixels in a neighborhood of p , which depend both on the masks used and the mathematical function of the masks and the image. We constructed a definition for a class of edge detectors, covering most of the ones used in applications.

Methods of edge detection can be divided into two main categories: the edge-fitting method; and the enhancement method. Edge detection methods of the second type were the only ones investigated during the 10-week summer research, and continued to be the sole interest of this research.

Before discussing the classification scheme, we list the edge detectors that were investigated:

Sobel
Prewitt
Roberts'
Kirsch
Gradient
 $\nabla^2 G$, the Laplacian of an image convolved with the Gaussian
 $\frac{\delta^2}{\delta n^2}$, the second directional derivative in the direction of the gradient
Logarithmic edge detector
Geometric edge detector

The techniques were translated into the image algebra in order to facilitate investigation into the properties of each technique. We omit discussion of the image algebra operands and operations and refer the reader to [6] for more details.

To facilitate the discussion of the edge detectors, we give a brief image algebra formulation of each.

1. Sobel. The image algebra expression

$$[(a \oplus t_1)^2 + (a \oplus t_2)^2]^{1/2},$$

where

$$t_1 = \begin{array}{|c|c|c|} \hline -1 & & 1 \\ \hline -2 & \text{circle} & 2 \\ \hline -1 & & 1 \\ \hline \end{array} \quad t_2 = \begin{array}{|c|c|c|} \hline -1 & -2 & -1 \\ \hline & \text{circle} & \\ \hline 1 & 2 & 1 \\ \hline \end{array}$$

represents the Sobel edge enhanced image.

2. Prewitt. The image algebra expression

$$[(a \oplus t_1)^2 + (a \oplus t_2)^2]^{1/2},$$

where

$$t_1 = \begin{bmatrix} -1 & & 1 \\ -1 & \bigcirc & 1 \\ -1 & & 1 \end{bmatrix} \quad t_2 = \begin{bmatrix} -1 & -1 & -1 \\ & \bigcirc & \\ 1 & 1 & 1 \end{bmatrix}$$

represents the Prewitt edge enhanced image.

3. Roberts'. The image algebra expression

$$[(a \oplus t_1)^2 + (a \oplus t_2)^2]^{1/2},$$

where

$$t_1 = \begin{bmatrix} -1 & \\ \bigcirc & 1 \end{bmatrix} \quad t_2 = \begin{bmatrix} & -1 \\ 1 & \bigcirc \end{bmatrix}$$

represents the Roberts' edge enhanced image.

4. Kirsch. The image algebra expression representing Kirsch algorithm is given by

$$1 \vee \left(\bigvee_{i=1}^8 |a \oplus t_i| \right),$$

where 1 denotes the unit image and t_i is defined as follows. For $i = 1, 2, \dots, 8$ define the parameterized template t_i by

$$t_{i,y} = \{(x, t_{i,y}(x)) : t_{i,y}(x) = 5 \text{ if } x = x_i, x_{i+1}, x_{i+2}, t_{i,y}(x) = 3 \text{ if } x = x_{i+3}, \dots, x_{i+7}, \text{ else } t_{i,y}(x) = 0\},$$

where the subscripts are modulo 8, and where the x_j 's denote the elements of the configuration $S(t_{i,y})$ as shown:

$$S(t_{i,y}) = \begin{bmatrix} x_4 & x_3 & x_2 \\ x_5 & y & x_1 \\ x_6 & x_7 & x_8 \end{bmatrix}$$

5. Gradient. Edge detection is accomplished by convolving the image with the following six 3x3 edge masks with each mask having a direction associated with it.

1	1	1
0	0	0
-1	-1	-1

m_1 180°

-1	0	1
-1	0	1
-1	0	1

m_2 90°

.7	1	1
-.8	0	.8
-1	-1	-.7

m_3 150°

1	1	.7
.8	0	-.8
-.7	-1	-1

m_4 210°

-.7	.8	1
-1	0	1
-1	-.8	.7

m_5 120°

1	.8	-.7
1	0	-1
.7	-.8	-1

m_6 240°

Define $f: \mathbb{R} \rightarrow \mathbb{R}^2$ by $f(r) = (|r|, 180\chi_{<0}(r))$, where χ is the characteristic function. Let a_i be the two-valued image $a_i = (0, \theta_i + f(a \oplus m_i))$, $i=1, \dots, 6$, where m_i are masks as shown above, and θ_i are the respective degrees associated with each m_i . Then the gradient edge detector, expressed in the multi-valued image algebra, is

$$\bigvee_{i=1}^6 a_i$$

6. The Laplacian of an image convolved with the Gaussian, $\nabla^2 G$, has the image algebra expression

$$a \oplus g$$

where g is a translation invariant template from \mathbb{Z}^2 to \mathbb{Z}^2 defined by

$$g_{(x,y)}(i,j) = \frac{1}{2\pi\sigma^2} \exp \left[\frac{-1}{2} \cdot ((i-x)^2 + (j-y)^2)/\sigma^2 \right]$$

7. The second directional derivative in the direction of the gradient, $\frac{\delta^2}{\delta n^2}$, has the image algebra expression

$$\frac{(a \oplus u)^2(a \oplus t) + 2(a \oplus u)(a \oplus w)(a \oplus z) + (a \oplus w)^2(a \oplus s)}{(a \oplus u)^2 + (a \oplus w)^2}$$

Here, the masks are as follows:

$$t = \begin{bmatrix} 1 & -2 & 1 \end{bmatrix} \quad u = \begin{bmatrix} -1 & & 1 \end{bmatrix} \quad s = \begin{bmatrix} 1 \\ -2 \\ 1 \end{bmatrix} \quad w = \begin{bmatrix} -1 \\ \\ 1 \end{bmatrix}$$

$$z = \begin{bmatrix} -1 & & 1 \\ & & \\ 1 & & -1 \end{bmatrix}$$

8. Logarithmic edge detector. The image algebra expression is

$$\ln(a) - [(\frac{1}{4} \ln(a)) \oplus t]$$

where

$$t = \begin{bmatrix} & 1 & \\ 1 & & 1 \\ & 1 & \end{bmatrix}$$

9. Geometric edge detector. The image algebra expression is

$$[(a \oslash t - a \oslash s)^2 + (a \oslash u - a \oslash w)^2]^{1/2},$$

where

$$t = \begin{bmatrix} 2 & 1 & 2 \end{bmatrix} \quad s = \begin{bmatrix} 1 & 2 & 1 \end{bmatrix} \quad u = \begin{bmatrix} 2 \\ 1 \\ 2 \end{bmatrix} \quad w = \begin{bmatrix} 1 \\ 2 \\ 1 \end{bmatrix}$$

Definition 1. Let F be a vector space over a field K . A *linear image operator* is a function $f: F^X \rightarrow F^Y$ such that

1. $f(ka) = kf(a)$,
2. $f(a + b) = f(a) + f(b)$, where $a, b \in F^X$, and $k \in K$.

Definition 2. A *semi-linear image operator* is a function $f: F^X \rightarrow F^Y$ such that

1. $f(ka) = kf(a)$, where $a \in F^X$, and $k \in K$.

Definition 3. A *semi-linear edge operator* is a function $E: F^X \times [(F^X)^X]^p \rightarrow F^Y$, for some fixed integer p , such that

1. $E(k, t_1, \dots, t_p) = 0$, for k a constant image
2. $E(ka, t_1, \dots, t_p) = kE(a, t_1, \dots, t_p)$, $k \geq 0$
3. $E(k + a, t_1, \dots, t_p) = E(a, t_1, \dots, t_p)$, k a constant image.

Thus, for example, the function $E: R^X \times (R^X)^X \rightarrow R^X$ defined by $E(a, t) = a \oplus t$, where t is either one of the Sobel templates [1], is a semi-linear edge operator, as well as the Sobel operator itself. Figure 2 lists the edge operators and their respective types.

Name of Edge Detector		Type	
		Semi-Linear	Other
1.	Sobel	X	
2.	Prewitt	X	
3.	Roberts'	X	
4.	Kirsch	X	
5.	Gradient	X	
6.	$\nabla^2 G$	X	
7.	$\frac{\delta^2}{\delta n^2}$	X	
8.	Logarithmic edge detector		X
9.	Geometric edge detector	X	

Figure 2. Edge Classification Scheme.

Proofs: Here we prove that the edge detectors satisfy the semi-linear edge properties, or not, as in the case of the logarithmic edge detector. We shall use the following proposition heavily:

Proposition 1. Let $t \in (\mathbb{R}^X)^X$ be an invariant template such that the sum of the weights over the template configuration is 0, and let $a \in \mathbb{R}^X$. Then $E(a,t)$ defined by

$$E(a,t) = a \oplus t$$

is a semi-linear edge operator.

Proof: Since $\{ (\mathbb{R}^X)^X, \mathbb{R}^X, \oplus, +, \bullet \}$ is isomorphic to the linear algebra [7], we know that $a \oplus t$ corresponds to the linear algebra operation $M_t v_a$, where M_t corresponds to the template t , v_a corresponds to the image a , and the matrix-vector product $M_t v_a$ corresponds to the image algebra product $a \oplus t$. Thus, even if t is a variant template, the function $E(a,t)$ is linear. Property 2 of the definition immediately follows,

and Property 3 follows from linearity and Property 1. For Property 1, the gray value of $\mathbf{a} \oplus \mathbf{t}$ at $\mathbf{y} \in \mathbf{X}$ is $c(\mathbf{y})$

$$c(\mathbf{y}) = \sum_{\mathbf{x} \in S(\mathbf{t}_y)} \mathbf{a}(\mathbf{x}) \mathbf{t}_y(\mathbf{x}) = \sum_{\mathbf{x} \in S(\mathbf{t}_y)} k \mathbf{t}_y(\mathbf{x}) = k \sum_{\mathbf{x} \in S(\mathbf{t}_y)} \mathbf{t}_y(\mathbf{x})$$

Thus, in order for $\mathbf{a} \oplus \mathbf{t}$ to have value 0 at location \mathbf{y} , the sum of the weights over the template configuration must be 0. But this is true by hypothesis.

Q.E.D.

Thus, for all templates \mathbf{t} of the Sobel, Kirsch, Prewitt, Roberts', gradient, and $\frac{\delta^2}{\delta n^2}$ operators, $E(\mathbf{a}, \mathbf{t})$ as defined in Proposition 1 is a semi-linear edge operator.

Now we proceed with the proofs that the edge operators themselves are semi-linear edge operators.

Proposition 2. Let $E: \mathbf{R}^X \times [(\mathbf{R}^X)^X]^2 \rightarrow \mathbf{R}^X$ be defined by

$$E(\mathbf{a}, \mathbf{t}_1, \mathbf{t}_2) = [(\mathbf{a} \oplus \mathbf{t}_1)^2 + (\mathbf{a} \oplus \mathbf{t}_2)^2]^{1/2},$$

where \mathbf{t}_i , $i=1,2$ are the Sobel templates, the Prewitt templates, or the Roberts' templates.

Then E is a semi-linear edge operator.

Proof: To show that Property 1 holds, we note that

$$E(\mathbf{k}, \mathbf{t}_1, \mathbf{t}_2) = [(\mathbf{k} \oplus \mathbf{t}_1)^2 + (\mathbf{k} \oplus \mathbf{t}_2)^2]^{1/2}$$

has gray value, at location $\mathbf{y} \in \mathbf{X}$, of

$$\begin{aligned} & \{ [\sum_{\mathbf{x} \in S(\mathbf{t}_{1y})} \mathbf{k}(\mathbf{x}) \mathbf{t}_{1y}(\mathbf{x})]^2 + [\sum_{\mathbf{x} \in S(\mathbf{t}_{2y})} \mathbf{k}(\mathbf{x}) \mathbf{t}_{2y}(\mathbf{x})]^2 \}^{1/2} \\ &= k \{ [\sum_{\mathbf{x} \in S(\mathbf{t}_{1y})} \mathbf{t}_{1y}(\mathbf{x})]^2 + [\sum_{\mathbf{x} \in S(\mathbf{t}_{2y})} \mathbf{t}_{2y}(\mathbf{x})]^2 \}^{1/2} = k * 0 = 0 \end{aligned}$$

as the sum of the weights of each template over its respective configuration is 0. Thus we have $E(\mathbf{k}, \mathbf{t}_1, \mathbf{t}_2) = \mathbf{0}$.

To show that Property 2 holds, we see that at $y \in X$ $E(ka, t_1, t_2)$ has gray value $c(y)$, where

$$c(y) = \{ [\sum_{x \in S(t_1)} k a(x) t_{1y}(x)]^2 + [\sum_{x \in S(t_2)} k a(x) t_{2y}(x)]^2 \}^{1/2} =$$

$$k \{ [\sum_{x \in S(t_1)} a(x) t_{1y}(x)]^2 + [\sum_{x \in S(t_2)} a(x) t_{2y}(x)]^2 \}^{1/2}$$

which is the same gray value at $y \in X$ as $kE(a, t_1, t_2)$.

Property 3 can be shown as follows: at location $y \in X$, $E(k + a, t_1, t_2)$ has gray value $c(y)$, where

$$c(y) = \{ [\sum_{x \in S(t_1)} (k + a(x)) t_{1y}(x)]^2 + [\sum_{x \in S(t_2)} (k + a(x)) t_{2y}(x)]^2 \}^{1/2} =$$

$$\{ [k \sum_{x \in S(t_1)} t_{1y}(x) + \sum_{x \in S(t_1)} (a(x) t_{1y}(x))]^2 + [k \sum_{x \in S(t_2)} t_{2y}(x) + \sum_{x \in S(t_2)} (a(x) t_{2y}(x))]^2 \}^{1/2} =$$

$$\{ [0 + \sum_{x \in S(t_1)} (a(x) t_{1y}(x))]^2 + [0 + \sum_{x \in S(t_2)} (a(x) t_{2y}(x))]^2 \}^{1/2}$$

which is the same gray value at $y \in X$ as $E(a, t_1, t_2)$.

Q.E.D.

The proof for the Kirsch operator is very similar to Proposition 2, and we omit it for that reason.

For the Gradient operator, we note that since it results in a 2-valued image, we cannot apply Proposition 2 directly to it. However, if we consider the magnitude image a and direction image d as two separate images, then we can consider the edge operator to be only the magnitude part, and Properties 1-3 follow.

The remaining edge operators, $\nabla^2 G$, $\frac{\delta^2}{\delta n^2}$, and the geometric edge detector, are shown in a similar way to be semi-linear edge detectors. For example, in the geometric edge operator, the fact that $k \geq 0$ in Property 2 allows us to pull the k outside the maximum sign in

the gray level value for $E(k, t_1, t_2, t_3, t_4)$:

$$\begin{aligned} & \{ [\sum_{x \in S(t_1)} (k \cdot a(x)t_{1y}(x) - k \cdot a(x)t_{2y}(x))]^2 + [\sum_{x \in S(t_3)} (k \cdot a(x)t_{3y}(x) - k \cdot a(x)t_{4y}(x))]^2 \}^{1/2} \\ &= k \{ [\sum_{x \in S(t_1)} (a(x)t_{1y}(x) - a(x)t_{2y}(x))]^2 + [\sum_{x \in S(t_3)} (a(x)t_{3y}(x) - a(x)t_{4y}(x))]^2 \}^{1/2} \end{aligned}$$

(Here we also use the fact that $S(t_{1y}) = S(t_{2y})$ and $S(t_{3y}) = S(t_{4y})$.)

We remark that since the problem of finding the derivative of an image is an ill-defined one in the sense of Hadamard (though it can be regularized), that not all edge operators need satisfy the semi-linear properties. For example, the logarithmic edge detector is not semi-linear, as it does not satisfy properties 2 and 3.

B. Image Complexity Measures. A literature search during the summer of 1986, performed while supported on the GSSSP disclosed a total lack of articles in the area of sensor independent automated edge detector selection. The purpose of investigating image complexity measures is to use a set of these measures in conjunction with the properties satisfied by an edge detector to arrive at a method of determining how "optimal" an edge detector is. This information, in turn, could be used to construct an automated rule-based algorithm which would select an optimal edge detector based on the degree of optimality obtained by the set of image measures. The initial literature search revealed that this approach had not been investigated.

We investigated measures from the following areas: algebraic topology (fractals), differential geometry (the gaussian average operator), and a few statistical measures. We discuss the purpose of each measure and the research performed on each.

I. Fractals. A method for calculating a unique measurement for an image was investigated. The method involves an application of the theory of fractals and Hausdorff dimension. We modify an iterative algorithm already existent in the literature [8]. The algorithm

results in a one-dimensional discrete function which uniquely identifies the image to which it was applied.

Measuring the area of a gray level surface is based on a method suggested by Mandelbrot [9] for curve length measurements. Consider all points with distance to the gray level surface of no more than ϵ . These points form a "blanket" of thickness 2ϵ , and the suggested surface area $A(\epsilon)$ of the gray level surface is the volume of the blanket divided by 2ϵ . Here we have $A(\epsilon)$ increasing as ϵ decreases.

To begin the computation of the surface area for $\epsilon = 1, 2, \dots$, an upper surface U_ϵ and a lower surface B_ϵ are defined iteratively in the following manner:

Let a be the input image. Let

$$u_0 = a, \quad b_0 = a$$

Then define u_ϵ and b_ϵ for $\epsilon = 1, 2, \dots$, by

$$u_\epsilon = u_{\epsilon-1} \boxtimes t$$

$$b_\epsilon = b_{\epsilon-1} \boxtimes t$$

where

$$t_x = \begin{array}{|c|c|c|} \hline & 0 & \\ \hline 0 & 1 & 0 \\ \hline & 0 & \\ \hline \end{array}$$

Then the volume $v(\epsilon)$ of the "blanket" between the upper and lower surfaces is calculated for each ϵ by computing

$$p_1(\epsilon) = u_\epsilon \oplus s, \quad q_1(\epsilon) = b_\epsilon \oplus (-s)$$

for

$$s_x = \begin{array}{|c|c|} \hline 0.67 & 0.33 \\ \hline 0.33 & 0.67 \\ \hline \end{array}$$

Let $v_1(\epsilon) = \sum [p_1(\epsilon) + q_1(\epsilon)]$.

Since this adds in values from the top and right edge pixels, which overestimates the volume, we correct for it by applying a variant template effective only on those edge pixels:

Let w = be defined by:

$$w_x = \begin{bmatrix} 0.33 & 0.67 \end{bmatrix}$$

if x is a top edge pixel and not the top right corner pixel,

$$w_x = \begin{bmatrix} 0.33 \end{bmatrix}$$

if x is the top right corner pixel,

$$w_x = \begin{bmatrix} 0.67 \\ 0.33 \end{bmatrix}$$

if x is a right edge pixel but not the top right corner pixel, and $w_x = 0$, if x is otherwise.

Then to correct for the extra volume added in on these edge pixels, we calculate

$$p_2(\epsilon) = u(\epsilon) \oplus (-w), \quad q_2(\epsilon) = b(\epsilon) \oplus w$$

and let $volerr(\epsilon) = \sum [p_2(\epsilon) + q_2(\epsilon)]$. The correct volume $v(\epsilon)$ is

$$v(\epsilon) = v_1(\epsilon) + volerr(\epsilon)$$

The approximated surface area is

$$area(\epsilon) = \frac{v(\epsilon)}{2\epsilon}$$

The rate of change of $\log(area(\epsilon))$ with respect to $\log(\epsilon)$ contains important information about the image. The slope $s(\epsilon)$ of $area(\epsilon)$ versus ϵ is computed on a log-log scale for each ϵ by finding the best fitting straight line through the three points

$$(\log(\epsilon-1), \log(area(\epsilon-1))), (\log(\epsilon), \log(area(\epsilon))), (\log(\epsilon+1), \log(area(\epsilon+1)))$$

The graph of $s(\epsilon)$ versus ϵ is called the *signature* of the image.

This algorithm was run on the images accompanying this report. For each image, we show the input image, u_5 , u_{10} , b_5 , b_{10} , and the graph of the upper and lower signatures. Here, ϵ ranged from 1 to 50.

As ϵ increases, the computation of the images b_ϵ shrinks in size those regions of pixels that initially had the highest gray values. However, as ϵ increases, the images u_ϵ shrink the background regions. This asymmetry can, in theory, be taken advantage of. This corresponds roughly to: the graph of $S(\epsilon)$ for the $\{b_\epsilon\}$ represent the shape of objects with high gray values, and the graph of $S(\epsilon)$ for the $\{u_\epsilon\}$ represent the shape of objects with low gray values. Since our images are infrared, we are mainly interested in the $S(\epsilon)$ for the b_ϵ .

The magnitude of the curve $S(\epsilon)$ is related to the information lost on objects with details less than ϵ in size. The more gray level variation at distance ϵ , the higher the values for $S(\epsilon)$. Thus, if at small ϵ $S(\epsilon)$ is large, then there is "high-frequency" gray level variations, and if at large ϵ $S(\epsilon)$ is large, then we have "low-frequency" gray level variations. The curve $S(\epsilon)$ thus gives us information about the rate of change of variations in the gray level surface.

After running the program on a dozen images, we have concluded that this algorithm is too sensitive to the great variance in outdoor scenery. For example, in Image 1, we have a background of trees only, no targets, while in Image 2 we have 2 distinct targets and no trees as background. Yet they both have similar graphs for the lower signatures. The lower signature represents more of the shape of the hot objects in the image, but in one we have 2 distinct hot objects (Image 2) and in the other (Image 1), none. Also, in Image 3, we have a target with a road and a field as background, and in Image 4 we have the same, yet the graphs for the upper signatures for these images have a very distinct difference. The upper signatures should represent similar backgrounds, but we cannot draw that conclusion from

this data. The examples given in [8] are of a very regular texture and in a controlled environment.

It was hoped that these graphs would give a measure of gray level variation within an image, so that images with more variation would benefit from using more sensitive masks, such as the gradient masks. But this use of the algorithm did not produce data that leads to this conclusion.

II. The gaussian average operator. This operator has been utilized [10] to perform edge segmentation. This particular algorithm uses Gaussian filtering at different "scales" (different σ 's). Recall the Gaussian function

$$g(x,y) = \frac{1}{2\pi\sigma^2} \exp \left[\frac{-1}{2} \cdot (x^2 + y^2)/\sigma^2 \right]$$

Convolution with a Gaussian kernel function acts as an averaging filter, and using different values for σ gives different "resolutions" of details in the image. The image is convolved with the Gaussian kernel, and then an edge detector applied, one of a gradient type. This is done for decreasing values of σ . At each value of σ , that is, at each level, varying amounts of detail appear, with smooth, broad edges at higher values of σ down to disjoint short segments at smaller values of σ . The main thrust of this idea is to try to overcome the conflict of eliminating noise and insignificant edges while at the same time preserving the basic edges present in the image.

Each template that the image is convolved with represents a digital approximation of the Gaussian average operator. The Gaussian is chosen as it has been shown theoretically to *regularize* the ill-posedness of the derivative problem, (see [4], for example), and also because it is computationally inexpensive.

Convolution with a Gaussian blurs the image, and the degree of blurring is dependent on the size of the operator. An approximation of the Gaussian is used as convolution with the Gaussian itself is computationally too intensive. Let \mathbf{X} be a rectangular coordinate set, that is, $\mathbf{X} = \{ (i,j) : 0 \leq i \leq n, 0 \leq j \leq m \}$. The Gaussian average operator acts on an image $\mathbf{a} \in 2^{\mathbf{X}}$ and produces a blurred image \mathbf{b} in the following manner:

$$\mathbf{b} = \mathbf{a} \oplus \mathbf{g}$$

where $\mathbf{g} \in (\mathbb{R}^{\mathbf{X}})^{\mathbf{X}}$ and

$$g_{(x,y)}(i,j) = \frac{1}{2\pi\sigma^2} \exp \left[\frac{-1}{2} \cdot ((i-x)^2 + (j-y)^2) / \sigma^2 \right]$$

The parameter σ is called the resolution parameter. The smaller σ is, the more detail the Gaussian convolution will pick up. Thus, larger values of σ give broadly curving edges, and as σ decreases, the resolution becomes finer, that is, more detail is shown.

First, the initial image is convolved with σ large, say $\sigma = 4.2$. Then a gradient type edge detector is applied to this image. To this image is applied a weak thresholding, and a "coarse-level" edge image is produced. Then, σ is reduced by 0.5 to 3.7, and the thresholded image is convolved. Then the gradient edge detector is applied to this blurred image. There is no more thresholding done after the first one. This process is repeated until $\sigma < 1$. However, the edge detector algorithm has some decision rules about which pixels to keep for edge points, and when the new edge points are found, the old ones are thrown away. Since only a weak threshold is done, edge points at finer levels of resolution (= smaller σ) are kept. These edges are often collections of small, disjoint segments, "fuzzy" looking. Since at coarser levels the edges are usually strong and broad in comparison, this gives us a method for classifying different types of edges: the small, fuzzy edge segments often are texture borders or borders of shadows, and the strong "continuous" segments locate where the image can be modeled

closely to a step edge.

This algorithm was dependent on a specific edge detector algorithm, namely that of Canny's in an MIT Technical Report, which unfortunately was not made available in time for us to implement it. It appears that this approach to locating edge points is more useful than most. First, it distinguishes between the two main types of edges, those of textures and those created by a step edge model. Second, it can be made automated by implementation of an automated thresholding on the initial image, as the rest of the procedure is totally self-standing.

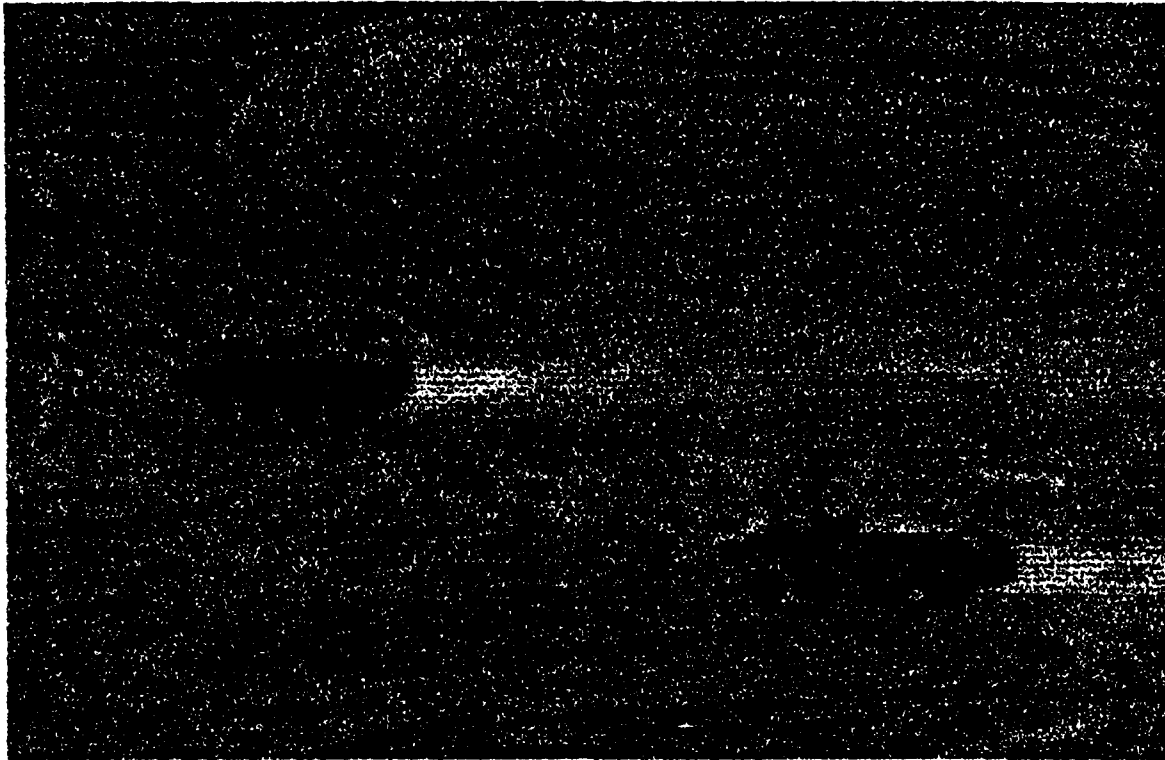
The value σ at which there is a distinct break between resolutions, if indeed there exists such a break, could be used for distinguishing between edges in texture and discrete step edges. This in turn could be utilized to decide which type of processing on the image was needed next, depending on the type of target sought, texture targets or otherwise. Also, if there was much noise in the image, there might be a value for σ at which the step or continuous edges broke up into "fuzzy" pieces, and the edge algorithm could then be stopped. This might then be declared as the "optimal" edge segmentation for this image.

III. Statistical Operators. During the course of this project, investigation of two well-known statistical transforms, the Karhunen-Loeve transform and the statistical differencing image enhancement method was performed. The Karhunen-Loeve transform is applicable to a series or sequence of images (multispectral images). It is a computationally intensive algorithm used for data compression, for example, and possibly not as "good" as simpler methods [11]. We decided not to research this transform any further, in the interest of time.

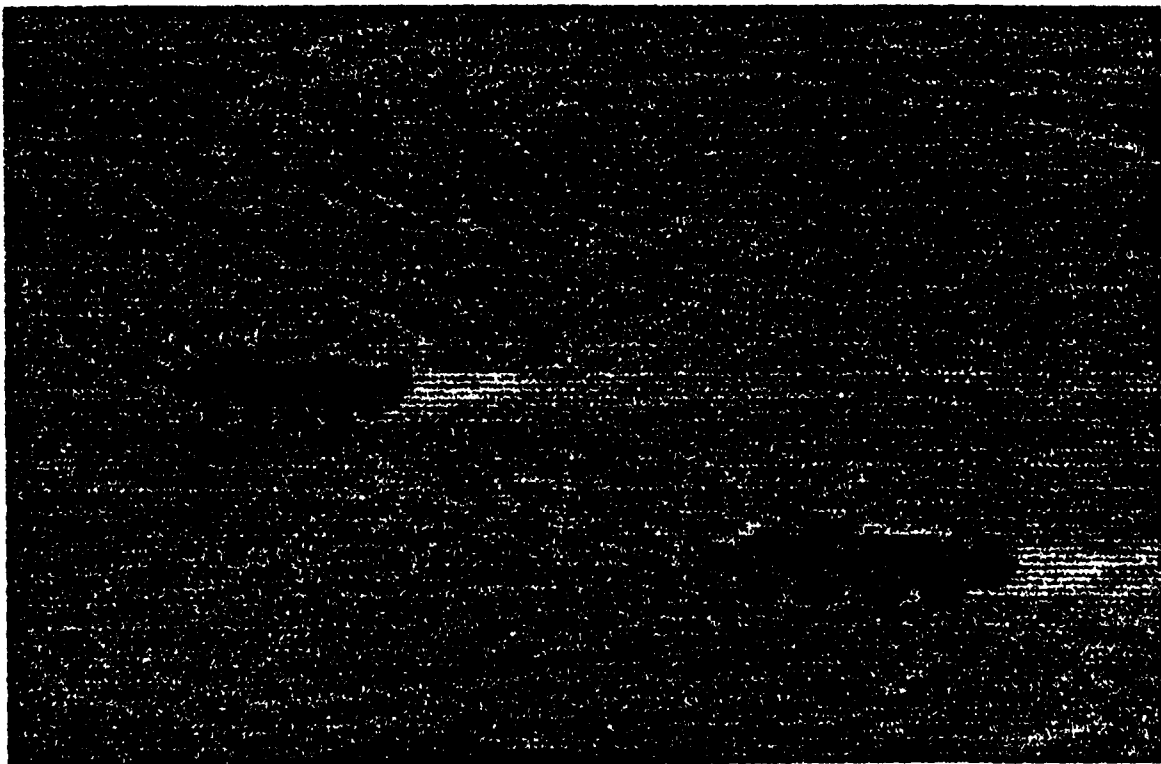
The statistical differencing method is used as an image enhancer [1], and we present a example of the generalized statistical differencing operator here. The mathematical computation, pointwise, is

$$b(i,j) = [a(i,j) - \bar{a}(i,j)] \cdot \left[\frac{gf \cdot \sigma_d}{gf \cdot \sigma(i,j) + \sigma_d} \right] + \alpha m_d + (1 - \alpha) \bar{a}(i,j)$$

where \mathbf{a} is the input image, \mathbf{b} the output image, $\sigma(i,j)$ is the mean value of the image at point (i,j) (the averaged image), m_d and σ_d represent desired mean and standard deviation factors, gf is a gain factor that prevents overly large output values when $\sigma(i,j)$ is small, and α is a proportionality factor controlling the ratio of edge to background composition of the enhanced image. We present an example of this algorithm implemented on the image algebra Preprocessor on the following page.



The Input Image



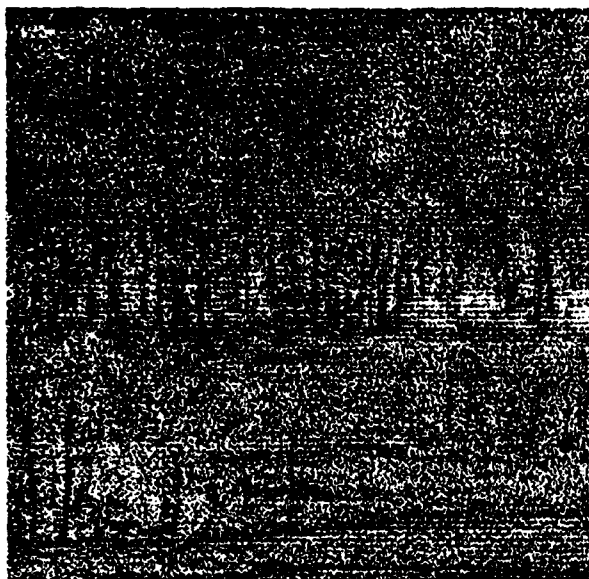
The Output Image

6. Conclusion. A search of the few pieces of available ATRWG literature revealed no useful image "metrics." A partial report on image metrics, the one by ERIM, was made available too near the end of the project to investigate. This report should be researched to see if there is any useful information applicable to edge detection. While global image measures described in the literature have already been tried, most do not give useful measures for ATR problems. One novel method we investigated, the fractal measure, also proved not too useful. Since there was a lack of positive results, it may be that this approach to solving the edge segmentation problem is not a valid one. Though there does not seem to be one "best" edge detector for any given image, Pratt [1] has shown in an edge performance comparison that the Sobel is one of the better performing ones on an image with synthetically produced edges. This does not mean, however, that it will work the best on a given specific image. Thus, until more useful measures are found, any approach that utilizes global measures of an image will not be a fruitful one, and so the approach to edge detection that we have taken cannot be investigated any further. Perhaps our lack of positive results shows that this is not a worthwhile approach to use in the edge segmentation portion of image processing. Since there are rarely exact step edges in real image data, edge detector algorithms that are based on locating single step edges will not be the most useful, as texture edges will not be correctly represented. Methods using a sequence of edge detectors in conjunction with a smoothing operator, such as edge focusing methods, may be more useful in locating both sharp edges and texture edges.

REFERENCES

1. W.K. Pratt, *Digital Image Processing*, John Wiley, New York (1978).
2. D. Marr and E. Hildreth, "Theory of Edge Detection," *Proc. R. Soc. London B* **207** (1980).

3. K. Shanmugan and et al., "An Optimal Frequency Domain Filter for Edge Detection in Digital Pictures," *IEEE Trans. on PAMI* 1 (Jan. 1979).
4. V. Torre, T. Poggio, "On Edge Detection," *IEEE Transactions on Pattern Analysis and Machine Intelligence PAMI-8* (1986), 147-163.
5. G. X. Ritter and et. al., "Image Algebra Tutorial, Version I," TR Image Algebra Project, F08635-84-C-0295, Eglin AFB, FL (1985).
6. G.X. Ritter, J.N. Wilson, J.L. Davidson, "AFATL Standard Image Algebra," UF-CIS Technical Report TR-87-04, Dept. of Comp. and Info. Sci., Univ. of Florida, Gainesville, FL (October 1987).
7. P. D. Gader, *Image Algebra Techniques for Parallel Computation of Discrete Fourier Transforms and General Linear Transforms*, Ph.D. Dissertation, University of Florida,, Gainesville, Fl. (1986).
8. S. Peleg and et. al., "Multiple Resolution Texture Analysis and Classification," TR, Center for Automation Research, University of Maryland, College Park, MD (July 1983).
9. B.B. Mandelbrot, *The Fractal Geometry of Nature*, Freeman, San Francisco (1983).
10. F. Bergholm, "Edge Focusing," *IEEE Transactions on Pattern Analysis and Machine Intelligence PAMI-9* (1987), 726-741.
11. P.C. Coffield, "Image Enhancement through Multispectral Data Fusion," Master's Thesis, University of Florida (1986).



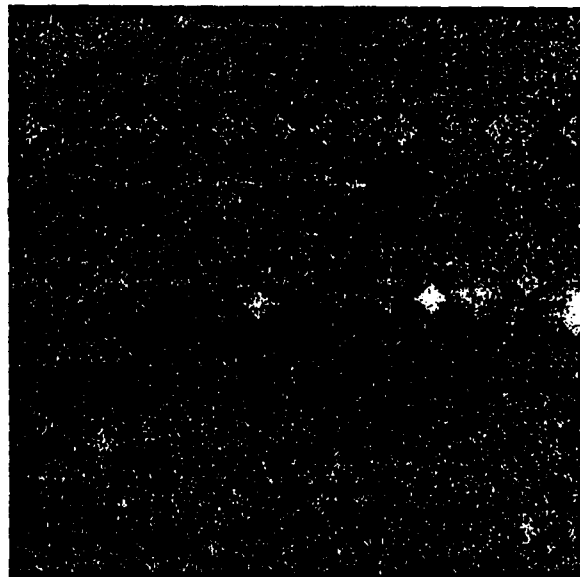
ORIGINAL 200 x 200 SUBIMAGE OF ERIM IMAGE im005.img



TENTH UPPER ITERATION FOR im005.img

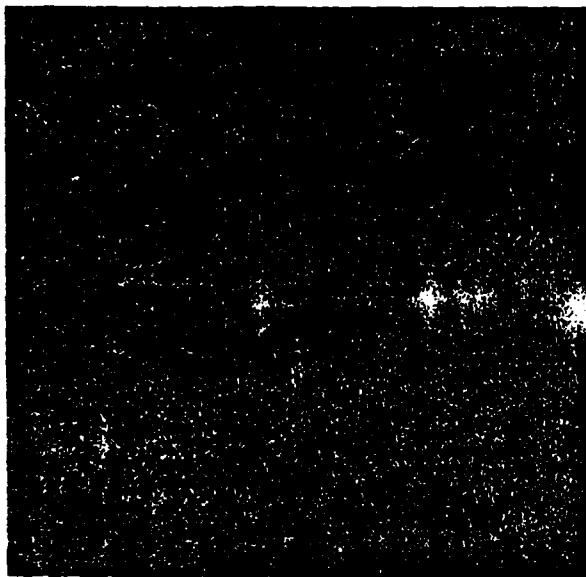


FIFTH UPPER ITERATION FOR im005.img

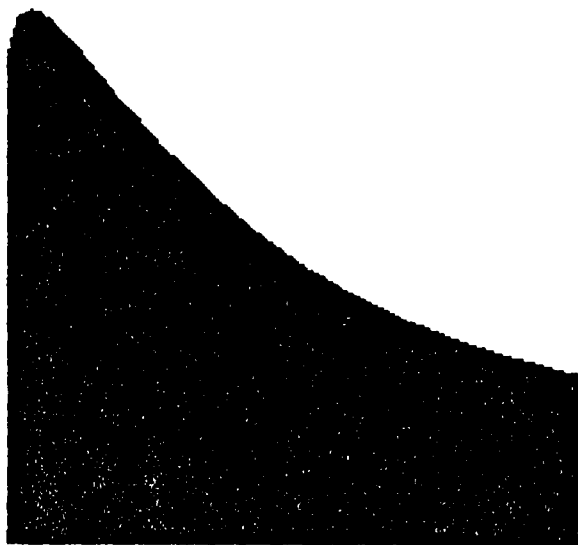


FIFTH LOWER ITERATION FOR im005.img

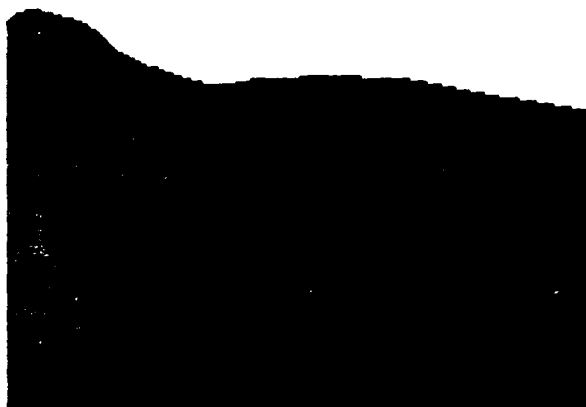
IMAGE I



TENTH LOWER ITERATION FOR im005.img

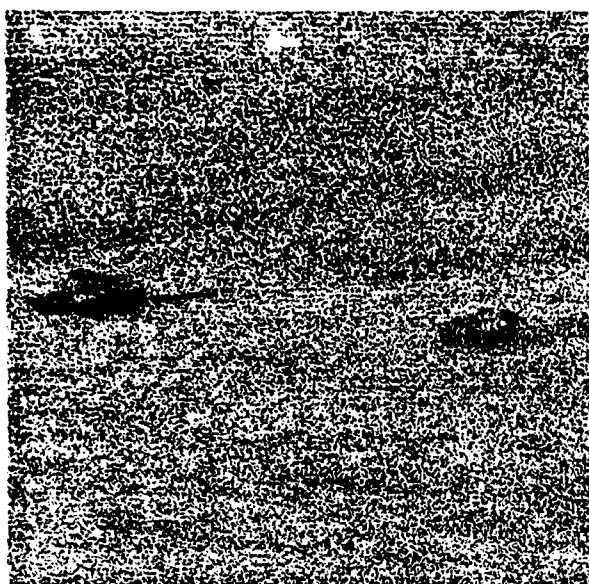


GRAPH OF LOWER SIGNATURE FOR im005.img

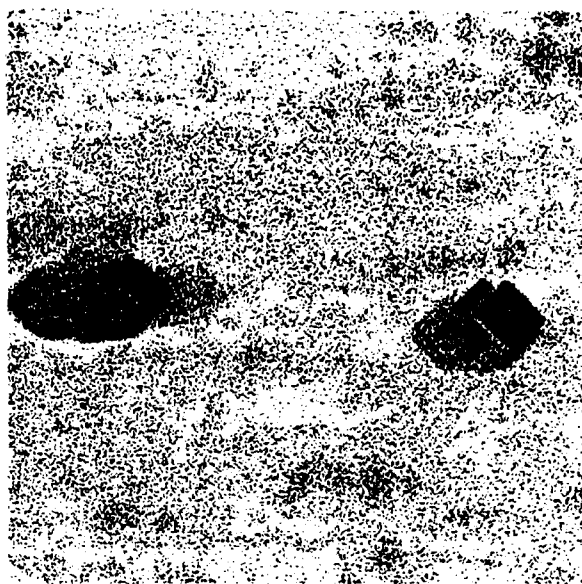


GRAPH OF UPPER SIGNATURE FOR im005.img

IMAGE I



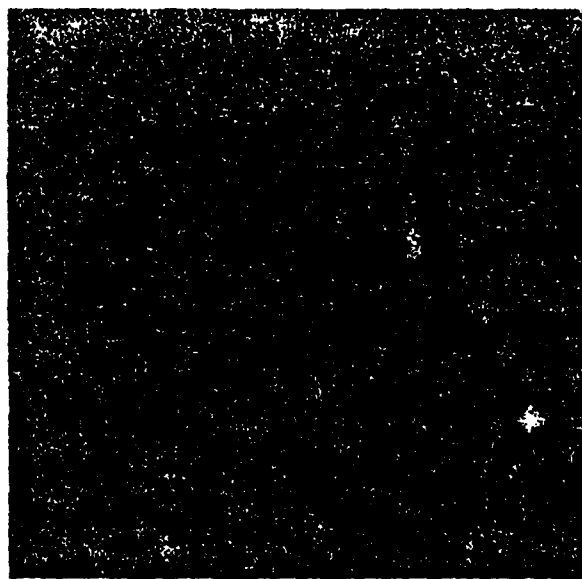
ORIGINAL 200 x 200 SUBIMAGE OF ERIM IMAGE im078.img



TENTH UPPER ITERATION FOR im078.img

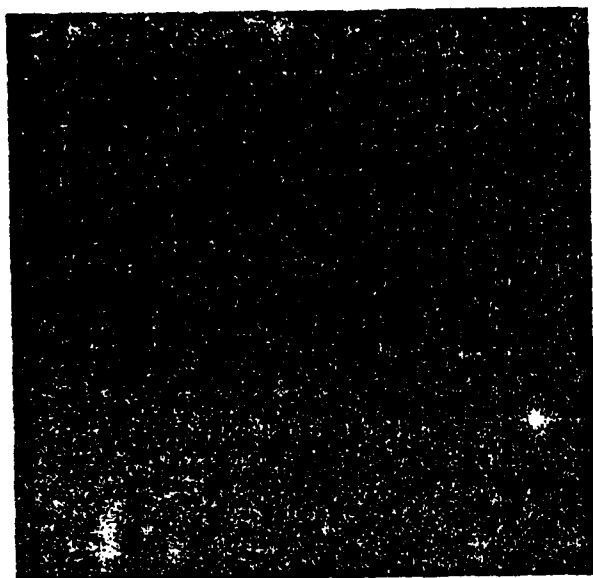


FIFTH UPPER ITERATION FOR im078.img

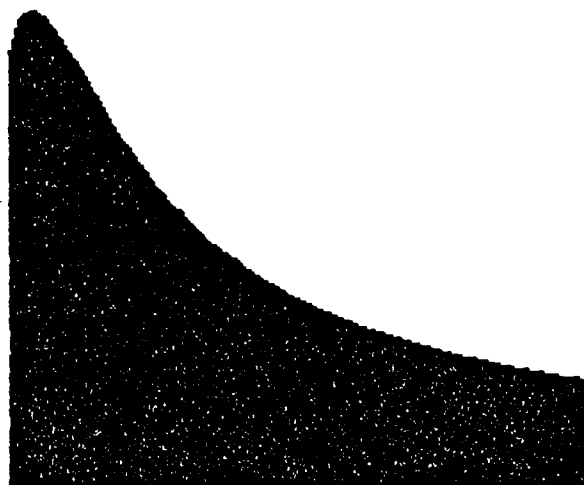


FIFTH LOWER ITERATION FOR im078.img

IMAGE II



TENTH LOWER ITERATION FOR im078.img

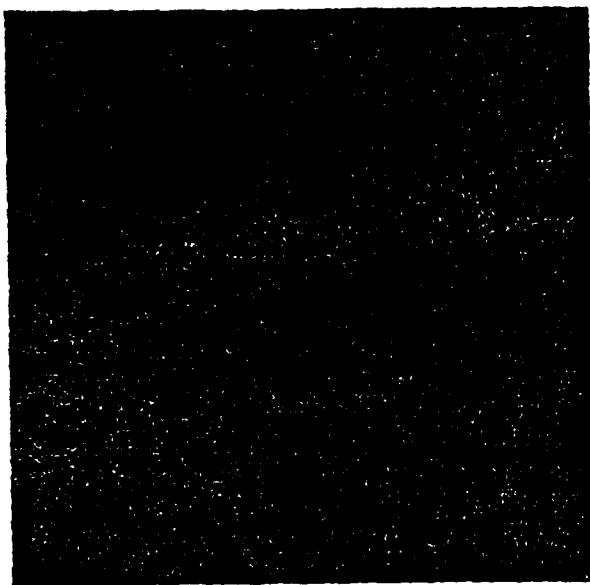


GRAPH OF LOWER SIGNATURE FOR im078.img

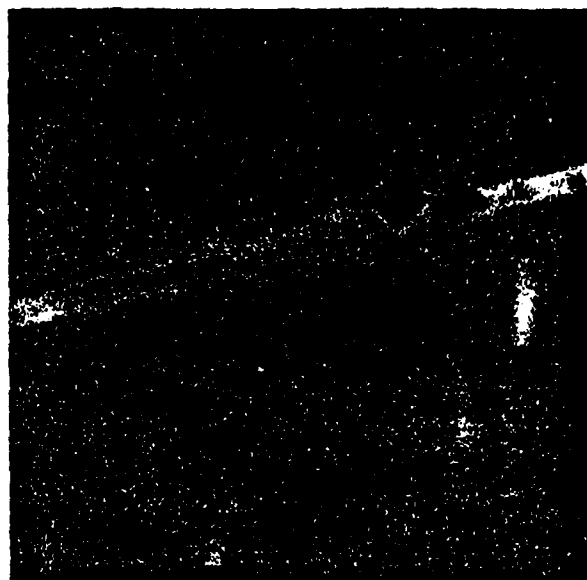


GRAPH OF UPPER SIGNATURE FOR im078.img

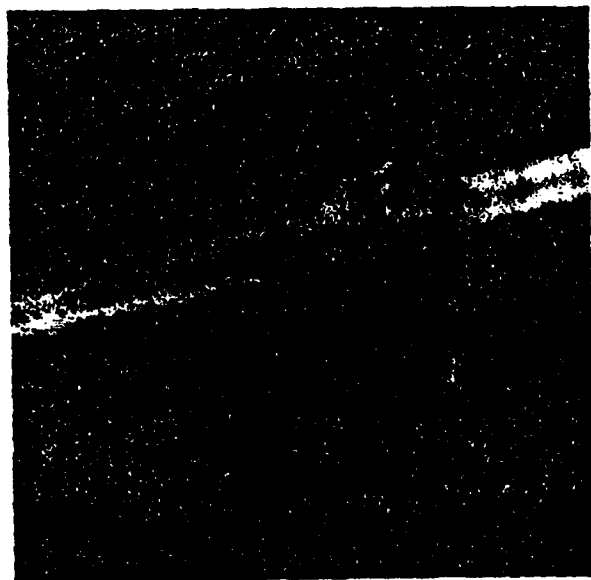
IMAGE II



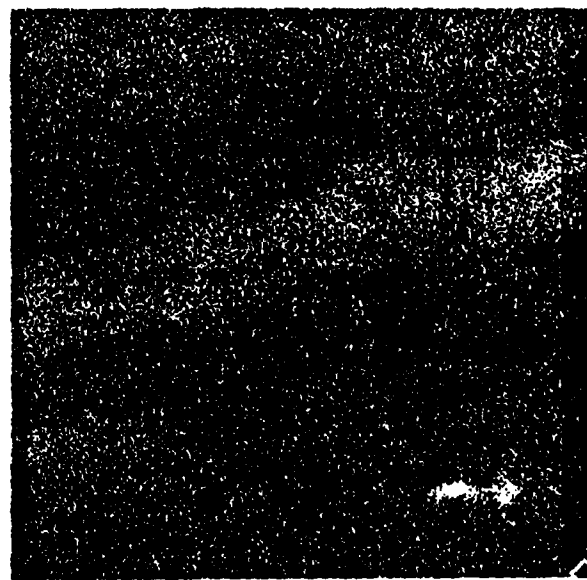
ORIGINAL 200 x 200 SUBIMAGE (#1) OF ERIM IMAGE im001.img



TENTH UPPER ITERATION FOR im001.img (#1)



FIFTH UPPER ITERATION FOR im001.img (#1)

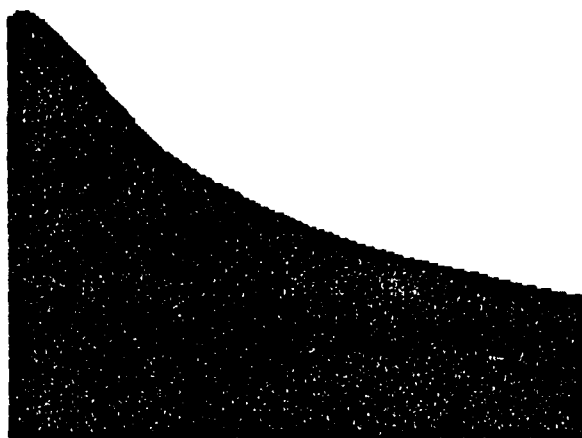


FIFTH LOWER ITERATION FOR im001.img (#1)

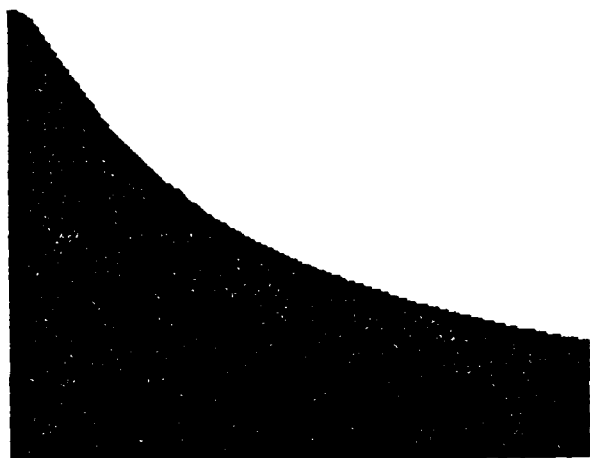
IMAGE III



TENTH LOWER ITERATION FOR im001.img (#1)

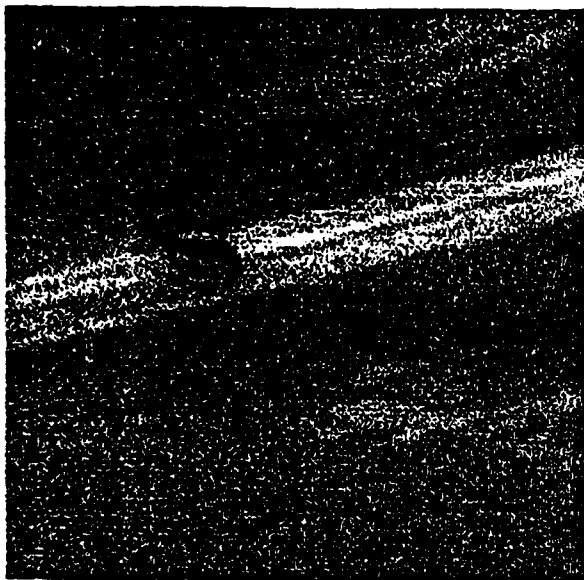


GRAPH OF LOWER SIGNATURE FOR im001.img (#1)

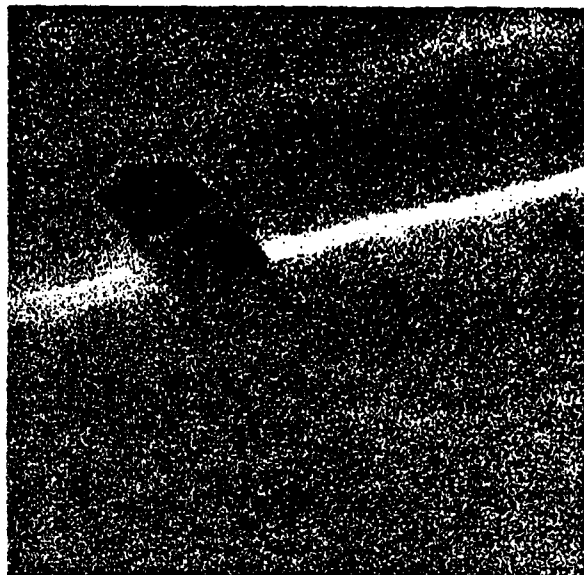


GRAPH OF UPPER SIGNATURE FOR im001.img (#1)

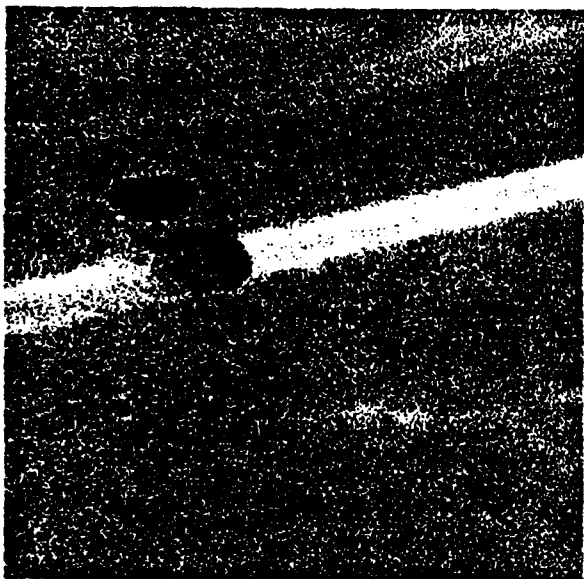
IMAGE III



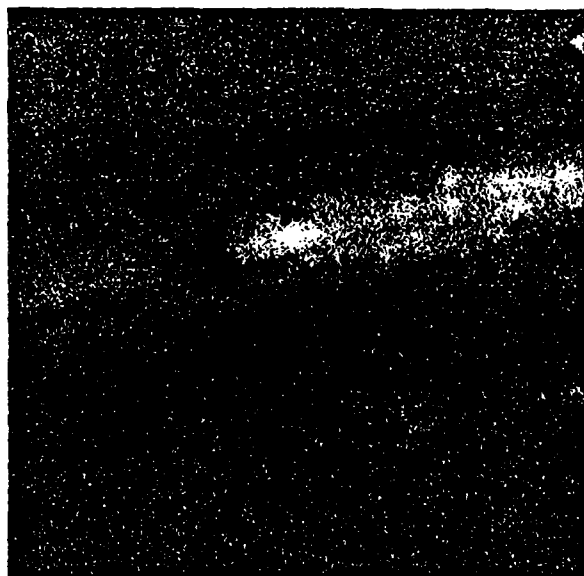
ORIGINAL 200 x 200 SUBIMAGE (#2) OF ERIM IMAGE im001.img



TENTH UPPER ITERATION FOR im001.img (#2)

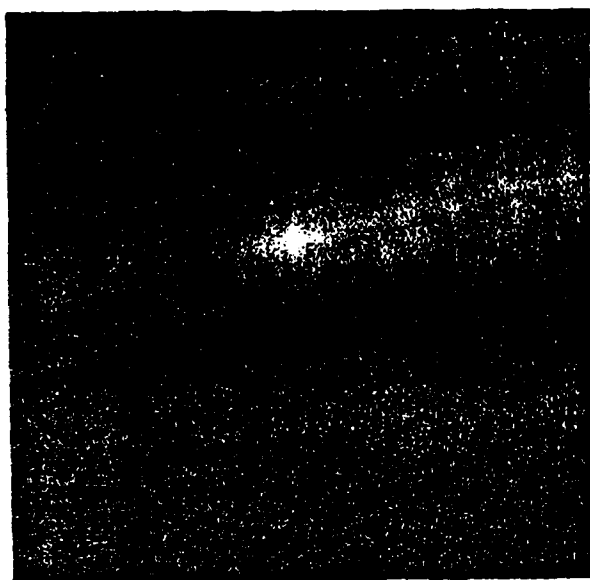


FIFTH UPPER ITERATION FOR im001.img (#2)

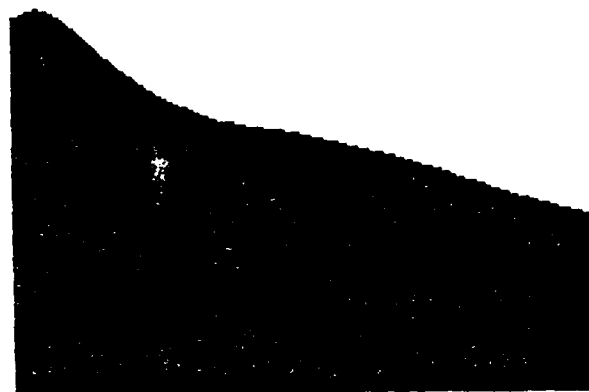


FIFTH LOWER ITERATION FOR im001.img (#2)

IMAGE IV



TENTH LOWER ITERATION FOR im001.img (#2)



GRAPH OF LOWER SIGNATURE FOR im001.img (#2)



GRAPH OF UPPER SIGNATURE FOR im001.img (#2)

IMAGE IV

FINAL REPORT NUMBER 4
REPORT NOT AVAILABLE AT THIS TIME
Dr. Joseph J. Feeley
760-7MG-070

FINAL REPORT
ADVANCED GUN GAS DIVERSION

Sponsored by the
AIR FORCE OFFICE OF SCIENTIFIC RESEARCH

Conducted by the
Universal Energy Systems, Inc.

Prepared by:	Elmer C. Hansen
Institution:	Department of Mechanical Engineering University of Florida
Date:	December 15, 1988
Contract Number:	F49620-85-C-0013

ACKNOWLEDGEMENTS

This research was sponsored by the Air Force Office of Scientific Research/AFSC Bolling AFB, DC, under contract F49620-85-C-D013 with Universal Energy Systems. I would like to thank the Air Force Office of Scientific Research and Universal Energy Systems for this support.

This project was successful because of the many people who helped by bringing their expertise to bear on the problem. I was given excellent support by Branch Chief Ron Boulet and the staff of the Fuses and Guns Branch at Eglin AFB. Project managers Ken Welzyn and Kirk Herzog helped in oversight of the project. Nunzio Zummo and the personnel of the Model Shop constructed precision hardware for the project. Ralph Terrero helped with designs, drawings, and testing of some of the hardware.

Finally, I would like to give due respect to God for giving the insight and understanding of the physical processes upon which this work was based.

INTRODUCTION

Definition of Problems

Advanced aircraft cannons produce large amounts of gun gas which can cause significant problems to the aircraft. When the gas is ingested by the engine it quickly fouls the engine and causes performance deterioration. The A-10 aircraft is a good example of this. The gun gas can also produce secondary flash which temporarily blinds the pilot and produces extra energy release near the airplane skin. Because the new generation of fighter aircraft will have cannons placed within the wing or fuselage, it is essential to understand the physics of diverting and controlling the gun gas.

Literature Review

A substantial body of information was found concerning secondary flash and various methods control it mechanically and chemically (Ref. 1-6). However, literature was not found which gave quantitative effects of various geometries on muzzle flow fields. This lack of design information required the following experimental work.

Objectives

1. Test various symmetrical and asymmetrical diverters using compressed nitrogen to determine diversion efficiency over a range of supply pressures.
2. Write and test a computer program to estimate the pressures, flows and average diversion efficiencies during the blowdown process.
3. Determine methods which might be able to reduce secondary flash.
4. Design and test diverters on high speed guns to test their effectiveness of gas diversion and of secondary flash suppression.

STEADY STATE DIVERSION

Experimental Apparatus

Because of the difficulty in measuring the flow out the muzzle of a gun, a simpler steady flow compressed gas apparatus was built to measure diversion efficiencies. The diversion efficiency was defined as the ratio of the mass diverted to the mass that continues along the muzzle axis downstream of the muzzle.

The apparatus consisted of a sonic nozzle run at an underexpanded condition. Various diversion devices were placed downstream of the nozzle. Three pressure transducers were used to measure the needed data. The apparatus is shown in Figure 1. The flow was from left to right. The pressure transducer upstream of the sonic nozzle measured the stagnation pressure of the gas.

The pressure transducer on the right measured the stagnation pressure of the flow which was continuing along the nozzle axis. Note that there must always be a hole along this axis to allow for travel of the projectile. The third transducer shown on the top measured the stagnation pressure of the diverted flow. The dimensioned shop drawing of the device is shown in Figure 2.

The hole downstream of the nozzle was 20% larger in diameter than the nozzle to allow for yaw of the projectile in an actual gun. The nozzle and the downstream hole run under choked conditions. Data were not used at pressures below choking. Diversion efficiency was obtained using the following equations.

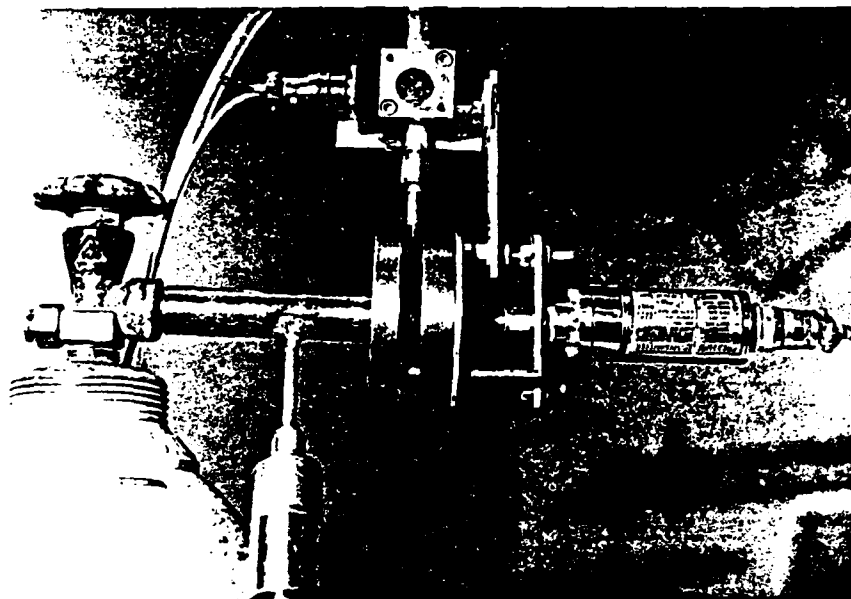


Figure 1 Photograph of the steady state gas flow apparatus used to measure diversion efficiency.

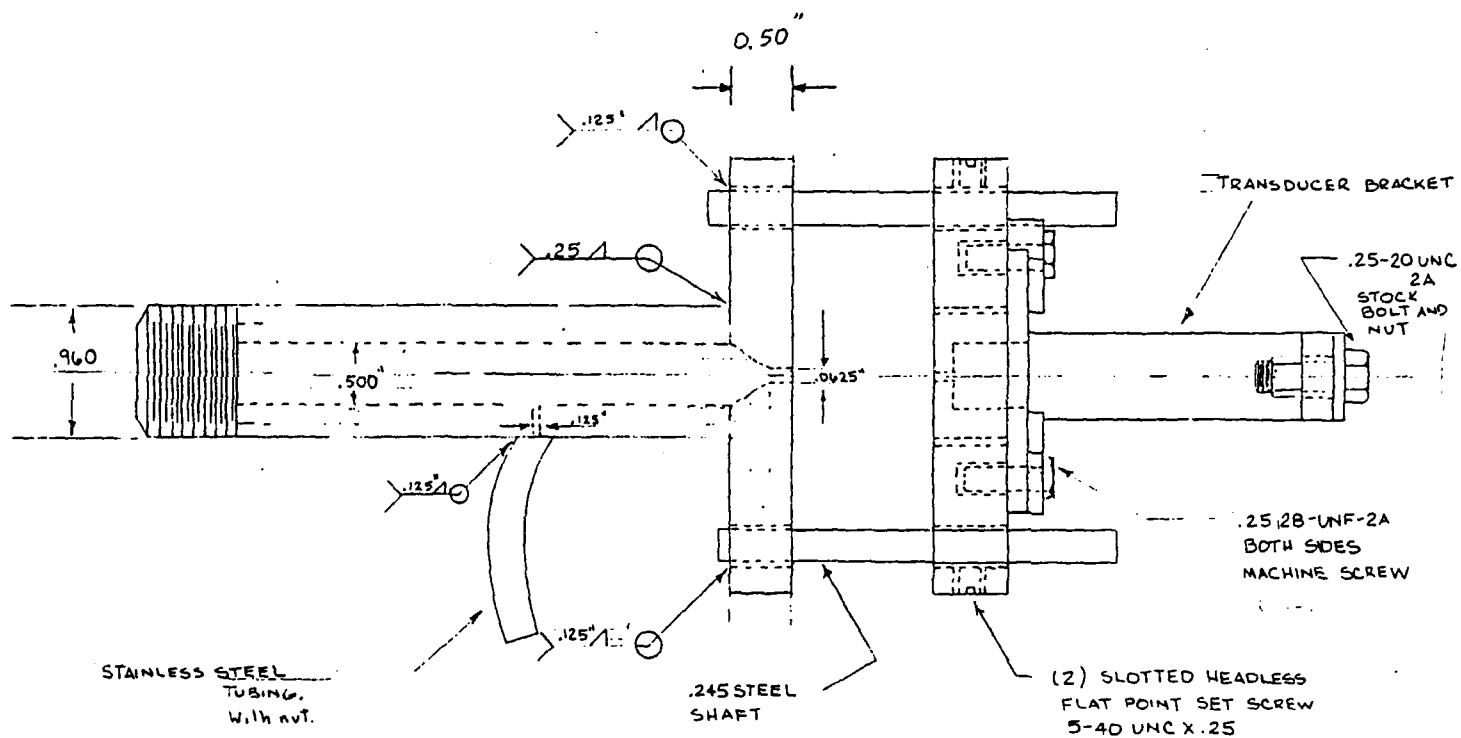


Figure 2 Drawing of the steady state gas flow apparatus used to measure diversion efficiencies.

choked flow

$$\dot{m} = A \rho_0 \left(\frac{2}{\gamma+1} \right)^{\frac{\gamma+1}{2(\gamma-1)}} \sqrt{\gamma R T_0}$$

diversion efficiency

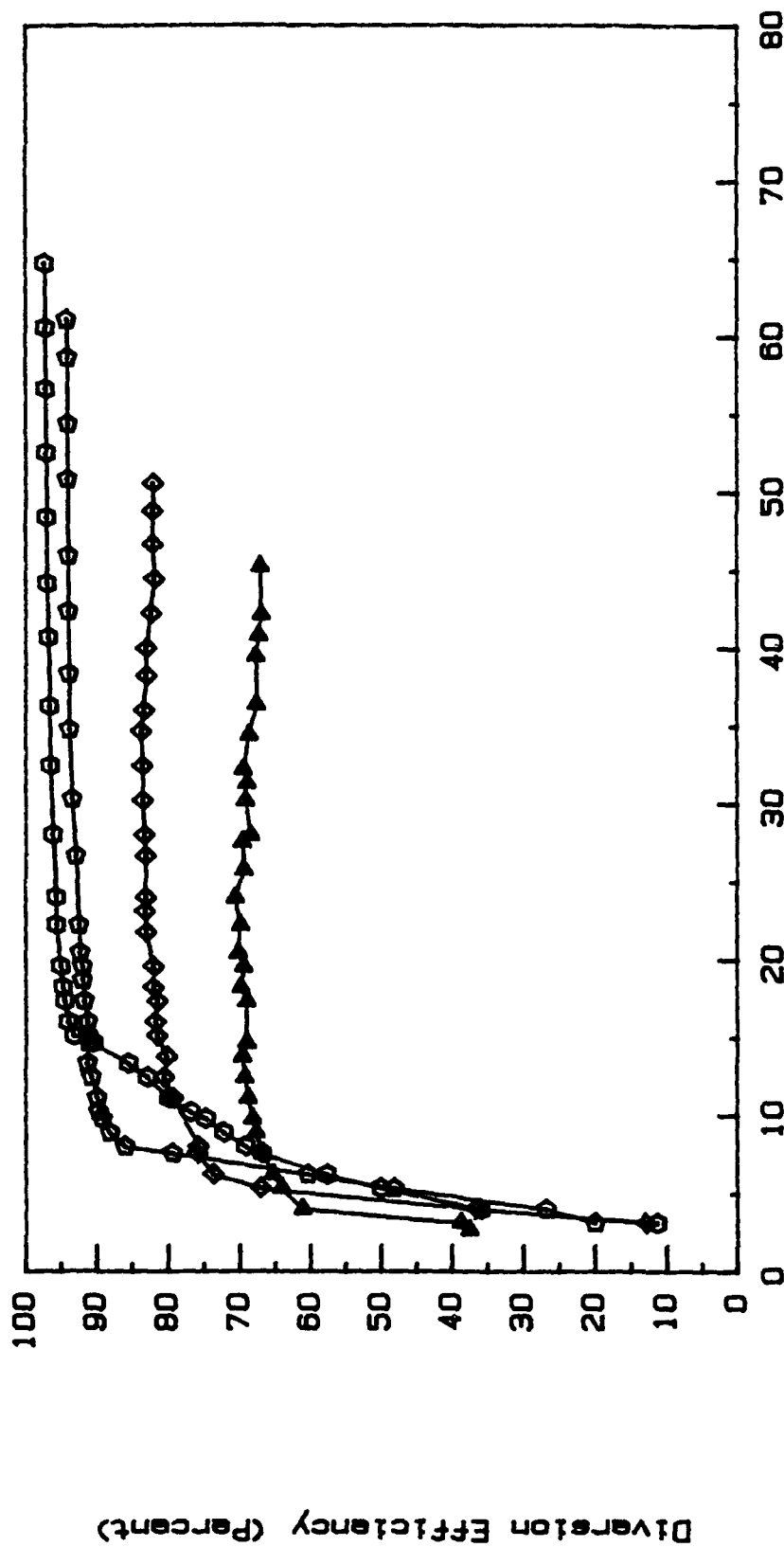
$$\eta = 1 - \frac{\dot{m}_{\text{not diverted}}}{\dot{m}_{\text{into diverter}}}$$

The amount of underexpansion of the nozzle was given by the ratio of the static pressure at nozzle to the stagnation pressure of the diverted flow. The diversion efficiency was considered to be dependent upon the underexpansion pressure ratio, the geometry of the diverter, and the specific heat ratio of the gas.

Single Plate Geometries

The simplest geometry to use for a diverter was a flat plate with one hole in it directly downstream of the sonic nozzle. This type of geometry is also the building block for multiple baffle diverters. The diversion efficiency for this type diverter is shown in Figure 3. The gas used in this test was nitrogen.

Efficiencies of 90% to 97% were attainable at $L/D = 7$. At the close spacing of $L/D = 1$, the efficiency may be as low as 67% to 70%. Figure 3 would suggest that L/D from 4 to 7 would be the best type of



Pressure Ratio P_{muzzle} / P_o diverter

Figure 3 Diversion efficiency of a flat perforated plate diverter using nitrogen gas. $L/D = 1$ ▲ ◻ 4, ◻ 7 ○.

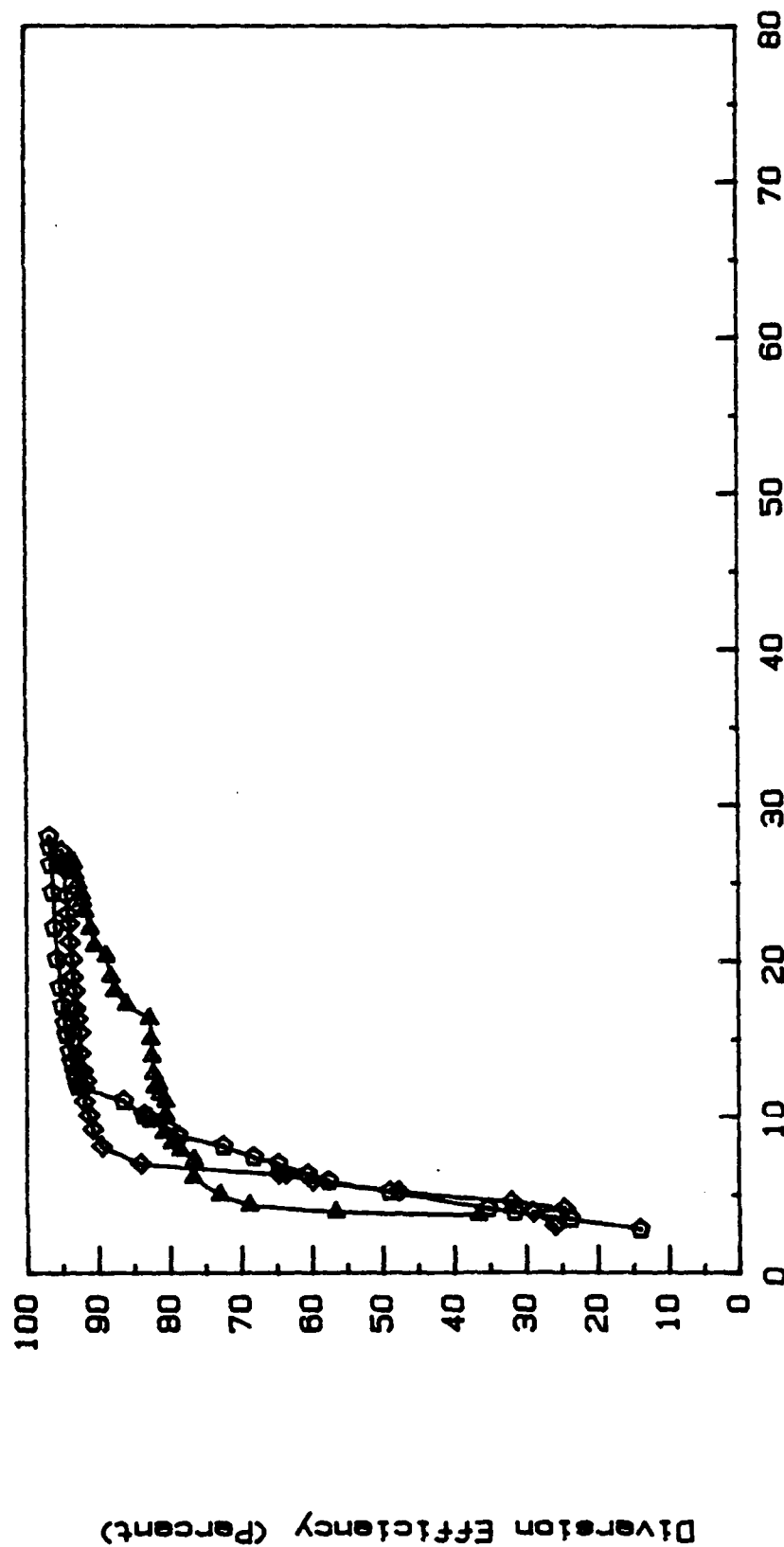
single plate diverter. Note that at low pressure ratios the small L/D geometries have better efficiencies than the larger L/D geometries. This phenomena will show itself again in double plate geometries.

The effect of the specific heat ratio was determined next. Nitrogen has a specific heat ratio of 1.4 and carbon dioxide has a specific heat ratio of 1.3. The approximate specific heat ratio of gun gas is 1.25. Figure 4 shows the diversion efficiency of a single plate diverter using carbon dioxide. For the most part the results are quite similar to the nitrogen case of Figure 3. Large pressure ratios were not obtained because of a limitation on the pressure of the carbon dioxide in the tank.

Nitrogen was used in all the tests except for the tests shown in Figure 4 which used carbon dioxide. Because the results shown in Figures 3 and 4 were so close it was assumed that nitrogen would be an acceptable gas to model gun gas for the following geometries. Two additional advantages of nitrogen are that it is easier to work with and that the bottles come at a pressure 2.5 times that of carbon dioxide.

Double Plate Geometries

Next two plates were used as the diverter geometry. The first plate was placed at $L/D = 3.5$ downstream of the sonic nozzle. The plate was $L/D = 0.4$ thick. The second plate was placed $L/D = 3.5$ downstream



Pressure Ratio $P_{\text{muzzle}} / P_{o \text{ diverter}}$

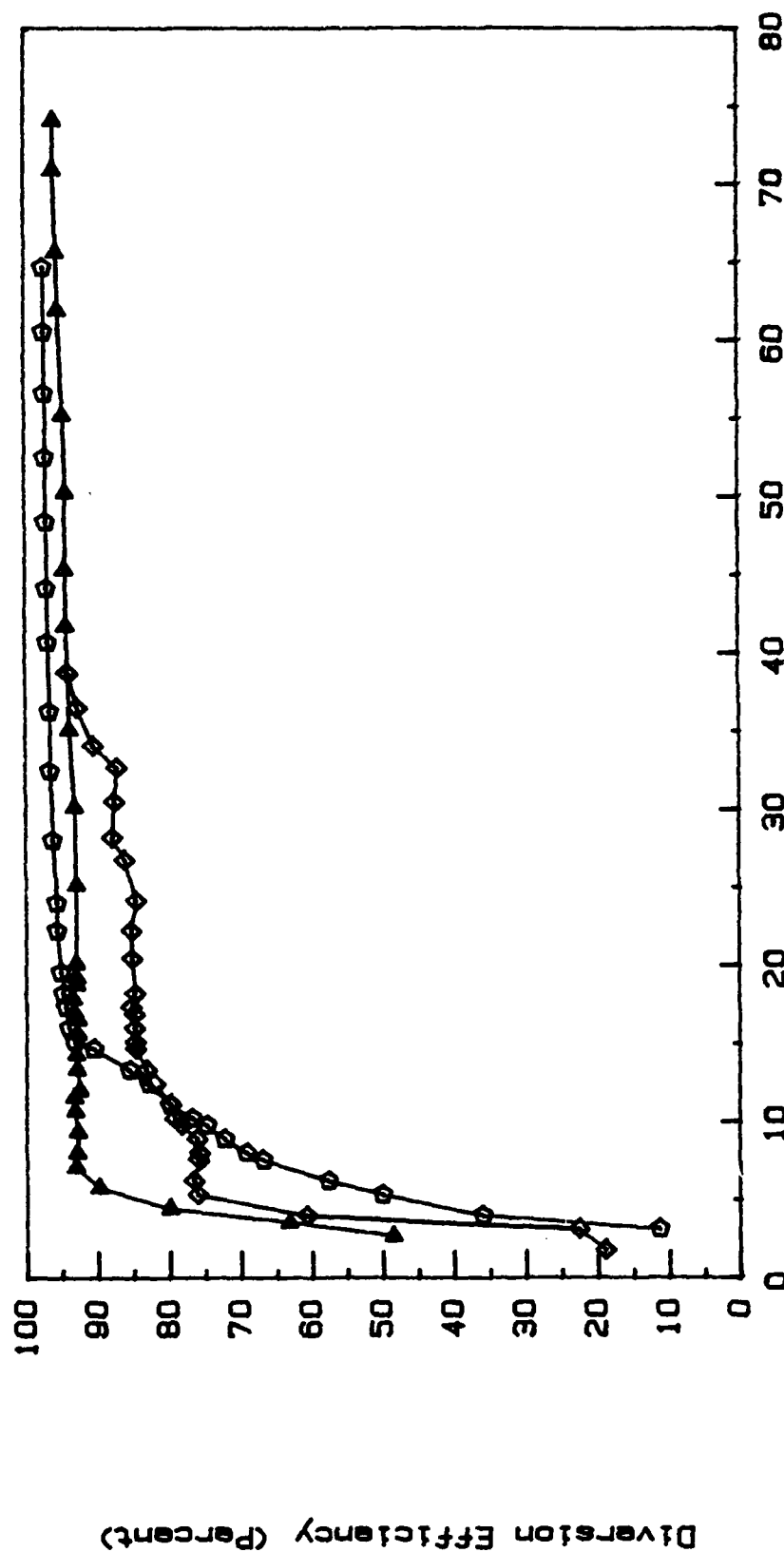
Figure 4 Diverion efficiency of a flat perforated plate diverter using carbon dioxide gas. $L/D = 2$ \blacktriangle ; 4 \diamond ; 7 \circ .

of the back of the first plate. A second two plate diverter with plate to plate distances of $L/D = 2$ was also tested. The resulting efficiencies are shown in Figure 5. At high pressure ratios the two plate diverters do not have as high an efficiency as the single plate $L/D = 7$ diverter. However, the two plate diverters do have the feature that at low pressure ratios they retain a diversion efficiency higher than the single plate diverter.

The effect of the position of the first plate on efficiency was determined and shown in Figure 6. Each of the three diverters shown in Figure 6 has an overall length of $L/D = 7$. The distance of the first plate to the nozzle was $L/D = 2$ or 3.5 or 5. The results show very little difference at high pressure ratios. At medium pressure ratios (20) the plate farther from the nozzle has an advantage of over 4% as compared to the closest plate. At pressure ratios below 7 the closest plate has the advantage over the other geometries.

Asymmetrical Geometries

Three asymmetric geometries were studied next as possible diverters. The wide and narrow v's with an $L/D = 7$ are shown in Figure 7. The pipe with three holes is shown in Figure 8. The efficiencies of these geometries are shown in Figure 9. The v's have quite high efficiencies which extend to very low pressure ratios. The wide v efficiency was 94% to 99% at pressure ratios above 10. The narrow v had an efficiency from 90% to 97% over the same pressure ratio range. The pipe with holes only had an efficiency in the upper 70's. This is probably due to the lack of exit flow area.



Pressure Ratio $P_{\text{muzzle}}/P_{o \text{ diverter}}$

Figure 5 Diverseion efficiency of two flat perforated plates using nitrogen $L/D = 7$ ▲ $L/D = 14$ ◆ . Compared with a single perforated plate diverter $L/D = 7$ ◆ .

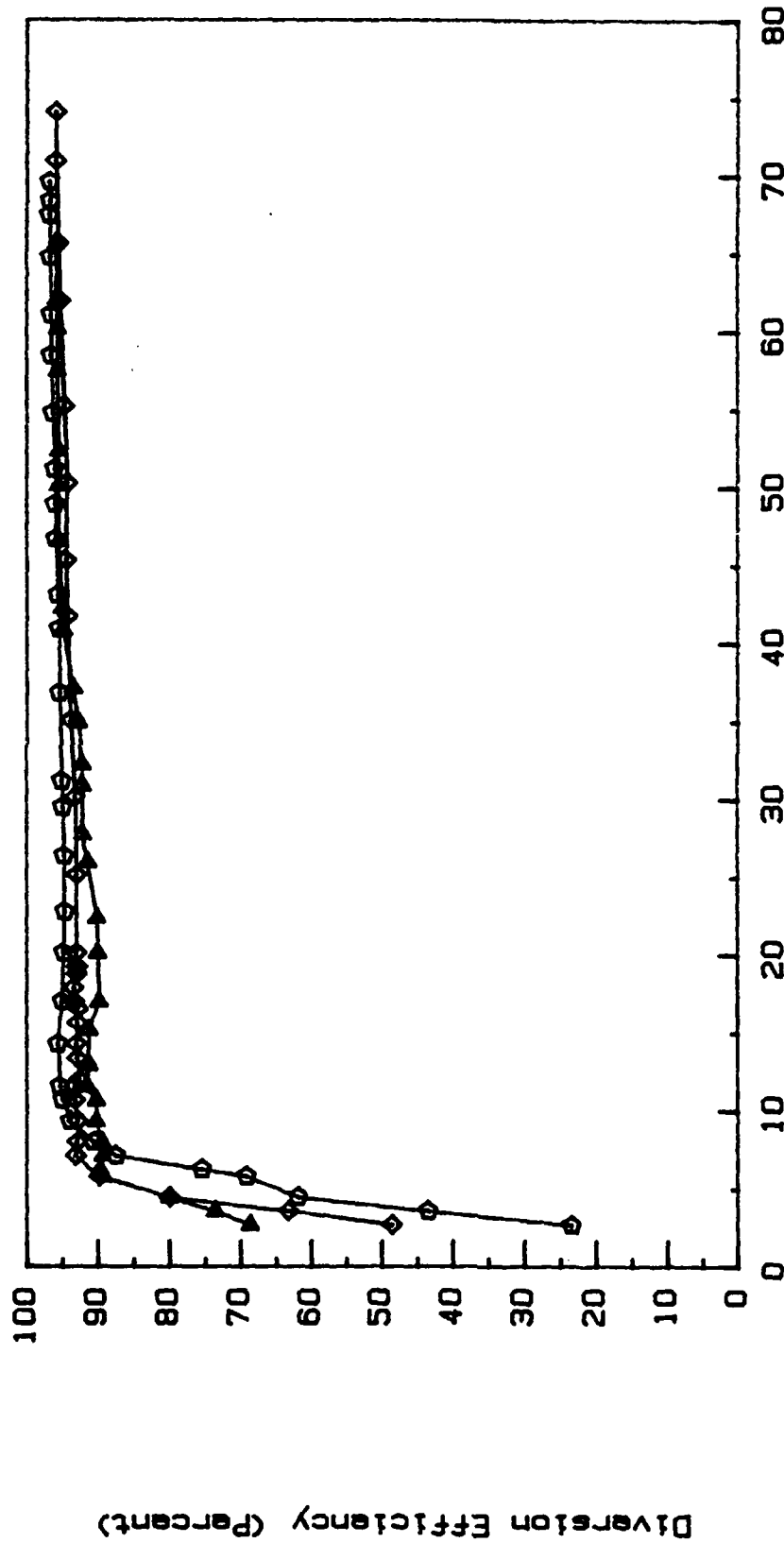


Figure 6 Diversion efficiency of three flat perforated plates using nitrogen. $L/D = 7$. The spacing of the first plate from the nozzle is $L/D = 2$ ▲ ; 3.5 ◆ ; 5 ○ .

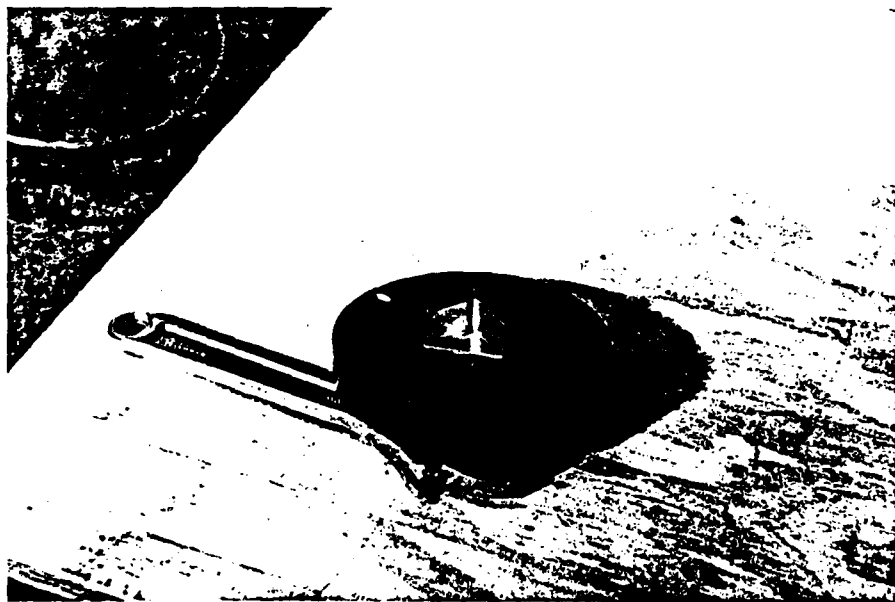
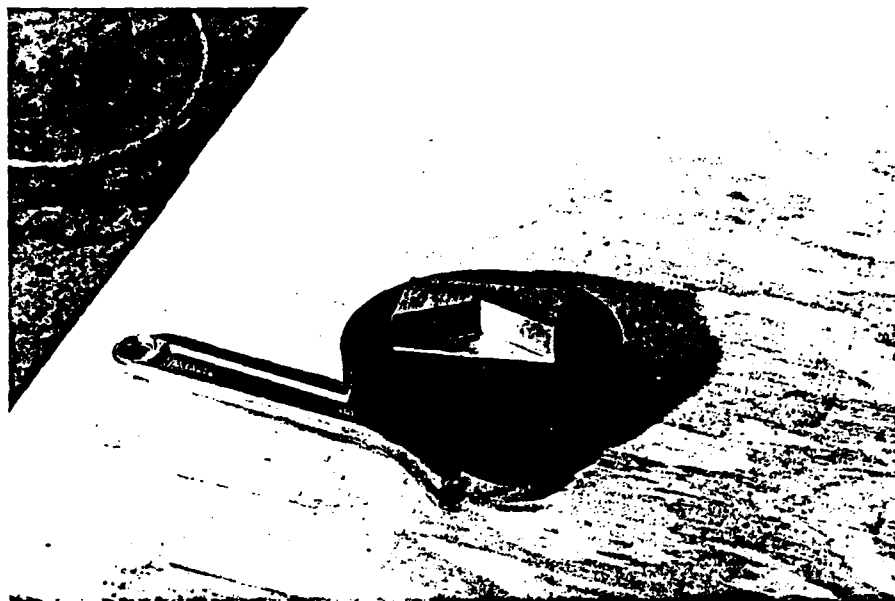


Figure 7 Wide v (upper) and narrow v (lower) used in the steady state test apparatus to measure diversion efficiency. $L/D = 7$.

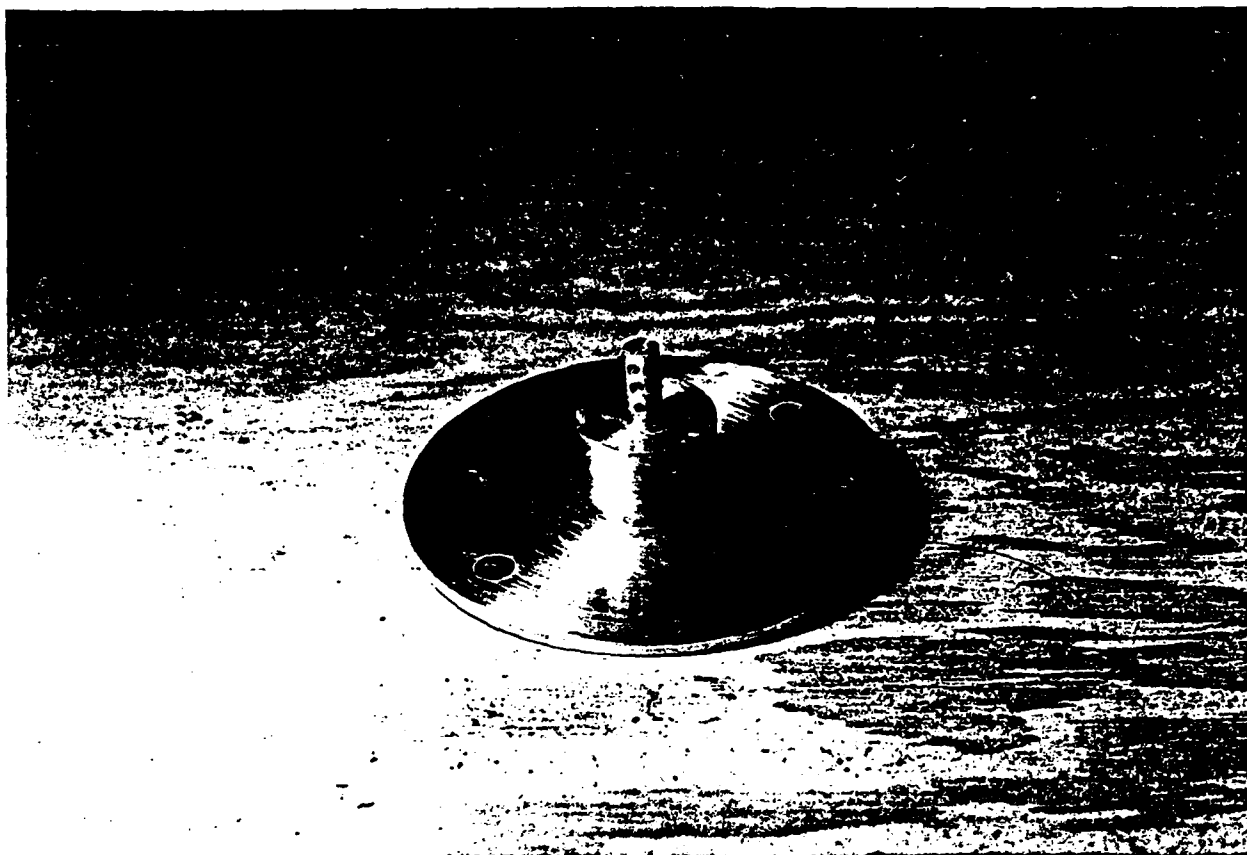


Figure 8 Pipe with holes geometry ($L/D = 8$) used in the steady flow apparatus to measure diversion efficiency.

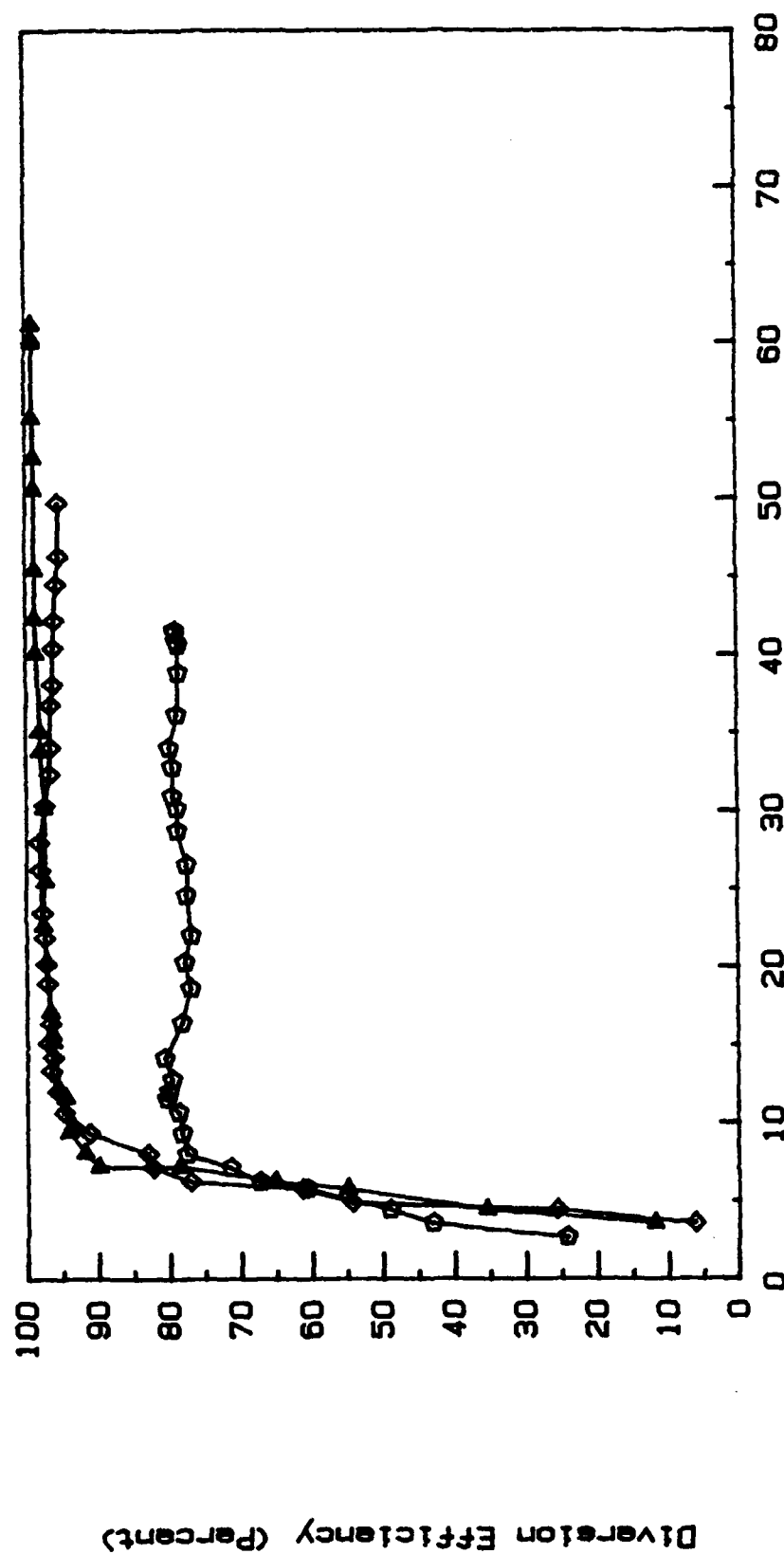


Figure 9 Diverston efficiency of a wide v ▲ , a narrow v ◊ , and a pipe with six side holes ○ . Each v has $L/D=7$ and pipe has $L/D = 8$.

Interpretation of Data

A cross-plot of the data in Figure 3 is shown in Figure 10 and reveals two phenomena which are divided at a pressure ratio of about 10. Above 10 the efficiency increases with length. Below 10 the efficiency peaks and then drops off. The physical reason for this is not yet understood. However, the practical use of this knowledge is quite evident. When diverter pressures are high (causing low pressure ratios), closely spaced multiple plate geometries are required to produce high overall diversion efficiencies.

UNSTEADY DIVERSION

Quasi-steady Equations of Motion

Using the previously measured efficiencies and a model for the flow out the throat of the diverter, a computer program was written to determine the pressure time history in the diverter and the average efficiency during the blowdown of the ballistic cycle. It was assumed that the flow out of the diverter was choked as long as the pressure was above 28 psia. The equations used to model the flow are given as follows.

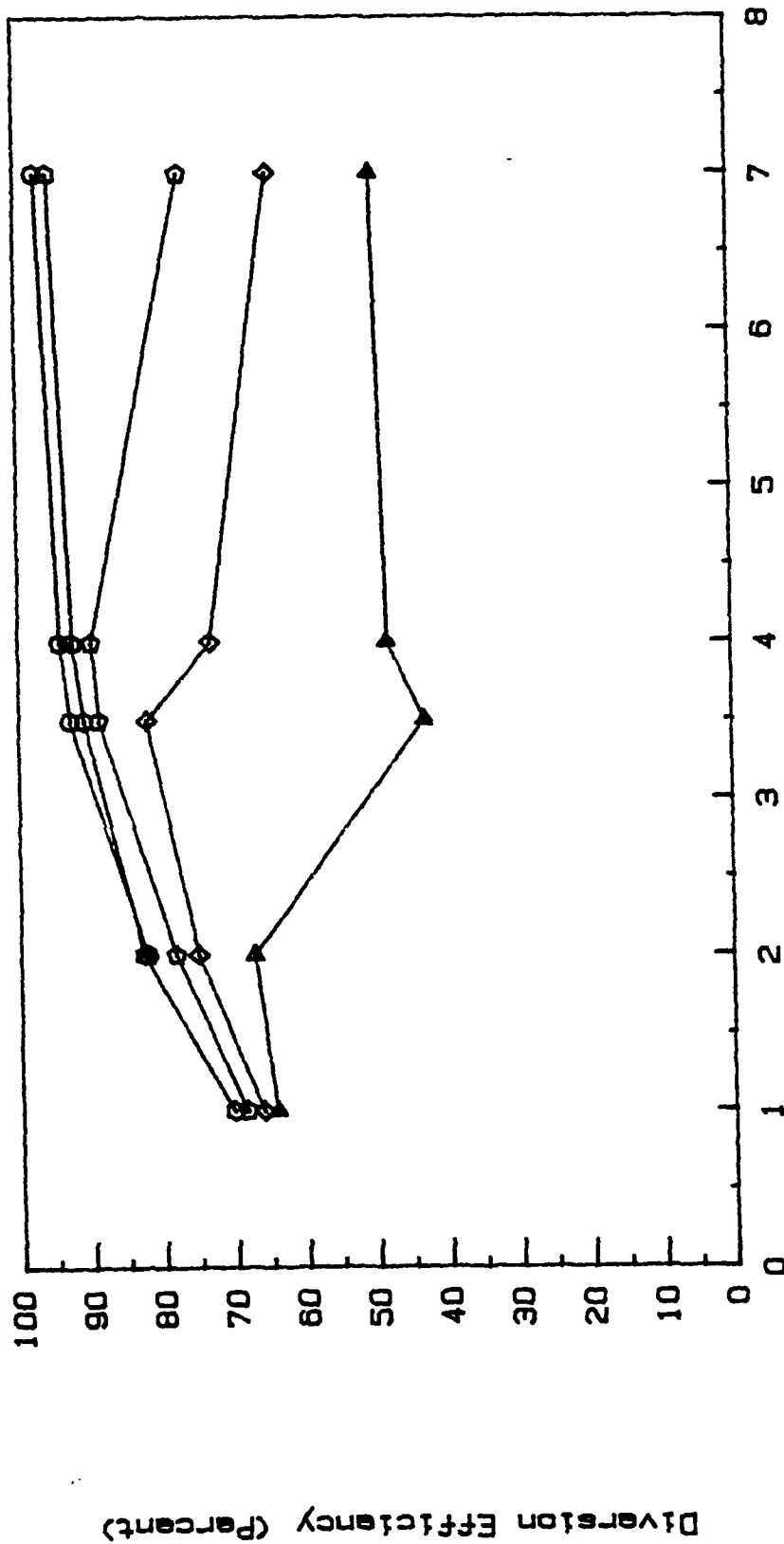


Figure 10 Crossplot of data for the efficiency of a single perforated plate diverter using nitrogen gas. Pressure ratios of 5 ▷ ; 7 ◇ ; 10 ◊ ; 20 ○ and 50 ◌ .

choked flow

$$\dot{m}_{out} = A_{throat} \rho_0 \left(\frac{2}{\gamma+1} \right)^{\frac{\gamma+1}{2(\gamma-1)}} \sqrt{\gamma R T_0}$$

conservation of mass

$$V_{diverter} \frac{d\rho_0}{dt} = \dot{m}_{in} - \dot{m}_{out}$$

$$\text{mass flow rate from muzzle } \dot{m}_{in} = 8 m_{propellant} \left(1 + (65.7 - 6190t) t \right)^{-9} (65.7 - 12,380t)$$

This computer program (Appendix B) was used to model a rectangular diverter (details of which will be discussed later) during an advanced gun blowdown. The results are shown in Figure 11. Several volumes were used to show the effect of volume on the blowdown process. The computer model assumes that the volume is filled with gas at the stagnation density. This is not quite true. The average density will probably be significantly less than the stagnation value. To account for this in the computer program the diverter volume can be reduced.

Generic Diverter Design

The computer program (Appendix C) was then run for 575 combinations of volume and outlet area for two kind of diverters. The first diverter was a single plate diverter with $L/D = 7$. The result

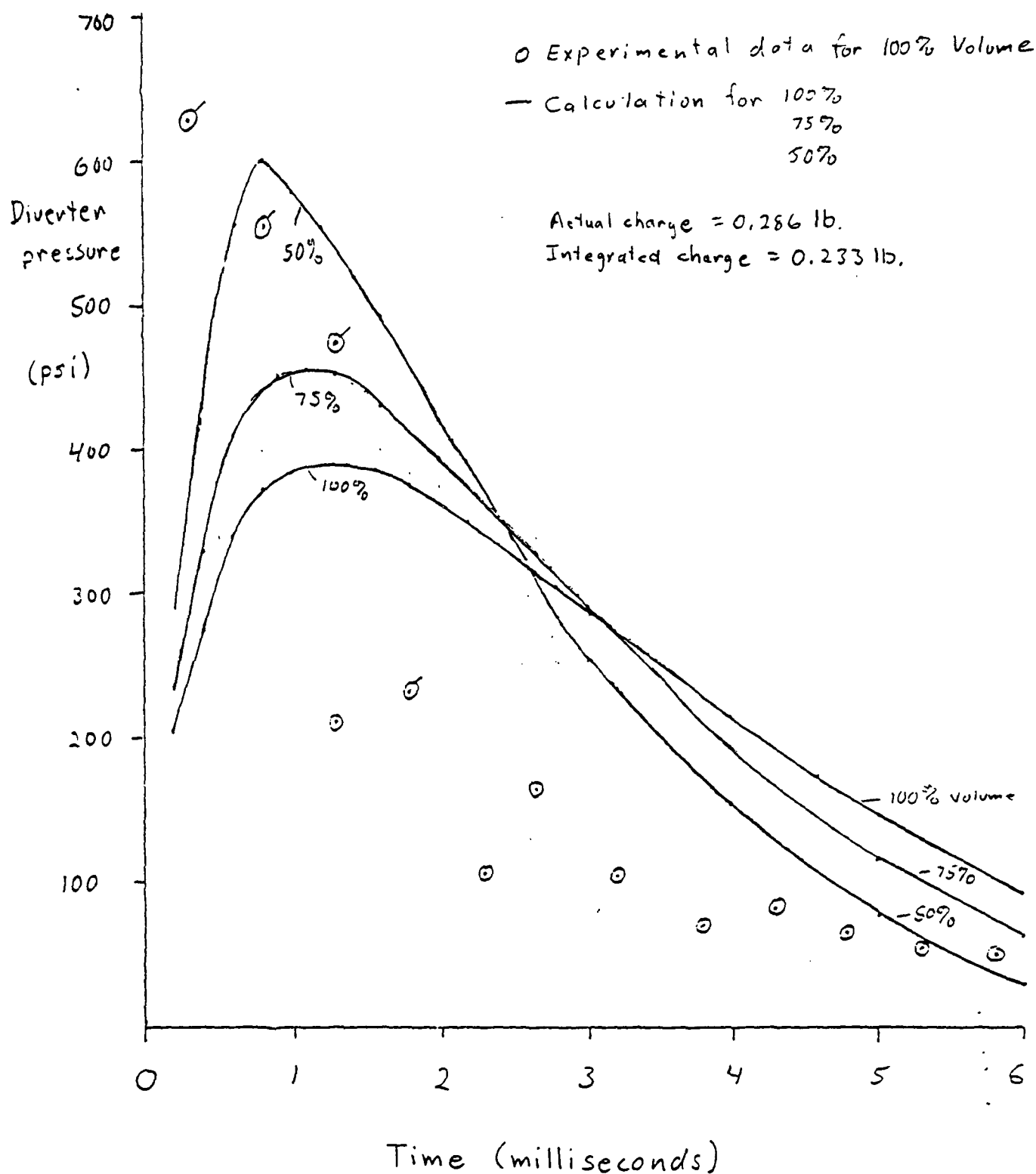


Figure 11. Pressure time traces, measured and computed, using advanced gun and rectangular diverter.

Area
sq.in.

Figure 12 Variation of diversion efficiency for 575 generic diverter designs. Outlet area increases down the page from 2 to 50 square inches. Volumes increase from 120 cubic inches at the left to 1000 cubic inches on the right. The diverter simulated has one downstream perforated plate $L/D = 7$.

(Figure 12) shows that a 90% efficient diverter will result if the throat area is greater than 34 square inches. The volume can range from 120 to 1000 cubic inches. The efficiencies of a double plate diverter with $L/D = 7$ are shown in Figure 13. Again diverters with throat areas over 34 square inches will produce an average diversion efficiency of 90%. The double plate diverter produced a diversion efficiency of 85% at an throat areas as low as 18 square inches.

By using the experimental data to obtain diversion efficiencies, gun gas diverters can be designed to use minimum volume and minimum throat area. The operation of these diverters can be predicted using the computer program found in Appendix B. The rectangular diverter that will be described in the following section is a example of a diverter that was successfully designed based using these principles.

SECONDARY FLASH REDUCTION MECHANISMS

Secondary Flash

Although diverters can be designed to turn gun gas using minimum volumes and minimum flow areas, the problem of secondary flash is not eliminated. Secondary flash in a minimum volume and area

Area
sq.in.

Figure 13 Variation of diversion efficiency for 575 generic diverter designs. Outlet area increases down the page from 2 to 50 square inches. Volumes increase from 120 cubic inches at the left to 1000 cubic inches on the right. The diverter simulated has two downstream perforated plates $L/D = 7$, $(3.5+3.5)$.

diverter will occur at the exit area using the advanced gun ammunition. The question was then asked "What can now be done to the geometry of the diverter to eliminate secondary flash?"

Secondary flash is the result of two mechanisms, heat and mixing. The high temperature and velocity of the gases produce a high stagnation temperature. After exiting the muzzle, the highly underexpanded gas accelerates to a Mach number of at least 5. This was indicated in the steady state nitrogen tests. The flow then passes through a normal shock producing a subsonic velocity and returning the static temperature to near stagnation values. At the same time, the flow in the shear layer at the boundary of the gas and the air curls up in a smoke ring. This smoke ring moves downstream from the muzzle and entrains air into the central hot core of gas. When enough oxygen is present, the secondary flash occurs. The two major problems to be overcome to prevent secondary flash are temperature and mixing.

Heat and Mass Transfer

The methods investigated to overcome the problems of temperature and mixing were heat transfer, mass transfer, and rapid expansion. Heat transfer to a large area of fins seemed to theoretically be able to lower the temperature of a short burst firing. Multiple firings soon deplete the ability of the fins to absorb the heat. To overcome this the fins could be made of an

ablating material with a large heat of evaporation. Zinc was identified as one such material. An attempt was made to test the effect of heat transfer. However, a needed rectangular test fixture had been rendered inoperative and could not be used.

Rapid Expansion

Before the heat transfer concepts could be tested a much more viable and useful method was found. This method is called rapid expansion. It serves to address the problems of temperature and mixing. This method can be thought of in thermodynamic terms as an isentropic expansion of the gun gas that does work on the surrounding air. Doing work on a large amount of air will substantially reduce the temperature of the gun gas. To accomplish this the gun gas must flow through a widely diverging supersonic nozzle. This large exit area then tends to prevent the formation of a smoke ring and the subsequent rapid mixing of air and gun gas. The round and v diverters described in the gun test results are examples of such devices.

A computer program (Appendix D) was written to determine the flow of gas behind the shock wave of the expanding gun gas. Figure 14 shows the predicted travel of the gas compared to the bounded results from highspeed photographs of tests using the round diverter.

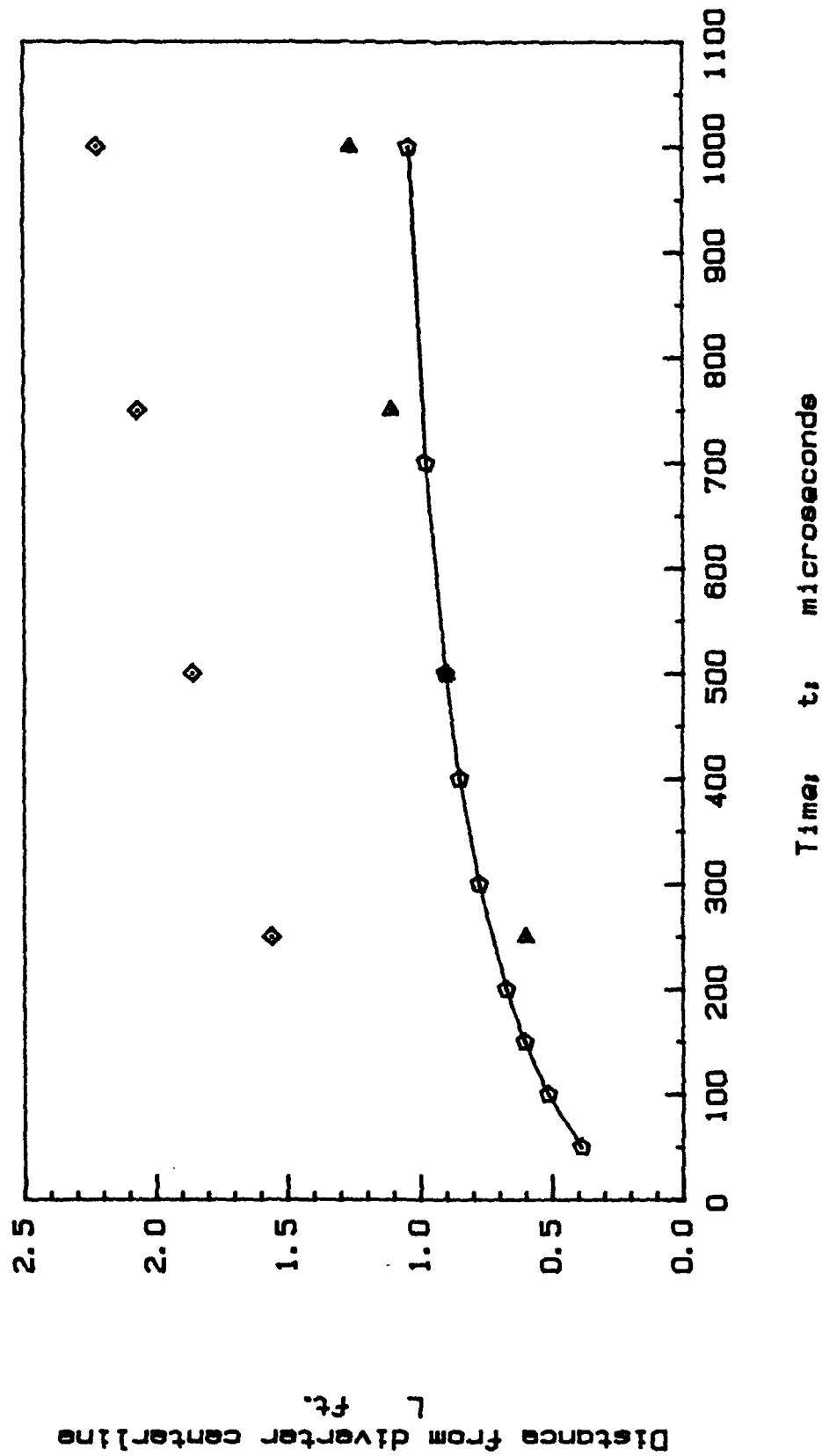


Figure 14 Movement of the gun gas behind the shock as a function of time as it leaves the diverter radially. Lower bound of experimental data \blacktriangle ; upper bound \diamond ; computer estimate \circ .

GUN TEST RESULTS

The following diverters were tested at the muzzle of the advanced gun. Highspeed photos were taken of the gun gas flow.

Rectangular Diverter

The rectangular diverter shown Figure 15 was tested mainly for the purpose of diversion and not flash suppression. High speed photos showed that the great majority of the flow had been diverted but that secondary flash still existed. The diverter pressure as a function of time was used in Figure 11 to help validate the computer blow down model.

Round Diverter

The round diverter shown in Figure 16 was used to demonstrate the effects of heat and mass transfer and rapid expansion. Eighteen square feet of finned surface area was mounted within the round diverter. The fins were zinc coated. The geometry of the round diverter was a continuously diverging channel and was thus a good geometry to use for rapid expansion.

The results of the test showed a very substantial reduction in primary flash and a complete elimination of secondary flash in all seven tests. A typical example of the highspeed photos showing the gun gas with no secondary is shown in Figure 17. In some of the tests two-thirds of the surface area was removed to determine the effect of heat transfer. It appeared from the high speed photos that the

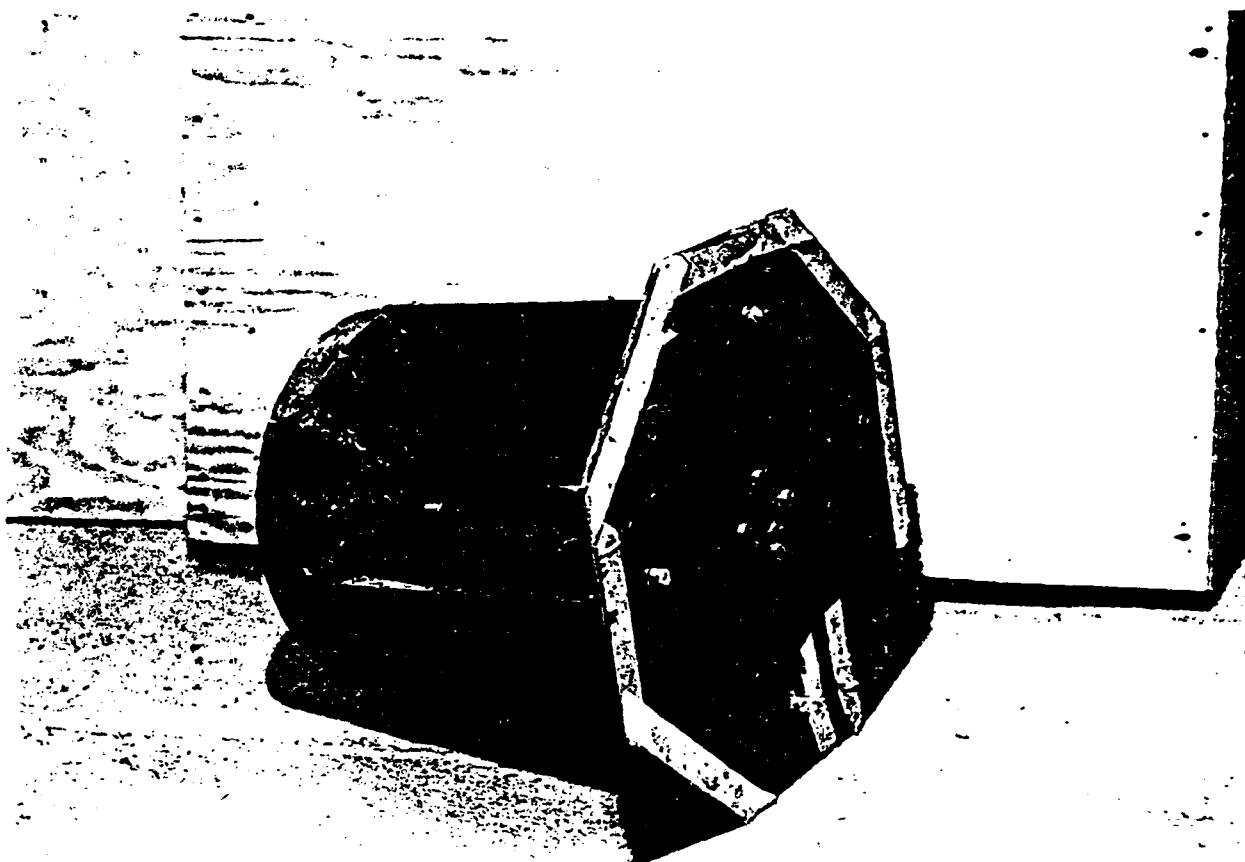


Figure 16 Round diverter. Rear round plate screws to the barrel and is 11 inches in diameter. Hexagonal plate is 16 inches across.



Figure 17 Highspeed photos of gas flow from round diverter.
4000 frames/sec. Hexagonal plate is 16 inches across.

addition surface area had little effect on the elimination of secondary flash. Finally only four square feet of surface area was left in place for structural reasons (this can be seen in Figure 16). The result was still an eliminated secondary flash.

V diverter

Because the round diverter was quite large (11" long, 11" diameter), a smaller version using the same operating principle was designed, constructed and tested on the advanced gun. This diverter was shaped as a v as seen in Figure 18. The larger style v had a 5.5" by 24" outlet. The smaller style v had a 5.5" by 18" outlet area.

The results for the larger v showed a short (0.75 millisecond) primary and a 2.3 millisecond secondary. One of three tests showed no secondary. The smaller v had a small nose piece added. This piece was added to reduce the amount of hot gas coming through the projectile hole. This gas seemed to ignite the secondary was seen in the high speed photos. There was only one secondary flash seen in the four tests of the smaller v. It is possible that that secondary may have been externally caused by the heat detector five feet directly above the diverter. The detector triggered simultaneously with the gun firing.

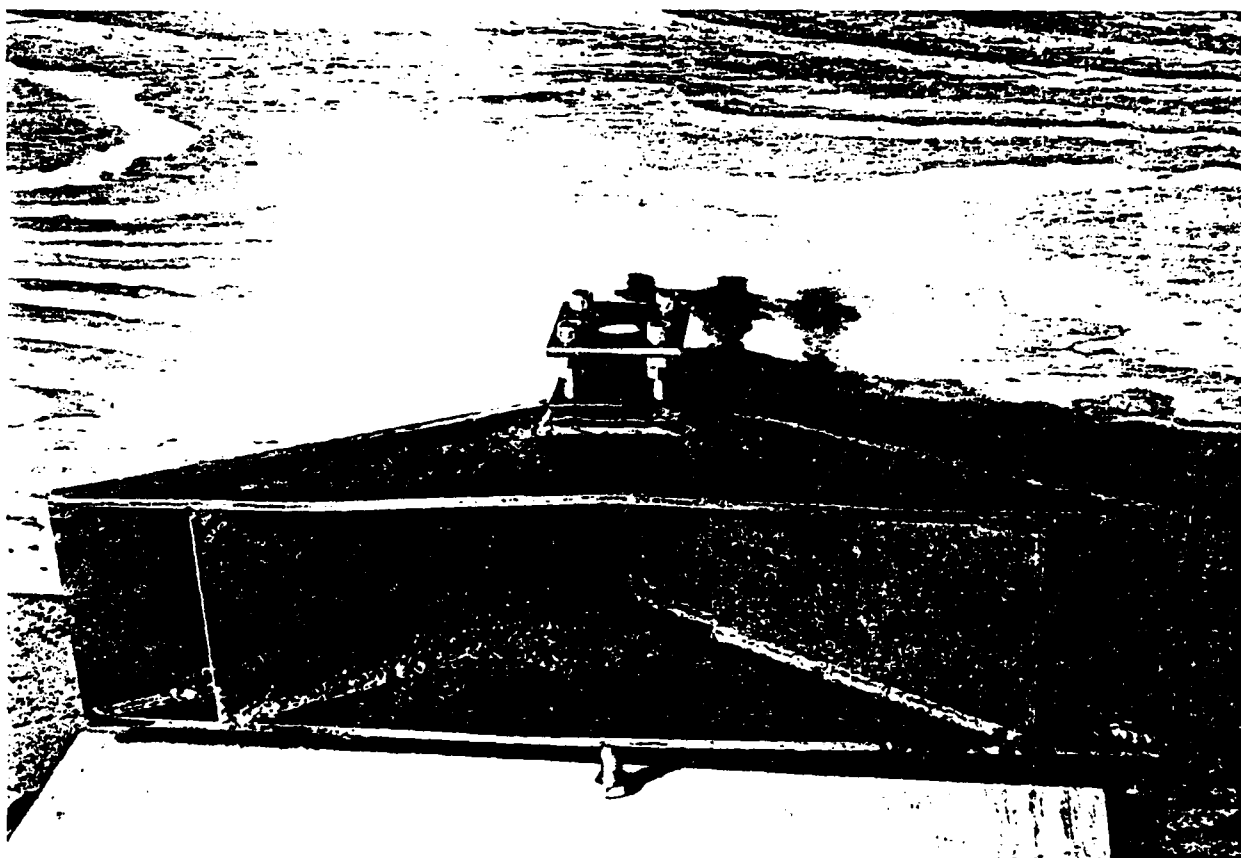


Figure 18 Wedge diverter (24" x 5.5") shown with insert plates to reduce outlet to 18" x 5.5".

Bare Muzzle

High speed photos of firings with a bare muzzle were taken to observe the secondary flash phenomena and be used as a base to determine the amount of secondary flash reduction achieved using various diverters. The time duration of the primary and secondary are shown in Table 1.

Comparisons of tests

A test matrix of the results of the gun gas diverters is shown in Table 1. The results in the table show that the round and the v diverters have been able to bring secondary flash under control. The 18" v should be able to eliminate secondary flash with a very small cost in volume and a reasonable outlet area. It should also be noted that the 18" v diverter also reduced the duration of the primary by two-thirds.

Table 1. Gun gas diverter test results. All test were run using the advanced gun.

	Bare Muzzle	Rectangular	Round	24" v	18" v
Volume of diverter cubic in.	---	900	1045	396	297
Outlet area sq. in.	0.5	49	380	132	99
Average time duration of primary milliseconds	3.8	3.4	0.6	0.75	1.1
Average time duration of secondary milliseconds	18.9	15.3	none	2.3	1.5*
Total number of tests	2	6	7	3	4
Number with secondary flash	1	5	0	2	1*

* This result is questionable.

CONCLUSIONS

1. The recommended geometries for $L/D = 7$ listed in order of good to best are given as:

Geometry of diverter	Diversion efficiency, pressure ratios 10 to 50
one plate	77%-97%
narrow v	94.9%-95.5%
two plate	90.2%-96.8%
wide v	93.7%-99%

2. Diverter design considerations for maximum diversion efficiency during a actual blowdown cycle are as follows:

a. Geometry of the diverter should have a length of seven times the bore diameter and use a geometry similar to one of the four geometries listed above.

b. The throat area in the diverter should have an area equal to or greater than 36 square inches to maintain an overall diversion efficiency greater than 90%.

3. Diverter design considerations for flash suppression during firing of the advanced gun are as follows:

a. The geometry of the diverter should have a continuously increasing cross sectional area from muzzle exit to diverter exit (similar to the v geometry).

b. The cross sectional area at the exit of the diverter should be equal to or greater than 99 square incnes.

REFERENCES

1. May, I.W. and S.I. Einstein, "Prediction of Gun Muzzle Flash", 14th JANNAF Combustion Meeting, August 1977.
2. Carfagno, S.P., "Handbook on Gun Flash", Franklin Institute, 1961.
3. Heiney, O.K. and R.J. Powers, "Secondary Muzzle Gas Combustion Considerations in Aircraft Cannon", 14th JANNAF Combustion Meeting, August 1977.
4. Heimerl J.M. and G. Klingenberg, "Combustion Following Turbulent Mixing in MUzzle Flows", 21st International Symposium on Combustion, August 1986.
5. Schmidt, E.M., "Muzzle Flow Gasdynamics", in Gun Propulsion Technology, Ed. L. Stiefel, Progress in Astronautics and Aeronautics, Vol. 109, 1988.
6. Engineering Design Handbook, Gun Series, Muzzle Devices, AD 838748, AMCP 706-251, 1968.

Appendix A. Tabulated Data for Figures 3 - 7
Table 1A
Diversiion efficienciies L/D = 1 using nitrogen.

Pressure Ratio	Diversiion Efficiency
2.68459	37.60316
3.128954	38.85725
4.017684	61.26911
5.350777	64.24578
6.239506	65.52359
7.5726	66.87793
8.905692	67.82681
9.794422	68.3159
11.12752	68.90305
12.46061	69.36456
13.7937	69.73688
14.68243	69.13693
17.34862	69.07793
18.23735	69.93222
19.57044	69.54782
20.45917	70.28893
22.23663	69.98775
24.01409	70.72237
25.79155	69.50993
27.569	69.74894
28.01337	68.52941
30.23519	69.26749
31.35516	69.05726
32.23789	69.53785
34.44471	68.74398
36.39445	67.65624
39.49972	67.79258
40.83055	67.38741
42.16139	67.00781
45.26666	67.17128

Table 2A
 Diversion efficiencies L/D = 2 using nitrogen.

Pressure Ratio	Diversion Efficiency
3.128954	13.00887
4.017684	36.75552
5.350777	67.16648
6.228921	73.77653
7.5726	76.00342
8.016963	75.82878
11.12752	79.33324
12.46061	80.57615
13.7937	80.267
15.1268	81.60729
16.01552	81.8747
17.34862	81.52911
18.23735	82.09848
19.57044	82.08508
21.79226	83.08125
23.12536	83.2741
24.01409	83.13958
26.68027	83.24196
28.01337	83.3935
30.23519	83.61636
32.45701	83.62289
34.67883	83.8025
36.01193	83.39715
38.23375	83.09991
40.01121	83.09693
42.23303	82.41518
44.45486	81.93726
46.67668	82.15094
48.81555	82.22185
50.58999	82.13127

Table 3A
 Diversion efficiencies L/D = 3.5 using nitrogen

Pressure Ratio	Diversion Efficiency
3.128954	15.71356
4.017684	30.99922
5.350777	43.77653
6.683871	76.69469
7.5726	82.99395
8.016963	83.93656
9.350058	87.67011
10.23879	88.74035
11.12752	89.03326
12.46061	89.66503
15.1268	89.7024
18.23735	90.34882
20.90353	90.77282
24.45845	91.28633
27.12464	91.52094
30.67956	91.9536
32.90138	91.98427
35.95084	92.3019
37.72528	92.30689
39.94333	92.39681
42.01883	92.47726
45.55572	92.61923
50.33384	92.79856
53.86476	92.89737
56.95431	92.98848
60.41674	93.00561
63.58686	93.18614
65.88593	93.10496
67.41948	93.18996
71.27873	93.19819

Table 4A
 Diversion efficiencies L/D = 4 using nitrogen.

Pressure Ratio	Diversion Efficiency
3.128954	20.02644
4.017684	26.80063
5.350777	48.19009
6.239506	60.43599
7.5726	79.42983
8.016963	86.04066
8.905692	88.19137
9.794422	89.26286
10.23879	89.72886
11.12752	89.94281
12.46061	90.74803
13.34934	91.36398
14.68243	91.22898
15.1258	91.26359
16.01552	91.32709
17.34862	91.79908
18.68171	92.02309
19.57044	92.04056
20.45917	92.38631
22.23663	92.53975
26.68027	93.02357
30.33829	93.50908
34.79709	93.85439
38.36413	93.98459
42.37705	94.07493
45.94409	94.01918
50.84877	94.19662
54.4158	94.07936
58.67452	94.12526
61.104	94.2842

Table 5A
 Diversion efficiencies L/D = 7 using nitrogen.

Pressure Ratio	Diversion Efficiency
3.128954	11.40065
4.017684	36.03751
5.350777	50.08161
6.239506	57.73248
7.5726	66.95538
8.016963	69.20781
8.905692	72.28067
9.794422	74.79587
10.23879	76.87824
11.12752	79.93767
12.46061	82.89628
13.34934	85.5513
14.68243	90.53964
15.1268	93.27086
16.01552	94.06557
17.34862	94.52158
18.23735	94.78856
19.57044	95.14355
22.23663	95.72583
24.01409	95.76122
28.01337	96.24593
32.45701	96.55201
36.27139	96.65262
40.69249	96.85133
44.15473	97.02724
48.40499	97.0904
52.54066	97.18282
56.63103	97.24598
60.58233	97.27999
64.6988	97.37755

Table 6A

Diversion efficiencies L/D = 2 using carbon dioxide.

Pressure Ratio	Diversion Efficiency
3.68441	36.66149
3.906592	56.67208
4.358362	68.85111
5.026044	72.98907
6.138846	76.7844
7.251648	76.61875
7.905873	78.59003
8.364451	79.72937
9.032131	80.85368
10.14493	80.62203
11.03518	80.65408
11.4803	81.40418
11.92542	82.09828
12.14798	81.59168
12.81566	82.28703
13.92846	82.48905
15.04126	82.66117
16.3488	82.83685
17.23753	86.07037
18.12626	87.68394
19.04735	88.25958
20.34808	88.86294
21.01463	90.50052
22.12554	91.12998
23.23645	91.84441
23.903	92.21298
24.3888	92.3551
25.05648	92.82856
25.68045	93.27744
26.347	93.44752

Table 7A
 Diversion efficiencies L/D = 4 using carbon dioxide.

Pressure Ratio	Diversion Efficiency
3.017863	26.02583
3.906592	29.03705
4.128774	24.68457
4.573139	32.00285
5.239686	47.7355
5.906233	59.91712
6.350597	63.7843
6.350597	64.84678
7.017144	84.05171
8.128055	89.55202
9.238966	90.80831
10.1277	91.28178
11.01642	91.98511
11.90515	92.01666
12.34952	91.75754
13.01607	92.17964
14.12698	92.55579
15.46007	92.54304
16.3488	92.9484
17.01535	93.22463
18.12626	93.26763
19.01499	93.5823
20.1259	93.60128
21.23681	93.936
22.42393	94.08648
23.09275	94.25775
24.20745	94.52216
25.99097	94.89806
26.21391	94.94145
27.10566	95.10788

Table 8A
 Diversion efficiencies L/D = 7 using carbon dioxide.

Pressure Ratio	Diversion Efficiency
2.795681	14.11306
3.462228	23.82695
3.906592	31.62784
4.128774	35.30715
5.239686	49.02325
5.906233	57.63228
6.350597	60.59684
7.017144	64.82046
7.461509	68.272
8.155773	72.53416
8.824592	78.83553
9.238966	80.21863
9.939292	82.91209
10.16223	83.62009
11.05399	86.47272
11.98663	92.86681
12.43403	93.12348
12.88144	93.36231
13.55255	93.691
14.22365	93.98868
15.34217	94.42692
16.04072	94.6605
17.16115	95.00911
18.34446	95.31498
20.14331	95.73337
22.16702	96.12289
24.41559	96.34011
26.21445	96.59125
27.33873	96.73144
28.0133	96.81014

Table 9A
 Diversion efficiencies L/D = 7 using nitrogen
 and a two plate diverter.

Pressure Ratio	Diversion Efficiency
2.689159	48.57399
3.579401	63.25257
4.469643	80.02288
5.805005	89.85779
7.140368	93.17441
8.03061	92.87901
9.365972	92.81183
10.70134	93.23511
11.59158	93.31734
12.0367	92.58179
13.37206	92.94351
14.31102	93.02855
15.65095	92.86706
16.57253	92.84227
17.01994	93.32979
17.91475	93.47335
18.80956	92.97118
19.25697	92.95809
20.15178	93.01794
25.15933	92.96591
30.14944	93.21408
35.09629	93.87871
41.77016	94.33517
45.3617	94.48312
50.30006	94.31325
55.23841	94.72909
61.97254	95.30185
65.67682	95.55921
70.95136	95.96845
74.09396	95.90944

Table 10A
 Diversion efficiencies L/D = 4 using nitrogen
 and a two plate diverter.

Pressure Ratio	Diversion Efficiency
1.795861	18.96557
3.128954	22.64731
4.017684	60.77594
5.350777	76.18446
6.239506	76.67659
7.5726	76.00342
8.016963	75.82878
8.905692	76.20907
9.794422	78.36781
10.23879	79.30666
11.12752	79.87529
12.46061	82.02832
13.34934	83.22479
14.68243	84.74789
15.1268	84.79719
16.01552	84.88761
16.90425	84.9685
17.34862	85.35351
18.23735	84.74433
20.45917	85.22181
22.23663	85.31809
24.17843	84.64661
26.77126	86.18089
28.20508	87.91508
30.49428	87.60619
32.67913	87.15375
34.07965	90.51662
36.50821	92.77661
38.694	93.98516
38.76066	94.14292

Table 11A

Diversion efficiencies L/D = 7 (2+5) using nitrogen
and a two plate diverter.

Pressure Ratio	Diversion Efficiency
2.680036	68.68111
3.567257	73.6381
4.454479	80.02288
5.785311	89.27564
6.228921	89.76904
7.116143	89.38811
8.003364	89.51244
9.334196	90.28607
10.66503	90.23503
11.55225	91.56808
12.92694	91.26268
15.2043	91.31936
17.01994	89.83718
20.15178	90.06812
22.3888	90.15018
25.96805	91.44241
27.75767	92.17769
30.88951	92.20102
32.23173	92.26233
34.91616	92.75993
37.15318	93.51586
40.87228	94.87786
42.29171	95.08164
46.5487	95.55437
50.12794	95.60074
52.36497	95.52921
57.48312	95.73541
60.17677	95.69974
62.07911	95.87935
65.67682	95.89712

Table 12A

Diversion efficiencies $L/D = 7$ (5+2) using nitrogen
and a two plate diverter.

Pressure Ratio	Diversion Efficiency
2.689159	23.44009
3.579401	43.42564
4.469643	61.8767
5.805005	69.19104
6.250126	75.44045
7.140368	87.49495
8.03061	90.5645
9.365972	93.89429
10.70134	94.97199
11.59158	95.35814
14.31102	95.63499
17.01994	95.0262
20.15178	94.78782
22.79721	94.65679
26.37034	94.73782
29.49683	94.95071
31.17689	95.07647
36.83181	95.42646
40.94257	95.46162
43.11699	95.65836
46.70852	95.9922
48.95323	96.03672
51.19794	96.11062
54.78947	96.36559
58.4814	96.58916
61.07465	96.60008
64.77739	96.70984
67.47567	96.81612
68.3751	96.80806
69.60455	96.82086

Table 13A

Diversión efficiencies $L/D = 7$ using nitrogen
and a wide vee geometry.

Pressure Ratio	Diversión Efficiency
3.579401	12.03301
4.469643	35.60256
5.805005	55.07361
6.282206	65.3023
7.201658	78.6208
7.201658	89.97971
8.099542	91.93217
9.446366	94.16492
9.895309	93.74074
11.65107	94.70217
12.09848	95.45962
15.28261	96.39326
15.7586	96.49619
17.16679	96.77251
20.39604	97.2741
22.69949	97.69818
25.55415	97.40272
30.21941	97.56608
33.88007	98.03413
35.12988	98.11069
40.14573	98.60544
42.35182	98.76199
45.4788	98.76033
50.61876	98.88424
52.64395	98.92339
55.21873	99.04045
60.0299	99.05585
60.27871	99.12099
61.1987	99.07714
61.1987	99.07714

Table 14A
 Diversion efficiencies L/D = 7 using nitrogen
 and a narrow vee geometry.

Pressure Ratio	Diversion Efficiency
3.579401	6.368172
4.454479	25.77339
4.914764	54.49956
5.805005	61.4774
6.271476	77.19773
7.164758	82.4071
8.058041	83.09492
9.365972	91.27834
10.70134	94.89304
12.0367	95.74038
13.37206	96.67121
14.2623	96.40508
15.15254	97.06235
16.40414	96.68537
18.96495	97.14743
20.21868	97.3333
21.90168	97.54646
23.49508	97.72806
26.23312	98.11298
28.01361	98.25585
30.37249	97.52144
32.36875	96.67564
34.08185	96.56009
36.80828	96.62205
38.12346	96.233
40.43742	96.15399
42.18924	96.04386
44.5203	95.74081
46.31918	95.30299
49.73291	95.49648

Table 15A

Diversion efficiencies L/D = 8 using nitrogen
and a pipe with six side holes.

Pressure Ratio	Diversion Efficiency
2.689159	24.3034
3.579401	43.13009
4.469643	49.12263
5.805005	60.82628
6.250126	67.43103
7.140368	71.49164
8.03061	77.62103
9.365972	78.26598
10.70134	78.74997
11.59158	80.38199
12.0367	80.11702
12.81785	79.64184
14.18984	80.71205
16.43197	78.25421
18.65002	77.01806
20.32105	77.85126
22.04929	76.9456
24.61009	77.50222
26.5826	77.58998
28.76002	78.88109
30.20021	78.94
30.96047	79.52467
32.83942	79.46294
34.06267	79.89806
36.20364	78.8096
38.88162	78.61863
40.66402	78.67143
40.88425	78.88678
41.38322	79.03961
41.57858	79.03961

```

C      THIS PROGRAM CALCULATES THE DENSITY AND PRESSURE- TIME
C      RELATIONSHIP DURING DIVERTER OPERATION
C
C
0001      REAL MDOTIN,MDTOUT,MDTPEA
0002      DIMENSION PR(20),EFF(20)
0003      OPEN (UNIT=5,NAME='PTINP.DAT',TYPE='OLD',READONLY)
0004      OPEN (UNIT=6,NAME='PTOUT.DAT',TYPE='NEW')
C      READ IN THE INPUT DATA
C      1. Gun chamber volume m3
C      2. Gun gas diverter volume m3
C      3. Diverter outlet nozzle cross sectional area m2
C      4. Initial density in chamber kg/m3
C      5. Density blowdown constant sec-1
C      6. Slope of blowdown constant sec-2
C      7. Time step sec
C
0005      DO 100 IR=1,16
0006      READ (5,*) VCHAM,VDIV,ANOZ,RHOI,A,B,DT,NEFF
0007      DO 10 J=1,NEFF
C      ORDER PRESSURE RATIOS LOW TO HIGH
0008      10 READ (5,*) PR(J),EFF(J)
0009      WRITE (6,*) 'VOL CHAMBER=',VCHAM,' m3; VOL DIVERTER=',VDIV,
1      ' m3'
0010      WRITE (6,*) ' AREA NOZZLE=',ANOZ,' m2'
0011      WRITE (6,*) ' INITIAL DENSITY IN CHAMBER=',RHOI,' kg/m3;',
0012      WRITE (6,*) ' A=',A,' sec-1; B=',b,' sec-2'
0013      WRITE (6,*) ' TIME STEP=',DT,' TIME DELAY=',TIMEDE,' SEC'
C      A Constant used in density blowdown sec-1
C      ANOZ Outlet area of the sonic nozzle m2
C      B Slope of the density blowdown constant sec-2
C      DT time step sec
C      EFF diversion efficiency array
C      ETA diversion efficiency
C      FRTMAS mass out the front hole
C      GAM specific heat ratio
C      GAMCON constant derived from gam used in sonic nozzle equati
C      I loop counter
C      MDOTIN mass flow rate into diverter kg/sec
C      MDTOUT mass flow rate out of diverter kg/sec
C      NEFF elements in efficiency array
C      PRESS diverter pressure Pa
C      PSI diverter pressure psi
C      PR pressure ratio array
C      RHOD gas density in diverter at beginning of time step kg/
C      RHODN gas density in diverter at end of time step kg/m3
C      RHODN1 gas density estimate 1 kg/m3
C      RHODN2 gas density estimate 1 kg/m3
C      RHOI density of gas in gun as projectile uncorks kg/m3
C      RHOO stagnation density estimate of leaving gas
C      RTO gas constant times stagnation temperature m2/s2
C      TIMEDE time delay until shock wave passes through volume
C      TIME current time sec
C      TOTMAS total mass leaving diverter

```

```

      C      VCHAM      volume of gun chamber m3
      C      VDIV      volume of diverter m3
      C
0014      ETA=1.0
0015      RTO=700000.
0016      GAM=1.25
0017      TIMEDE=VDIV/ANOZ/SQRT(GAM*RTO)
0018      WRITE (9,*) 'TIME DELAY',TIMEDE
0019      TOTMAS=0.0
0020      FRTMAS=0.0
0021      WRITE (6,*) ' PRESSURES AND DENSITIES IN DIVERTER WITH TIME'
0022      WRITE (6,*)
0023      WRITE (6,*) ' TIME SEC*DENS KG/M3*PRESS PA *PRESS PSI'
0024      WRITE (6,*)
0025      RHOD=1.2
0026      GAMCON=(2/(GAM+1))*((GAM+1)/2./(GAM-1))
      C      BEGIN CALCULATION LOOP
0027      DO 100 I=1,40
0028      TIME=DT*(I-1)
0029      RHOO=RHOD
      C      DETERMINE MASS FLOWS IN AND OUT
      C      PREDICTION AT TIME
0030      MDOTIN=VCHAM*8*RHOI*(1+(A+B*TIME)*TIME)**(-9)*(A+2.*B*TIME)
0031      MDTOUT=ANOZ*SQRT(GAM*RTO)*RHOO*GAMCON/ETA
0032      IF (TIME.LT.TIMEDE) MDTOUT=0.0
0034      IF (TIME.GT.TIMEDE.AND.PSI.LT.28.) MDTOUT=MDOTIN
0036      RHODN1=RHOO+(MDOTIN-MDTOUT)*DT/VDIV
0037      WRITE (9,*) 'MDOT',MDOTIN,MDTOUT
0038      TIME=TIME+DT
      C      PREDICTION AT TIME+DT
0039      MDOTIN=VCHAM*8*RHOI*(1+(A+B*TIME)*TIME)**(-9)*(A+2.*B*TIME)
0040      MDTOUT=ANOZ*SQRT(GAM*RTO)*RHODN1*GAMCON/ETA
0041      IF (TIME.LT.TIMEDE) MDTOUT=0.0
0043      IF (TIME.GT.TIMEDE.AND.PSI.LT.28.) MDTOUT=MDOTIN
0045      MDTPEA=MDTOUT*(1.-ETA)
0046      TOTMAS=TOTMAS+MDTOUT*DT
0047      FRTMAS=FRTMAS+MDTPEA*DT
0048      RHODN2=RHOO+(MDOTIN-MDTOUT)*DT/VDIV
0049      WRITE (9,*) 'MDOT',MDOTIN,MDTOUT
      C      AVERAGE OVER THE TIME STEP
0050      RHODN=(RHODN1+RHODN2)/2
0051      PRESS=RHODN*RTO
0052      PSI=PRESS/6895.
0053      PRATIO=12400.*((1.+(A+B*TIME)*TIME)**(-10)/PSI)
0054      DO 50 J=1,NEFF
0055      K=J
0056      50 IF (PR(J).GE.PRATIO) GO TO 60
0058      60 IF (K.EQ.1) K=2
0060      ETA=EFF(K-1)+(EFF(K)-EFF(K-1))*(PRATIO-PR(K-1))/(PR(K)-PR(K-1))
0061      IF (K.EQ.NEFF) ETA=EFF(NEFF)
0063      IF (ETA.LE.0.25) ETA=0.25
0065      RHOD=RHODN
0066      IF (TOTMAS.GT.0.0) AVEFF=FRTMAS/TOTMAS
0068      WRITE (9,200) TIME,RHODN,PRESS,PSI,TOTMAS,FRTMAS,AVEFF

```

```
0069    200  FORMAT (F10.5,F10.4,F10.0,F10.1,3F10.5)
0070      WRITE (6,200) TIME,RHODN,PRESS,PSI,TOTMAS,FRTMAS,AVEFF
0071    100  CONTINUE
0072      STOP
0073      END
```

```

C      THIS PROGRAM CALCULATES THE DENSITY AND PRESSURE- TIME
C      RELATIONSHIP DURING DIVERTER OPERATION
C
C
0001      REAL MDOTIN,MDTOUT,MDTPEA
0002      DIMENSION PR(20),EFF(20),IAVE(50)
0003      OPEN (UNIT=5,NAME='PTINP.DAT',TYPE='OLD',READONLY)
0004      OPEN (UNIT=6,NAME='PTOUT.DAT',TYPE='NEW')
C      READ IN THE INPUT DATA
C      1. Gun chamber volume m3
C      2. Gun gas diverter volume m3
C      3. Diverter outlet nozzle cross sectional area m2
C      4. Initial density in chamber kg/m3
C      5. Density blowdown constant sec-1
C      6. Slope of blowdown constant sec-2
C      7. Time step sec
C
0005      READ (5,*) VCHAM,VDIV,ANOZ,RHOI,A,B,DT,NEFF
0006      DO 10 J=1,NEFF
C      ORDER PRESSURE RATIOS LOW TO HIGH
0007      10 READ (5,*) PR(J),EFF(J)
0008      DO 400 IA=1,25
0009      ANOZ=FLOAT(IA)*0.00129
0010      DO 300 IV=3,25
0011      VDIV=FLOAT(IV)*0.0006556
0012      WRITE (9,*) 'IA IV',IA,IV
C      A Constant used in density blowdown sec-1
C      ANOZ Outlet area of the sonic nozzle m2
C      B Slope of the density blowdown constant sec-2
C      DT time step sec
C      EFF diversion efficiency array
C      ETA diversion efficiency
C      FRTMAS mass out the front hole
C      GAM specific heat ratio
C      GAMCON constant derived from gam used in sonic nozzle equation
C      I loop counter
C      MDOTIN mass flow rate into diverter kg/sec
C      MDTOUT mass flow rate out of diverter kg/sec
C      NEFF elements in efficiency array
C      PRESS diverter pressure Pa
C      PSI diverter pressure psi
C      PR pressure ratio array
C      RHOD gas density in diverter at beginning of time step kg/m3
C      RHODN gas density in diverter at end of time step kg/m3
C      RHODN1 gas density estimate 1 kg/m3
C      RHODN2 gas density estimate 1 kg/m3
C      RHOI density of gas in gun as projectile uncorks kg/m3
C      RHOO stagnation density estimate of leaving gas
C      RTO gas constant times stagnation temperature m2/s2
C      TIMEDE time delay until shock wave passes through volume
C      TIME current time sec
C      TOTMAS total mass leaving diverter
C      VCHAM volume of gun chamber m3
C      VDIV volume of diverter m3

```

```

C
0013  ETA=EFF(NEFF)
0014  RTO=700000.
0015  GAM=1.25
0016  TIMEDE=VDIV/ANOZ/SQRT(GAM*RTO)
0017  WRITE (9,*) 'TIME DELAY V A',TIMEDE,VDIV,ANOZ
0018  TOTMAS=0.0
0019  FRTMAS=0.0
0020  RHOD=1.2
0021  GAMCON=(2/(GAM+1))*((GAM+1)/2./(GAM-1))
C
0022  BEGIN CALCULATION LOOP
0023  DO 100 I=1,40
0024  TIME=DT*(I-1)
0025  RHOO=RHOD
C
0026  DETERMINE MASS FLOWS IN AND OUT
C
0027  PREDICTION AT TIME
0028  MDOTIN=VCHAM*8*RHOI*(1+(A+B*TIME)*TIME)**(-9)*(A+2.*B*TIME)
0029  MDTOUT=ANOZ*SQRT(GAM*RTO)*RHOO*GAMCON/ETA
0030  IF (TIME.LT.TIMEDE) MDTOUT=0.0
0031  IF (TIME.GT.TIMEDE.AND.PSI.LT.28.) GO TO 101
0032  RHODN1=RHOO+(MDOTIN-MDTOUT)*DT/VDIV
0033  TIME=TIME+DT
C
0034  PREDICTION AT TIME+DT
0035  MDOTIN=VCHAM*8*RHOI*(1+(A+B*TIME)*TIME)**(-9)*(A+2.*B*TIME)
0036  MDTOUT=ANOZ*SQRT(GAM*RTO)*RHODN1*GAMCON/ETA
0037  IF (TIME.LT.TIMEDE) MDTOUT=0.0
0038  IF (TIME.GT.TIMEDE.AND.PSI.LT.28.) GO TO 101
0039  MDTPEA=MDTOUT*(1.-ETA)
0040  TOTMAS=TOTMAS+MDTOUT*DT
0041  FRTMAS=FRTMAS+MDTPEA*DT
0042  RHODN2=RHOO+(MDOTIN-MDTOUT)*DT/VDIV
C
0043  AVERAGE OVER THE TIME STEP
0044  RHODN=(RHODN1+RHODN2)/2
0045  PRESS=RHODN*RTO
0046  PSI=PRESS/6895.
0047  PRATIO=12400.*((1+(A+B*TIME)*TIME)**(-10)/PSI)
0048  DO 50 J=1,NEFF
0049  K=J
0050  IF (PR(J).GE.PRATIO) GO TO 60
0051  60 IF (K.EQ.1) K=2
0052  ETA=EFF(K-1)+(EFF(K)-EFF(K-1))*(PRATIO-PR(K-1))/(PR(K)-PR(K-1))
0053  IF (K.GE.NEFF) ETA=EFF(NEFF)
0054  IF (ETA.LE.0.25) ETA=0.25
0055  RHOD=RHODN
0056  IF (TOTMAS.GT.0.0) AVEFF=1.0-FRTMAS/TOTMAS
0057  100 CONTINUE
0058  101 BVEFF=100.*AVEFF+0.5
0059  WRITE (9,*) 'AVE',BVEFF,TIME,PSI
0060  IF (BVEFF.GT.100.) BVEFF=EFF(NEFF)*100.
0061  IAVE(IV)=INT(BVEFF)
0062  300 CONTINUE
0063  WRITE (6,200) IA*2,(IAVE(IVV),IVV=3,25)
0064  200 FORMAT (I4,25I3)
0065  400 CONTINUE
0066  STOP
0067  END

```



```
C
C      SHOCK IN FRONT OF THE GUN GAS
C
0001      OPEN (UNIT=6,NAME='SHOCK1.OUT')
0002      VOL=0.025
0003      VOLI=0.025
0004      P=8000.
0005      PI=8000.
0006      XS=0.07
0007      XG=0.07
0008      DT=1.E-6
0009      WRITE (9,*) 'N OUTER  M MICROSECONDS PER PRINT'
0010      READ (9,*) N,M
0011      WRITE (6,*) 'MICROSECONDS  SHOCK DISTANCE FT  GAS DISTANCE',
1      'SHOCK VELOCITY  PRESSURE'
0012      DO 100 I=1,N
0013      DO 50 J=1,M
0014      SM=((P/14.7+1./6.)*6./7.)**0.5
0015      VS=SM*1100.
0016      GM=((SM*SM+5.)/(7.*SM*SM-1.))**0.5
0017      VG=VS-GM*1100.
0018      XS=XS+VS*DT
0019      XG=XG+VG*DT
0020      DVOL=2.*3.1416*XG*1.*VG*DT
0021      VOL=VOL+DVOL
0022      P=PI*VOLI**1.25/VOL**1.25
0023      50  CONTINUE
0024      WRITE (6,*) I*M,XS,XG,VS,P
0025      WRITE (9,*) I*M,XS,XG,VS,P
0026      100 CONTINUE
0027      STOP
0028      END
```

1987-88 USAF-UES RESEARCH INITIATION PROPOSAL

Sponsored by the
AIR FORCE OFFICE OF SCIENTIFIC RESEARCH
Conducted by the
Universal Energy Systems, Inc.

FINAL REPORT

A PHYSICAL AND NUMERICAL STUDY OF PRESSURE
ATTENUATION IN SOLIDS

Prepared by:	James Steven Hoffmaster, Ph. D.
Academic Rank:	Associate Professor
Department and	Physics Department
University:	Gonzaga University
Research Location:	Air Force Armament Laboratory Munitions Division Energetic Materials Branch Dynamics Laboratory Eglin AFB FL 32542-5434
USAF Researcher:	David R. Wagnon
Date:	29 July 1988
Contract No.:	F49620-85-C-0013/SB5851-0360

A PHYSICAL AND NUMERICAL STUDY OF PRESSURE
ATTENUATION IN SOLIDS

by

James Steven Hoffmaster

ABSTRACT

The peak pressure in a material produced by a shock wave decreases as the wave passes through the object. The rate of decrease depends on the size, shape, and molecular structure of the object. Pressure is a key consideration when evaluating insensitive high explosive candidate materials. Current state-of-the-art computer codes are extremely complex and are difficult, time consuming affairs to apply. A simpler computer program is described in this report. It is capable of giving peak shock wave pressure at interfaces as well as pressure attenuation as a function of distance in selected materials. The results obtained, although less accurate than those of the more complex codes, are far easier to obtain and are sufficiently accurate to be useful in choosing experimental parameters in IHE evaluative testing.

Improvements over earlier work by this investigator include more accurate determination of parameters describing shock wave behavior. Errors on these parameters have been determined. A more realistic, more general, and more accurate relationship between shock wave pressure and attenuation distance has been modeled. These changes have been incorporated into the computer program associated with the initial work over the summer of 1987.

Acknowledgements

I wish to thank the Air Force Systems Command and the Air Force Office of Scientific Research for sponsorship of this research, as well as Universal Energy Systems for their assistance in facilitating the administrative aspects of the program.

Many people are responsible for making this an enjoyable and rewarding research experience. I would first like to thank Dr. Sam Lambert for his efforts on my behalf in the initial selection process. At Gonzaga; Steven Lewis, Craig Looney, and Walter Lowe have assisted with some of the programming work. Discussions with them have helped us all to better understand the physical principles involved. Finally, and most significantly, I am pleased to thank Mr. David Wagnon for his suggestions and guidance. They were always constructive and informative.

I. INTRODUCTION:

Insensitive high explosives (IHEs) have been an area of major interest in the armed services. Because of the tremendous energy releases associated with even conventional explosives, the safe handling, storage, and transportation of high explosives is literally a matter of life and death to those involved in these processes. IHEs are those whose behavior is such that they have passed certain cookoff, impact, and sympathetic detonation tests. These are tests which in essence try to ensure that IHEs do not detonate by accident or under enemy attack, but at the same time are reliable and effective in times of military action (Corley, 1986).

For the summers of 1985 and 1986 in a faculty research program run by the US Navy, I was involved in the investigation of effective armoring of Navy and Marine facilities and equipment. In evaluating armor many threats must be considered and, of course, one of these is conventional explosives. At Eglin AFB in the USAF-UES Summer Faculty Research Program the author was associated with the High Explosives Research and Development Facility and hence was able to continue research initiated in the earlier programs.

Because of the destructive nature of the process and the expense associated with sacrificing facilities to destructive testing, much of the evaluation of IHEs is done by computer simulation and modeling. Many of the techniques used in the modeling of effective armoring can also be applied to similar modeling of the IHEs themselves. These procedures involve the use of state-of-the-art techniques, such as finite differences and finite elements analysis as

well as more traditional but still useful methods involving least squares curve fitting and other numerical analysis techniques. The success of these models varies with the problem analyzed and with the type of analysis.

II. OBJECTIVES OF THE RESEARCH EFFORT:

The problems associated with the understanding and prediction of detonation characteristics are extremely complex. They involve several fields of both chemistry and physics and often several states of matter within those fields (Fickett and Davis, 1979). As such, they have not lent themselves to a simple tractable solution (Davis, 1987). The most successful approach is one that has developed over the last thirty years and has increasingly involved the use of rather sophisticated computer analysis. The software associated with this analysis started with a "SIN" code and led to several spin-offs. All of these are finite difference approximations. Differences between; burning and detonation, heterogeneous and homogeneous materials, and various geometries can all be approximated by additions to the original program, such as Forest Fire and Sharp-Shock Burn (Mader, 1979). This, of course, adds to the complexity of the analysis.

Currently, the situation is such that in the ordinary day-to-day operations of the laboratory, these models are far too complex to be of any use. Typically, they will take an expert in the field several months to enter the appropriate initial and boundary conditions, run the program, and then check to see if the results make sense. Hence, these computer codes are really viable only at the large research facilities such as Los Alamos and Sandia.

At the smaller laboratories, there is a need for a more simple approach to obtain reasonably accurate predictions for explosive parameters as new IHEs are developed and tested. The major objective of this research was to continue the development of one such model started at Eglin over the summer of 1987.

III.

a. Last summer it was decided that the most reasonable analytical procedure would permit a shock wave to be transmitted between two different materials and then look at pressure attenuation of that shock wave in the second material as a function of the thickness of this second substance. Such a strategy would then, with some minor modifications, allow analysis of shock transmission and pressure attenuation in several materials in contact with one another.

The starting point for the model developed is the Hugoniot curve for the material being considered. This curve is the set of all possible shock states in the material. There are several such curves for each material just as there are several interrelated parameters that can describe a particular state. One can experimentally determine the shock wave speed in the material with a standard streak photograph, pressure pins, or some other similar technique. If the density is known, one can then obtain the corresponding pressure and particle velocity (Fickett and Davis, 1979).

In the current research, material density, ρ , and shock wave speed, u_s , were assumed. Then, from the relationship in equation (1)

$$P = \rho \cdot u_s \cdot u_p \quad (1)$$

one can find the slope of the straight line extending from the origin to the Hugoniot Curve where the pressure, P , and the particle speed, u_p , have been plotted for the material in question. In this case, it is the material through which the shock wave initially travels. The analytical form of the Hugoniot curve was obtained from a least squares curve fitting analysis from experimental data in Marsh (1980). In most cases, it was found that the best fit for pressure versus particle speed was quadratic and of the general form given by equation (2)

$$P = a + bu_p + cu_p^2 \quad (2)$$

where each material will have its own unique a , b , and c values. Results for the other materials are presented in table (1). In some cases the fit for quadratic and cubic approximations were about equally effective. In the name of simplicity and uniformity, equation (2) was used for all materials (Dunn and Clark, 1974; Taylor, 1982; Young, 1962).

Typical graphs for least squares fits are shown in figures (1)-(3). The similarity among materials can easily be seen as can the good nature of the fit.

Table (2) provides the adjusted R square value for each of the materials that were modeled. This is a measure of goodness of fit between the data and the approximation. A perfect fit would give a value of 1. As can be seen both quadratic and cubic approximations are quite good. In general, the slightly larger number for the cubic fit is typical of the extra degree of freedom associated with the

TABLE 1
COEFFICIENTS OF EQUATION (2)

Material	a	b	c
Aluminum	-1.00	15.95	3.31
Beryllium	0.23	14.45	2.17
Brass	0.02	13.73	11.91
Calcium	-0.12	5.78	1.44
Cesium	-1.17	2.35	2.21
Copper	-1.65	38.01	12.49
Lithium	0.25	2.21	0.65
Magnesium	0.44	7.35	2.31
PMMA	-0.57	4.05	1.46
Silver	2.53	29.26	18.13
NaCl	0.22	7.03	2.92
Titanium	-0.16	23.16	4.24
Tungsten	-1.43	82.51	21.09
Water	-1.14	3.32	1.17
Zinc	2.26	17.70	12.39

The units associated with the quantities are
speed (km/s) and pressure (GPa)

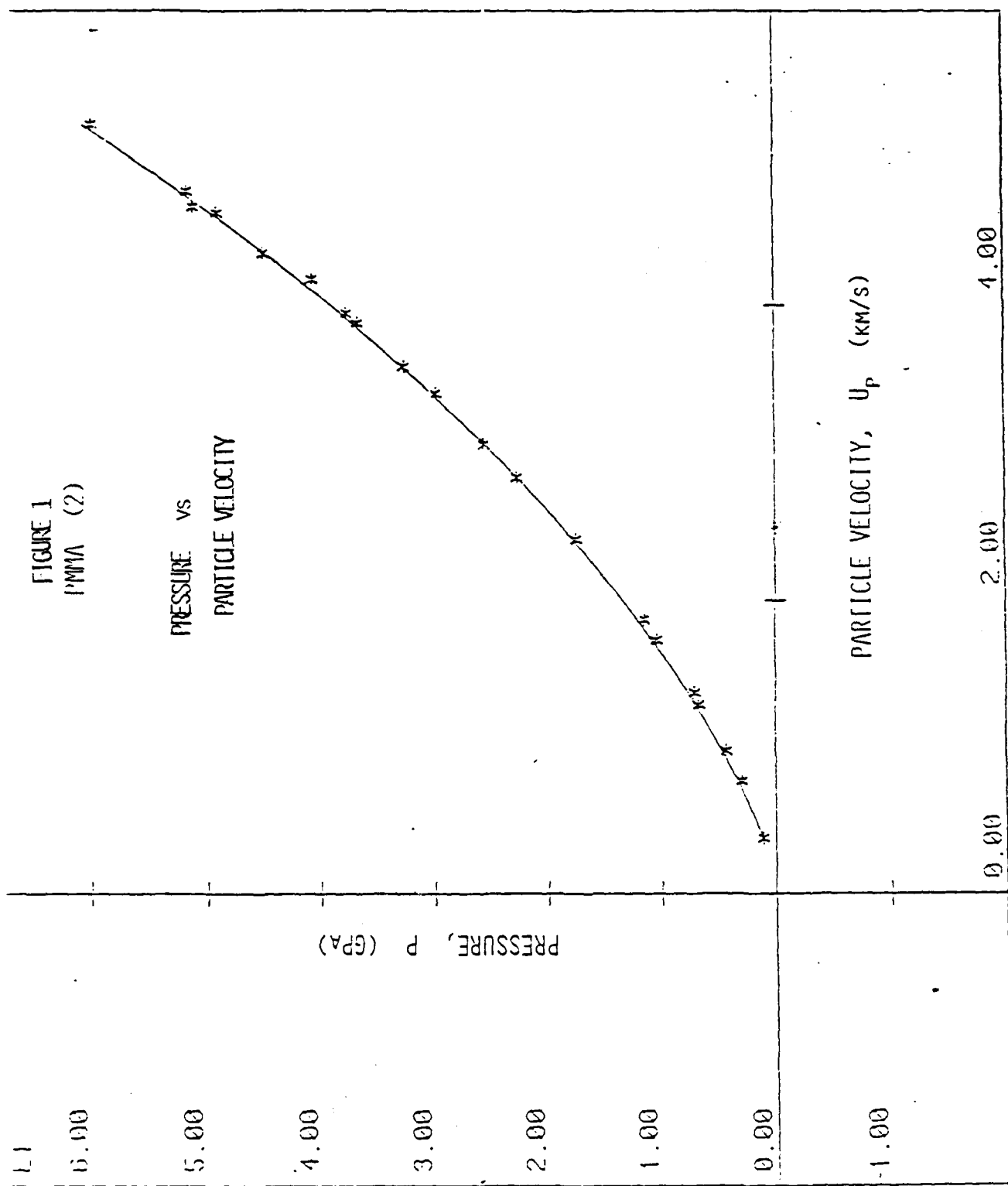


FIGURE 2
ALUMINUM 6061 (2)

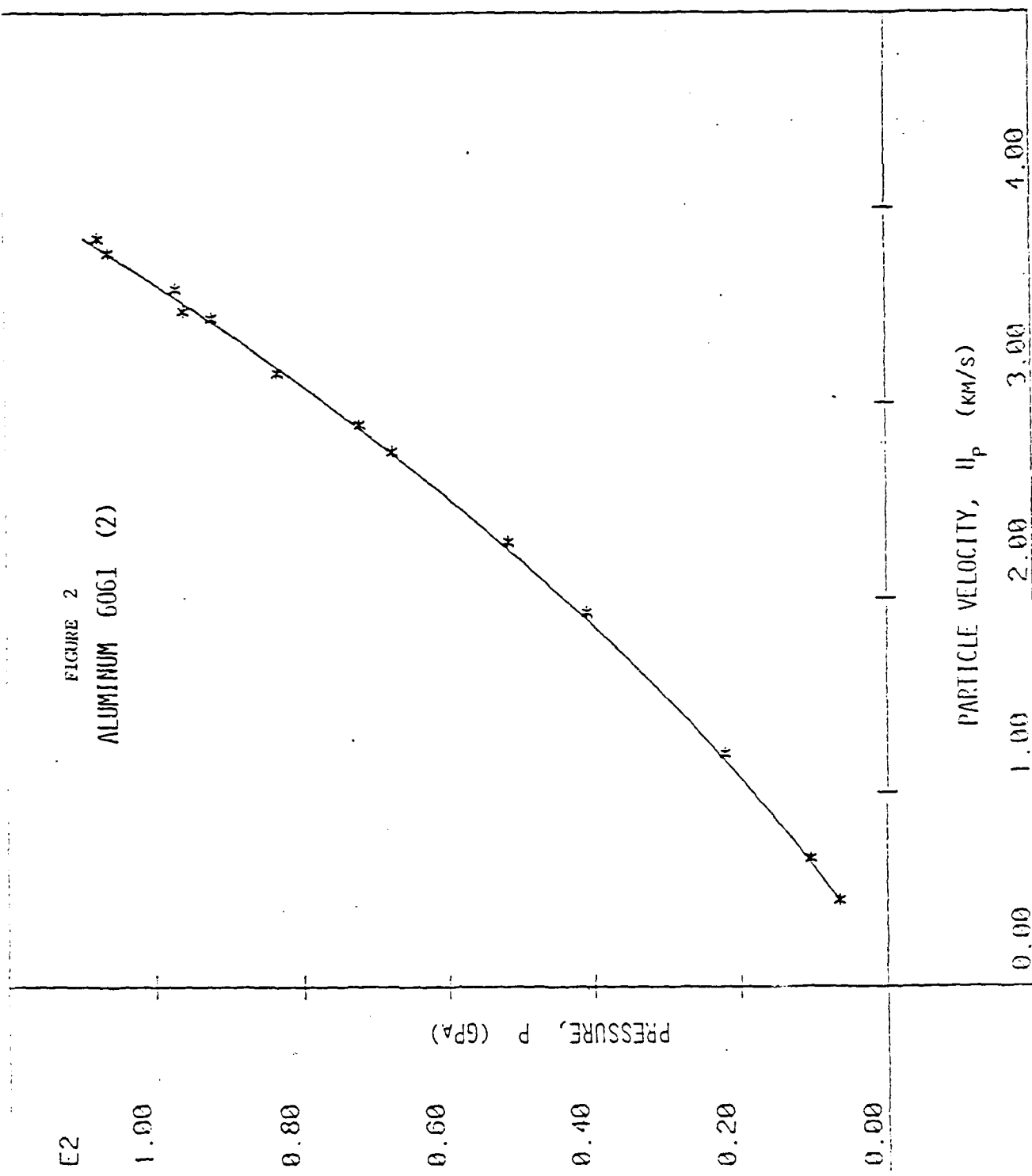


FIGURE 3
SILVER (2)

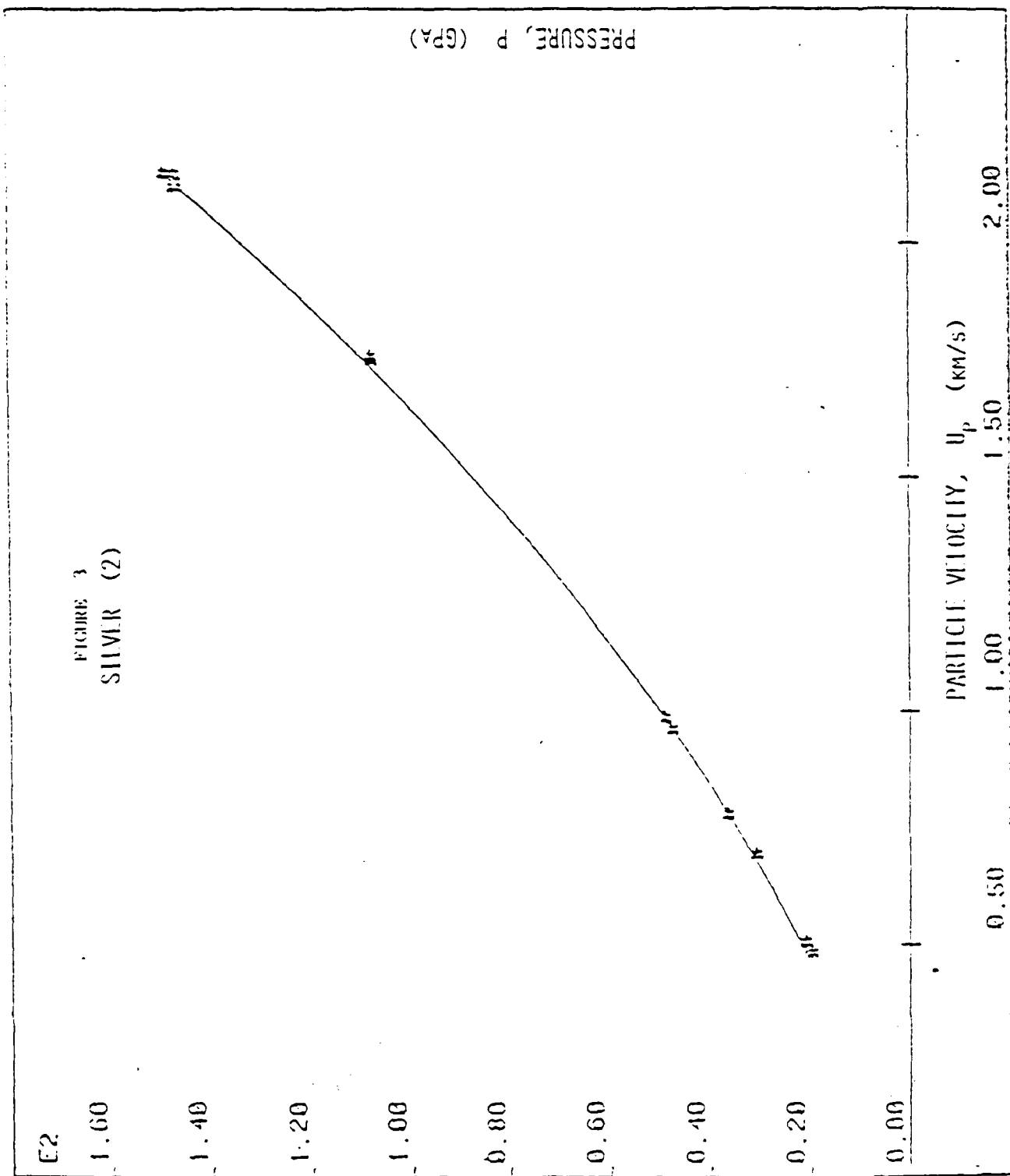


TABLE 2
ADJUSTED "R SQUARE" VALUES

Material	Quadratic	Cubic
Aluminum	0.99922	0.99940
Beryllium	0.99986	0.99986
Brass	0.99987	0.99987
Calcium	0.99907	0.99915
Cesium	0.99998	0.99999
Copper	0.99902	0.99898
Lithium	0.99971	0.99978
Magnesium	0.99992	0.99991
PMMA	0.99945	0.99945
Silver	0.99968	0.99979
NaCl	0.99965	0.99974
Titanium	0.99983	0.99994
Tungsten	0.99982	0.99983
Water	0.99988	0.99995
Zinc	0.99986	0.99991

cubic. Because of this there is no real reason either physically or statistically to prefer the cubic to the quadratic fit.

Additional analysis of the fit to equation (2) provides confidence levels on the coefficients. These results are shown in table (3). Both the coefficients and their errors are given. The errors are in parentheses and were calculated at the 95% confidence level. It can easily be seen that the linear and square terms are known rather accurately. This gives some added confidence to the particular modeling process.

The point of intersection of the straight line of equation (1) and the Hugoniot curve of equation (2) represents the incident pressure at the boundary between two materials. At this point, the Hugoniot of material one must be "flipped" (rotated 180 degrees around a vertical axis passing through this point). Then the point of intersection of the Hugoniot curve for material one with the corresponding curve for material two will give the pressure in the second material the one the shock wave enters. Boundary conditions require that transmitted pressure be equal to reflected pressure in the first material.

The flipped curve for material one is given by equation (3)

$$P = (a + 2bu_p^* + 4cu_p^{*2}) - (b + 4cu_p^*)u_r + cu_r^2 \quad (3)$$

where u represents the particle velocity at the intersection of equations (1) and (2).

The second material can be represented by equation (2) with the appropriate values for a , b , and c given in table (1). This leads to equation (4).

$$P = a_2 + b_2 u_p + c_2 u_p^2 \quad (4)$$

TABLE 3
COEFFICIENTS OF EQUATION (2)
WITH (ERRORS)

Material	a	b	c
Aluminum	-1.00 (1.26)	15.95 (1.35)	3.31 (0.30)
Beryllium	0.23 (0.39)	14.45 (0.44)	2.17 (0.10)
Brass	0.02 (0.86)	13.73 (1.47)	11.91 (0.49)
Calcium	-0.12 (0.57)	5.78 (0.54)	1.44 (0.10)
Cesium	-1.17 (0.23)	2.35 (0.19)	2.21 (0.04)
Copper	-1.65 (1.56)	38.01 (2.57)	12.49 (0.82)
Lithium	0.25 (0.32)	2.21 (0.23)	0.65 (0.04)
Magnesium	0.44 (0.35)	7.35 (0.32)	2.31 (0.06)
PMMA	-0.57 (0.39)	4.05 (0.33)	1.46 (0.06)
Silver	2.53 (1.93)	29.26 (3.51)	18.13 (1.28)
NaCl	0.22 (0.36)	7.03 (0.46)	2.92 (0.12)
Titanium	-0.16 (0.50)	23.16 (0.68)	4.24 (0.20)
Tungsten	-1.43 (1.29)	82.51 (2.68)	21.09 (1.18)
Water	-1.14 (0.22)	3.32 (0.19)	1.17 (0.03)
Zinc	2.26 (0.75)	17.70 (1.13)	12.39 (0.36)

Standard Errors Have Been Calculate At The 95%
Confidence Level

Units: a-GPa, b-GPa(s/km), c-GPa(s/km)²

When equations (2) and (4) are solved simultaneously, the value for P will be the pressure in material two as the shock wave enters. A straightforward but algebraically unpleasant process will yield two answers. One will typically make no physical sense and can be eliminated.

b. Also modeled was the attenuation of the pressure once the shock wave is in the second material. Initially in the summer research a polynomial modeling between pressure and attenuation distance was used. Analytically this is given by equation (5).

$$P = A + BR + CR^2 + DR^3 + ER^4 \quad (5)$$

In this equation R is the attenuation distance and P is the shock wave pressure. A least squares fit provided values for the parameters A-E. This was a very unsatisfactory model. Mathematically it only gave reasonable results for a limited range of distances and physically it made no sense at all. Experimental data for pressure attenuation is not easily found in the literature, if indeed it exists, so that equation (5) was only evaluated for PMMA (Jaffe et al., 1965).

The current research attempted to find a more general and more pleasing (from a physical point of view) model. As a first approximation it was decided to try an exponential decay. This is shown by equation (6).

$$P = A \exp(-BR) \quad (6)$$

where P is the shock wave pressure in kbar and R is the distance the shock wave has moved into the second material, measured in mm. A and B are to be determined from the data. The results are shown in table (4). Also shown in this table, in parentheses, are the standard errors for these two

TABLE 4
COEFFICIENTS OF EQUATION (6)
WITH (ERRORS)

A (kbar)	144	(1)
B (1/mm)	0.043	(0.001)

parameters at the 95% confidence level. The adjusted R square value for this approximation is 0.99765, indicating an excellent fit.

A typical extension to this approximation would be to include more terms in the exponential. The next two approximations are given by equations (7) and (8).

$$P = A \exp(-BR - CR^2) \quad (7)$$

$$P = A \exp(-BR - CR^2 - DR^3) \quad (8)$$

However upon the evaluation of the coefficients for equations (7) and (8) the values of C and D were zero to the accuracy of the data. Further the R square value did not change significantly. Thus because of its simplicity and large R square value, equation (6) is to be preferred over (7) and (8). Also it should be pointed out that the new expression, (6), is perfectly general and can be used to approximate the attenuation at any distance.

Several researchers in the field at Eglin AFB suggested that equation (6) might have different parameters for different pressure values. In other words, that there might be two different pressure attenuation curves that joined smoothly. If this were so, it would tend to indicate that high pressure attenuation might proceed through a different physical process than that for low pressure attenuation.

In order to test this hypothesis, the parameters A and B were evaluated for high and low pressure ends of the attenuation data. The results are given in table (5) with errors on the parameters given in parentheses. Clearly from a statistical point of view the two results are not consistent. However, with only 15 total data points and the results so close to one another, I would suggest the acquisition of more data before attempting to justify the physically and mathematically unpleasant assumption of two different pressure attenuation processes.

TABLE 5
COEFFICIENTS OF EQUATION (6)
WITH (ERRORS)

	A (kbar)	B (1/mm)
High Pressure	138 (1)	0.039 (0.000)
Low Pressure	130 (1)	0.037 (0.000)

c. Both equations (2) and (6) can be generalized to any number of materials by evaluating the coefficients. The data for equation (2) are readily available, that for equation (6) are not. There are some limitations on the generality of the results obtained. The major one pertains to the fact that the PMMA results for equation (6) are for samples two inches in diameter. It would seem reasonable to expect different coefficients for samples of different diameters.

This particular analysis, although rather limited in scope, offers the opportunity to quickly and accurately approximate peak pressure values in different materials. The computer program can be run on any personal or scientific computer and gives immediate results. Although clearly not of the accuracy of the complex computer codes using finite difference methods, it is far easier to use and its accuracy is good enough for choosing masses and geometries that are useful in testing new explosives, their effects, and their suitability as IHEs.

IV. RECOMMENDATIONS:

a. Because of the demands of opening new facilities and of the reassigning of key personnel, many of the tests and data to be performed by Eglin AFB employees were not done. Hence the scope of the analysis was severely limited and the research was not able to completely follow the directions initially indicated. Generalization of the analytical method and of the results to cylinders of different diameters and materials would seem in order.

b. In conclusion, let me restate that the computer model developed was at no time meant to replace the more sophisticated, more accurate, and more detailed computer codes that now exist. Instead, it is intended to be easier to use and, hence, can be used by scientists and technicians in related fields who might not have the time or expertise to use the more complex programs.

c. The computer program, if taken further, will provide appropriate data, pressure values, both forward and backward in space, and will give them quickly. It is this data that is useful in the design and testing of IHEs. And, it is the ease with which this data will be available that will make it a useful research tool.

d. Appendix A provides a similar analysis for explosive materials prior to detonation.

REFERENCES

- Corley, John D., 1Lt, USAF. "Insensitive High Explosives Evaluation Techniques." Internal Report, Eglin Air Force Base, Florida, AD-PA-86-233, 1986.
- Davis, William C. "The Detonation of Explosives." Scientific American, May 1987, pp 106-112.
- Dunn, Olive Jean and Virginia A. Clark. Applied Statistics: Analysis of Variance and Regression, New York, John Wiley and Sons, 1974.
- Fickett, Wildon and William C. Davis. Detonation, Berkeley, California, University of California Press, 1979.
- Jaffee, I., et al. "The NOL Large Scale Gap Test. Compilation of Data for Propellants and Explosives II." NOLTR 65-177, White Oak, Maryland, Naval Ordnance Laboratory Technical Report, 1965, pp 35-42.
- Mader, Charles L. Numerical Modeling of Detonations, Berkeley, California, University of California Press, 1980.
- Marsh, Stanley P. (editor). LASL Shock Hugoniot Data, Berkeley, California, University of California Press, 1980.
- Taylor, John R. An Introduction to Error Analysis: The Study of Uncertainties in Physical Measurements, Mill Valley, California, University Science Books, 1982.
- Young, Hugh D. Statistical Treatment of Experimental Data, New York, McGraw-Hill Book Company, 1962.

APPENDIX A

MODELING OF EXPLOSIVE MATERIALS

The generality of the analytical methods described in this paper can be shown, in part, by its further applicability to undetonated explosive materials in addition to those previously mentioned in the text. The results of a similar analysis are given in tables (A1) and (A2) which parallel the results presented in tables (2) and (3).

In comparing the results of tables (A2) and (3), one can readily see that the errors for (A2) are much larger (in a relative sense) than those for (3). The adjusted R square values in table (A1) are somewhat lower than those for non explosive materials. In both comparisons, the differences can be at least partially attributed to the few available data points and the added difficulty of obtaining reliable data from explosive materials.

In the explosives community the general shock wave/velocity behavior of an explosive is often modeled by using the parameters of salt. A simple analysis tends to add validity to this assumption. If one takes the eight explosives described in tables (A1) and (A2) and calculates the mean and standard error for the coefficients a , b , and c one obtains the results shown in table (A3). The b and c values for sodium chloride (the two that "matter") are within the extremes of similar parameters for explosives. Thus this model predicts that the behavior of salt and undetonated explosives will be similar. This can, perhaps, more easily be seen in figure (A1) which presents the same data graphically. In figure (A1) the notations represent:

P_s -- shock wave pressure in salt
 P_{exp} -- mean explosive shock wave pressure
 P_{max} -- maximum explosive shock wave pressure
 P_{min} -- minimum explosive shock wave pressure

TABLE A1

ADJUSTED "R SQUARE" VALUES

Explosive	Quadratic	Cubic
Baratol	0.98423	0.99166
HMX(pressed)	0.98332	0.98417
PBX	0.99923	0.99929
PETN(pressed)	0.95589	0.94790
PETN(crystal)	0.99845	0.99832
RDX(20% Al)	0.99979	0.99967
TATB(pure)	0.99727	0.99743
TNT(cast)	0.99342	0.99249

TABLE A2

COEFFICIENTS OF EQUATION (2)
WITH (ERRORS)

Explosive	a	b	c
Baratol	-0.53 (1.71)	8.84 (4.59)	1.51 (2.91)
HMX(pressed)	-0.71 (3.87)	7.71 (10.3)	2.16 (6.48)
PBX	0.30 (0.17)	3.60 (0.46)	4.38 (0.23)
PETN(pressed)	0.11 (0.61)	2.46 (3.10)	6.89 (3.85)
PETN(crystal)	-0.09 (0.18)	5.12 (0.54)	3.01 (0.33)
RDX(20% Al)	-0.38 (0.34)	6.77 (1.07)	0.88 (0.74)
TATB(pure)	-0.03 (0.44)	3.69 (1.25)	4.82 (0.74)
TNT(cast)	-0.47 (0.81)	5.52 (1.70)	2.02 (0.76)

Units: a-GPa, b-GPa(s/km), c-GPa(s/km)²

TABLE A3
COEFFICIENTS OF EQUATION (2)
SALT VERSUS EXLOSIVES

Explosives	a	b	c
Mean	-0.22	5.46	3.21
Error	0.24	1.53	1.40
Sodium Chloride	0.28	6.93	2.95

Errors have been calculated at the
95% Confidence level

Units: a-GPa, b-GPa(s/km), c-GPa(s/km)²

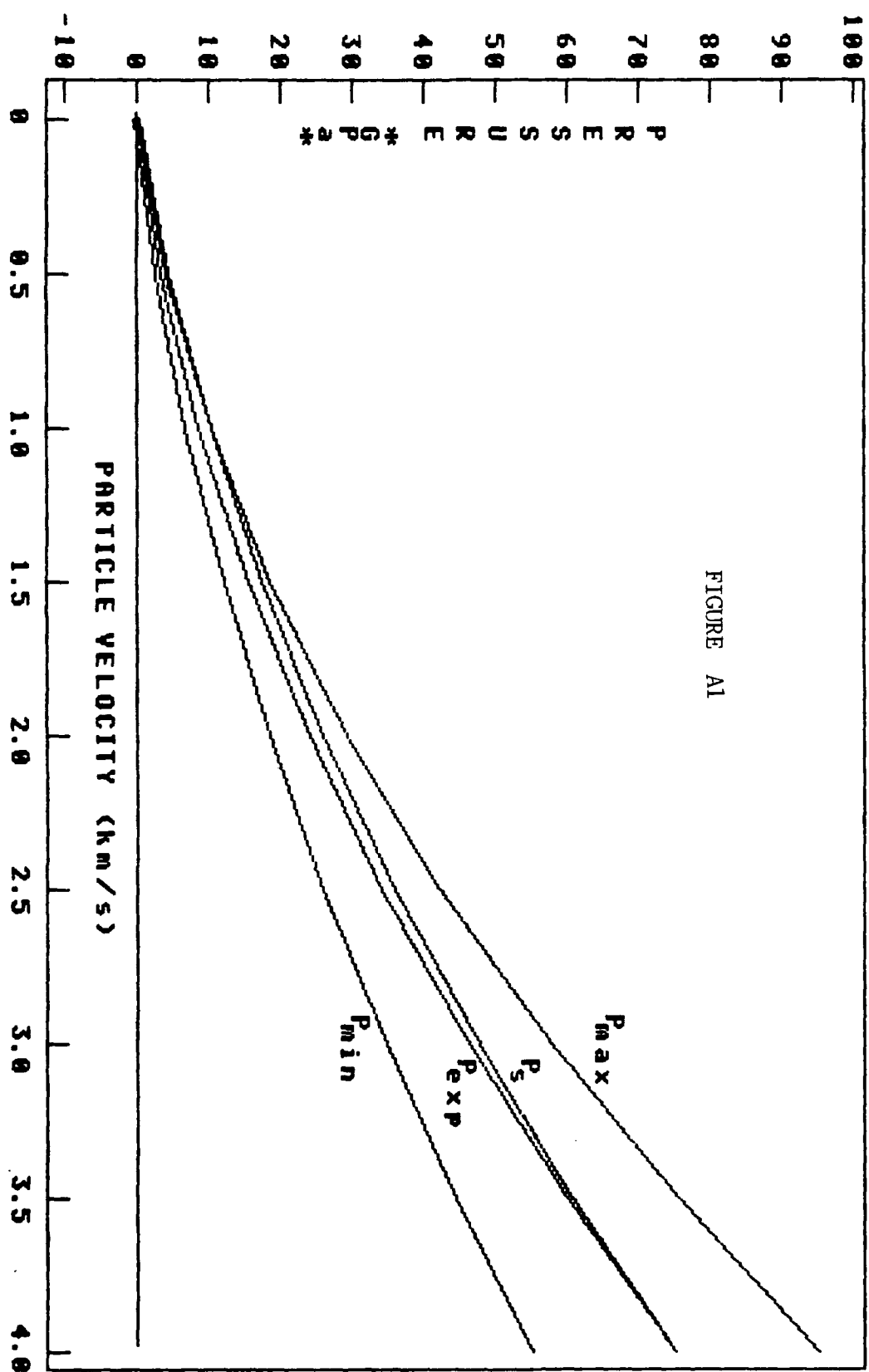


FIGURE A1

FINAL REPORT
PYROELECTRIC SENSING FOR POTENTIAL MULTI-MODE USE

1988 USAF-UES
RESEARCH INITIATION PROGRAM

Sponsored by the
AIR FORCE OFFICE OF SCIENTIFIC RESEARCH
BOLLING AFB, DC

Administered by
Universal Energy Systems, Inc.

James Bert Nail, Ph.D., Associate Professor
John Fryer, Master of Science Candidate

Electrical Engineering Department
Mississippi State University

30 May 1988

F49620-85-C-0013/SB5851-0360

ACKNOWLEDGEMENTS

This research was made possible through the Air Force Office of Scientific Research, Bolling AFB, DC, with contract management through Universal Energy Systems. We wish to express our appreciation for this support, and our hope for useful application in the future. We are also indebted to Bob McIntyre of the Institute for Technological Development for expertise and helpful suggestions regarding microelectronic fabrication, and especially to Dr. Steven F. Butler of Eglin AFB, who provided the creative environment from which this research began.

ABSTRACT

This research focused on the potential microelectronic fabrication of piezofilm sensing devices, with emphasis on application of the pyroelectric effect. Experimental work, however, was done on discrete film samples. Simple patterns were etched on the film surfaces and connected differentially to achieve sufficient rejection of the microphonic noise components. Several interface schemes were attempted, none of which were consistently acceptable. The problems encountered were then analyzed in the context of circuit reduction by microelectronic fabrication.

General conclusions are presented that may be applicable for discrete film applications. Specific issues dealing with promising microelectronic fabrication are presented, with a report of continuing research.

INTRODUCTION

This research is a first attempt to merge Polyvinylidene Fluoride (PVDF) Piezo-Film and microelectronics technology to accomplish pyroelectric sensing. The original proposal emphasized: (1) experimental work with optomechanical techniques to posture the signal for easy detection, (2) experimentation with interface circuitry to prove the concepts for common-mode rejection and enhancement of the sensor response, and to explore potential problems, and (3) a limited attempt at scaling to microelectronic proportions. As it worked out, most of the effort and frustration revolved around point (2), and little was expended on point (1). Quite a bit of thought has been applied to point (3), which we consider the real contribution. Physical effects are analyzed to arrive at a pixel dimension, and several alternative approaches are postulated that hold promise within these dimensions.

There are two general approaches to interfacing PVDF film. The most common is simply to attach to the gate of a FET, which is used for impedance matching. Inherent in this approach is acceptance of an extremely long electrical time constant, which makes the sensor useless for applications requiring both speed and sensitivity.

The second approach is to maintain near-zero voltage across the film with operational amplifier circuitry. A simple current-to-voltage configuration will accomplish this function, provided the op-amp input impedance is in the same range as the film resistance. Only FET-input amps with unprotected inputs approach this value. The signal levels expected from the piezoelectric effect are much larger than the pyroelectric signals and require external resistors to limit input

current. Furthermore, in order to reject microphonic noise, dual lines must be routed in a completely symmetric fashion to differential inputs, as shown in Figure 1. The protection resistors, R_p , have relatively little effect on the operation of the circuit, except for setting the new electrical time constant. These resistors could also be moved to the amp inputs, as shown in Figure 2, with similar results.

The important point is that the feedback resistor (which is typically much less than the film source resistance) represents a proportionally lower resulting output signal. The obvious way to retain signal level is to choose R as large as possible. There are a few suppliers who provide resistors in the range of $10^9 - 10^{12}$ ohms. Matching resistance (and tracking) is difficult for these values. Although several circuits exhibit excellent common-mode signal rejection, each is extremely dependent on resistance match and tracking. This means that amplifier gain based on large resistor values will experience a significant piezoelectric contribution at the output. It is possible to shunt much of the current from the feedback resistors, making them appear to have much larger value, and this will achieve the same gain with better matching. Unfortunately, the amplifier noise will be enhanced in this configuration.

The previous discussion is believed adequate to follow the logic applied in the experimental work. For more information on noise, shielding, and circuit contamination, refer to Appendix B. For additional information on the pyroelectric effect, refer to Appendix C.

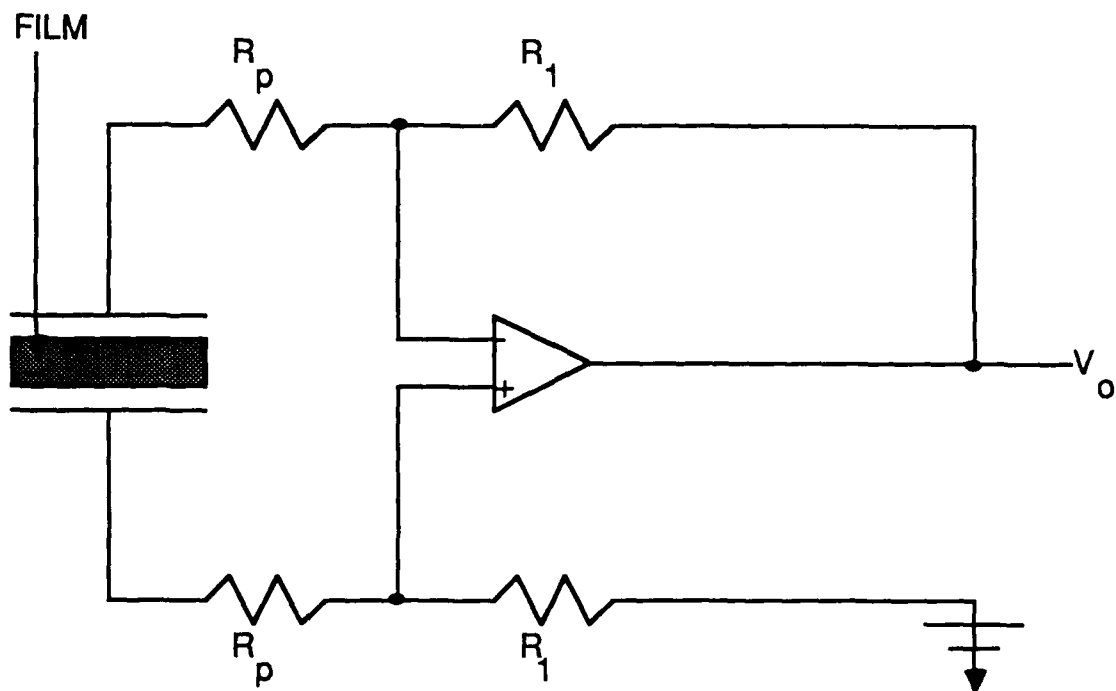


FIGURE 1. CURRENT - TO - VOLTAGE CONVERTER

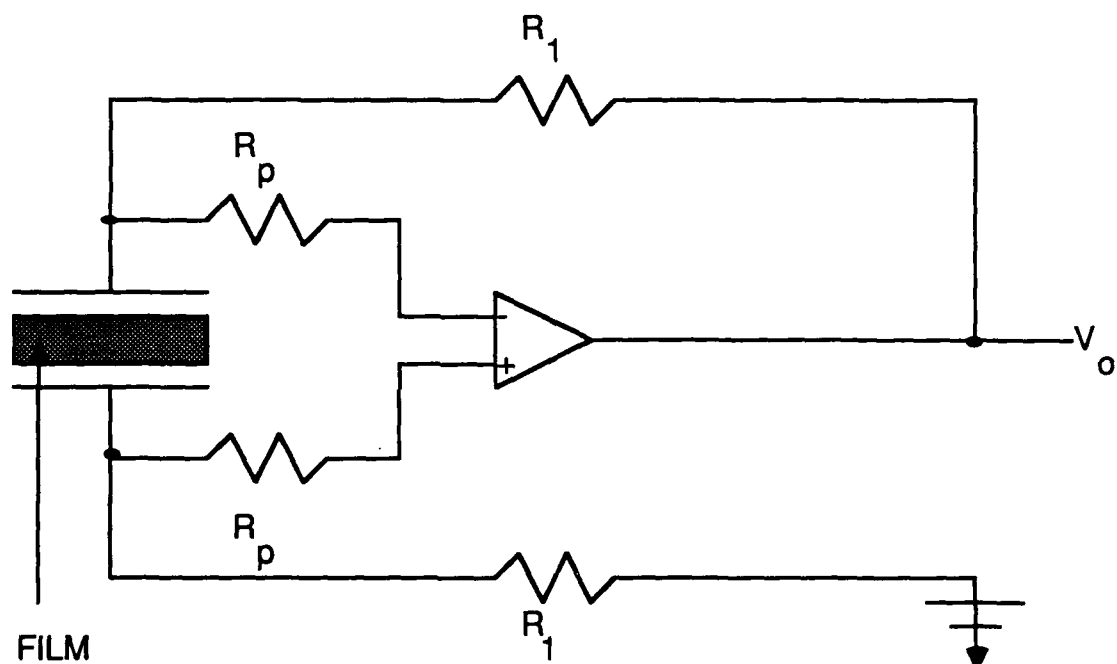


FIGURE 2. CURRENT - TO - VOLTAGE CONVERTER
ALTERNATE PROTECTION SCHEME

EXPERIMENTAL DEVELOPMENT

A .5 mW He-Ne laser was selected as a repeatable source for experimentation. A 6-tooth chopper wheel was fabricated and mounted on a small dc motor with an integral tachometer for easy observation of signal frequency. An additional adjustment was provided for duty cycle control, and the whole assembly was mounted on an optical rail for added repeatability. This device worked so well for providing a time varying signal for observation that no further alterations were made. The modulation frequency ranged from 10Hz to 1000Hz, and duty cycle was adjustable from 0% to 100%. The unmodified beam width was approximately .020", well within the pixel dimension. A pinhole was fabricated to further diminish the signal.

The extremely high film resistance dictated the use of FET-input operational amplifiers, with unprotected inputs. One of the very few amplifiers of this type is the Burr-Brown OPA-104, which we used in several circuits. From the Burr-Brown application notes, we determined that Teflon was the only fabrication medium that would eliminate leakage current problems. The first circuit was fabricated with Teflon standoffs mounted in aluminum and connected to film captured between frames machined from Teflon. The film was etched exactly as proposed, with a 10 x 10 crosshatch of interconnected pixels about .030" on a side. From experimentation with this circuit and film combination, we discovered problems in surface leakage, shielding, film etch accuracy, and connection to the film. No pyroelectric signal was distinguishable in this circuit. The overall dimensions of the assembly were about 4" x 4" x 6".

In order to improve pattern definition, a simpler 6 x 6 crosshatch of .040" interconnected pixels was fabricated, with considerable emphasis on etching techniques. Piezofilm is very difficult to process, and much of our effort was expended developing a workable technique. For those who would like to develop the same capability, Appendix A explains the process that we used, which allows definition adequate for line widths of about .040". The Teflon frame was similarly reduced and modified for an easy clamp-connection to the film. At this point, several interface circuits were fabricated, usually in printed circuit, but with critical input lead connections made off-the-board to avoid leakage currents. These circuits ranged from one to three amplifiers in complexity, with the least complex showing the most promise. At this point, we did have indication of a pyroelectric response, but enclosure in a shielding assembly was an absolute necessity.

Shielding was then incorporated by redesigning the assembly to stack in 2" x 2" modules, to be enclosed except for a small hole for light entry. The film was sandwiched in Teflon, which in turn was sandwiched between Aluminum plates, a printed circuit was attached, batteries connected, and the whole assembly enclosed in a 2" x 2" x 4" can. The film pattern is shown in Figure 3, assembly layout is shown in Figure 4, and three promising circuits are shown in Figures 1, 5 and 6.

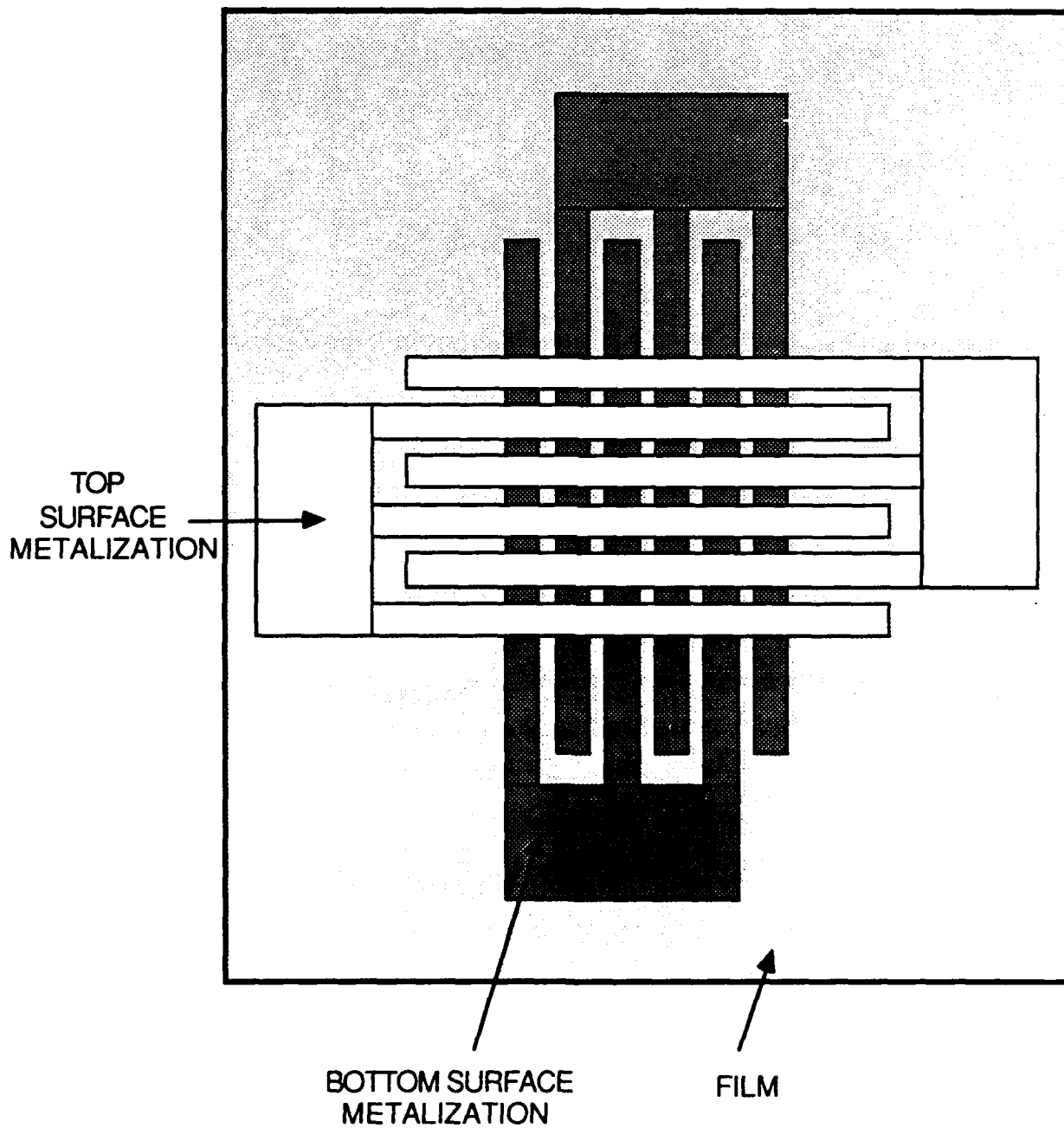


FIGURE 3. PYROELECTRIC FILM WITH ELECTRODE PATTERN

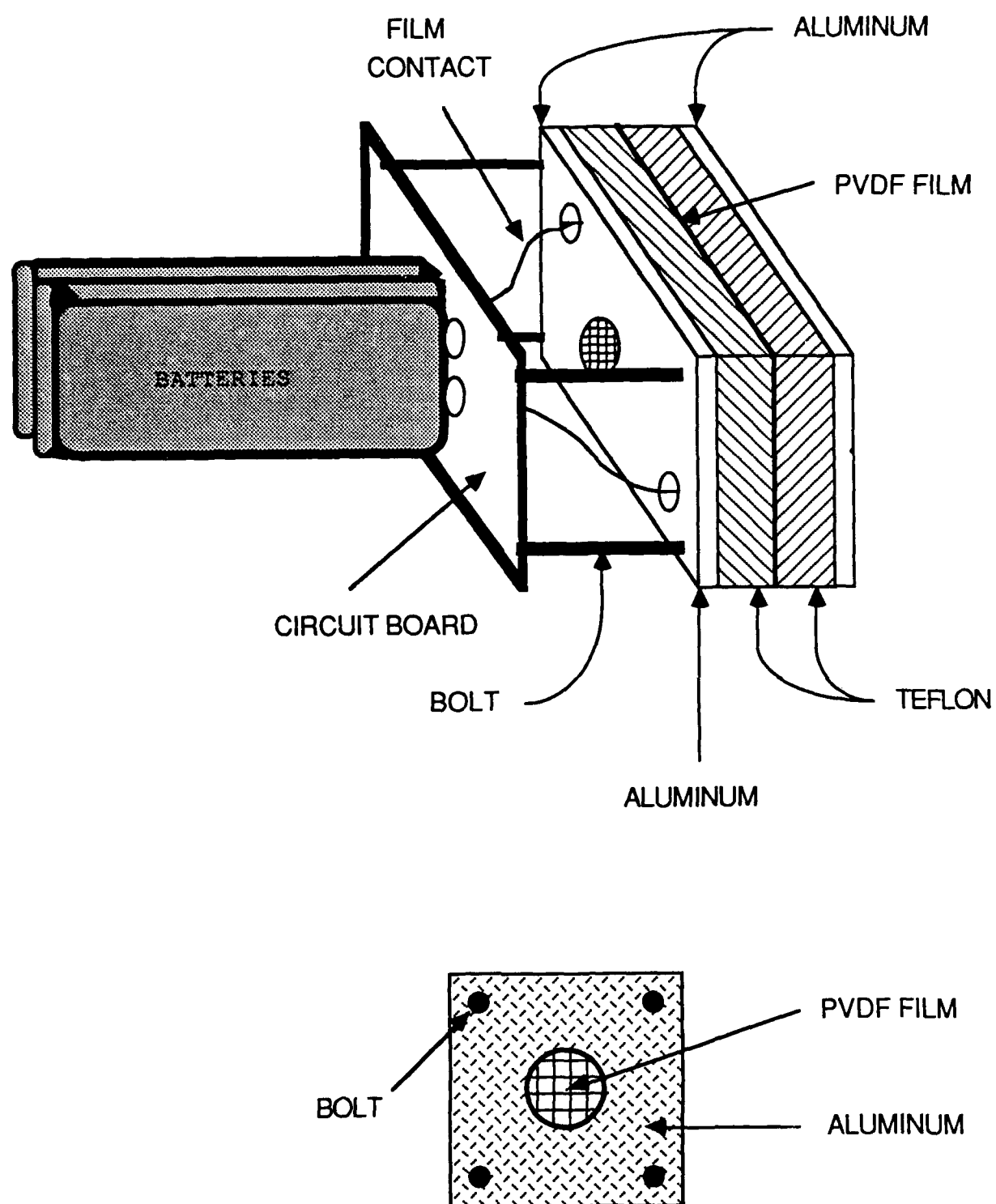


FIGURE 4. SENSOR ASSEMBLY -- PROFILE AND FRONT VIEWS

EXPERIMENTAL RESULTS

The ability to reject common-mode microphonic noise was obvious in these circuits. The circuit of Figure 5 responded with approximately a 4V peak-to-peak signal to a pinhole of light from a .5 mW He-Ne laser, and that of Figure 6 was nearly as responsive. These circuits have a shunt resistor provided, which can effectively leverage the feedback resistance by diverting a portion of the feedback current. (This increased the effective R from 10^6 to 10^9 ohms in the circuits used). Both circuits had a noticeable, but very diminished response to microphonic noise, such as a whistle. They also responded strongly to the fluorescent lights in the laboratory, as expected. The tradeoff between gain and frequency response inherent in these circuits is shown in Figure 7. The sloped line represents the electrical response of the film itself. Comparison with the circuit response (flat line) shows that above 7 Hz the compensation vastly improves the signal gain. At 7 KHz, the difference is 60 dB.

The assembly was fairly repeatable in the short term, and early efforts were applied to increasing the gain, when the available gain should have been quantified. Over a period of two or three days, the response became increasingly more unstable and intermittent, until the circuit remained consistently unstable and oscillatory. Leakage currents were suspect, but repeated disassembly and cleaning were ineffective. The problem was finally located at the connection to the film itself.

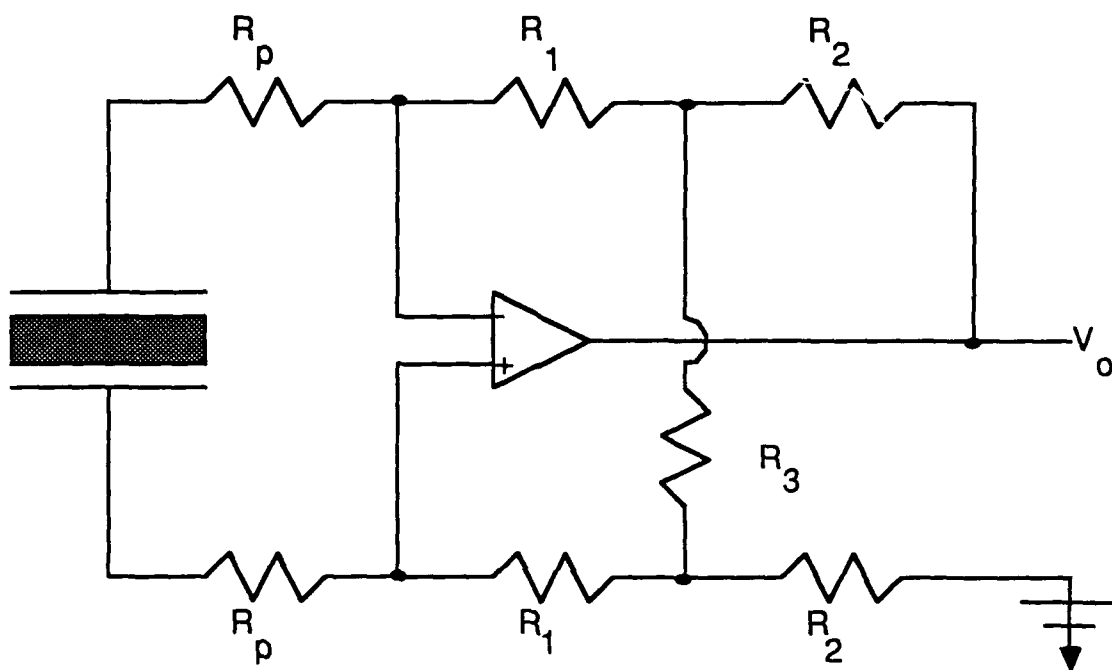


FIGURE 5. EXPERIMENTAL CIRCUIT

LEVERAGED FEEDBACK SCHEME

R_1 , R_2 AND R_p ARE MATCHED PAIRS OF 10^6 OHM RESISTORS

$$R_3 = 10^3 \text{ OHMS}$$

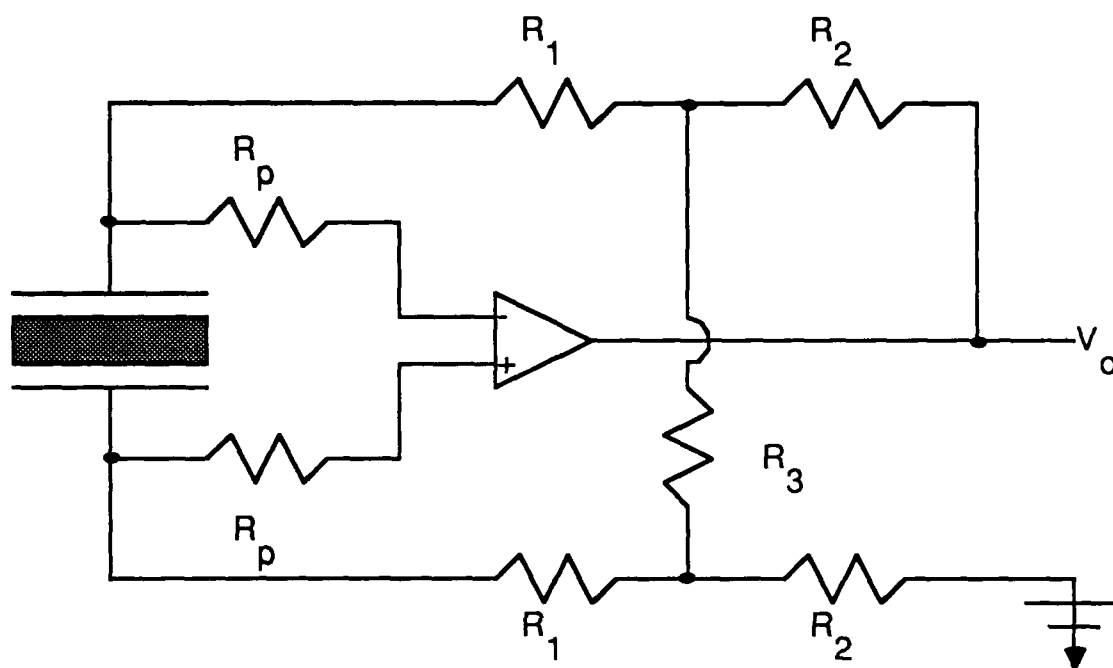


FIGURE 6. ALTERNATE PROTECTION SCHEME

R_1 , R_2 AND R_p ARE MATCHED PAIRS OF 10^6 OHM RESISTORS

$$R_3 = 10^3 \text{ OHMS}$$

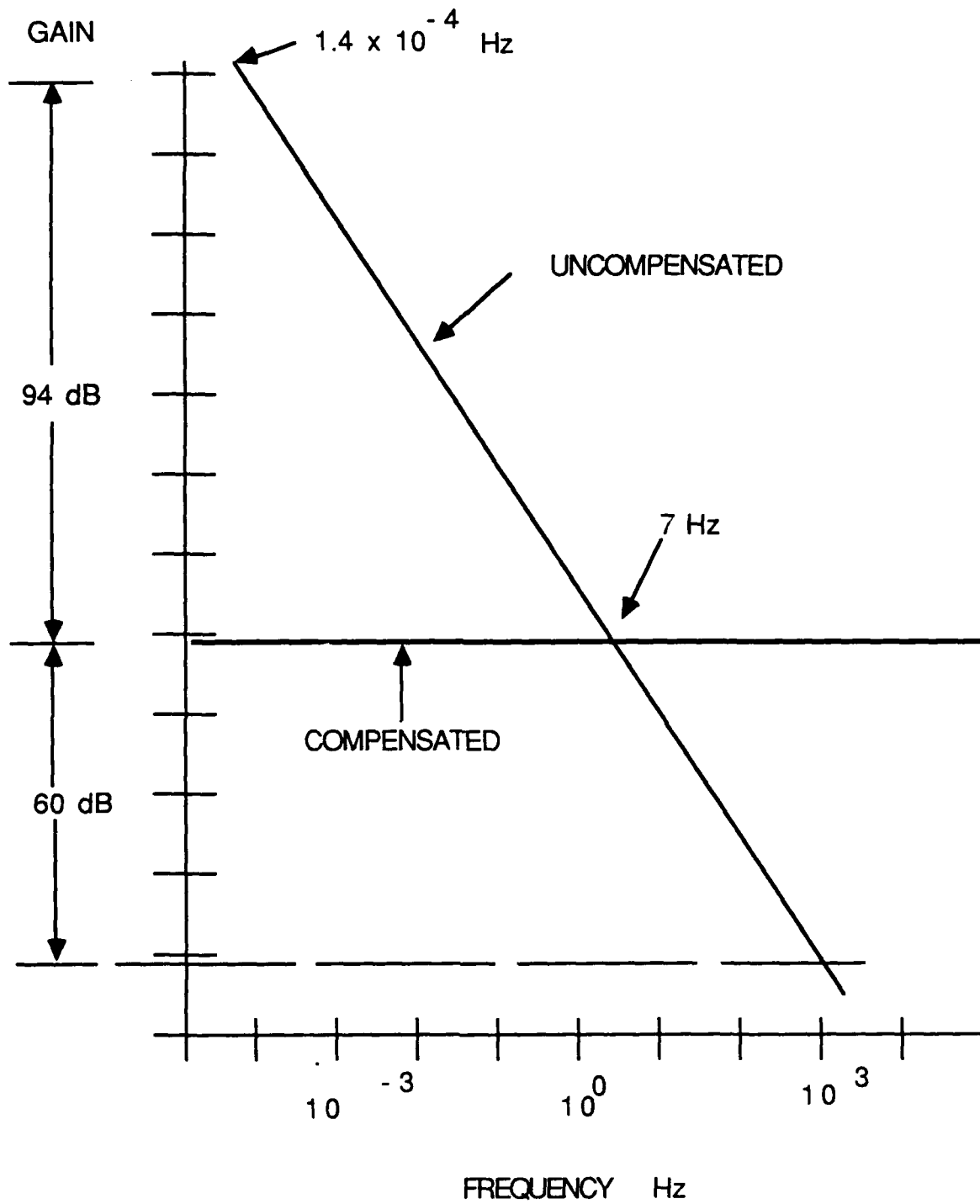


FIGURE 7. GAIN vs FREQUENCY TRADEOFF

A clamp connection to the film is the obvious approach, since soldering is not possible. The outer metallization is Aluminum, well known for the ability to oxidize. The resulting Aluminum oxide is an excellent insulator, and essentially replaces the terminal connections with a small capacitive coupling. This was an unexpected problem, for which the discrete solution and microelectronic solution would be markedly different. At this plateau, microelectronics fabrication processes and dimensions held more promise than additional research with discrete components.

MICROELECTRONICS SCALING STUDY

Several negative conclusions regarding the use of piezofilm follow naturally from the research which we conducted. These can be grouped into three major areas: (1) off-chip processing and connection difficulty, (2) limiting leakage and noise in high impedance interfaces, (3) active common-mode rejection and input current limiting problems.

Despite these obvious drawbacks to bulk piezofilm, some very positive conclusions can be drawn when microelectronic processing is considered. The compatibility with microelectronic fabrication is striking. The purity of the melt must approach that of silicon, metallization is applied by sputtering, poling is done by an applied electrostatic field, at temperatures in the range used for "softbake" of photoresist.

The microelectronic environment also provides a medium that totally eliminates film connection problems, since all processing to the hermetic seal is done in vacuum or nitrogen. This also does much to limit the leakage (which comes partly from the circuit layout, and partly from surface contaminants). Greatly compacted dimensions limit susceptibility to electrical noise, make shielding much simpler, and opens the possibility of passive common-mode rejection.

Microphonic noise is the major factor to be considered in common-mode rejection techniques. The wavelength of audible or ultrasonic noise is given by

$$\lambda = V_s / f,$$

where λ represents the wavelength, V_s is the speed of sound, and f is the frequency of vibration. If we assume standard temperature and pressure conditions, the speed of sound is approximately 330 meters/second. A cutoff frequency of, at most, 100 KHz seems reasonable for a film that is backed by a chip. At this frequency, a wavelength of 3.3 mm results. If we limit pixel size to a factor of 30 smaller (100 μ m), the impinging vibrations on two adjacent pixels will be essentially equal. Then it remains to develop a technique to make the impinging noise cancel, while incident infrared (IR) adds. One such technique was suggested in the proposal originating this research. In that discussion, one of the stringent requirements was that of selectively poling small adjacent pixel sections in opposing directions. A technique that avoids this complex processing task is indicated in Figure 8. Notice that adjacent pixel halves are cross-coupled, and poled in the same direction. Noise impinging on the surface will produce identical currents, but these flow only in the metal surface layers on the film, due to the cross-coupling. The same thing will happen for incident IR at equal intensity on the two halves. Thus some external mechanism must be provided to alternate incident IR on the pixel halves. The important point is that passive common-mode rejection allows simplification of the multiplexing requirements, and avoids the need for amplifier input protection.

The pixel size is sufficient to consider passive common-mode rejection techniques. These techniques eliminate complex multiplexing requirements and dependency on accurately tracking resistors. This is fortunate, since the multiplexing problem requires unconventional approaches. If we assume a signal frequency of 1 KHz, a reasonable

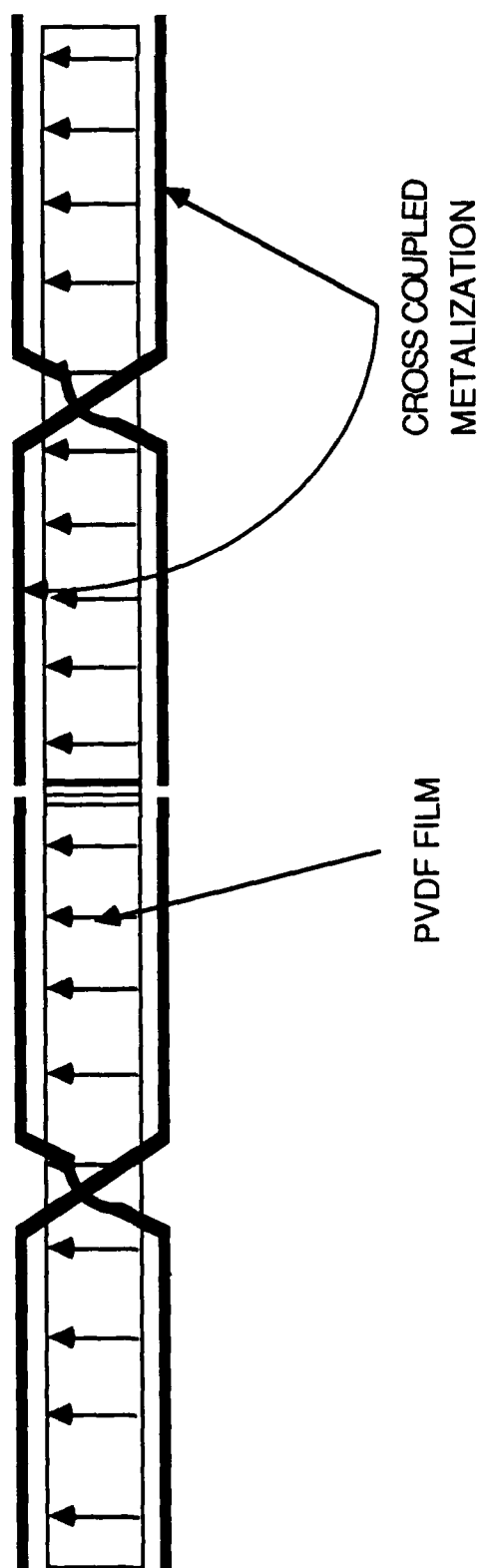


FIGURE 8. COMMON MODE CANCELATION SCHEME

detection time is approximately 3 milliseconds. If a 32 x 32 pixel array is fabricated, conventional multiplexing would consume about 3 seconds---totally unacceptable. There are two approaches to alleviating the problem. One is to provide an amplifier for each pixel, each continuously sensing the state of that pixel. With the amplification required for this application, this approach, explored in a later section, is probably the more difficult of the two. The second approach is to "multiplex" prior to conversion. Any image that is "vibrated", optically or mechanically, will be detectable only at the "edge" pixels. This provides a rather interesting multiplexing possibility wherein there are two amplifiers, one of which typically views many pixels simultaneously. The best way to describe the algorithm is to start at initial target search. This amplifier would be connected to every pixel at this stage. If any action appears, an interval-halving algorithm can be invoked to isolate the active location. Once action is detected, the second amplifier can strobe suspect pixels and adjacent pixels to continuously verify detection. Meanwhile, the first amplifier remains connected to the majority of the imaging circuitry, and detects activity encroachment, or additional incident radiation. This approach also allows synchronized inversion of input lines to the first amplifier, thus providing an integration mode for better detection at range.

There is an obvious problem with this approach, involving the number of lines required to multiplex each pixel individually and simultaneously. One way to avoid this is to provide one bit of random access memory to control each pixel connection. The memory can be set as desired to map appropriate pixels, and detection can proceed at a 3-millisecond rate, which is more acceptable. In the previous

discussion on passive noise cancellation, a nominal pixel dimension of 100 μm was estimated. This dimension allows adequate space for a bit-controlled multiplexer pair. For an array 32 pixels on a side, an overall die dimension is about 3mm, for which a reasonable yield can be expected. This is also about right for proper alignment relative to the focal plane.

A crude circuit to accomplish the multiplexing task is shown in Figure 9. It should be noted that the algorithms for multiplexing and detection are expected to be complicated, and additional circuitry will likely be required. This is simply a first attempt to establish feasibility. At a minimum, it appears that 8 lines must enter or exit the pixel area: Power busses (V_{cc} and Gnd), Bit lines (D and \bar{D}), Address lines (Row and Col), and Amplifier busses (Bus1 and Bus2). In order to guarantee detection, as many as 4 amplifier busses may be required.

At some point, an amplifier is required. The limitations of a discrete solution are sufficiently convincing. Our goal in this section is to explore the possibility of a separate amplifier under each pixel. Linearity, flexibility, and current drive are some of the attributes of operational amplifiers that are non-essential for this application. In addition, the PVDF film is an excellent insulator (disregarding the source characteristics). These properties can be used to advantage in conserving space and current. One interesting approach is to use the film itself as gate dielectric; this may lend features that conserve functional blocks. Approximately 30 transistors can be fabricated in the 100 micron square underneath each pixel. This is certainly enough

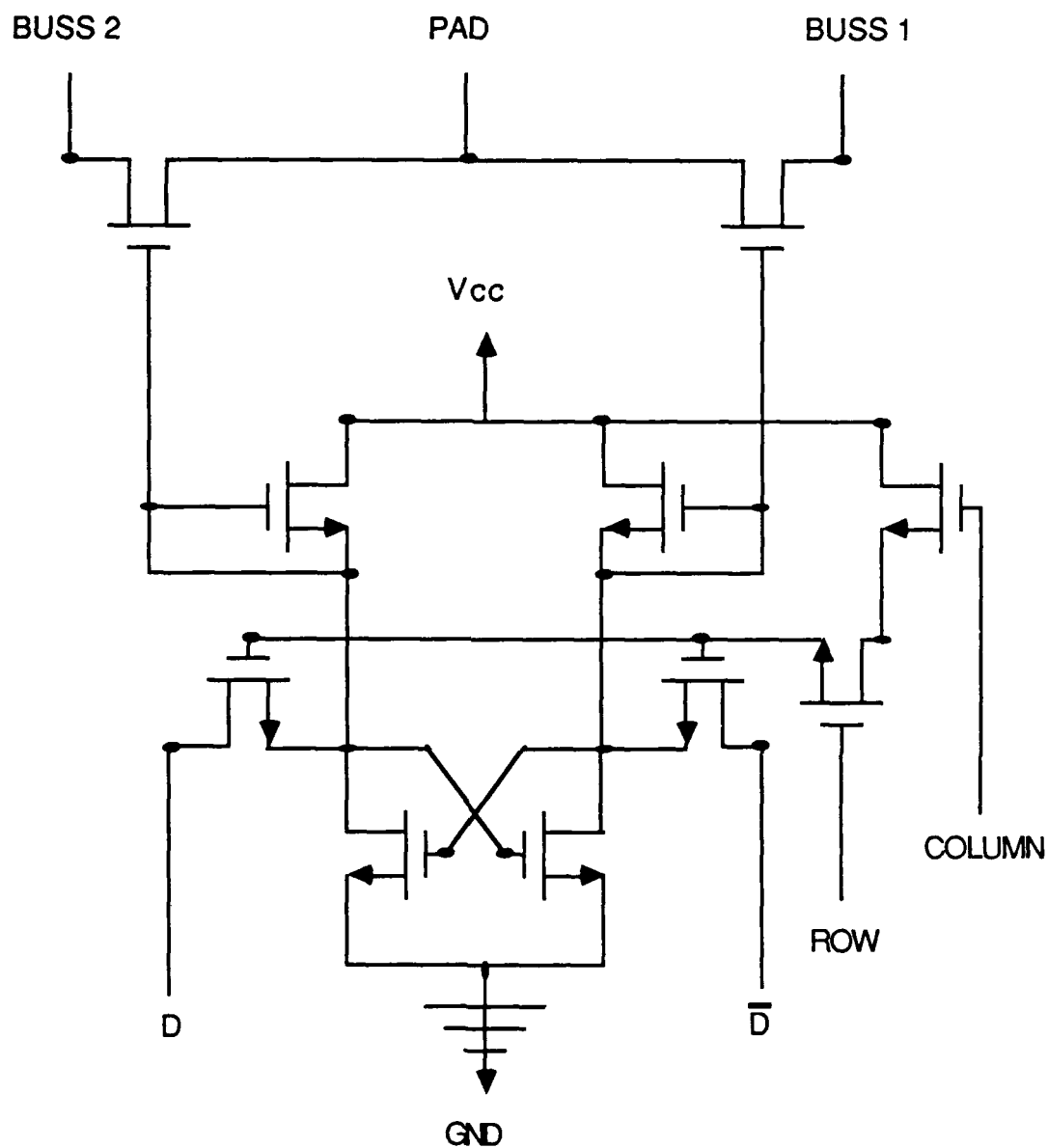


FIGURE 9. RAM CONTROLLED MULTIPLEXING

to provide most of the features of a conventional op-amp, and should include space for a fabricated feedback structure to maintain constant film voltage. There are two primary difficulties: (1) The large resistor values required must be derived from FET or diode tricks, and (2) Low amplifier noise figures are attained at the expense of junction area. It may be possible to limit the amplifier noise problem, since the output current drive capacity of the circuit can still be minute. Taken together, however, it is unlikely that a linear amplifier with low noise figure can be fabricated in the space allotted. It may, however, be desirable to build two amplifiers on the same chip (adjacent to the pixel area) to process the multiplexed signals.

CONCLUSIONS

Microelectronic fabrication techniques will eliminate several problems encountered in application of piezofilm: circuit and film contamination, etching difficulty, oxidation of film connections, and resistor matching and tracking errors. In addition, microelectronic dimensions allow passive common mode rejection of piezoelectric (microphonic) noise, eliminating the need for amplifier input protection.

Other problems remain to be solved, such as incorporating high-gain low-noise amplifiers on-chip, and multiplexing and interpreting the acquired data. Conventional solutions for these problems are expected. Attaining the high Beta-phase film content is a questionable area, but one with two alternative solutions. Centrifuge processing on the chip is possible, and there are some materials which exhibit adequate response with no additional processing. Poling the finished film can be accomplished easily. Compatibility with microelectronics fabrication is remarkable.

APPENDIX A

PIEZOFILM PROCESSING ALTERNATIVE

Etching a desired pattern on piezofilm is no easy task. Two alternatives were presented by Pennwalt. The first is simply to provide artwork to Pennwalt and wait for them to process. This is certainly the easiest approach, but does involve up to 8 weeks delay.

A second alternative is to etch the material as suggested by Pennwalt. Unfortunately, the processing techniques are complicated and dangerous. In addition to photographic steps, a silk-screen is required, then an unusual protectant, and finally an etch in concentrated hydrochloric acid. Although this can be accomplished, it lacks the simplicity and safety desired for extended development.

We chose to experiment with conventional printed-circuit chemicals and techniques, in an effort to develop a third alternative. The technique we developed still lacks finesse, but it works---at least for 9 micro Pennwalt Kinar film, marked 5009NA-MR87029. The following description is provided in the hope that it may provide a plateau from which other piezofilm research can build.

STEP 1. One of the more notable properties of piezofilm is a pronounced similarity to Saran-Wrap. A more rigid frame is required and can be made from acetate film. First, decide on the dimensions of the film to be processed. Then cut a square from the acetate so that the film will just overlap the rectangle, when skewed 45 degrees. Tape the acetate down, leaving the removable square in position. Then carefully cut the film and transfer to span the square, with the corners overlapping to

the solid acetate. Tape the film corners to the acetate outside the square. Then take up the acetate, drop out the removable square, and trim the acetate border as desired. Leave the film on this acetate frame for all the remaining processing steps.

STEP 2. Temporarily mount the acetate (with film) on a rigid frame for use in a spin-table. We used .032 aluminum, with a hole large enough to access both sides of the film, when mounted. Spray Type "B" Etch Resist Sensitizer (Negative Type) on both sides, and spin to provide a thin, even coat. Allow to dry overnight in a dust-free area. The sensitizer is available from GC Electronics, Rockford, Illinois, Catalog #22-248.

STEP 3. Remove the acetate and film from the rigid frame provided for the spin-table. Expose the film by placing it, with an appropriate negative of the artwork, in a UV light frame. If double-side exposure is desired, do so.

STEP 4. Develop for about 90 seconds in "Negative Type" P.C. Board Developing Solution, Catalog #22-235, also available from GC Electronics.

STEP 5. Wash the developer off, taking care not to touch the film. You should now be able to see a faint pattern on the film. You may now turn on as much light as desired without damaging the film.

STEP 6. Agitate the film in Ammonium Persulfate Etchant, at about 120 degrees F, for about 3 minutes. You will detect very little etching

activity at this point. This etchant is available from Mouser Electronics.

STEP 7. Agitate the film in Ferric Chloride Etching Solution, Catalog #E-1G, also available from GC Electronics. Only a few seconds are required in this etchant to complete the process. Wash off the film as soon as etching is complete.

STEP 8. Clean the film in Photoresist Stripper, available from Kepro Circuit Systems, Fenton, Missouri, Catalog #PRSK-1G. You may touch the film at this point. Note that the film polarity and identification marks have survived the processing.

STEP 9. When the film is dry, mount and remove the acetate frame.

APPENDIX B

NOISE, SHIELDING, AND CIRCUIT CONTAMINATION

There are four types of noise to be considered: electromagnetic, microphonic, light and thermal.

Electromagnetic noise may be from external sources or may be generated by the amplifier circuitry. External noise may be blocked by placing the circuit and sensor in a grounded metal enclosure. However, some provision must be made to allow the desired light signal to enter. One way to let the light in and keep out lower frequency noise is to borrow from waveguide theory. A waveguide will attenuate transmit a signal whose wavelength is longer than twice the diameter of the waveguide. For example, a circular waveguide with .250 inch inside diameter has a cutoff frequency of 27.638 GHz. Frequencies below this are severely attenuated, so a 1/4" pipe attached to the enclosure may be used to admit light.

Large value resistors are a source of noise that is dependent upon the circuit bandwidth and temperature of the feedback circuit. This terminal noise is given by:

$$E_n = (4KTBR)^{1/2} , \quad (1)$$

where: E_n is the rms value of the noise,

K is Boltzmann's constant (1.38 E-23 J/K),

T is the Kelvin temperature,

B is the bandwidth,

R is the resistance that generates the noise.

This is a normal input noise caused by the thermal action in the feedback and input resistances. For practical purposes, the value of R is the parallel combination of these resistances. Since R must be very large for gain and impedance matching, and we do not want to cool the system, the only way to reduce this noise is to severely limit the bandwidth. For our circuit this is:

$$E_n = 4.0694 \times 10^{-6} \text{ B} \quad (2)$$

where: $R = 10^9 / 10^{13} = 10^9,$

$$T = 300 \text{ K},$$

$$K = 1.38 \times 10^{-23} \text{ J/K}.$$

The output signal voltage is:

$$E_s = iR, \quad (3)$$

where: i is the signal current,

R is the feedback resistor.

The signal-to-noise ratio is thus

$$\frac{E_s}{E_n} = \frac{iR}{(4KTBR)^{1/2}} \quad (4)$$

Assuming a minimum signal-to-noise ratio of 1, and solving for i yields

$$i = (4KTb/R)^{1/2} . \quad (5)$$

For values of: $T = 300 \text{ K}$, $B = 100 \text{ Hz}$, $K = 1.38 \times 10^{-23} \text{ J/K}$, $R = 10^9 \text{ ohms}$, then $i = 40.7 \times 10^{-15} \text{ A}$.

The signal-to-noise ratio is proportional to the square root of R , so increasing R increases the signal faster than it increases the noise.

It may be possible to limit the effects of noise by using another communications technique called Coherent Detection. Since the signal is periodic, it is possible to integrate it over a half period. The integral of the signal plus the noise over a half period should be positive if the signal is positive, negative if the signal is negative. At the end of the half period, short the integrating capacitor and begin integrating again. This technique depends on the noise being relatively constant and requires very accurate timing of the integrator. The output will be either positive, negative, or zero (if desired).

PVDF is an excellent sound transducer, being used in high quality musical instruments such as violins and guitars. For pyro applications, sound is a major source of unwanted signals. Common mode rejection of sound may be accomplished by reducing the geometry of sensor pixels so that an incident wave covers adjacent oppositely polarized pixels. The signals produced then cancel out. If the film is suspended such that only air is in direct contact with the sensory part, an incident sonic wave will stretch the whole sheet from end to end. If the electrodes are asymmetrically arranged on the film surface, the sound will produce a signal. For this experiment, the metal can was lined with foam to reduce the level of sound reaching the sensor.

The waveguide mentioned above will keep out radio frequency noise, but not light. Background light, especially the fluorescent lighting, easily saturated the sensor. For this work it became necessary to enclose the path of the laser beam to eliminate all background light. A more desirable approach would be to filter out all light frequencies except those desired using IR filtering mirrors. It is possible to coat the surface of the film with materials for selective absorption and reflection of incident light; however, this will add to the thermal time constant, slowing the system response.

Thermal noise consists of fluctuations of the temperature of the sensor environment. With the other types of shielding already in place, this was not a problem.

It is necessary to keep the circuit, film, and all mounting equipment as clean as possible. The atmosphere should be free from contaminants such as dust and humidity. For discrete experimentation, it may be desirable to operate in a nitrogen environment. One of the chief advantages of microelectronic fabrication of the sensor is that the connections to the film can be made with no oxidation at all. For discrete work, an ultrasonic vibrator may be used to break through the oxide layer and then apply a conductive epoxy to make the connection.

APPENDIX C

POLYVINYLIDENE FLUORIDE (PVDF) PIEZO-FILM

Pyroelectric detectors have existed long enough to develop a reputation of fragility and poor detectivity. Pyroelectric films such as Polyvinylidene Fluoride (PVDF) are helping to change this reputation, and the potential for even better characteristics is being developed. The application of this material appears plausible because:

- * It can conform to practically any shape.
- * Pyroelectric response is in the audio range at least.
- * The material has a wide, adjustable optical span.
- * The overrange capacity of the film is exceptional.
- * The temperature limit is 100°C.
- * Several similar films are under development.
- * Microelectronics fabrication techniques apply.

This interesting material was developed in 1971 at Bell Laboratories, and results from proper stretching and quenching of the original plastic material. A resulting crystalline structure is formed in the plastic that is found to be piezoelectric, with response to approximately 10 Ghz, and additional passband above 40 Ghz. The usual configuration is to provide a thin metallic coating to both sides, which makes the contact for the sensor. Pressure and acceleration transducers are obvious applications, and the film also serves as a large-area audio transducer (both ways). The film is relatively inexpensive, and is now employed under carpet to detect illegal entry.

The interesting aspect is that it is also a pyroelectric detector. Unfortunately, the passband is limited, and in early research, the material was discarded for applications requiring fast response. Recent research has been applied to a 30nm film that is much more encouraging. The film was pulsed with a laser, and exhibited a response from excitation to peak much less than 1 millisecond. Pennwalt produces the KINAR film, which set new records for speed of response reported in the literature. Douglas Kerhung (215-337-6710), Applications Engineer at Pennwalt, mentioned picosecond pyroelectric response in some advanced research! The ensuing discussion is a focused analysis on the pyroelectric application to seekers.

PYROELECTRIC MEASUREMENT

Pyroelectric devices are deceptive. Pyroelectrics would appear to have a very slow response, due to thermal time constants. Surprisingly, this is not the case. Figure 10 is a common model for thermal response analysis, where C_T is the thermal capacity, G_T is the thermal conductivity, T is the film temperature, ϵ is the emissivity of the surface, and $P(t)$ is the incident power. A straightforward analysis yields:

$$\begin{aligned} C_T \dot{T} + G_T T &= \epsilon P(t) , \\ C_T s T(s) + G_T T(s) &= \epsilon P(s) , \\ T(s) &= \epsilon P(s) / (s C_T + G_T) . \end{aligned} \tag{6}$$

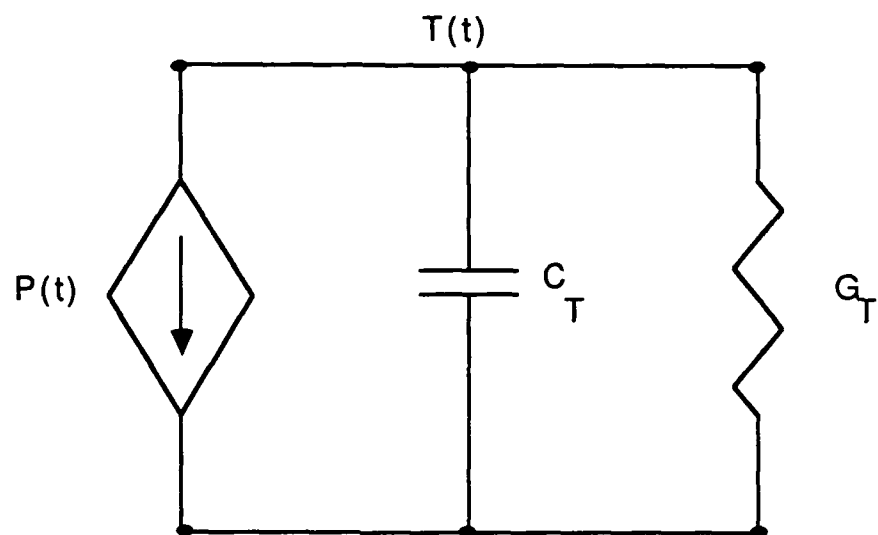


FIGURE 10. THERMAL MODEL FOR FILM ANALYSIS

The thermal response to a step input is obviously slow, as expected. But the pyroelectric response is related to temperature change:

$$i(t) = p A \dot{T} ,$$

where $i(t)$ is the current produced, p is the pyroelectric coefficient, and A is the detection area. Thus,

$$\begin{aligned} I(s) &= p A s T(s) , \\ I(s) &= p A s \epsilon P(s) / (s C_T + G_T) . \end{aligned} \quad (7)$$

The time constant, C_T / G_T , is thus seen to limit the low frequency response, which we don't need anyway. Above this frequency,

$$I = p A \epsilon P / C_T . \quad (8)$$

Although the time constant is of little consequence (provided we can work at higher frequencies), it is obviously desirable to decrease the heat capacity.

A simple analysis on the bulk material is informative. The thermal conductivity is

$$G_T + .13 A / t \quad (W / ^\circ K) , \quad (9)$$

where A is the detector area and t is the thickness. The heat capacity is

$$C_T = 2.314 \times 10^6 A t \text{ (J / } ^\circ\text{K)} . \quad (10)$$

The thermal break frequency then occurs at

$$f_T = 8.94 \times 10^{-9} / t^2 . \quad (11)$$

Interface circuitry must operate above this frequency (110 Hz, for 9 μ m film). Mounting techniques can affect this frequency significantly. Substituting equation (5) into equation (3) yields

$$i(t) = p A \epsilon P / 2.314 \times 10^6 A t . \quad (12)$$

Before cancelling terms, recall that optic elements may be used to concentrate incident infrared to the order of pixel size, A. Thus,

$$\begin{aligned} P &= P_i A_o / A , \\ i &= -10.8 \times 10^{-12} \epsilon P_i A_o / A t . \end{aligned} \quad (13)$$

It is now evident that response is increased by decreasing detector area or thickness, but the thermal break frequency can move out of range and is very sensitive to thickness. Remember, however, that the bulk material is sandwiched between conductive material. As dimensions shrink, conductor and spatial effects become dominant, and this analysis

is no longer valid. It does explain the effort to achieve very thin piezo-films.

The electrical properties are more severe and less controllable. The resistance is

$$R = 10^{13} t / A \text{ (ohms) ,} \quad (14)$$

and the capacitance is

$$C = 116.76 A / t \text{ (pF) .} \quad (15)$$

The electrical break frequency then occurs at 1.4×10^{-4} Hertz, and we have no control over it! Interface circuitry must defeat this problem.

Surprisingly, the electrical parameters are more unforgiving than the thermal. The model shown in Figure 11 is simple, but foreboding. The usual logic is as follows: The time constant is improved with low impedance interface circuitry, but signal transfer is improved with very high impedance. This conflict usually ends the analysis, and a poor combination of response and sensitivity is accepted as inevitable.

REFERENCES

1. Boyd, Robert W., Radiometry and the Detection of Optical Radiation, John Wiley and Sons, 1983.
2. Carlisle, Ben H., "Piezoelectric Plastics Promise New Sensors," Machine Design, October 23, 1986, pp 105-110.
3. Day, G. W., Hamilton, C. A., Gruzensky, P. M., and Phelan, R. J., Jr., "Performance and Characteristics of Polyvinylidene Fluoride Pyroelectric Detectors," Ferroelectrics, Vol. 10, pp 99-102, 1976.
4. Hudson, Richard D., Jr., Infrared System Engineering, John Wiley and Sons, 1969.
5. Korn, U., Rav-Noy, Z., and Shtrikman, S., "Pyroelectric PVF₂ Infrared Detector Arrays," Applied Optics, Vol. 20, No. 11, June 1, 1981.
6. Pennwalt Kynar Piezo-Film Technical Manual.
7. Ravich, Leonard E., "Pyroelectric Infrared Detectors," Sensors, June, 1984, pp 66-72.
8. Liao, Samuel Y., "Microwave Devices and Circuits," Second Edition, Prentice Hall, Inc., 1985.
9. Carr, Joseph J., "The Complete Handbook of Amplifiers, Oscillators & Multivibrators," TAB Books, Inc., #1230, C1981.

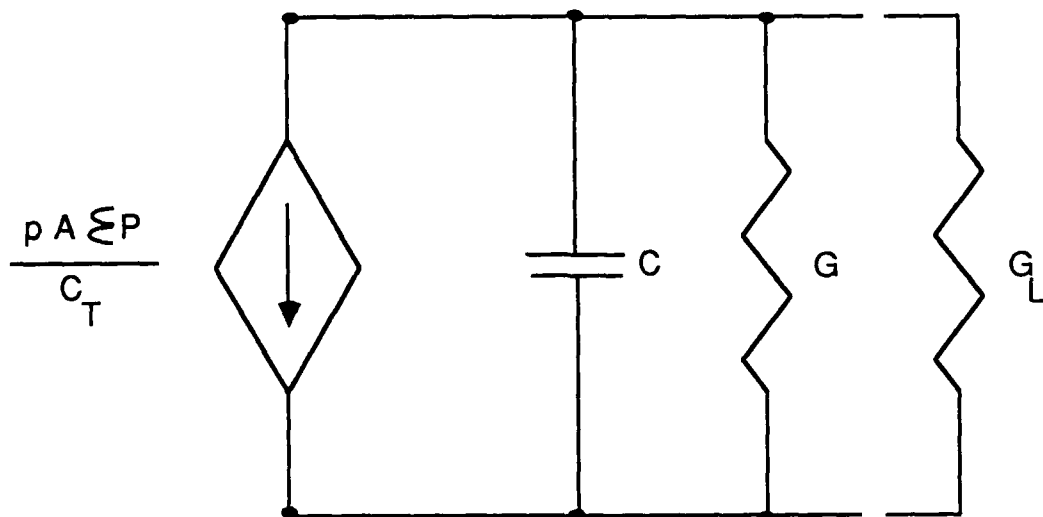


FIGURE 11 MODEL DEMONSTRATING ELECTRICAL RESPONSE PROBLEM

GASEOUS FUEL INJECTION AND MIXING IN A SUPERSONIC COMBUSTOR

M. Samimy and D.E. Erwin
Department of Mechanical Engineering

For the Period
December 1, 1986 - June 30, 1988

UNIVERSAL ENERGY SYSTEMS
Dayton, Ohio 45432

Subcontract No. S-760-6MG-059

June 1988

NOMENCLATURE

b	Span of the tunnel
DELTA	Incoming boundary layer thickness
H	Step Height; Figure 3
P	Static pressure
P ₁	Static pressure before the step
R _{uv}	Correlation coefficient
SIG ₁	10 times standard deviation of streamwise velocity
U ₁	Streamwise velocity
U _{inf}	Incoming boundary layer freestream velocity
Y	Transverse coordinate starting from top surface of the splitter plate
X	Axial coordinate starting from the step
Z	Spanwise coordinate starting from center of the tunnel

ABSTRACT

The existing 152.4 mm x 152.4 mm supersonic wind tunnel at the Ohio State University Aeronautical and Astronautical Research Laboratory was modified to accomodate a model to study a cold flow simulation of a sonic injection of gaseous fuel into a supersonic stream. The new configuration of the tunnel has a 152.4 mm span and a 76.2 mm height at the exit of a Mach 1.83 nozzle. The model used is a backward facing step configuration with a 6.35 mm step height. The flow before the step has a fully developed turbulent boundary layer with a freestream Mach number and velocity of 1.83 and 470 m/s. The boundary layer thickness and momentum thickness determined from velocities measured by LDV are 7.5 mm and 0.48 mm, respectively. The Reynolds number based on momentum thickness is 26000. There is a single injection nozzle with a 5 mm exit diameter located at the center of the tunnel 3 step heights downstream of the step. A two-component coincident LDV system with a 5 watt argon laser was acquired for use in this research. A 3-component traversing table for the LDV was designed and fabricated. This report contains some preliminary Schlieren photographs and pressure measurements. The future plans are to obtain detailed LDV measurements with air and helium injection and to explore the possibilities of enhancing mixing by means such as pulsating the injection and/or by acoustic excitation of the structure in the mixing region.

1. INTRODUCTION

Hypersonic flight has received renewed interest in recent years. This flight regime is generally defined as flight Mach numbers of 5 or greater. In many aspects, propulsion for hypersonic flight is different than for subsonic and supersonic flights. The airflow through a hypersonic vehicle's engines will be supersonic rather than subsonic. This situation is necessary due to the large stagnation pressure losses associated with decelerating a hypersonic flow to subsonic speeds. Passing a supersonic flow through the engines and obtaining efficient mixing and combustion will present challenges to the engine design. The high velocities associated with supersonic flow will result in a short residence time for the fuel and air mixture. Mixing and combustion must occur quickly to obtain efficient operation. The mixing of the fuel and air in a supersonic stream will be more difficult than for a subsonic flow. This effect is due to the slower growth and entrainment rates of supersonic shear layers as compared to subsonic shear layers. These effects must be considered when designing a hypersonic engine configuration.

A typical hypersonic engine configuration will emerge after considering the above effects. The flight vehicle forebody and engine inlet will act as a diffuser to decelerate the flow to low supersonic Mach numbers. The diffused flow Mach numbers will be perhaps 1 to 4, depending on the flight Mach number. After passing through the diffuser, the flow will encounter the fuel addition region. This region will contain fuel injectors which will inject fuel normally, tangentially, or at an angle to the flow. The injection region will be isolated from the incoming section

by centerbodies, struts, and rearward facing steps. This is to minimize the upstream influence of the fuel injection and also to provide some sort of flameholding mechanism. Too much upstream influence could cause inlet unstart.

The injection region is therefore a critical area in the engine design. This region must enable rapid mixing without causing inlet unstart. Control of these effects can be achieved by proper design of the injection nozzle configuration and by adjusting the injection flow. Parameters to control in the nozzle design are the nozzle diameter, proximity to steps and struts, and the longitudinal and lateral spacing of the nozzles. The jet injection pressure has a direct effect upon plume penetration and spreading. Once the plume penetration and spreading characteristics of a single jet are known, multiple jets may be placed in the injection region to study the effects of the jets on each other and on overall mixing and combustion.

Much research has been done to study injection into a supersonic airstream. Several basic research configurations have been studied. These configurations are used to study the penetration and mixing of single jets. One such configuration is injection from flat plates and straight ducts[1-6]. These configurations allow the study of injection through boundary layers with a zero pressure gradient. Another basic configuration is a strut or a rearward facing step[7-13]. As stated, the step will isolate the incoming boundary layer to prevent inlet unstart and also will act like a flameholder. Struts act to decelerate the incoming flow and to isolate the injection from the incoming flow. Struts also duplicate generic engine inlets and provide a study of lateral injector spacing and opposing injection[1,2,7].

Several gases have been used in injection studies. Air is used for jet penetration and spreading studies[2,3,6-9,11,13]. An understanding of the effects of nozzle positioning and injection pressure can be obtained. Combustion studies generally use hydrogen as the fuel[1,3,12]. When only cold mixing studies are being performed, helium is used to simulate hydrogen[4,5,10]. The combustion studies obtain data about the completeness of mixing and the efficiency of combustion[7,10,12]. The injection pressures used are generally for a ratio of injectant static pressure to freestream static pressure of less than 12 [2,9,10,11,13]. Higher pressure ratios will not promote jet penetration or mixing to a useful extent[13]. There is also the possibility of inlet unstart at higher injection pressures and mass flow rates.

Various types of data are taken in these experiments. The most basic data are total and static pressure surveys[2,5-8,12]. This data indicates the extent of the jet plume penetration and lateral influence. The injection jet penetration can also be studied from Schlieren and shadowgraph photographs[5,6,8,11]. These photographs indicate the edge of the jet plume and the height of the injection jet Mach disc[3]. A more accurate determination of the jet penetration boundary is obtained with densitometer analysis of the photographs[4]. Another visualization technique is laser induced fluorescence (LIF) [9,11,13]. LIF provides data as in the Schlieren and shadowgraph cases. An advantage of LIF over the Schlieren and shadowgraph techniques is that only a thin sheet of the flowfield is illuminated, and this sheet may be in either the vertical or horizontal plane. Illumination in the vertical plane provides data on jet penetration, and illumination in the horizontal plane indicates the extent

of injectant lateral spreading.

Gas concentration measurements are also obtained [2,4-6,10,12]. Gas samples are removed from the flowfield for both reacting and nonreacting cases. For the nonreacting case, the gas samples will provide data about the extent of mixing. In the reacting case the gas samples indicate the completeness of combustion.

The objective of this research was twofold. The first objective was to develop an experimental flow facility and instrumentation to enable us to conduct research on injection into a supersonic stream. The second objective was to use this facility/instrumentation for a detailed analysis of injection flowfield and to explore ideas to enhance mixing in this type of configuration. This report covers the work performed under the first task. From the second task only preliminary results will be presented.

2. TEST FACILITY AND INSTRUMENTATION

The test facility is the 152.4 x 152.4 mm supersonic wind tunnel at the Ohio State University Aeronautical and Astronautical Research Laboratory (AARL). The blowdown tunnel is operated with a test section Mach number of 1.83 and a Reynolds number of $54 \times 10^6/\text{m}$. The air is fed into the stagnation chamber through a line which is connected to the laboratory high pressure tanks. The air is stored in these tanks at 2400 psi and the tanks are large enough to provide run times of over two minutes. The tunnel stagnation chamber pressure is controlled by a Vogt series 1871 valve which is in the air line leading into the tunnel. The test section has a line of static pressure taps to monitor the static pressure distribution in the test section.

2.1 Modifications to the facility

Before using the tunnel, several modifications were necessary to make the facility more versatile. The tunnel was modified to accommodate configurations for injection into a supersonic stream with different angles from tangential to vertical and also to accommodate configurations to study constant pressure supersonic mixing and reattaching shear layers. In order to carry out these modifications, the tunnel had to be completely disassembled. Several new parts were designed and manufactured, and these parts were included in the tunnel during reassembly.

The first modification was to lengthen the stagnation chamber by lengthening the top, bottom, and side walls. This change was necessary to accommodate the new nominal Mach 2 nozzle which was placed in the top stream of the tunnel as shown in figure 1. A new splitter plate and a new

converging nozzle were also manufactured and installed. With the configuration shown in figure 1, we are capable of investigating the mixing of a supersonic and a sonic or a subsonic flows. Figure 1 also shows the viewing area of the test section. The viewing area covers part of the incoming boundary layers and approximately 50 cm of the mixing region. In order to provide injection into the supersonic stream, a step block was designed and fabricated to fit to the trailing edge of the splitter plate and an injection plate was designed and fabricated to accomodate the injection nozzle. Details of the step block and the injection plate are given in Section 2.4.

Two high pressure control valves were used to control the flows to the primary Mach 1.83 and the secondary Mach 0-1 streams. These valves were procured when the tunnel was assembled. It was necessary to procure replacement seats and discs for the valves due to wear and deterioration from the high pressure airstream.

It was necessary to design and manufacture new glass windows and aluminum window frames for the tunnel. The tunnel had existing 2 inch thick plexiglass windows, but these existing windows were not suitable for use with LDV and Schlieren systems. The new glass windows were 1/2 inch thick and were designed so that different blocks of glass could be mounted in the window frame. The design used beveled glass mounted to the window frame by epoxy. Figure 2 shows the window frame with its accompanying access panel. The access panel makes cleaning the windows and the model very convenient while minimizing the time between runs. In addition, the positions of the frame and the access panel could be easily exchanged to provide approximately 50 cm optical access to the flowfield.

2.2 Data Acquisition Systems

The data acquisition system was assembled from existing components and from equipment obtained for this project. Schlieren photographs, pressure data, and some LDV data in the incoming boundary layer were taken with the data acquisition system.

The Schlieren system used existing 8 inch diameter, 5 foot focal length parabolic mirrors. A general Radio Corporation stroboscope light source was used with the Schlieren system. The light source could be operated in the continuous mode or as a single flash. The flash durations used were .5 and 1.2 microseconds. A single one-sided knife edge was used in front of a 35mm camera. The camera's lens was removed and a single convex lens was used to focus the image on the film. The film speeds used were 1000 ASA and 1600 ASA. The stand which held the knife edge and camera would vibrate slightly while taking photographs. This vibration changed the sensitivity setting slightly and degraded the quality of the photographs. A new stand was designed and assembled to eliminate this problem. The new stand allows for consistent and repeatable Schlieren pictures.

Pressure data was obtained with the use of the AARL data acquisition system. The tunnel and model pressure taps were connected to a 48 port scanivalve. The scanivalve contained a 100 psi transducer, and the transducer was connected to the laboratory Harris 800 computer. During a run, the scanivalve would step through each port and the transducer would measure the pressure. Existing software would then process the data and provide the pressures at the end of each run. Since the transducer could measure pressures up to 100 psi, the test section static pressure taps and the tunnel stagnation chamber taps were connected to the same transducer.

It would be ideal to measure the stagnation pressure taps with the 100 psi transducer and use a lower pressure range transducer to measure the test section pressures. However, for these preliminary results the 100 psi transducer was used for all pressure measurements. A pitot probe was also placed in the test section to measure the test section stagnation pressure.

A two-component laser Doppler velocimeter system was procured and set up to measure velocity profiles for this project. The system used a 5-Watt Spectra Physics argon laser with TSI optics and electronics. The data was taken by an Everex 1800 IBM AT compatible computer. The data was transferred to the Harris 800 for data reduction. Data reduction consisted of calculating mean and turbulence properties of the flowfield and accounting for velocity and fringe biasing. Those regions of interest for LDV measurements were the incoming boundary layer, the injection jet, and the mixing region downstream of the jet. For now, LDV has been used only to measure properties of the incoming boundary layer.

A 3-dimensional traversing table was designed and manufactured for the LDV system. This table is capable of positioning the laser measurement volume independently in 3 directions. A cross beam, which is mounted to the table, reaches over the top of the tunnel and holds a smaller receiving platform for the forward scatter LDV receiving optics. This traversing table is extremely stable and enables us to map a three dimensional flowfield without realigning the LDV optics for different locations.

2.3 Operation of the Facility

The tunnel modifications and reassembly were performed first. After the tunnel was reassembled, the Schlieren and pressure data acquisition

systems were brought online. The LDV system was then acquired. The LDV required a substantial amount of assembly and alignment for proper operation. Once the assembly and adjustments were completed, the tunnel became fully operational and data could be taken efficiently.

2.4 Design of the Model

After the tunnel was assembled, the model was designed and built. A step block was designed and fabricated to fit to the trailing edge of the splitter plate and an injection plate was designed and fabricated to accomodate the injection nozzle. Figure 3 shows an illustration of the model(the step block and the injection plate) installed in the tunnel. As shown in Figure 3, for injection experiments the tunnel lower stream was closed off and the injection plate formed the tunnel floor. The backward facing step height was set at 6.35 mm which was scaled up from others[9,11,13] to account for the thicker incoming boundary layer in this tunnel.

The injection nozzle was placed 3 steps heights after the rearward facing step. This location was chosen after examining the results of other tests[9,11]. Those results indicated that placing the injection nozzle 4 step heights downstream of the step resulted in no injectant flow reaching the recirculation region. Placing the nozzle at 3 step heights after the step would place the jet in the shear layer reattachment region and would allow injectant flow to reach the recirculation region. The nozzle exit diameter is 5 mm and the flow is choked to provide sonic injection. The nozzle has a straight converging section with a short constant area channel

before the exit. A curved converging nozzle was considered but was not implemented due to the expense involved. The start of the converging section had an area of 126.7 mm^2 and the nozzle exit had an area of 20.1 mm^2 , yielding an area ratio of 6.3. Figure 4 illustrates the nozzle design.

The air for the injection nozzle was provided by the AARL high pressure air supply. A control valve adjusted the pressure. After passing through the valve, the air went to a stagnation chamber for stagnation pressure measurement and then passed through a hose to the injection nozzle. Figure 5 is a schematic of the injection line. Due to the length of the hose connecting the stagnation chamber and the nozzle, there was a stagnation pressure loss. This loss was calibrated by measuring the stagnation pressure in the stagnation chamber and the pitot pressure at the nozzle exit.

2.5 Model Instrumentation

The model was instrumented with 25 static pressure taps. In addition to these pressure taps, the freestream static and stagnation pressures and the injector stagnation pressure were recorded. The model static pressure taps were divided into 3 groups. The first group of taps was in the centerline of the tunnel floor downstream of the injector. The other 2 groups were arranged laterally, one group before the nozzle and one group after the nozzle. The first lateral group was 1 step height after the step and the second lateral group was 5 step heights after the step. The lateral taps were used to verify the two-dimensionality of the flow without injection and to observe the lateral spreading of the jet during injection. Figures 6a and 6b show the arrangement of the pressure taps.

3. PRELIMINARY RESULTS

Preliminary data was obtained first with no injection and then with different injection pressure levels. In each case the freestream static pressure was identical. Therefore, the injection pressures were referenced by the ratio of injectant static pressure to the static pressure before the step. The cases are denoted by the titles case 1, case 2, case 3, and case 4. The corresponding static pressure ratios are: 1.36, 2.85, 4.29, and 5.64. The data acquired consisted of static pressure measurements and Schlieren photographs for each injection case and for no injection. The incoming boundary layer was probed by LDV to obtain a mean velocity profile and turbulence information. The Mach 1.83 boundary layer with a freestream velocity of 492 m/s was turbulent and fully developed. The thickness, to 99% of freestream velocity, was 8.0 mm and the momentum thickness was 0.5 mm. The Reynolds number based on incoming momentum thickness was approximately 26000.

3.1 Flowfield Visualization

Schlieren photographs of the flowfield were taken first for no injection. These photographs for two trials are shown in figure 7. The incoming freestream flow is at Mach 1.83 and expands past the rearward facing step to a Mach number of approximately 2.3. The shear layer angle is approximately 18 degrees below the horizontal and surface oil flow visualizations showed that it reattaches approximately 3 step heights after the step. The reattachment shock and the large scale structures in the boundary layer downstream of the reattachment are seen in the photographs.

The next set of Schlieren photographs are for injection. Figures 8 and 9 show photographs for injection case 2 and case 3. For injection case 2, the incoming Mach 1.83 flow expands past the step to Mach 2.28. The shear layer is approximately 14 degrees below the horizontal, which is 4 degrees less than for no injection. This smaller angle indicates that shear layer reattachment has been delayed. The Schlieren photographs for case 2, static pressure ratio 2.85, shows that the injection shock protrudes into and interacts to some degree with the expansion fan. For case 3 the shock also protrudes into and interacts with the expansion fan. It was be seen that the injection generated shock wave is not smoothly curved but instead has a wavy appearance. This is due to shock wave and expansion wave interaction.

3.2 Pressure Data

The pressure data is shown in figures 10, 11, and 12. The lateral pressures for no injection provide a check of the two dimensionality of the flow. At both $X/H = 1$ (Fig. 10) and $X/H = 5$ (Fig. 11) the lateral pressures for no injection are uniform which shows that flowfield without injection was two-dimensional. The longitudinal data for no injection (Fig. 12) shows the pressure drop after the step and the downstream pressure recovery. The last data point, at $X/H = 20$, is after a shock wave impinges on the model. This relatively weak shock wave is originated from the juncture of the nozzle. Therefore, the last tap has a slight pressure rise.

The no injection data provides a reference for the effects of injection. Figures 10 and 11 show the lateral influence of the jet. The data at $X/H = 1$ shows a substantial pressure increase throughout the

recirculation region. Since the recirculation region is subsonic and the jet is at the downstream edge of subsonic region, injection increases the pressure throughout the subsonic region. The higher injection pressures of cases 3 and 4 have a more pronounced effect than cases 1 and 2. The lateral data at $X/H = 5$ is outside the recirculation region and is therefore different. The lateral spreading of the jet does not go beyond 30% of the span on either side of the centerline. This indicates that the injection plume is narrow and lateral spreading is limited. The longitudinal pressure data indicates that cases 3 and 4 have a more dominant effect than cases 1 and 2. For injection pressure cases 3 and 4, the constant pressure base region extends up to 6 step heights while cases 1 and 2 have a smaller constant pressure base region. All of the injection cases show similar downstream pressure recovery.

In summary, the Schlieren data show that for low injection pressures the injection shock is smoothly curved and is located just downstream the expansion fan. For higher injection pressures the injection shock protrudes into and interacts with the expansion fan. The shock structure in this case is wavy with inflections. The pressure data indicates that injection at $X/H = 3$ acts to increase the pressure in the recirculation region. Shear layer reattachment is also delayed, and the lateral spreading of the injection plume is also confined.

3.3 Incoming Flow Data

The incoming boundary layer was a Mach 1.83 flow with the boundary layer thickness of 8 mm and the momentum thickness of 0.5 mm. Figure 13 shows the mean velocity profile, the streamwise turbulence intensity, and

the correlation coefficient. The mean flow profile is typical of a fully developed turbulent supersonic boundary layer[15]. The maximum turbulence intensity is about 8% which is comparable to the results obtained with the other researchers in supersonic boundary layers[16]. The general trend of the correlation coefficient is similar to that of the subsonic boundary layer flows but lower in magnitude[17]. The correlation coefficient results agree well with the Mach 2.9 boundary layer results of Johnson and Rose[18].

REFERENCES

1. Weidner, Elizabeth H. and Drummond, J. Philip, "Numerical Study of Staged Fuel Injection for Supersonic Combustion", AIAA Journal, Vol. 20 No. 10, pp. 1426-1431, 1982.
2. Rogers, Clayton R., "Mixing of Hydrogen Injected from Multiple Injectors Normal to a Supersonic Airstream", NASA TN D-6476, Sept. 1971.
3. Schetz, Joseph A., Hawkins, Paul F., and Lehman, Harry, "Structure of Highly Underexpanded Transverse Jets in a Supersonic Stream", AIAA Journal, Vol. 5 No. 5, pp. 882-884, 1967.
4. Hersch, Martin, Povinelli, Louis A., and Povinelli, Frederick A., "Optical Study of Sonic and Supersonic Jet Penetration from a Flat Plate into a Mach 2 Airstream", NASA TN D-5717, March 1970.
5. Zukoski, Edward E. and Spaid, Frank W., "Secondary Injection of Gases into a Supersonic Flow", AIAA Journal, Vol. 2 No. 10, Oct. 1964.
6. Torrence, Marvin G., "Concentration Measurements of an Injected Gas in a Supersonic Stream", NASA TN D-3860, Oct. 1966.
7. Uenishi, K., Rogers, R. C. and Northam, G. B., "Three Dimensional Numerical Predictions of the Flow Behind a Rearward Facing Step in a Supersonic Combustor", AIAA 87-1962, July, 1987.
8. Walker, D. A., Campbell, R. L. and Schetz, J. A., "Turbulence Measurements for Slot Injection in Supersonic Flow", AIAA 88-0123, Jan., 1988.
9. Fletcher, D. G. and McDaniel, J. C., "Quantitative Measurement of Transverse Injector and Freestream Interaction in a Nonreacting Scramjet Combustor Using Laser Induced Fluorescence", AIAA 87-0087, Jan. 1987.
10. McClinton, Charles R., Torrence, Marvin G., Gooderum, Paul B. and Young, Irene G., "Nonreactive Mixing Study of a Scramjet Swept-Strut Fuel Injector", NASA TN D-8069, Dec. 1975.
11. McDaniel, J. C. and Graves, J., "A Laser Induced Fluorescence Visualization Study of Transverse, Sonic Fuel Injection in a Nonreacting Supersonic Combustor", AIAA 86-0507, Jan., 1988.
12. Eggers, James M., Reagon, Patricia G. and Gooderum, Paul B., "Combustion of Hydrogen in a Two-Dimensional Duct with Step Fuel Injectors", NASA TP 1159, May 1978.
13. Graves, John, "Flowfield Visualization in a Model Scramjet Combustor Using Laser Induced Iodine Fluorescence", Master's Thesis, University of Virginia, August, 1985.

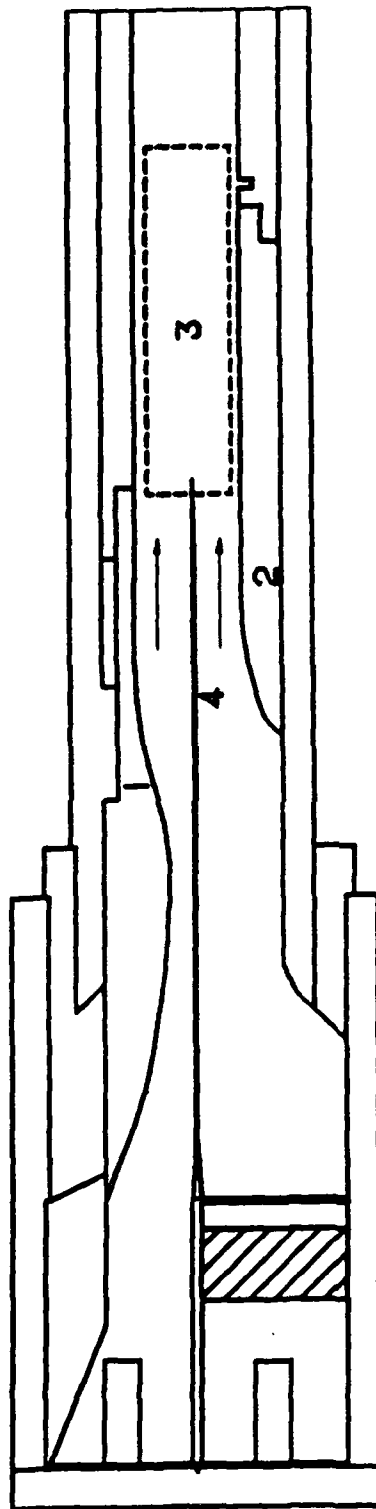
14. Diskin, Glenn S. and Northam, G. Burton, "Effects of Scale on Supersonic Combustor Performance", AIAA 87-2164, July, 1987.

15. Samimy, M., Petrie, H.L., and Addy, A.L., "A Study of Compressible Turbulent Reattaching Free Shear Layers," AIAA Journal, Vol. 24, pp. 261-267, 1986.

16. Petrie, H.L., Samimy, M., and Addy, A.L., "Compressible Separated Flows," AIAA Journal, Vol. 24, pp. 1971-1978, 1986.

17. Klebanoff, D.S., "Characteristics of Turbulence in a Boundary Layer with Zero Pressure Gradient," NACA Report 1247, 1955.

18. Johnson, D.A. and Rose, W.C., "Laser Velocimeter and Hot-Wire Anemometer Comparison in a Supersonic Boundary Layer," AIAA Journal, Vol. 13, pp. 512-515, 1975.



1. Mach 2 Nozzle

2. Mach 1 Nozzle

3. Test Section (Viewing area
is outlined)

4. Splitter Plate

Fig. 1 Schematic of the dual-stream wind tunnel

WINDOW FRAME AND ACCESS PANEL
 DIMENSION, MILLIMETERS
 MATERIAL, ALUMINUM

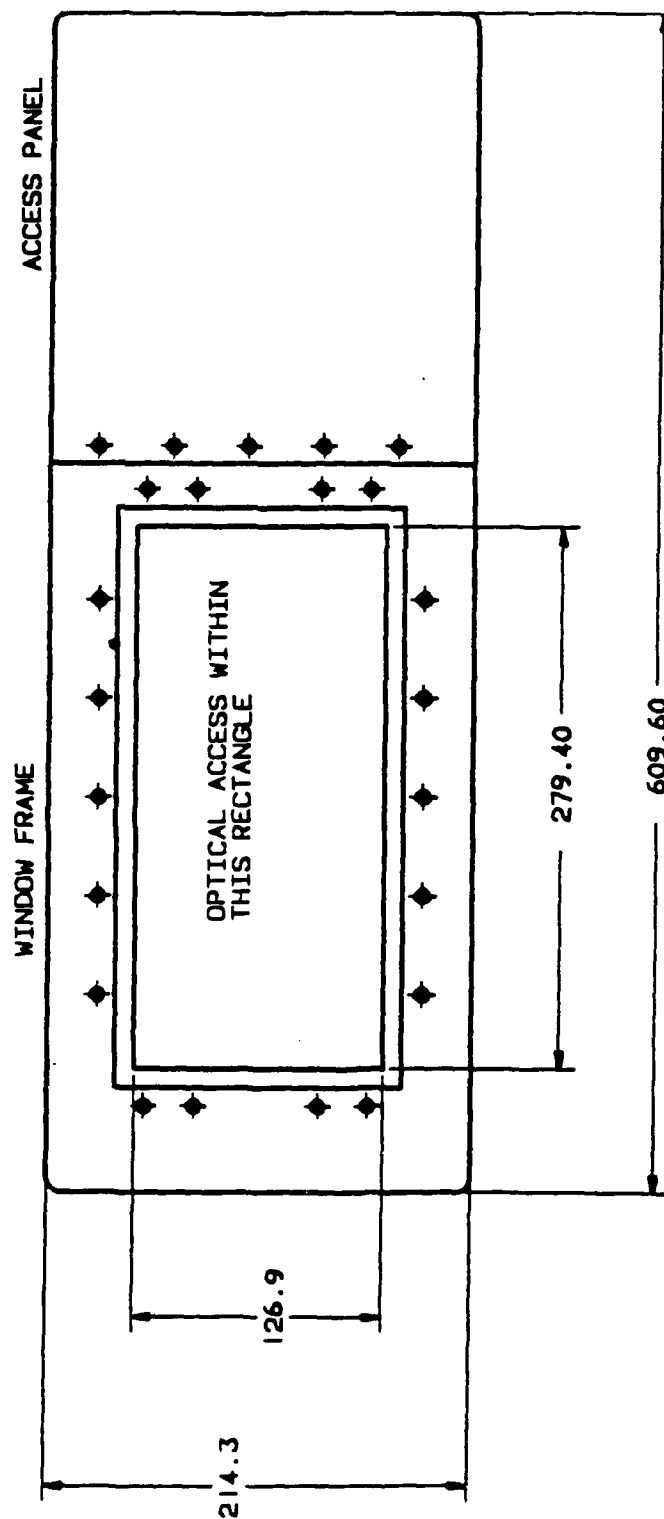
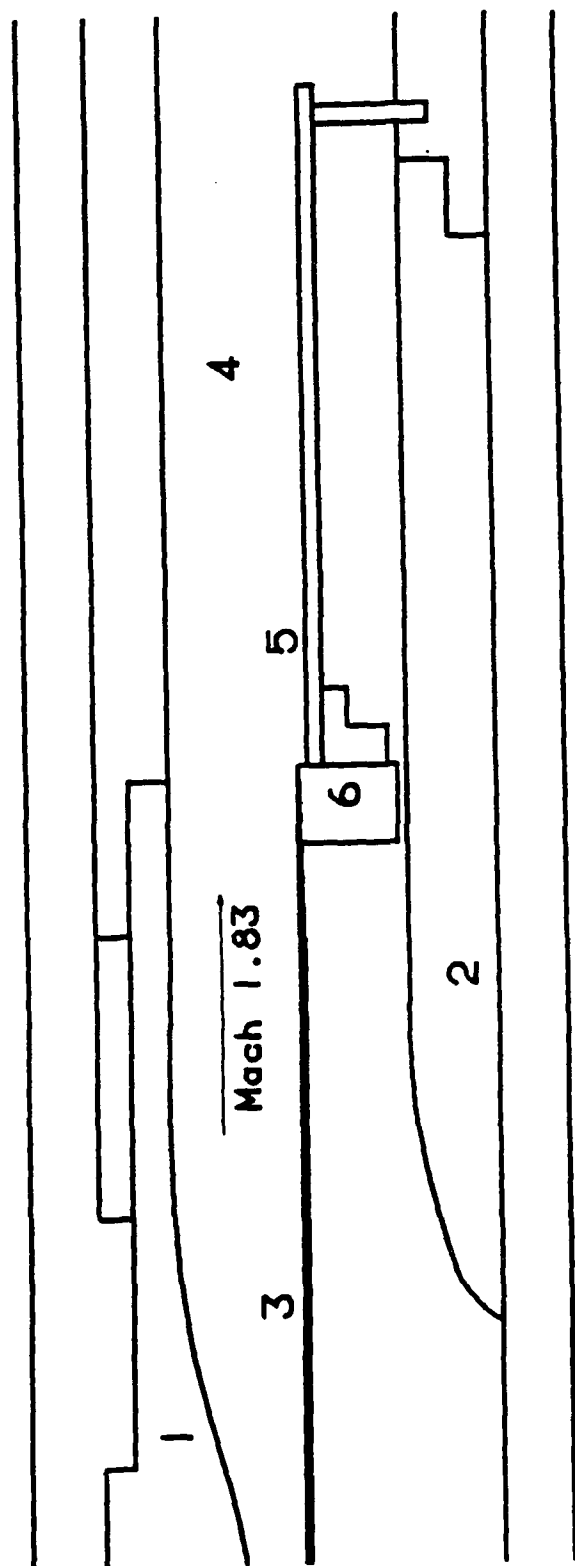


Fig. 2 Window frame with the access panel



- | | |
|-------------------|--------------------|
| 1. Mach 2 Nozzle | 4. Test Section |
| 2. Mach 1 Nozzle | 5. Injection Plate |
| 3. Splitter Plate | 6. Step Block |

Fig. 3 Schematic of the tunnel with the injection plate and the step block installed

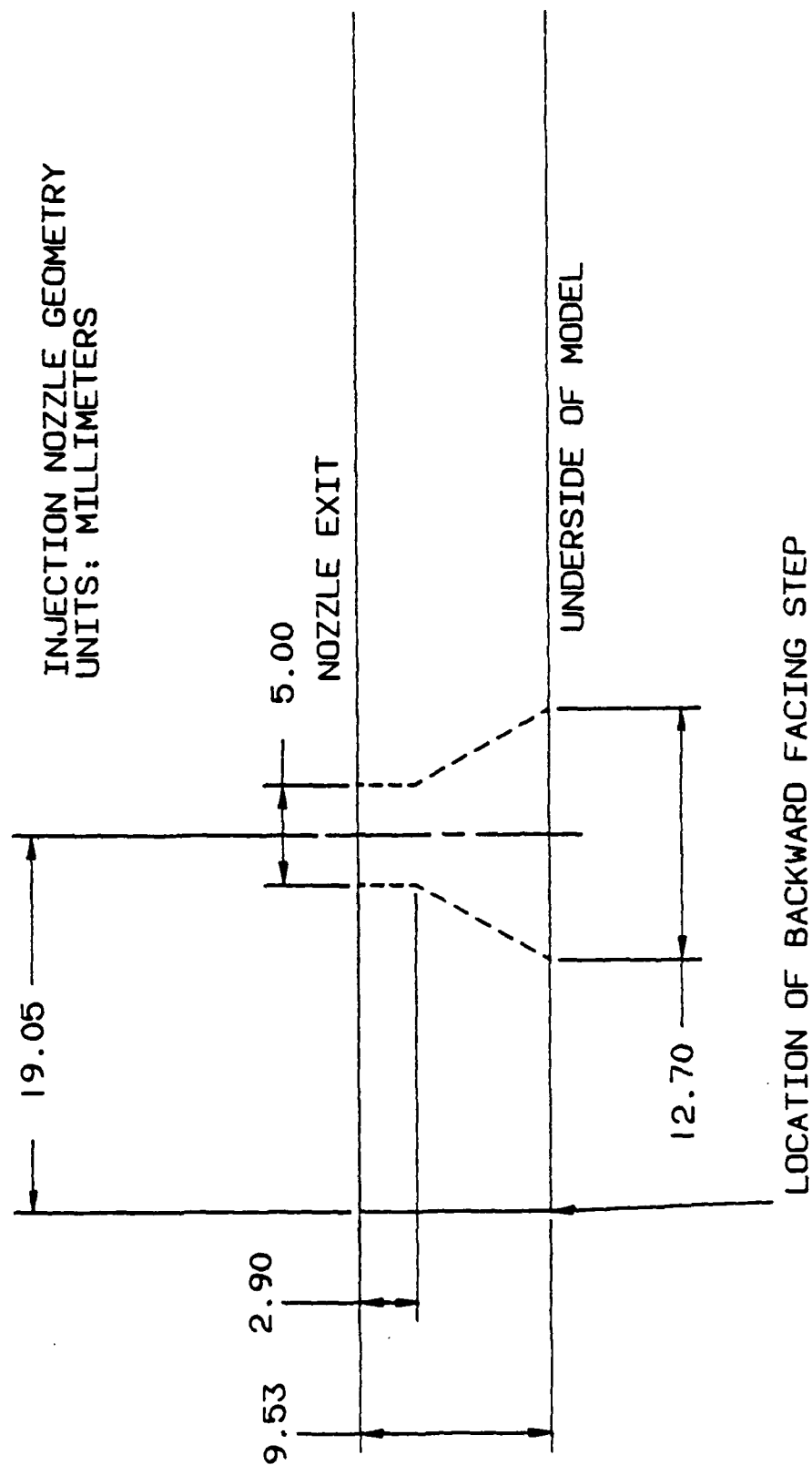


Fig. 4 Injection nozzle geometry

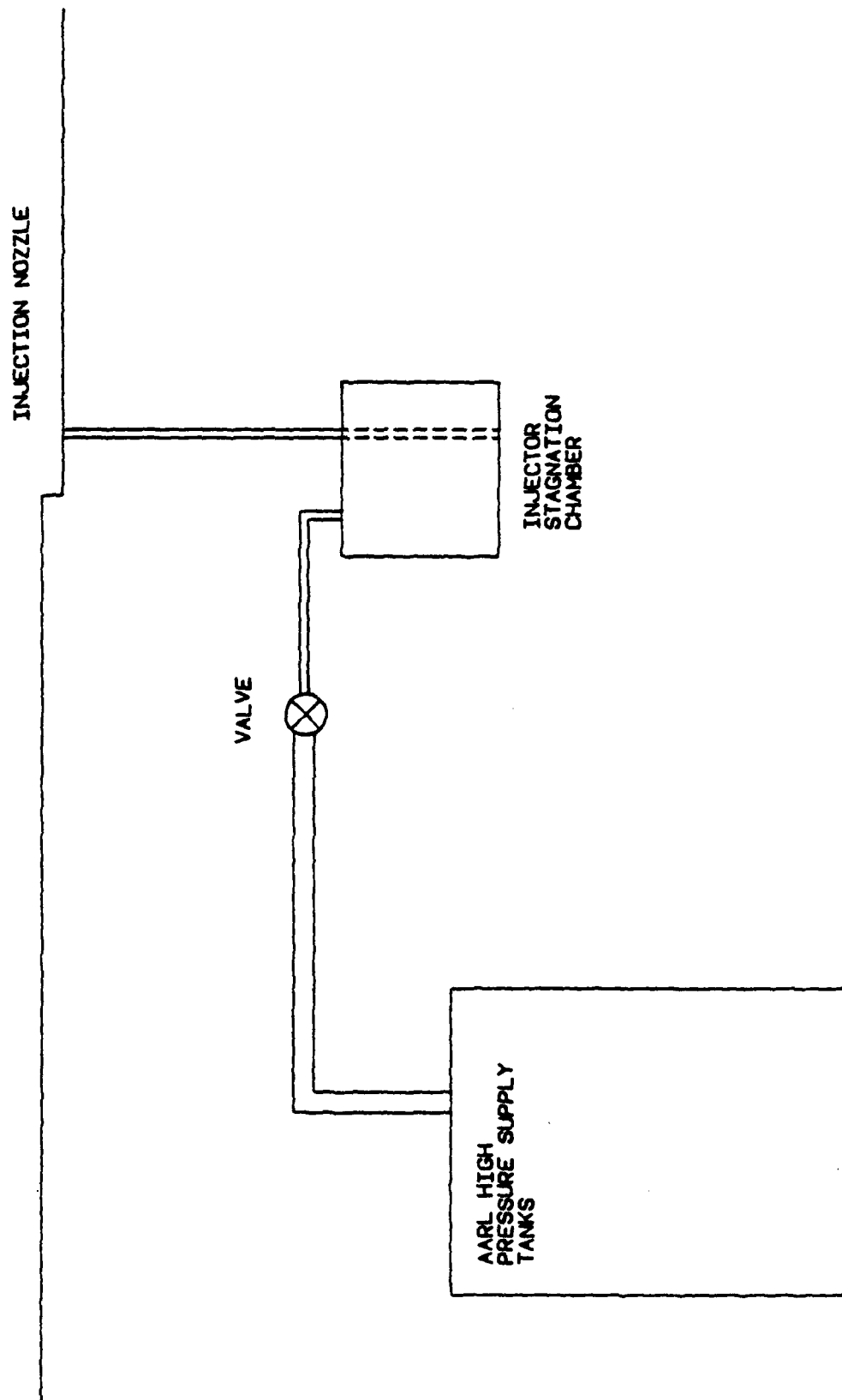


Fig. 5 Schematic of the injection line

FLOOR OF WIND TUNNEL WITH INJECTION NOZZLE
 LONGITUDINAL SPACING OF PRESSURE TAPS
 UNITS: MILLIMETERS

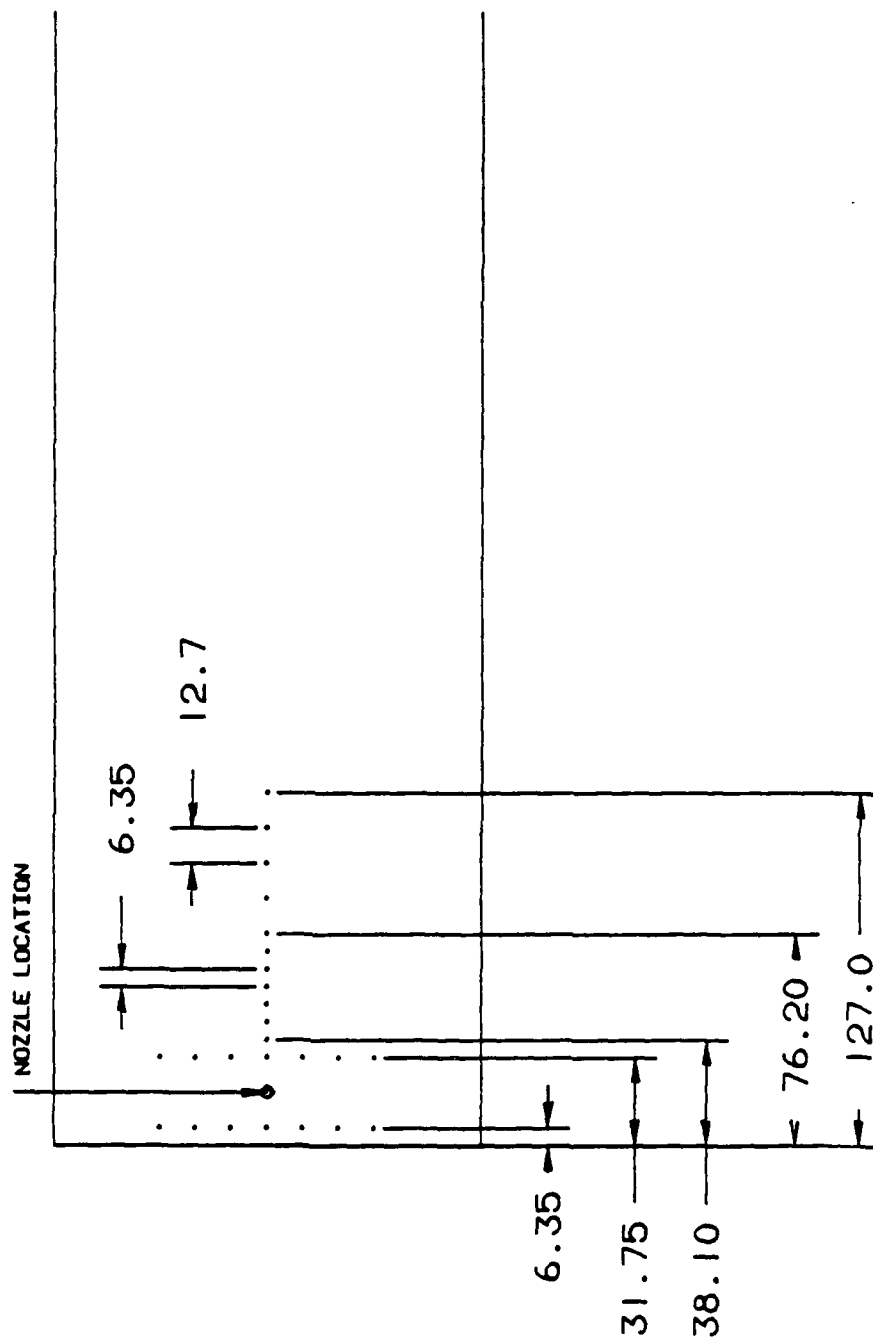


Fig. 6a Longitudinal spacing of pressure taps

FLOOR OF WIND TUNNEL WITH INJECTION NOZZLE
 LATERAL SPACING OF PRESSURE TAPS
 UNITS: MILLIMETERS

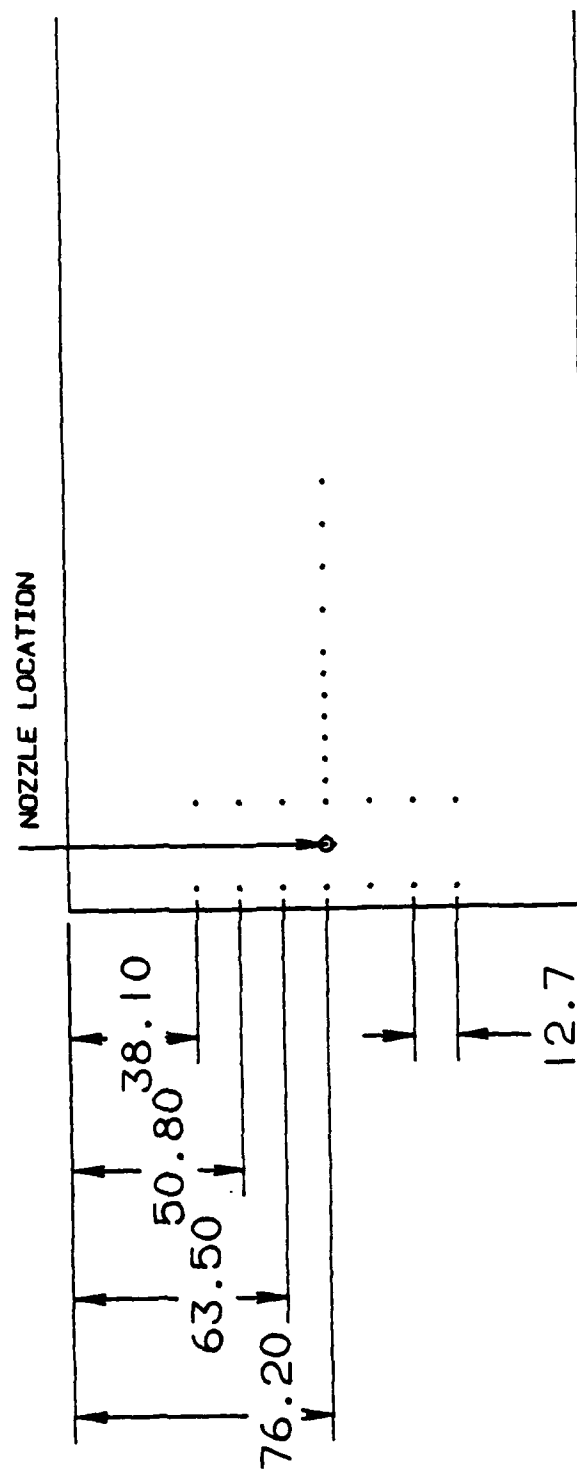


Fig. 6b Lateral spacing of pressure taps



Fig. 7 Schlieren photographs for no injection case (two different trials)



Fig. 8 Schlieren photographs for case 2, $P/P_1 = 2.85$

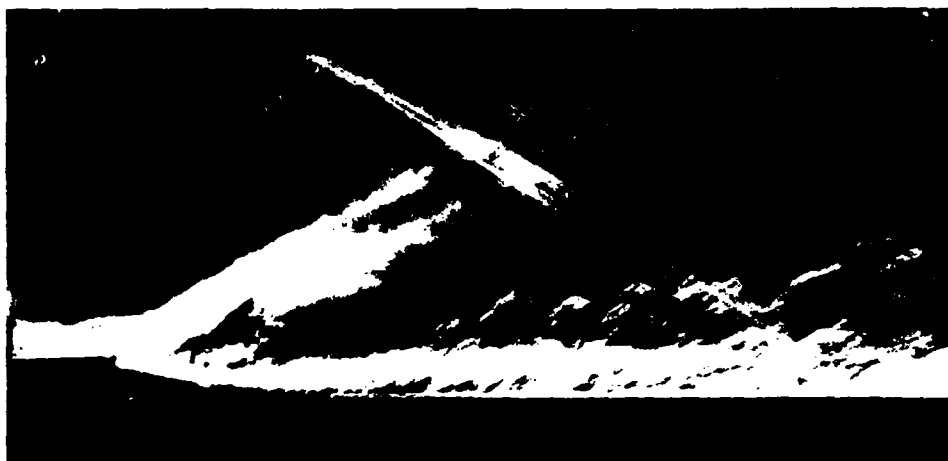


Fig. 9 Schlieren photograph for case 3, $P/P_1 = 4.29$

Normalized Static Pressure on the Plate Surface: $X/H=1$.

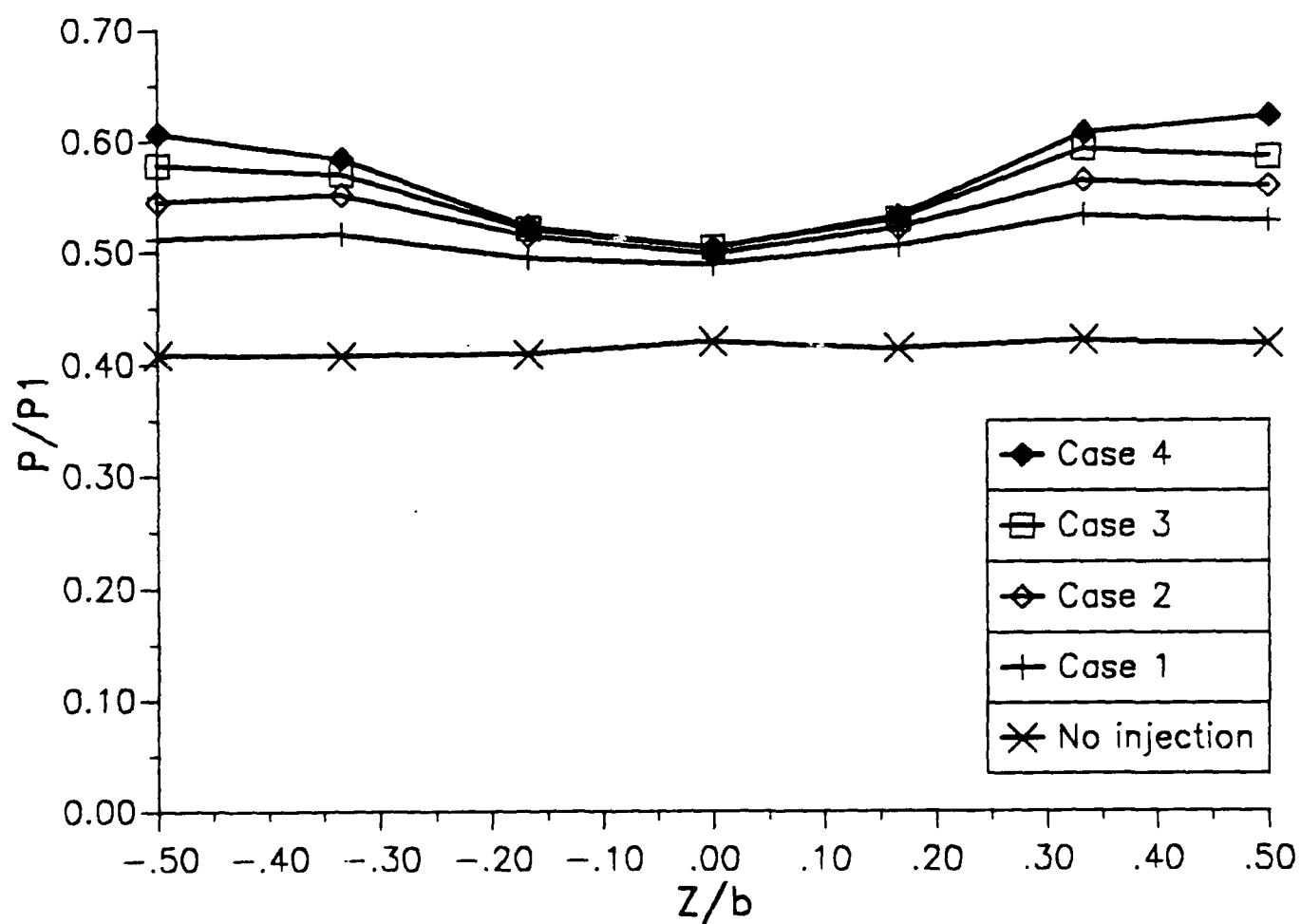


Fig. 10 Spanwise static pressure distributions at $X/H=1$

Normalized Static Pressure on the Plate Surface: $X/H=5$.

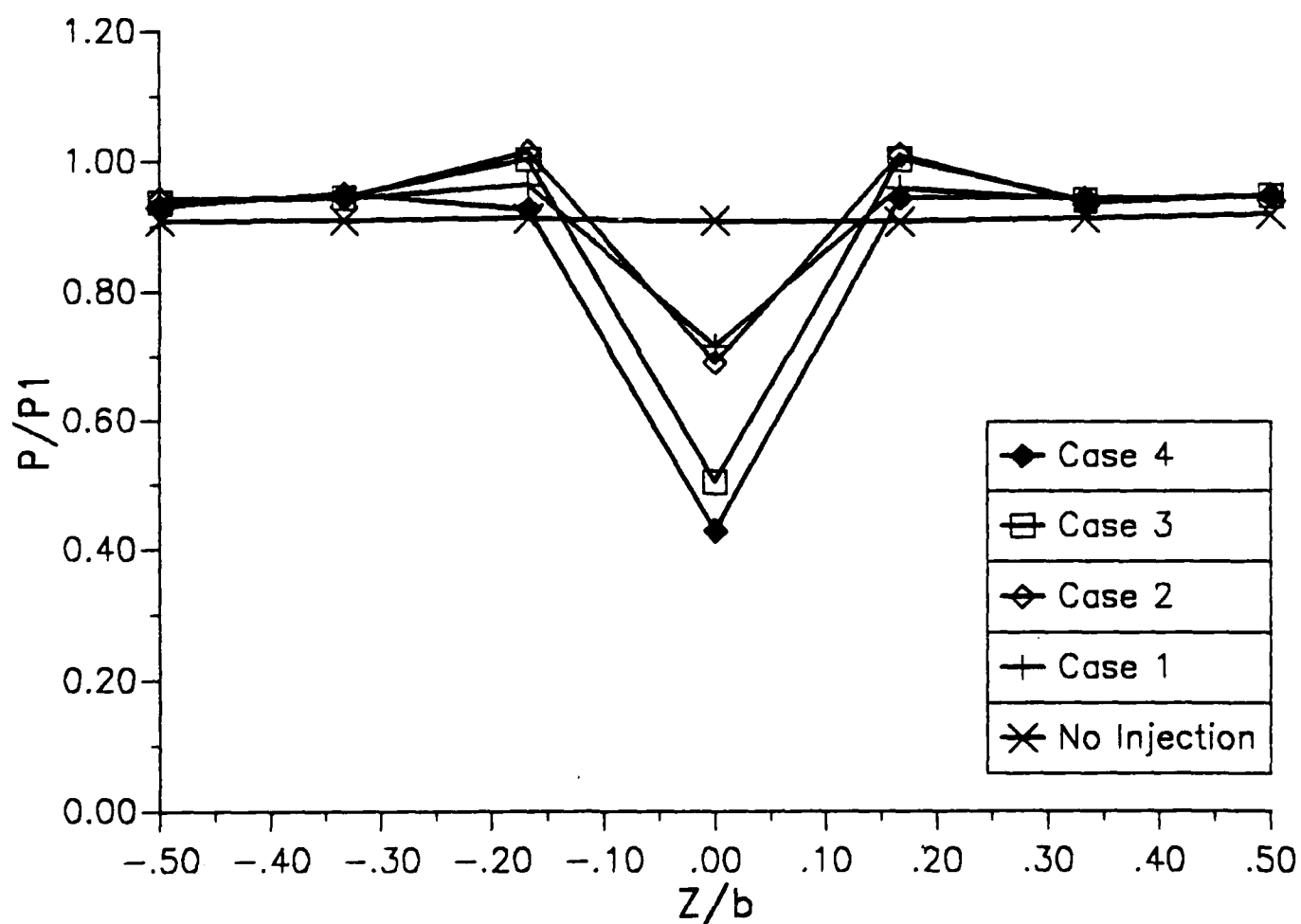


Fig. 11 Spanwise static pressure distributions at $X/H=5$

Normalized Static Pressure on the Plate Surface

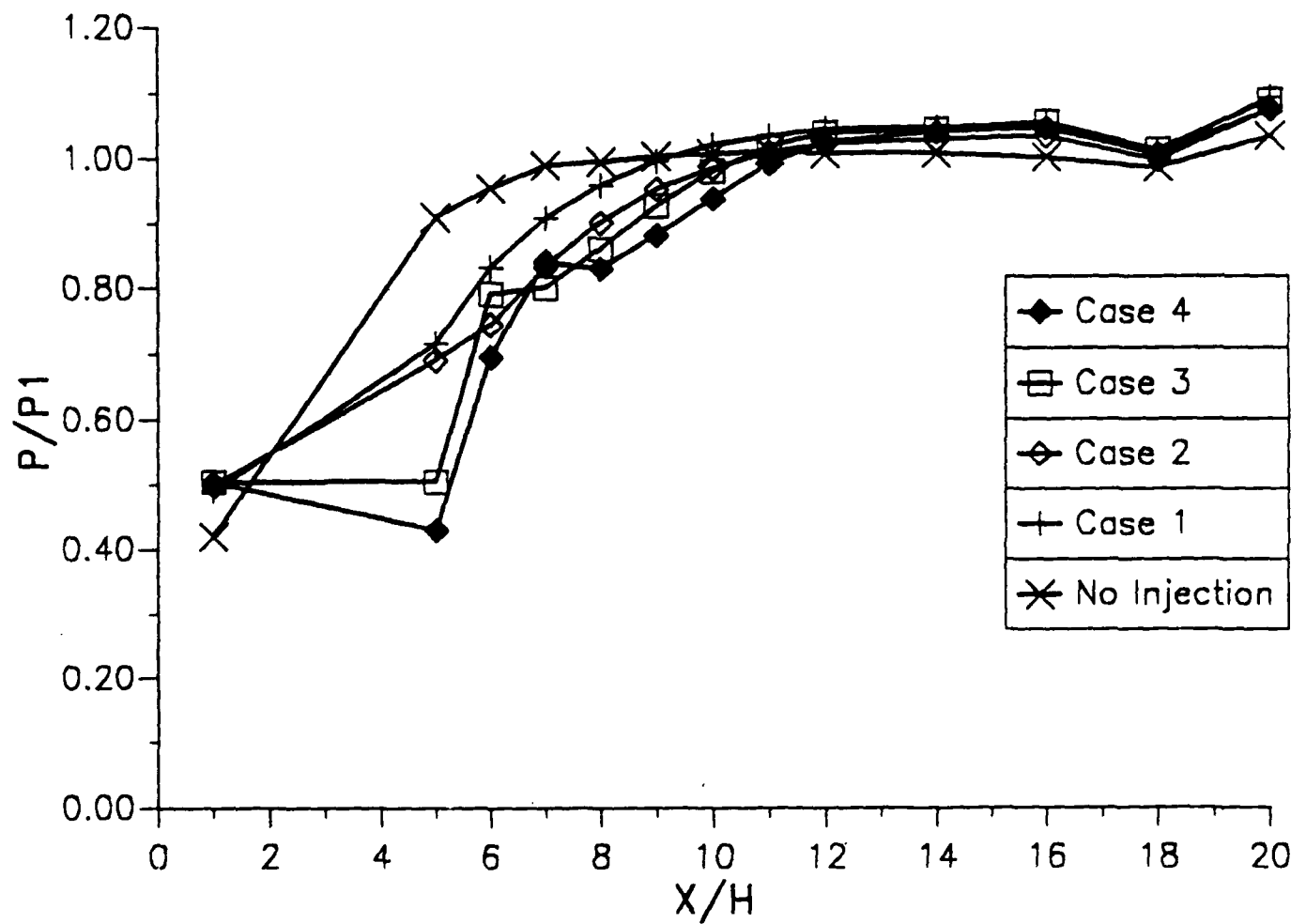


Fig. 12 Axial static pressure distributions

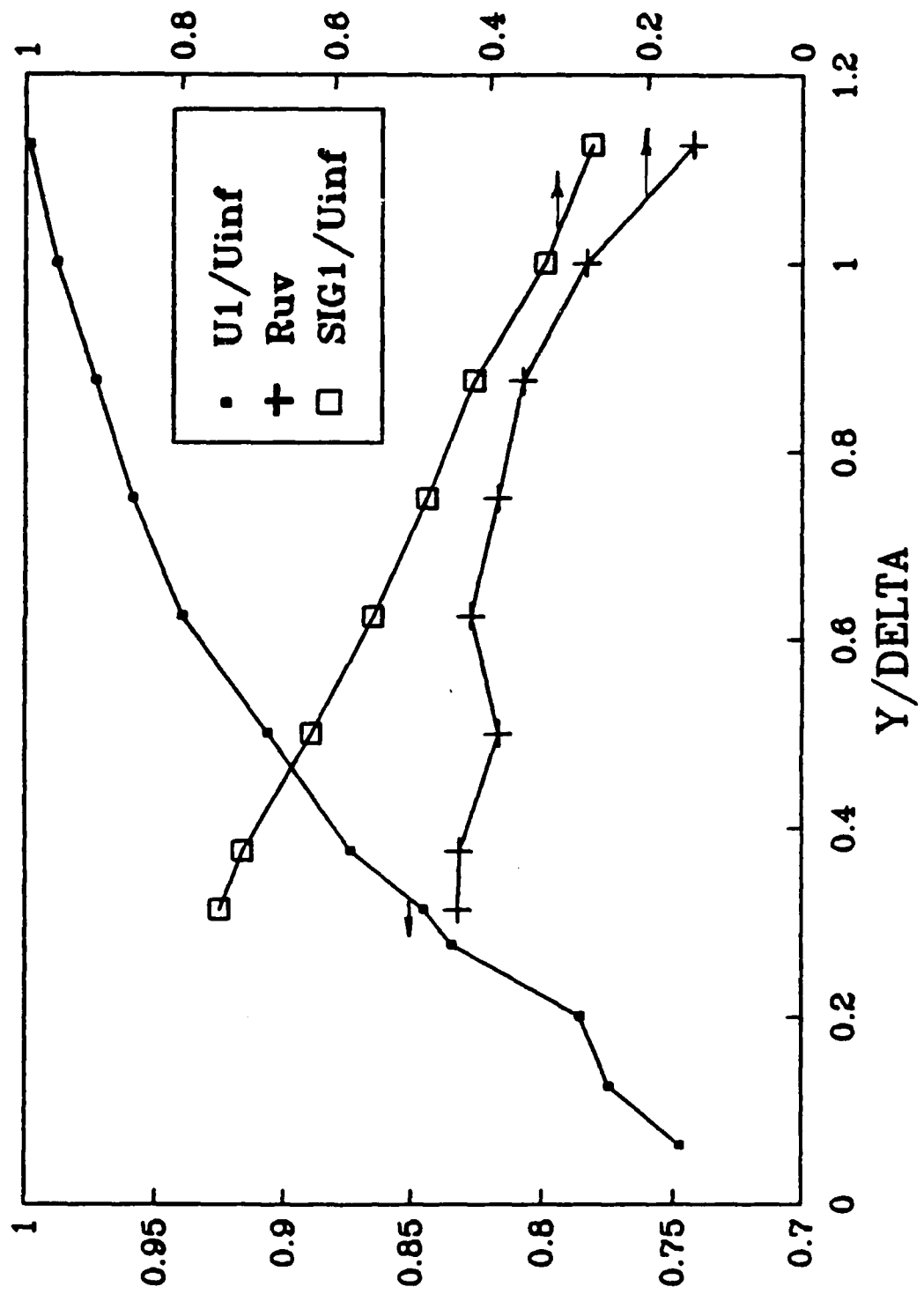


Fig. 13 Incoming boundary layer data obtained by LDV

USAF-UES Research Initiation (Mini Grant) Program

Sponsored by the
Air Force Office of Scientific Research

Conducted by the
Universal Energy Systems, Inc.

FINAL REPORT

SYSTEMS EFFECTIVENESS FOR TARGETS WITH REPAIR OR
REPLACEMENT FACILITIES OF DAMAGED COMPONENTS

by

Meckinley Scott
Professor of Mathematics
University of Alabama
Tuscaloosa, AL 35487

May 12, 1988

Contract No: F49620-85-C-0013/SB5851-0360

ABSTRACT

This report describes the work done in the development and improvement of some methodologies useful for evaluating target effectiveness. The study consists of two parts, the first of which is a continuation of the 1986 summer research effort at Eglin AFB. Specifically, it deals with system effectiveness after weapon impact on targets where use of some components is shared by two or more subsystems. The second part of this report is concerned with system effectiveness where after weapon impact, damaged components are either repaired or replaced. In this case, several models are analyzed. The analysis for each model includes the determination of the distribution of time taken to restore the system to full efficiency after weapon impact.

INTRODUCTION

This project is concerned with developing and improving methodologies for evaluating systems effectiveness with particular reference to vulnerability of hardened targets to a variety of conventional weapons. A target usually consists of a large collection of different components which interact in a complex manner in order to achieve a specific goal. These components are divided into a number of groups called phases. Each phase must be operational (possibly with degraded effectiveness) for the target to function. Again, each phase may have one or more ways of handling its function which are referred to as modes. As discussed in [4], there are three basic most common configurations of the modes of a phase and these are known as (i) hierarchical, (ii) parallel, and (iii) series configurations.

This report consists of two parts, the first of which is a continuation of the research carried out at Eglin AFB during the Summer of 1986 under the USAF-UES Summer Faculty Research Program. Methods in current use for evaluating systems effectiveness concerning targets have rather limited applications. In particular, these methods are incapable of evaluating effectiveness where use of some components is shared by two or more subsystems of the target. Some aspects of this problem has been dealt with in the 1986 summer research report [9] and in this report further results have been obtained which include more general cases.

In part I of this report, effectiveness of the system is evaluated after weapon impact on the target along one shotline. No other assumptions are made about the damaged components. For a large number

of targets in actual applications, it is important that damaged components be repaired or replaced as soon as possible. In part II of this report we consider target models where facilities are available for repair or replacement of damaged components caused by weapon impact. The degree of complexity for analyzing such models depends upon the repair or replacement times distributions, the repair policy for damaged components and a number of other variable factors. Our attention will be directed primarily to two basic problems of interest and these deal with the determinations of (i) system efficiency at any given time after weapon impact on the target, and (ii) the distribution of time measured from the instant of weapon impact on the target until all damaged components have been repaired. The repair times of various components are assumed to be independent random variables and that each follows the exponential type of distribution.

PART I

A. System Effectiveness Where Use of Some Components is Shared by Two or More Modes.

When the same components are used by two or more modes of a phase, the calculation of probabilities for the functioning of the various modes is no longer straightforward. In [9], an example was considered to indicate how to treat the case when two modes share a single component in the hierarchical phase model. The example is not general enough and gives little indication to modify the formulas for generalization. Below we discuss several cases of interest for the hierarchical phase model. The methodology for the other types of phases is similar and will not be discussed.

A.1. In the hierarchical model suppose there are m modes and mode j , ($j = 1, 2, \dots, m$) can function if and only if each of the components A_1, A_2, \dots, A_k functions and also another component M_j functions. Note that the latter is used exclusively by mode j alone whereas components A_1, A_2, \dots, A_k are used by every mode. Let U_j , ($j = 1, 2, \dots, m$) denote the event that the most efficient mode available to function is the j th one. U^c will denote the event that none of the m modes can function. Using standard notation and avoiding the use of intersection symbol for the joint occurrence of events, let

$$A = A_1 A_2 \dots A_k.$$

the event that each of the components A_1, A_2, \dots, A_k is operational. Now, we can represent the events U_1, U_2, \dots, U_m and U^c as follows:

$$U_1 = AM_1$$

$$U_j = AM_1^C M_2^C \dots M_{j-1}^C M_j, (j = 2, 3, \dots, m)$$

$$U^C = A^C \cup AM_1^C M_2^C \dots M_m^C.$$

For the probabilities of these events, we can write

$$P(U_1) = P(AM_1) = P(A)P(M_1/A),$$

where $P(M_1/A)$ is the conditional probability that the component M_1 of mode 1 functions given that each of the components A_1, A_2, \dots, A_k functions. Similarly for $j = 2, 3, \dots, m$ we have

$$\begin{aligned} P(U_j) &= P(AM_1^C M_2^C \dots M_{j-1}^C M_j) \\ &= P(A)P(M_1^C/A)P(M_2^C/A) \dots P(M_{j-1}^C/A)P(M_j/A), \end{aligned}$$

since the functioning of the various modes are dependent among themselves only through the components A_1, A_2, \dots, A_k . Let $P(M_j/A) = g_j$, $P(A_i) = p_i$ and $P(A) = p$, i.e., $p = p_1 p_2 \dots p_k$.

Thus,

$$P(U_1) = p g_1,$$

$$P(U_j) = p(1 - g_1)(1 - g_2) \dots (1 - g_{j-1})g_j, (j = 2, 3, \dots, m).$$

Also,

$$P(U^C) = (1 - p) + p(1 - g_1)(1 - g_2) \dots (1 - g_m).$$

It has been verified that

$$P(U_1) + P(U_2) + \dots + P(U_m) = 1 - P(U^C),$$

as is to be expected.

Suppose we have a system where each mode can function if at least one of the components A_1, A_2, \dots, A_k is functional and the other requirements remain the same as in the model discussed above. In this case, the

formulas for the probabilities of the various events are the same as those obtained above except that here

$$p = P(A_1 \cup A_2 \cup \dots \cup A_k) \\ = \sum p_i - \sum_{i < j} p_i p_j + \dots + (-1)^{k-1} p_1 p_2 \dots p_k.$$

which is a standard text book formula.

The case where each mode can function if at least i out of k components A_1, A_2, \dots, A_k are functional can similarly be done. However, the formula for p here is quite cumbersome and we shall write it down only for the case where the components A_1, A_2, \dots, A_k are identical. In this case, letting $a = p_i$, ($i = 1, 2, \dots, k$), we have

$$p = \sum_{j=i}^k \binom{k}{j} a^j (1-a)^{k-j},$$

where $\binom{k}{j}$ is the usual symbol for a binomial coefficient.

A.2. In this section we consider some models where some modes share more common components than the rest. Because of the numerous possibilities of sharing different types of components by various modes it is not possible to derive a general formula for the probabilities of the associated events. We shall instead consider three simple models, each of which consists of three modes 1, 2, and 3.

A.2.1. In this model, mode j , ($j = 1, 2, 3$) can function if and only if (i) component M_j is functional and (ii) for modes 1 and 2, two components A_1 and A_2 should be functional whereas mode 3 only requires that component A_1 be functional.

Using the same notations as before, we can write

$$U_1 = (A_1 A_2) M_1. \quad U_2 = (A_1 A_2) M_1^C M_2.$$

$$U_2 = (A_1 A_2) M_1^C M_2^C M_3 \cup (A_1 A_2^C) M_3.$$

$$U^C = A_1^C \cup (A_1 A_2^C) M_3^C \cup (A_1 A_2) M_1^C M_2^C M_3^C.$$

The corresponding probabilities of these events are:

$$P(U_1) = p_1 p_2 g_1. \quad P(U_2) = p_1 p_2 (1 - g_1) g_2.$$

$$P(U_3) = p_1 p_2 (1 - g_1)(1 - g_2) g_3 + p_1 (1 - p_2) g_3.$$

$$P(U^C) = (1 - p_1) + p_1 (1 - p_2)(1 - g_3) + p_1 p_2 (1 - g_1)(1 - g_2)(1 - g_3).$$

A.2.2. Here we assume that mode j , ($j = 1, 2, 3$) can function if and only if (i) component M_j is functional and (ii) for modes 1 and 3, two components A_1 and A_2 should be functional whereas mode 2 only requires that component A_1 be functional.

In this case,

$$U_1 = (A_1 A_2) M_1.$$

$$U_2 = (A_1 A_2) M_1^C M_2 \cup (A_1 A_2^C) M_2.$$

$$U_3 = (A_1 A_2) M_1^C M_2^C M_3.$$

$$U^C = A_1^C \cup (A_1 A_2^C) M_2^C \cup (A_1 A_2) M_1^C M_2^C M_3^C.$$

The corresponding probabilities of these events are:

$$P(U_1) = p_1 p_2 g_1.$$

$$P(U_2) = p_1 p_2 (1 - g_1) g_2 + p_1 (1 - p_2) g_2.$$

$$P(U_3) = p_1 p_2 (1 - g_1)(1 - g_2) g_3.$$

$$P(U^C) = (1 - p_1) + p_1 (1 - p_2)(1 - g_2) + p_1 p_2 (1 - g_1)(1 - g_2)(1 - g_3).$$

A.2.3. In this model we assume that mode j , ($j = 1, 2, 3$) can function if and only if (i) component M_j is functional and (ii) for modes 2 and 3, two components A_1 and A_2 should be functional whereas mode 1 only requires that component A_1 be functional.

Here

$$U_1 = A_1 M_1, \quad U_2 = (A_1 A_2) M_1^C M_2,$$

$$U_3 = (A_1 A_2) M_1^C M_2^C M_3,$$

$$U^C = A_1^C \cup (A_1 A_2^C) M_1^C \cup (A_1 A_2) M_1^C M_2^C M_3^C,$$

and the corresponding probability of these events are given by

$$P(U_1) = p_1 g_1,$$

$$P(U_2) = p_1 p_2 (1 - g_1) g_2,$$

$$P(U_3) = p_1 p_2 (1 - g_1) (1 - g_2) g_3,$$

$$P(U^C) = (1 - p_1) + (p_1 (1 - p_2) (1 - g_1) + p_1 p_2 (1 - g_1) (1 - g_2) (1 - g_3)).$$

B. System Effectiveness Where Various Phases Share the Use of Certain Components

In the preceding sections, the assumption has been that the various phases of the system consist of mutually subgroups of components, even though within each phase modes may share the use of certain components. Thus, the random variables representing the effectiveness of the various phases are independent and the expected effectiveness E of the system is given by

$$E = \prod_{i=1}^n E_i.$$

where E_i is the expected effectiveness of the i th phase [4]. The probabilities of functioning of the various modes of a phase i , say, are needed to calculate E_i . In practice, there may be systems where the components comprising the different phases are not mutually exclusive. Each phase may require the use of a group of components (subsystem) $C: \{C_1, C_2, \dots, C_k\}$. Each phase i , ($i = 1, 2, \dots, n$) may be considered as comprising of two subsystems C and S_i . Specifically, each phase i is functional if and only if subsystems C and S_i are operational. Thus the various phases are no longer mutually exclusive even though subsystems S_1, S_2, \dots, S_n are mutually exclusive subgroups of components which are assumed to be independent of one another.

Let Y_1, Y_2, \dots, Y_n be random variables representing the effectiveness of phases $1, 2, \dots, n$ respectively. In this case, these random variables are no longer independent and the expected effectiveness of the system will no longer be the product of the expected effectiveness of the various phases. In order to provide a meaningful way of defining the effectiveness of the system in these cases, we associate with a subsystem S_i , ($i = 1, 2, \dots, n$) a random variable X_i which represents the

effectiveness of the subsystem S_i . Likewise we introduce a random variable X_c which represents the effectiveness of the subsystem C. With these definitions, the random variable Y_i can be expressed as

$$Y_i = X_c X_i. \quad (i = 1, 2, \dots, n)$$

where X_c and X_i are independent. Furthermore, from the assumption about the subsystems S_1, S_2, \dots, S_n , the random variables X_1, X_2, \dots, X_n are independent. The random variables Y_1, Y_2, \dots, Y_n are obviously correlated. Below we present the values of the mean, $E(Y_i)$ variance, $V(Y_i)$ and also the correlation coefficient ρ_{ij} between Y_i and Y_j in terms of the means, variances and second moments of X_c, X_i and X_j .

$$E(Y_i) = E(X_c)E(X_i),$$

$$V(Y_i) = E(X_c^2)E(X_i^2) - \{E(X_c)E(X_i)\}^2,$$

$$\rho_{ij} = \frac{E(X_i)E(X_j)V(X_c)}{\sqrt{V(Y_i)V(Y_j)}}.$$

The effectiveness X of the system is defined by

$$X = \left(\prod_{i=1}^n X_i \right) X_c$$

and not as the product of the random variables Y_1, Y_2, \dots, Y_n , i.e., the expected effectiveness of the system is given by

$$E = \left(\prod_{i=1}^n E_i \right) E_c$$

where E_i is the expected effectiveness of the subsystem S_i of the i th phase and E_c is the expected effectiveness of the subsystem C.

At this time we will no longer continue to pursue further study of this topic. Instead, we will turn our attention to a new area which is carried out in part II of the report.

PART II

Some Target Models with Repair Facilities for Damaged Components.

In this part of the report we consider target systems where upon weapon impact, damaged components are repaired or replaced. In dealing with such systems, note that (i) the number of damaged components is a random variable, and (ii) the repair times of damaged components are also random variables. The degree of complexity for analyzing such models depends upon the repair times distributions, repair policy for various components and a number of other factors. Problems of interest for such models include the determinations of (a) the state of the system, equivalently the system's effectiveness, at any time t units after weapon impact on the target, and (b) the distribution of time measured from the instant of weapon impact upon the target until all damaged components have been completely repaired or replaced. Several models will be discussed based on different assumptions. However, it is to be noted that the configuration of the various components within the system plays no part or little, if any, in the analyses of problems of interest at this time. Hence we will not include this factor in our assumptions. Also, at this time, we will not consider the case where an attack on the target may take place again while the damaged components are being repaired. We will assume that the system has k components.

Let $N(t)$ be the number of unrepaired components at time t units after weapon impact. Thus, $N(0)$ is the number of components damaged by weapon impact. As mentioned before $N(t)$, ($t \geq 0$) is a random variable and data should be available to permit the determination of the

probability density function (p.d.f.) of $N(0)$. Let

$$d_i = \text{Prob}[N(0) = i], \quad (i = 0, 1, 2, \dots, k)$$

$$p_i(n, t) = \text{Prob}[N(t) = n | N(0) = i], \quad (n = 0, 1, 2, \dots, i).$$

Note that $p_0(0, t) = 1$ and $p_i(i, 0) = 1$. Also, let T_i be a random variable which denotes the time to restore the system to full efficiency when i components are damaged upon weapon impact. The p.d.f. of T_i will be denoted by $g_i(t)$. We will first discuss three simple models and then analyze a few other more general models when the number of components in the system is small.

Model I. The assumptions for this model are:

- (A) the repair facilities are such that all damaged components can be repaired simultaneously, and
- (B) the repair times of components follows exponential distributions, the repair rate being λ_r when r components are being repaired.

With these assumptions, the probabilities of the various states of the system satisfy the following set of differential-difference equations:

$$\frac{d p_i(i, t)}{dt} + \lambda_i p_i(i, t) = 0$$

$$\frac{d p_i(n, t)}{dt} + \lambda_n p(n, t) = \lambda_{n+1} p_i(n+1, t), \quad (n = 1, 2, \dots, i-1).$$

$$\frac{d p_i(0, t)}{dt} = \lambda_1 p_i(1, t).$$

where $p_i(i, 0) = 1$ and $p_i(n, 0) = 0$, $n \neq i$, $(i \geq 1)$.

The solution to the above system of equations is

$$p_i(i,t) = e^{-\lambda_i t}.$$

$$p_i(n,t) = \left(\prod_{r=n+1}^i \lambda_r \right) \sum_{j=n}^i \frac{e^{-\lambda_j t}}{\prod_{\substack{k=n \\ (k \neq j)}}^i (\lambda_k - \lambda_j)}. \quad (n = 1, 2, 3, \dots, i-1).$$

$$p_i(0,t) = \left(\prod_{r=1}^i \lambda_r \right) \sum_{j=1}^i \frac{(1 - e^{-\lambda_j t})}{\lambda_j \prod_{\substack{k=1 \\ (k \neq j)}}^i (\lambda_k - \lambda_j)}.$$

Note that $p_i(0,t)$ is the probability that at time t the system has already been restored to full efficiency starting initially with i damaged components. Also,

$$p_i(0,t) = \text{Prob}(T_i \leq t),$$

and the p.d.f. of T_i is

$$\begin{aligned} g_i(t) &= \frac{d}{dt} p_i(0,t) \\ &= \left(\prod_{r=1}^i \lambda_r \right) \sum_{j=1}^i \frac{e^{-\lambda_j t}}{\prod_{\substack{k=1 \\ (k \neq j)}}^i (\lambda_k - \lambda_j)}, \end{aligned}$$

with expected value

$$E(T_i) = \sum_{j=1}^i (1/\lambda_j).$$

Let T denote the time measured from the instant of weapon impact until all damaged components have been repaired or replaced irrespective of the number of components damaged by weapon impact. Also, let $g(t)$ be the p.d.f. of T . The relationship between $g(t)$ and $g_i(t)$. ($i = 0, 1, 2, \dots, k$) is given by

$$g(t) = \sum_{i=0}^k g_i(t) d_i.$$

where $g_0(t) = \delta(t)$, the dirac delta function, and

$$E(T) = \sum_{i=0}^k E(T_i) d_i = \sum_{i=1}^k \left(\sum_{j=1}^i 1/\lambda_j \right) d_i.$$

Model II. In this model we consider the case where

- (A) the repair facilities are restricted so that damaged components can only be repaired one at a time, and
- (B) the repair times of components follow the exponential distribution with equal repair rate λ .

The differential equations for the state probabilities can be written down as in model I (special case where $\lambda_i = \lambda, i = 1, 2, \dots, k$). However, as expected the solution assumes quite a different but much simpler form. We have,

$$p_i(n, t) = \frac{(\lambda t)^{i-n} e^{-\lambda t}}{(i-n)!}, \quad (n = 1, 2, \dots, i)$$

and

$$p_i(0, t) = \frac{1}{(i-1)!} \int_0^{\lambda t} u^{i-1} e^{-u} du,$$

which is an incomplete gamma function. The p.d.f. of T_i is given by

$$g_i(t) = \frac{\lambda^i t^{i-1} e^{-\lambda t}}{(i-1)!}, \quad (i \geq 1)$$

with expected value

$$E(T_i) = (i/\lambda).$$

Using the same definition for T as in model I, we have

$$E(T) = \frac{1}{\lambda} E\{N(0)\}.$$

where $E\{N(0)\}$ is the expected number of damaged components upon weapon impact.

Model III. The assumptions for this model are:

- (A) all of the damaged components are repaired simultaneously whenever the number of components undergoing repair does not exceed c (i.e., the facilities can repair up to a maximum of c components at a time), and
- (B) the repair times of components follow the exponential distribution with equal repair rate λ .

Note that model III reduces to that of model II when $c = 1$. The differential equations associated with this model can also be easily written down, the solution of which depends upon i , the number of damaged components upon weapon impact relative to c .

Case 1. For $1 \leq i \leq c$, we have

$$p_i(n, t) = \binom{i}{n} (e^{-\lambda t})^n (1 - e^{-\lambda t})^{i-n}, \quad (n = 0, 1, 2, \dots, i),$$

and the p.d.f. of T_i is

$$g_i(t) = i(1 - e^{-\lambda t})^{i-1} \lambda e^{-\lambda t},$$

with expected value

$$E(T_i) = \sum_{r=1}^i (1/r\lambda).$$

Case 2. For $i > c$, we have

$$p_i(n, t) = \frac{(c\lambda)^{i-n} t^{i-n} e^{-c\lambda t}}{(i-n)!}, \quad (n = c, c+1, \dots, i),$$

$$p_i(n, t) = \left\{ \frac{(c\lambda)^{i-c} t^{i-c-1} e^{c\lambda t}}{(i-c-1)!} \right\} * \binom{c}{n} (e^{-\lambda t})^n (1 - e^{-\lambda t})^{c-n}, \quad (n = 1, 2, \dots, c-1),$$

where $*$ denotes the convolution operation.

Also,

$$p_i(0,t) = \int_0^t \left\{ \frac{(c\lambda)^{i-c+1} u^{i-c-1} e^{-c\lambda u}}{(i-c-1)!} \right\} * \left\{ e^{-\lambda u} (1 - e^{-\lambda u})^{c-1} \right\} du.$$

The p.d.f. of T_i is

$$g_i(t) = \left\{ \frac{(c\lambda)^{i-c+1} t^{i-c-1} e^{-c\lambda t}}{(i-c-1)!} \right\} * \left\{ e^{-\lambda t} (1 - e^{-\lambda t})^{c-1} \right\}.$$

with expected value

$$E(T_i) = \frac{(i-c)}{c\lambda} + \sum_{r=1}^c (1/r\lambda).$$

Although the formulas obtained in the preceding sections are fairly general, they have been derived under rather restrictive conditions.

In model I, we assume that all damaged components can be repaired simultaneously, the repair rate being λ_r when r components are being repaired. This assumption does not make any distinction between different types of components. If distinction is to be made as is the case in many real life situations, the problem becomes unmanageably cumbersome when the number of components k is large.

Model I.a. This model is a generalization of model I when the system comprises of only three components c_1 , c_2 and c_3 which are vulnerable to damage by weapon impact. Components c_1 , c_2 and c_3 are all different and their repair times follow the exponential distributions with repair rates α_1 , α_2 and α_3 respectively.

Let

$p^i(c_i:t)$ = probability that component c_i alone is damaged upon weapon impact and at time t it is still under repair, ($i = 1, 2, 3$).

$p^i(0:t)$ = probability that component c_i alone is damaged upon weapon impact and by time t , repair on it has already been completed.

$p^{i,j}(c_i, c_j; t)$ = probability that components c_i and c_j are damaged upon weapon impact and both of them are still under repair at time t .
($i \neq j = 1, 2, 3$).

$p^{ij}(c_i; t)$ = probability that components c_i and c_j are damaged upon weapon impact and by time t repair on c_j has been completed but not c_i .

$p^{i,j}(0:t)$ = probability that components c_i and c_j are damaged upon weapon impact and by time t , repair on both of them has been completed.

Similar meanings can be attached to

$p^{1,2,3}(c_1, c_2, c_3; t)$, $p^{1,2,3}(c_i, c_j; t)$, $p^{1,2,3}(c_i; t)$ and $p^{1,2,3}(0:t)$.

For this model, it has been verified that

$$p^i(c_i; t) = e^{-\alpha_i t},$$

$$p^i(0:t) = 1 - e^{-\alpha_i t},$$

$$p^{i,j}(c_i, c_j; t) = e^{-(\alpha_i + \alpha_j)t}$$

$$p^{i,j}(c_i; t) = e^{-\alpha_i t} \{1 - e^{-\alpha_j t}\},$$

$$p^{i,j}(0:t) = \{1 - e^{-\alpha_i t}\} \{1 - e^{-\alpha_j t}\},$$

$$p^{1,2,3}(c_1, c_2, c_3; t) = e^{-(\alpha_1 + \alpha_2 + \alpha_3)t},$$

$$p^{1,2,3}(c_i, c_j; t) = e^{-(\alpha_i + \alpha_j)t} \{1 - e^{-\alpha_k t}\}, \quad (i \neq j \neq k = 1, 2, 3)$$

$$p^{1,2,3}(c_i; t) = e^{-\alpha_i t} \{1 - e^{-\alpha_j t}\} \{1 - e^{-\alpha_k t}\},$$

$$p^{1,2,3}(0:t) = \{1 - e^{-\alpha_1 t}\} \{1 - e^{-\alpha_2 t}\} \{1 - e^{-\alpha_3 t}\}.$$

Let T^i denote the time to restore the system to full efficiency when at the instant of weapon impact only component c_i is damaged. The p.d.f. of T^i will be denoted by $g^i(t)$. Similar meanings can be given to the random variables $T^{i,j}$ and $T^{1,2,3}$ with corresponding p.d.f.'s $g^{i,j}(t)$ and $g^{1,2,3}(t)$ respectively. In this case, it follows that

$$g^i(t) = \alpha_i e^{-\alpha_i t}.$$

$$E(T^i) = 1/\alpha_i.$$

$$g^{i,j}(t) = \alpha_i e^{-\alpha_i t} + \alpha_j e^{-\alpha_j t} - (\alpha_i + \alpha_j) e^{-(\alpha_i + \alpha_j)t}.$$

$$E(T^{i,j}) = 1/\alpha_i + 1/\alpha_j - 1/(\alpha_i + \alpha_j).$$

The expression for $g^{1,2,3}(t)$ is long and cumbersome but it can compactly be written as

$$g^{1,2,3}(t) = \frac{d}{dt} \{1 - e^{-\alpha_1 t}\} \{1 - e^{-\alpha_2 t}\} \{1 - e^{-\alpha_3 t}\}.$$

and

$$\begin{aligned} E(T^{1,2,3}) = & 1/\alpha_1 + 1/\alpha_2 + 1/\alpha_3 - 1/(\alpha_1 + \alpha_2) - 1/(\alpha_1 + \alpha_3) - 1/(\alpha_2 + \alpha_3) \\ & + 1/(\alpha_1 + \alpha_2 + \alpha_3). \end{aligned}$$

Model II.a. This is a generalization of model II when the system has only three components c_1 , c_2 , and c_3 . In this case, components can only be repaired one at a time. Thus, some more assumption is needed as to the order in which repair is to be made when more than one component is damaged. We will adopt a policy whereby priority for repair of components is implemented in the order c_1 , c_2 and c_3 . Adopting the same notation as

in model I.a. we can show that

$$p^i(r_i; t) = e^{-a_i t}.$$

$$p^i(0; t) = (1 - e^{-a_i t}).$$

$$E(T^i) = 1/a_i.$$

$$p^{1,2}(c_1, c_2; t) = e^{-a_1 t}.$$

$$p^{1,2}(c_2; t) = a_1 e^{-a_1 t} * e^{-a_2 t}.$$

$$p^{1,2}(0; t) = \int_0^t (a_1 e^{-a_1 u}) * (a_2 e^{-a_2 u}) du.$$

$$g^{1,2}(t) = a_1 e^{-a_1 t} * a_2 e^{-a_2 t}.$$

$$E(T^{1,2}) = 1/a_1 + 1/a_2.$$

Similar expressions can be written down for the probabilities, etc., when the components c_1 and c_2 are replaced by c_1 and c_3 or c_2 and c_3 .

$$p^{1,2,3}(c_1, c_2, c_3; t) = e^{-a_1 t}.$$

$$p^{1,2,3}(c_2, c_3; t) = a_1 e^{-a_1 t} * e^{-a_2 t},$$

$$p^{1,2,3}(c_3; t) = a_1 e^{-a_1 t} * a_2 e^{-a_2 t} * e^{-a_3 t}.$$

$$p^{1,2,3}(0; t) = \int_0^t (a_1 e^{-a_1 u}) * (a_2 e^{-a_2 u}) * (a_3 e^{-a_3 u}) du.$$

$$g^{1,2,3}(t) = a_1 e^{-a_1 t} * a_2 e^{-a_2 t} * a_3 e^{-a_3 t},$$

$$E(T^{1,2,3}) = 1/a_1 + 1/a_2 + 1/a_3.$$

Model III.a. In this model which again is a generalization of model III, we assume that there are three components c_1 , c_2 and c_3 . Two components are repaired simultaneously when at least two of them need repair. We assume that components c_1 and c_2 have priority over c_3 for repair purposes.

The expressions for the various quantities of interest in this case are the same as those of model I.a when the number of damaged components upon impact is not more than two. Below we write down the results for the case when all three components are damaged upon weapon impact

$$p^{1,2,3}(c_1, c_2, c_3; t) = e^{-(a_1 + a_2)t}.$$

$$p^{1,2,3}(c_2, c_3; t) = (a_1 e^{-a_1 t} * e^{-a_3 t}) e^{-a_2 t}.$$

$$p^{1,2,3}(c_1, c_3; t) = (a_2 e^{-a_2 t} * e^{-a_3 t}) e^{-a_1 t}.$$

Note that for this model $p^{1,2,3}(c_1, c_2; t)$ does not exist.

$$p^{1,2,3}(c_1; t) = \left\{ \int_0^t (a_2 e^{-a_2 u} * a_3 e^{-a_3 u}) du \right\} e^{-a_1 t}.$$

$$p^{1,2,3}(c_2; t) = \left\{ \int_0^t (a_1 e^{-a_1 u} * a_3 e^{-a_3 u}) du \right\} e^{-a_2 t}.$$

In order to avoid long expressions we will also write down $p^{1,2,3}(c_3; t)$ in terms of integrals given by

$$\begin{aligned} p^{1,2,3}(c_3; t) = & a_1 a_2 e^{-a_3 t} \left[\int_0^t \int_0^{t_2} e^{-(a_1 - a_3)t_1} e^{-a_2 t_2} dt_1 dt_2 \right] \\ & + a_1 a_2 e^{-a_3 t} \left[\int_0^t \int_0^{t_2} e^{-(a_2 - a_3)t_1} e^{-a_1 t_2} dt_1 dt_2 \right]. \end{aligned}$$

Also, we can write

$$p^{1,2,3}(0; t) = \int_0^t \{ a_1 p^{1,2,3}(c_1; u) + a_2 p^{1,2,3}(c_2; u) + a_3 p^{1,2,3}(c_3; u) \} du.$$

The p.d.f. of $T^{1,2,3}$ is given by

$$g^{1,2,3}(t) = a_1 p^{1,2,3}(c_1; t) + a_2 p^{1,2,3}(c_2; t) + a_3 p^{1,2,3}(c_3; t).$$

and its expected value can be found from

$$E(T^{1.2.3}) = \int_0^{\infty} t g^{1.2.3}(t) dt.$$

We now conclude this part of the report with a remark that for the last three models considered, since the number of components in the system is small, it is possible to obtain expressions for the various quantities of interest even when the repair times distributions do not follow exponential distributions.

Acknowledgements

I would like to thank the Air force Command and the Air Force Office of Scientific Research for sponsoring this project. Special thanks go to Mr. George C. Crews, Chief of the Technology Assessments Branch at Eglin AFB, who provided me with all the support and directions to successfully complete this project. It has been a great pleasure working with him and his staff.

REFERENCES

- [1] Barlow, R.E. and F. Proschand, Statistical Theory of Reliability and Life Testing, New York, Holt, Rinehart and Winston, Inc., 1975.
- [2] Collins, J.A., H.E. Page, and C.M. Guglielmoni, "Weapons Effects/Target Vulnerability (WETV) Computer Program", Vol. I - User Manual, Technical Report, Datatec, Inc., Fort Walton Beach, Florida, December 1985.
- [3] Feller, W., An Introduction to Probability Theory and Its Applications, New York, John Wiley and Sons, 1968.
- [4] Gregory, L.D., "Hardened Sam Site Vulnerability Analysis (U)", Vol. II - SAMV User Manual, Technical Report, Vought Corporation, Dallas, Texas, April 1981.
- [5] Karlin, S. and H.M. Taylor, A First Course in Stochastic Processes, 2nd Edition, New York, Academic Press, 1975.
- [6] Kozlov, B.A. and I.A. Ushakov, Reliability Handbook, New York, Holt, Rinehart and Winston, Inc., 1970.
- [7] Rickower, E.B., "Reliability in a Random Environment", Preprint (Technical Report), Naval Postgraduate School, Monterey, California, October 1986.
- [8] Scott, M., "Distribution of the Number of Tasks by a Repairable Machine", Operations Research, vol. 20, 851-59, 1972.
- [9] Scott, M., "Systems Effectiveness Concerning Vulnerability of Hardened Targets to a Variety of Weapons", Summer Faculty Research Program Report, Eglin AFB, Florida, July 1986.
- [10] Williams, R.L., "Systems Functional GO Models for Vulnerability Analysis", Technical Report, Kuman Sciences Corporation, Colorado Springs, Colorado, October 1985.

A Pattern Recognition Application in Elastic-
Plastic Boundary Element, Hybrid Stress Analysis

Jim Sirkis
Aerospace Engineering, Mechanics, and Engineering Science
University of Florida, Gainesville, Florida 32611

April 1988

Final Report

Submitted to Universal Energy Systems
as the Required Report for USAF Mini Grant Program

ABSTRACT

This report contains a description of the major findings of the year long study into displacement pattern matching applications in hybrid stress analysis. As a result of this effort, a two-dimensional elastic-plastic boundary element (EPBEM) code was produced. Also, the pattern recognition technology necessary to automatically discern boundary conditions for the EPBEM structural code was developed.

INTRODUCTION

Hybrid, experimental-numerical stress analysis is currently an intense area of technical interest. Experimentalists have long been able to produce full-field information about the deformation or stress fields experienced by structural members. But producing this information is not enough. Extraction and interpretation of the data must follow if the experimentation is to have any meaning. The tedious nature of manual data extraction has cost an untold number of man hours. Automated data extraction is a logical step in producing more economical experimental procedures. If one can automatically extract displacement, stress or strain data from the experimental results, then it is a simple matter to format this information so that it is acceptable for use in some structural analysis computer code.

In this effort, two relatively new technologies are merged to address the problem of manual data extraction and interpretation; they are pattern recognition and elastic-plastic boundary element methods. A new technique called "displacement pattern matching" is introduced to find all but the free surface boundary conditions. This technique uses computer vision hardware and pattern recognition concepts to track the centroids of black spots adhered to the surface of a white painted structure. These spots are placed at locations where the displacement information is desired. The displacement information from displacement pattern matching, coupled with free surface conditions, are supplied to an initial strain, elastic-plastic boundary element code. The EPBEM code is then used to analyze of internal state of stress. Boundary element methods are used since they have an advantage over finite element and finite difference methods in that only the plastically deforming region needs to be domain discretized. The Appendix gives a brief theoretical development of the hybrid method and then gives a description of the hybrid analysis of a perforated strip under uniaxial tension.

APPENDIX

ABSTRACT

A two-dimensional hybrid experimental-numerical technique for elastic-plastic stress analysis is presented. This technique results from merging two relatively new technologies in engineering mechanics: boundary element methods and image processing. A syntactic pattern recognition scheme termed "Displacement Pattern Matching" (DPM) determines displacement boundary conditions to be used in an elastic-plastic boundary element (EPBEM) code. The result is an automated stress analysis tool.

Displacement pattern matching is a process where displacements are measured by tracking an arbitrary array of 'black' spots on a 'white' specimen. The digitized images of the specimen are compared in a double exposure format to determine displacements. Displacement pattern matching is a full field technique, with spatial resolution on the order of .00254 mm.

Displacement pattern matching supplies the actual specimen displacement increments to the von Mises, isotropic work hardening, boundary element code. Given these displacements and free surface conditions, EPBEM is able to incrementally calculate the internal state of stress at selected locations. Results obtained for a variety of geometries and loading conditions compared well with ANSYS finite element and selected published experimental solutions and therefore are encouraging.

INTRODUCTION

Substantiating postulations through experimentation, or using experimentation to draw new conclusions, is fundamental to science and engineering. This service is provided to theoretical mechanics by the field of experimental mechanics. Before coming to any conclusions, experimentalists demand confidence in their work; as a result, many time consuming experiments are repeated "just to be sure." Experimental stress analysis is no different. Repeating experimental procedures, often including more than one technique, is the norm when searching for the solution to engineering problems [1]. The tedious nature of manual data extraction and reduction led researchers to explore automated extraction and reduction schemes. Hence, hybrid experimental-numerical stress analysis techniques evolved.

The shear difference method [2] is an early example of an experimental-numerical hybrid method in stress analysis. Since then, researchers have acknowledged the need for improved and more encompassing hybrid techniques [3]. Prior to the development of digital image processing, most hybrid stress analysis techniques suffered from the need for manual data extraction. Here, boundary element methods and pattern recognition concepts are combined to develop a hybrid technique for elastic plastic stress analysis.

Moslehy and Ranson [4], Umeagukwu et al. [5], and Balas et al. [6] introduced early BEM-experimental hybrid techniques, but all require manual data extraction and all are restricted to the elastic regime. Liu [7] was first to introduce a hybrid method using digital image processing for automated data extraction and elastic BEM for structural analysis. Hybrid elastic boundary element-experimental methods are presently an important research area [8-9]. Equally important are elastic-plastic boundary element-experimental methods, but there seems to be a absence of research in this topic. Elastic-plastic boundary element methods (EPBEM) were first conceived by Swedlow and Cruse [10] in 1971 and then implemented by Riccardella [11] in 1973. Since then, EPBEM have grown in popularity. Telles [12] gives an excellent historical review of the development of this numerical method. Elastic-plastic boundary element methods have the similar attributes as the elastic boundary element methods, the main difference being that EPBEM require the plastic region to be domain discretized.

In the natural progression of coupling boundary element methods and image processing techniques, this report introduces a two-dimensional experimental-EPBEM technique. The experimental technique used here, displacement pattern matching, is a spin-off of the pattern mapping technique, first introduced by Fail [13]. The pattern recognition technique called image matching is used to follow the motion of black spots placed on a white painted structure. Spots are placed at or near the locations where the

displacements are desired. These displacements, and any free surface conditions, provide enough information for the boundary element method to evaluate the interior stress field. Since this image processing based experimental procedure provides only displacements, it is named "displacement pattern matching" (DPM). The combination of displacement pattern matching for data extraction and elastic-plastic boundary element methods for structural analysis leads to a fully automated technique for measuring plastic stress and strain.

a perforated strip under uniaxial tension is used to explore the ability of the automated hybrid technique as a nondestructive stress analysis tool. The specimens for this plane stress test are produced from 1100-H14 aluminum, and a MTS testing machine is used to apply controlled loads. This experiment serves to show the usefulness of this hybrid DPM-EPBEM technique in elastic-plastic stress analysis.

THE ELASTIC-PLASTIC BOUNDARY ELEMENT METHOD

The governing equations in elastic-plastic boundary element methods are derived using virtual work. The virtual work approach sheds light on the some of the fundamental concepts of boundary element methods and shows how powerful the method can be. Following this development, the initial strain concept and its effect on the solution procedure is described. Additionally,

the need for a second equation is illustrated and a plastic flow rule is introduced to meet that need.

Elastic-plastic boundary element methods are based on the numerical solution of the integral equations governing the deformation in an elastic-plastic solid. These integral equations can be derived by starting with the following rate form of the virtual work statement:

$$\int_{\Gamma} \mathbf{t}_i^*(s) \dot{u}_i(s) d\Gamma + \int_{\Omega} \mathbf{b}_i^*(p) \dot{u}_i(p) d\Omega = \int_{\Omega} \sigma_{ij}^*(s, p) \dot{\epsilon}_{ij}(p) d\Omega; \quad (1)$$

where t_i , u_i , and b_i denote the traction, displacement and body force vectors respectively. The stress tensor is σ_{ij} and the strain tensor is ϵ_{ij} . The differential $d\Gamma$ is an element on the bounding curve and the differential $d\Omega$ is an interior surface element. Also, the *-superscript denotes an arbitrary equilibrium set and no superscript denotes an arbitrary compatible set [14]. The total strain tensor can be decomposed into elastic and plastic parts; thereby, rewriting Equation (1) as

$$\begin{aligned} \int_{\Gamma} \mathbf{t}_i^*(s) \dot{u}_i(s) d\Gamma + \int_{\Omega} \mathbf{b}_i^*(p) \dot{u}_i(p) d\Omega = & \int_{\Omega} \sigma_{ij}^*(s, p) \dot{\epsilon}_{ij}^p(p) d\Omega \\ & + \int_{\Omega} \sigma_{ij}^*(s, p) \dot{\epsilon}_{ij}^e(p) d\Omega. \end{aligned} \quad (2)$$

During each load increment both elastic and plastic deformation are present. Even though plastic deformation occurs, the stress rate is still related to the elastic strain rate by

Hooke's law [15]. Therefore the substitution $\sigma_{ij}^* \dot{\epsilon}_{ij}^e = \epsilon_{ij}^* \dot{\sigma}_{ij}$ can be made. Equation (2) can be further expanded by applying the rate form of virtual work (with the significance of the superscripts interchanged) to the $\epsilon_{ij}^* \dot{\sigma}_{ij}$ term;

$$\begin{aligned} \int_{\Gamma} \dot{t}_i^*(s) \dot{u}_i(s) d\Gamma - \int_{\Gamma} \dot{t}_i(s) u_i^*(s) d\Gamma + \int_{\Omega} \dot{b}_i^*(p) \dot{u}_i(p) d\Omega \\ - \int_{\Omega} \dot{b}_i(p) u_i^*(p) d\Omega = \int_{\Omega} \sigma_{ij}^*(s, p) \dot{\epsilon}_{ij}^p(p) d\Omega. \end{aligned} \quad (3)$$

The difference between this integral equation and its elastic counterparts is the integral which includes the plastic strain rate term.

Since the choice is arbitrary, \dot{u}_i , \dot{t}_i , and \dot{b}_i are chosen as the traction rate, displacement rate, and body force rate of the true body. The choice of the *-superscript set is also arbitrary; therefore, it is chosen as Kelvin's solution to the response of an infinite, two-dimensional, elastic medium which is subjected to arbitrarily located, mutually orthogonal point loads. These designations lead to Somigliano's Identity for inelastic materials;

$$\begin{aligned} \dot{u}_j(s) = \int_{\Gamma} U_{ij}^*(s, p) \dot{t}_i(s) d\Gamma - \int_{\Gamma} T_{ij}^*(s, p) \dot{u}_i(s) d\Gamma + \\ \int_{\Gamma} U_{ij}^*(s, p) \dot{b}_i(p) d\Omega + \int_{\Omega} \sigma_{ij}^*(s, p) \dot{\epsilon}_{ij}^p(p) d\Omega. \end{aligned} \quad (4)$$

Choosing Kelvin's solutions as the boundary element fundamental solution, without explanation, is common in boundary element methods. The virtual work derivation shows the choice is completely arbitrary. This derivation underscores the fact that many choices are available. One may choose any elastic or elastic-plastic solution as long as it satisfies equilibrium and compatibility. The virtual work approach allows the boundary element solution to be completed with a renewed appreciation.

As with its elastic counterpart, a limiting process is required to find the elastic-plastic boundary element constraint equation. The results are identical to the elastic case since the plastic strain rate integral exists and has no contribution to C_{ij} .

$$\begin{aligned}
 C_{ij}(s) \dot{u}_j(s) + \int_{\Omega} T_{ij}^*(s, \ell) \dot{u}_i(\ell) d\Gamma = \int_{\Omega} U_{ij}^*(s, \ell) \dot{t}_i(\ell) d\Gamma \\
 + \int_{\Gamma} U_{ij}^*(s, \ell) \dot{b}_i(\ell) d\Omega + \int_{\Gamma} S_{jki}^*(s, \ell) \dot{\epsilon}_{ki}^p(\ell) d\Omega;
 \end{aligned}
 \tag{5}$$

where $S_{jki}^*(s, p)$ is the stress associated with Kelvin's solution.

An initial strain algorithm is introduced in order to numerically solve the above integral equations governing elastic-plastic deformation. Swedlow and Cruse [10] were first to formulate the initial strain boundary element theory. Since then, Riccardella [11], Mendelson and Albers [16], Mukherjee [17], Telles [12] and others have developed initial strain algorithms to solve engineering problems. Although initial strain theory is not restricted to a particular flow rule, it

will be described in the context of isotropic work hardening and incremental plasticity. In accordance with accepted terminology and notation, rate and increment will be used interchangeably and superior dots denote time differentiation.

In an elastic-plastic body, strains can be categorized as either elastic or plastic. In initial strain EPBEM, the plastic strain is assumed to act as a residual strain; each load increment is just a deviation from that residual strain. The adjective "residual" refers to the idea that the solid knows, by some internal mechanism, the plastic strain increment before the application of the load increment. When the increment is applied, the material only deforms elastically. Loosely interpreted, the initial strain concept states that plastic deformation occurs before elastic deformation. This idea of initial strain is analogous to Martin's discussion of convergence by the superposition of elastic and residual stresses [18]. As an aside, initial strain has little meaning in finite strain plasticity since numerically, this is a load and unload process. Initial strain, however, is acceptable in incremental plasticity.

If the plastic strain is known apriori and if the problem is well posed, then Equation (5) yields the unknown boundary conditions. The boundary information could then be used to find the displacements in an elastic-plastic solid (Equation (4)). The problem here is that prior knowledge of the plastic strain rate is just an idealization of the initial strain solution approach. In reality, the plastic strain rate is an

unknown quantity; therefore, an additional relation is needed.

An isotropic work hardening, von Mises flow rule is introduced to satisfy the above requirement for an additional relation. Although a multitude of flow rules have been proposed [19], an isotropic work hardening flow rule provides an easily understood constitutive model. It also provides a reasonable approximation to material response while loading takes place. However, one should be aware that the von Mises yield criterion is limited in that it does not provide for hysteresis [20].

In an effort to be concise, the functional form of the constitutive relation used in this initial strain algorithm is given below. A detailed development can be given in Ref [21].

$$\dot{\epsilon}_{ij}^p = \frac{3 S_{ij} S_{mn} \dot{\epsilon}_{mn}}{2 \sigma_{eq}^2 (1 + E_T/3G)} \quad (6)$$

In Equation (6), E_T is the tangent modulus of the uniaxial stress-strain curve, G is the shear modulus, S_{ij} is the stress deviator, and σ_{eq} is the von Mises equivalent stress.

Numerical Implementation of EPBEM

Simple domains, simple boundary conditions and knowledge of the loading history are all needed if exact solutions to the elastic-plastic boundary element equations are to be found. Some exact solutions are documented [22], but seldom are researchers so fortunate.

The proposed EPBEM algorithm strives for a balance between simplicity and accuracy. To this purpose, the boundary displacements are assumed to vary linearly along the boundary segments. Correspondingly, the tractions are assumed constant over each segment. The plastic strain rate must also be quantized before the numerical procedure can be described. The plastic zone is discretized much like FEM. Triangular cells are chosen with the plastic strains assumed to be constant over each cell. This may seem identical to FEM but in contrast to FEM, the cells are used only to evaluate the domain integral. If the interpolating functions are given, then the constraint equation (5) and interior displacement equation (4) can be rewritten as

$$\dot{u}_j(p) = \sum_{m=1}^N \dot{t}_i(s) \int U_{ij}^*(s,p) d\Gamma_m - \sum_{m=1}^N \int T_{ij}^*(s,p) \dot{u}_i(s) d\Gamma_m + \sum_{q=1}^d \dot{\epsilon}_{ki}^p \int S_{jki}^*(s,p) d\Omega_q \quad (7)$$

$$C_{ij} \dot{u}_j(s) + \sum_{m=1}^N \int T_{ij}^*(s,l) \dot{u}_i(l) d\Gamma_m = \sum_{m=1}^N \dot{t}_i \int U_{ij}^*(s,l) d\Gamma_m + \sum_{q=1}^d \dot{\epsilon}_{ki}^p \int S_{jki}^* d\Omega_q \quad (8)$$

Equation (II-29.A) represents a system of 2N equations for 2N unknowns.

The line integrals are evaluated just as in elastic BEM, but the elastic-plastic BEM also requires domain integration.

Special care must be observed when evaluating these domain integrals. The initial strain solution procedure requires a boundary element formulation for the interior strain rate. As a consequence, the correct formulation introduces an additional singular kernel. The strain at any point in the domain is defined by $2\dot{\epsilon}_{ij} = (\dot{u}_{i,j} + \dot{u}_{j,i})$; therefore, one may use the boundary element displacement rate equation (Equation 4) to find the interior strain rates. Many early researchers failed to recognize that the integration path around the domain singularity changes with the load; this path change prevents pulling the derivative directly under the plastic strain rate integral [18]. Bui [22] was the first to recognize this error and formulated the correct derivative; Telles and Brebbia [23] expanded Bui's ideas and then later carried them out [24]. The above techniques are both elegant and independent of the plastic strain rate shape function but they are sometimes difficult to use. Since the EPBEM algorithm presented here is of the constant cell type, the general approach championed by Telles and co-workers will be foregone in lieu of an implementationally easier technique.

The assumption that plastic strain rate is constant over each interior cell is not only computationally simple, it also makes the above discussion inconsequential. The constant cell approximation enables direct evaluation of the plastic strain rate integral [11,16] by subdividing the cell (Figure 1). The integrals over triangle 1 and triangle 2 are algebraically added to the integral over triangle 3 to give the desired

integral over the cell (triangle 4). The unit directions are defined so that the algebraic signs are correct. Since the plastic strain rate kernel is singular at the base point, a small region surrounding this point is excluded in the kernel evaluation [17]. This integration scheme is equally valid when the source point coincides with the load point. No great difficulty exists in evaluating the integrals, and the question surrounding the existence of the derivatives is moot since plastic strain rates are found via direct differentiation. The boundary element, internal strain rate equation is given below.

$$\begin{aligned} \dot{u}_{i,k} = & \dot{t}_j(s) \int U_{ij,k}^*(s,p) d\Gamma - \int \dot{u}_j(s) T_{ij,k}^*(s,p) d\Gamma \\ & + \dot{p}_{jm} \frac{\partial}{\partial x_k} \int S_{ijm}^*(s,p) d\Omega \end{aligned} \quad (9)$$

The iterative elasto-plastic boundary element solution technique used in the solution to Equations (4), (5) and (9) are similar to the successive approximation scheme used by Roberts and Mendelson for stress function solutions [25]. The iterative approach used here is less cumbersome since the total strain rates are found directly. Figure 2 provides a flow chart of the numerical solution procedure. This iterative solution is efficient and has acceptable accuracy. The technique is sufficiently general so that it is easily extended to other than boundary element methods. When large scale yielding occurs, there is a possibility that the plastic zone will exceed the

celled region. If such a case arises, one expects a reduction in EPBEM accuracy.

DISPLACEMENT PATTERN MATCHING

The spread of image processing applications in photomechanics is a consequence of the availability of equipment at affordable costs. Hardware prices continue to decline and the power of personal computers continues to increase. Economical mass storage, networking, graphics, and application specific software all have increased the proliferation of image processing in the photomechanics field [26]. For the most part, image processing techniques in photomechanics are grouped into two categories, fringe analysis [27-29] and correlation techniques [30-31]. A third category, pattern mapping [13], is emerging as alternative with many attractive qualities. Pattern mapping is a non-destructive technique measuring displacement and strain and is based on image processing and syntactic pattern recognition. It is a process by which "black" spots on a "white" background are followed in a double exposure type scheme. This highly automated technique offers: full field measurement, sub-pixel registration, and greatly reduced CPU time.

Pattern mapping was originally developed as a general purpose strain measurement technique capable of discerning large rigid body rotation and translations. It also included a variety of strain definitions. Fail [13] suggested that reductions in

run time were achievable by tailoring the pattern mapping to a specific class of problems. Displacement pattern matching (DPM) is a result of this suggestion. The displacement pattern matching algorithm is developed by assuming that the experimenter can prevent appreciable rigid body motion and that displacements are the only information of interest. As a result, a highly automated, very fast displacement tracking scheme emerged.

A decided advantage of displacement pattern matching is the limited prior knowledge required for success. Success of the technique hinges on the placement of high contrast spots (dark spots on a light background) at locations where displacement is desired. Implicit in this knowledge is the idea that the images are binary, that is, the gray levels should be either black or white [35]. In keeping with the automated methodology, DPM does not need prior knowledge about the number of spots, spot area or any other distinguishing feature.

Displacement pattern matching starts by raster scanning the underformed image until a black pixel is found, then the gray levels of that pixel's eight nearest neighbors are checked. If at least one neighbor is black then DPM has located a spot. If none of its neighbors are black, then DPM considers the center pixel as a false spot. Once a true spot is located, a general border following scheme developed by Rosenfeld [33] and specialized to only find outside edges [34,13] 'frames' the spot. Framing the spot is the process by which a complete clockwise circuit around the border is traversed, storing only the left

most, right most, highest, and lowest pixel locations (L, R, T, B respectively) for the feature extraction. To account for the transition between black and white, the frame automatically expands by two pixels in all directions. With the first spot framed, the raster scanning continues. This process is repeated until the entire image is examined.

False spots larger than one pixel in diameter are entirely possible, especially when the scene is significantly magnified. An automated method of discerning false from true spots is therefore required. Experience indicates that the areas of false spots are much smaller than their legitimate cousins (area is defined as $A = [R-L][B-T]$). A spot area larger than one third the average spot area (averaged over every framed spot) is a true spot. This definition is completely arbitrary but it proved to be 99% reliable for the spot sizes used in this research.

Once all the true spots are found, their centroids are calculated using the true gray levels in the frame and pixel locations (i,j) in the matrix [32].

At this point pattern matching [35] is introduced to the spot tracking algorithm. Here, spot motion is measured by local matching of the segmented spots. In essence, the location of a spot in the image is assumed near its location in the previous sequential image. Therefore, instead of raster scanning the entire new image, only the previous framed area is scanned.

If the displacement field carries the spot out of the original frame area then the search region is expanded to

$$A_n = [L-R][B-T]n^2, \quad n=2,3,4\ldots \quad (10)$$

where A_n is the area of the search region and n is the number of search region expansions required to find the spot (Figure 3). When the search region encompasses more than one spot or a wrong spot only, a one-to-one match is not guaranteed and the matching process may fail. Therefore, over-expansion defines a restriction on DPM. The spot displacement must be smaller than or equal the distance from the original spot to the closest spot in the current image. This critical distance is easily gaged. For example, in a square array of spots, the maximum displacement can never be greater than 0.7071 times the smallest original spot spacing.

A special search region expansion case occurs near the image edge. When the displacement field carries a spot close to the perimeter of the image, the expansion may try to extend the search region beyond the image border, the results of which are unpredictable. The search region is therefore contoured to the image edge if the region encounters the perimeter

With a one-to-one correspondence established between segments in successive images, statistical feature extraction can proceed. The centroid of each spot is calculated and the x- and y-coordinates of the centroids in sequential images are

subtracted to find the displacements

$$u_x = X_n - X_{n-1} \quad (11)$$

and

$$u_y = Y_n - Y_{n-1}. \quad (12)$$

In these displacement definitions, n refers to the current image. The units of displacement are pixels but can be converted to a units of length through calibration.

Images are captured with an personal computer based image processing system. The image device is Sony XC-38 CCD camera. A Datacube IVG-128 Video Acquisition and Display Board quantizes the image with its digital form displayed on a PVM-1271Q/1371QM Sony studio monitor. All image processing is done on a PC's Limited 286-8 Personal computer equipped with a math co-processor and EGA graphics. All DPM calculations are performed on the 80287-8 based personal computer and written in C. Run times average about 31 seconds per load increment.

HYBRID DPM-EPBEM TECHNIQUE

Both the elastic-plastic boundary element and displacement pattern matching algorithms have been individually discussed, but the ultimate goal here is to construct a single successful stress analysis tool by meshing these two techniques. Accordingly, this section presents a hybrid DPM-EPBEM and its experimental verification.

Experimental Setup and Specimen Preparation

Since EPBEM is a two-dimensional code, only plane stress or plane strain loading conditions can be examined. All specimens are of the plane stress type and are produced from a ductile aluminum alloy (1100-H14, $E=73.88$ GPa., $\nu=.33$, and $Y_0=103.45$ MPa.). Loads are applied by a Material Testing System (MTS) machine. A schematic of the setup is given in Figure 4. The testing machine is manually controlled to produce either constant load or constant stroke.

DPM depends on the application of high contrast spots to the specimen. The aluminum specimens are painted flat white in order to produce the high contrast background for the black spots. The spots are applied by using typical "rub-ons" commonly found in office supply stores; the grammatical periods are far more consistent in area and darkness than any attempted painting or staining procedures. The periods are simply "rubbed on" at the locations where the displacement is desired.

Perforated Strip Tensile Test

The perforated strip exposes DPM-EPBEM to a stress state containing high stress gradients and is representative of

realistic engineering problems. The dimensions of the perforated strip specimens used in these experiments are 228.6mm in length, 25.4mm wide, 1.59mm thick with a centrally located 12.7mm diameter circular cutout. The stresses calculated by the hybrid technique are compared to both ANSYS finite element and Theocaris and Marketos' experimental results [38].

The spots are applied to the specimen at the locations specified in Figure 5 and shown in Figure 6; and the domain enclosed by the spots is modelled as seen in Figure 7. A careful comparison between Figure 7 and Figure 5 reveals that not all of the DPM spots and EPBEM nodes are found at the same locations. The finite size of the spots establishes a practical limit to the spot spacing; therefore, DPM-EPBEM uses quadratic interpolation to find the displacements at nodes which do not coincide with spots.

The homogeneous, isotropic hardening option (von Mises yield condition) and two-dimensional, four point, isoparametric plate elements (two degrees of freedom) are used in the finite element solution to this problem. ANSYS follows an initial stress [37] solution procedure, modelling the stress-strain curve with five piecewise linear segments. One symmetric quarter of the specimen is modelled and is loaded with 345. kPa. traction increments, added to the initial traction of 20.7 Mpa. The load steps are applied until a value of 43.45 MPa. is reached. The DPM-EPBEM, ANSYS, and Theocaris' normalized stress at ($x=6.35$ mm, $y=0.0$ mm) as a function of load step are given in Figure 8. The

normalized stress is defined as the current y-component of stress divided by the applied stress. The finite element and DPM-EPBEM results compare well, with DPM-EPBEM exhibiting one larger excursion at the sixth load step. No immediate explanation for this anomaly is apparent. Since the next increment's result does not seem to be affected, one might presume that some grip slippage had occurred.

Perhaps even more comforting are the experimental points produced by Theocaris and Marketos [38]. The material they tested was also an aluminum alloy. It exhibited a similar uniaxial stress-strain curve to the one used here, but with a higher yield strength (237.93 MPa.). Although the normalized stress curves are not identical, which is not to be expected, the purely experimental, hybrid and purely numerical behaviors are remarkably similar.

The difference in the response could be caused by one of many reasons. Theocaris and Marketos use a bi-linear approximation of the uniaxial stress-strain curve in their analysis whereas the DPM-EPBEM uses a combination of Ramberg-Osgood and linear fits. Theocaris and Marketos make no mention of whether they did or did not anneal their specimens, nor do they discuss their loading apparatus in any detail. Therefore, one would not necessarily expect perfect agreement.

Other interesting information produced by the hybrid technique is the load-displacement curve for ($x=0.0$ mm, $y=6.35$ mm) which is given in Figure 9. The load-displacement results mimic

(in shape) the load-maximum strain curves reported by Zienkiewicz [38]. Although not definitive, they certainly are supportive of DPM-EPBEM reliability. In his study, Zienkiewicz used the material properties reported by Theocaris and Marketos.

A final plot, Figure 10, demonstrates the extent of the plastic zone by giving the normalized stress at various radial locations from the root of the hole (for $t_y=41.38$ MPa.). The slight inflections at $x=10.17$ mm and $x=6.93$ mm are apparent in all of the graphs provided by Theocaris and Marketos [36] and are therefore reassuring.

CONCLUSIONS

The two-dimensional numerical-experimental hybrid technique described herein combines context-free syntactic pattern recognition (DPM) and elastic-plastic boundary element methods (EPBEM) to produce a useful, non-destructive stress analysis tool. Within a certain load range, all of the presented DPM-EPBEM results compare well with finite element and purely experimental (where available) solutions.

DPM-EPBEM works well in load ranges above approximately 90% of the proportional limit. Below this value, the resolution of DPM is insufficient to accurately measure the spot locations. In these experiments, the DPM resolution is on the order of .1 pixel. Experimentation with synthetic images indicate that the geometric character of the spot influences the DPM resolution.

Optimum spot shape, size and gray level profile may exist which produce an improved resolution.

Another area which needs improvement deals with the elastic-plastic boundary element method. The convergence of the initial strain elastic-plastic boundary element solution is sensitive to load increment step size. It is not always possible to apply the loads in such way as to stay within the realm of incremental plasticity and thereby guarantee convergence. Therefore a solution procedure which is less sensitive to increment size would be more desirable. Fortunately, the initial stress solution approach has just this quality [39]. It is anticipated that an initial stress solution procedure would greatly enhance the load range in which this hybrid technique is applicable. By incorporating the above suggestions, the displacement pattern matching, elastic-plastic boundary element hybrid method can be shaped to provide good solutions over an even wider load range.

REFERENCES

1. Durelli, A. J., APPLIED STRESS ANALYSIS, Prentice-Hall, Englewood Cliffs, N. J., 1967.
2. Frocht, M.M., PHOTOELASTICITY, Vol. 1, Wiley, New York, 1941.
3. Kobayashi, A. S., "Hybrid Experimental-Numerical Stress Analysis," in HANDBOOK ON EXPERIMENTAL MECHANICS (A. S. Kobayashi ed.), Prentice-Hall, Englewood Cliffs, N. J., pp. 739-768, 1987.
4. Moslehy, F. A., and Ranson, W. F., "Laser Speckle Interferometry and Boundary Integral Techniques in Experimental Stress Analysis," in DEVELOPMENTS IN THEORETICAL AND APPLIED MECHANICS, Vol. X (J. E. Stoneking, Ed.), Chattanooga, Tenn., Univ. of Tenn., pp. 473-492, 1980.
5. Umeagukwu, I., Peters, W., and Ranson, W.F., "The Experimental Boundary integral Method in Photoelasticity," in DEVELOPMENTS IN THEORETICAL AND APPLIED MECHANICS, Vol. XI (T. J. Chung and G. R. Karr, Eds.), Huntsville, Ala., Univ. of Ala., pp. 181-191, 1982.
6. Balas, J., Sladek, J., and Drzik, M., "Stress-Analysis by Combination of Holographic Interferometry and Boundary Integral Method," Exp. Mech. 23, pp.196-202, 1983.
7. Liu, C., Development of a Consistent Boundary Integral Equation Method for Use with Image Processing Method in Experimental Mechanics, Ph.d. Dissertation, University of South Carolina, Columbia, 1984.
8. Mitsui, Y., and Yoshida, S., Separation of Principal Stresses Using Boundary Element Method, "DEVELOPMENTS IN THEORETICAL AND APPLIED MECHANICS, VOL. XIII (W. F. Ranson and J. M. Biedenbach Eds.), Columbia, S.C., University of South Carolina, pp. 263-268, 1986.
9. Shukla, A., Sadd, M. H. and Saliba, E., Two Dimensional Contact Stress Analysis Using a Hybrid Technique of Photoelasticity and Boundary Element Methods," DEVELOPMENTS IN THEORETICAL AND APPLIED MECHANICS, VOL XIII (W. F. Ranson and J. M. Biedenbach Eds.), Columbia, S. C., University of South Carolina, pp. 590-594, 1986.

10. Swedlow, J., L., and Cruse, T. A., "Formulation of Boundary Integral Equations for Three Dimensional Elastoplastic Flow," Int. Jou. Sol. Struc., 7, pp. 1673-1683, 1971.
11. Riccardella, P. C., "An Implementation of the Boundary-Integral Technique for Planar Problems of Elasticity and Elasto-Plasticity," Ph.d. Dissertation, Carnegie-Mellon University, Pittsburgh, 1973.
12. Telles, J. F. C., THE BOUNDARY ELEMENT METHOD APPLIED TO INELASTIC PROBLEMS, Springer-Verlag, New York, 1983.
13. Fail, R. W., "Pattern Mapping in Plane Motion Analysis," Ph.d. Dissertation, University of Florida, Gainesville, 1987.
14. Drucker, D. C., "Variational Principles in the Mathematical Theory of Plasticity," Proc. Symp. Appl. Math., 8, pp. 7-22, 1958.
15. Chen, W., LIMIT ANALYSIS AND SOIL PLASTICITY, Elsevier Scientific Publishing Company, New York, 1975.
16. Mendelson, A., and Albers, L. U., "Application of Boundary Integral Equation Method to Elasto-Plastic Problems," in PROC. ASME CONF. ON BIEM, AMD-Vol. 11 (T. A. Cruse and F. J. Rizzo Eds.), ASME, Troy, New York, pp.47-84, 1975.
17. Mukherjee, S., BOUNDARY ELEMENT METHODS IN CREEP AND FRACTURE, Applied Science Publishers, New York, 1982.
18. Martin, J. B., PLASTICITY: FUNDAMENTALS AND GENERAL RESULTS, The MIT Press, Cambridge, Mass., 1975.
19. Drucker, D. C., "Conventional And Unconventional Plastic Response and Representation," to appear in Appl. Mech. Rev., 1988.
20. Johnson, W., and Mellor, P. B., PLASTICITY FOR MECHANICAL ENGINEERS, D. Van Nostrand Co., Ltd., London, 1966.
21. Sirkis, J. S., "A Two-Dimensional Hybrid Numerical-Experimental Technique For Elastic-Plastic Stress Analysis," Ph.D. Dissertation, University of Florida, Gainesville, 1988.
22. Bui, H. D., "Some Remarks about the Formulation of Three Dimensional Thermoelastoplastic Problems by Integral Equations," Int. Jou. Sol. Struc., 14, pp. 935-939, 1978.

23. Telles, J. F. C., and Brebbia, C. A., "On the Application of the Boundary Element Method to Plasticity," Appl. Math. Model., 3, pp. 466-470, 1979.
24. Telles, J. F. C., and Brebbia, C. A., "The Boundary Element Method in Plasticity," Proc. 2nd. Sem. on RECENT ADVANCES IN BOUNDARY ELEMENT METHODS (C. A. Brebbia Ed.), University of Southampton, Southampton, pp. 295-317, 1980.
25. Roberts E., and Mendelson A., "Analysis of Plastic Thermal Stress and Strain in Finite Thin Plate of Strain-Hardening Material," National Aeronautics and Space Administration Report, Huntsville, Ala., NASA TN D-2206, pp. 3-8, 1964.
26. Wetzler, F. U., "Digital Imaging Technology: Applications Are Expanding Everywhere," SPIE Opt. Eng. Reports, No. 48, pp. 3a-5a, Dec., 1987.
27. Chen, T. C., "Application of Digital Image Processing and Computer Graphics Techniques in Photomechanics," Ph.d. Dissertation, University of Florida, Gainesville, 1985.
28. Burger, C. P., "Automated Moire' and Photoelastic Analysis with Digital Image Processing," PROC. 1984 SEM FALL CONF. ON EXP. MECH., Milwaukee, Wisc., 1984.
29. Robinson, D. W., "Automatic Fringe Analysis With a Computer Image-Processing System," Appl. Opt., 22, pp. 2169-2176, 1983.
30. Chu, T. C., Ranson, W. F., Sutton, M. A., and Peters, W. H., "Applications of Digital-Image-Correlation Techniques to Experimental Mechanics," Exp. Mech., 25, pp. 232-244, 1985.
31. Sutton, M. A., Wolters, W. J., Peters, W. H., Ranson, W. F., and McNeil, S. R., "Determination of Displacements Using an Improved Digital Correlation Method," Image and Vision Comp., pp. 133-139, 1983.
32. Rosenfeld, A., and Kak, C., DIGITAL PICTURE PROCESSING, Vol. 1, Academic Press, New York, pp. 214-250, 1982.
33. Rosenfeld, A., and Kak, A., DIGITAL PICTURE PROCESSING, Vol. 2, Academic Press, New York, pp. 191-240, 1982
34. Susuki, S., and Abe, K. 'Topological Structural Analysis of Digitized binary Images by Border Following,' Com. Vis., Graph., and Im. Pr., V. 30, pp. 32-46, 1985.
35. Mantas, J. "Methodologies in Pattern Recognition and Image Analysis-A Brief Survey," Pat. Rec., 20, pp. 1-6, 1987.

36. Theocaris, P. S., and Markedos, E., "Elastic Plastic Analysis of Perforated Thin Strips of a Strain Hardening Material," *Jou. Mech. Phys. Solids*, 12, pp. 377-390, 1964.
37. Kohnke, P. C., ANSYS, ENGINEERING ANALYSIS SYSTEM THEORETICAL MANUAL, Swanson Analysis Systems, Inc., Houston, Pa., pp. 4.0.1-4.1.33, 1983.
38. Zienkiewicz, O. C., THE FINITE ELEMENT METHOD, McGraw-Hill Book Co., London, pp. 469-471, 1955.
39. Nayak, G. C., and Zienkiewicz, O. C., "Elasto-Plastic Stress Analysis. A Generalization for Various Constitutive Relations Including Strain Softening," *Inter. Jou. Num. Meth.*, 5, pp. 113-135, 1972.

LIST OF FIGURES

1. Scheme used in domain integration.
2. Flow chart of the iterative elasto-plastic (initial strain) boundary element solution procedure.
3. Search region expansion.
4. Schematic of the experimental set up.
5. Schematic of the spot locations on the perforated strip.
6. Photograph of the spots applied to the perforated strip.
7. Boundary element domain discretization of the perforated strip.
8. Plot of normalized stress versus load step for the perforated strip.
9. Load-displacement plot for ($x=0.$ mm, $y=6.35$ mm) on the perforated strip.
10. Plot of the normalized stress versus x -position on the perforated strip.

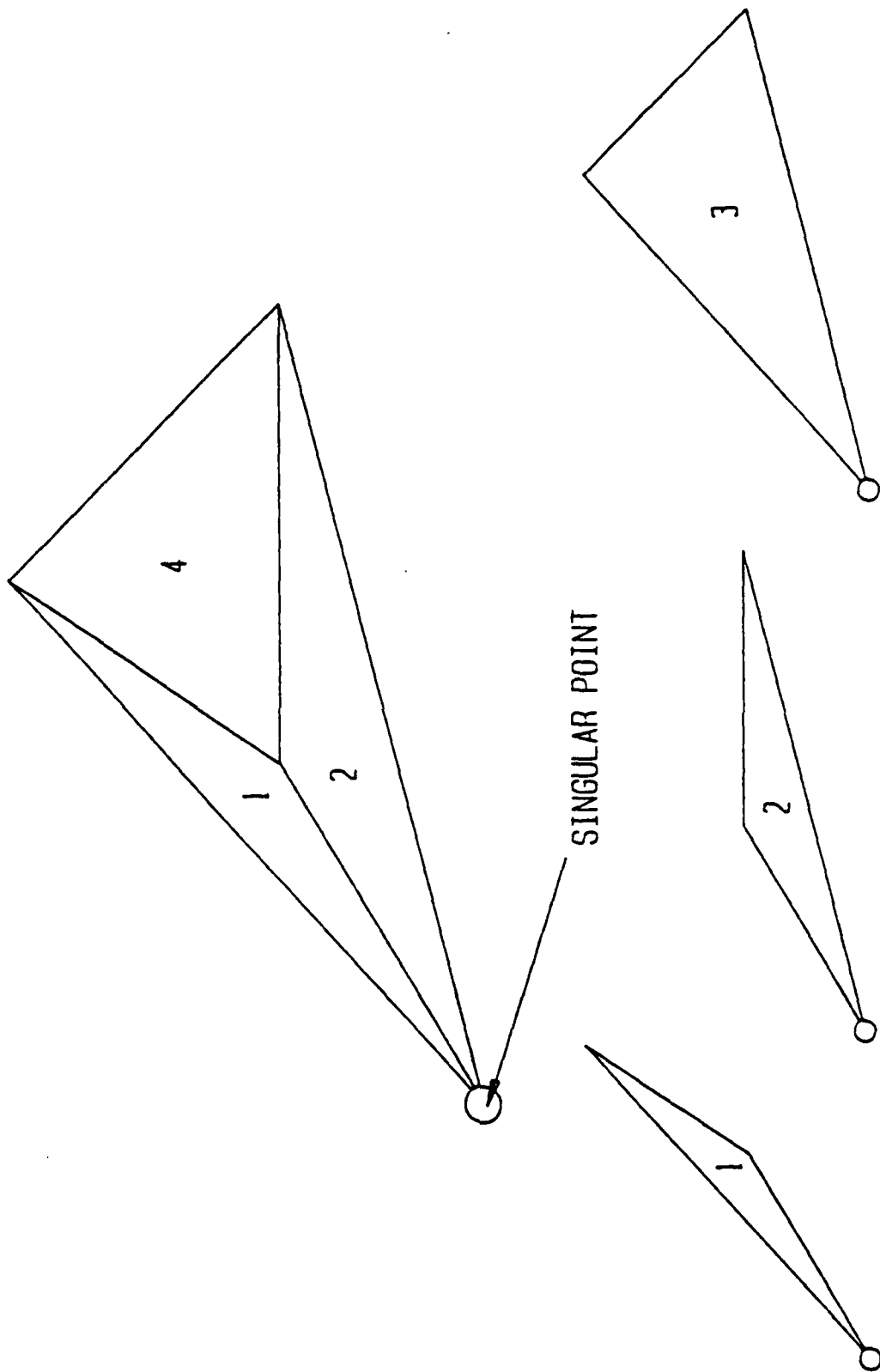


Figure 1.

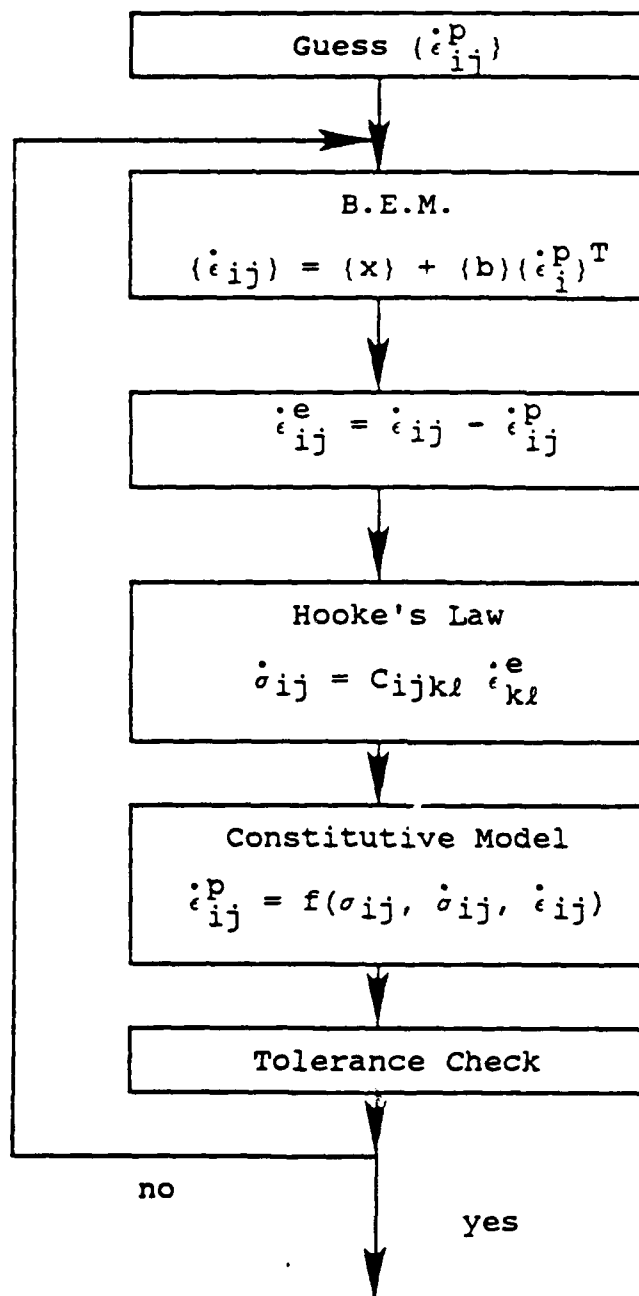


Figure 2.

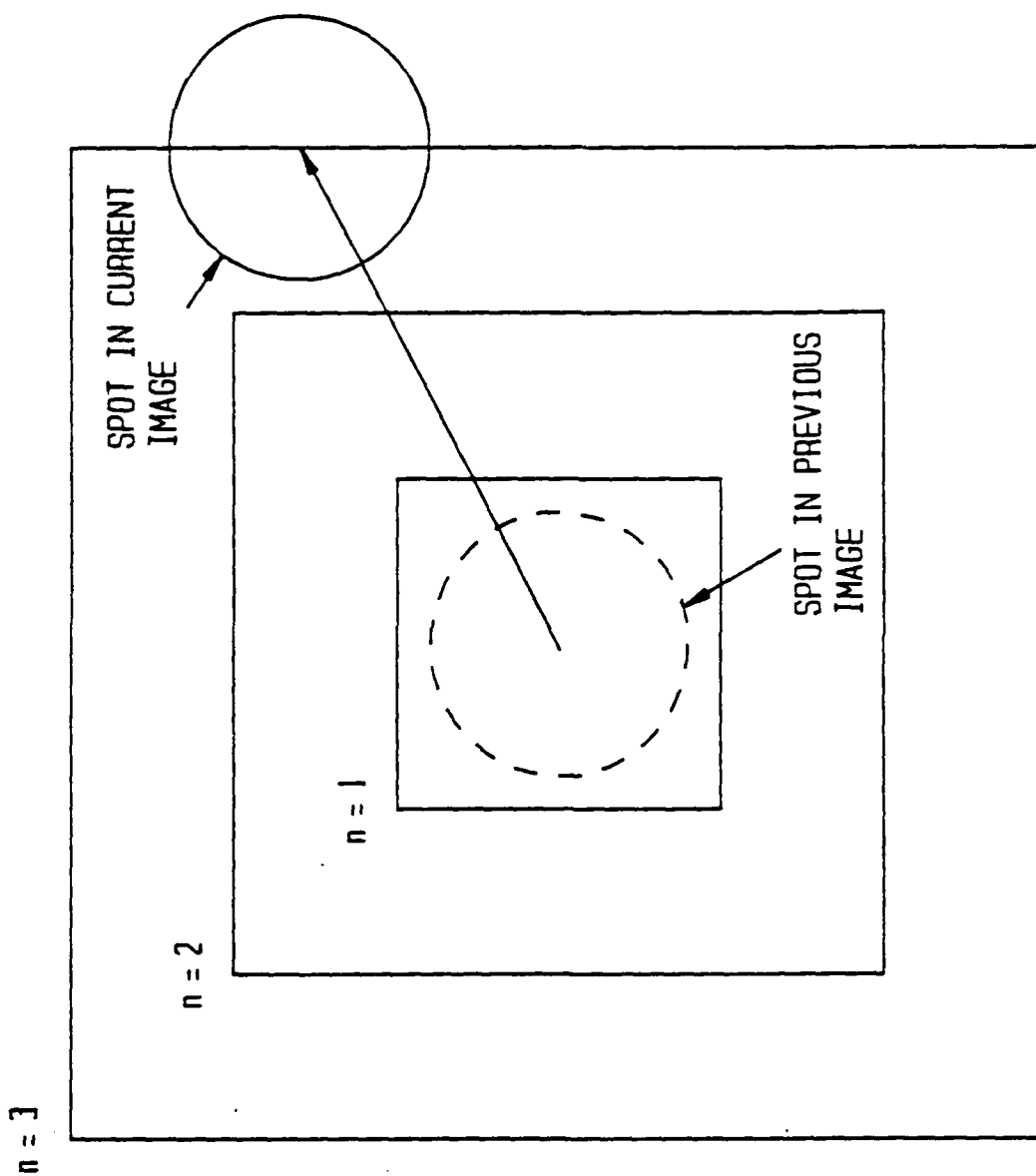


Figure 3.

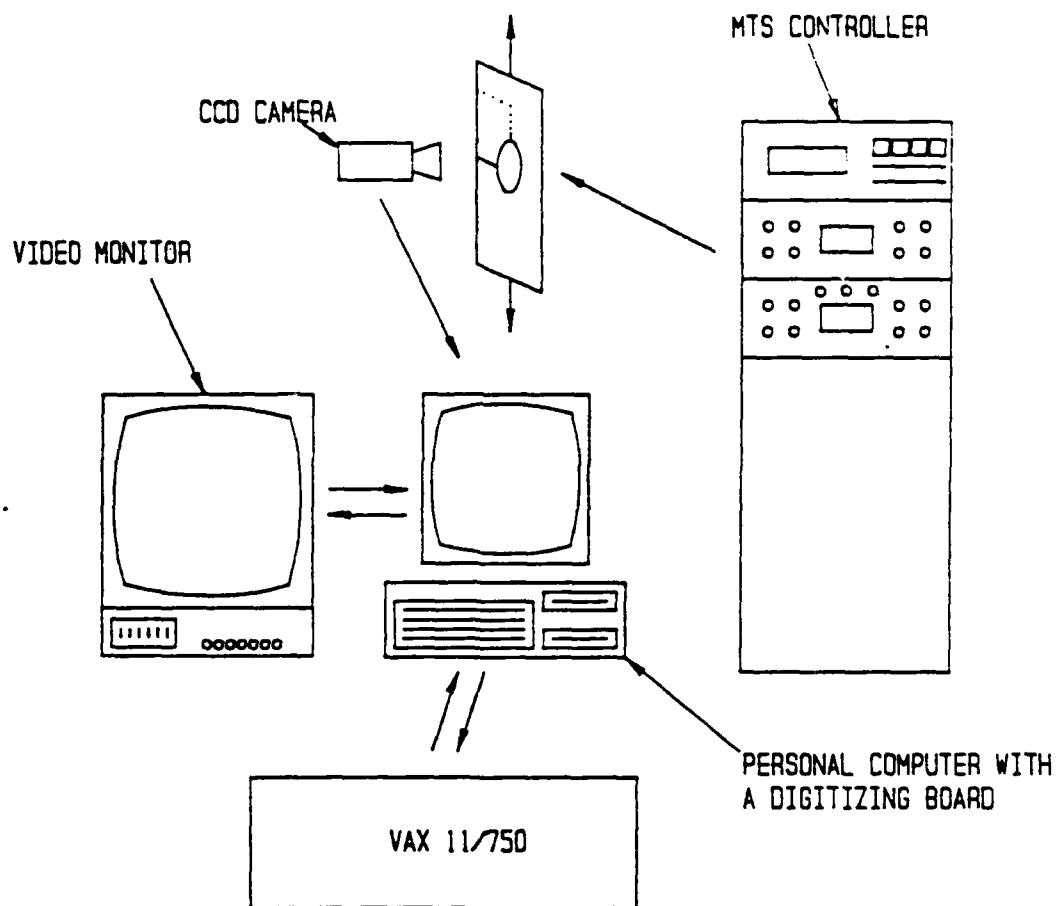


Figure 4.

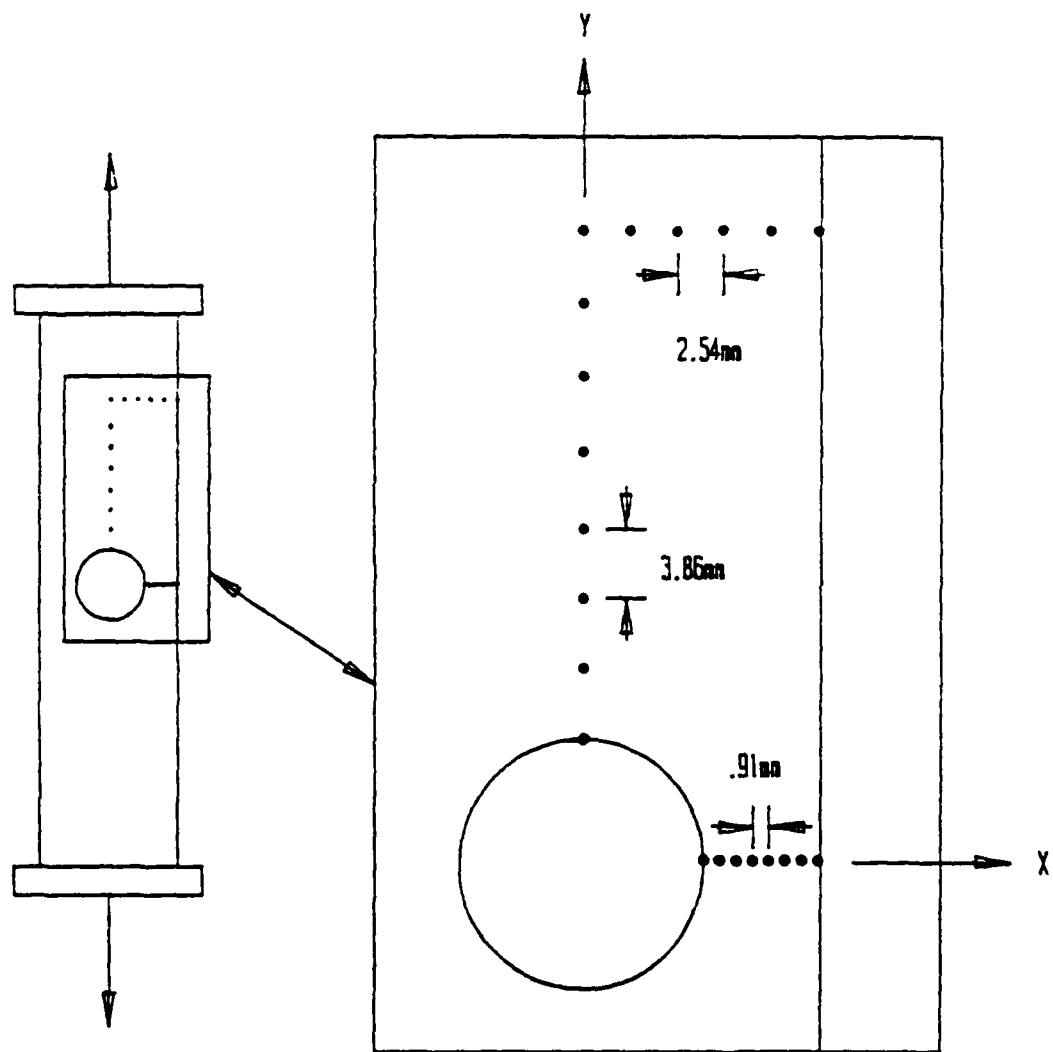


Figure 5.

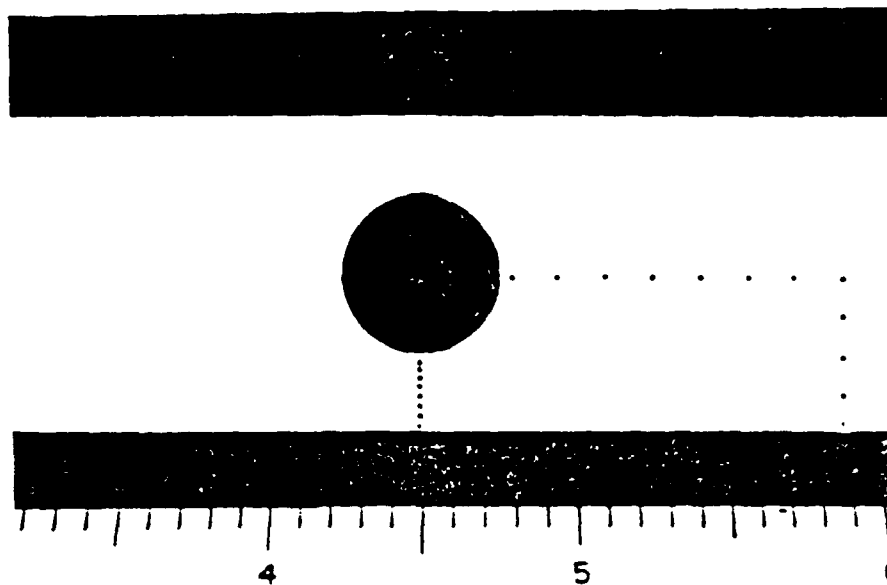


Figure 6.

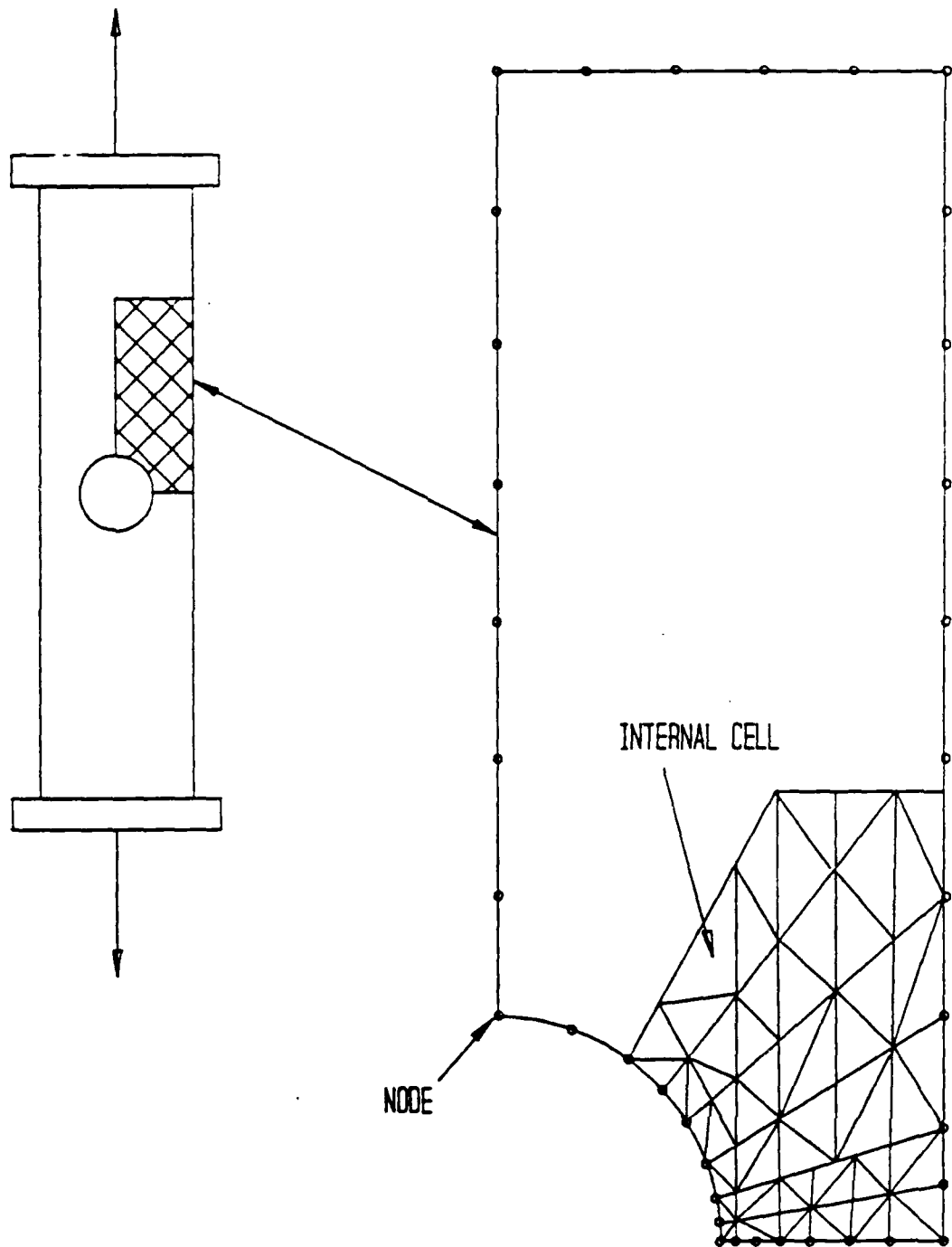


Figure 7.

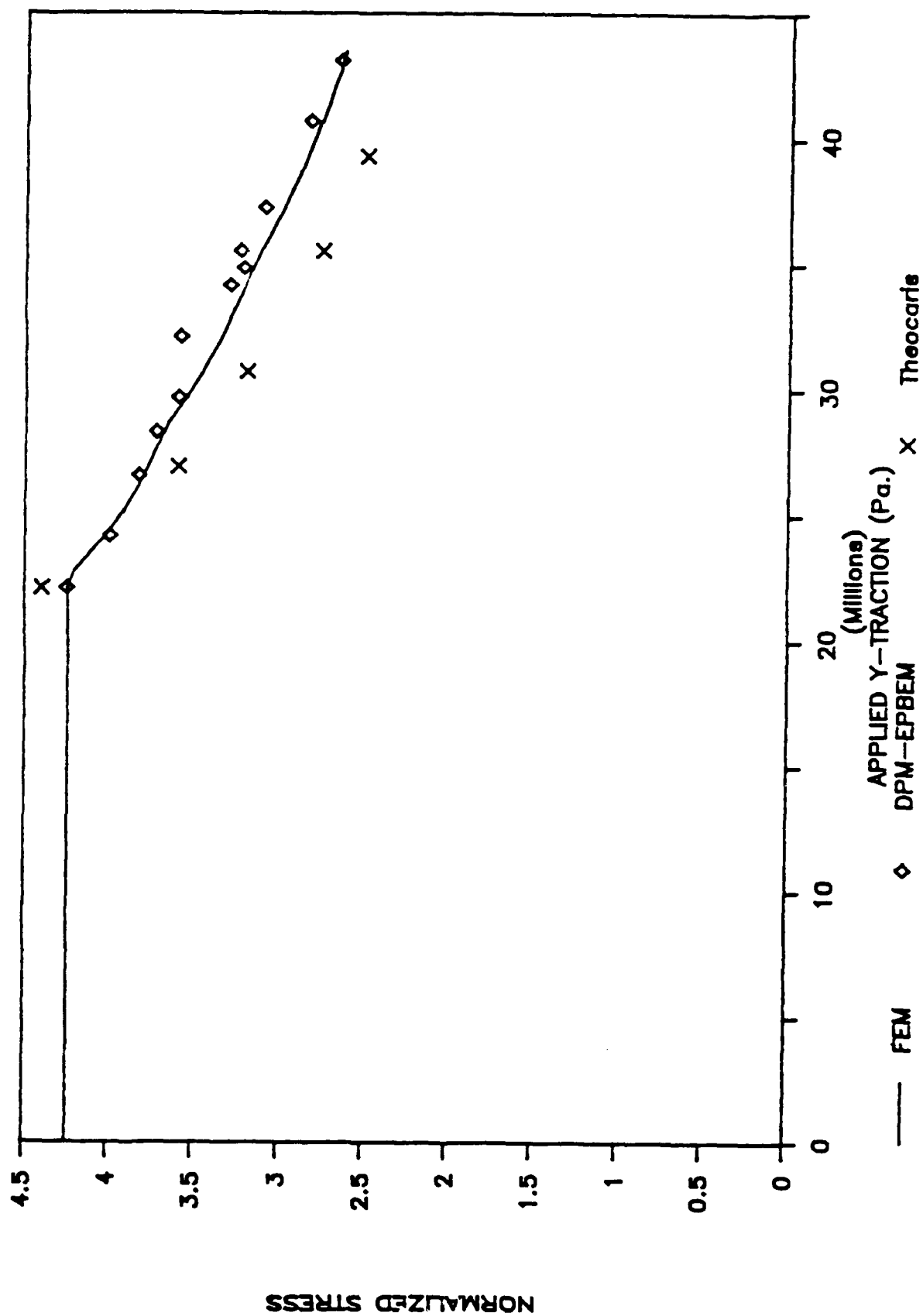


Figure 8.

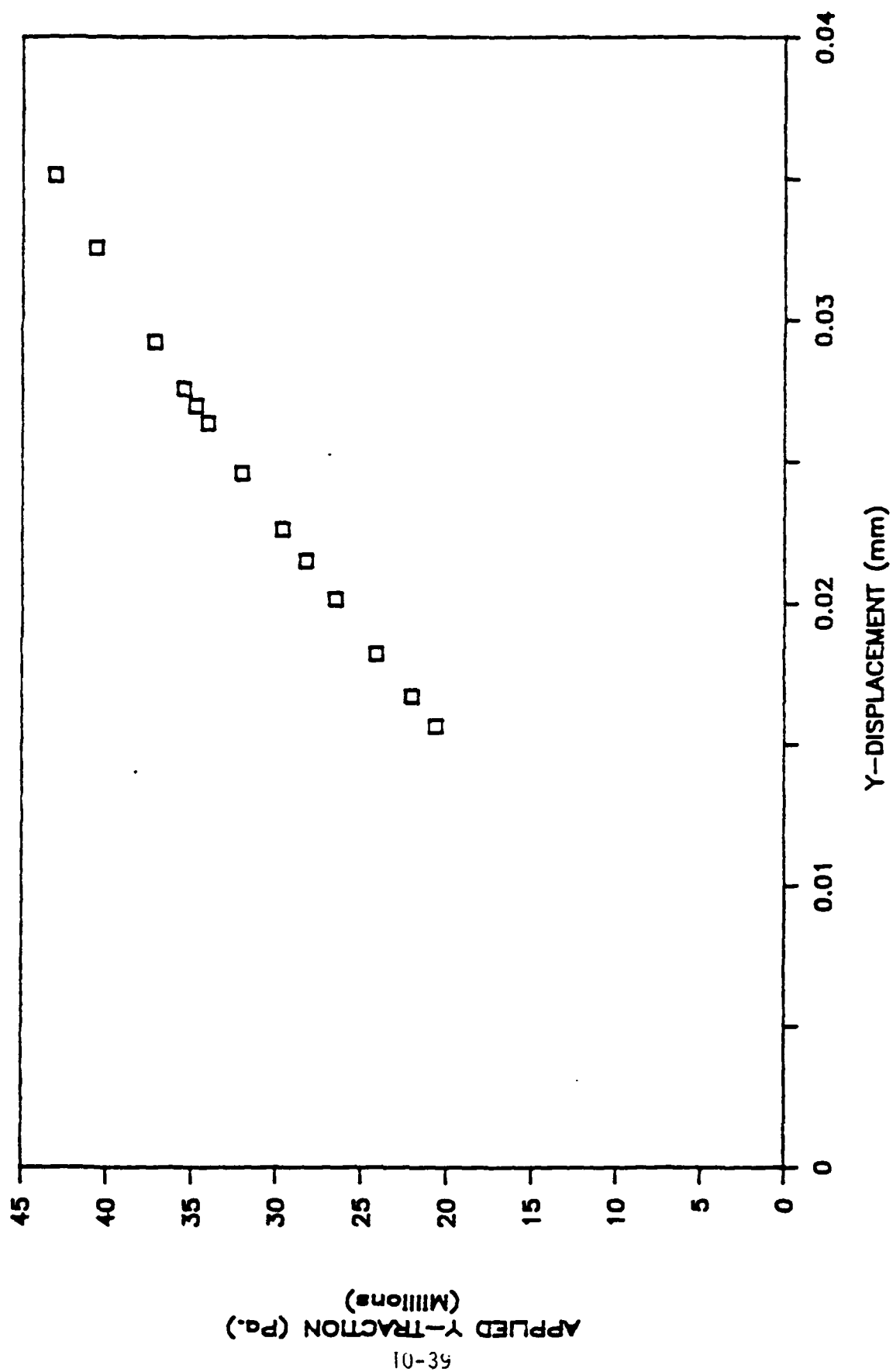


Figure 9.

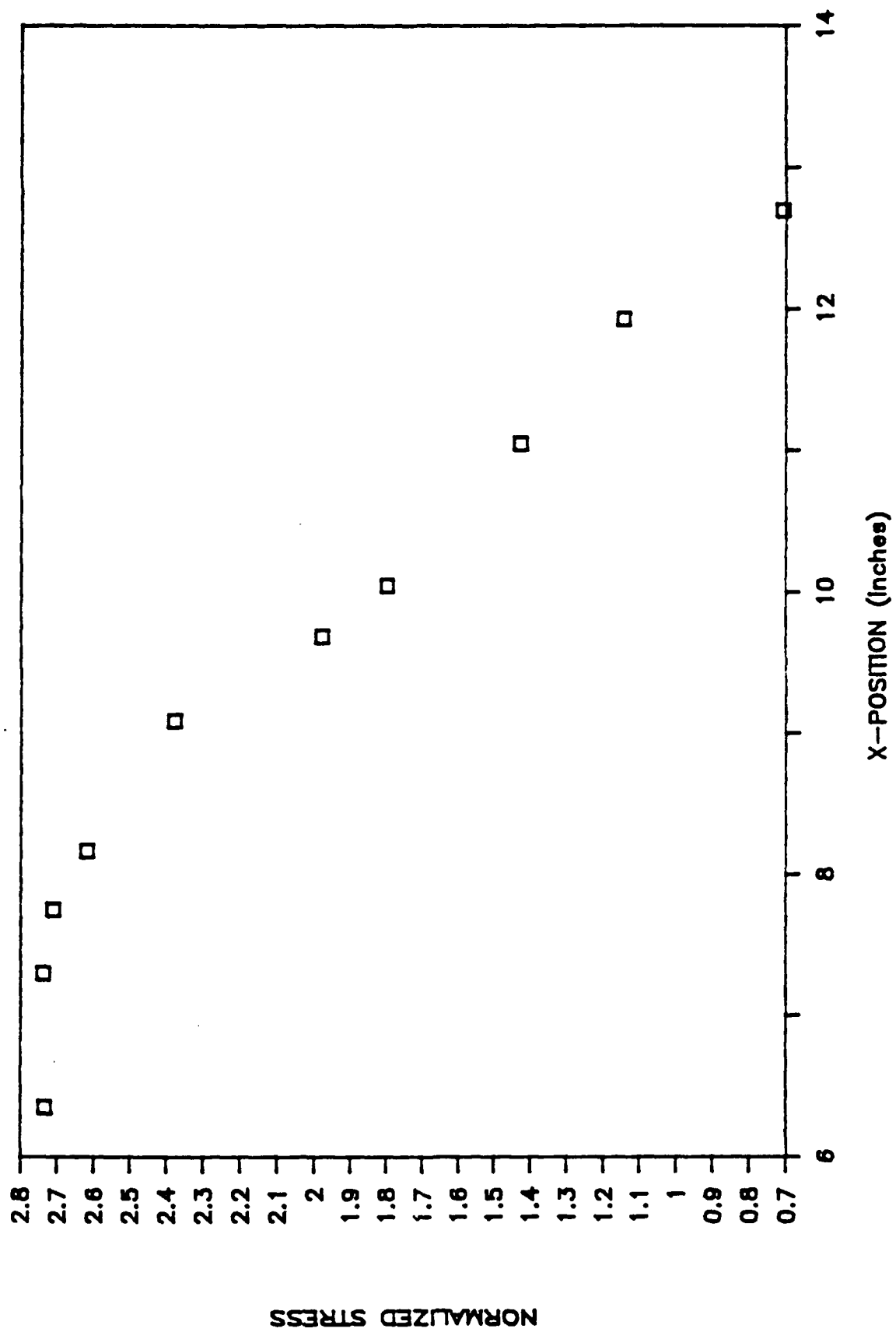


Figure 10.

VECTORIZED PERTURBED FUNCTIONAL ITERATIVE SCHEME (VPFIS):
A LARGE-SCALE NONLINEAR SYSTEM SOLVER.

S. K. Dey

Department of Mathematics
Eastern Illinois University
Charleston, Illinois 61920

Abstract

VPFIS is a computational technique to solve nonlinear systems of equations. The algorithm is fully vectorized. It is an iterative scheme where unique perturbation parameters are added to functional iterates which bring them closer to the actual solution. These parameters are computed applying partial linearization and are damped out as convergence is approached, restoring thereby all the essential nonlinear properties of the system. Thus VPFIS generates very accurate results. There are two versions of VPFIS: An explicit VPFIS where the numerical procedure which is totally matrix free and an implicit VPFIS where the numerical procedure requires inversions of Jacobians whose orders are determined by the number of unknown elements to be computed simultaneously. If there are n number of equations and all the unknown elements are perturbed simultaneously, then a matrix of the order $n \times n$ must be inverted to compute n number of perturbation parameters. However, the entire system may be subdivided into two

subsystems one containing m and the other containing $(n-m)$ number of equations. Then, the first m number of perturbation parameters are computed simultaneously inverting a $m \times m$ matrix and the rest $(n-m)$ number of perturbation parameters are computed simultaneously inverting a $(n-m) \times (n-m)$ matrix. The system may be subdivided into more than two subsystems. The number of such subsystems and the size of each subsystem may be predetermined by the user. In general, they should depend on some of the properties of the nonlinear system, the unknown elements, software packages for inversion of matrices, size of computers to be used, etc., etc. This version of VPFIS is an implicit VPFIS. If on the other hand, each perturbation parameter for each unknown element is computed one at a time, no matrix inversion is needed which gives the explicit version of VPFIS. Although both versions seem to be quite effective for solving nonlinear systems, implicit VPFIS seem to demonstrate better convergence properties for certain problems which will be discussed later. In this work, we have solved some parabolic and some hyperbolic PDE's and the results seem to be quite encouraging.

1. Introduction

Let us consider a system of nonlinear equations

$$F(U) = 0 \quad (1.1)$$

$$U = (U_1 \ U_2 \ \dots \ U_I)^T \in D \subseteq R^I$$

where R^I = real I-dimensional space.

Let $U = U^* \in D$, be the root.

Then,

$$F(U^*) = 0 \quad (1.2)$$

Our objective is to develop an algorithm to compute U^* . Possibly, the most standard method to compute U^* is Newton's method which has a quadratic rate of convergence. However, the algorithm requires inversion of the Jacobian matrix $(F'(U^p))$ at each pth iteration and generally requires the initial guess U^0 sufficiently close to U^* in order that it may work. In spite of these, this method produced excellent results solving implicit finite difference analogs of nonlinear initial-value models. For one dimensional models, if there are I-number of points in the field of computation, I-order Jacobians are computed. If I is large, computations of large Jacobians pose some difficulties. Still this is

routinely done by many researchers. However, for large-scale computations with regard to two (and especially three dimensional) models, Newton's method requires inversions of block (and block of block) matrices at each iteration level. Since for most models these matrices are sparse, inversions of block matrices (or block of block matrices) are done using L U decompositions or other techniques of matrix factorization by most researchers. But one must admit that such techniques often cause a great deal of computational difficulties.

VFFIS eliminates most of these difficulties. The explicit algorithm of VFFIS is completely matrix free. It uses only the diagonal terms of the Jacobians at each iteration. The implicit algorithms of VFFIS require inversions of matrices whose sizes may be selected apriori. However, regardless of the nature of the model VFFIS does not require inversion of any block (or block of block) matrices. It is a fully vectorized scheme and could be easily implemented in a supercomputer.

We will now derive the algorithm of VFFIS and analyze its convergence properties.

2.0 Algorithm of VPFIS

A nonlinear system (1.1) may be expressed as

$$U = G(U) \quad (2.1)$$

$$G : D \dashrightarrow D \subseteq R^I$$

A nonlinear Jacobi-type iteration is:

$$U^{p+1} = G(U^p) \quad (2.2)$$

where,

$$U^p = (U_1^p \ U_2^p \ \dots \ U_I^p)^T \in D \ \forall \ p.$$

and U_i^p = value of U_i at the p th iteration. In (2.2) we introduce a perturbation parameter w^p and write a perturbed functional iterative scheme as:

$$U^{p+1} = w^p + G(U^p) \quad (2.3)$$

where $w^p = (w_1^p \ w_2^p \ \dots \ w_I^p)^T \in R^I$, is yet to be known.

In the element form (2.3) is:

$$U_i^{p+1} = w_i^p + G_i(U^p) \quad (2.4)$$

$$i = 1, 2, \dots, I.$$

Let us perturb m ($m \leq I$) number of elements simultaneously.
Assuming convergence after the p th iteration,

$$U_i^p = G_i^p = U_i^* = U_i^{p+1} \quad (2.5)$$

$$i = 1, 2, \dots, I.$$

where $G_i^p = G_i(U_1^p, U_2^p, \dots, U_I^p).$

(2.5) gives:

$$w_i^p + G_i^p = G_i(w_1^p + G_1^p, w_2^p + G_2^p, \dots,$$

$$w_m^p + G_m^p, G_{m+1}^p, \dots, G_I^p)$$

Expanding the right side by Taylor's series and truncating after the second term, we get:

$$w_i^p + G_i^p = G_i(G_1^p, G_2^p, \dots, G_I^p) +$$

$$\sum_{s=1}^m w_s^p \frac{\partial G_i(G^p)}{\partial U_s}$$

$$i = 1, 2, \dots, m.$$

This gives,

$$(I - J_m(G^P)) w^{m,P} = b_m^P \quad (2.6)$$

where, I = the identity matrix

$$J_m(G^P) = \begin{bmatrix} G_{1,1}(G^P) & G_{1,2}(G^P) & \dots & G_{1,m}(G^P) \\ G_{2,1}(G^P) & G_{2,2}(G^P) & \dots & G_{2,m}(G^P) \\ \vdots & \vdots & \ddots & \vdots \\ G_{m,1}(G^P) & G_{m,2}(G^P) & \dots & G_{m,m}(G^P) \end{bmatrix} \quad (2.7)$$

$$w^{m,P} = (w_1^P \ w_2^P \ \dots \ w_m^P)^T \quad (2.8)$$

$$b_m^P = \begin{bmatrix} G_1(G^P) - G_1(U^P) \\ G_2(G^P) - G_2(U^P) \\ \vdots \\ G_m(G^P) - G_m(U^P) \end{bmatrix} \quad (2.9)$$

$$\text{and } G_{i,s}(G^P) = \left. \frac{\partial G_i}{\partial U_s} \right| \text{ evaluated at } G_1^P, G_2^P, \dots, G_I^P$$

Assuming $(I - J_m(G^P))$ to be nonsingular and solving (2.6), the values of perturbation parameters may be obtained. Thus we get the first m iterates

$$U_i^{P+1} = w_i^P + G_i^P, \quad i = 1, 2, \dots, m.$$

In a similar way, the next $(I-m)$ iterates may be computed solving,

$$(I - J_{I-m}(G^P)) w^{I-m,P} = b_{I-m}^P \quad (2.10)$$

for the perturbation parameters,

where,

$$J_{I-m}(G^P) = \begin{bmatrix} G_{m+1,m+1}(G^P) & G_{m+1,m+2}(G^P) & \dots & G_{m+1,I}(G^P) \\ G_{m+2,m+1}(G^P) & G_{m+2,m+2}(G^P) & \dots & G_{m+2,I}(G^P) \\ \cdot & \cdot & \cdot & \cdot \\ G_{I,m+1}(G^P) & G_{I,m+2}(G^P) & \dots & G_{I,I}(G^P) \end{bmatrix}$$

and $w^{I-m,P}$ and b_{I-m}^P are also defined following (2.8) and (2.9).

This shows how one can subdivide the entire system into two subsystems, perturb each subsystem simultaneously and thereby generate a new system of iterates. Obviously, the entire system may be subdivided into more than two subsystems.

The algorithm, when we have two subsystems, may be expressed as:

At some p th iteration,

#1. Compute $G^P = (G_1^P \ G_2^P \ \dots \ G_I^P)^T$ where

$$G_i^P = G_i(U_1^P, U_2^P \ \dots \ U_I^P).$$

#2. Compute $G(G^P)$ and $b^P = G(G^P) - G^P$.

#3. Compute w^P solving (2.6) and (2.10).

#4. Compute $U^{P+1} = w^P + G^P$

Criterion for convergence is at some $p > P$,

$$|| w^b || < \epsilon \quad (2.11)$$

for some norm. (ϵ = a positive preassigned quantity chosen arbitrarily small).

The significance of (2.11) will be discussed in section 3.

The algorithm discussed above is an implicit version of VPFIS where two subsystems are used. Clearly, this algorithm is fully vectorized. If no subsystems are used, all perturbation parameters are computed simultaneously by solving an equation of the form (2.6) where $m = j$. If $m = 1$ it means each perturbation parameter is computed individually. In such a case, the algorithm is:

$$U_i^{p+1} = w_i^p + G_i (U^p) \quad (2.12)$$

where

$$w_i^p = (1 - G_{i,i}(G^p))^{-1} (G_i(G^p) - G_i(U^p)) \quad (2.13)$$

The only requirements are $G_{i,i}(G^p) \neq 1 \forall i$ and p . No matrix computation is required. This matrix-free version of VPFIS is the explicit algorithm of VPFIS.

3. Analysis of Convergence

First, a simple theorem may be proved.

Theorem: 1 A necessary condition for convergence is:

$$\lim_{p \rightarrow \infty} ||w^p|| = 0 \quad (3.1)$$

Proof: If (2.3) converges $\lim_{p \rightarrow \infty} U^p = U^*$ and

$$\lim_{p \rightarrow \infty} G(U^p) = G(U^*) = U^*.$$

This implies that (3.1) is valid.

Let both equations (2.6) and (2.10) be jointly expressed as:

$$A(G^p) W^p = b^p \quad (3.2)$$

Assuming $A(G^p)$ is bounded for all p , it may be proved:

Theorem 2 (3.1) is a sufficient condition for convergence.

Proof: Let for some $p > P$, $\|w^p\| < \epsilon/a$ where $a = \|A(G^p)\|$, then from (3.2)

$$\|b^p\| \leq \|w^p\| \|A(G^p)\| < \epsilon \quad (3.3)$$

which gives $\|G(G^p) - G^p\| < \epsilon$ for $p > P$, proving the theorem.

To analyze the rate of convergence, let us consider the explicit VFFIS (equations (2.12) and (2.13)).

Let $F_i(U) = U_i - G_i(U)$. $F_{i,i} = 1 - G_{i,i}$. Then the iterative scheme is:

$$U_i^{p+1/2} = G_i(U_1^p, U_2^p, \dots, U_I^p) \quad (3.4)$$

$$U_i^{p+1} = U_i^{p+1/2} - \frac{F_i(U_i^{p+1/2})}{F_{i,i}(U_i^{p+1/2})} \quad (3.5)$$

This means that the explicit VFFIS is a combination of two iterative procedures. If r_1 = rate of convergence of (3.4) and r_p = rate of convergence of (3.5), then the rate of

convergence of the combined algorithm is $r_1 r_2$. The rate is not quadratic.

$$\text{Let } \epsilon_i^p = G_i^* - G_i^p \quad (3.6)$$

where $G_i^* = G_i(U_1^*, U_2^* \dots U_I^*)$

$$\text{and } \delta_i^p = U_i^* - U_i^p \quad (3.7)$$

A linearized analysis gives,

$$\epsilon^p = J(U^p) \delta^p \quad (3.8)$$

where,

$$J(U^p) = \begin{bmatrix} G_{1,1}(U^p) & G_{1,2}(U^p) & \dots & G_{1,I}(U^p) \\ G_{2,1}(U^p) & G_{2,2}(U^p) & \dots & G_{2,I}(U^p) \\ \cdot & & & \\ \cdot & & & \\ \cdot & & & \\ G_{I,1}(U^p) & G_{I,2}(U^p) & \dots & G_{I,I}(U^p) \end{bmatrix}$$

If we combine (2.12) and (2.13) we get

$$\delta^{p+1} = M_p(G^p) \cdot J(U^p) \cdot \delta^p \quad (3.9)$$

where

$$M_p(G^p) = \begin{bmatrix} 0 & \frac{G_{1,2}(G^p)}{1-G_{1,1}(G^p)} & \frac{G_{1,3}(G^p)}{1-G_{1,1}(G^p)} & \dots & \frac{G_{1,I}(G^p)}{1-G_{1,1}(G^p)} \\ \frac{G_{2,1}(G^p)}{1-G_{2,2}(G^p)} & 0 & \frac{G_{2,3}(G^p)}{1-G_{2,2}(G^p)} & \dots & \frac{G_{2,I}(G^p)}{1-G_{2,2}(G^p)} \\ \frac{G_{I,1}(G^p)}{1-G_{I,I}(G^p)} & \frac{G_{I,2}(G^p)}{1-G_{I,I}(G^p)} & \dots & 0 & \end{bmatrix} \quad (3.10)$$

We assume that $\forall p, U^p \in D$ and $G(D) \subseteq D$. It may now be shown that if for some norm, and for $\forall p > P$

$$||J(U^p)|| \leq \alpha < 1 \quad (3.11)$$

it will imply that for the same norm

$$||M_p(G^p)|| \leq \beta < 1 \quad (3.12)$$

If we combine (3.9), (3.11) and (3.12) we get

$$\| \delta^{p+1} \| \leq \alpha \beta \| \delta^p \|$$

If $\max(\alpha, \beta) = r$, this gives

$$\| \delta^{p+1} \| \leq r^2 \| \delta^p \| \quad (3.13)$$

It may be seen that, if

$$(3.14) \quad \left(\sum_{\substack{s=1 \\ s \neq i}}^I |G_{i,s}(G^p)| \right) / (1 - |G_{i,i}(G^p)|) \leq \alpha < 1$$

both (3.11) and (3.12) are valid.

Thus applying a linearized analysis it may be seen that if the Jacobian matrix $G'(U)$ is diagonally dominant on D , (3.13) is valid. This is only a linearized sufficient condition.

If we consider the algorithm of VPFIS where all the elements are perturbed simultaneously, the algorithm is:

$$U^{p+\frac{1}{2}} = G(U^p) \quad (3.15)$$

$$U^{p+1} = U^{p+\frac{1}{2}} - F'(U^{p+\frac{1}{2}})^{-1} F(U^{p+\frac{1}{2}}) \quad (3.16)$$

where $F(U) = U - G(U)$. It is a combination of nonlinear Jacobi-type iteration and Newton's method. The rate of convergence is

$$\| \delta^{p+1} \| \leq r \| \delta^p \|^2 \quad (3.17)$$

If $0 < r < 1$, the rate of convergence is faster than quadratic. It should be noted that unless all the perturbation parameters are computed simultaneously, the rate of convergence is not quadratic.

It may be noted that if $G:D \rightarrow D$ does not satisfy (3.14), we may introduce,

$$U = \hat{G}(U)$$

where, $\hat{G}(U) = (I - \Gamma) U + \Gamma G(U)$

$$= \text{diag} (\gamma_1, \gamma_2, \dots, \gamma_I)$$

where γ_i 's may be computed such that (3.14) is true [1].

4. Algorithms of VPFIS for Coupled Two and Three Dimensional Models.

VPFIS is developed primarily to solve large-scale models for two and three dimensional problems. The applications of VPFIS to solve coupled systems will be the topic of our present discussion.

Let us consider a coupled two-dimensional model:

$$U = F(U, V) \quad (4.1)$$

$$V = G(U, V) \quad (4.2)$$

where, $U = (U_1 \ U_2 \ \dots \ U_I)^T$ and

$$U_i = (U_{i1} \ U_{i2} \ \dots \ U_{iJ})^T.$$

The same is true for V . Thus $F: R^{IJ} \rightarrow R^{IJ}$
and the same is true for G .

At some $(p + 1)$ th iteration, VPFIS is:

$$U_{ij}^{p+1} = \alpha_{ij}^p + F_{ij}(U^p, V^p) \quad (4.3)$$

$$i = 1, 2, \dots, I; \quad j = 1, 2, \dots, J$$

$$V_{ij}^{p+1} = \beta_{ij}^p + G_{ij}(U^{p+1}, V^p) \quad (4.4)$$

where α_{ij}^p and β_{ij}^p are perturbation parameters which are yet to be computed.

Now, $F^P = (F_1^P \ F_2^P \ \dots \ F_I^P)^T$; $F_i^P = (F_{i1}^P \ F_{i2}^P \ \dots \ F_{iJ}^P)^T$

$$F_{ij}^P = F_{ij}(U^P, V^P).$$

VPFIS may be applied rowwise or columnwise. Let us apply it columnwise. This means that all the elements of a given column will be perturbed simultaneously. When all the U_{ij} 's are computed at the $(p+1)$ th iteration, this new information may be used to compute V_{ij} 's at the $(p+1)$ th iteration. This should not affect the vectorization property of the algorithm.

If we assume convergence after p iterations,

$$\alpha_{ij}^P + F_{ij}^P = F_{ij}(F_1^P \ \dots \ F_{ij}^P; \alpha_1^P + F_1^P; F_{i+1}^P \ \dots \ F_I^P; G^P)$$

This gives:

$$\alpha_{ij}^P + F_{ij}^P = F_{ij}(F_1^P \ \dots \ F_{i-1}^P; \alpha_{i1}^P + F_{i1}^P; \alpha_{i2}^P + F_{i2}^P \ \dots$$

$$\alpha_{iJ}^P + F_{iJ}^P; F_{i+1}^P \ \dots \ F_I^P; G^P) \quad (4.5)$$

$j = 1, 2, \dots, J.$

Expanding the right side by Taylor's series and using the first order approximation of α_{ij} 's, we get:

$$(I - J_i(F^P, G^P)) \alpha_i^P = b_i^P \quad (4.6)$$

$$i = 1, 2, \dots, I$$

where

$$J_i(F^P, G^P) =$$

$$\begin{bmatrix} F_{i1,i1}(F^P, G^P) & F_{i1,i2}(F^P, G^P) & \dots & F_{i1,iJ}(F^P, G^P) \\ F_{i2,i1}(F^P, G^P) & F_{i2,i2}(F^P, G^P) & \dots & F_{i2,iJ}(F^P, G^P) \\ F_{iJ,i1}(F^P, G^P) & F_{iJ,i2}(F^P, G^P) & \dots & F_{iJ,iJ}(F^P, G^P) \end{bmatrix}$$

(4.7)

$$b_i^p = \begin{bmatrix} F_{i1}(F^p, G^p) - F_{i1}^p \\ F_{i2}(F^p, G^p) - F_{i2}^p \\ F_{iJ}(F^p, G^p) - F_{iJ}^p \end{bmatrix} \quad (4.8)$$

$$\text{and } F_{ij, is}(F^p, G^p) = \frac{\sigma F_{ij}(F^p, G^p)}{\sum U_{is}} \quad (4.9)$$

Assuming that in (4.6), the coefficient of α_i^p is nonsingular, (4.6) may be solved to compute

$$\alpha_i^p = (\alpha_{i1}^p \quad \alpha_{i2}^p \quad \dots \quad \alpha_{iJ}^p)^T \text{ for each } i = 1, 2, \dots, I.$$

Once U^{p+1} are computed, α_{ij}^{p+1} may be computed by solving:

$$(I - J_i(U^{p+1}, G^p)) \alpha_i^p = C_i^p \quad (4.10)$$

where

$$J_i(U^{p+1}, G^p) =$$

$$\begin{bmatrix} G_{i1,i1}(U^{p+1}, G^p) & G_{i1,i2}(U^{p+1}, G^p) & \dots & G_{i1,iJ}(U^{p+1}, G^p) \\ G_{i2,i1}(U^{p+1}, G^p) & G_{i2,i2}(U^{p+1}, G^p) & \dots & G_{i2,iJ}(U^{p+1}, G^p) \\ \vdots & \vdots & \ddots & \vdots \\ G_{iJ,i1}(U^{p+1}, G^p) & G_{iJ,i2}(U^{p+1}, G^p) & \dots & G_{iJ,iJ}(U^{p+1}, G^p) \end{bmatrix}$$

(4.11)

$$\text{and } C_i^P = \begin{bmatrix} G_{i1}(U^{P+1}, G^P) - \tilde{G}_{i1}^P \\ G_{i2}(U^{P+1}, G^P) - \tilde{G}_{i2}^P \\ \vdots \\ G_{iJ}(U^{P+1}, G^P) - \tilde{G}_{iJ}^P \end{bmatrix} \quad (4.12)$$

$$\tilde{G}_{ij}^P = G_{ij}(U^{P+1}, v^P)$$

$i = 1, 2, \dots, I$; and for each i , $j = 1, 2, \dots, J$.

Solving (4.10) for β_i^P , v_{ij}^{P+1} are computed using (4.4).

The condition for convergence is:

At some $p > P$,

$$\max_{i,j} (|\alpha_{ij}^P|, |\beta_{ij}^P|) < \epsilon \quad (4.13)$$

where ϵ is a small preassigned positive quantity.

This is the algorithm of the implicit VPFIS. There is no requirement to invert any block matrix. The procedure is rather simple and straight forward.

The algorithm of the explicit VPFIS may now be stated:
First compute

$$\alpha_{ij}^p = \frac{F_{ij}(F^p, G^p) - F_{ij}(U^p, v^p)}{1 - F_{ij,ij}(F^p, G^p)} \quad (4.14)$$

$i = 1, 2, \dots, I$; $j = 1, 2, \dots, J$ for each i

Now (4.3) may be used to compute U_{ij}^{p+1} . β_{ij} 's are now given by:

$$\beta_{ij}^p = \frac{G_{ij}(U^{p+1}, G^p) - G_{ij}(U^{p+1}, v^p)}{1 - G_{ij,ij}(U^{p+1}, G^p)} \quad (4.15)$$

$i = 1, 2, \dots, I$; $j = 1, 2, \dots, J$ for each i .

Now (4.4) may be used to compute v_{ij}^{p+1} . The criterion for convergence is (4.13).

In this procedure no matrix computation is required.

Let us consider a coupled nonlinear system with three unknowns:

$$U = F(U, V, W) \quad (4.16)$$

$$V = G(U, V, W) \quad (4.17)$$

$$W = H(U, V, W) \quad (4.18)$$

where $U = (U_1 \ U_2 \ \dots \ U_I)^T$, $U_i = (U_{i1} \ U_{i2} \ \dots \ U_{iJ})^T$

and $U_{ij} = (U_{ij1} \ U_{ij2} \ \dots \ U_{ijk})^T$, $U \in R^{IJK}$. Also $V \in R^{IJK}$

and $W \in R^{IJK}$; and $F : R^{IJK} \times R^{IJK} \times R^{IJK} \rightarrow R^{IJK}$.

The algorithm of the implicit VPFIS is

$$U_{ijk}^{p+1} = \alpha_{ijk}^p + F_{ijk}(U^p, V^p, W^p) \quad (4.19)$$

$i = 1, 2, \dots, I$; $j = 1, 2, \dots, J$; $k = 1, 2, \dots, K$.

$$V_{ijk}^{p+1} = \beta_{ijk}^p + G_{ijk}(U^{p+1}, V^p, W^p) \quad (4.20)$$

$i = 1, 2, \dots, I$; $j = 1, 2, \dots, J$; $k = 1, 2, \dots, K$

$$w_{ijk}^{p+1} = \gamma_{ijk}^p + H_{ijk}(u^{p+1}, v^{p+1}, w^p) \quad (4.21)$$

$$i = 1, 2, \dots, I ; j = 1, 2, \dots, J ; k = 1, 2, \dots, K$$

The perturbation parameters are given by:

$$(I - J_1(F^p, G^p, H^p)) \alpha_{ij}^p = \tilde{z}_{ij}^p \quad (4.22)$$

where

$$J_1(F^p, G^p, H^p) =$$

$$\begin{bmatrix} F_{ij1,ij1}(F^p, G^p, H^p) & F_{ij1,ij2}(F^p, G^p, H^p) & \dots & F_{ij1,ijk}(F^p, G^p, H^p) \\ F_{ij2,ij1}(F^p, G^p, H^p) & F_{ij2,ij2}(F^p, G^p, H^p) & \dots & F_{ij2,ijk}(F^p, G^p, H^p) \\ \vdots & \vdots & \ddots & \vdots \\ F_{ijk,ij1}(F^p, G^p, H^p) & F_{ijk,ij2}(F^p, G^p, H^p) & \dots & F_{ijk,ijk}(F^p, G^p, H^p) \end{bmatrix} \quad (4.23)$$

$$\alpha_{ij}^p = (\alpha_{ij1}^p \quad \alpha_{ij2}^p \quad \dots \quad \alpha_{ijk}^p)^T \quad (4.24)$$

$$\bar{\zeta}_{ij}^P = \begin{bmatrix} F_{ij1}(F^P, G^P, H^P) - F_{ij1}(U^P, V^P, W^P) \\ F_{ij2}(F^P, G^P, H^P) - F_{ij2}(U^P, V^P, W^P) \\ \vdots \\ F_{ijk}(F^P, G^P, H^P) - F_{ijk}(U^P, V^P, W^P) \end{bmatrix} \quad (4.25)$$

$i = 1, 2, \dots, I ; j = 1, 2, \dots, J$ for each i

and $k = 1, 2, \dots, K$ for each i and j

$$\text{Also } F_{ijk,ijs} = \frac{\partial F_{ijk}}{\partial U_{ijs}} \quad (4.26)$$

Once the values of α_{ijk} 's are computed solving (4.22) ,
we compute U's using (4.19)

Next we compute β_{ij} 's using

$$(I - J_2(U^{p+1}, G^p, H^p)) \beta_{ij}^p = \eta_{ij}^p \quad (4.27)$$

where

$$J_2(U^{p+1}, G^p, H^p) =$$

$$\begin{bmatrix} G_{ij1,ij1}^{(U^{p+1}, G^p, H^p)} & G_{ij1,ij2}^{(U^{p+1}, G^p, H^p)} & \dots & G_{ij1,ijk}^{(U^{p+1}, G^p, H^p)} \\ G_{ij2,ij1}^{(U^{p+1}, G^p, H^p)} & G_{ij2,ij2}^{(U^{p+1}, G^p, H^p)} & \dots & G_{ij2,ijk}^{(U^{p+1}, G^p, H^p)} \\ \vdots & \vdots & \ddots & \vdots \\ G_{ijk,ij1}^{(U^{p+1}, G^p, H^p)} & G_{ijk,ij2}^{(U^{p+1}, G^p, H^p)} & \dots & G_{ijk,ijk}^{(U^{p+1}, G^p, H^p)} \end{bmatrix}$$

(4.28)

$$\beta_{ij}^p = (\beta_{ij1}^p \quad \beta_{ij2}^p \quad \dots \quad \beta_{ijk}^p)^T \quad (4.29)$$

$$\eta_{ij}^p = \begin{bmatrix} G_{ij1}(U^{p+1}, G^p, H^p) - G_{ij1}(U^{p+1}, v^p, w^p) \\ G_{ij2}(U^{p+1}, G^p, H^p) - G_{ij2}(U^{p+1}, v^p, w^p) \\ \vdots \\ G_{ijk}(U^{p+1}, G^p, H^p) - G_{ijk}(U^{p+1}, v^p, w^p) \end{bmatrix} \quad (4.30)$$

$$\text{and } G_{ijk,ijs}(U^{p+1}, G^p, H^p) = \frac{\partial G_{ijk}(U^{p+1}, G^p, H^p)}{\partial v_{ijs}}$$

(Similarly, γ_{ij} 's are found).

Solving (4.27) β_{ij} 's are computed and used in (4.20) to compute v^{p+1} . To compute γ_{ij} 's U^{p+1} and v^{p+1} are used, and once γ_{ij} 's are known, (4.21) is used to compute w^{p+1} .

The criterion for convergence is:

$$\max_{i,j,k} (|\alpha_{ijk}^p|, |\beta_{ijk}^p|, |\gamma_{ijk}^p|) < \epsilon$$

for some $p > P$, ϵ being a small positive preassigned quantity.

5. Applications.

VPFIS has been applied to solve several text-book type problems which may not be of any significance for this article. However, several nonlinear PDE's were approximated by implicit finite differences and solved numerically by VPFIS. Some of them may be discussed now.

Ex: 1. Burgers' Equation

$$u_t + uu_x = \gamma u_{xx}$$

$$u(x,0) = -\sin 2\pi x, \quad u(0,t) = u(1,t) = 0.$$

Flux vector splitting approximation was used to derive finite difference equations.

$$\begin{aligned} u_j^n = & u_j^{n-1} + a \left((u_{j+1}^n - |u_{j+1}^n|) - u_{j+1}^n \right. \\ & \left. + 2u_j^n |u_j^n| - (u_{j-1}^n + |u_{j-1}^n|) - u_{j-1}^n \right) \\ & + b \left(u_{j-1}^n - 2u_j^n + u_{j+1}^n \right) \end{aligned}$$

where $u_j^n = u(x_j, t_n)$, $a = -\Delta t / (4 \Delta x)$

$$b = \gamma \Delta t / (\Delta x^2).$$

convergence criterion was $\|w_{\max}\| < 10^{-4}$. Figure 1 gives the velocity profiles after five time steps.

($\gamma = 0.1$, $\Delta x = 0.02$, $\Delta t = 0.08$)

A more interesting result is given in figure 2. Here we used $\bar{V} = 0$ and the following initial conditions:

$U(X,0) = 1$ if $X \leq 0.06$, else $U(X,0) = -0.5$. With $\Delta X = 0.02$, $\Delta t = 0.4$, the motion of the shock has been described in the figure. No artificial viscosity was used. (According to the figure the shock speed = 0.5 m/sec.). Thus, the shock speed is accurately found.

Ex: 2 A 3-D Model

$$u_t + uu_x + vu_y + wu_z = f_1(u, v, w, t)$$

$$v_t + uv_x + vv_y + wv_z = f_2(u, v, w, t)$$

$$w_t + uw_x + vw_y + ww_z = f_3(u, v, w, t)$$

where $f_1 = (v + w - 2u)/(1+t)$

$$f_2 = (w + u - 2v)/(1 + t)$$

$$f_3 = (u + v - 2w)/(1 + t)$$

This system has an analytical solution given by

$$u = (1 - x + y + z)/(1 + t)$$

$$v = (1 + x - y + z)/(1 + t)$$

$$w = (1 + x + y - z)/(1 + t)$$

$$0 \leq x, y, z \leq 1.$$

Here time derivatives were approximated by two-point backward differences and space derivatives were approximated by central differences. Use of central differences required extra boundary conditions at $x = y = z = 1$. Both explicit and implicit versions of VPFIS were applied for numerical solution. The implicit scheme was slightly faster. However, they produced almost identical results. The computations were conducted at the Arnold Air Force Station at Tennessee using the CRAY - XMP super computer. We used $\Delta x = \Delta y = \Delta z = 0.1$ and $\Delta t = 0.0025$. 2000 time steps were used. No artificial viscosity was ever needed to maintain numerical stability.

The following results were found (by applying explicit VPFIS)

<u>Time Step</u>	<u>No of Iterations</u>	<u>Max. Error in the Field</u>
100	6	1.6623E-05
500	5	4.4579E-03
1000	4	3.2437E-03
1500	4	2.0840E-03
2000	4	2.0959E-03

Max error in the field

$$= \max_{i,j,k} (| u_{ijk}^n - U_{ijk}^n | , | v_{ijk}^n - V_{ijk}^n | , | w_{ijk}^n - W_{ijk}^n |)$$

where $u_{ijk}^n, v_{ijk}^n, w_{ijk}^n$ = analytical values at $x = x_i$,

$y = y_j$, $z = z_k$, $t = t_n$, and $U_{ijk}^n, V_{ijk}^n, W_{ijk}^n$ =

computational values at the same point. The overall largest error in the field was 6.01E-03 at time step = 300.

6. Conclusion

VFFIS seems to be a computationally simple technique to solve nonlinear systems. Since matrix computations are minimized or even could be abolished, applications of VFFIS to large-scale models do not seem to create any computational difficulties. The nonvectorized version of this scheme which appeared in [2] seem to be less effective than the present vectorized version.

(Nonvectorized version failed with regard to Figure 2).

Experimentations conducted so far tend to suggest that VFFIS is effective to solve single or coupled nonlinear systems. But many more applications need to be studied so that one may recognize the conditions under which VFFIS will be most effective. These conditions are yet to be known. As such this work should be classified as a preliminary work. Suggestions from other researchers are welcome in this regard.

7. Acknowledgement

This research has been funded partially by the UES/Air Force Contract #F49620-85-C-0013/SB5851-0360, subcontract #S-760-7MG-037, Amendment #0002, and partially by Eastern Illinois University. Most computations were undertaken by Charlie Dey.

NO. OF ITERATIONS= 27

TIME STEP= 5

$\nu = 0.1$

$DX = 0.02$

$DT = 0.08$

BURGERS' EQUATION.

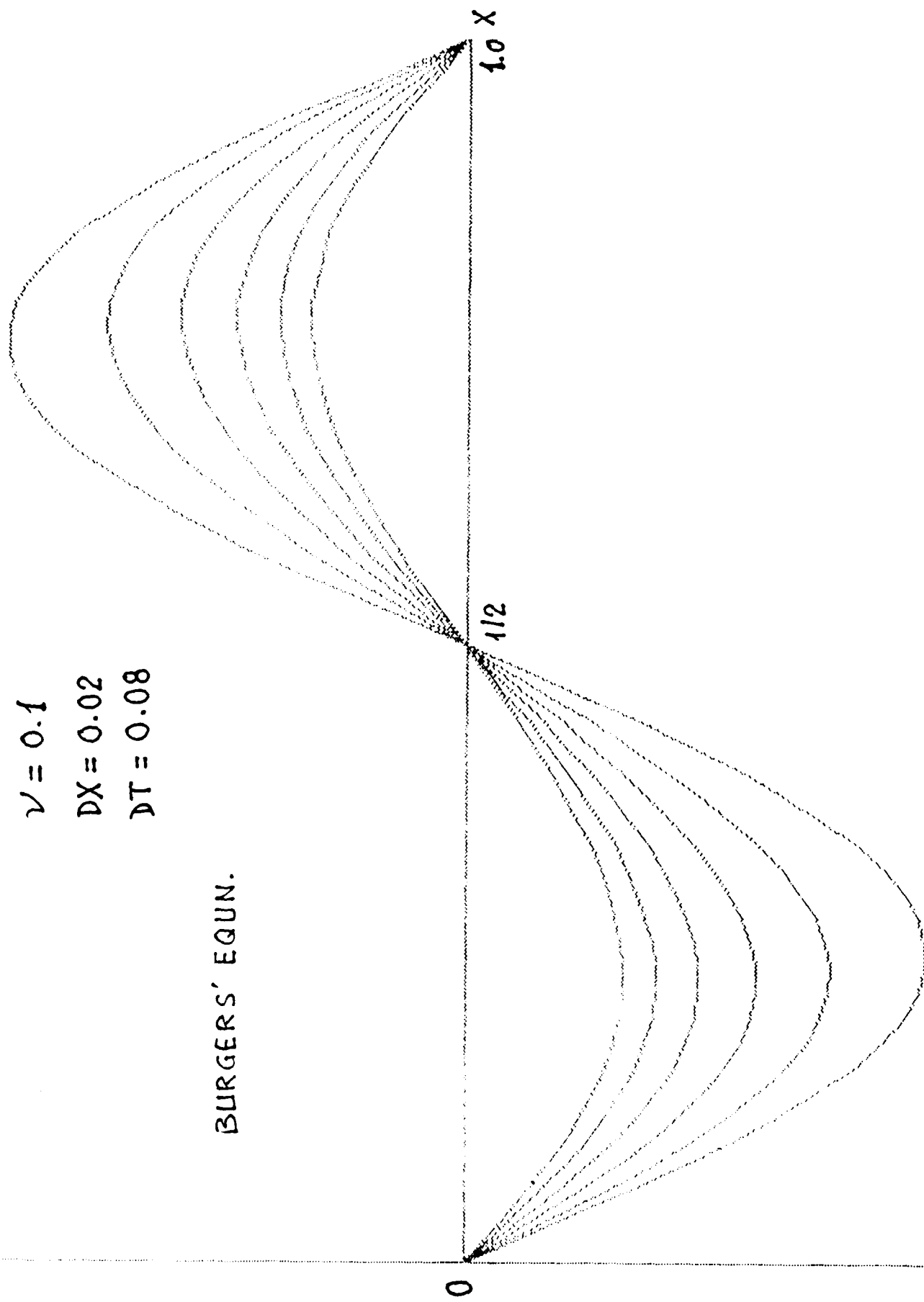


FIGURE 1.

NO. OF ITERATIONS= 53
TIME STEP= 8

U.

1.

0

-1/2.

I= 51 DX= .02 DT= .4 CFL#= 20

FIGURE 2.

References

1. S. K. Dey, "Linearized D-Mappings for Stiff Computations." Numerical Math and Comp. North-Holland, Amsterdam 1986.
2. S. K. Dey, "Implicit Finite Difference Solution of Flow Models by Perturbed Functional Iterations." Lecture Series on Computational Fluid Dynamics '78, von Karman Institute for Fluid Dynamics, Brussels, Belgium.

LIQUID FILM COOLING IN ROCKET ENGINES

William M. Grissom
Physics Department
Morehouse College
Atlanta, Georgia 30314

December 1988

Final Report

Contract: F49620-85-C-00137/SB5851-0360
Purchase Order: S-760-7MG-022
Universal Energy Systems, Inc.

sponsored by the Air Force Office of Scientific Research

WARNING

This document contains technical data whose export is restricted by the Arms Export Control Act (Title 22, U.S.C., Sec 2751 et seq.) or the Export Administration Act of 1979, as amended. Title 50, U.S.C., App. 2401, et seq. Violations of these export laws are subject to severe criminal penalties. Disseminate in accordance with the provisions of AFR 80-34.

PREFACE

The research reported herein was sponsored by the Air Force Office of Scientific Research/AFSC under Contract F49620-85-C-0013/SB5851-0361 as a follow-on to work done in the summer of 1987 on the Universal Energy Systems Summer Faculty Research Program at Arnold Engineering Development Center, Arnold AFS, Tennessee. The author was allowed to return to AEDC during the summer of 1988 to facilitate work on the project. Appreciation is due C.C. Limbaugh and W.K. McGregor for suggesting the topic, to M.H. Simmons for running the NASA equilibrium code, and to M. Powell of the Air Force Astronautics Laboratory for providing numerous references to rocket test reports. M. Kingery supervised the summer faculty program at AEDC.

1.0 INTRODUCTION

Many liquid rocket engines employ a film of liquid fuel as thermal protection for the combustion chamber walls. This process was experimentally studied in the 1950's and 1960's, however no general analysis procedure was established at that time. Since then a number of fundamental heat transfer studies have been performed which allow the liquid film cooling problem to be broken into discrete mechanisms for a more fundamental analysis.

The mechanisms involved in the liquid film cooling of rocket engines are depicted in Figure 1. Heat is transferred to the liquid film by both radiation and convection from the hot combustion gases. The vapor transpired from the film tends to decrease the convective heat transfer rate below what it would be for a dry wall. This vapor then mixes with the hot gases entrained in the boundary layer and lowers the boundary layer temperature by calorimetric mixing. This provides thermal protection downstream of the liquid film.

Most of the existing heat transfer correlations are for the flow of a low turbulence gas at constant velocity over a flat plate. Even for this classic problem many of the existing correlations differ considerably. The most fundamental of these correlations were selected and extended for use in developing, accelerating, and turbulent freestream flows. The goal was to develop a simple model suitable for design and test analysis. For this reason only simple lumped parameter models were considered.

2.0 LIQUID FILM EVAPORATION

2.1 Convective Heat Transfer

The flow over the combustion chamber walls is almost like that over a flat plate in a uniform freestream flow, the difference being that it arises from an effective stagnation point rather than an abrupt leading edge. However, for a turbulent boundary layer the exact starting conditions quickly become unimportant.

In the absence of the liquid film the "dry-wall" convective heat flux can be calculated using one of the many tested flat-plate correlations available (Reference 1). One commonly used correlation (Colburn's Eq.) is derived by assuming a 1/7th power law velocity profile (Reference 2). Expressed in terms of a non-dimensional friction coefficient, C_f , and the Reynold's number based upon the distance x from the leading edge:

$$C_f = 0.0592 \text{ Re}_x^{-0.2}$$

Using Reynold's momentum-heat analogy for turbulent convection, a non-dimensional heat transfer coefficient, termed the Stanton number, is expressed:

$$\text{St} = \frac{1}{2} C_f \text{ Pr}^{-0.6} \quad (\text{Equation 2.1})$$

In a rocket engine there is a large temperature difference between the combustion gases and the liquid film, hence the temperature at which the properties are evaluated is important. It has been common practice in boundary layer correlations to evaluate properties at the freestream gas temperature. A correction factor for the freestream to wall temperature ratio is then multiplied, the exponent being 0.26, 0.4, or 0.5 depending upon the author (References 3, 4, or 5, respectively). However, evaluating all of the properties at the mean temperature of the freestream and the wall usually eliminates such correction factors.

As the boundary layer thickness grows, the cylindrical geometry becomes important. Perhaps the most extensive measurements in fully-developed pipe flow at high temperatures was by Humble (Reference 6). He obtained a correlation in terms of a non-dimensional heat transfer coefficient, termed the Nusselt number, and the Reynold's number based on pipe diameter:

$$\text{Nu}_D = 0.023 \text{ Re}_D^{0.8} \text{ Pr}^{0.4} \quad (\text{Equation 2.2})$$

which can be rearranged to the form:

$$St = 0.023 Re_D^{-0.2} Pr^{-0.6} \quad (\text{Equation 2.3})$$

Humble found that if the property values were evaluated at the mean temperature of the freestream gas and wall, then no temperature correction factor was necessary. Such will be assumed to hold for Equation 2.1 as well.

Bartz (Reference 7) found Equation 2.3 to predict the heat transfer rate at the throat of an RFNA/N₂F₄ rocket if the constant was 0.026. This form has been extensively used to calculate convective heat fluxes in rocket engines. In Bartz' tests the flow was probably not completely developed, which explains the slightly larger constant.

For $x > 3.53 D$ the flat plate correlation of Equation 2.1 predicts a lower heat transfer rate than that for fully-developed flow, Equation 2.3. Certainly the heat transfer rate cannot fall below that for fully-developed flow. To patch these two limiting cases together, Equation 2.1 can always be used but with x replaced by an effective x_e :

$$x_e = 3.53 D \left[1 + \left[\frac{x}{3.53 D} \right]^{-m} \right]^{-1/m}$$

where the exponent $m = 4$ gives the gradual transition shown in Figure 2.

The Stanton number in Equation 2.1 is a local value at x . The average Stanton number over the region from 0 to x is higher by a factor of 1.25. However, in the present computer code this averaging is done implicitly as a summation over all local evaporation rates.

2.1.2 Transpiration Corrections

The convective heat flux vaporizes a mass flux (per surface area) of liquid:

$$\dot{m}_{\text{conv}} = \frac{h \Delta T}{\lambda^*} = \frac{G C_{pg} St \Delta T}{\lambda^*}$$

The total vapor, \dot{m}_v , generated by both convective and radiative heat transfer is "blown" into the boundary layer. This blown mass decreases the normal wall shear stress and convective heat flux by a factor dependant upon a "blowing parameter", F :

$$F = \dot{m}_v / G$$

The simplest analysis consists of calculating the velocity profile in the viscous

sublayer with blowing and ratioing the shear stress to that for the unblown wall, assuming no change in the sublayer thickness. This simple "Couette flow" model gives (References 5, 8):

$$\frac{\tau_w}{\tau_{wo}} = \frac{C}{e^C - 1} \quad ; \quad \text{where} \quad C = \frac{2F}{C_{fo}} = \frac{\dot{m}_v U_g}{\tau_{wo}}$$

and

$$\frac{h}{h_o} = \frac{\ln(1+H)}{H} \quad ; \quad \text{where} \quad H = \frac{F}{St} = C_{pg} \left[\frac{\Delta T}{\lambda} + \frac{\dot{m}_{rad}}{h} \right]$$

where C_{pg} is evaluated at the freestream temperature.

Results from more sophisticated transpiration analyses are compared with the Couette flow result in Figure 3. The curve due to Brunner (Reference 9) is a correlation of experimental results. Most experimental data has considerable scatter, but tends to follow the Couette flow model the closest (Reference 8). There appears to be no advantage in using much more complicated turbulent boundary layer models.

To account for different molecular weight injectants the parameter H should be multiplied by a correction factor, being either the vapor to gas specific heat ratio to the power 0.6 (References 5, 9) or the gas to vapor molecular weight ratio to the same power (Reference 10), when $M_c < M_g$. These two forms are identical for ideal gases with the same specific heat ratio. For the case $M_c > M_g$, Rubesin (Reference 10) gives the exponent as 0.35. Since Brunner's data (Reference 9) was only for the first case, it doesn't contradict this exponent. These corrections are substantially verified by Landis with a turbulent boundary layer model (Reference 3).

Since the Couette flow model includes the specific heat of the vapor, it would not be expected that an additional correction for specific heat differences would be necessary. However, a molecular weight difference could lead to effects requiring a separate accounting, namely the fact that with a lower density vapor the volume displaced in the boundary layer would be greater. This would tend to decrease the heat flux. For this reason the molecular weight ratio should be used in the correction term, as suggested by Rubesin.

2.1.1 Liquid Film Disturbances

Two different types of surface disturbance on the liquid film have been noted. Both have been studied in detail by Kinney (Reference 11), Knuth (Reference 12), and Gater (Reference 13).

The first type of disturbance is the appearance of random, small-scale structures with a pebbled appearance, possibly a reflection of the turbulent eddies in the boundary layer. These are always present and cause an effective surface roughness which may increase the heat transfer rate. Photographic studies have shown that the length scales of these disturbances decrease at higher velocities, although no general correlations were determined (References 11, 12).

The other type of disturbance, realized at higher coolant flow rates, is the appearance of large waves travelling in the flow direction. These waves exist only at the upstream positions where the liquid film is thick enough to sustain them. The mass loss rate in the regions where these waves do exist is 2 to 4 times the normal evaporation rate, independent of the film thickness. Entrainment of liquid from the crests of the waves without evaporation is considered the primary mechanism of mass loss.

The point of onset of these waves is well defined. Knuth was able to correlate both his data and that of Kinney for the transition point. Assuming that the mixture above the liquid film is mostly vapor and that the vapor to liquid viscosity ratio is greater than 0.03, Knuth's correlation may be written as:

$$\Gamma_{cr} = 1.01 \cdot 10^5 \mu_v^2 / \mu_l$$

Gater found quite different results. In photographic studies he noticed large waves only for water coolant. Mass was lost without evaporation for all of his test conditions. Furthermore, the mass loss rate was dependant upon the local film thickness, proportionate with the local flow rate.

These differences might be explained by the different experimental arrangements. Kinney and Knuth both measured the length of the liquid film for different circumferential mass flows by determining the dryout point using axially spaced thermocouples. Gater used a fixed film length and captured the excess liquid in a downstream slot. Obviously the potential existed for some of the liquid to flow past the capture slot. At high injection rates it is also difficult to insure that all of the liquid is placed on the wall. Knuth considered this problem in detail. Either of these problems might explain the different results of Gater. In favorably comparing his proposed correlation with Kinney's data, Gater employed an adjustable constant and failed to properly account for quantities on a unit area basis.

Other studies of liquid film waves have appeared in the chemical engineering literature. Hanratty and Hersham (Reference 14) give a correlation for the freestream velocity at the transition to large waves in terms of the gravitational constant. However,

they are unable to explain the results of Kinney and Knuth in a horizontal tube. Apparently their correlation is useful only in vertical tubes at lower velocities. Woodmansee and Hanratty (Reference 15) measured $\Gamma_{cr} = 0.0641$ kg/m-s for water, which is about 3 times lower than predicted by Knuth's correlation. Of related interest, Tatterson and Dallman (Reference 16) give a correlation for the mean diameter of the droplets sheared off of the liquid film.

2.2 Radiative Heat Transfer

In most rocket combustion chambers the radiant heat flux is negligible in comparison with the convective flux. However, the transpiration of the vapor from the liquid film greatly decreases the normally expected convective flux to such an extent that the radiant flux is often dominant in determining the liquid evaporation rate.

The radiation from combustion products is difficult to calculate from first principles due to the complicated molecular spectra of the many species present. Molecular band models attempt to replace the actual spectral lines present with a statistical distribution of lines with the same gross properties. Such modelling is a major research effort and is not warranted in the present study. However, with access to available spectral codes, it should be preferred to the methods described here.

Fortunately, in a high temperature and pressure environment many of the gas spectral properties can be more simply treated. High temperatures cause each spectral line to be "doppler broadened" due to kinetic motion. Even more significant is "collision broadening" due to high pressure. This broadening tends to smear the spectrum lines together into continuous bands. With a large number of different species radiating there would be few gaps in the spectrum. Soot aids in filling the gaps. In the limit a very dense gas mixture in thermodynamic equilibrium would radiate as a blackbody.

2.2.1 Total Emittance of Gas

A useful quantity is the total emittance of the gas, which is the ratio of the radiant intensity of the gas to that of a blackbody at the same temperature, averaged over the entire spectrum. Indeed this quantity is much easier to measure than the detailed spectral data and has been available for many years. The problem is that only data for H_2O and CO_2 are readily available. However, this covers many cases of combustion interest since symmetric molecules such as N_2 in the products do not significantly radiate.

The most recent emittance data is compiled by Siegel and Howell (Reference 17). This data is replotted in Figure 4 as a function of the optical density, ρ_{opt} , which is the gas partial pressure times the path length through the gas. Note that at very high optical densities the emittances reach limiting values, ϵ_f , of 0.825 for H_2O and 0.231 for CO_2 . These curves may be analytically fit to a function:

$$\epsilon = \epsilon_f \left[1 + \left[\frac{\rho_{opt}}{c} \right]^{-n} \right]^{-1/n}$$

with coefficients:

H_2O			CO_2		
$T(^{\circ}K)$	$c(atm \cdot m)$	n	$T(^{\circ}K)$	$c(atm \cdot m)$	n
1000	0.165	0.45	1000	0.05	0.6
2000	0.90	0.65	1500	0.075	0.6
3000	2.05	0.61	2000	0.15	0.6

In order to use these fits at different temperatures a three point interpolation among the three temperature curves should be used. The coefficients cannot be separately interpolated. A correction must be made for a total pressure different than 1 atm by multiplying a correction factor, K_p , to each emittance. The curves for these pressure corrections can be fit analytically by:

$$H_2O: \quad K_p = 1 + C_1 \{ 1 - \exp[(1-P[1+\rho_{H_2O}])/C_2] \}$$

$$\text{where:} \quad \begin{aligned} C_1 &= 0.26 + 0.74 \exp(-2.5 \rho_{H_2O}) \\ C_2 &= 0.75 + 0.31 \exp(-10 \rho_{H_2O}) \quad atm \\ \rho_{H_2O} &<> atm \cdot m \end{aligned}$$

$$CO_2: \quad \log_{10} K_p = 0.036 \rho_{CO_2}^{-0.483} [1 + (2 \log_{10} P)^{-m}]^{-1/m}$$

$$\text{where:} \quad \begin{aligned} m &= 100 \rho_{CO_2} \\ P &<> atm \\ \rho_{CO_2} &<> atm \cdot m \end{aligned}$$

An additional correction factor is necessary to account for overlaps in the two spectra. This correction can be expressed analytically for $T > 1200K$ as:

$$\Delta\epsilon = 0.0551 K_x [1 - \exp(-4 \rho_{opt})] [1 - \exp(-12.5 \rho_{opt})]$$

$$\text{where:} \quad K_x = 1 - \left| \frac{2 N_w}{N_w + N_c} - 1 \right|^n$$

$$n = 5.5 [1 + (1.09 \rho_{opt})^{-3.88}]^{-1/3.88}$$

$$\rho_{opt} <> atm \cdot m$$

N_w = mole fraction of water in mixture

N_c = mole fraction of CO_2 in mixture

The total gas emittance is then:

$$\epsilon_g = \epsilon_w + \epsilon_c - \Delta\epsilon$$

In evaluating these terms it is necessary to input the optical path length through the gas. Since this generally varies over the sight angle, the most direct method would be to calculate the emittance at a number of sight angles and to average them, weighted by the projected area at each angle. However, a simpler approach is to use an overall effective length. A very simple expression is quite accurate in determining the effective length (Reference 17):

$$L_{eff} = 0.95 (4V/A)$$

where V is the chamber volume and A is the surrounding surface area.

In applying this formula, the downstream section of the chamber can be assumed to be an infinite cylinder, for which $L_{eff} = 0.95 D$. If the cloud of droplets coming out of the injector is assumed to be perfectly reflective, then the upstream direction can also be considered an infinite cylinder. Since the droplets have numerous partially reflecting surfaces compared with the volume of absorbing liquid, this is probably the best assumption. Alternatively, if the droplets are assumed to be perfectly absorbing then the upstream effective length is:

$$L_{eff}|_{upstream} = 0.95 D \left[\frac{4x}{D + 4x} \right]$$

The upstream and downstream emittances are then averaged to obtain the total emittance. With this assumption the radiant heat flux must be calculated at every axial position.

It is also necessary to consider the possibility of reflective walls. In this case the effective sight paths will be longer. The simplest correction, due to Egleti (Reference 18), is to multiply the above effective length by a factor of A_w to the power -0.85 ; where A_w is the wall absorptivity. This factor works best with highly absorbing walls, as exist in most rocket chambers.

With the gas emittance so determined the radiant heat flux is calculated as:

$$\dot{Q}_{\text{rad}} = \sigma A_w \epsilon_g [T_g^4 - T_v^4]$$

$$\text{where: } \sigma = 5.67 \cdot 10^{-8} \text{ W/m}^2 \cdot ^\circ \text{K}^4$$

$$\text{which vaporizes a mass flux, } \dot{m}_{\text{rad}} = \dot{Q}_{\text{rad}} / \lambda^*$$

A final concern is that the above relations are for the radiation from hot gases in chemical and thermodynamic equilibrium. However, there is evidence that the radiation from transient species can be important. Ziebland (Reference 18) measured an emittance of 0.22 in a small O_2/H_2 rocket operating at 10 atm. The radiation peak, which occurred at a position 8 cm from the injector face, was almost three times the expected value. Some 20 cm downstream the emittance settled to the expected value. This initially large radiation was attributed to radiation by transient OH. While the radiation from OH in atmospheric flames contributes only a faint blue glow of no significant intensity, at high pressures it becomes significant (Reference 19).

2.2.2 Liquid Film Burnout

The radiant heat can penetrate the liquid film and be absorbed directly at the combustion chamber walls. It is then conducted into the liquid film by boiling heat transfer. With a high enough heat flux the surface can become covered by poorly conducting vapor, causing the surface temperature to rapidly rise, usually with catastrophic results. This rather abrupt transition is termed "burnout".

The same geometry of a thin liquid film flowing across a heated surface has been studied by Katto et al (References 20, 21). From measurements with water, freon® 113, and α -trichloroethane, a correlation for the burnout heat flux was found:

$$\dot{Q}_{\text{bo}} = 0.0164 \lambda \rho_\ell^{0.534} \rho_v^{0.133} \left\{ \frac{U_\ell \sigma_\ell}{1} \right\}^{0.333}$$

They noted that at the burnout point the liquid was deflected away from the surface. With water this deflection occurred on first contact with the surface, whereas with the organics the liquid was deflected near the end of the heated plate.

One would expect the burnout point to depend only upon local conditions, such as the local film thickness, rather than global quantities such as the downstream distance, l , used in the correlation above. For this reason the general applicability of the correlation must be questioned.

For comparison purposes the burnout heat flux for several rocket fuels is calculated below for the case: $l = 5 \text{ cm}$, $U_l = 1.5 \text{ m/s}$ (average film velocity), at a pressure of 100 psia (data Reference 22):

Fuel	Tsat (°K)	λ (10^3 J/kg)	ρ_l (kg/m^3)	ρ_v (kg/m^3)	σ_l (10^{-3} N/m)	\dot{Q}_{bo} (kW/m^2)
MMH	433	663	720	9.79	20.2	419
Az50	413	870	778	9.50	18.	548
H ₂	29	335	70	5.75	0.6	17.6

In most rocket engines the radiant flux will exceed these limiting values. However, it can be expected that a significant fraction of the radiant heat will be absorbed by the liquid film and vapor. Since hydrogen does not absorb infrared radiation it is doubtful that it could be used for liquid film cooling, although its large specific heat does makes it very suitable as a gaseous film coolant.

The fraction of radiation transmitted through the liquid film is: $\exp(-\alpha t)$; where α is the absorptivity of the liquid, weighted over the spectrum of the radiation, and the liquid film thickness, t , can be calculated from the wall shear stress. Assuming laminar flow:

$$t = \sqrt{\frac{2 \nu \Gamma}{\tau_w}}$$

where Γ is the local coolant mass flow (per circumference).

Katto et. al. suggest a correction factor when the liquid is injected at a temperature below the saturation temperature (Reference 21), however it was not correlated over a large range and is significantly larger than such correction factors for pool boiling. If the burnout point is controlled only by local conditions and the liquid is heated to the saturation temperature at the burnout point, then no sub-cooling correction should be necessary.

2.3 Comparison With Other Analyses

2.3.1 Perdue University Jet Propulsion Center:

A number of liquid film cooling analyses have been presented by researchers from the Jet Propulsion Center at Perdue. In early studies Zucrow and Graham

(Reference 23) attributed the increased mass loss rate after transition not to large surface waves, but to instabilities in the termination point of the liquid film. Zucrow and Sellers (Reference 24) later attempted to model the convective mass transfer.

In a later analysis Warner and Emmons (Reference 25) give a result which has been quoted by others. For the no blowing case it reduces to an unusual result:

$$St = C_f K_v / (2C_{pg} U_g)$$

It was not possible to reproduce their calculations with the suggested constants, even after correcting for an apparent sign error in their Equation 5.

Gater et al (Reference 26) attempted to relate all of the previous expressions from the Center. In a later report (Reference 13) he mentions the transpiration analysis of Sec. 2.1.2, but discounts it due to the anomalies in his data mentioned in Section 2.1.1 .

2.3.2 Shembharkar and Pai (S&P) (Reference 27)

These authors present a Prandtl mixing length turbulence model for the gas convection, coupled to a viscous flow model for the liquid film. Landis (Reference 3) and Economis (Reference 28) have reported similar turbulent boundary layer models which give no real improvement over the simple Couette flow transpiration model. The main addition of the S&P model is the inclusion of the liquid interface motion. Since the interface velocity is only 1% of the freestream velocity, this is insignificant.

In their "datum case" the starting boundary layer thickness is 12.5 mm, corresponding to a downstream starting position of $x = 0.812$ m, by the boundary layer growth relations of Sec. 3.0 Since the boundary layer is well developed upon contacting the relatively short liquid film, the evaporation rate should be almost constant. Instead, they calculate an initially high evaporation rate of 0.2 kg/s-m^2 , dropping exponentially to 0.124 kg/s-m^2 . This may be due to numerical transients. The simpler analysis of the present report predicts an almost constant evaporation rate of 0.106 kg/s-m^2 . The difference between this and their final evaporation rate is exactly accounted for by the blowing correction factor h/h_0 . It is not apparent that the momentum of the transpiring vapor was properly included as a boundary condition in their model. This vapor momentum is the important term in providing the heat flux decrease with transpiration cooling.

3.0 VAPOR FILM COOLING

After the liquid film has vaporized it continues to provide thermal protection to the wall by calorimetric mixing with the hot gases in the boundary layer. Numerous correlations have been presented for this process, termed "gaseous film cooling". They are normally expressed in terms of a "cooling effectiveness":

$$\eta = \frac{T_g - T_{aw}}{T_g - T_c}$$

versus a dimensionless distance along the wall:

$$X = K x ; \quad \text{where: } K = G \mu_g^{0.25} M_c^{-1.25}$$

where: \dot{M}_c = coolant vapor mass flow (per circumference)

$G = \rho_g U_g$ = freestream gas mass flow rate
per chamber cross-sectional area

x = distance downstream from injection point

Most authors arrange the constant K above in terms of a coolant flow Reynolds number, giving the false impression that the injection conditions are important. As long as the coolant is injected with low relative velocity so that there are no jet effects, the geometry of the injection point is unimportant.

The most successful of the flat-plate integral solutions is that due to Kutateladze, et al (Reference 29) and Stollery, et al (Reference 30, Equation 27). In determining the boundary layer growth rate they conceptually replace the injected coolant with an equivalent mass of freestream gas. To provide the proper boundary layer growth rate, they identify an effective starting point a distance x_0 upstream of the injection point. Their analysis assumes that the injection point is at the leading edge. It can be extended to the case of injection at a point x_i downstream of the leading edge as follows, with the nomenclature defined in Figure 5.

From the $1/7^{\text{th}}$ power law results (Reference 2), the boundary layer growth from the fictitious point x_0 is:

$$\delta = 0.371 x' \text{Re} x'^{-0.2} ; \quad \text{where: } x' \equiv x + x_0$$

$$\dot{M}_{bl} = 7/8 \rho_g U_g \delta = 0.325 \dot{M}_c [X + X_0]^{0.8} \quad (\text{Equation 3.1})$$

The fictitious upstream point X_0 is found from a mass balance at the injection point:

$$\begin{aligned}\dot{M}_{bl}|_{x=x_i} &= \dot{M}_C + \dot{M}_g \\ 0.325 \dot{M}_C (X_i + X_0)^{0.8} &= \dot{M}_C + 0.325 \dot{M}_C X_i^{0.8} \quad (\text{Equation 3.2})\end{aligned}$$

$$X_0 = (3.08 + X_i^{0.8})^{1.25} - X_i$$

$$\text{where: } X_i = K x_i$$

The freestream gas entrained in the boundary layer at position x is:

$$\dot{M}_g = \dot{M}_{bl} - \dot{M}_C \quad (\text{Equation 3.3})$$

From a calorimetric heat balance:

$$\begin{aligned}\eta &= \left[1 + \frac{C_{pg} \dot{M}_g}{C_{pc} \dot{M}_C} \right]^{-1} \\ \text{or,} \\ \eta &= \left[1 + \frac{C_{pg}}{C_{pc}} (0.325 [X + X_0]^{0.8} - 1) \right]^{-1} \quad (\text{Equation 3.4})\end{aligned}$$

Other correlations based upon less reasonable assumptions about the effect of the injectant upon the boundary layer growth rate have been proposed (Reference 30, 31, 32). At large downstream distances most reduce to the same form. The correlation above gives excellent comparison with most experimental data (Reference 30, 33).

The analysis can be extended to the case of distributed injection, however the result is unwieldy. In any event, the effective injection point is of minor concern. In the analysis of Librizzi and Cresci (Reference 32), which gives predictions close to the present analysis, the upstream position of coolant injection is not even specified.

The present analysis contains two basic assumptions which are known to be wrong. These are that all of the vapor remains in the boundary layer and that all of the gases in the boundary layer are at the same temperature, T_{aw} . In fact, measurements of the concentration and temperature profiles show an "S-shaped" profile for both (Reference 38). However, these profiles do maintain a similar shape with x , growing away from the wall at the same rate as the boundary layer thickness. This suggests that the the derivation above can be reinterpreted.

This "S-shaped" profile can be conceptually divided into a two domain region, with an outer layer at the freestream temperature and an inner layer at T_{aw} . Since this inner layer thickness will always be a constant fraction of the total boundary layer thickness, then the same relative masses of hot gases will be entrained as in the original analysis. However, in this case the interpretation is, more properly, that T_{aw} is the temperature only in the region very close to the wall.

Even with this conceptual reinterpretation a difficulty remains in that the above analysis would predict no freestream gas entrainment in a fully-developed flow in a pipe, which is certainly unrealistic. In the present study Equation 3.4 is assumed to hold equally well in a fully-developed flow. That the analysis which leads to this equation is apparently flawed should not detract from the fortuitous result that Equation 3.4 correlates the existing data extremely well.

A number of corrections to Equation 3.4 are necessary to account for effects not considered in the standard flat-plate boundary layer analysis. Corrections for freestream turbulence, foreign gas injection, thermal radiation, and changing freestream conditions are itemized below.

3.1 Freestream Turbulence Effects

The flat-plate boundary layer relations used in deriving Equation 3.4 assume no freestream turbulence. Two experiments considered the effects of turbulence upon gaseous film cooling (References 34 and 35). A possible correction might be to multiply X by a factor $K_t = 1 + C_t$. When applied to the data of Marek and Tacina (Reference 35), C_t is found to be constant with X and varies with the freestream turbulence rms fraction, e , as: $C_t = 8.67 e$; for $e = 0.07, 0.14$, and 0.23 . For the 35% turbulence case the data follows this relation for $X < 1.5$, thereafter C_t increases as $X^{0.3}$.

Unlike Marek and Tacina, Carlson and Talmor (Reference 34) did not directly measure the turbulence level, but rather inferred it based on screens placed in the flow. The length scales of the turbulence may also have differed considerably. Nonetheless, their data give $C_t = 11.7 e$. In this case C_t varied slightly with X for all turbulence levels. Since their greatest turbulence level was 22%, the increased mixing found by Marek and Tacina at 35% turbulence was not confirmed. Averaging the two results gives:

$$K_t = 1 + 10.2 e \quad \text{(Equation 3.7)}$$

Two studies have experimentally determined the turbulence intensities in rocket engines. The results are given below:

- $e = 0.10$ to 0.05 at distances 2 to 8 inches from the injector in a LOx/GH_2 engine (Reference 36)
- $e = 0.20$ to 0.15 at distances 6 to 23 inches from the injector in an $\text{N}_2\text{O}_4/\text{Az50}$ engine (Reference 37)

3.2 Foreign Gas Injection

Goldstein, et. al. (Reference 38) found that the effectiveness values were about 30% higher than expected when helium replaced air as the coolant injected into a heated airstream. These results were confirmed by Burns and Stollery (Reference 39). However, it is not certain that the effect is due to the coolant properties since the helium injection velocities were lower than the air velocities at the same effectiveness values (Reference 34). Assuming the effect is real, it might be attributed to the molecular weight difference, similar to the assumption made Section 2.1.2 .

The results with helium coolant are well fit by the empirical Equation 12 of Goldstein (Reference 38). This can be put into the form of Equation 3.4 by adding a multiplier of 0.76 to the C_{pg}/C_{pc} ratio. In general, this multiplier can be written as:

$$K_M = (M_c/M_g)^{0.14} \quad (\text{Equation 3.6})$$

With these correction factors Equation 3.4 becomes:

$$\eta = \left[1 + K_M \left[\frac{C_{pg}}{C_{pc}} \right] \left[0.325 (K_t X + X_o)^{0.8} - 1 \right] \right]^{-1} \quad (\text{Equation 3.9})$$

3.3 Thermal Radiation

The thermal radiation is transmitted with little absorption through the boundary layer and absorbed at the wall. From there it is conducted back into the boundary layer gases, requiring a wall temperature, T_w , in excess of the boundary layer temperature, T_{aw} :

$$T_w = T_{aw} + \frac{\dot{Q}_{rad}}{h} \quad (\text{Equation 3.7})$$

This form is suggested for gaseous film cooling with a non-adiabatic wall (Reference 40). The heat transfer coefficient is calculated by Equation 2.1, evaluated at $x' = x + x_o$, with freestream gas properties.

The radiant heat will also go into the heat balance of the boundary layer gases. Assuming that it is spread evenly over the entire boundary layer mass, the temperature increase with distance will be:

$$\frac{\Delta T_{aw}}{\Delta x} = \frac{\dot{Q}_{rad}}{M_{bl} C_{pg}}$$

3.4 Non-uniform freestream flow

Equation 3.4 was derived assuming a constant freestream gas flowrate and temperature. If these quantities change at a downstream point then Equation 3.4 cannot be directly applied. To demonstrate this, consider a sudden decrease in the flow rate per area, G . Attempting to apply the expression locally would lead to a step decrease in the non-dimensional distance, X , and a step increase in the effectiveness, η . This would imply that the gases spontaneously unmix, violating the second law of thermodynamics.

It is possible, however, to obtain a proper local expression from Equation 3.4. Due to the parabolic nature of the boundary layer the local conditions determine only the rate of change, in the downstream direction, of the boundary layer properties. The present expression is an integral result for the special case of constant flow conditions. From it a differential equation in terms of the local properties can be determined.

The rate of change with position of η is determined by differentiating Equation 3.9. All parameters are held constant in differentiating, since such was done in deriving the integral expression. The result is expressed in terms of the local value of η instead of the global variable X .

$$d\eta/dx = -0.1963 K K_t K_M \left[\frac{C_{pg}}{C_{pc}} \right] \eta^2 \left[1 + \frac{C_{pc}}{K_M C_{pg}} \left(\frac{1}{\eta} - 1 \right) \right]^{-\frac{1}{2}}$$

The rate of change of T_{aw} is then found as:

$$\frac{dT_{aw}}{dx} = - \frac{(T_g - T_c)}{\eta} \frac{d\eta}{dx}$$

T_{aw} is found by numerically integrating this expression. Equation 3.9 could be used to calculate T_{aw} at the injection point. However, this predicts $T_{aw} > T_c$ at the injection point for downstream injection. It seems more realistic to use $T_{aw} = T_c$ as the initial condition for the differential equation in all cases. The above approach will be

termed the "differential η " formulation to distinguish it from the "integral correlation" of Equation 3.9 .

The freestream mass flow-rate per area, G , varies inversely with the local cross-sectional area as:

$$G = G_{ch}(A_{ch}/A)$$

Increases in G as the nozzle converges increases the rate of freestream gas entrainment through the constant K . The distance x should be measured along the nozzle contour.

The other effect of freestream acceleration is a drop in the static temperature of the freestream gas. Upon entrainment into the boundary layer the original stagnation temperature is recovered as the kinetic energy is converted back into thermal energy. However, some of this heat is then lost by conduction back into the cooler freestream gas. The result is that the freestream gas attains a temperature in the boundary layer lower than the stagnation temperature. This is termed the "recovery temperature", T_r , and is normally a constant fraction of the difference between the static and stagnation temperatures:

$$T_r = T_o - (1-r)(T_o - T_s)$$

where: T_o = stagnation temperature of freestream gas
 T_s = static temperature of freestream gas
 r = recovery factor

This recovery temperature should replace T_g everywhere. For a flat-plate boundary layer without entrainment it can be shown that $r = Pr^{1/3}$ (Reference 41), however it is not likely that this relation will hold in the gaseous film cooling case.

From the isentropic relations for compressible flow:

$$T_r = T_o [1 - (1-r)b / (1+b)]$$

where: $b \equiv \frac{1}{2}(\gamma - 1)M^2$

The local Mach number, M , is found implicitly from one of two forms:

$$M = \frac{1}{A_t} \left[\frac{2}{\gamma + 1} + \frac{M^2}{\gamma} \right]^{\gamma/2} \quad \text{for } M < 1$$

or

$$M = \left[\gamma_r (M A_t)^{2/\gamma_r} - \frac{2}{\gamma-1} \right]^{1/2} \quad \text{for } M > 1$$

where: $A_t = (A/A_{\text{throat}})$

$$\gamma_r = \frac{\gamma+1}{\gamma-1}$$

3.4.1 Differential Entrainment Formulation

If the freestream gas recovery temperature changes ($r < 1$) then the "differential η " formulation above cannot be used, for the subtle reason that the local value of η no longer uniquely determines the entrainment rate of freestream gases. This problem is remedied by recognizing that the entrainment rate is a function of only the local boundary layer mass flow rate \dot{M}_{bl} . From Equation 3.1:

$$\left. \frac{d\dot{M}_{bl}}{dx} \right|_e = 0.1963 G \left[\frac{\mu_g}{\dot{M}_{bl}} \right]^{-0.25} \quad (\text{Equation 3.10})$$

The calorimetric heat balance in differential form is:

$$\dot{M}_{bl} C_{pg} (T_r - T_{aw}) = (\dot{M}_g C_{pg} + \dot{M}_c C_{pc}) dT_{aw}$$

The specific heat on the left side of the equation should be evaluated at the mean temperature between T_r and T_{aw} , while those on the right should be evaluated at T_{aw} .

Substituting Equation 3.3:

$$\frac{dT_{aw}}{dx} = \left. \frac{d\dot{M}_{bl}}{dx} \right|_e (T_g - T_{aw}) \left[\dot{M}_{bl} + \left[\frac{C_{pc}}{C_{pg}} - 1 \right] \dot{M}_c \right]^{-1} \quad (\text{Eq. 3.11})$$

The initial condition on \dot{M}_{bl} is found from Equation 3.2:

$$\dot{M}_{bl}|_{x_i} = \dot{M}_c [1 + 0.325 X_i^{0.8}]$$

As with the "differential η " formulation, the initial condition on T_{aw} is taken to be T_c . For the case of constant freestream gas temperature, where the local value of η can be directly related to \dot{M}_{bl} , the formulation above can be equated to the prior "differential η " formulation.

To include the effects of freestream turbulence and molecular weight differences of Sections 3.1 and 3.2, a multiplier of k_t should be added to the coefficient

in Equation 3.10 and a multiplier of $1/k_M$ should be added to the C_{pc}/C_{pg} ratio in Equation 3.11. This is consistent with the placement of these correction terms in the differential η formulation.

3.4.2 Circumferential Change:

In a rocket engine the contraction of the nozzle decreases the circumference, causing an increase in the boundary layer flow rate per circumference as:

$$\left. \frac{d\dot{M}_{bl}}{dx} \right|_c = - \dot{M}_{bl} \frac{1}{D} \frac{dD}{dx}$$

Since this increase is not due to freestream entrainment it does not enter into the energy balance. However, it is important in that it affects the total boundary layer flow rate, which is found by adding the changes due to freestream entrainment and this circumferential change. This total boundary layer flow rate determines the local rate of freestream gas entrainment, as given by Equation 3.10. It should be mentioned that in using this addition that the coolant flow rate per circumference be calculated locally, by scaling the chamber value.

3.5 Turning Effects

Carlson and Talmor (Reference 34) measured the effectiveness downstream of a sharp turn in a rectangular duct. Their results can be expressed as:

$$\eta = [1 + cX^n]^{-1}$$

with coefficients (at 12% turbulence):

turning angle	C	n
30°	0.40	2.2
45°	0.75	2.1
60°	1.40	2.0

To reduce approximately to Equation 3.4 the exponent, n , should approach 0.8 as the turning angle approaches 0°. Since the exponent is increasing in the opposite direction their results appear to be anomalous. For unturned flows in a circular duct their results followed Equation 3.4. Possibly these results were due to disturbance of the boundary layer by the sharp turn in their wind tunnel.

Rousar and Ewen (References 42-44) studied gaseous film cooling in a converging nozzle. Their data is analyzed in Section 4.2.1.

4.0 COMPARISON WITH EXPERIMENTS

4.1 Liquid Film Cooling

4.1.1 G.R. Kinney et al air-water experiment (Reference 11)

These heat transfer measurements were performed at fairly low temperatures in a tube with fully-developed flow. The evaporation rates were therefore fairly constant with distance.

Gas:

air ($M = 29$)
 $P = 2.54 \text{ atm}$
 $Pr = 0.697$

Coolant:

water ($M = 18$)
 $T_v = 367 \text{ K}$
 $T_c = 300 \text{ K}$
 $C_{pl} = 4196 \text{ J/kg-K}$
 $\lambda^* = 2.59 \cdot 10^6 \text{ J/kg}$

The test conditions are reported in terms of Re_D at the freestream temperature. To convert to the mean temperature, each Re_D is multiplied by the appropriate density and viscosity ratio. The heat transfer coefficient is then calculated from Eq. 2.2. Radiation is negligible at these low temperatures.

T_g (F)	800	900	1000	1200	1400	1600
T_g (K)	700	756	811	922	1033	1144
ρ_g (kg/m ³)	1.278	1.187	1.104	0.973	0.867	0.783
C_{pg} (J/kg-K)	1075	1087	1100	1126	1148	1168
μ_g (E-5 kg/m-s)	3.332	3.499	3.656	3.959	4.238	4.551
H	0.184	0.217	0.252	0.321	0.393	0.466
h/h_o	0.918	0.905	0.892	0.867	0.843	0.821
properties at:						
T_{mean} (K)	534	562	589	645	700	756
K_g (E-2 W/m-K)	4.257	4.436	4.606	4.922	5.230	5.544
ρ_g (kg/m ³)	1.676	1.597	1.521	1.390	1.278	1.206
C_{pg} (J/kg-K)	1036	1043	1052	1063	1075	1087
μ_g (E-5 kg/m-s)	2.784	2.887	2.974	3.159	3.332	3.654
$Re_D _{T_m} / Re_D _{T_g}$	1.570	1.631	1.694	1.790	1.875	1.918

Using these values the calculations for the different tests are:

TEST	Re_D (10^5)	$\overline{Re_D}$ (10^5)	U_g (m/s)	Nu	h_o ($\frac{W}{m^2 K}$)	\dot{m}_{vcalc} ($\frac{kg}{s \cdot m^2}$)	\dot{m}_{vexp1} ($\frac{kg}{s \cdot m^2}$)	\dot{m}_{vexp2} ($\frac{kg}{s \cdot m^2}$)
2 in smooth:								
800F	4.4	6.91	226	935	783	0.0924	0.141	---
800F	5.6	8.79	287	1133	949	0.112	0.200	---
1200F	3.5	6.27	280	865	838	0.156	0.236	0.450
1600F	2.5	4.80	286	698	762	0.188	---	0.611
4 in smooth:								
900F	6.0	9.79	174	1235	539	0.0733	0.0794	0.326
900F	8.2	13.37	238	1585	692	0.0941	0.109	0.226
900F	9.9	16.15	287	1843	805	0.109	0.153	0.366
1400F	5.3	9.94	255	1250	644	0.139	---	0.440
1600F	4.7	9.01	269	1156	631	0.155	---	0.629
4 in rough:								
800F	6.8	10.68	175	1324	555	0.0655	0.131	---
800F	11.	17.27	282	1945	815	0.0962	0.226	0.458
1400F	5.4	10.1	260	1269	653	0.142	0.326	0.930
1400F	6.7	12.6	322	1507	776	0.168	---	0.896

The \dot{m}_{vexp1} listed above are the experimentally determined evaporation rates for normal film evaporation. The \dot{m}_{vexp2} are for the case after the transition to large waves. The comparison between the calculated and experimental (\dot{m}_{vexp1}) values is shown in Figure 6.

While the calculations do not compare favorably with the measured values in an absolute sense, they do correlate the data well. The greatest difference between the calculated and measured values is for the "4 inch rough tube". Since tube roughness is known to increase the wall shear stresses and heat transfer rates, this result is expected. The remainder of the discrepancy might be explained by the "pebbling" of the liquid surface observed which would also give a roughness effect and possibly mass transfer augmentation of the evaporation due to the freestream being unsaturated. A multiplying factor of 1.4 to the calculated evaporation rates would best bring the calculations into comparison with the data for the two "smooth tubes".

4.1.2. E.L. Knuth air-water tests (Reference 12)

These tests were done shortly after Kinney in a similar set-up.

Gas: air

P= 1 atm

D= 2.9 in; Ach=0.00426 m²

Liquid: water

Tv= 339 K (Knuth Fig.11)

Tc= 300 K

λ^* = 2.59E06 J/kg

TEST	20-30:	45-54:	89-99:
Tg (K)	613	901	1230
Cpg (J/kg-K)	1057	1121	1184
ρ_g (kg/m ³)	0.575	0.393	0.159
h/ho	0.932	0.866	0.799
properties at:			
Tmean (K)	476	620	785
ρ_g (kg/m ³)	0.741	0.569	0.450
Cpg (J/kg-K)	1025	1060	1092
μ_g (E-5kg/m-s)	2.57	3.08	3.58
Pr	0.682	0.681	0.688

With these property values the evaporation rates are calculated using Equation 2.3:

TEST	$\rho_g U_g$ (kg/s-m ²)	U_g (m/s)	Re _D (10 ⁵)	Sto (10 ⁻³)	h (W/m ² -K)	\dot{m}_{vcalc} (kg/s-m ²)	\dot{m}_{vexp} (kg/s-m ²)
20-30	181.0	315	5.19	2.08	463	0.0490	0.0586
45-54	91.6	233	2.19	2.48	302	0.0656	0.0586
89-99	69.2	435	1.42	2.68	457	0.1574	0.0633

In this case the calculated values are generally higher than the measured evaporation rates. However, there is not enough data to discern any trends.

4.1.3. G. Morrell LOX/ammonia rocket (Reference 45)

These test were performed in a 4 inch diameter rocket chamber with a liquid film cooled section 2.8 inches downstream of the injector. Water, ethanol and ammonia were tested as liquid coolants. However, the ammonia was at super-critical conditions and no sharp evaporation points were determined, hence it is omitted here. At 17.4 atm:

coolant	Mc	Tv (K)	λ $\left[\frac{10^6 \text{ J}}{\text{kg}} \right]$	μ_v $\left[\frac{10^{-6} \text{ kg}}{\text{m-s}} \right]$	μ_l $\left[\frac{10^{-6} \text{ kg}}{\text{m-s}} \right]$	σ $\left[\frac{10^{-3} \text{ N}}{\text{m}} \right]$	ρ_l $\left[\frac{\text{kg}}{\text{m}^3} \right]$	ρ_v $\left[\frac{\text{kg}}{\text{m}^3} \right]$	Γ_{cr} $\left[\frac{\text{kg}}{\text{m-s}} \right]$
water	18	481	1.91	15.9	129	33.0	950	9.09	0.198
ethanol	46	448	0.742	13.0	120	7.91	608	27.6	0.142

The freestream gas properties are given in the report as a function of the O/F ratio. Several of the properties can be evaluated at O/F = 1.41 (stoichiometric) and Tmean = 1722 K:

$$0.75 \text{ H}_2\text{O}, 0.25 \text{ N}_2, M_g = 20.5, \mu_g = 6.50 \cdot 10^{-5} \text{ kg/m-s}$$

The remaining properties are strong functions of the O/F ratio, as given in Morrell's Figure 5, and are evaluated for each run. The properties at Tmean are taken as:

$$G = G(T_g/T) \quad \text{and} \quad C_{pg} = 0.725 C_{pg}$$

Test	O/F	T _g (K)	P (atm)	G $\left[\frac{\text{kg}}{\text{s-m}^2} \right]$	C _{pg} $\left[\frac{\text{J}}{\text{kg-K}} \right]$	Pr	Γ $\left[\frac{\text{kg}}{\text{s-m}} \right]$	L _{meas} (cm)	L _{calc} (cm)
water:									
1	1.61	2950	17.4	226	3033	1.02	0.269	21.2	31.0
2	1.56	2960	17.8	234	3179	1.02	0.258	19.4	28.4
3	1.64	2945	17.0	225	3012	1.01	0.213	14.2	24.2
4	1.42	2978	17.4	233	3681	1.07	0.219	14.6	23.1
5	1.50	2963	17.0	207	4141	1.03	0.209	16.2	24.1
6	1.66	2940	17.1	229	3012	1.01	0.130	7.01	14.0
7	1.72	2935	17.5	220	2907	1.00	0.128	9.86	14.2
8	1.41	2978	17.1	209	3700	1.08	0.262	18.8	30.2
9	1.51	2963	16.9	214	2494	1.03	0.262	20.7	30.3
10	1.75	2930	17.7	225	2886	0.99	0.290	20.4	34.1
11	1.67	2942	17.7	224	2970	1.01	0.296	21.7	34.7

ethanol:

12	1.18	2858	17.8	223	4727	1.23	0.809	14.2	60.9
13	1.10	2714	17.4	222	5145	1.28	0.869	16.2	69.5
14	1.17	2840	17.8	225	4768	1.24	0.834	17.4	63.2
15	1.12	2750	17.4	211	5019	1.27	0.859	19.4	70.0
17	1.25	2915	18.0	209	4371	1.18	0.872	17.7	67.5
18	1.17	2840	17.7	228	4768	1.24	0.869	18.0	65.6
19	1.13	2768	17.6	224	4978	1.27	0.716	16.2	--
20	1.25	2915	18.0	224	4371	1.18	0.713	16.2	--
22	1.41	2978	18.1	236	3681	1.08	0.570	14.6	--
23	1.37	2968	17.9	225	3848	1.10	0.598	15.8	--
25	1.48	2965	18.1	230	3388	1.04	0.535	11.0	--
26	1.31	2940	18.2	237	4099	1.14	0.525	10.4	--
28	1.54	2958	18.0	238	3242	1.02	0.341	10.3	--
29	1.53	2960	17.8	225	3250	1.03	0.369	9.55	25.8
30	1.59	2952	18.2	231	3095	1.02	0.318	10.2	--

In these calculations radiation from H_2O in the products is significant. Since the freestream parameters for each run varied significantly, the liquid film length must be separately calculated for each run condition. The results given by the computer code are listed above. In all of the ethanol tests the liquid coolant flow rate greatly exceeded Knuth's critical values for the formation of large waves, hence the poor comparison with calculations is not surprising. Some representative calculated values are listed above.

The comparison with the experimental data for water coolant is given by the squares in Figure 7. In the computer code the local burnout heat flux is calculated, as discussed in Section 2.2.2. As the liquid film thickness decreases, the velocity decreases, decreasing in turn the burnout heat flux. At some point before complete evaporation, the radiant heat flux exceeds the burnout heat flux. The liquid film length determined by this burnout condition is shown by the asterisks in Figure 7.

Most of the water coolant tests slightly exceeded Knuth's critical flow rates, however no such transition was noticed in the data. All of the data shows an evaporation rate consistently 1.55 times higher than calculated. With the burnout condition included the calculations agree much better with the data. However, this must be considered merely fortuitous, since for the ethanol tests the burnout condition predicted liquid film lengths of only 2 to 4 cm. The burnout calculation is most sensitive to the latent heat of the liquid.

In the calculations the convective heat flux accounted for 47% of the total evaporation, the remainder due to radiation. From the data of Kinney, et. al. it can be inferred that the convective evaporation rate is actually 40% higher than calculated, with Knuth's data dissenting. The present 55% difference between calculations and experiment could be attributed to a number of factors, all of which would decrease the liquid film length:

- 1) the turbulence in a rocket engine may significantly increase the convective heat transfer
- 2) Knuth's stability criterion being slightly exceeded may have caused some droplet entrainment.
- 3) the radiative heat flux may be higher than assumed due to OH and other transient species at the high pressures (Sec. 2.2.1)
- 4) burnout of the liquid film before complete evaporation is not unlikely and probably accounts for some length decrease, however questionable the use of Katto's correlation.

As in most models it is difficult to determine what percentage each of the above factors contribute to the difference between the calculations and data. Use of a multiplying factor of 1.55 to the calculated evaporation rates could be justified by the above unknowns.

4.1.4. Warner and Emmons H₂/air rocket (Reference 25)

These tests were in a 7.98 cm diameter rocket burning air and H₂. The tests were performed far downstream of the rocket chamber so that fully-developed flow is assumed. The test conditions of their Figure 5 are reported at a freestream $Re_D = 68,000$. This can be converted to mean temperature conditions by multiplying by the temperature ratio to the power 1.64 .

The gas is assumed due to the stoichiometric reaction of air and H₂ giving:

$$T_g = 2222 \text{ K}, Pr = 0.797, k_g = 0.0849 \text{ W/m-K.}$$

65.3% N₂ , 34.7% H₂O

Three different coolants were tested. The properties of each at the 34 atm test pressure are given in Reference 13, Table 5:

Coolant	T (K)	T _v (K)	λ^* (E6 J/kg)	$\frac{C_{pg}\Delta T}{\lambda^*}$	μ_v/μ_l	Γ_{cr} (kg/m-s)
water	1327	431	2.71	1.41	0.0884	0.137
NH ₃	1275	328	1.20	3.41	0.0596	0.0667
ethanol	1299	376	1.12	2.33	0.0383	0.0445

The radiative heat flux can be calculated as 484 kW/m², which vaporized 0.178, 0.404, and 0.432 kg/s-m² of water, NH₃, and ethanol coolant, respectively.

The convective evaporation rates are calculated from Eq. 2.3 with the blowing correction, giving the total calculated evaporation rates:

Coolant	h ₀ (W/m ² -K)	h (W/m ² -K)	\dot{m}_{vconv} (kg/s-m ²)	\dot{m}_{vcalc} (kg/s-m ²)	\dot{m}_{vexp} (kg/s-m ²)
water	323	203	0.081	0.259	0.459
NH ₃	340	149	0.080	0.484	0.855
ethanol	332	173	0.132	0.564	1.157

The flow rates for the ammonia and ethanol tests exceeded Knuth's stability criteria, however the data did not show any such transition. For water and ammonia the measured evaporation rates are a factor 1.77 larger than calculated. The ethanol rate is 2.05 times larger than calculated. In this case radiation accounted for about 70% of the evaporation. This would imply that the differences are not due entirely to errors in the calculation of the convective heat transfer rate.

4.1.5. R.C. Kesselring, et al OF₂/B₂H₆ rocket test (Reference 46)

Gas: NASA Equil. Code
0.537 HF, 0.225 BOF
0.063 H₂O, 0.036 H₂
0.031 OH

P = 6.8 atm

T_g = 3900 K

M_g = 31.1

U_g = 396 m/s

C_{pg} = 4232 J/kg-C

properties at:

T = 2080 K

C_{pg} = 3660 J/kg-C

ρ_g = 1.16 kg/m³

μ_g = 8.37 10⁻⁵ kg/m-s, Pr = 0.80

Coolant: B₂H₆

(many values not certain)

T_v = 260 K (from data)

Mc = 27.67

λ = 1.51 10⁶ J/kg (at 1 atm)

C_{pl} = 2055 J/kg-C

assume T_v=T_c

Radiation is dominant in this case. In the absence of better data it is initially assumed that the combustion products radiate as a black body. This gives:

$$\dot{q}_{\text{rad}} = 13.12 \text{ MW/m}^2, \quad \dot{m}_{\text{rad}} = 8.687 \text{ kg/s-m}^2$$

The convective evaporation rate can be calculated from Eq. 2.1. Assuming a film-cooled length of 15 cm gives, with the blowing correction:

$$h_o = 4665 \text{ W/m}^2\text{-K}, \quad h = 9 \text{ W/m}^2\text{-K}, \quad \dot{m}_{\text{conv}} = 0.0217 \text{ kg/s-m}^2$$

At such high temperatures the blown vapor generated by the radiant flux is so large as to make the convective evaporation negligible. The total evaporation rate is then almost constant with distance at 8.71 kg/s-m^2 , giving a film-cooled length:

$$L_c = \Gamma / \dot{m}_v = 0.115 \Gamma \text{ m}^2\text{-s/kg}$$

From the thermocouple readings given in the report the film-cooled length can be determined to ± 2 inches as:

TEST	Γ (kg/m-s)	L_c (in)
1	0.583	$3 < L_c < 5$
3	0.445	$1 < L_c < 3$
4	0.451	$1 < L_c < 3$
6	0.191	$1 < L_c < 3$
9	0.306	$1 < L_c < 3$
10	0.532	≈ 3
11	0.435	$1 < L_c < 3$

Surprisingly, the authors assume that the liquid is immediately evaporated, based upon calculations of the "dry-wall" heat flux without transpiration. They interpret the thermocouple data as meaning that this vapor refrains from mixing with the hot gases until some arbitrary distance downstream.

While the bracketing of the data is wide, the film-cooled length is fairly well defined, as shown in Figure 8. The data is best fit with an emittance of 0.77, instead of the 1.0 assumed above. This is reasonable since the optical density (64 atm-cm) is not terribly high.

4.2 Gaseous Film Cooling

4.2.1 Rousar and Ewen (References 42-44)

The tests in the first two reports were performed in a hot nitrogen freestream flow with hydrogen and nitrogen coolants. The freestream turbulence was measured to be 4.1% for all of these tests. The tests in the last report were performed in a LOx/H₂ rocket engine using hydrogen, nitrogen, and helium coolants. The O/F mixture ratio was varied to obtain different combustion temperatures.

The authors present an empirical analysis with which they analyze their data. Although their analysis bears some relation to the present differential entrainment model, it is difficult to relate to any of the standard correlations. For this reason only their raw data is considered here. The comparison with the present model is given below.

Test	hot gas	coolant	x _{in} (mm)	e (%)	Δet (%)	comparison
1972:						
3	N ₂	H ₂	20.	4.1	38.	good
5A	N ₂	H ₂	32.	4.1	28.	good
8	N ₂	H ₂	0.	4.1	6.	fair
11A	N ₂	H ₂	0.	4.1	0.	good
1973:						
101L	N ₂	N ₂	0.	4.1	0.	good
101H	N ₂	N ₂	0.	4.1	0.	good
102	N ₂	H ₂	0.	4.1	16.	good
103A	N ₂	H ₂	0.	4.1	18.	good
104AL	N ₂	N ₂	0.	4.1	0.	good
104AH	N ₂	N ₂	0.	4.1	0.	good
105A	N ₂	H ₂	0.	4.1	0.	good
1977: (O/F)						
102	3.89	H ₂	0.	5.	0.	good
103	3.81	H ₂	0.	4.	0.	good
105	5.75	H ₂	0.	2.	0.	good
110	7.71	H ₂	0.	0.	0.	good
111	7.99	H ₂	0.	0.	0.	good
114	6.27	H ₂	0.	0.	0.	good
115	5.93	H ₂	0.	1.5	0.	good
116	7.60	H ₂	0.	0.	0.	good
117	4.00	H ₂	0.	3.	0.	good
119	7.76	He	0.	0.	0.	bad
120	7.46	He	0.	0.	0.	bad
122	7.75	He	0.	0.	0.	bad

A "good comparison" above means that the calculated wall temperatures (using the adjustable parameters listed) varied from the data points within 5% of the total temperature increase, in the region upstream of the throat.

In the first two reports the heated nitrogen flow was fully developed upon entering the film cooling test chamber. This made it uncertain what injection distance from the "leading edge" to input into the calculations, as discussed in Section 3.0 . For this reason this injection point, x_{in} , was varied in the calculations to obtain the best fit to the data. Interestingly, taking $x_{in} = 0$, gave the best comparison with the data for most of the runs, the exception being tests 3 and 5A of 1972, the first of which was a "check-out run". This assumption is supported by heat transfer data taken in the same study which shows the initially high convective heat transfer rates of a leading edge, as depicted in Figure 2, at the injection point. Apparently the coolant injection disrupts the flow such that a new boundary layer grows from the injection point.

In the 1977 rocket engine tests the freestream turbulence intensity, e , was unknown. In the computer runs for these tests this parameter was varied to give the best comparison with the data. This assumed turbulence, e , is well correlated to the O/F mass ratio, O_f , by a function:

$$e = 7.25 \{ 1 - [1 + (0.132 O_f)^{-1.0}]^{-0.1} \}$$

as shown in Figure 9. This effect may be due to having assumed the freestream gas to be pure water vapor in the calculations. The calculations must be rerun using the actual combustion products at each mixture ratio to verify if this turbulence dependance on mixture ratio is real. A representative comparison between the calculations and data in the rocket engine is given in Figure 10 for test 102 of 1977. It was not possible to obtain a reasonable comparison with the data of tests 119-122 which used helium coolant, for undetermined reasons.

In some of the tests it was necessary to assume that the entrainment rate increased at the beginning of the converging turn in order to obtain a comparison with the data. This was expressed as an effective increased freestream turbulence of Δe_t . This might be attributed to an unstable condition when a denser freestream gas is above a lighter boundary layer flow in the converging turn. Similar correction terms are necessary with 3-D turbulence models (Reference 47).

This extra "turning turbulence" is fairly well correlated by a "centrifugal force":

$$F_c = (\rho_g - \rho_c) \frac{v^2}{r} = \frac{G^2}{r\rho_g} \left[1 - \frac{\rho_c}{\rho_g} \right]$$

The function:

$$\begin{aligned} \Delta e_t &= 5.26 \{ [1 + (0.029 F_c)^8]^{1/8} - 1 \} && \text{for } \rho_g > \rho_c \\ &= 0. && \text{for } \rho_g < \rho_c \end{aligned}$$

well correlates the results, as shown in Figure 11. The aberrant point is due to test 8 of 1972 for which it was not possible to obtain a satisfactory comparison with the data. A typical comparison between the calculations and data, requiring this turning turbulence, is given in Figure 12 for test 102 of 1973. It should be noted that without the circumferential terms of Section 3.4.2 much less "turning turbulence" is required in the calculations to force a data comparison. However, this is not a suitable reason for discounting this effect.

In all of the calculations it was not possible to account for the rapid decrease of the wall temperature downstream of the throat. Since the wall temperature decreased even faster than the freestream gas static temperature, increased mixing with the freestream gases could not account for this decrease. Instead, it might be attributable to the static temperature change of the boundary layer gases as they accelerate. Since the present formulation lumps together all of the boundary layer gases, it would be difficult to incorporate such an effect into the model. A turbulent boundary layer model, which considers the velocity profile across the boundary layer, would be better suited to this task.

All of the calculated results above assume a recovery factor of zero, meaning that the entrained freestream gas is at its static temperature. However, upstream of the nozzle throat there is little difference between the static and stagnation temperatures, so that the choice of recovery factor is not very significant. Downstream of the throat the present model is unable to accurately predict the wall temperature, regardless of the choice of recovery factor, as described above.

A thorough description of the computer codes used in these calculations and a more thorough reporting of the calculated results is being prepared as a limited distribution second volume of a technical report on the project work to be submitted to Arnold Engineering Development Center.

5.0 CONCLUSIONS

It is possible to correlate the existing liquid film data from rocket engine tests using a model based on simple heat transfer correlations. In rockets with moderate combustion temperatures (2000-3500 K), both convective and radiant heat transfer must be considered. Knuth's criterion is useful for estimating the critical coolant flow rate to avoid droplet shearing from the liquid film, but is not definitive. Radiant burnout of the liquid film before complete evaporation is likely, however existing correlations for burnout are questionable. Downstream of the liquid film a standard gaseous film cooling correlation, modified to a differential form, is successful in calculating the wall temperatures upstream of the throat as the vapor mixes with the freestream gas.

REFERENCES

1. Cebeci, T. and Bradshaw, P. Phys. and comp. aspects of Convective Heat Transfer. Springer-Verlag, 1984.
2. Schlichting, H. Boundary Layer Theory. McGraw-Hill, 1981.
3. Landis, R.B. "Num. Sol. of Var. Prop. Turb. Boundary Layers with Foreign Gas Inj.". PhD. Thesis, UCLA, 1971.
4. Reynolds, W.C., et. al. NASA Memo 12-1-58W, 1958.
5. Kays, W.M. Convective Heat and Mass Transfer. McGraw-Hill, 1966.
6. Humble, L.V., et. al. NACA Report 1020, 1951.
7. Bartz, D.R. Jet Propulsion - ARS Journal, Jan. 1957, p. 49 .
8. Hartnett, J.P. et. al. Heat and Mass Transfer in Boundary Layers. Vol.1 . N. Afgan, editor, Pergamon, 1972.
9. Brunner, M. J. ASME Paper no. 64-WA/HT-50.
10. Rubesin, M.W. et al. Handbook of Heat Transfer. W.M. Rosenhow, editor. McGraw-Hill, Ch. 8, p. 171.
11. Kinney, G.R. et al. NACA Report 1087, 1952.
12. Knuth, E.L. "The Mechanics of Film Cooling". JPL Memo 20-85, September 1953.
13. Gater, R.A. et al. Jet Propulsion Center TM-69-1, Purdue Univ., contract Nonr 1100(21), 1969.
14. Hanratty, T.J. and Hersham, A. "Initiation of Roll Waves", AIChE Journal, vol. 7, no.3, Sept. 1961, p. 488.
15. Woodmansee, D.E. and Hanratty, T.J. "Base Film over which Roll Waves Propagate", AIChE Journal, vol. 15, no. 5, Sept. 1969, p. 712.
16. Tatterson, D.F., et. al. "Drop Sizes in Annular Gas-Liquid Flows", AIChE Journal, vol. 23, no. 1, Jan. 1977, p. 68.
17. Siegel, R. and Howell, J.R. Thermal Radiation Heat Transfer, second edition, Hemisphere, (1981), Section 17.5 - 17.6 .
18. Ziebland, H. and Parkinson, R.C. "Heat Transfer in Rocket Engines", AGARD-AG-148-71, Sept 1971, Ch.6 .
19. Burrows, M.C. NASA TND - 2541, 1964.
20. Monde, M. and Katto, Y. Int. Journal of Heat and Mass Transfer, Vol.21, 1978, p.295.
21. Katto, Y. and Ishii, K. 7th Int. Heat Transfer Conf., Vol.4, Toronto, 1978, p.435.
22. CPIA Liquid Propellants Manual, Chemical Propulsion Information Agency, Laurel, Md.
23. Zucrow, M.J. and Graham, A.R. Jet Propulsion - ARS Journal, June 1957, p. 650.
24. Zucrow, M.J. and Sellers, J.P. ARS Journal, May 1961, p. 668.
25. Warner, C.F. and Emmons, D.L. Trans. ASME Journal of Heat Transfer, May 1964, p. 271.

26. Gater, R.A. et al. Jet Propulsion Center TM-65-6, Purdue Univ., Contract Nonr 1100(21), October 1965.
27. Shembharkar, T. R. and Pai, B.R. Int. Journal of Heat and Mass Transfer, Vol. 29, No. 6, 1986, p. 899.
28. Economos, C. "The Comp. Turb. Boundary Layer with Mass Transfer". Phd thesis, Polytechnic Inst. of Brooklyn, 1968.
29. Kutateladze, S.S. et al. High Temperature (Soviet), Vol.1, Sept-Oct 1963.
30. Stollery, J.L. and El-Ehwany, A.A.M. Int. Journal of Heat and Mass Transfer, Vol.8, 1965, p.55 .
31. Hatch, J.E. and Papell, S.S, NASA TND-130, 1959.
32. Librizzi, J. and Cresci, R.J. AIAA Journal, Vol.2, No.4, April 1964.
33. Goldstein, R.J. et al. Trans. ASME Journal of Heat Transfer, August 1965, p.353 .
34. Carlson, L.W. and Talmor, E. Int. Journal of Heat and Mass Transfer, Vol.11, 1968, p. 1695. (or Ref. 8 p. 177)
35. Marek, C.J. Tacina, R.R. NASA TN D-7958, June 1975.
36. Hersch, M. ARS Journal. Vol. 31, (1961), p. 39 .
37. Talmor, E. A.I.Ch.E. Journal, Vol. 12, (1966), p. 1092 .
38. Goldstein, R.J. et al. Int. J. of Heat and Mass Transfer, Vol. 9, 1966, p.1341.
39. Burns, W.K. and J.L. Stollery, Int. J. of Heat and Mass Transfer, Vol. 12, 1969, p. 935.
40. Hartnett, J.P. et al Handbook of Heat Transfer. W.M. Rosenhow, editor, McGraw-Hill, Ch. 17, Figure 69, 1973.
41. Eckert, E.R.G. and Drake, R.M. Analysis of Heat and Mass Transfer. McGraw-Hill, 1972.
42. Ewen, R.L. "Hydrogen Film/Conductive Cooling", NASA CR-120926, November 1972 (Aerojet).
43. Rousar, D.C. and Ewen, R.L. "Hydrogen Film Cooling Investigation", NASA CR-121235, August 1973 (Aerojet).
44. Rousar, D.C. and Ewen, R.L. "Combustion Effects on Film Cooling", NASA CR-135052, February 1977 (Aerojet).
45. Morrell, G. NACA RM E51E04, July 1951.
46. Kesselring, R.C. et al. "Boundary Cooled Rocket Engines for Space Storable Propellants". NAS7-767, NASA-CR-129260, June 1972, (Rocketdyne).
47. Gibson, M.M. and Younis, B.A. "Modeling the Curved Turbulent Wall Jet", AIAA Journal, 20, no. 12, December 1982.

NOMENCLATURE

- $a = 0.6$ if $M_c < M_g$ or 0.35 if $M_c > M_g$
 A_w = absorptivity of chamber walls
 C = mass fraction
 C_f = skin friction factor $\equiv 2\tau_w/\rho_g U_g^2$
 C_p = specific heat per mass
 C_t = correction constant for turbulence
 D = diameter of combustion chamber at position x
 e = freestream turbulence intensity
 F = blowing parameter $= m_v/G$
 G = freestream mass flow per area $= \rho_g U_g$
 h = convective heat transfer coeff.
 $H = F/St$
 $K = G \mu_g^{0.25} / M_c^{1.25}$
 K_g = thermal conductivity of freestream gas
 K_t = correction factor for turning
 L = optical path length
 L_c = film-cooled length
 L_{eff} = average optical path length
 m = mass fraction in b.l. at x
 m_v = total liquid evaporation rate per surface area
 M = molecular weight
 \dot{M} = mass flow rate (per circumference) in b.l. at x
 n = no. of moles
 N = mole fraction of vapor
 Nu_D = Nusselt no. based on diameter $\equiv hD/K_g$
 Pr = Prandtl no of gas $\equiv \mu_g C_{pg}/K_g$
 P = absolute pressure
 P_g = partial pressure of species
 Q = heat flux
 r = radius of convergence arc in nozzle
 Re_D = Reynold's no based on diameter $\equiv G D/\mu_g$
 $Rex = \quad \quad \quad$ position $\equiv G x/\mu_g$
 St = Stanton no $\equiv h/(G C_{pg})$
 T = absolute temperature
 T_c = temperature of liquid or gaseous coolant
 T_v = saturation temperature of coolant
 $\Delta T = T_g - T_v$
 U = axial velocity

x = axial position
 x' = x corrected for developing pipe flow
 X = dimensionless distance = Kx
 y = distance from wall

Greek Symbols:

δ = boundary layer thickness
 ϵ = gas emissivity
 λ = latent heat of vaporization of coolant
 $\lambda^* = \lambda + C_{pl}(T_v - T_c)$
 γ = specific heat ratio
 Γ = liquid coolant mass flow rate per circumference
 η = film cooling effectiveness
 ρ = mass density
 ρ_{opt} = optical density $\equiv PgL$
 σ = surface tension of coolant or Stephan's const.
 μ_g = dynamic viscosity
 ν = kinematic viscosity $\equiv \mu/\rho$

subscripts:

bl - boundary layer
bo - burnout point
c - coolant, gaseous or liquid
conv - convective
cr - at transition to "large waves"
g - freestream gas
l - coolant liquid
o - for "dry-wall" conditions, without transpiration
rad - due to radiation
v - vapor
w - evaluated at wall

superscript:

() - properties evaluated at mean temperature $(T_g + T_w)/2$

Figure 9. Freestream Turbulence
vs. Mixture Ratio

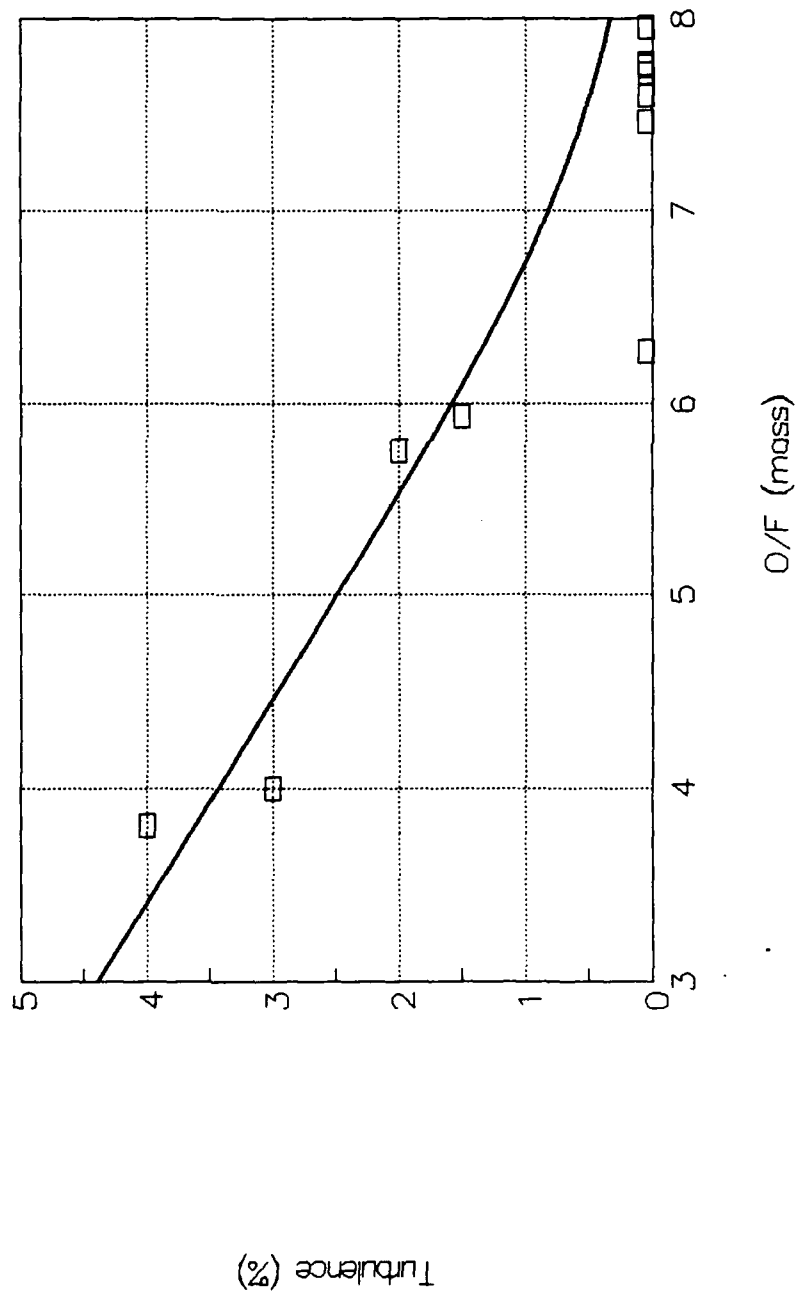


Figure 10. Rousar and Ewen

NASA CR-135052, 1977, test 102

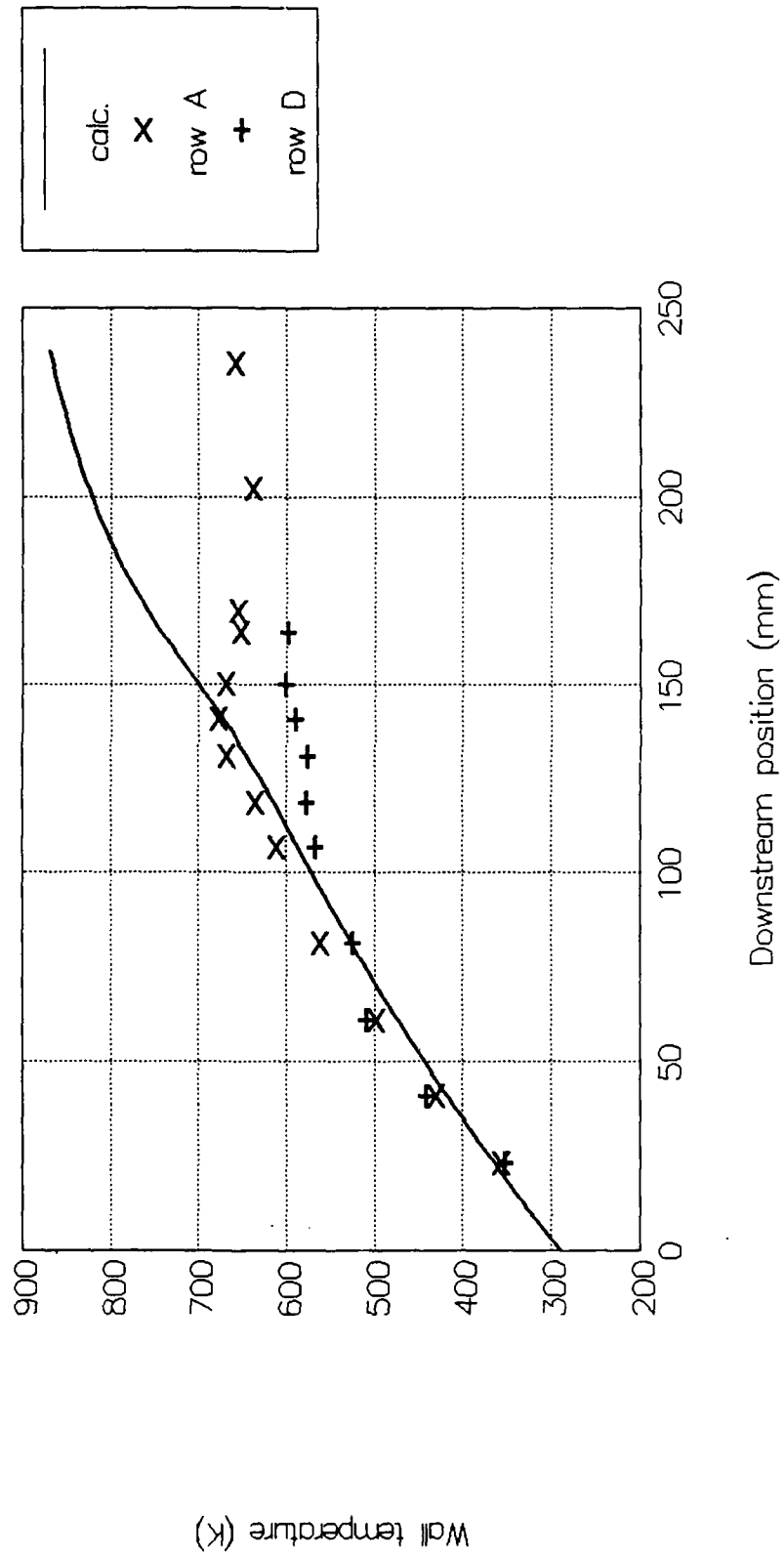


Figure 11. Turn Turbulence vs.

Centrifugal Force

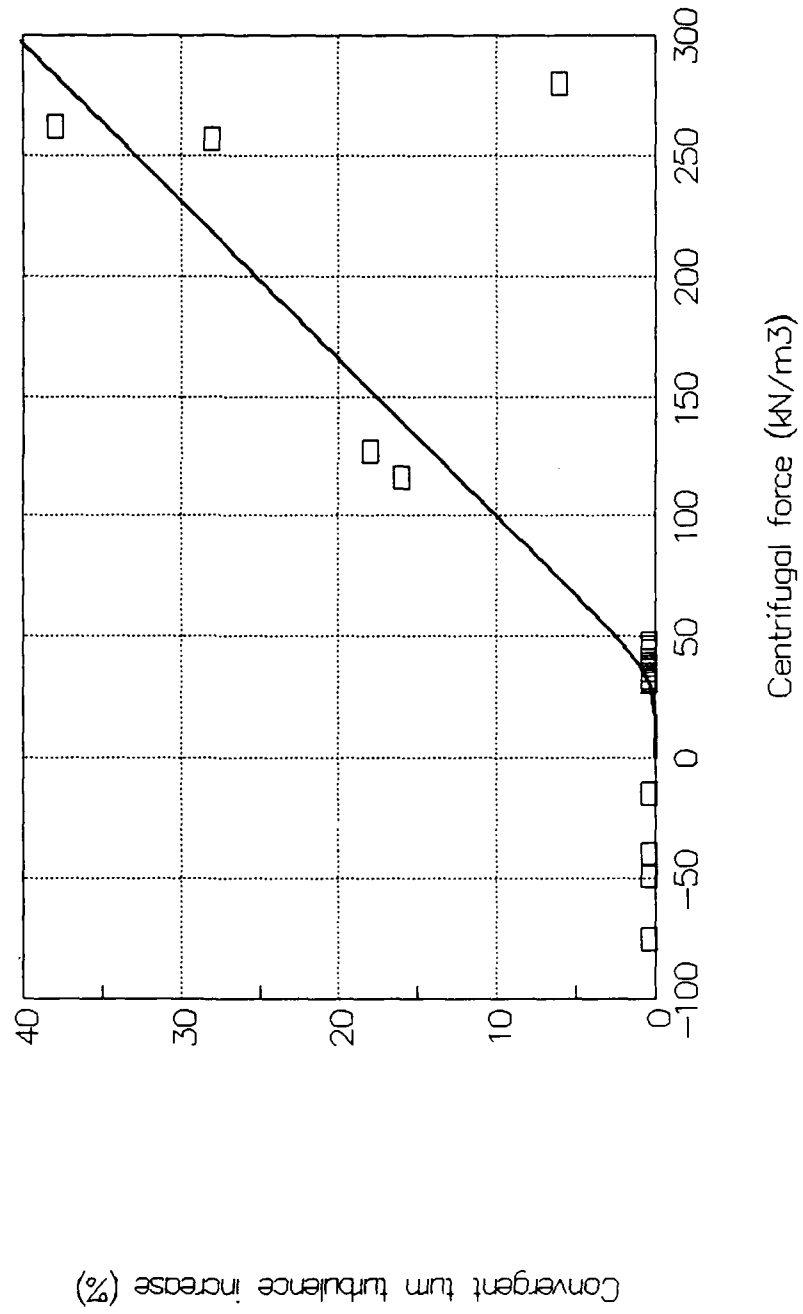
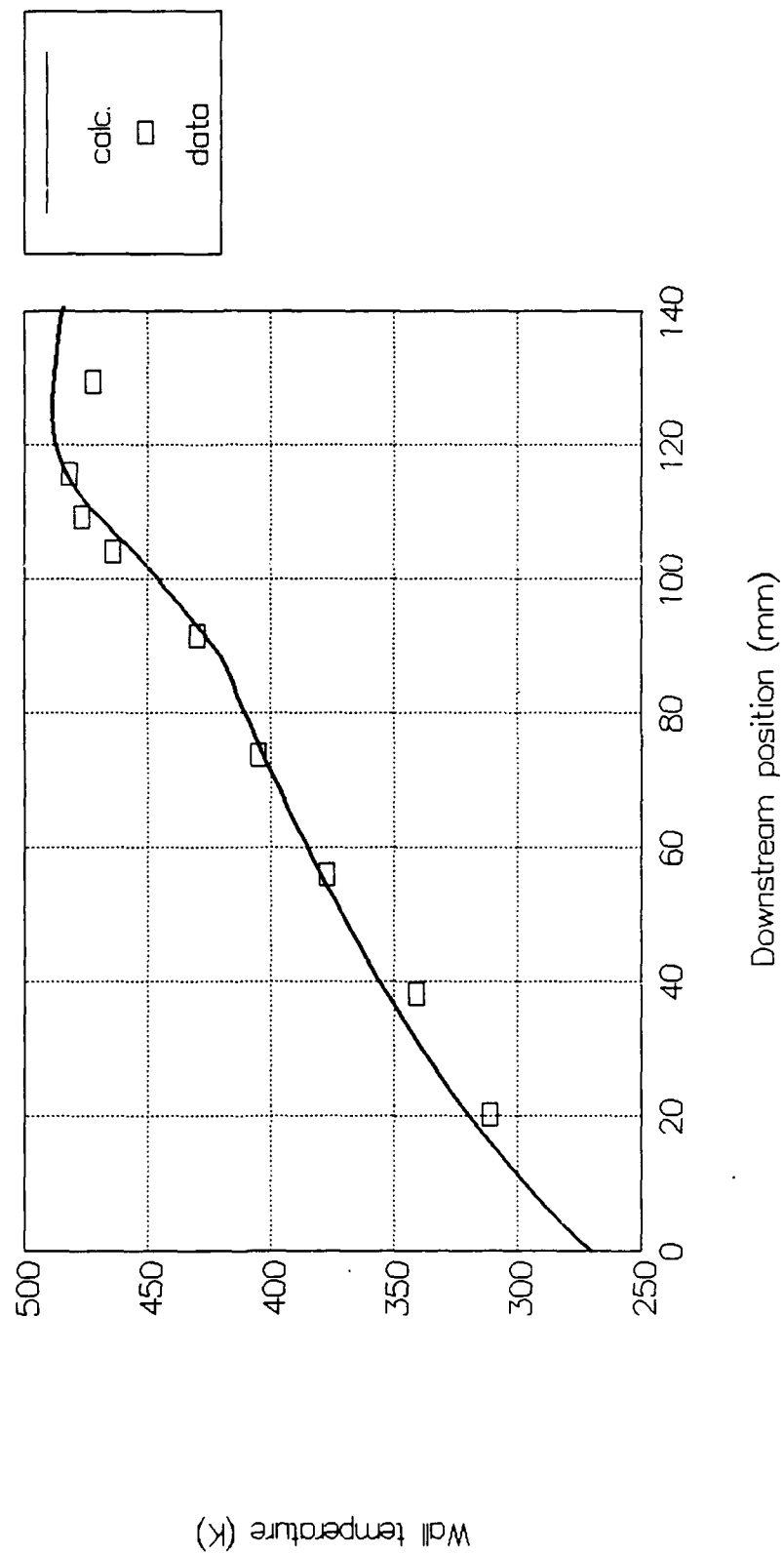


Figure 12. Rousar and Ewen
NASA CR-121235, 1973, test 102



ESTIMATION OF AUTOCORRELATION AND POWER SPECTRAL DENSITY FOR RANDOMLY SAMPLED SYSTEMS

S. A. PATIL

Tennessee Technological University, Cookeville, Tennessee 38505

Abstract. Spectral density estimates and autocorrelation estimates are proposed under random sampling plans. The estimators are applied to simulated population of Gaussian process. The laser velocimetry data obtained in the Laboratory under practical conditions are tested for randomness of the arrival times of the process. Different spectral density estimators based on direct Fourier Transform as well as autocorrelation based approaches are developed when the samples are obtained randomly. The estimators suggested by Gastor & Roberts (1975, 1977), Roberts (1986) and Mayo (1973) are applied to sinusoidal, Gaussian and LDV data. Merits and shortcomings of these estimators to LDV data are discussed and a suitable estimator is recommended for randomly sampled data.

I. INTRODUCTION

Techniques for the estimation of the spectrum of randomly sampled records have been investigated over the last two decades. In typical applications the sampling instants are best approximated by a poisson distribution.

Conventional methods of spectral estimation require constant sampling rates. These must be modified to suit randomly sampled records. The various techniques for spectral estimation are compared with respect to accuracy and computational speed.

The computation of spectra is generally done through one of the two methods. In the direct approach (Cooley & Tukey algorithm, 1) the discrete fourier transform of the discretized data is applied. The square of the magnitude of the Fourier transform then gives the spectrum. A suitable window function is used to avoid leakage. In the indirect approach (Blackman & Tukey algorithm, 3) first the correlation function is estimated, a window is applied and then the fourier transform is taken. To reduce variability the record is divided into a number of blocks and then averaged to give the spectrum.

For the data sampled at constant rates the fast fourier transform (FFT) algorithm significantly reduces the computation times. Such an algorithm has not been developed for randomly sampled records and therefore the computation of the spectrum is time intensive. Present research is centered about trying to obtain algorithms that

resolve the random arrival times to equispaced set of data or correlation estimates so that the FFT algorithm may be applied.

The spectral estimators involving the direct transform of the time series are compared with those obtained from correlation based approaches. It is seen that an additional variability is introduced due to the random nature of the sampling instants. Extensive simulation tests are done over a wide range of sampling instants and the bandwidth of the signal. Several types of signals are used and the behavior of the algorithms is seen to be dependent on the nature of the signal.

A typical application of the analysis of randomly sampled signals is the laser anemometer in fluid mechanics which measures the velocity of dust particles as they randomly cross a narrow focused ray of light. At times when the particles are sparse (corresponding to low sampling rates), the spectral density cannot be estimated by conventional algorithms using regular sampling. In other cases it may be more appropriate to randomly sample a broadband continuous signal to avoid impractical large sampling rates. Unfortunately we still do not have fast estimators which could handle randomly sampled data effectively at high aliasing factors. The state of art research is focused on obtaining consistent estimators with good alias free properties and secondly practical means of implementing them to random signals.

Initial research was centered about the study of the alias free properties of the poisson point process and the obtaining of consistent estimators (references 4,9,10,11). However research in the practical implementation of these estimators has been realized only over the last decade or so (references 1,2,3,5,6,12,16).

In this report a number of algorithms are performed and compared for aliasing, accuracy and computational speed. These algorithms are tested using both deterministic and random data and actual LV data. The autocorrelation and spectral density; also the aliasing, variability, consistency and frequency discrimination properties of these algorithms are studied in detail.

II. PERIODOGRAM APPROACHES

In this method the power spectrum is found by applying the Discrete Fourier Transform to the time series. A suitable window is applied to avoid leakage, Gastor & Roberts (1). For equispaced records the estimator is

$$\hat{s}(w) = \frac{1}{T} \left| \int_0^T x(t) D(t) \delta(t - t_n) e^{-j\omega t} dt \right|^2 \quad (1)$$

where δ is the dirac delta function, T is the total observation time, D(.) is a data

window. The discrete form of the above estimator is

$$\hat{s}_1(w) = \frac{1}{T} \left| \sum_i x(t_i) D(t_i) e^{-j\omega t_i} \Delta t_i \right|^2 \quad (2)$$

As in, Gastor & Roberts (1), if we assume that the average spacing between samples is $\frac{1}{\nu}$, where ν is the average sampling rate then

$$\hat{s}_1(w) = \frac{1}{\nu^2 T} \left| \sum x(t_i) D(t_i) e^{-j\omega t_i} \right|^2 \quad (3)$$

The above estimator guarantees positive spectral values but the accuracy is poor. The estimate is accurate at only very high sampling rates and there is a constant false shift in the spectrum. The variability of the estimate is high and it is not consistent for random data, as shown in Bell (2). Further it is computationally intensive.

Gastor & Roberts (1) modified this estimator as follows:

$$\begin{aligned} \hat{s}_1(w) &= \frac{1}{\nu^2 T} \left| \sum x(t_i) D(t_i) e^{-j\omega t_i} \right|^2 \\ &= \frac{1}{\nu^2 T} \left\{ \sum_{i \neq j} \sum x(t_i) x(t_j) D(t_i) D(t_j) e^{-j\omega(t_i - t_j)} + \sum_i x^2(t_i) D^2(t_i) \right\} \quad (4) \end{aligned}$$

$$\begin{aligned} \hat{s}_2(w) &= \hat{s}_1(w) - \frac{1}{\nu^2 T} \sum_i x^2(t_i) D^2(t_i) \\ &= \frac{1}{\nu^2 T} \left| \sum x(t_i) D(t_i) e^{-j\omega t_i} \right|^2 - \frac{1}{\nu^2 T} \sum_i x^2(t_i) D^2(t_i) \quad (5) \end{aligned}$$

The second term on the right hand side (RHS) was subtracted to remove the constant false shift in the spectrum. In Gastor & Roberts (1), it is shown that the bias of the estimator approaches 0 as N approaches ∞ . Also the variance is of the form

$$\text{Var}\{\hat{s}_2(w)\} = \alpha + \frac{\beta}{\nu} + \frac{Y}{\nu^2}$$

and

$$\text{Var}\{\hat{s}_2(w)\} \rightarrow \alpha \text{ as } N \rightarrow \infty \quad (6)$$

The variance of the estimate is seen to be high, consequently averaging needs to be done over several blocks to reduce the variability.

In the slotted periodogram type of approach, Bell (2), the time scale is divided into N slots over the observation time T. Thus each slot is of width Δt ,

$$\Delta t = \frac{T}{N} \quad (7)$$

The maximum frequency is thus,

$$f^* = \frac{1}{2\Delta t} \quad (8)$$

The spectral estimate is then obtained by an N point Fourier transform of the data. The FFT algorithm may be applied because the slots are equi-spaced.

The accuracy of the estimate in the slotted periodogram approach improves with an increase in the sampling rate. The computation time is less, but for a reasonable accuracy a large number of samples are needed. The spectral estimate for this method is

$$\hat{s}_3(w) = \frac{1}{T} \left| \sum x(t_i) D(t_i) e^{-j\omega t_i} \right|^2, \quad (9)$$

$$t_i = i\Delta t; \quad i = 0, 1, \dots, N-1$$

III. CORRELATION BASED APPROACHES

The power spectral density by the correlation method or indirect method is by first computing the autocorrelation function. The autocorrelation function $R_{xx}(\tau)$ of a signal $x(t)$ is given by

$$R_{xx}(\tau) = \lim_{T \rightarrow \infty} \frac{1}{T - \tau} \int_{-\frac{T}{2}}^{\frac{T}{2}} x(t)x(t + \tau) d\tau, \quad (10)$$

τ = time lag

T = Total observation time.

The spectrum is then given by

$$s_{xx}(w) = \int_{-\infty}^{\infty} R_{xx}(\tau) e^{-i\omega\tau} d\tau \quad (11)$$

Gastor & Roberts (3) give a discretized form of the above equation,

$$\hat{s}_4(w) = \frac{4}{\nu^2 T} \sum_{j < k}^N \sum_{j < k}^N D(t_k - t_j) \cos w(t_k - t_j) x(t_j) x(t_k) \quad (12)$$

where N is the number of samples over time T , $D(\cdot)$ is a data window. A similar estimator is also reported by Masry & Lui (4). The mean square error of the estimator is defined as

$$e_n^2(w) = E[s_N(w) - \hat{s}(w)]^2 \quad (13)$$

then Masry & Lui prove that the estimate is mean square consistent for all positive w as N approaches ∞ . The estimator is unbiased and the variance of the estimator is

$$\text{Var}\{\hat{s}_4(w)\} \cong \frac{3\tau_m}{4T} \left[s(w) + \frac{\sigma^2}{2\pi\nu} \right]^2 \quad (14)$$

τ_m = max lag time

σ = standard deviation of signal

For finite T the estimator has more terms for shorter lags because of neglecting the $(T-\tau)$ term in equation (10). However for $T \gg \tau$ equation (12) gives a good approximation since the effect of neglecting the $(T-\tau)$ term becomes negligible.

This estimate requires $\nu^2 T \tau_m$ crossproducts and is computationally intensive, but has been seen to be the most accurate for the same record length N .

There have been efforts to speed up the estimate $\hat{S}_4(w)$ by dividing the correlation plane into N slots of equal width Δt . If τ_m is the maximum lag time then

$$\Delta\tau = \frac{\tau_m}{N} \quad \text{and} \quad f^* = \frac{1}{2\Delta\tau}. \quad (15)$$

The correlation estimates are then equispaced at

$$\tau_k = k\Delta\tau; \quad k = 0, 1, \dots, N-1 \quad (16)$$

and are

$$R(\tau_k) = \frac{1}{N_k} \sum_{i,j} x(t_i) x(t_j) \quad (17)$$

where the summation is over crossproducts such that $(k - \frac{1}{2})\Delta\tau \leq t_j - t_i < (k + \frac{1}{2})\Delta\tau$ and N is the number of cross products in the k th slot.

The spectral estimator can then be obtained by an FFT:

$$\hat{s}_5(w) = \frac{1}{T} \sum R(t_i) e^{-j w t_i}; \quad t_i = i \Delta \tau \quad (18)$$

The slotting reduces the computation time of $\hat{S}_4(w)$ (from $2N^2M$ computations) to $\frac{MN}{2}$ computations for $\hat{S}_5(w)$.

Mayo (6) describes a similar slotting procedure, except that the slots are integral values apart and the spectral estimate is given by a form similar to equation (18),

$$\hat{s}_6(w) = \Delta \tau \left[c(1) + 2 \sum_{\kappa=2}^k w(\kappa) c(\kappa) \cos \left(i \frac{\kappa - 1}{k} \pi \right) \right] \quad (19)$$

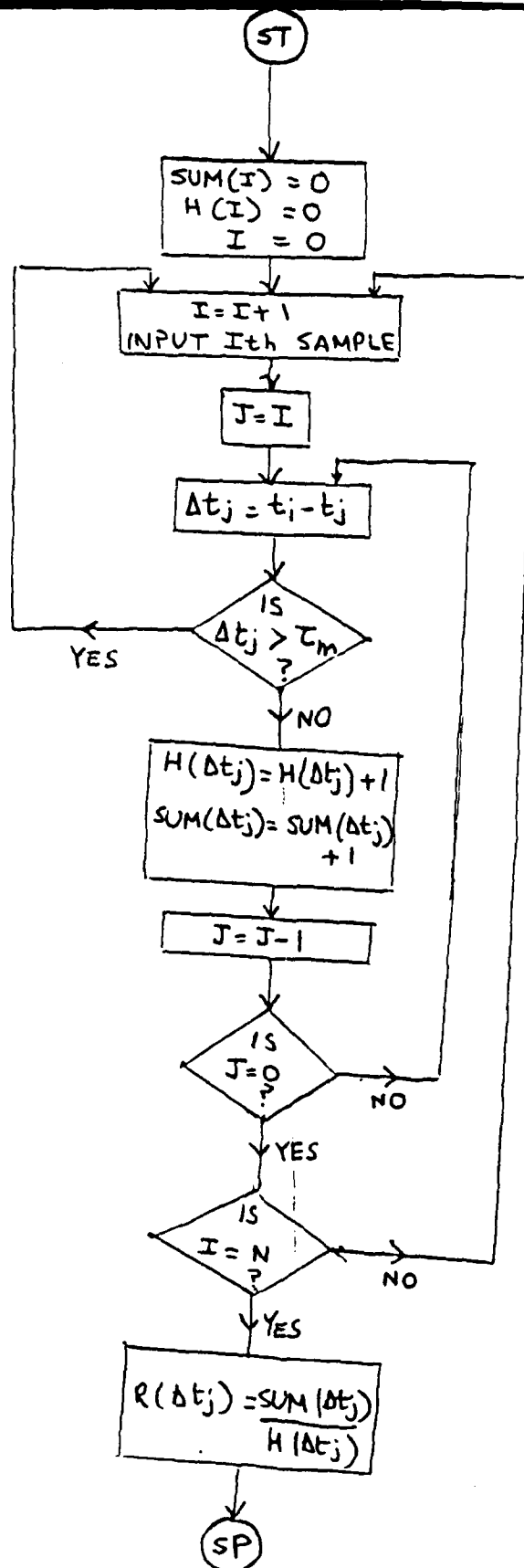
The spectrum estimate $\hat{S}_5(w)$ is seen to be sensitive to the choice of slot width, $\Delta \tau$. A very small value of $\Delta \tau$ leads to scattering in the tail of the spectrum; a large value of $\Delta \tau$ may lead to an aliased estimate. Thus one has to be careful in selecting $\Delta \tau$. The correlation based slotting technique seems to be the best compromise in accuracy and speed.

A practical means of implementing the correlation slotting algorithm can be conceived as in Plumlee (7). Here basically the latest sample value recorded is used to update the correlation values by checking the time differences w.r.t. the previous samples. The velocity data samples are processed serially as they are recorded. Each sample is first correlated with itself to update the zero lag correlation value. The time difference with the previous element is used to update the corresponding correlation lag value. This process of finding time differences with elements down the time history, and updating corresponding correlation lag values, is continued until the time difference exceeds the maximum lag time. At this point the next sample is inputted and the process is repeated. Thus when all the samples are obtained the correlation array is completed. The power spectrum can then be obtained from equation (19). A simple flowchart of the method is given in Figure 1.

IV. COMPUTATION OF PARTICLE ARRIVAL TIMES

The sampling instants are taken to be generated by a poisson point process on $[0, \infty)$. For such a process the inter arrival times are exponentially distributed. Thus if ν is the mean rate then the inter-arrival times, which are independent identically distributed (i.i.d.) random variables, are given by

$$\alpha_n = -\frac{1}{\nu} \ln(1 - a_n) \quad n = 1, 2, \dots \quad (20)$$



Flow-chart for :
Real-time version of Mayo's algorithm

Figure 1

where a_n are random numbers uniformly distributed between [0,1). The sampling instants, as in Patil (16), are then given by,

$$\begin{aligned} t_n &= t_{n-1} + \alpha_n \\ t_0 &= 0 \end{aligned} \quad (21)$$

The α_i 's are independent and exponentially distributed with mean $\frac{1}{\nu}$. A chi-square test on the α_i 's is performed, which are then used as the required sampling instants in the various algorithms. The classes for the chi-square test were obtained such that each class had approximately same number of samples. Thus because of the exponential nature of the distribution the width of each class was different. In a typical test the observed χ^2_{obs} value was 7.73 while the theoretical value of χ^2_{th} is 11.07. Thus the inter-arrival times are verified to be exponentially distributed. This can be indeed seen from Figure 2.

V. DATA GENERATION

The various types of data used for testing the algorithms was:

1. sine wave
2. gaussian data
3. first and second order random data
4. actual LV data

Sine data may easily be generated. If $t(i)$ are the sample arrival times then the sample values are given by,

$$x(i) = \sin(2 \times \pi \times f \times t(i)) \quad (22)$$

where f is the frequency of the sine wave.

For gaussian and first and second order random data a near continuous signal comprising of very closely spaced points in time is generated. This is the primary time series. This near continuous signal is then seeded with poisson instants to give the secondary time series. The sample values of primary time series are at integral values but the poisson instants are arbitrary real numbers. Here we have taken one out of every ten samples of the primary series giving an accuracy of upto the first decimal place at the poisson instant. The primary time series consists of equispaced instants and a FFT algorithm applied to that gives the actual or exact reference spectrum.

The simulation of the gaussian process with independent components can be obtained by using the Box-Muller transform, viz.

$$\begin{aligned} x_1 &= (-\ln U_1)^{\frac{1}{2}} \cos(2\pi U_2) \\ x_2 &= (-\ln U_2)^{\frac{1}{2}} \sin(2\pi U_2) \end{aligned} \quad (23)$$

Chi Square Test For Inter-Arrival Times Data Number: 10,000

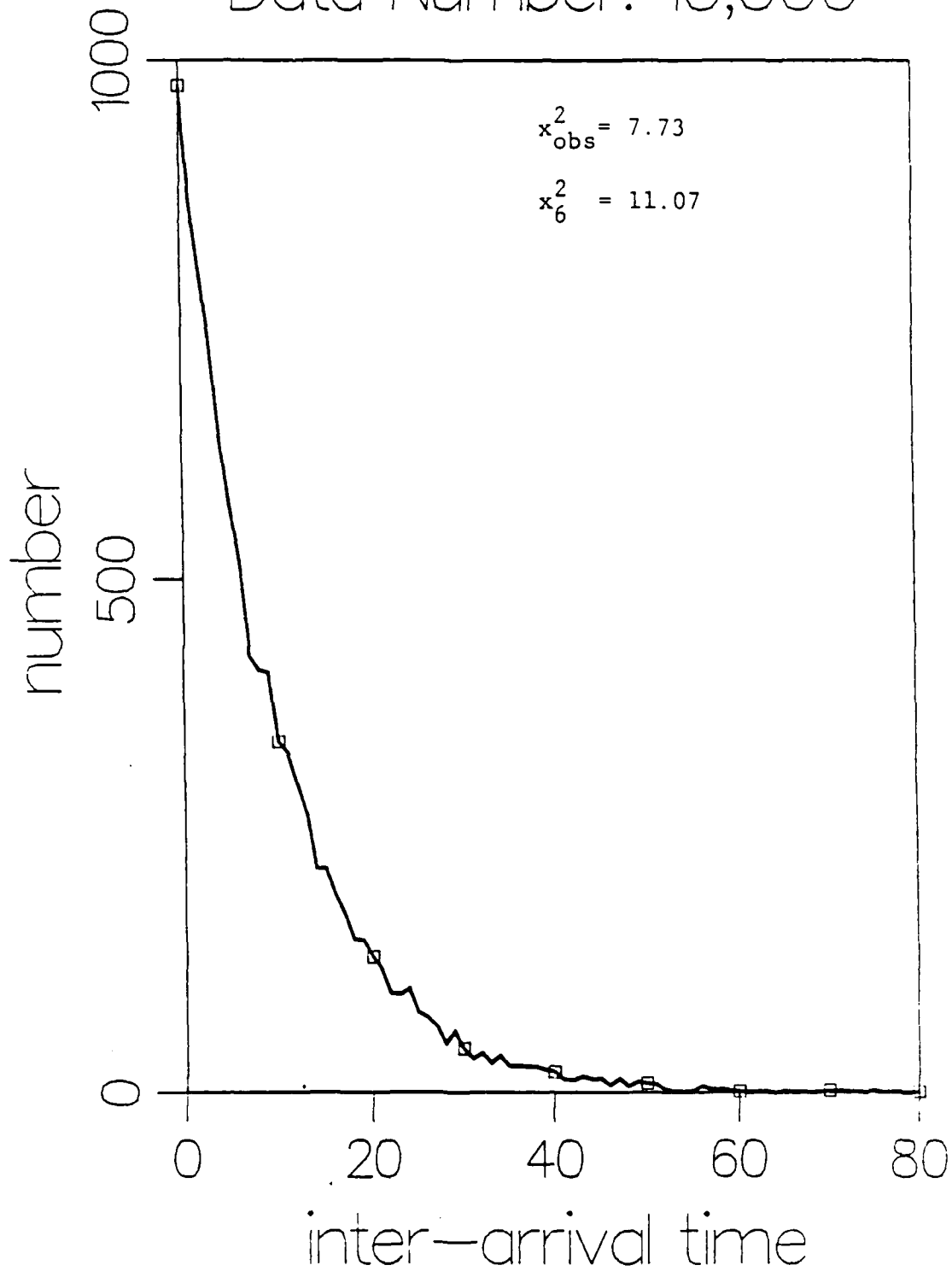


Figure 2

where U_1 and U_2 are uniform random variables in $[0,1)$ and are obtained by using pseudorandom numbers generating technique. A chi-square test is then performed on the gaussian samples. A total of 19 classes was used. In a typical case the observed χ^2_{obs} value was 19.65 while χ^2_{th} is 30.14, thus giving a positive test. Figure 3 shows that the samples are indeed $N(0,1)$.

First and second order random data may be generated by using an autoregressive model of order 2, Tropea (15). The required model is

$$z_k = \phi_1 z_{k-1} + \phi_2 z_{k-2} + a_k$$

$$\phi_1 + \phi_2 < 1, \quad \phi_2 - \phi_1 < 1, \quad -1 < \phi_2 < 1 \quad (24)$$

where $a_k \sim N(0, \sigma_a^2)$ is a gaussian random number and z_k 's are generated recursively. It can be easily shown that the resulting time series has energy up to 0.5 Hz. and the spectrum is given by,

$$s(f) = \frac{2\sigma_a^2}{1 + \phi_1^2 + \phi_2^2 - 2\phi_1(1 - \phi_2) \cos 2\pi f - 2\phi_2 \cos 4\pi f} \quad (25)$$

where σ_a^2 is the variance of a_k .

The above time series are then seeded with the poisson instants.

VI. VARIABILITY OF ESTIMATES

It is seen that the mean estimation error is the same for both direct and correlation based approaches. This is shown in the sample plots Figure 4 and Figure 6. The mean error goes to zero as the number of samples are increased.

The variability plots shown in Figure 5 and Figure 7 illustrate the fact that the direct approach has greater variability. In the direct approach the variability is about 100 times that in the correlation based approach. The expected error for the correlation approach as in (3) is,

$$e = \sqrt{\frac{3\tau_m \nu}{N}} \left[s(w) + \frac{\sigma^2}{2\pi\nu} \right] \quad (26)$$

where σ is the standard deviation of the signal and τ_m is the max. lag time. However this is true only for $T \gg \tau_m$, so that there are enough averages for each lag value estimate.

Though the direct periodogram approach is twice as fast as the correlation slotting technique, more data is needed in the direct approach to reduce the variability. Thus there is a trade off in speed and accuracy of estimate.

chi *2 test
gaussian data
data samples: 100,000

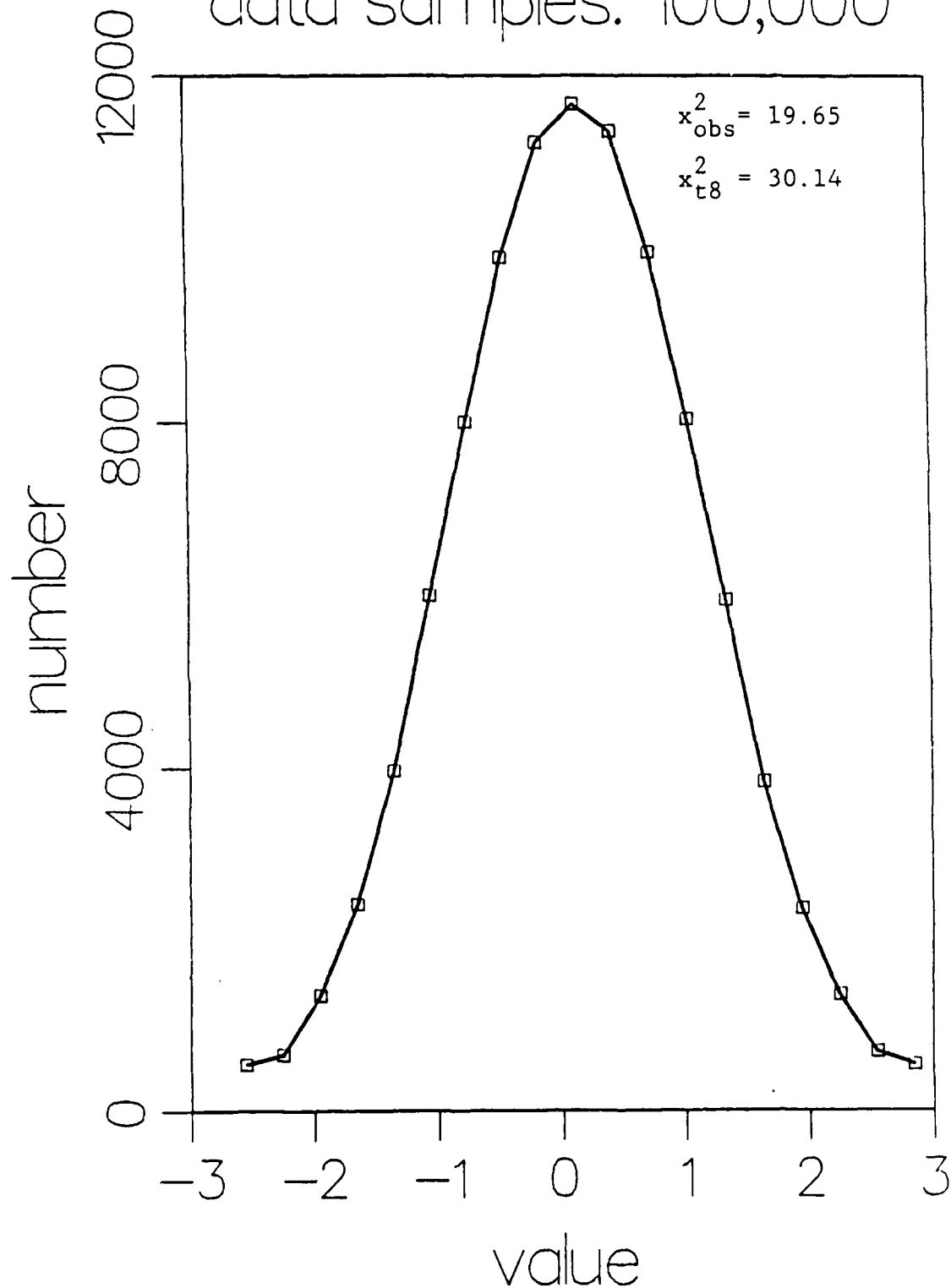
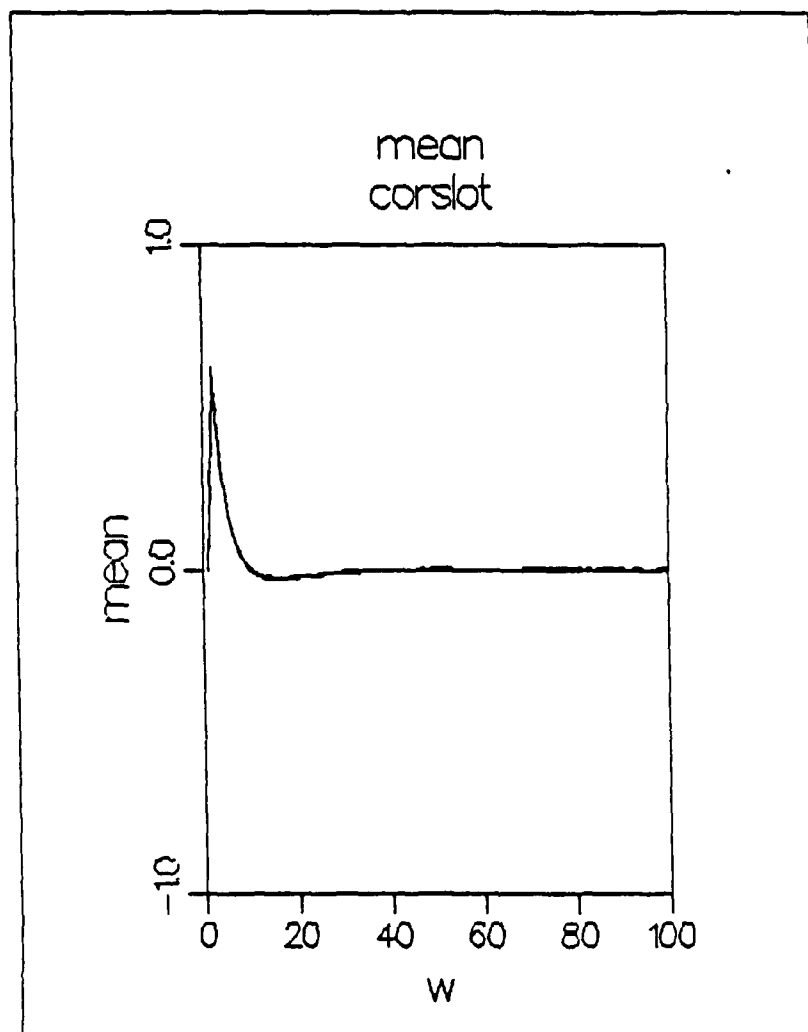


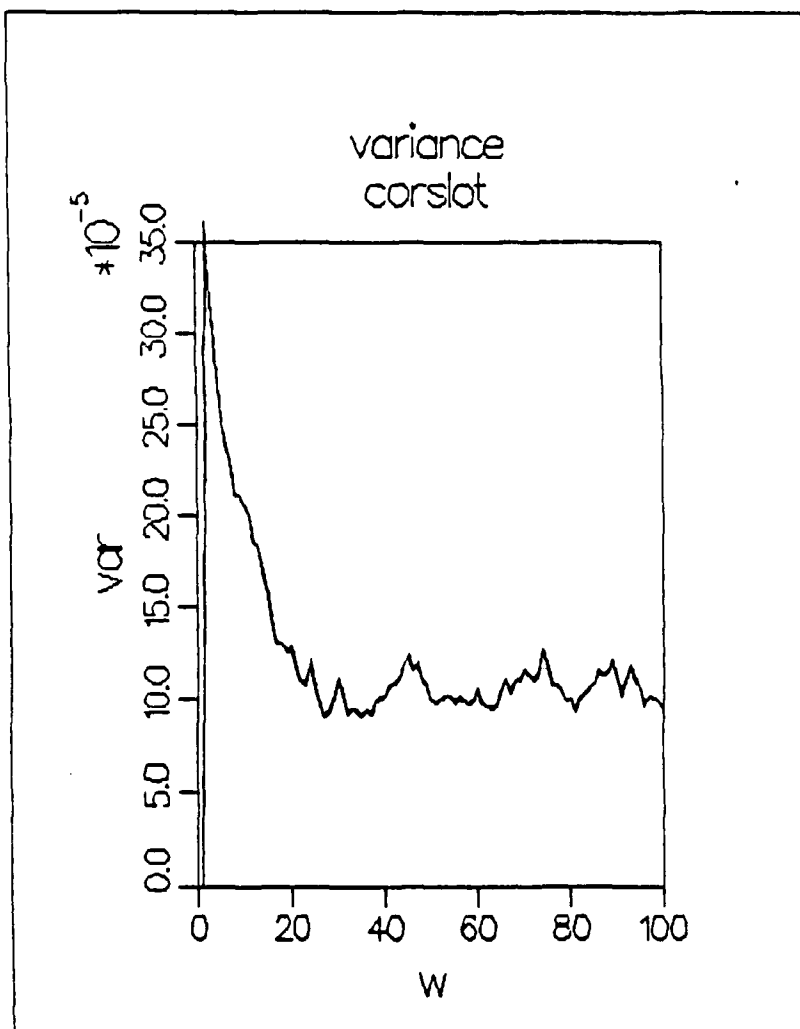
Figure 3



Mean error curve \pm correlation slotting technique

aliasing factor = 1
 samples / block = 200
 slot width = 1 second
 frequency range = (0, 0.5) Hz.

Figure 4



Error variance curve - correlation slotting

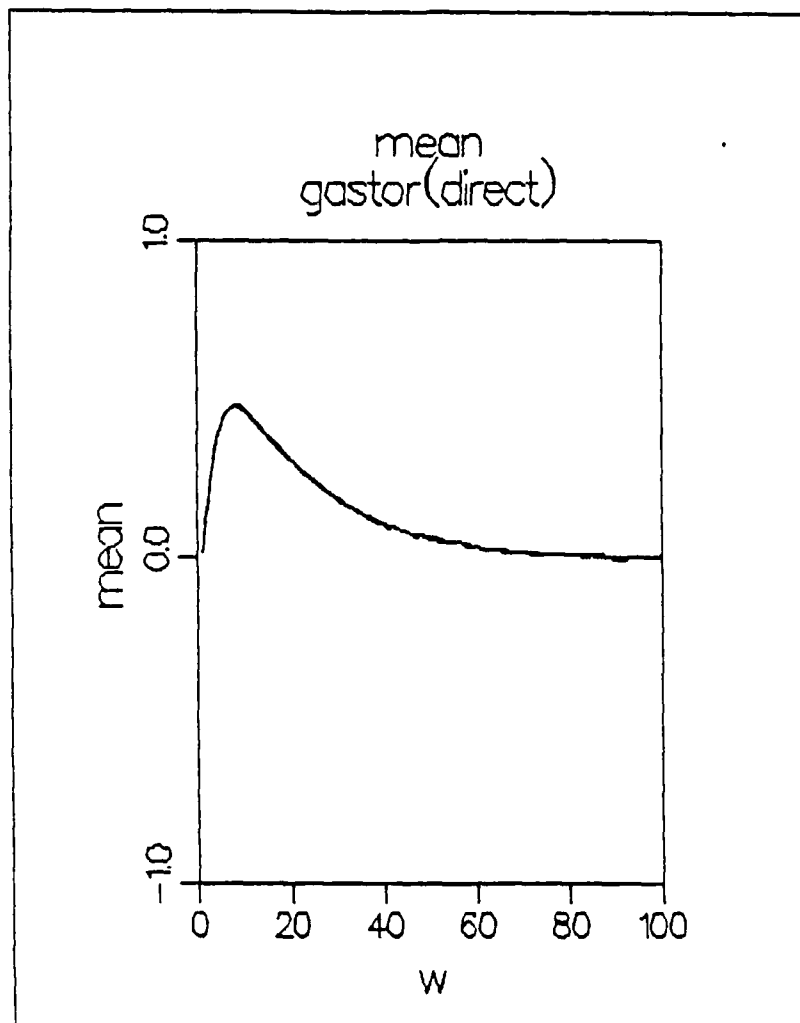
aliasing factor = 1

number of slots = 200

slot width = 1 second

frequency range = (0,0.5) Hz.

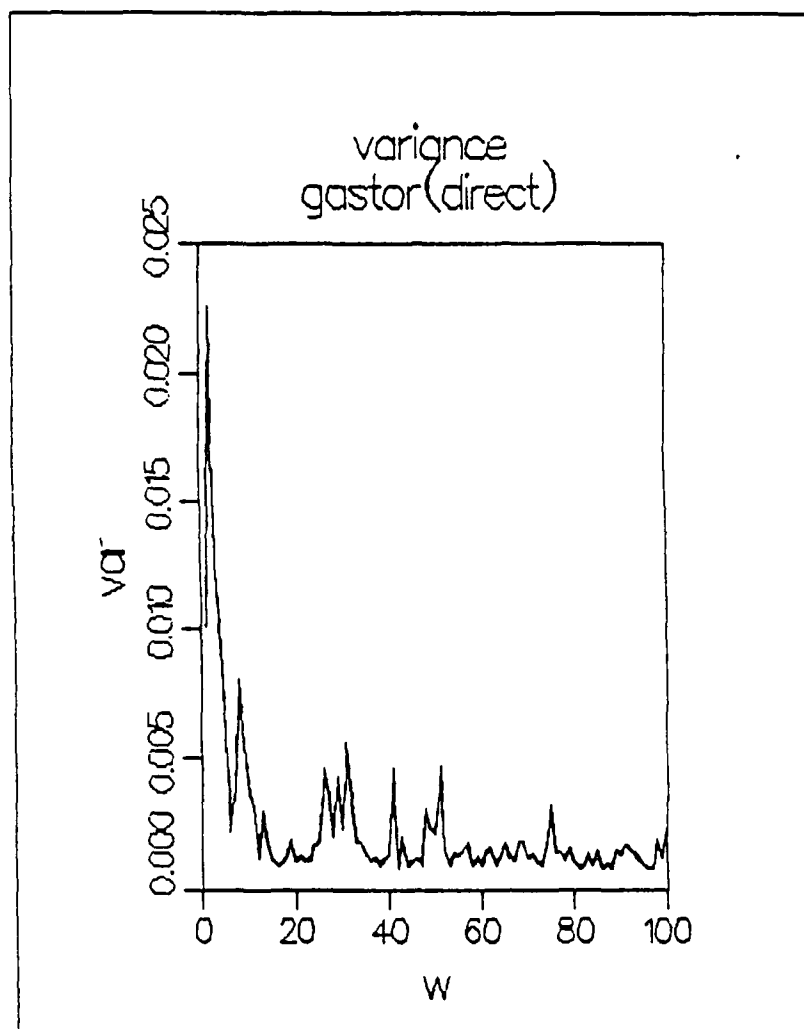
Figure 5



Typical Mean Error Curve

aliasing factor = 1
 samples/block = 280
 frequency range = (0.0.5) Hz.
 number of averages = 100

Figure 6



Typical error variance curve

aliasing factor = 1
 samples/block = 200
 frequency range = (0,0.5) Hz.
 number of averages = 100

Figure 7

VII. DISCUSSIONS

All the algorithms have an improvement in performance when the sampling rate is increased. The slotting type of algorithms give better results as the number of crossproducts in each slot is increased.

The correlation slotting algorithm is equivalent to Mayo's algorithm. The process of finding the correlation array in each case is the same except that Mayo talks of integral slot widths. The correlation slotting method uses the FFT to obtain the spectrum. This may be shown to be similar to equation (19) used by Mayo. The FFT is given by,

$$s(i\Delta w) = \Delta\tau \sum_{\kappa=-\frac{(k-1)}{2}}^{\frac{(k-1)}{2}} c(\kappa) e^{-j\frac{2\pi i\kappa}{k} w(\kappa)}$$

The correlation function is even i.e. $c(-\kappa) = c(\kappa)$, $\forall \kappa$

k = Total lag values (odd)

$\Delta\tau$ = slot width

Hence

$$\begin{aligned} s(i\Delta w) &= \Delta\tau \left\{ c(0) + 2 \sum_{\kappa=1}^{\frac{(k-1)}{2}} c(\kappa) e^{-j\frac{2\pi i\kappa}{k} w(\kappa)} \right\} \\ &= \Delta\tau \left\{ c(0) + 2 \sum_{\kappa=1}^{\frac{(k-1)}{2}} c(\kappa) \cos\left(\frac{2\pi i\kappa}{k} w(\kappa)\right) \right\}. \end{aligned}$$

In Mayo(6) equation (19), the correlation array is $c(1)$, $c(2)$, \dots , $c(k)$ where $c(1)$ is the zero'th lag and so on. Thus the above equation reduces to

$$s(i\Delta w) = \Delta\tau \left\{ c(1) + 2 \sum_{\kappa=2}^{\frac{(k+1)}{2}} c(\kappa) w(\kappa) \cos \frac{2\pi i(\kappa-1)}{k} \right\}$$

Putting $\frac{k+1}{2} = L$, we get

$$s(i\Delta w) = \Delta\tau \left\{ c(1) + 2 \sum_{\kappa=2}^L c(\kappa) w(\kappa) \cos \frac{\pi i(\kappa-1)}{\frac{2L-1}{2}} \right\}$$

as given by Mayo in equation(19) except there is a slight difference in the denominator of the last item.

For sine type of data the correlation based slotting algorithm is seen to perform well even at sampling rates as low as (1/200)th of the Nyquist frequency, for relatively short record lengths. This is seen in Figure 8. The direct periodogram approach, shown in Figure 9 shows more scattering at low sampling rates. The lag approach (equation 12), as shown in Figure 10, also has scattering especially at aliasing factor of 40 or more. The correlation slotting algorithm also is seen to have better frequency discrimination property.

However, for gaussian data relatively longer record lengths are needed for acceptable accuracy, Figure 11. All algorithms are seen to deteriorate in their performance. At low aliasing the direct periodogram approach is seen to give best results. Further it is seen that the correlation slotting algorithm has a number of negative spectral points at the point of discontinuity in the actual spectrum (we have used brick wall filtering to have a band limited gaussian spectrum). This has not been reported earlier and needs to be studied more.

A similar observation is with random data from the auto regressive model, Figure 12. It seems that all algorithms tend to have more scattering at high aliasing. Again the direct periodogram approach performs best at low aliasing.

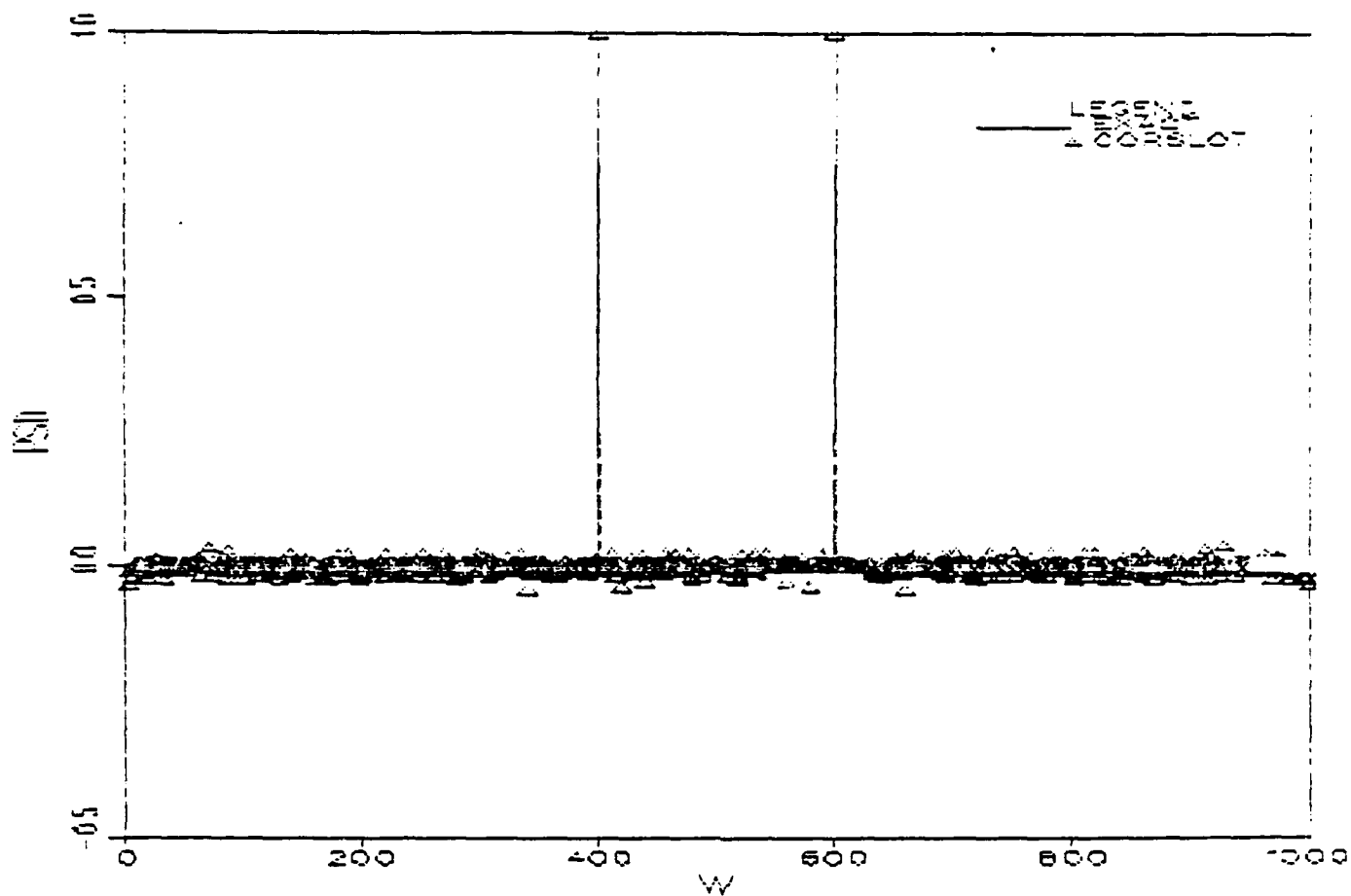
The correlation based slotting algorithm is seen to have more scattering and negative spectral values if the slot width is chosen too small ie. $\Delta\tau \ll \frac{f_{max}}{2}$. Thus an apriori knowledge of the maximum frequency content (approximate) of the spectrum is needed.

The randomness of the inter-arrival times of the LV data was verified by performing a test for exponential distribution. Figure 13 shows the estimated spectrum for LV data using the correlation based slotting technique. The correlation between the velocity values and the time instants was seen to be close to 0, as expected. The LV data analyzed comprised of 147 blocks of 1000 samples each. The blocks were from 1 second up to 110 seconds in time duration. In the first case the spectrum was averaged over 15 blocks (each less than 2 sec.). Similarly blocks of the same order of time duration were grouped and the spectrum was averaged over them. From initial observations at 6.67 KHz. and 1.33 KHz. it seemed that there was too much scattering in the high frequency region. So the slot width was subsequently increased. The spectrum in Figure 13 seems to be a close estimate of the actual spectrum. This is verified using the direct periodogram approach which gave similar results (Figure 14). This confirms that LV data has frequency components up to about 500 Hz. and can be seen by comparing graphs in Figure 13 and Figure 14.

VIII. CONCLUSION

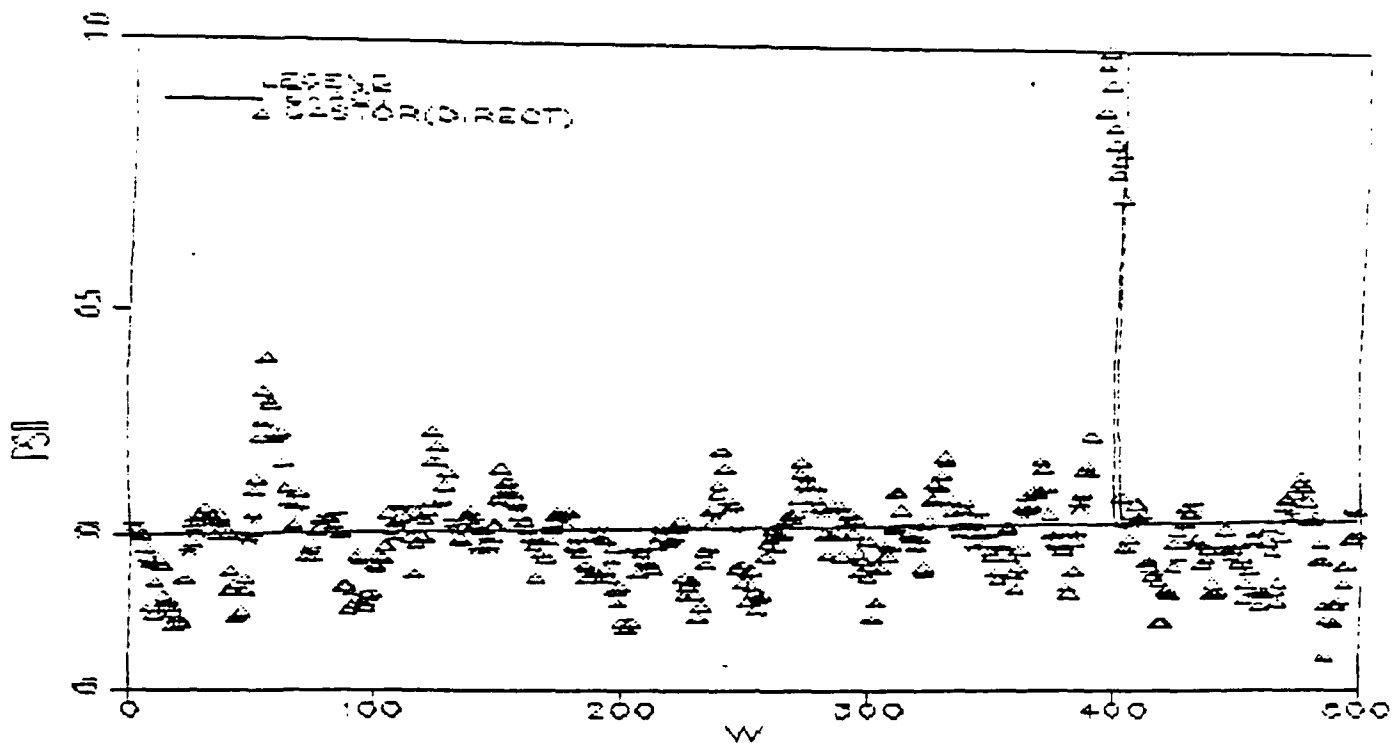
Simulation results show that the direct periodogram approach gives good results at high sampling rates, but gives a distorted spectrum at high aliasing factors.

POWER SPECTRUM



sampling frequency = 1 Hz.
 sine frequency = 40 Hz.
 aliasing factor = 80
 number of blocks = 20
 samples / block = 100
 max. lag time = 10 seconds
 number of slots = 1000
 max. frequency = 50 Hz.

Figure 8

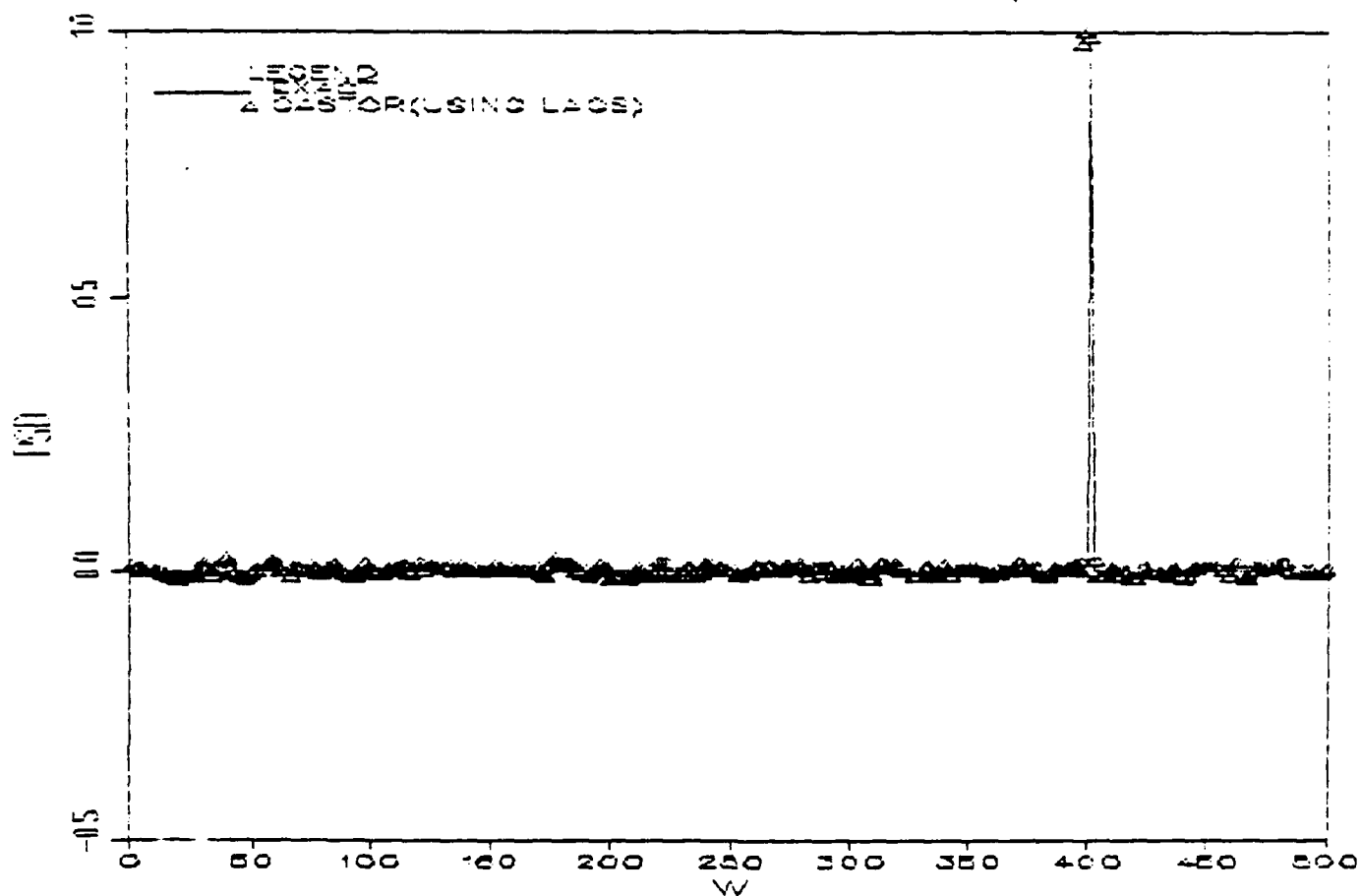


sampling frequency = 1 Hz.
 sine frequency = 16 Hz.
 aliasing factor = 32
 number of blocks = 10
 samples /block = 500
 max. frequency = 20 Hz

Figure 9

POWER SPECTRUM

SINE DATA

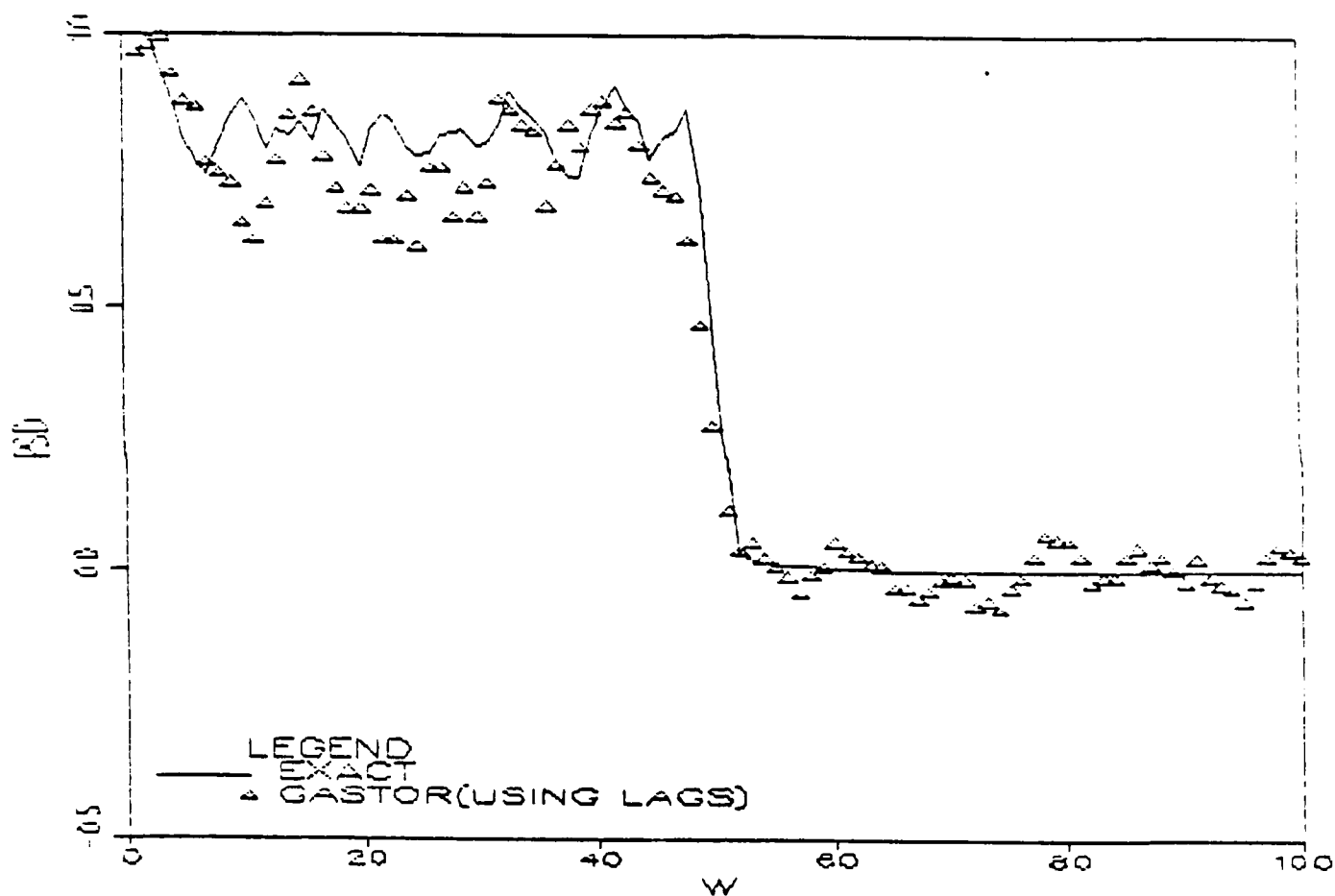


sampling frequency = 1 Hz.
 sine frequency = 16 Hz.
 aliasing factor = 32
 number of blocks = 10
 samples/block = 400
 max lag time = 400 seconds
 number of slots = 500
 max. frequency = 20 Hz.

Figure 10

POWER SPECTRUM

gaussian data

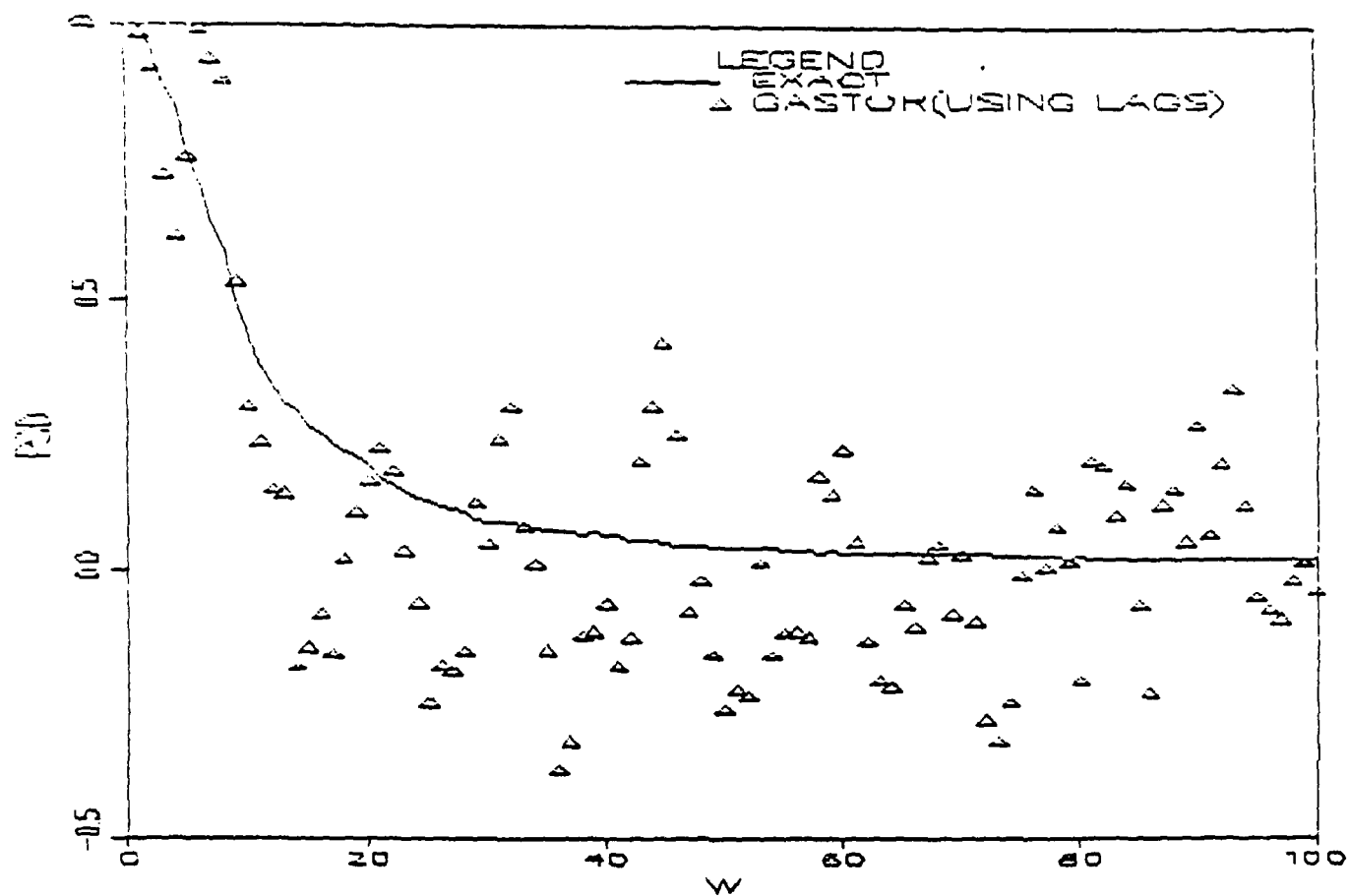


sampling frequency = 0.1 Hz.
 max. frequency = 0.05 Hz.
 aliasing factor = 1
 number of blocks = 49
 samples / block = 200
 max. lag time = 2000 seconds
 number of slots = 100
 frequency range = (0,0.1) Hz.

Figure 11

POWER SPECTRUM

random data



$$\phi_1 = 0.75$$

$$\phi_2 = 0$$

number of blocks = 10

samples / block = 500

max lag time = 500 seconds

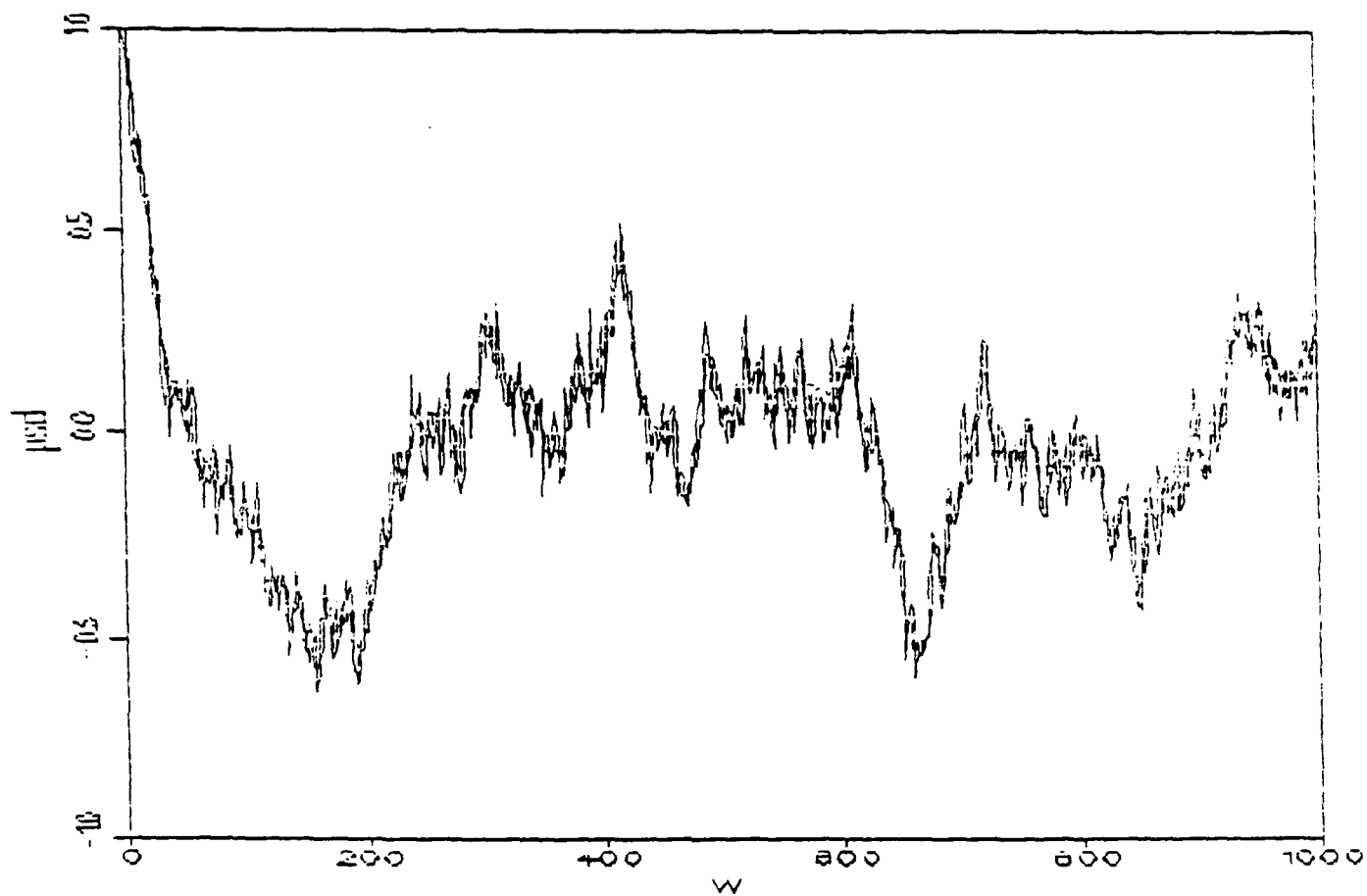
number of slots = 100

max. frequency = 0.5 Hz.

aliasing factor = 10

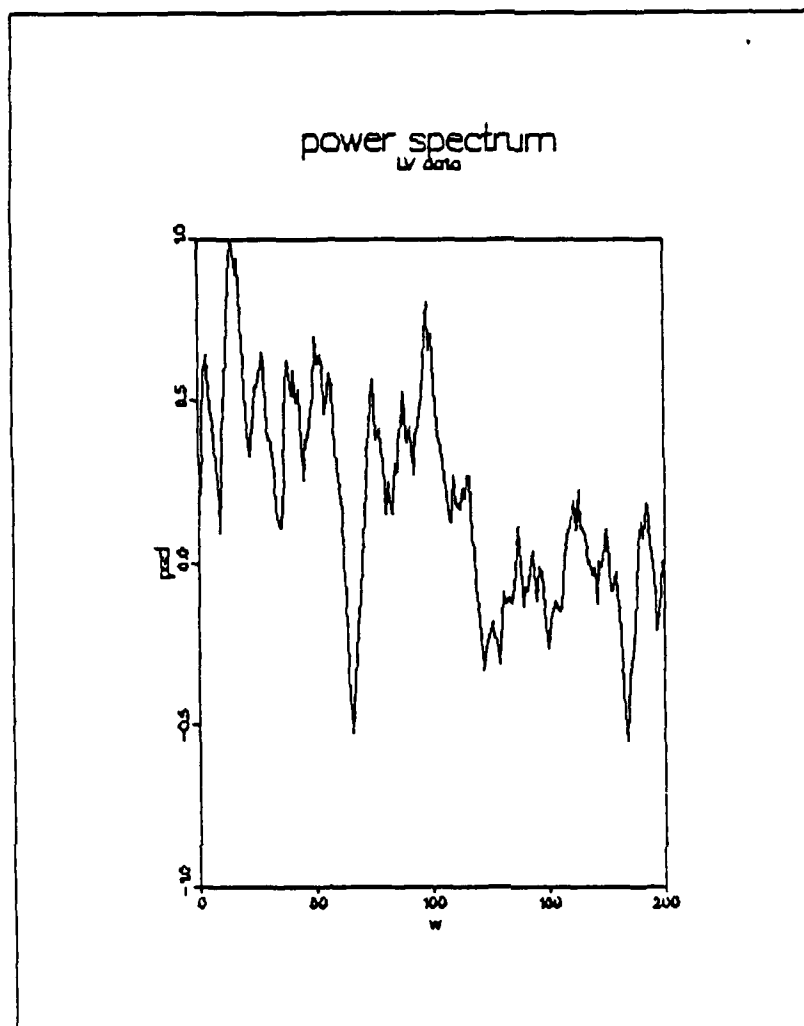
Figure 12

power spectrum LV data



number of blocks = 15
max. lag time = 0.15 seconds
number of slots = 2000
slot width = 0.15/2000
max. frequency = 6.67 KHz.

Figure 13



Power spectrum of LV data by Gastor (Direct) technique

samples/block = 200

number of blocks = 75

frequency range = (0 0.5) Hz.

Figure 14

This is because of the overlapping of spectra above the folding frequency. This approach though has the disadvantage that it is computationally intensive. The direct approach using lags is the most time consuming and results show that it is not practical to use for most applications. The correlation based slotting method seems to be the best compromise between computational speed and accuracy of the estimate (in terms of variability and the mean square error). However the negative spectral values are of concern and need to be investigated further. Such negative spectral values are also reported in Gastor (1986) and Mayo (1973) and arise because of random inter-arrival times.

It is observed that for the same record length all the algorithms work better for deterministic data. For random data the variability of the estimate increases. This is seen in the results from analyzing gaussian and first order random data.

Though it appears that the correlation based slotting approach is the most appropriate to date, the proper choice of the slot width is an important decision. This is all the more so when the bandwidth of the signal is not known apriori. The slot width becomes a tricky choice because too large a slot width leads to aliasing and too small a values causes scattering in the tail of the spectrum. Thus as in the case of the LV data repeated trials of different slot widths may be necessary to properly gauge the spectrum.

IX. ACKNOWLEDGMENT

The author is thankful to Sanjay Gupta for computational help and to Dr. C. E. McHenry for some suggestions.

X. BIBLIOGRAPHY

1. Gastor, M. and Roberts, J.B., "Spectral Analysis of Randomly Sampled Records by a Direct Transform", Proc. Royal Society of London, Ser A, Vol. 354, 1977, pp 27-58.
2. Bell, W.A., "Spectral Analysis Algorithms of Laser Velocimeter-A Comparative Study", AIAA Journal, Vol. 21, No. 5, 1982, pp 714-719.
3. Gastor, M. and Roberts, J.B., "Spectral Analysis of Randomly Sampled Signals", JIAM, Vol. 15, 1975, pp 195-216.
4. Masry, E. and Lui, M.C., "Discrete Time Spectral Estimation of Continuous Parameter Processes - A New Consistent Estimate", IEEE Transactions - IT, Vol. IT - 22, No. 3, May 1976, pp 298-312.

5. Roberts, J.B. and Ajamani, D.B.S., "Spectral Analysis of Randomly Sampled Signals Using a Correlation Based Slotting Technique", IEE Proceedings, Vol. 133, Pt. F, No. 2, April 1986, pp 153-162.
6. Mayo, W.T. Jr., Shay, M.T. and Riter, S., "The Development of New Digital Data-Processing Techniques for Turbulence Measurements with Laser Velocimeter", Interim Report, Texas A&M Remote Sensing Center, October, 1973.
7. Plumblee, M.E. Jr. (editor), "The Generation and Radiation of Super-Sonic Jet Exhaust Noise", Technical Report AFAPL- TR-74-24, June 1974.
8. Hogg, R.V. and Tanis, E.A., "Probability and Statistical Inference", second edition, MacMillan Publishing Co., Inc., 1983.
9. Masry, E., "Poisson Sampling and Spectral Estimation of Continuous Time Processes", IEEE Transactions on Information Theory, Vol.IT-24, No. 2, March 1978, pp 173- 183.
10. Masry, E., "Alias-Free Sampling: An Alternative Conceptualization and Its Applications", IEEE Transactions on Information Theory, Vol. IT-24, No. 3, May 1978, pp 317-324.
11. Beutler, F.J., "Alias Free Randomly Timed Sampling of Stochastic Processes", IEEE Transactions on Information Theory, Vol. IT-16, No. 2, March 1970, pp 147-152.
12. Kar, M.L., Hornkohl, J.O. and Farmer, W.M., "An Algorithm for Spectral Estimation of Randomly Sampled Data", Proceedings of the Southeastcon '81, Huntsville, Ala., 1981.
13. Oppenheim, A.V. and Schafer, R.W., "Digital Signal Processing", Prentice-Hall, Englewood, N.J., 1975.
14. Bendat, J.S. and Piersol, A.G., "Engineering Application of Correlation and Spectral Analysis", John Wiley & Sons, New York, 1980.
15. Tropea, C., "Turbulence-Induced Spectral Bias in Laser Anemometry", AIAA Journal, Vol. 5, No. 2, Feb. 1987. pp 306-309.
16. Patil, S.A., "Estimation of Spectral Density by Random Samples", 1987 USAF-UES Summer Faculty Research Report.

Additional References-

17. Beutler, F. and Leneman, O., "The Spectral Analysis of Impulse Processes", Information and Control, Vol. 12, 1968. pp 236-258.

18. Beutler, F. and Leneman, O., "The Theory of Stationary Point Processes", *Acta Mathematica*, Vol. 116, 1966. pp 160-197.
19. Brillinger, D., "The Spectral Analysis of Stationary Interval Functions", *Proceedings of the Sixth Berkley Symposium on Mathematical Statistics and Probability*, Vol. 1, 1972. pp 483-513.
20. Jones, R., "Aliasing with Unequally Spaced Observations", *Journal of Applied Meteorology*, Vol. 11, 1972. pp 245-254.
21. Kay, S. and Marple, S., "Spectral Analysis - A Modern Perspective", *Proceedings of the IEEE*, Vol. 69, 1981. pp 1380-1419.
22. Leneman, O., "Random Sampling of Random Processes", *Information and Control*, Vol. 9, 1966. pp 347-363.
23. Leneman, O. and Lewis, J.B., "Random Sampling of Random Processes: Mean-Square Comparision of Various Interpolators", *IEEE Transactions of Automatic Control*, Vol. AC-11, 1966. pp 396-403.
24. Roberts, J.B. and Gastor, M., "Rapid Estimation of Spectra from Irregularily Sampled Records", *Proc. IEEE*, Vol. 125, No. 2, 1978. pp 92-96.
25. Thompson, R., "Spectral Estimation from Irregularily Spaced Data", *IEEE Transactions on Geoscience Electronics*, Vol. GE-9, No. 2, 1971. pp 107-110.
26. Kryukov, V.I., "Calculation of the Correlation Function and the Spectral Power Density of Random Sampling", *Radio Engineering and Electronic Physics*, Vol. 12, 1967. pp 169- 176.

FINAL REPORT NUMBER 14
REPORT NOT AVAILABLE AT THIS TIME
Dr. Gurbux S. Alag
760-7MG-042

FINAL REPORT NUMBER 15
REPORT NOT AVAILABLE AT THIS TIME
Dr. John Kenney
760-7MG-019

Final Report

on

**FRACTURE IN SOLID PROPELLANT:
DAMAGE EFFECTS UPON CRACK
PROPAGATION**

Air Force Office of Scientific Research
Research Initiation Program Mini-Grant
Contract No. F49620-85-C-0013/SB5851-0360

December 31, 1988

Principal Investigator
Lawrence Schovanec

INTRODUCTION

This report presents the results of research efforts that were initially undertaken while the principal investigator was a participant in the Summer Faculty Research Program in 1987 and then continued under the support of the AFOSR Research Initiation Program in 1988. In addition to the principal investigator, three graduate students were supported during the tenure of the RIP mini-grant. As a result of this work, 4 refereed journal articles and 2 conference proceeding papers were published or accepted for publication during this period. These papers are listed in the Publication section of this report and are reproduced in the Appendices. In addition two of the students that were supported on this grant wrote masters theses based on this work. These theses are listed in the Advanced Degrees section and are also included in the Appendices.

SUMMARY OF RESEARCH OBJECTIVES AND PROGRESS

For recently developed propellants the issue of crack formation and propagation is complicated by damage that may develop in these propellants. One approach to modelling the effects of damage undertaken at the Air Force Astronautics Laboratory focused on the aspect of material inhomogeneity and its suitability for characterizing damage effects. The research supported by this grant was primarily concerned with analyzing crack behavior in a medium where material inhomogeneity, as introduced by an appropriately chosen variable modulus, corresponded to a particular state of damage in the body.

Experimental evidence indicates that damaged material often occupies wedge-shaped regions emanating from the crack tip or a small "process zone" about the crack tip. To model the former situation the shear modulus was assumed to be piecewise constant with values chosen in such a way as to correspond to the size, location, and degree of the damaged material. The analysis for this scenario is presented in the papers of Appendices A and B. Among the conclusions of these works are 1) damage effects significantly influence the stress field near the crack tip as well as the crack surface displacements, 2) the direction of crack propagation may be altered by the presence of damage ahead of the crack, and 3) conventional fracture theories (for example, those based on the concept of critical values of the stress intensity factor or the energy release rate) may not be applicable in damaged media.

The concept of the process zone alluded to previously was incorporated into the crack model by adopting a continuously varying power-law form of the modulus, corresponding to a reduced rigidity at the crack tip. In the case of an antiplane shear crack explicit formulas for the stresses and displacements, valid throughout the body, were derived in the paper of Appendix C. The qualitative behavior summarized by conclusions 1) - 3) above was again observed. A study of various criteria for determining the onset of crack initiation was carried out in a subsequent paper (Appendix D) by explicitly calculating the energy release rate, the strain energy density, the maximum cleavage stress, and zones of plasticity. The presence of damage near the crack tip as modelled by the reduced modulus results in

a dramatically lowered energy release rate, severe crack tip blunting, and enlarged zones of plasticity near the crack tip. The implications of these results with regard to possible modes of failure at the crack tip were also investigated in this paper. The analysis for the opening mode crack was subsequently carried out in Appendix H. For this more complicated mode the same qualitative behavior was deduced by a numerical analysis of the problem.

Microcracking or void nucleation near the crack tip are two common manifestations of damage. As a first step toward modelling these effects in a viscoelastic material the investigation in Appendix E was undertaken. In addition, a process zone at the crack tip was incorporated into the model. The energy release rate was then calculated by carrying out a dynamic, steady state analysis. The effects of crack interaction, crack speed, material properties and a process zone upon the energy release rate were deduced. The implications of these results with regard to predicting crack speeds and unstable fracture were also analyzed.

PUBLICATIONS

Journal Papers and Conference Proceeding Papers
Published with AFOSR Support

1. "A mode III crack problem in a bonded composite material," *Engng. Fracture Mech.*, Vol. 31, pp. 437-449, 1988.
2. "An antiplane shear crack in a nonhomogeneous elastic material," accepted for publication in *Engng. Fracture Mech.*, to appear in 1988 issue.
3. "Some aspects of crack behavior in a nonhomogeneous material" (with T. Timmons), accepted for publication in *Engng. Fracture Mech.*, to appear in 1989 issue.
4. "The dynamic energy release rate for two parallel steadily propagating mode III cracks in a viscoelastic body" (with J. R. Walton), accepted for publication in *Int. J. of Fracture*, to appear in 1989 issue.
5. "The dynamic energy release rate for crack propagation in viscoelastic media" (with J. R. Walton), to appear in *Proceedings of the Pan American Congress of Applied Mechanics*, Rio de Janeiro, Brazil, January, 1989.
6. "A mode III crack terminating asymmetrically at a wedge-shaped inhomogeneity" (with B. Pashaie), to appear in *Proceedings of the ASME Pressure Vessels and Piping Conference*, July, 1989.

ADVANCED DEGREES AWARDED

1. William Todd Timmons, M.S., "An Analysis of an Antiplane Shear Crack in a Nonhomogeneous Elastic Medium," August, 1988.
2. Scott Douglass Brisendine, M.S., "An Opening Mode Crack in a Nonhomogeneous Elastic Material," December, 1988.

Appendices can be obtained from
Universal Energy Systems, Inc.

FINAL REPORT

PROJECT TITLE:	Novel Conversion of Organometallics to Energetic Nitro Compounds
CONTRACT NO.:	F49620-85-C-0013/SB5851-0360
PURCHASE ORDER NO.:	S-760-6MG-130
PRINCIPAL INVESTIGATOR:	Dr. Nicholas E. Takach

REPORT SUBMITTED TO UNIVERSAL ENERGY SYSTEMS, INC.
DECEMBER 8, 1988

ACKNOWLEDGEMENT

The Principal Investigator gratefully acknowledges the support and assistance of the Air Force Office of Scientific Services (Bolling AFB, DC), The University of Tulsa Research Office, Universal Energy Systems, Inc., and Dr. Robert D. Chapman (Astronautics Laboratory, Edwards AFB, CA).

INTRODUCTION

The author ("NET") participated in the 1986 USAF Summer Faculty Research Program. Subsequently, a proposal was submitted for funding of follow-on research through the Research Initiation Program (RIP). This report discusses progress made during the follow-on period.

The research proposed for the RIP was essentially an extension of the SFRP project: to investigate the feasibility of a new single-step nitration technique for organolithiums. The nitrating agent of interest was nitronium triflate ("NO₂OTf"), NO₂OSO₂CF₃. During the SFRP period several nitration reactions using the new technique were attempted. As a result, the supply of nitronium triflate was consumed about half-way through the summer research period. Because this compound is not commercially available, another batch had to be synthesized. The scientist at Edwards Air Force Base with whom NET collaborated, Dr. Robert D. Chapman ("RDC"), had earlier attempted a number of different synthetic routes for the triflate that were published in the chemical literature. Eventually, RDC was able to prepare the desired product in high purity and yield by carrying out two individual reactions in succession. NET attempted to reproduce the synthesis by following the notes in RDC's laboratory notebook. The two reactions were: 1. synthesis of N₂O₅ by dehydration of 100% nitric acid using P₂O₅ under an ozone atmosphere, according to the procedure reported by Andrieth¹; 2. reaction of N₂O₅ with triflic acid to form nitronium triflate and nitric acid, as described by Effenberger and Geke.² NET encountered several problems in trying to repeat the synthesis, particularly the first reaction, and was unsuccessful in each of four attempts. A subsequent attempt by RDC working alone, followed by two attempts in which RDC and NET worked together, were also unsuccessful. The main obstacles were perceived to be the difficulty in controlling the exothermicity of the reaction between P₂O₅ and the 100% nitric acid, and physical problems associated with trapping the intermediate product, N₂O₅. In the final analysis, there was still no nitronium triflate available at the start of the RIP period and its synthesis was the first task facing NET.

At The University of Tulsa, site of the RIP project, a different route for synthesizing nitronium triflate was chosen. The method described above was abandoned because of the difficulties encountered earlier and because it required a specialized piece of equipment (ozonator) that was neither available nor readily accessible to the principal investigator. The new synthesis also consisted of two successive reactions; it differed from RDC's synthesis only in the method of obtaining N₂O₅. Formation of N₂O₅ would then be followed by its reaction with triflic acid, as described

earlier. The "new" method of preparing N_2O_5 utilized a procedure reported by Robson in 1954, in which trifluoroacetic anhydride ("TFAA") was reacted with absolute nitric acid.³

When the RIP proposal was submitted, there was insufficient laboratory space available for research of this type in the Chemistry Department. However, in the spring of 1987 the Administration of the College of Engineering and Applied Sciences (to which the Chemistry Department belongs) committed the funds needed to convert a room vacated by another department into a chemistry research laboratory for NET. It was anticipated that the room would be completed by the summer of 1987. Later in the spring, before money for the lab actually became available, it was announced that the Dean of the College would be replaced. While the Chairman of the Chemistry Department was still optimistic that funds would eventually be available for the room conversion, it became apparent that even in the best-case scenario the job would not be completed for several months. In the meantime NET and RDC discussed the type of equipment that would be best-suited for carrying out the new procedure for preparing nitronium triflate. NET then ordered the necessary chemicals and special glassware. When funding was informally re-approved late in the summer, NET immediately began work on a design plan for the laboratory's layout and furnishing. A purchase order was issued in the fall and completion of the work was projected for January, 1988. NET requested and later received a no-cost extension of the RIP project's deadline from 31 December 1987 to 30 September 1988. The laboratory was not actually ready for occupation until late March, 1988, and its new fume hood was not completely functional for another month after that. Consequently, NET and a student spent the first part of the Spring, 1988 semester modifying the fume hood of a freshman teaching laboratory so that it could be used as the site for preparation of 100% nitric acid. As soon as furniture installation in the new lab was complete and all of the various utilities were functional, NET and the student prepared the room for more elaborate experiments, such as the synthesis of nitronium triflate and subsequent nitration reactions. Preparation included construction of support-rod networks in the fume hood and at two lab counter locations, setup of glove bags and their internal support frames, and numerous other minor tasks associated with organizing the lab and making it functional.

Originally, NET was reluctant to enlist student help for the RIP project. Exposure of undergraduate students with limited laboratory experience to the intricacies and potential dangers of the experiments represented risks was thought to be incommensurate with the potential benefits. However, as the lab was being set up it became apparent, for reasons discussed

later, that performing some of the experiments without one or preferably two assistants would be extremely difficult. Unfortunately, student help is generally not available during the summer months, particularly in an undergraduate Department such as ours, unless money is available to pay for it. NET did not make student support a line item in the RIP budget simply because there were not enough funds available. Consequently, NET was forced to request another extension of the project's deadline. An extension to 30 November 1988 was granted. Fortunately, NET was able to recruit two very capable and highly motivated Senior Chemistry Majors to work on the project in the fall semester, 1988. The next section discusses results obtained during this period.

RESULTS AND DISCUSSION

The procedure described by Robson for the preparation of N_2O_5 involves the following steps, all of which were performed under a nitrogen atmosphere:

1. 100% nitric acid was added dropwise to TFAA, maintaining the temperature at $0-5^\circ\text{C}$.
2. When the addition was complete, the resulting yellow solution was cooled to -30°C .
3. Upon cooling, the solution formed a crystalline slurry. After the slurry was filtered and washed twice with cold TFAA (-50°C), a white solid resulted. The solid was dried for two hours at -30°C and 1 mm pressure.

Robson reported that, due to the difficulty of handling the product (nitrogen pentoxide decomposes above 0°C), determination of the yield was not attempted. Uncertainty concerning the yield of N_2O_5 was also significant in our work, as discussed later.

The following is a description of the apparatus used to carry out Robson's procedure. Due to the reactivity of the reaction components, they were only allowed to contact glass or teflon. A refrigerated bath capable of externally circulating coolant was connected to a jacketed reaction vessel using plastic tubing. The vessel was fitted with a matching flask head by means of a ground-glass connection. The top center joint of the flask head was fitted with a glass bearing, through which a teflon-coated stirring shaft was inserted. A small teflon stirring blade was connected to the bottom of the shaft and the top was connected to a mechanical stirring motor. The other top joints of the flask head allowed attachment of an addition funnel, a thermometer adapter, and an stopcock-adapter connected to a nitrogen gas source.

The entire vessel was enclosed inside a small glove bag. Four holes were cut in the bag to allow access to the female joints at the top of the flask head. By continuously purging the bag with a small positive pressure of nitrogen, formation of frost on the outside of the vessel was prevented and it was possible to see the contents of the vessel throughout the course of the reaction. Regular-grade nitrogen gas passed through a dessicant before entering one of the manifolds of a five-port, dual manifold. The other manifold could be connected to a vacuum source. The multi-port, dual manifold allowed nitrogen gas to be simultaneously distributed to the inside of the reaction vessel, to the small glove bag surrounding the vessel, and to a large glove bag where moisture-sensitive reagents were handled and stored. Figure 1 is a depiction of the flask head and reaction vessel, photocopied from the vendor's catalog (note: all Figures are located in the Appendix). Figure 2 is a photograph of the left side of the apparatus, including the circulating bath, the enclosed vessel/flask-head assembly, and the hoses connecting the bath and the vessel. In the background, to the left of the hood, a portion of the large glove bag can be seen. Insulating hoses were wrapped around the plastic hoses through which coolant actually flowed between the bath and the vessel. This arrangement allowed liquids inside the vessel to be stay within 1-2° of the thermostated internal bath temperature. Figure 3 is a photograph of the right side of the apparatus, including the dual manifold and connected vacuum system. The vacuum system was permanently mounted to a cart. When the vacuum system was not needed it could easily be disconnected from the dual manifold using plastic "Quick-Disconnect" joints and rolled out of the way. Reagents such as absolute nitric acid, TFAA, and triflic acid, each of which are extremely moisture sensitive, were transported between the large glove bag and the reaction vessel using a pressure-equalizing addition funnel. The funnel has an additional stopcock on its side arm that allowed each reagent to be isolated from air when the funnel was outside the glove bag.

With the type of apparatus described above and the sensitive, noxious reagents involved, it was essential to have at least two persons working together during an experiment. Someone needed to be available if the person using the glove bag (Figure 4) required assistance. Just as important was assistance with the dual manifold. For example, while one person moved the addition funnel from the glove bag to the reaction vessel, the other person adjusted the relative pressures of nitrogen gas flowing to the two sites (Figure 5).

Prior to each attempted synthesis of nitronium triflate, all glassware was thoroughly cleaned, kept overnight in an oven at 110°C, and allowed to

cool in the presence of nitrogen. All chemicals (except 100% nitric acid) were obtained from vendors in the highest purity available and used without further purification. Observations made during the preparation of N_2O_5 were completely consistent with those described by Robson. Though this method of preparing N_2O_5 was much easier to control than the dehydration of 100% HNO_3 by P_2O_5 , there was still the problem of not knowing the yield. In the paper by Effenberger and Geke, 78 mmole of N_2O_5 was reacted with 39 mmole of triflic acid in the reaction that produced nitronium triflate. The 2:1 excess of N_2O_5 relative to triflic acid was very important because, as NET's experience at Edwards Air Force Base demonstrated, it was very difficult to obtain pure nitronium triflate if the latter contained even traces of unreacted triflic acid. The quantities of HNO_3 and TFAA used in our reaction were the amounts needed to prepare 78 mmole of N_2O_5 , assuming a quantitative yield of the latter.

The reaction between N_2O_5 and triflic acid also produced no unexpected observations. After washing the reaction product several times, it was dried under vacuum for one hour at ambient temperature. Then the hoses connecting the reaction vessel to the circulating bath were removed and the entire vessel was moved to the large glove bag. Attempts to separate the flask head from the vessel were unsuccessful and the product had to be removed through one of the flask head's necks using a teflon-coated spatula. The product was not completely dry and fumed slightly. The fuming and traces of moisture inside the reaction vessel suggested that some unreacted triflic acid was present in the product. It was also discovered that the large glove bag had a small hole in it. This presumably occurred when a few drops of triflic acid spilled as it was being measured into a graduated cylinder. The product was placed in a teflon vial, which was covered with a kimwipe and put inside a vacuum dessicator containing P_2O_5 . The dessicator was the type that sealed by compression of a large silicone rubber o-ring that fit between the lid and body. After evacuating the dessicator over the weekend a significant portion of its o-ring was literally pulverized--another indication that triflic acid contamination had occurred. By then, the product had a slushy appearance and was discarded. Further attempts to separate the flask head and vessel were unsuccessful. There were signs that the teflon casing of the flask head's lower joint had been chemically attacked, presumably by triflic acid. Eventually, an upper neck of the flask head was broken while trying to separate it from the vessel. A professional glassblower was finally able to separate the two pieces by heating them with his torch; but, in the process, the vessel cracked in the vicinity of its stopcock and the remainder of the flask head's teflon casing was charred. After the separation, the portion of the

vessel below the frit was rebuilt and the glass stopcock was replaced by a high-vacuum teflon stopcock similar to the type used in the dual manifold. Several minor adjustments to other parts of the apparatus were also necessary before the second attempt to prepare nitronium triflate. Stirring was made more efficient and practically vibration-free. With the residue of its teflon casing completely burned off, the flask head's male joint had a clean, ground-glass surface. In an attempt to prevent another potential separation problem, a small amount of an aerosol form of teflon lubricant was applied to the joint.

The second synthesis of N_2O_5 proceeded routinely. Other than seepage of a few mL of liquid below the frit during the addition of nitric acid to TFAA, the rebuilt vessel functioned exactly as before. Again, N_2O_5 was obtained in apparently good yield and purity. In the first attempted synthesis of nitronium triflate, completion of both reactions required a total of 13 hours. Therefore, we decided to interrupt the second attempt after N_2O_5 was isolated. Thus, instead of drying the latter for only two hours before reacting it with triflic acid, it was left under vacuum at -30°C overnight. The following morning we were surprised to find that the product had completely sublimed and the vessel was empty! This was unexpected, considering the low temperature at which the N_2O_5 was dried.

A third attempt to prepare nitronium triflate was recently completed. The quantities of reagents used in the reaction to produce N_2O_5 were the same as in the first attempt. In the second stage of the synthesis only 3.0 mL triflic acid was added, as an extra precaution against potential contamination by unreacted triflic acid. Both stages of the procedure were free of complications. The product of the reaction between N_2O_5 and triflic acid appeared to be pure and dry soon after its final wash with dichloroethane. Unlike the first attempt, the inside walls of the flask were also dry at this stage, an important indication that the nitronium triflate was not being attacked by moisture. However, after the product was dried under vacuum for another 15 minutes, traces of moisture were seen inside the vessel. Hydrolysis of the product was attributed to contamination by air resulting from a vacuum leak in the flask-head/vessel assembly.

CONCLUSION AND FUTURE STUDIES

Numerous difficulties were encountered during attempts to prepare nitronium triflate, both at Edwards AFB and the University of Tulsa. Consequently, only a few nitration reactions between the triflate and organolithiums have been carried out. Additional work is needed before

conclusions can be made regarding the feasibility of the single-step nitration reaction of interest. The method described by Robson for preparing N_2O_5 was clearly superior in terms of manageability to the procedure attempted by NET at Edwards AFB. We are confident that this step in the preparation of nitronium triflate was successful. We also have a better understanding of how to control the reaction between N_2O_5 and triflic acid.

As this report is being written, a final attempt to synthesize nitronium triflate is in progress. Preparations for this experiment focussed mainly on ways to prevent exposure of the product to moisture. We were able to isolate and eliminate the vacuum leak in the flask-head/vessel assembly. Also, a drying tube filled with partially-crushed, granular phosphorus pentoxide was inserted into the joint of the flask head where nitrogen gas entered the vessel. Another concern was the addition of triflic acid to N_2O_5 at room temperature. In our final attempt, we will carry out this step at -5°C , then allow the mixture to gradually warm to room temperature. We hope that this modification will minimize thermal degradation of N_2O_5 prior to its reaction with triflic acid.

NET will continue to work on the RIP project's objectives. In addition, one of the students currently working on the project has committed to continue through the end of the Spring, 1989, semester (the other student graduates in December). The former student recently submitted an abstract to present our results at the Student Affiliate Poster Session of the National ACS Meeting in Dallas in April, 1989.

In a recent discussion with RDC it was agreed that if the current attempt to synthesize nitronium triflate is unsuccessful, alternative nitrating agents should be investigated.* One interesting possibility is the use of N_2O_5 itself. After it is formed (using Robson's procedure), N_2O_5 could conveniently be treated *in situ* with an organolithium. Nitronium tetrafluoroborate, NO_2BF_4 , is another nitronium salt that will be investigated if the synthesis of nitronium triflate is unsuccessful. The former is an attractive candidate because it is commercially available.

***NOTE:** After the text of this report was written, the final attempt to prepare nitronium triflate was completed. The experiment was a success: the melting point of the final product was $198-199.5^\circ\text{C}$ (reported value is $198-200^\circ\text{C}$).

REFERENCES

1. L. F. Audrieth, Inorganic Syntheses, Vol. III, McGraw-Hill Book Co., New York (1950), p. 78.
2. Effenberger, F., and J. Geke, Synthesis, 1975, 1, 40.
3. J. H. Robson, J. Am. Chem. Soc., 1955, 77, 107.

APPENDIX

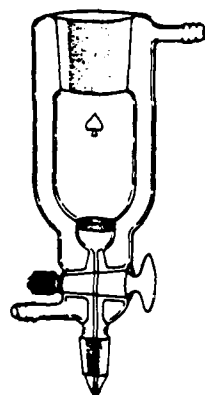
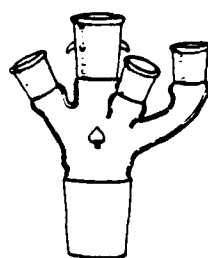


Figure 1. Flask head (Ace Catalog No. 9446-10) and jacketed vessel (Ace Catalog No. 9454-06) used in the attempted preparation of nitronium triflate (photocopied from Ace Glass, Inc., Catalog 900, pp. 342 and 343, respectively).

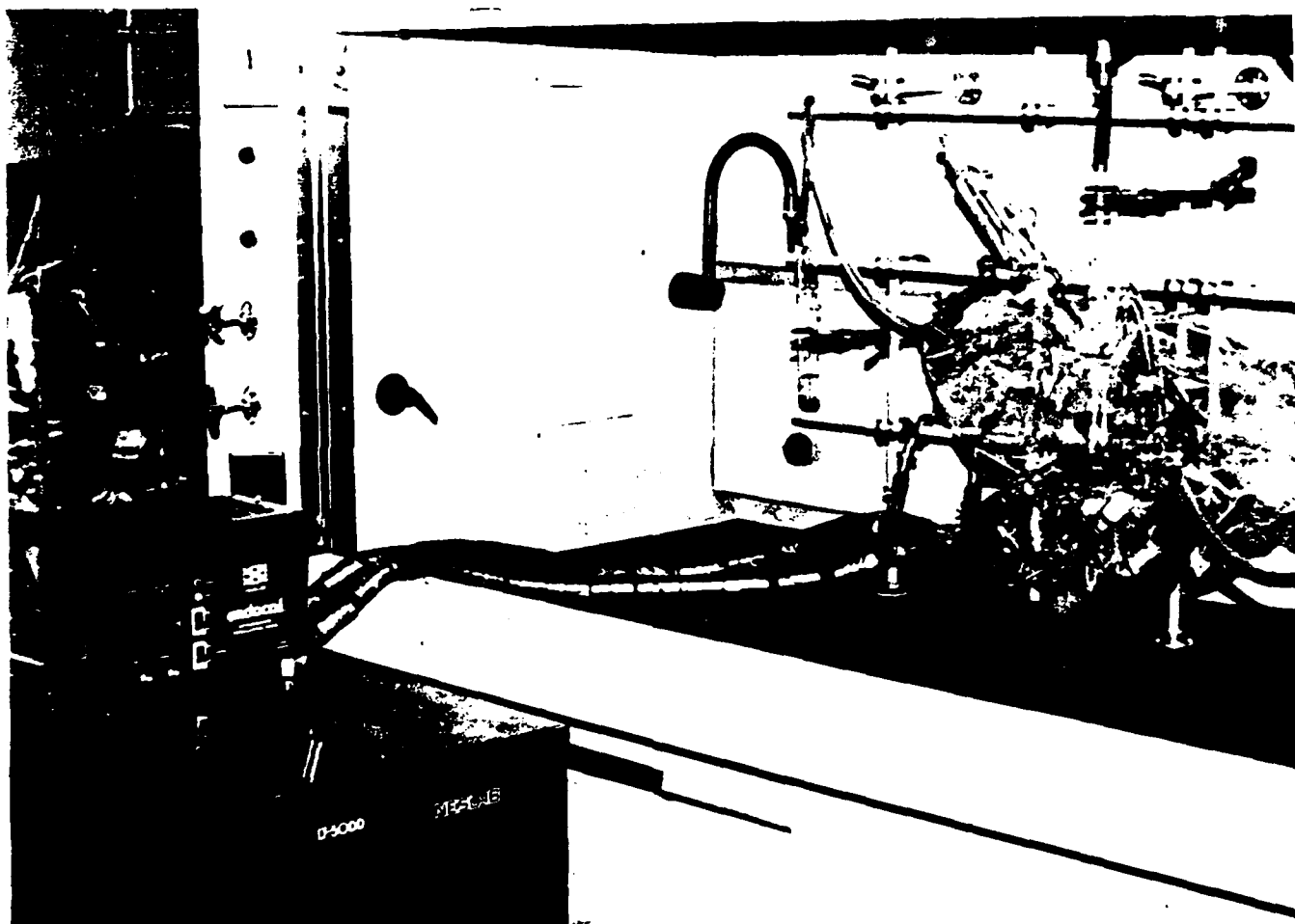


Figure 2. Photograph showing the left side of the apparatus, including the circulating bath and the vessel/flask-head assembly.

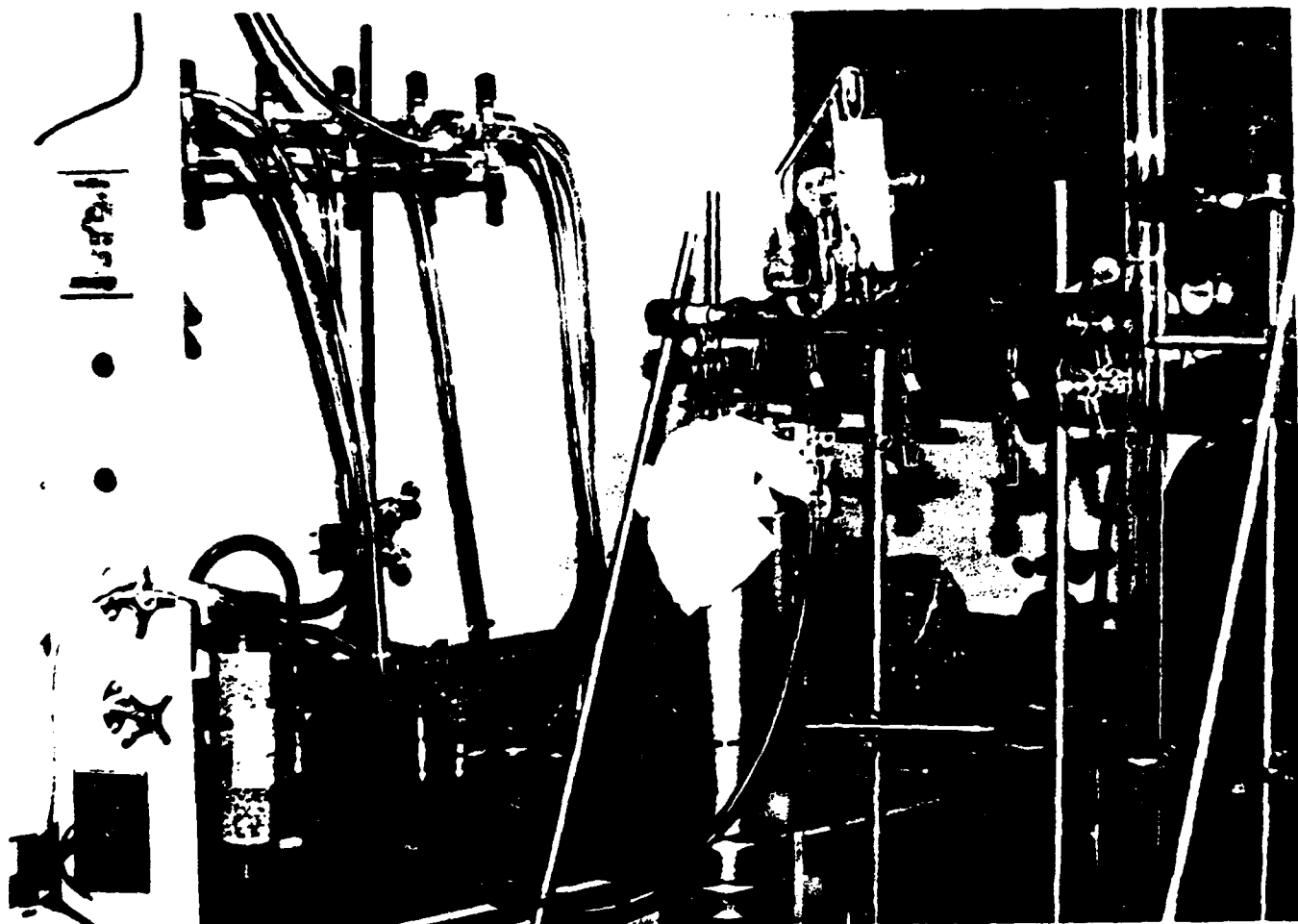


Figure 3. Photograph showing the right side of the apparatus.
including the dual manifold and connected vacuum system.

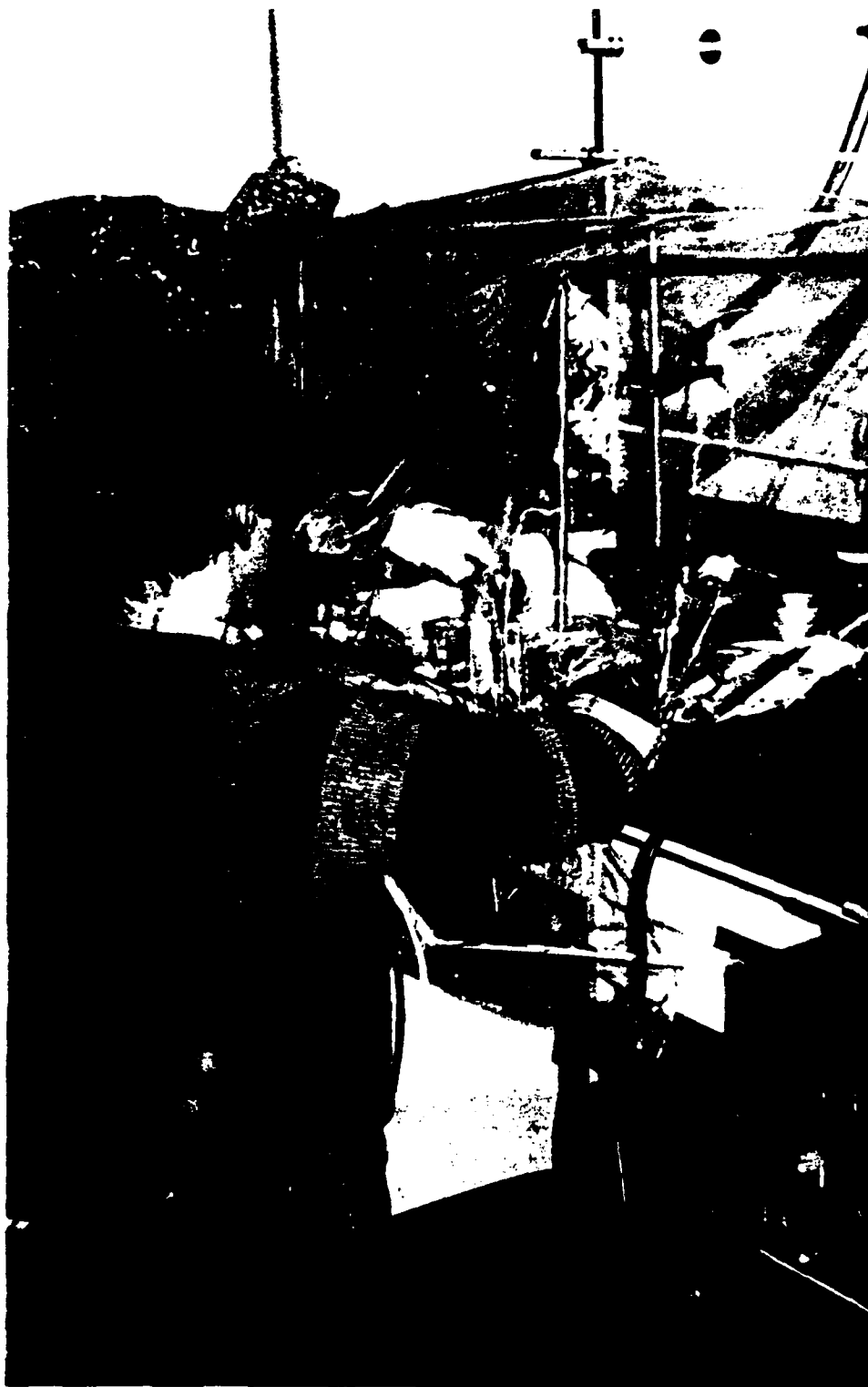


Figure 4. Photograph showing student manipulating reagents in the large glove bag.



Figure 5. Photograph showing student regulating the relative nitrogen gas pressures flowing out of the dual manifold.

AUTOIGNITION. II. CORRELATIONS OF SPONTANEOUS IGNITION TEMPERATURES
WITH MOLECULAR STRUCTURES OF FLAMMABLE COMPOUNDS

AIR FORCE OFFICE OF SCIENTIFIC RESEARCH RESEARCH INITIATION PROGRAM

FINAL REPORT TO UNIVERSAL ENERGY SYSTEMS, INC., DAYTON, OHIO

William W. Bannister,* Stuart B. Clough and Sukant Tripathy
Department of Chemistry, University of Lowell, Lowell, MA 01854

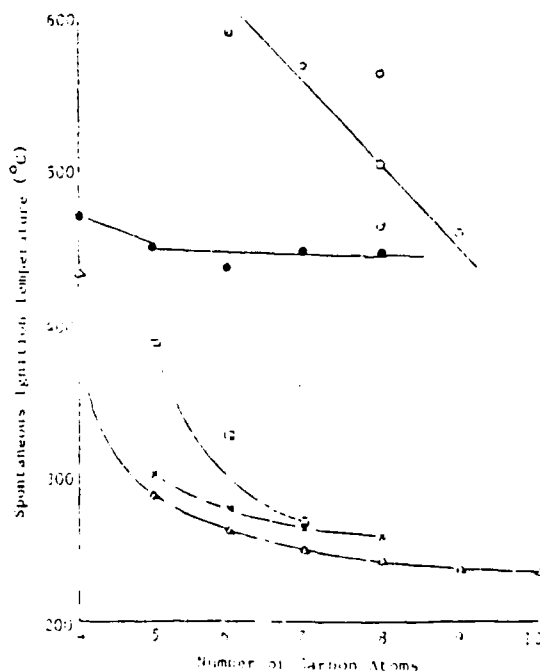
ABSTRACT

As noted in the previous paper of this series, a reversed relationship exists between molecular weight and spontaneous ignition temperature (IT), occasioned by contact with hot surfaces: up to a point, less volatile higher molecular weight fuels have lower IT's and are more easily ignited. For higher members of the alkane family this trend may reverse, resulting in minimum IT's for the C₅ - C₉ alkanes. Branched chain alkanes, arenes and olefins also have higher IT's than analogous straight chain alkanes. Important parameters in governing IT's of fuel components include: (1) the effect of molecular weight on the velocity of the fuel molecule near the hot surface; (2) the effect of rigidity of the fuel molecule on its ability to recoil from the hot surface; and (3) the effect of specific heat of the molecule with regard to ability for dissipation of heat energy within the molecule. Molecular modelling considerations will be discussed to explain anomalous trends.

As can be seen in Figures 1 and 2, there is a decrease in IT values for alkanes with increasing molecular weight, for the range of alkanes from methane (C₁) through octane (C₈).

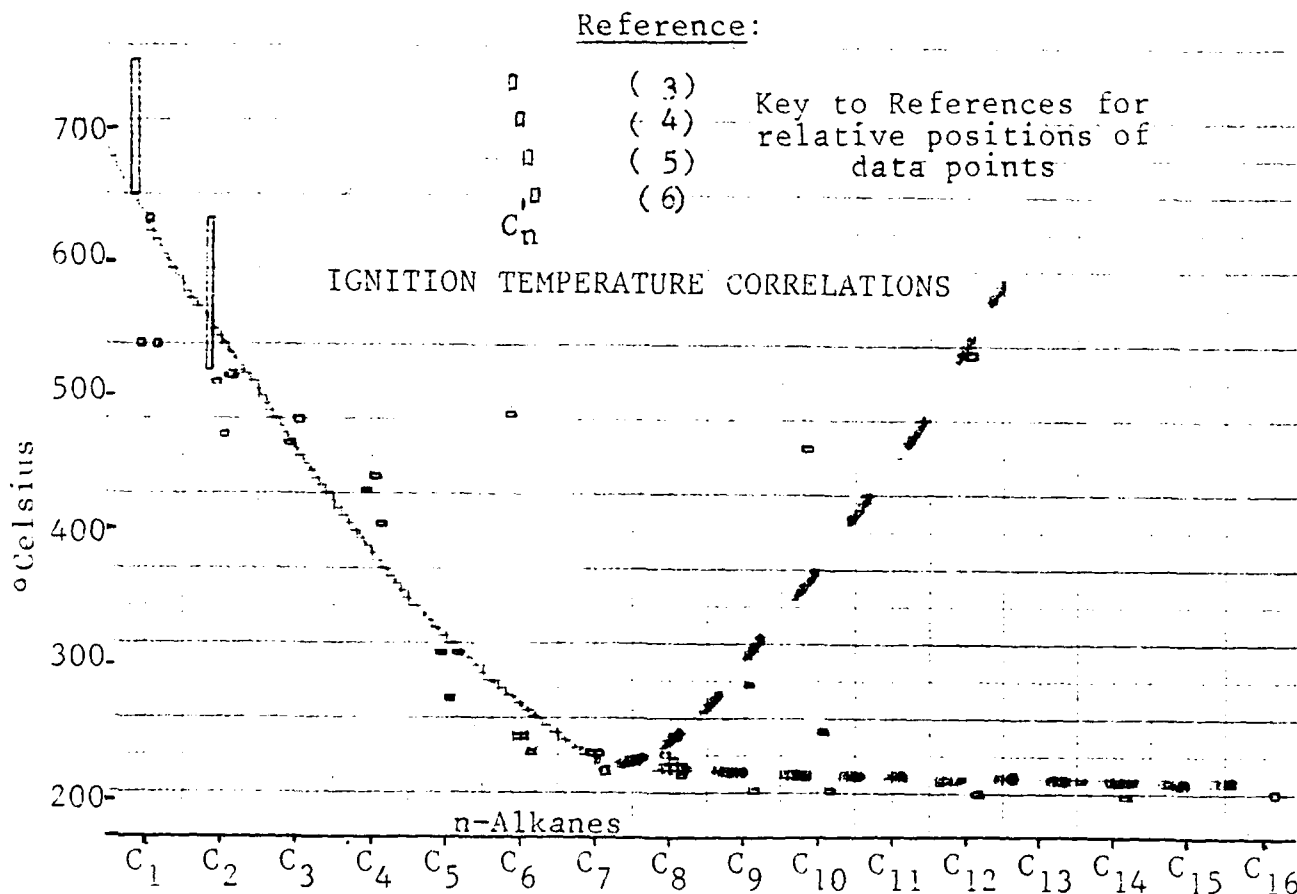
Figure 1. Spontaneous Ignition
Temperatures for
Typical Hydrocarbons
(References 1 and 2)

- Branched Alkanes
- ▲ Paraffins
- Aromatic Hydrocarbons
- ◻ Cycloalkanes
- x Olefins



Precise data is not available for higher alkanes. As shown in Fig. 2, in the lower projected track of IT values, one possibility lies in an asymptotic sweep along a 200° isotherm for alkanes beyond C₈. (Thermal cracking may occur at this temperature, if the hydrocarbons are permitted to linger at the heated surface in accordance with current ASTM procedures.^{7,8} Thus, larger alkanes could conceivably have higher ignition temperatures; but by undergoing slow pyrolysis at 200°, some alkanes in the minimum IT region characteristic of C₅ - C₉ would form, with these igniting at this spuriously low temperature.

Figure 2. Correlations of Ignition Temperatures for n-Alkanes



Frank observed increased IT values for C₁₄ through C₂₀ alkanes, attributing this to decreasing volatilities,⁹ and several other anomalously high IT values have been observed for decane and higher alkanes. Thus, a minimum zone of IT's may exist for C₅ - C₉ alkanes. This is shown in Figure 2 as the upper projected track for the alkanes beyond C₉. Obviously, either track could actually pertain; currently available data is insufficient and good values are probably poorly available with existing equipment and technique.

Fuel component characteristics which have been identified as having possible impact on the ignition temperatures are discussed on page 3 and illustrated on page 4 of this paper.

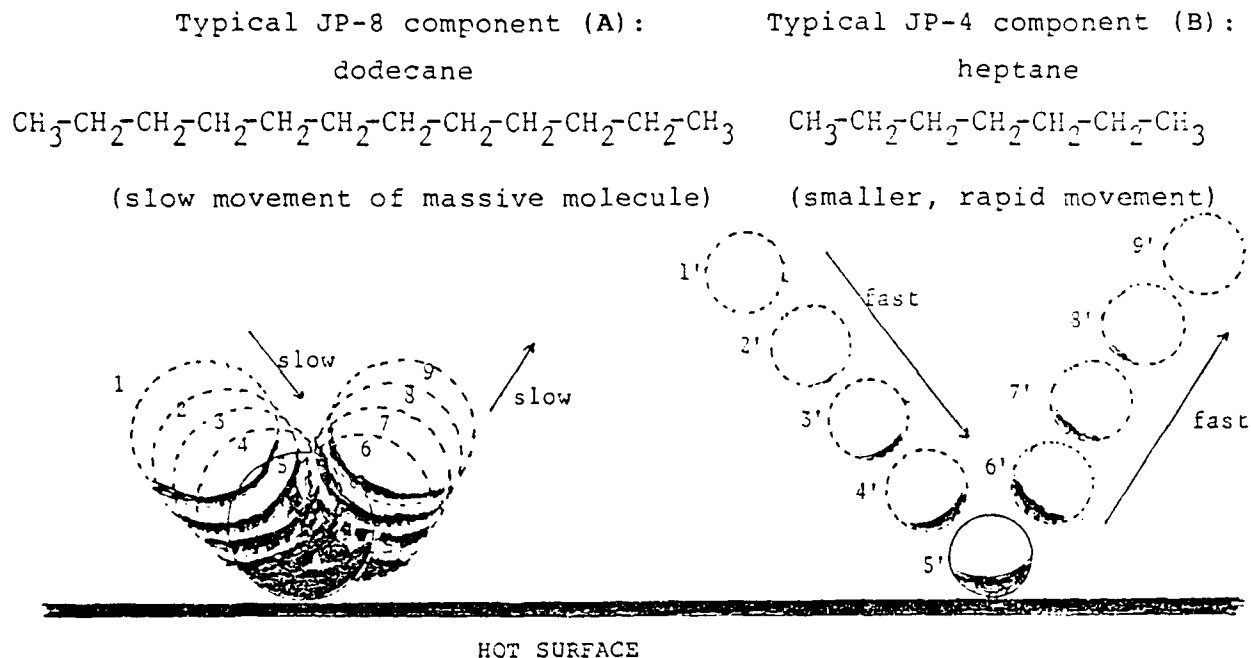
1. Molecular weight effects on speed and inertia for heavier molecules. These effects increase residence time in the vicinity of a hot surface, with increased time for energy transfer.
2. Molecular rigidity. Rigid molecules have reduced rotational degrees of freedom within the molecular structures. This would significantly decrease "floppiness" of the molecule in its impact with a hot surface, allowing the more rigid structure to rebound readily and rapidly with correspondingly reduced residence times in the vicinity of the hot surface, and considerably reduced energy transfer from the surface to the fuel molecule.
3. Specific molecular heat. For smaller molecules relative speed and relative rigidity are important. For the lower alkanes, each addition of a methylene unit imparts a significant increase in molecular weight and in internal degrees of rotational freedom. In going from ethane to propane, for example, there is a 17% decrease in speed at 500°C, whereas decane is only 5% slower than nonane at this temperature. Internal rotational degrees of freedom are even more considerably enhanced for propane, which is very flexible compared with the very rigid ethane; but decane and nonane have very little difference in "mushiness" due to this effect. Thus, decreased speed and rigidity arising from increased molecular weight are much less important for the higher alkanes.

Moreover, higher alkanes begin to enjoy the benefit of increased "molecular specific heat". When lower alkanes such as propane are energized by radiational heat, all atoms of the small molecule are fairly equally irradiated. For larger molecules, some atoms will be in the shadow of others. The hotter surface atoms can then transfer some of their increased energies to the cooler internal atoms. Thus, a higher ignition temperature will be required to attain decomposition energies for a molecule large enough to provide shadowing by some of its atoms to other neighboring atoms.

REFERENCES

1. Jackson, J. L. Ind. Eng. Chem. **1961**, 43, 2869.
2. Miller, R. G. Symp. #6, Major Aircraft Fires (Proc.), Fire Research Station, Boreham Wood, Herts, England, Dec. 1966, pp. 54-65.
3. Lange, N. A. "Handbook of Chemistry", 9th ed., Handbook Publishing Co., Sandusky, OH, 1956, p. 824.
4. McCracken, D. J. "Hydrocarbon Combustion and Physical Properties", BRL-1496; Ballistic Res. Lab, Aberdeen Proving Ground, MD (1970).
5. Perry, R. H. "Chemical Engineering Handbook", 3rd ed., McGraw-Hill Book Co., New York, 1950, pp. 1584-1585.
6. "Fire Hazard Properties of Flammable Liquids, Gases and Volatile Solids", National Fire Protection Association, Boston, MA, 1960.
7. "Autoignition Temperature of Liquid Chemicals", ASTM Designation E 659 - 78 (Reapproved 1984).
8. Affens, W. A.; Johnson, J. E.; Carhart, H. E. J. Chem. Eng. Data **1961**, 6, 613-619 (and references cited therein).
9. Frank, C. E.; Blackham, A. U. Ind. Eng. Chem., **1952**, 44, 862-867.

Figure 3. Molecular Characteristics Affecting Ignition Temperatures.



[(1), (2), (3) ... (8), (9) above indicate positions of molecules A and B at same time intervals, relative to hot surface area.]

Molecular velocity at temperature (T, °K) is inversely proportional to the molecular weight (M); smaller molecules have greater speed.

$$\text{Average velocity} = 14,600 (T/M)^{1/2} \text{ cm/sec}$$

The slow moving heavy molecule A (above) is therefore near the hot surface longer than the lighter and faster B, and A has more time available to absorb energy from the hot radiating surface.

The larger molecule A has more mobile C-C bonds and therefore more rotational degrees of freedom than the smaller B. Thus, A will tend to be "mushier" with less elastic recoil on impact with the hot surface than the smaller, more rigid B which can bounce away more readily. Again, molecule A will have more time to energize than B.

To offset this, and although the larger molecule has greater surface area enabling it to absorb more heat than the smaller molecule, the large molecule's volume is increased even more than is the surface area (by comparison with the smaller molecule). Absorbed heat is then dissipated more through the large molecule, which accordingly is cooler than the small molecule. This effect is more pronounced with increased molecular weights (and volumes). In this case A (dodecane) needs more heat (with a higher ignition temperature) to energize it to its decomposition point than does B (heptane). For smaller molecules (e.g., comparing hexane [C₆] and propane [C₃]), this offsetting factor of increased molecular specific heats is not as important as the molecular speed and rigidity effects: in such cases the heavier molecule has the lower ignition temperature.

ACKNOWLEDGMENTS

This research was sponsored and supported by the US Air Force Systems Command and the Air Force Office of Scientific Research. Support was also extended by the College of Pure and Applied Science of the University of Lowell (Massachusetts). Grateful acknowledgement is extended to Universal Energy Systems, Inc. for administration of work under the aegis of the Air Force Summer Faculty Research Program. We are also grateful for valuable information, advice and suggestions provided by Mr. James Sartain and Mr. Andrew Poulis of the Air Force Engineering and Services Center at Tyndall Air Force Base; Dr. Robert Levine, Dr. Kermit Smyth and Dr. J. Houston Miller of the National Institute of Standards and Technology; Mr. William Westfield, Mr. Eugene Klueg and Dr. George Geyer of the Federal Aviation Administration's Engine/Fuel Safety Branch and Services Center at Atlantic City, NJ; Dr. Joseph Leonard and Dr. Homer Carhart of the Naval Research Laboratory; Mr. Michael Beltran of Beltran, Inc.; and Achal Thakkar and Robert Zsofka, and Professors Albert Kowalak and James Pierce of the University of Lowell.

REFERENCES

1. Jackson, J. L. Ind. Eng. Chem. **1961**, 43, 2869.
2. Miller, R. G. Symp. #6, Major Aircraft Fires (Proc.), Fire Research Station, Boreham Wood, Herts, England, Dec. 1966, pp. 54-65.
3. Lange, N. A. "Handbook of Chemistry", 9th ed., Handbook Publishing Co., Sandusky, OH, 1956, p. 824.
4. McCracken, D.J. "Hydrocarbon Combustion and Physical Properties", BRL-1496; Ballistic Res. Lab, Aberdeen Proving Ground, MD (1970).
5. Perry, R. H. "Chemical Engineering Handbook", 3rd ed., McGraw-Hill Book Co., New York, 1950, pp. 1584-1585.
6. "Fire Hazard Properties of Flammable Liquids, Gases and Volatile Solids", National Fire Protection Association, Boston, MA, 1960.
7. "Autoignition Temperature of Liquid Chemicals", ASTM Designation E 659 - 78 (Reapproved 1984).
8. Affens, W. A.; Johnson, J. E.; Carhart, H. E. J. Chem. Eng. Data **1961**, 6, 613-619 (and references cited therein).
9. Frank, C. E.; Blackham, A. U. Ind. Eng. Chem., **1952**, 44, 862-867.
10. Brooks, B.; Bruccoleri, R.; Olafson, B.; States, D.; Swaminathan, S.; and Karplus, M. J.Comp.Chem. **1983**, 4, 187.
11. Allen, M.; Tildesley, D. "Computer Simulation of Liquids", Oxford Science Publications (Clarendon Press, Oxford), 1987.

THE ESTIMATION OF STATURE FROM FRAGMENTS OF THE FEMUR:
A Revision of the Steele Method

Final Report submitted to
Universal Energy Systems
Sept. 23, 1988

by

William M. Bass

Richard L. Jantz

Tal Simmons

Department of Anthropology
University of Tennessee
Knoxville, TN 37996-0720

INTRODUCTION

The estimation of stature from various skeletal elements has been an area of critical interest to physical anthropologists for many years. Past studies concerning stature estimation have included those by Manouvrier (1892), Stevenson (1929), Allbrook (1961), Genoves (1967), Lundy (1983) and Lundy and Feldesman (1987). These papers presented data and statistical formulae for the estimation of stature for geographic and racial groups as diverse as the Chinese and the South African Black. The formulae most often employed in the United States are those provided by Trotter and Gleser (1951a; 1951b; 1952; 1958) and Trotter (1970). All of these studies have shown a high correlation between the length of any whole, long limb bone and stature, with the highest single correlation being the femur.

Forensic anthropologists are often confronted with fragmentary remains while the estimation of stature by conventional formulae is dependent upon whole limb bones. The estimation of living stature from long bones is based upon the principle that the various long limb bones correlate positively with stature. Since this is true, the parts of each individual long bone should also be related to stature even though they may not correlate as highly as the length of the whole bone. Stature estimation from fragmentary long bones has been attempted by Muller (1935), Steele and McKern (1969), and Steele (1970). In practice, these methods are difficult to apply because of difficulty in identifying the exact location of necessary anatomical landmarks. Steele (1970:87) himself recognized this problem when he stated:

Another landmark not used in the present study, but used previously by the author and Dr. McKern, involves the humerus alone. The landmark in question is the point of greatest narrowing at the middle of the diaphysis. Although this narrowing can be related to a point, posterolaterally in the radial groove where the lateral supracondylar ridge becomes indistinct (on a level with the distal termination of the surface for m. deltoideus), in practice the point proved impossible to locate with sufficient constancy to give useful results.

Most practicing physical anthropologists have also experienced difficulties in locating many of the other anatomical landmarks used to predict stature from fragmentary long bones. Indeed many do not use either the Steele and McKern (1969) or the Steele (1970) formulae, and hence do not attempt to estimate stature when no whole long limb bones are present because of this very difficulty. However, since skeletal remains are often fragmentary, it would be useful to devise a more reliable technique for stature estimation from smaller segments of long bones.

OBJECTIVE

The objective of this study is to assess the feasibility of stature estimation using small fragments of the femur. As described above, the Steele and McKern (1969) and Steele (1970) methods are plagued by the difficulty of identifying the anatomical landmarks which define the various segments of the limb bones from which estimations are calculated. The present approach seeks to avoid this pitfall by using standard, clearly defined measurements taken on the distal, proximal, and midshaft regions of the bone. Many of these measurements are already familiar to physical anthropologists, who regularly use them for

comparative population studies or in some cases, the estimation of gender. It is also hoped that, by presenting data and providing equations for the estimation of stature from small segments of all areas of the bone, any recovered section might be used to estimate stature. It will normally be the case that smaller segments of bone will exhibit weaker relationships to stature than larger segments. Because the emphasis of this study is on smaller segments, the equations generated are therefore expected to offer less accuracy for both maximum femur length and stature. However, when small segments alone are available, this approach will offer the best opportunity for estimation of stature. The relationship of these dimensions to maximum femur length and stature has never been systematically examined.

The femur was selected as the initial skeletal element to be analysed because in addition to its high correlation with stature, it is (along with the feet) one of the bones most frequently recovered from Air Force crash sites. It is a large, durable bone protected by both large amounts of soft tissue and the seat and harness mechanisms of the aircraft.

METHODOLOGY

The sample measured was obtained from the Terry anatomical collection housed at the Smithsonian Institution's National Museum of Natural History in Washington, D. C.. The skeletons in the Terry collection are from cadavers dissected at the Washington University School of Medicine, St. Louis, Mo. Accurate data for age, sex, race, and cadaver stature are

available. A sample of approximately 200 males and 200 females from Blacks and Whites, yielding a total sample of 800 individuals was obtained. To be included in the sample an individual must have race and sex recorded on the morgue record. Only femora exhibiting no gross pathological changes of the distal, proximal, or midshaft regions were included in the study. Left femora were measured whenever possible, though right femora were substituted if breakage or pathological conditions precluded the use of the left. Preference for inclusion in the sample was given to individuals for whom age and cadaver stature were also recorded. With few exceptions, photographs of the cadavers were examined in order to be certain that the stature was recorded when the body was placed vertically with the feet in natural plantar position.

The measurements employed are defined in Table 1 and illustrated in Figure 1. All seven measurements are standard and defined in Martin (1957). The definition of number 7 was modified from a midshaft diameter to a minimum transverse shaft diameter in order to avoid the necessity of locating a midpoint on a fragment. All the measurements can be recorded with ease. Maximum femur length was measured on an osteometric board; all other measurements were obtained with sliding calipers. All measurements were taken by Tal Simmons, a Ph.D. student in physical anthropology at the University of Tennessee.

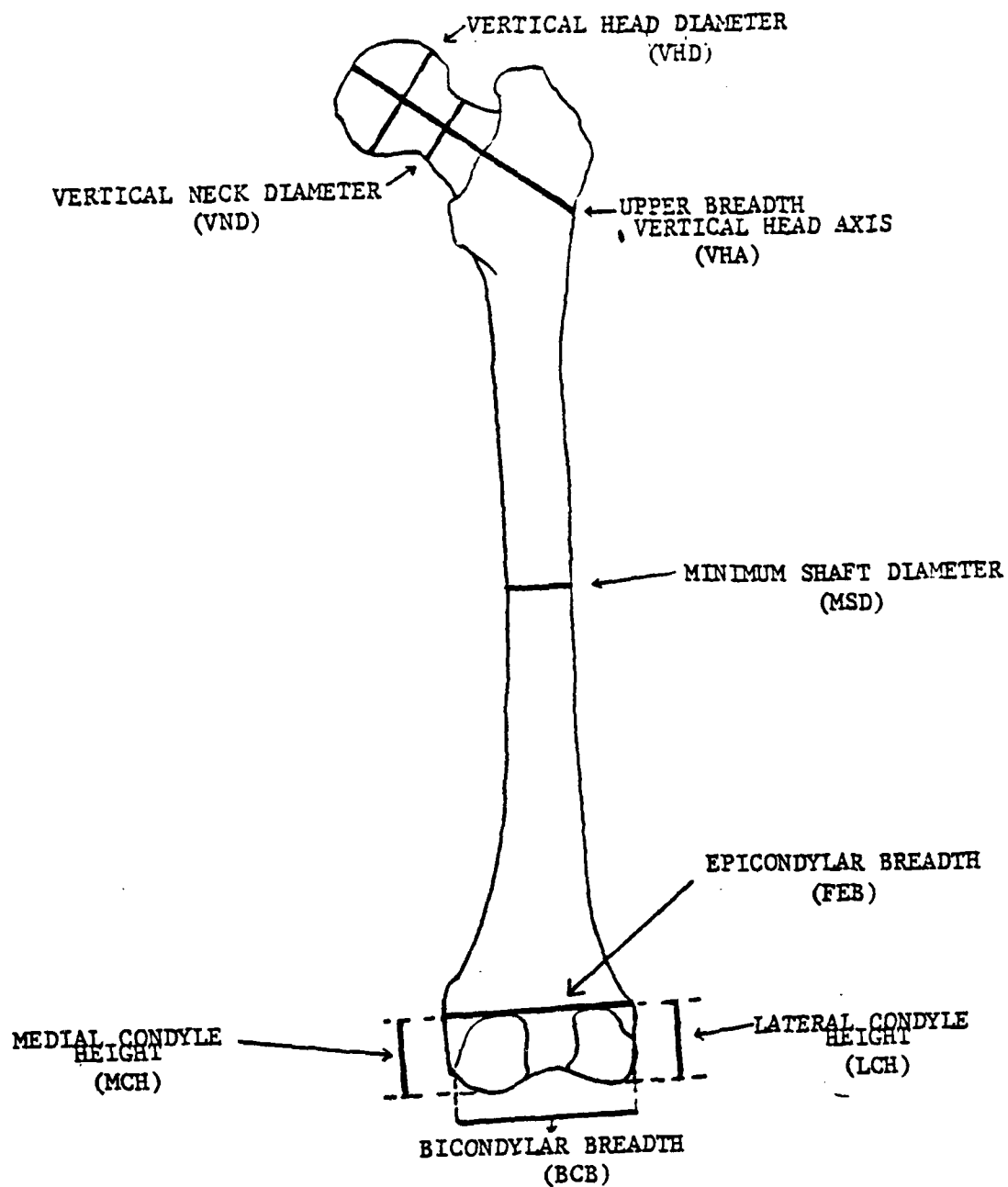


FIG.1 STANDARD MEASUREMENTS OF THE FEMUR USED IN THE REGRESSION EQUATIONS AGAINST MAXIMUM FEMUR LENGTH (FML).

Table 1 : Measurements (abbreviations in parentheses) used in estimating stature from femoral fragments.

<u>Martin No.</u>	<u>Measurement</u>
1	Maximum Femoral Length (FML)
18	Vertical diameter of the femoral head (VHD)
15	Vertical diameter of the femoral neck (VND)
13	Proximal Breadth of the Femur (VHA)
7	Transverse diameter of midshaft (minimum) (WSD)
-	Bicondylar Breadth (BCB)
21	Epicondylar Breadth (FDL)
25	Lateral Condyle Height (LCH)
26	Medial Condyle Height (MCH)

Data were entered on an IBM compatible PC using dBase III-plus. Analysis of the data was carried out using the SAS package on the University of Tennessee's Vax cluster. Equations for the prediction of stature were generated in two ways. First, stature estimation was performed by the usual method of regressing stature onto bone measurements. Second, because the Terry collection records do not always list the cadaver stature of the individual, maximum femur length was also regressed onto bone measurements. By determining the maximum femur length of an individual from a fragment, the stature may then be estimated also, though the standard error of the estimate will be increased.

RESULTS

Age, Stature, and Maximum Femoral Length

Stature, femur length and age of the present sample is compared to other samples which have been used in stature estimation in Table 2. The means and standard deviations for age, stature, and maximum femur length are quite close to those presented by Trotter and Gleser (1952) for the Terry Collection.

They differ, however, from those presented by Steele (1970) presumably because of that author's small sample size and his elimination of older individuals (those over age 70) from his study. Jantz and Moore-Jansen (1988) have shown that the Terry Collection differs from the contemporary White and Black population, present day populations exhibiting significantly longer femora. Table 2 also shows that Terry Collection heights are considerably below Trotter and Gleser's (1958) Korean war dead and Modern Forensic cases. Consequently, regression formulae developed from the Terry collection and applied to modern people may underestimate stature.

Summary of Fragment Measurements

Table 3 presents the means and standard deviations for each of the segments measured. Correlations for these measurements with femur length and cadaver stature are given in Table 4. The correlations show the strength of association between the segment measurements, stature and femur length. At the outset we had expected that VHA (proximal femur breadth) would be the best predictor and that is borne out by the correlations in males, but in females several other measurements are more highly correlated. In general, correlations rarely exceed 0.65.

Comparison with Steele's Results

Our goal at the outset was to attempt stature estimation from fragments which would equal or exceed Steele's in accuracy but would use standard measurements. We can examine this question by comparing our segment correlation with those from Steele that are more or less comparable. Steele's segment 1 is measured from

Table 2. Means and standard deviations of age(yrs), stature*(cm.) and femur length(cm.) of various samples compared to present sample.

White Males

Terry(1)	200	58.73	13.88	167.75	7.59	45.64	2.68
Terry(2)	255	61.66	12.55	167.89	7.34	45.66	2.45
Terry(3)	61	52.97	4.98	168.44	4.98	46.24	3.06
War dead(4)	545	23.14	4.31	173.90	6.63	47.29	2.36
War dead(5)	1265	--	--	174.39	6.55	47.17	2.30
Modern(6)	113	37.26	17.08	176.07	8.06	47.18	2.54

Black Males

Terry(1)	203	47.33	16.77	170.18	7.97	47.47	2.93
Terry(2)	360	49.46	15.51	170.23	7.81	47.42	2.97
Terry(3)	42	43.25	13.21	172.02	7.84	47.92	3.28
War dead(4)	54	25.07	4.98	172.11	6.14	48.34	2.26
War dead(5)	191	--	--	173.86	6.65	48.41	2.48
Modern(6)	29	37.45	21.52	179.15	6.68	48.24	2.81

White Females

Terry(1)	201	63.19	15.59	157.07	7.76	42.71	2.36
Terry(2)	63	63.93	16.07	158.18	7.51	42.96	2.53
Terry(3)	52	63.35	17.02	157.62	7.96	42.69	2.71
Modern(6)	89	37.14	21.52	165.54	5.94	43.72	2.02

Black Females

Terry(1)	199	48.11	18.44	159.04	6.63	43.99	2.41
Terry(2)	177	47.21	17.65	158.39	6.53	43.71	2.39
Terry(3)	57	39.58	15.52	159.88	6.22	43.96	2.30
Modern(6)	24	34.37	19.73	165.00	10.80	45.52	3.23

*Terry collection stature=cadaver stature-2.5cm. All others are stature obtained during life.

1. Present study
2. Trotter and Gleser (1952)
3. Steele (1970)
4. Trotter and Gleser (1952)
5. Trotter and Gleser (1958)
6. Jantz and Moore-Jansen (1988)

the proximal point on the head of the femur to the midpoint of the greater trochanter. It is comparable to our VHA (proximal femur breadth) in the size and location of the fragment.

Table 3. Means and standard deviations (mm.) of the Terry collection segments, by race and sex.

Variable	W Males		B Males		W Females		B Females	
	X	SD	X	SD	X	SD	X	SD
VHA	99.10	5.87	98.99	5.77	88.24	5.18	88.98	5.24
VHD	48.27	3.17	47.65	2.69	42.54	2.50	41.95	2.35
VND	33.09	3.05	31.16	2.60	29.27	2.62	27.17	2.48
WSD	28.26	2.16	28.05	2.21	25.10	2.13	25.18	2.03
LCH	41.35	2.91	42.33	3.00	36.30	2.53	37.05	2.34
MCH	40.92	3.01	41.94	3.22	37.22	2.90	37.75	2.70
BCB	77.81	4.30	77.71	4.57	68.44	3.75	67.74	3.94
FDL	83.42	4.47	83.00	4.22	74.57	3.54	73.94	3.95

Table 5 shows the correlations of our VHA (proximal femur breadth) and Steele's segment 1 with stature and maximum femur length. For stature, our correlations exceed Steele's in three of the four groups; only in White males is it slightly lower. For femur length, Steele's correlations are higher in three of the four groups. All 16 of the correlation coefficients are similar, indicating approximately equal predictive efficiency.

Steele's segment 4 is comparable to our MCH (medial condyle height). His correlations with height and femur length exceed ours in four cases while ours exceed his in four cases. However, our LCH (lateral condyle height) yields consistently higher correlations than MCH in our data (see table 4). Comparing LCH to Steele's segment 4 shows our correlations to exceed his in 7 of 8 comparisons. It is evident that lateral condyle height has the higher correlation with stature and femur length and is to be

preferred as the predictor variable when both condyles are present.

Table 4. Correlations of femur segments with maximum femur length and stature by race and sex.

Var.	W Males		B Males		W Females		B Females	
	Ht	FML	Ht	FML	Ht	FML	HT	FML
VHA	0.587	0.606	0.564	0.592	0.526	0.632	0.432	0.513
VHD	0.462	0.526	0.499	0.454	0.406	0.596	0.540	0.585
VND	0.312	0.384	0.393	0.315	0.409	0.409	0.461	0.422
WSD	0.386	0.281	0.251	0.276	0.428	0.295	0.367	0.277
LCH	0.557	0.571	0.503	0.452	0.677	0.665	0.571	0.585
MCH	0.417	0.459	0.391	0.404	0.595	0.518	0.470	0.403
BCB	0.512	0.541	0.509	0.440	0.294	0.445	0.220	0.345
FDL	0.493	0.521	0.560	0.465	0.428	0.537	0.329	0.415

Table 5. Correlations of upper femur breadth (VHA) and Steele's segment 1 with height and femur length

	Steele's Segment 1		VHA (Proximal Breadth	
	Height	Femur lgth	Height	Femur lgth
White males	0.602	0.651	0.588	0.607
White females	0.498	0.623	0.526	0.632
Black males	0.472	0.606	0.564	0.593
Black females	0.431	0.543	0.432	0.514

Formulae for the Estimation of Stature and Maximum Femur Length

In this section we present the statistical constants for estimating height and femur length from various fragments. We will present only those equations which offer the best predictive capability and seem useful in forensic work.

Table 6 presents the slopes, intercepts and standard errors of estimates for each race/sex group for stature and femur length using the variable VHA (proximal femur breadth) VHD (femur head diameter) LCH (lateral condyle height) MCH (medial condyle height) as predictor variables. While not presented as an equation, these constants are used in the same manner as traditional regression equations. Thus to estimate stature for a white male, using VHA one takes the slope times VHA and adds the intercept. The standard error of estimate then provides an indication of the range within which the true stature is likely to fall. For example, suppose femur fragments from a White male yield the following measurements: VHA=95mm.; LCH=40mm.; VHD=45mm. These measurements would be used to estimate stature as follows:

$$\text{Stature} = 0.78 \times 95\text{mm.} + 89.64 = 163.74\text{cm.} \pm 6.10\text{cm.}$$

$$\text{Stature} = 1.47 \times 40\text{mm.} + 107.09 = 165.89\text{cm.} \pm 6.24\text{cm.}$$

$$\text{Stature} = 1.11 \times 45\text{mm.} + 113.89 = 163.84\text{cm.} \pm 6.77\text{cm.}$$

The average ages for all groups in this study are similar to those presented by Trotter and Gleser (1952) in their work with the Terry Collection. In addition to concern regarding the secular trend in stature increase discussed above, Trotter and Gleser (1951a) addressed the issue of the effects of aging on stature. The correction of stature for age related effects is

Table 6. Regression constants for estimating stature* and femur length** from VHA, LCH and VHD. These are the three best predictor variables. See text for instructions.

	Height			Femur length		
	slope	intercept	S.E.	slope	intercept	S.E.
Predictor variable: VHA (proximal femur breadth)						
White males	0.78	89.64	6.10	0.29	14.81	2.10
White females	0.73	91.54	6.67	0.21	21.50	2.10
Black males	0.79	91.70	6.60	0.32	13.64	2.30
Black females	0.59	107.10	6.00	0.25	21.90	2.04
Predictor variable: LCH (lateral condyle height)						
White males	1.47	107.09	6.24	0.54	20.86	2.18
Black males	1.34	113.23	6.91	0.46	25.44	2.59
White females	1.94	86.10	5.77	0.42	24.96	2.09
Black females	1.59	100.07	5.47	0.56	20.80	2.03
Predictor variable: VHD (femur head diameter)						
White males	1.11	113.89	6.77	0.43	23.57	2.32
Black Males	1.51	97.82	6.92	0.54	19.45	2.56
White females	1.35	99.22	7.16	0.47	20.22	2.06
Black females	1.59	92.43	5.59	0.58	17.12	1.99
* Stature= predictor variable x slope + Intercept + S.E.						
** Femur length= predictor variable x slope + Intercept + S.E.						

given by Trotter and Gleser (1952); they suggest that this formula be applied to all individuals over the age of 35 for whom stature is to be estimated.

DISCUSSION

The method of femur length and stature estimation presented here has several advantages over previous attempts. First, the anatomical landmarks by which these measurements are defined are standard, well defined, and easy to locate. Many of them are already in standard usage for the estimation of sex or are standard measurements taken for comparative purposes on post cranial material. Second, the standard errors of estimates were equal to or lower than those presented by Steele (1970) for his smaller segments. And third, the sample size used in this study is approximately four times that used by Steele (1970), and thus the regression equations are more accurately estimated.

Perhaps the most significant comparison of the technique presented in this study with that of Steele (1970) concerns the standard errors of estimate. For comparable segments, such as those involving the proximal end (VHA) or the distal end (LCH) our standard errors of estimate are uniformly lower than Steele's. That in turn indicates that our stature estimates are more accurate. To some extent this results from higher standard deviations for femur length and height in Steele's sample. This is apparently a consequence of Steele's smaller sample size.

Our results have demonstrated the feasibility of estimating stature and femur length from small fragments using standard measurements. It is becoming increasingly clear that the Terry collection skeletons were drawn from a population considerably smaller than contemporary Americans. Therefore, our results should be viewed more as indicative of the feasibility of the technique than as providing formula applicable for forensic work

on contemporary people.

CONCLUSIONS

The technique for the estimation of stature from fragments of the femur presented in this report represents an improvement over methods which are currently in use. It is desirable to develop formulae using skeletons from contemporary populations, if possible. It is also possible that certain other bones likely to survive air crashes because of protection, such as the bones of the foot, calcaneous and metacarpals in particular, would lend themselves to stature estimation. Future research should be directed along these lines.

REFERENCES CITED

- Allbrook, D. (1961). The estimation of stature in British and East African Males. *Journal of Forensic Medicine* 8:15-28.
- Genoves, S. (1967). Proportionality of the long limb bones and their relation to stature among Mesoamericans. *American Journal of Physical Anthropology* 26:67-78.
- Jantz, R. L. and Moore-Jansen, P. H. (1988). A Data Base for Forensic Anthropology. Department of Anthropology Report of Investigations No. 47. Knoxville: The University of Tennessee.
- Lundy, J. (1983). Regression equations for estimating living stature from long limb bones in the South African Negro. *South African Journal of Science* 79:337-338.
- Lundy, J. and Feldesman, M. (1987). Revised equations for estimating living stature from the long bones of the South African Negro. *South African Journal of Science* 83:54-55.
- Manouvrier, L. (1892). Determination de la taille d'apres les grands os les membres. *Revue Mensuelle de l'Ecole d'Anthropologie* 2:227-233.
- Martin, R. (1957). *Lehrbuch der Anthropologie*. Revised Third Edition, Vol. 4. Karl Saller, Editor. Stuttgart: Gustav Fischer Verlag.
- Moore-Jansen, P. H. and Jantz, R. L. (1986). A computerized skeletal data bank for Forensic Anthropology. Knoxville: The University of Tennessee.
- Muller, G. (1935). Zur Bestimmung der Lange beschadigter Extremitatenknochten. *Anthropologischer Anzeiger* 12:70-72.
- Steele, G. (1970). Estimation of stature from fragments of long limb bones. In (T. D. Stewart, Ed.) *Personal Identification*

- in Mass Disasters, pp. 85-97. Washington, D. C.:
Smithsonian Institution Press.
- Steele, G. and McKern, T. (1969). A method for assessment of
maximum long bone length and living stature from
fragmentary long bones. American Journal of Physical
Anthropology 31:215-227.
- Stevenson, P. (1929). On racial differences in stature long bone
regression formulae with special reference to stature
reconstruction formula for the Chinese. Biometrika 21:303-321.
- Trotter, M. (1970). Estimation of stature from intact long limb
bones. In (Stewart, T. D. Ed.) Personal Identification in
Mass Disasters, pp. 71-83. Washington, D. C.: Smithsonian
Institution Press.
- Trotter, M. and Gleser G. (1951a). The effect of aging on
stature. American Journal of Physical Anthropology 9:311-324.
- Trotter, M. and Gleser, G. (1951b). Trends in stature of American
Whites and Negroes born between 1840 and 1924. American
Journal of Physical Anthropology 9:427-440.
- Trotter, M. and Gleser, G. (1952). Estimation of stature from
long bones of American Whites and Negroes. American
Journal of Physical Anthropology 10:463-514.
- Trotter, M. and Gleser, G. (1958). A re-evaluation of estimation
of stature based on measurements of stature taken during life
and of long bones after death. American Journal of Physical
Anthropology 16:79-123.

FINAL REPORT

1987-88 Mini-Grant Program

Sponsored by the
Air Force Office of Scientific Research

Conducted by
Universal Energy Systems

**"EFFECTS OF WATER SOLUBILITY AND FUNCTIONAL GROUP CONTENT ON THE
INTERACTIONS OF ORGANIC SOLUTES WITH SOIL ORGANIC MATTER"**

Prepared by: William T. Cooper, Ph.D.
Academic Rank: Associate Professor
Department: Chemistry
University: Florida State University
Research Location: Dittmer Laboratory of Chemistry
Florida State University
Tallahassee, Florida
Date: May 19, 1988
Contract No: F49620-85-C-0013/SB5851-0360
Purchase Order No: S-760-6MG-081

**PART I: CHARACTERIZATION OF POLAR SOLUTE - SOIL ORGANIC MATTER
INTERACTIONS BY HIGH PERFORMANCE LIQUID CHROMATOGRAPHY**

C.P. Antworth, R.R. Yates and W.T. Cooper*
Department of Chemistry
and
Center for Biomedical & Toxicological Research
Florida State University
Tallahassee, Florida 32306-3006

Presented in the "Symposium on Organic Geochemistry: Techniques
and Applications"
Division of Geochemistry
194th National Meeting of the American Chemical Society
New Orleans, LA
September, 1987

Submitted to **ORGANIC GEOCHEMISTRY**
December, 1987

* Author to whom correspondence should be addressed

In order to more fully understand the role of soil and sedimentary organic matter (SOM) in the migration and fate of organic pollutants in aquatic systems, a fast and accurate liquid chromatography method has been developed for the determination of sorption isotherms. The method is a modified Frontal Analysis by Characteristic Point (FACP) technique which accounts for hydrodynamic dispersion and which uses conventional HPLC equipment coupled with commercially available chromatography software. We have used this technique to generate sorption isotherms for various fractions of the total SOM. Isotherms are then fit to the Freundlich equation, from which water - organic carbon distribution coefficients (K_{OC} values) can be calculated. In this presentation we report on our studies of the roles played by various fractions of soil organic matter (lipids, humic/fulvic acids and humin) in the overall sorption process. By using solute probes which interact with solid phases in well-defined ways, we have been able to determine the contributions of acidic, basic and dipolar sites in the various SOM fractions, as well as the contribution of nonspecific hydrophobic partitioning, in the sorption of nonionic, polar organic solutes. It appears that these solutes interact with soil organic matter primarily through specific interactions with active sites in the humin fraction of the organic matrix, although there is some hydrophobic partitioning into the lipid fraction as well.

INTRODUCTION

It is now generally recognized that the sorption of sparingly soluble organic solutes onto soils and aquifer media is dominated by the natural organic carbon fraction of these materials. Lambert (1966,1968,1978) and Lambert et al. (1965) first demonstrated this principle with studies of neutral organic pesticide uptake onto a variety of soils. Lambert and co-workers (1965) also suggested that soil organic matter might act as an organic solvent in a solvent extraction process, and thus the movement of neutral organics in soils could be considered analogous to a chromatographic process, with dissolved solutes partitioning between a polar aqueous mobile phase and a non-polar stationary phase of soil organic matter coating an inorganic matrix. The partitioning of a neutral organic solute in such a system should then be correlated with the solute's partitioning between water and an immiscible organic solvent, and Briggs (1973) and Chiou et al. (1979) developed empirical equations which related sorption in soil systems to a solute's octanol-water partition coefficient.

The importance of sorption, including adsorption and/or partitioning on/into soil organic matter, in the transport of nonionic organic solutes can be addressed by first considering the relative residence time, or retardation factor, $(t_r)_i$, of a solute as it travels from source to observation point in an aquifer. This retardation factor is defined by equation 1:

$$(t_r)_i = \frac{t'_i}{t'_w} \quad (1)$$

where t'_i and t'_w represent the average travel times of solute i and water molecules, respectively. The effect of sorption on this factor can be quantitatively estimated through equation 2:

$$(t_r)_i = 1 + (K_d)_i \frac{\rho_{aq}}{\theta_{aq}} \quad (2)$$

where $(K_d)_i$ is the distribution coefficient for solute i between water and the aquifer media and ρ_{aq} and θ_{aq} represent the average bulk density and effective porosity of the media, respectively.

Distribution coefficients for the sorption of nonionic solutes on complex, heterogeneous soils and aquifer materials actually represent the weighted sum of all individual contributions:

$$(K_d)_i = \sum_j f_j (K_d)_{i,j} = f_{inorg} K_{inorg} + f_{org} K_{org} \quad (3)$$

where f_j represents the fraction of phase j and $(K_d)_{i,j}$ the distribution coefficient for solute i on that phase. However, Karickhoff et al. (1979) evaluated the sorption of many hydrophobic organic solutes on a variety of organic rich (>1% organic matter) natural sediments and found that sorptive effects of the inorganic matrix were negligible. Equation 3 could therefore be written

$$(K_d)_i = f_{oc} (K_{oc})_i \quad (4)$$

where $(K_{oc})_i$ is the distribution coefficient for the sorption of

i onto the organic fraction alone and f_{OC} is the mass percentage of this fraction in the mineral assemblage. Karickhoff et al. (1979) also evaluated the relationship between K_{OC} and a variety of solute properties and found first that, for sorption onto the fine fractions (<50 μm particles) of the sediments, a solute tended to have a reasonably constant K_{OC} , regardless of the origin of the organic matter. These workers also observed, in agreement with previous studies, a highly significant correlation between K_{OC} and a solute's octanol/water partition coefficient, K_{OW} .

$$\log K_{OC} = a * \log(K_{OW}) + b \quad (5)$$

Sorption onto the sand fraction (particles >50 μm) could also be described by equation 5, but the fitting coefficients were different than those for the fine fraction.

Substituting equations 4 and 5 into equation 2 yields

$$(t_r)_i = 1 + C * f_{OC} * (K_{OW})_i * \frac{a_q}{a_q} + C' \quad (6)$$

The relative residence time of organic solutes in aquifers can therefore be predicted from equation 6 if accurate measurements or estimates of f_{OC} , $(K_{OW})_i$, a_q and a_q are available.

Numerous studies have confirmed the conclusions of Lambert and co-workers, Briggs, Chiou et al. and Karickhoff et al.

(Hamaker and Thompson, 1972; Schwartzbach and Westall, 1981; Chiou et al., 1983; Chiou et al., 1985; Karickhoff, 1984). These studies invariably involve hydrophobic organic solutes, such as halogenated hydrocarbons, and organic rich soils and sediments. For such systems it is generally accepted that interactions between solutes and soil organic matter result from hydrophobic effects (Tanford, 1980). The driving force for such 'hydrophobic interactions' is the increase in entropy associated with the removal of the structured hydration region that surrounds a solute in water. This hydrophobic model also has been shown to be valid when organic cosolvents are present, and therefore is more generally termed a 'solvophobic' model (Banerjee et al., 1980; Rao et al., 1985; Nkedi-Kizza et al., 1985).

In spite of these advances in understanding the thermodynamic driving forces that control the adsorption and/or partitioning of organic solutes between water and soils, there are still many questions which have not been answered. Even for hydrophobic solutes which should interact only through hydrophobic forces, $(K_{OC})_i$ values have been observed to vary by as much as factors of 3 to 5 for different mineral/organic assemblages (Curtis et al., 1986). Mingelgrin et al. (1983) found literature values of K_{OM} (K_d expressed on an organic matter rather than organic carbon basis) that varied by more than an order of magnitude. This is an indication that the fitting coefficients of equation 5 could be a function of the nature of the soil organic matter involved. It is well known in the field of organic geochemistry that the chemical character of organic

matter in sediments depends both on the paleoecological conditions at the time of deposition and the extent of diagenesis within the sediment (Tissot and Welte, 1984). It should not be surprising, therefore, to find that soil and sedimentary organic matter might be highly variable in its ability to interact with organic solutes. Indeed, Lambert et al. (1965) suggested this in their original work. Hartley (1960) argued that the fats-waxes-resins fraction of soil organic matter was actually responsible for the sorption of nonionic organic solutes. In probably the most definitive study to date on this subject, Garbarini and Lion (1986) showed that different components of soil organic matter had widely varying affinities for toluene and trichloroethylene (TCE), both nonionic, hydrophobic organic solutes.

As noted previously, virtually all the studies cited involved nonpolar, hydrophobic organic solutes. If soil organic matter does vary in its affinity for organic solutes, this variability would become more pronounced as the water solubility of the organic solute increases. With increasing water solubility the non-specific hydrophobic effect becomes less important in the sorption process, while specific solute-organic matter interactions correspondingly increase in importance. In such cases it would therefore be necessary to consider the specific adsorptive characteristics of soil and aquifer organic matter.

In this and the following paper we report the results of our initial studies of the sorptive properties and chemical characteristics of several fractions of soil organic matter using the 'Inverse Chromatography' technique. In this approach the

column material itself is characterized by observing the retention behavior of solutes which are chosen because they are known to interact in chemically well-defined ways. The explosive growth in more conventional chromatographic separations that has occurred over the past 15 years has overshadowed the rather unique ability of chromatographic methods to measure meaningful physiochemical parameters.

In order to ensure that the organic matter under investigation is indeed variable in both composition and adsorptive character, we have chosen to study fractions of a single organic matter sample rather than a variety of different samples. An organic rich sediment (peat) was first fractionated into standard organic geochemical classes: lipids, humic and fulvic acids, and non-extractable humin. By comparing the sorption of the chosen solutes on these various organic matter fractions with the sorption observed with the total organic matter, we have been able to define the relative importance of each of these fractions in determining the overall, specific chemical character of soil organic matter.

In this first paper we report on our studies of the interactions of polar organic solutes with soil organic matter fractions using a dispersion corrected High Performance Liquid Chromatography (HPLC)/ Frontal Analysis by Characteristic Point (FACP) technique. We will also present the results of structural and compositional studies carried out primarily by solid state ^{13}C NMR spectroscopy. This is a powerful technique for studying

insoluble organic material, but a technique which has not yet found significant applications in environmental chemistry. Analyses of the solid state NMR spectra have allowed us to correlate soil organic matter structure with sorption properties.

EXPERIMENTAL

Substrate Preparation

Commercially available peat was prepared for fractionation by lyophilizing for 24 hours to obtain what will be termed the total soil organic matter (SOM) fraction. Non-bound lipid material was then removed by repeated methylene chloride-methanol (2:1) extractions, followed by vacuum filtration until a clear organic phase was achieved. The resulting lipid material was rotary-evaporated to dryness. The residue (SOM-Lipid) was split and one-half subjected to a 48 hour saponification in 1N NaOH, followed by repeated washings with 0.01N NaOH until the supernatant became clear. This procedure removed the humic and fulvic acids. The non-extractable residue was subsequently washed with methylene chloride to remove bound lipids freed during the saponification. The remaining residue is termed the Humin fraction. The entire fractionation scheme is summarized in Figure 1.

Column Preparation

The three insoluble residue fractions were each dried by lyophilization, frozen in liquid nitrogen and ground in a mortar and pestle. The material was then dry-sieved to isolate a 38-53 micron size fraction. To ensure reasonable chromatography retention times an appropriate amount of organic matter was weighed and mechanically mixed with 37-44 micron pellicular

silica gel to yield a 5% w/w organic matter mixture. Lipid material was solublized in methylene chloride and rotary-evaporated onto the silica gel support to yield a 1% w/w coated packing material. The prepared materials were dry packed into stainless steel HPLC analytical columns (4.1 mm I.D.) fitted with 5 micron column frits. Prior to analysis each column was allowed to equilibrate for 4-6 hours under continuous flow of deionized water. After analysis packing material was removed from the columns, dried, and percent organic carbon determined using a Horiba model PIR 2000 General Purpose Infrared Gas Analyzer.

Materials and Reagents

Solute probes were purchased from Mallinkrodt (St. Louis, Mo.) and were of analytical reagent grade. Aniline was purified by distillation prior to use. Vydac pellicular silica gel (37-44 micron) was purchased from Alltech Associates Inc. (Deerfield, Ill.). Water used in the analysis was purified by distillation and deionized using a Millipore Milli-Q system.

NMR Spectroscopy

^{13}C CP-MAS NMR spectra were obtained with a Bruker WP-200 SY spectrometer equipped with an IBM solids accessory operating at 50 MHz for carbon. The spectrometer was tuned with t-butyl benzene and the chemical shifts are reported as parts per million downfield from tetramethylsilane. Lyophilized samples were spun at the magic angle at 4 KHz. Use and optimization of this instrument for studying sedimentary organic carbon has been

described previously (Cooper et al., 1985; 1986). Dipolar dephasing delay spectra were obtained using a contact time of 1 millisecond and a 50 microsecond delay period prior to data acquisition during which the proton decoupler is turned off. A 180° refocusing pulse was inserted at the mid-point of this delay period.

HPLC System

Frontal chromatograms used in the dispersion corrected FACP technique were generated using a conventional HPLC system consisting of a Valco six-port valve outfitted with a 13 mL sample loop, a Waters Model 510 Solvent Delivery System, and a Waters Model 440 Absorbance Detector operating at 254 nm wavelength. All data was collected by and processed using a Hewlett-Packard HP-1000 Lab Automation System.

Isotherm Generation

Isotherms were calculated from the rear diffuse boundary (i.e. the desorption branch) of a single frontal chromatographic peak. This technique is termed Elution by Characteristic Point (ECP), or Frontal Analysis by Characteristic Point (FACP). It was first introduced by Cremer (1961) and Huber and Kuelemans (1962), and has been thoroughly discussed by Conder and Young (1979). With this technique each point on the isotherm is calculated according to equation 7.

$$q(C) = \frac{1}{m} * \int_0^C (V-V_0) * dC \quad (7)$$

where $q(C)$ is the uptake, or the concentration of adsorbed solute in equilibrium with the aqueous mobile phase concentration C , m is the mass of organic matter present in the column, V is the volume eluted at concentration C , and V_0 is the void volume contribution. Void volumes were determined from frontal chromatograms of non-retained solutes.

The FACP technique, in contrast to the more familiar Frontal Analysis (FA) method, does not take into account dispersional broadening that occurs in the column. In order to refine the FACP technique we have introduced a dispersion correction which employs the diffuse rear boundary of a non-retained solute breakthrough curve. The advantage of this approach is that the entire, dispersion corrected isotherm can be determined from the diffuse rear boundary of a single chromatogram, whereas the FA method requires a separate chromatogram for each isotherm point. Solutes were determined to be non-retained by comparing their retention volumes to those of calcium chloride, as well as column void volumes determined gravimetrically (Jacobson et al., 1984). These comparisons agreed within 3%.

RESULTS

Reliability of the HPLC/FACP Method

The dispersion corrected HPLC/FACP method was compared with both a frontal chromatography technique and the more conventional batch isotherm method. K_{OC} values calculated by the uncorrected FACP method differed from frontal K_{OC} values by up to 14%, but when the dispersion correction was applied the difference was reduced to within 2%. When compared to K_{OC} 's obtained by the batch isotherm method, dispersion corrected HPLC/FACP K_{OC} values differed by as little as 1% to a maximum of 11%. Comparisons of K_{OC} values generated by these various methods are summarized in Table 1, where the worst cases observed are included.

The dispersion corrected HPLC/FACP method is therefore seen to produce results which are in substantial agreement with those obtained by other, more conventional techniques. It is important to note, however, that an entire isotherm can be generated from a single chromatogram by this method. The frontal chromatography technique requires separate chromatograms for each data point on the isotherm, while the batch method involves an individual experiment for each data point (extraction, analysis, etc.). Once a column has been prepared, the HPLC/FACP method can generate an isotherm approximately every 30 minutes. The speed of this technique thus allows a wide spectrum of solute probes to be investigated in a relatively short time and with a minimum of sample required.

Soil Constituent Trends

Isotherm data for the four isolated soil organic matter fractions were generated using four solute 'probes'. These solute probes were chosen because they are known to interact with surfaces in well defined ways (Snyder, 1974, 1978). Cresol is a 'soft' acid and interacts strongly with basic sites; aniline a 'soft' base that interacts with acidic sites; nitrobenzene interacts strongly with dipolar sites; and benzene is non-functionalized and therefore interacts via non-specific dispersion forces. While both cresol and aniline are weakly ionizable, at neutral pH their dissociation constants are such that they exist in essentially unionized form ($pK_a[\text{cresol}] = 10.2$, $pK_b[\text{aniline}] = 9.3$).

Sorption data for the four probes and four organic matter fractions are summarized in Figure 2, where experimental K_{OC} values are plotted vs. calculated K_{OW} 's. The fitting coefficients (a and b of equation 5) are summarized in Table 2. Interestingly, all fractions exhibit a reasonably linear relationship between K_{OC} and K_{OW} , as predicted by equation 5, although in some cases this linear relationship holds for only three of the four solutes. Surprisingly, however, it is only the lipid fraction that exhibits the positive slope observed by others when using nonpolar, hydrophobic solutes. Soil Organic Matter (SOM), SOM-Lipids, and Humin all show a negative relationship between K_{OC} and K_{OW} . We interpret these results as indicating that only

sorption onto the lipid fraction of SOM is driven by non-specific hydrophobic (or solvophobic) partitioning. Sorption onto the other fractions appears to result from specific interactions between polar sites in the organic matter and the polar solutes. Since polarity generally increases with increasing water solubility, and therefore decreases with increasing octanol-water partition coefficients, such specific interactions would then be expected to decrease as K_{OW} values increase. This, of course, is precisely the behavior we have observed with the insoluble soil organic matter fractions.

Consideration of the chemical nature of the solute probes used in these studies gives insight into the observed behavior. Aniline ($K_{OW} = 0.98$), the soft base probe, exhibits the highest K_{OC} values on all three insoluble SOM fractions, indicating a relatively large population of acidic sites in these fractions. These sites are probably due to carboxyl and phenolic groups, a conclusion which is confirmed by the NMR spectra (Figure 3). Nitrobenzene ($K_{OW} = 1.85$) shows the next highest K_{OC} values, indicating numerous polar but non acidic sites. Again, ^{13}C NMR is helpful in interpreting the nitrobenzene data, as the spectra show substantial methoxy (carbohydrate) structure. Benzene ($K_{OW} = 2.13$), the non-specific probe, shows the smallest affinity for the insoluble fractions, again suggesting that these materials are highly polar and functionalized. The soft acid probe cresol ($K_{OW} = 1.94$) exhibits erratic behavior which we attribute to either strong hydrogen bonding with the aqueous solvent or exclusion from the largely acidic organic matrix.

It is interesting to note from the data of Table 2 that removal of the lipid material from the intact SOM increases the slope and intercept of the $\log K_{oc}$ vs. $\log K_{ow}$ plot. This indicates that binding of polar solutes, when normalized for the fraction of organic carbon comprising the sorbent, increases once the lipid fraction is removed. This increased sorptivity may be a result of the lipid components hindering access to polar sites in the remaining organic matter matrix, or a concentration of polar sites in the residue. A similar effect is observed when the humic and fulvic acids are removed, with the humin fraction exhibiting the largest sorptive capacity for polar solutes per mass of organic carbon than any of the fractions studied. We interpret this trend in increasing sorptivity with removal of extractable organic matter as an indication that the polar, active sites in soil organic matter are concentrated in the non-extractable humin fraction.

Relationship Between Sorptive Characteristics and Structure of Soil Organic Matter

With the development of high power decoupling, cross polarization and magic angle spinning techniques (Pines et al., 1973; Schaefer and Stejskal, 1976), it is now possible to obtain ^{13}C NMR spectra of solid, insoluble materials that, in favorable situations, approach the quality of solution spectra. However, the inherent heterogeneity of soil and sedimentary organic matter results in peaks which are sufficiently broad so as to preclude any realistic interpretation of the 'fine structure' that may be

observed. For that reason solid state ^{13}C NMR spectra of SOM are normally analyzed by comparing relative intensities in four spectral 'windows': 0-50 ppm (aliphatic carbon), 50-100 ppm (methoxy [carbohydrate] carbon), 100-160 ppm (olefinic and aromatic carbon), and 160-190 ppm (carboxyl and amide carbon).

NMR spectra of SOM, SOM-Lipid, and Humin are displayed in Figure 3. One of the most striking features of these spectra is the pronounced relative decrease in the aliphatic peak (ca. 30 ppm) when the lipids are removed (i.e. Figure 3(b) compared to 3(a)). This indicates that non-functionalized, hydrophobic aliphatic carbon is the chief component of the lipid fraction. This explains the sorption results for both the isolated lipid fraction (hydrophobic partitioning), as well as the differences between the SOM and SOM-Lipid fractions. While both of these fractions appear to interact with the polar solute probes through specific interactions at polar sites in the organic matter matrix, the relative number of sites in the SOM-Lipid fraction appears to be greater than the relative number of sites in the unextracted SOM. In other words, the lipid fraction appears to dilute the concentration of active polar sites in the total SOM fraction. The lipid fraction might also physically and/or chemically block some active sites from interacting with the solute probes.

Removal of humic and fulvic acids (Humin, Figure 3(c)) does little to the overall structure of the organic matter, except to reduce the relative intensity of the carboxyl peak (ca. 170-180

ppm). This is an entirely expected result, of course, since humics and fulvics are thought to be primarily polycarboxylate type materials. The important feature of the Humin spectrum is that peaks arising from the important polar carbon functional groups persist after extraction of lipids and humic/fulvic acids, and the relative intensities of these peaks are approximately the same as those observed in the spectrum of unextracted SOM (4(a)). These persistent polar carbon functional groups include methoxy (70-80 ppm), olefinic (100-120 ppm), aromatic (120-140 ppm), substituted aromatic (primarily phenolic, 140-160 ppm), and to a lesser extent carboxyl/amide (170-190 ppm). Also of interest in the Humin spectrum is the intense aliphatic peak at ca. 40 ppm, which is slightly downfield from the aliphatic peaks in the other two spectra. We attribute this peak to $-CH_2-$ groups adjacent to methoxy carbon, suggesting that a large percentage of aliphatic carbon in the Humin fraction is tied up in polar carbohydrate material, thus reducing the hydrophobic character of this aliphatic carbon. Interpretation of the NMR spectra thus explains nicely the increased polar sorptivity of the Humin fraction relative to SOM and SOM-Lipid.

Figure 3 also includes the 50 usec dipolar dephased spectra of each SOM fraction. Dipolar dephasing (DD) exploits the time dependence of magnetic relaxation to further enhance spectral resolution, and this technique represents what has been termed the 'second generation' of solid state NMR technology (Maciel, 1984). DD-CP-MAS ^{13}C NMR is finding utilization in a variety of studies of organic matter in soils (Wilson et al., 1983), resins

(Wilson et al., 1984), anoxic marine sediments (Cooper et al., 1985; 1986), and peats (Orem and Hatcher, 1987).

To a first approximation, relaxation of ^{13}C nuclei in the dipolar dephasing experiment is directly related to the number of bonded protons. Thus, intensities arising from $-\text{CH}_2-$ groups decay faster than those from $-\text{CH}-$ groups, which will themselves decay faster than quaternary aliphatic carbon. Similarly, unsubstituted aromatic carbon nuclei decay faster than substituted aromatic carbon. The exception to this general trend are $-\text{CH}_3$ groups, which have long relaxation times due to their rotational mobility. Our previous work (Cooper et al., 1985; 1986) and that of others indicate that spectra obtained with a 50 μsec delay show resonances arising only from non-protonated ^{13}C nuclei, as well as from $-\text{CH}_3$ groups.

Comparisons of the 50 μsec DD spectra of the various SOM fractions support previous conclusions regarding the sorptivity and structure of these materials. Removal of the lipids from the SOM has little effect on the DD spectra (Figure 3(b) compared to Figure 3(a)). Distinct resonances in the DD spectrum of humin (Figure 3(c)) are for the most part obscured due to the low signal to noise ratio that results from the lower carbon content of this fraction. However, the broad peak between 100 and 150 ppm, and the carboxyl peak at 175 ppm, indicate substantial non-protonated, functionalized olefinic, aromatic and carboxyl/amide carbon in the humin. The dipolar dephasing NMR experiment thus supports the conclusion that active, polar sorption sites in SOM are located in the non-extractable humin fraction.

CONCLUSIONS

We have shown that polar, nonionic organic solutes interact with soil organic matter primarily through specific interactions with active sites in the humin fraction of the organic matrix, and not as a result of the hydrophobic forces that are responsible for the sorption of nonpolar organic solutes. It is only sorption onto the lipid component of soil organic matter that appears to be a true hydrophobic phenomenon. Our results therefore substantiate the arguments of Hartley (1960), who described the fats-waxes-resins fraction of soils (i.e. soil lipids) as a solvent for organic pesticides. Our results are also in substantial agreement with those of Garbarini and Lion (1986), who observed wide variations in K_{OC} values for nonpolar, hydrophobic solutes with different soil organic matter fractions. Interestingly, Garbarini and Lion also observed the highest K_{OC} values with nonextractable humin.

We believe that these results and the results of others cited have important implications for the modeling of organic solute migration in ground water. For example, with regard to hydrophobic solutes, it may be necessary to recast equation 6 in terms of the weight fraction of lipids in the soil matrix, not the total organic matter fraction. On a broader scale, however, it is probably unreasonable to expect a single empirical parameter (e.g. K_{OC}) to adequately predict sorption in soils, sediments and aquifers, given the variations in organic matter composition which are to be expected, as well as our data and

those of others which indicate that the various organic matter fractions differ substantially in their sorptive characteristics. Qualitative interpretation of the conventional and dipolar dephased ^{13}C NMR spectra indicate that polar sorption sites in the humin fraction arise from aromatic, carboxyl/amide and carbohydrate carbon nuclei, many of which are non-protonated. These qualitative observations are in agreement with the statistical analyses of Garbarini and Lion (1986), who concluded that elemental C,H and O data are necessary parameters for accurately describing solute-soil organic matter interactions.

We also believe that much more work is necessary before accurate, a priori estimates of polar solute sorption can be made. Current efforts underway in our laboratory are directed toward the development of a more general model of sorption of polar solutes based on Snyder's concept of liquid chromatographic selectivity (1974,1978).

ACKNOWLEDGMENTS

This work was supported by the Air Force Office of Scientific Research through Faculty (Cooper) and Graduate Student (Antworth) Summer Fellowships, as well as by a follow-up Mini Grant that is a part of the Summer Research Program. Much of the work reported here was performed at the Environics Laboratory, Engineering and Services Center, Tyndall Air Force Base, FL. The authors would like to acknowledge the assistance of Dr. Thomas Stauffer of that lab, as well as the helpful discussions with Dr. William MacIntyre of the Virginia Institute of Marine Sciences.

References

- Banerjee S., Yalkowsky S. H. and Valvani S. C. (1980) Water solubility and octanol/water partition coefficients of organics. Limitations of the solubility-partition coefficient correlation. Env. Sci. Technol. 14, 1227-1229.
- Briggs G. G. (1973) A simple relationship between soil sorption of organic chemicals and their octanol/water partition coefficient. Proc. 7th Bri. Insecticide Fungicide Conf. 11, 475-478.
- Chiou C. T. (1979) A physical concept of soil-water equilibria for nonionic organic compounds. Science 206, 831-832.
- Chiou C. T., Porter P. E. and Schmedding D. W. (1983) Partition equilibria of nonionic organic compounds between soil organic matter and water. Env. Sci. Technol. 17, 227-231.
- Chiou C. T., Shoup T. D. and Porter P. E. (1985) Mechanistic roles of soil humus and minerals in the sorption of nonionic organic compounds from aqueous and organic solutions. Org. Geochem. 8, 9-14.
- Conder J. R. and Young C. L. (1979) Physicochemical Measurements By Gas Chromatography, 632 pp. J. Wiley and Sons.
- Cooper W. T., Heiman A. S. and Yates R. R. (1985) Early diagenesis of organic carbon in sediments from the Peruvian Upwelling Zone. In Organic Marine Geochemistry (edited by M. Sohn) pp. 158-172. ACS Symp. Series #305.
- Cooper W. T., Heiman A. S. and Yates R. R. (1986) Spectroscopic and chromatographic studies of organic carbon in recent marine sediments from the Peruvian Upwelling Zone. Org. Geochem. 10, 725-732.
- Cooper W. T. and Antworth C. P. (1986) Final Report USAF-UES Summer Faculty Research Program.
- Cremer E. (1961) Mikrobestimmung von Adsorptionisothermen durch Gas-Chromatographie Monatsh. Chem. 92, pp. 112-115.
- Curtis G. P., Reinhard M. and Roberts P. V. (1986) Sorption of hydrophobic organic solutes by sediments. In Geochemical Processes at Mineral Surfaces (edited by J. A. Davis and K. F. Hayes) ACS Symp. Series.
- Franks F. (1985) The hydrophobic interaction. In Water: A Comprehensive Treatise (edited by F. Franks), Vol. 4, pp. 1-94, Plenum Press.

- Garbarini D. R., Lion L. W. (1986) Influence of the nature of soil organics on the sorption of toluene and trichloroethylene. Env. Sci. Technol. 20, 1263-1269.
- Hamaker J. W. and Thompson J. M. (1972) Adsorption In Organic Chemicals in the Soil Environment (edited by Goring C. A. I. and Hamaker J. W.), Vol. 1, pp. 49-144, Marcel Dekker Inc.
- Hartley G. S. (1960) In Herbicides in the Soil (edited by Woodford E. F. and Sager G. R.), pp. 63-78, Blackwell Scientific.
- Huber J. F. K. and Keulmans A. I. M. (1962) Nonlinear ideal chromatography and the potentialities of linear gas-solid chromatography. In Gas Chromatography 1962 (edited by van Swaay M.), pp. 26-62, Buttersworth.
- Jacobson J., Frenz J. and Horvath C. (1984) Measurement of adsorption isotherms by liquid chromatography. J. Chromatogr. 316, 53-68.
- Karickhoff S. W., Brown D. S. and Scott T. A. (1979) Sorption of hydrophobic pollutants on natural sediments. Water Res. 13, 241-248.
- Karickhoff S. W. (1984) Organic pollutant sorption in aquatic systems. J. of Hydraulic Engineering 110, 707-735.
- Lambert S. M. (1966) The influence of soil moisture content on herbicidal response. Weeds 14, 273-275.
- Lambert S. M. (1967) Functional relationship between sorption in soil and chemical structure. J. Agric. Food Chem. 15, 572-576.
- Lambert S. M. (1968) Omega, a useful index of soil sorption equilibria. J. Agric. Food Chem. 16, 340-343.
- Lambert S. M., Porter P. E. and Schieferstein R. H. (1965) Movement and sorption of chemicals applied to the soil Weeds 13, 185-190.
- Maciel G. E. (1984) High resolution nuclear magnetic resonance of solids. Science 226, 282-287.
- Mingelgrin U. and Gerstl Z. (1983) Reevaluation of partitioning as a mechanism of nonionic chemicals adsorption in soils. J. Environ. Qual. 12, 1-11.
- Nkedi-Kizza P., Rao P. S. C. and Hornsby A. G. (1985) Influence of organic cosolvents on sorption of hydrophobic organic chemicals by soils. Env. Sci. Technol. 19, 975-979.
- Orem W. H. and Hatcher P. G. (1987) Early diagenesis of organic matter in a sawgrass peat from the Everglades, Florida. Int. J. of Coal Geol. 8, 33-54.

- Pines A., Gibby M. G. and Waugh J. S. (1973) Proton Enhanced NMR of dilute spins in solids. J. Chem. Physics. 59, 569-590.
- Rao P. S. C., Hornsby A. G., Kilcrease D. P. and Nkedi-Kizza P. (1985) Sorption and transport of hydrophobic organic chemicals in aqueous and mixed solvent systems. Model development and preliminary evaluation. J. Environ. Qual. 14, 376-383.
- Schaefer J. and Stejskal E. O. (1976) Carbon-13 nuclear magnetic resonance of polymers spinning at the magic angle. J. Am. Chem. Soc. 98, 1031-1033.
- Schwarzenbach R. P. and Westall J. (1981) Transport of nonpolar organic compounds from surface water to groundwater. Laboratory sorption studies. Env. Sci. Technol. 15, 1360-1367.
- Snyder L. R. (1974) Classification of the solvent properties of common liquids. J. Chromatogr. 92, 223-230.
- Snyder L. R. (1978) Classification of the solvent properties of common liquids. J. Chromatogr. Sci. 16, 223-234.
- Tanford C. (1980) The Hydrophobic Effect, 2nd ed., 233 pp. Wiley-Interscience.
- Tissot B. P. and Welte D. H. (1984) Petroleum Formation and Occurrence, 2nd ed., 699 pp. Springer-Verlag.
- Wilson M. A., Pugmire R. J. and Grant D. M. (1983) Nuclear magnetic resonance spectroscopy of soils and related materials. Relaxation of ^{13}C nuclei in cross polarization nuclear magnetic resonance experiments. Org. Geochem. 5, 121-129.
- Wilson M. A., Collin P. J., Vassallo A. M. and Russell N. J. (1984) The nature of olefins and carboxyl groups in Australina brown coal resin. Org. Geochem. 7, 161-168.

Table 1. Comparison of K_D Values Obtained by Different Techniques.

<u>Method</u>	<u>System</u>	
	Aniline/Humin	o-Cresol/Humin
Uncorrected HPLC/FACP	----	10.5
Corrected HPLC/Facp	----	9.5
Frontal Analysis	----	9.3
Corrected HPLC/FACP (dynamic)	40	----
Conventional Batch (static)	39	----

Table 2. Linear Fitting Coefficients fro Equation 5.

<u>Surface</u>	<u>a</u>	<u>b</u>	<u>correlation coefficient</u>
Lipid*	0.31	1.24	0.95
SOM	-0.36	1.97	0.80
Som-Lipid	-0.44	2.53	0.92
Humin	-0.61	3.16	0.92

* o-cresol was excluded

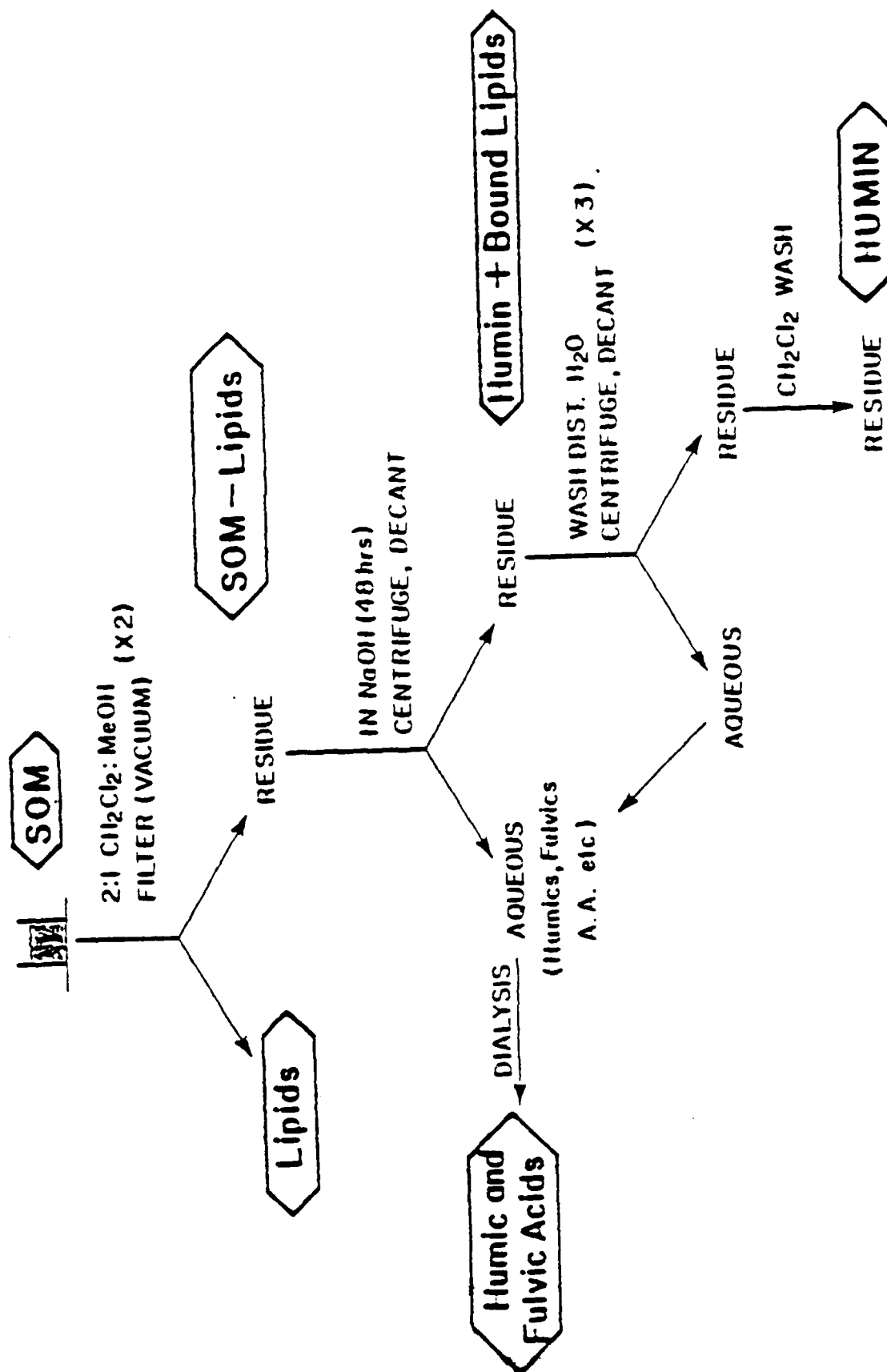
FIGURE CAPTIONS

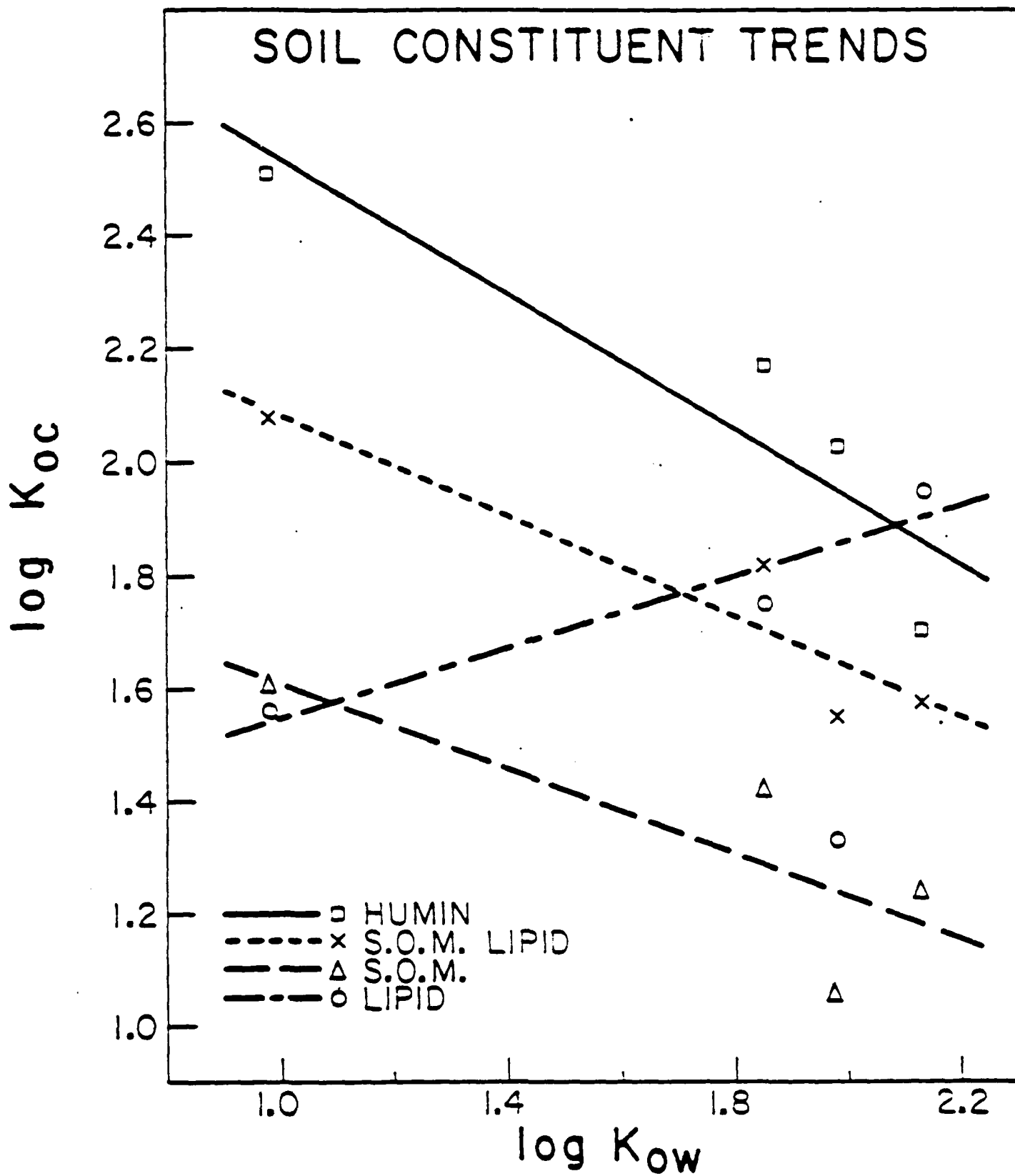
Figure 1. Extraction scheme used to isolate soil organic matter fractions.

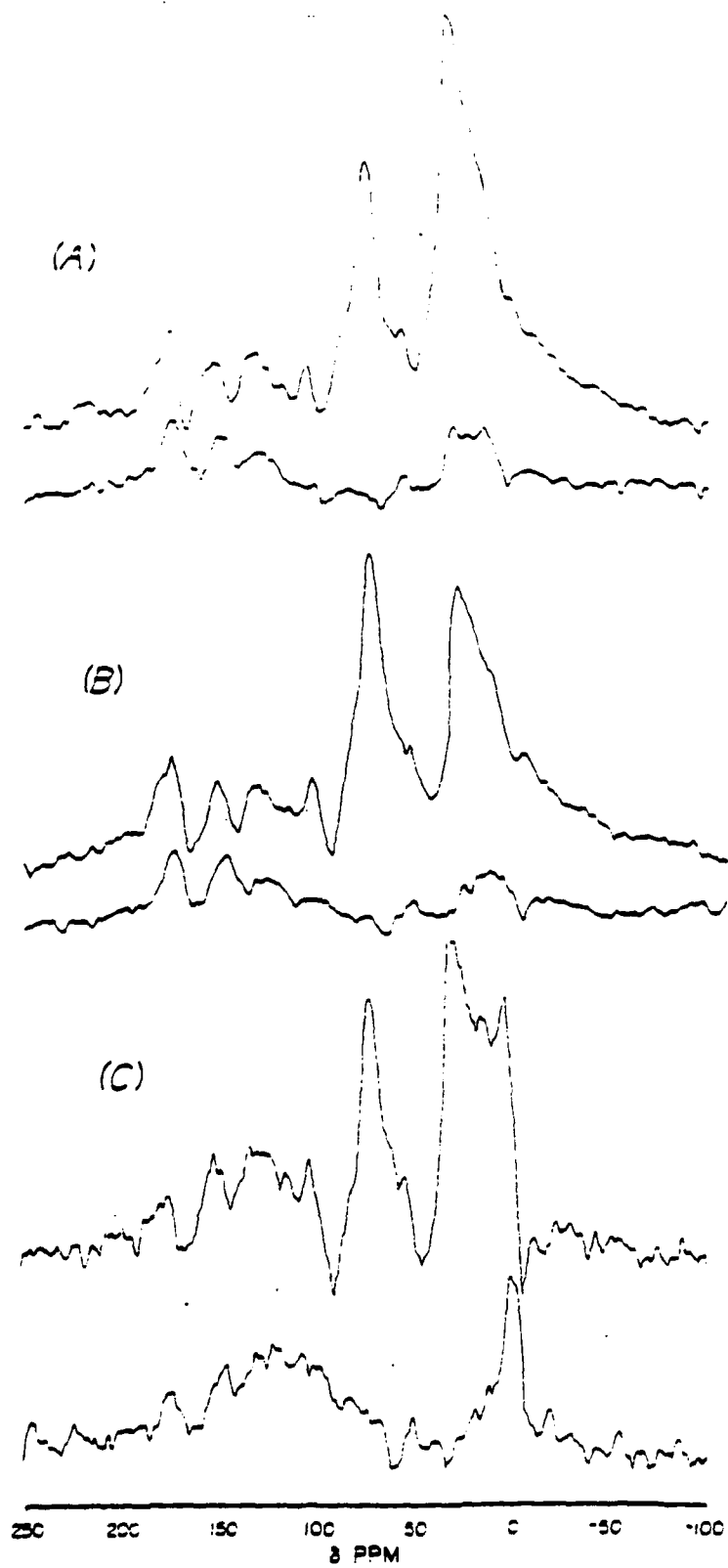
Figure 2. Plot of $\log K_{OC}$ versus $\log K_{OW}$ for the isolated organic matter fractions.

Figure 3. CP-MAS ^{13}C NMR spectra of (a) total soil organic matter (SOM) (b) SOM-Lipids (c) Humin. Top spectra represent 0 usec DD delay, while bottom represent 50 usec delay.

FRACTIONATION OF SOM







PART 2: MEASUREMENT OF SOLUTE ACTIVITY COEFFICIENTS IN ORGANIC
GEOPOLYMERS BY GAS CHROMATOGRAPHY

H. Collazo-Lopez, R.R. Yates and W.T. Cooper*
Department of Chemistry
and
Center for Biomedical & Toxicological Research
Florida State University
Tallahassee, Florida 32306-3006

Presented in the "Symposium on Organic Geochemistry: Techniques
and Applications"
Division of Geochemistry
194th National American Chemical Society Meeting
New Orleans, LA
September, 1987

Submitted to ORGANIC GEOCHEMISTRY
December, 1987

*Author to whom correspondence should be addressed

Gas chromatography has been used to measure the molal activity coefficients of a series of nonpolar organic solutes in sedimentary organic matter and its various extractable components. Organic matter from a peat deposit of higher plant origin in the Florida Everglades was isolated at three depths in the peat core. The organic matter was then fractionated into its lipid, humic acid and humin components, and the activity coefficients measured for solutes ranging in electronic polarizability from pentane to dichloroethane. Activity coefficients, which are a thermodynamic measure of the affinity of a solute for a polymeric solution, show a reasonable correlation with electronic polarizability for the total organic matter and its lipid and humin fractions. There is also a marked increase in the lipophilic character of the humin fraction with increasing depth of burial. In spite of this change in humin solution capabilities, however, all of the solutes exhibit decreased affinities for the deeper total organic matter, which we believe is due to its lower lipid content, as well as a somewhat lower affinity for the more mature lipid fraction. Solid state ^{13}C NMR spectra of the unfractionated organic matter and the humic acid and humin fractions give some insight into the relationship between their structure and sorption characteristics, although the chemical basis for the evolution of the nonpolar, lipophilic humin at depth is not readily apparent.

INTRODUCTION

In the preceding manuscript (Antworth et al., 1987) we demonstrated that the sorption of polar, nonionic organic solutes onto fractions of soil organic matter depended on the composition of the organic matter fraction. The results presented in that paper suggest that hydrophobic (solvophobic) partitioning of these solutes occurs only with the lipid fraction, and that specific polar interactions between the solutes and active sites in the nonextractable humin fraction actually dominate the sorption of polar solutes. It would thus appear that the empirical relationship between octanol-water partition coefficients and soil and sedimentary organic matter partitioning (Briggs, 1973; Chiou et al., 1979; Karickhoff et al., 1979) cannot be extended to polar organic solutes with water solubilities greater than that of benzene (~1000 ppm). It would also appear that the composition and structure of the organic matter involved must also be considered. Indeed, the work of Garbarini and Lion (1986), who correlated the sorption of toluene and trichloroethylene into a variety of organic matter samples with C and O content of the organic matter, suggest that soil organic matter composition must be considered for accurately predicting sorption of even hydrophobic solutes (solubilities less than ~100 ppm). Garbarini and Lion also observed that, when normalized for organic carbon content, humin showed the highest affinity for hydrophobic solutes of all the organic matter studied. Interestingly, we observed the same phenomenon with polar, more soluble solutes.

Accurate predictions of solute - organic matter partitioning would thus appear to require some knowledge of the organic matter involved. However, for such predictions to be included in realistic models of the movement and behavior of organic solutes in hydrologic systems, they must rely on parameters which can be reasonably acquired in a laboratory. We suggest that the relative proportions of lipids, humic/fulvic acids, and humin comprising soil and sedimentary organic matter, along with the elemental composition (C,H,N,O) of each fraction which was first suggested by Garbarini and Lion, represent a reasonable first approximation of the character of organic matter.

In order to more fully understand the chemical nature of these organic matter fractions, as well as to provide a more thorough scientific rationale for these suggestions, we have embarked on a detailed study of the solution properties of soil lipids, humic/fulvic acids and humin. We have again chosen organic-rich peat as our model soil organic matter since this material, low in inorganic content, can be considered essentially pure organic matter. This greatly simplifies the experimental aspects of the work. We do not mean to imply, however, that all soil and sedimentary organic carbon will behave as does peat. At this point our primary interest is more in understanding the differences in chemical properties of organic matter fractions, rather than the differences between peat and low-carbon soils and sediments. The similarities between the various organic fractions of peat and analogous fractions from other environments will be the subject of future investigations.

We have chosen to characterize these organic matter fractions, which can be considered mixtures of discrete geopolymers, by one form of the Inverse Chromatography Technique. Specifically, we have measured activity coefficients of organic solutes in these polymeric mixtures by gas chromatography. It has been experimentally verified that, under the proper conditions, gas chromatography can provide reliable thermodynamic values which can be used to study the interactions of molecules with different solvents (Conder et al., 1977; Conder et al., 1986). Particularly attractive features of the gas chromatographic approach are its essential simplicity, non-destructive nature, the speed with which large amounts of data can be obtained, and the ability to work at solute concentrations close to what is considered infinite dilution.

In this work we have again used different fractions of total organic matter as stationary phases. Solute is injected in the gaseous state, and their retention volumes then related to molal activity coefficients by equation 1.

$$\ln a_i = \ln \frac{RTW_2}{P_i V_n 10^3} - \frac{P_i^0 (B_{11} - v_i)}{RT} + \frac{P_0 (2B_{12} - v_i) J_3^4}{RT} \quad (1)$$

where a_i is the activity coefficient, T the absolute temperature, R the gas constant, W_2 the weight of stationary phase in the column, P_i^0 the saturation pressure of the pure solute, P_0 the pressure at the column outlet, V_n the net retention volume, and B_{11} and B_{12} the second virial coefficients of the pure solute and

the solute in the carrier gas, respectively. This equation was first derived by Martire (1974) and it has been shown that if the column pressure differential is less than two atmospheres, the carrier gas can be treated as an ideal gas, and the contributions of the last two terms are insignificant. Activity coefficients less than one are interpreted as an indication of high affinity for the stationary phase, while values greater than one indicate low affinity, or unfavorable mixing of the solute with the stationary phase.

The activity coefficient measurements just described have been supported by both conventional (CP-MAS) and dipolar dephased (DD-CP-MAS) Cross Polarization-Magic Angle Spinning ^{13}C NMR spectroscopy. The dipolar dephasing experiment takes advantage of the faster relaxation of protonated carbons. By allowing protonated carbons to dephase during a dipolar coupling period prior to data acquisition, the resonances of C-H and C-H₂ groups can be suppressed so that the remaining signal corresponds to non-protonated carbons, as well as methyl carbons that couple weakly because of their rapid rotational mobility. By using an optimum delay period (40-50 usec) the protonated carbon signal can be removed from the total signal, leaving resonances primarily from non-protonated carbon atoms.

EXPERIMENTAL

Gas Chromatography.

All chromatographic measurements were performed with a Varian 3700 gas chromatograph equipped with a flame ionization detector that was maintained at 200°C. For infinite dilution retention volume measurements the oven was kept at 25°C and the temperature of the column was monitored to $\pm 0.1^\circ\text{C}$ with a copper-constantan thermocouple. The inlet and outlet pressures were monitored with an amplified pressure transducer (105 series, Omega).

^{13}C NMR Spectroscopy

NMR spectra were obtained with a Bruker WP-200 SY spectrometer equipped with an IBM solids control accessory operating at 50 MHz for carbon. The spectrometer was tuned with t-butyl benzene and chemical shift scales are reported as parts per million downfield from tetramethylsilane. Samples were spun at the magic angle at approximately 4.5 KHz. A contact time of 1 msec was used throughout, and for dipolar dephasing experiments a 40 usec delay was inserted prior to data acquisition. This delay consisted of two 20 usec intervals separated by a 10 usec, 180° refocusing pulse. The repetition rate for all NMR experiments was 3 sec. The data was acquired as 2K sets, zero-filled to 8K and exponentially multiplied prior to Fourier transformation.

Extractions

The sedimentary organic matter used in this study was from a 2 meter peat core obtained from the Everglades National Park (FL)

during March of 1986. The core was taken from a Mahogany Hammock adjacent to the PaHayOkee visitor site. The core was refrigerated and stored in a sealed plastic container under a nitrogen atmosphere in the field, then frozen upon return to the lab until it was ready for use. Three horizons of 8 cm were cut from the core at 12, 35 and 151 cm and labeled as horizons A, B and C, respectively. Each sample horizon was lyophilized, mechanically homogenized and stored in sealed vials before analysis.

The total organic matter (TOM) from each horizon was continuously extracted with a 2:1 mixture of dichloromethane and methanol until a clear supernatant was achieved. The material extracted in this operation was defined as the lipid fraction. The residue left after the lipid extraction was then extracted with 0.5 N NaOH under a nitrogen atmosphere to remove humic and fulvic acids. The insoluble material was separated from the supernatant by centrifugation at 12000 RPM. This operation was repeated until no further material could be extracted from the residue and the supernatant was clear. The remaining residue was then washed with distilled water and lyophilized. This is the humin fraction. The NaOH solution was acidified with HCl to a pH of 1.0 and the humic acids that precipitated were separated by centrifugation at 12000 RPM, resuspended in an aqueous solution of pH 3 to protonate phenolic and carboxylic sites, and then lyophilized. The isolated fulvic acids were not used in this study.

After extraction of the lipids, the residue was dried and re-weighed. Lipid contents in horizons A, B and C were found to be

4.3%, 3.8% and 1.3% by weight, respectively.

Activity Coefficient Measurements

Activity coefficients were determined according to the procedures described by Conder and Young (1977) . The carrier gas flow rate was adjusted until the retention volumes of each probe showed no dependence on flow rate. This procedure was done separately for each of the fractions. Columns were made with 1/16 inch ID glass capillary tubes. Lipids were coated onto carefully silanized 100/200 mesh silica gel. Humic acids, humin and TOM were lyophilized and size fractionated to 100/200 mesh, then packed into columns without any additional silica support particles. The probes were injected as head space vapor and the amount injected was adjusted individually for each sample so that the infinite dilution condition was achieved (i.e. no dependence of sample size on retention volume).

RESULTS AND DISCUSSION

Activity Coefficients

Activity coefficients for the organic matter fractions from the deeper, more altered horizons B (35-42 cm) and C (151-158 cm) are summarized in Table 1. The solutes used in these studies are arranged from top to bottom in Table 1 according to increasing electronic polarizability. Electronic polarizability determines the contribution of nonspecific interactions to the total interaction energy involved in the chromatographic process (Barrer, 1966), and a correlation between sorption affinity and polarizability is an indication that nonspecific dispersion forces are responsible for the observed sorption, thus implying a partition process.

Solute activity coefficients are lowest for the lipid fractions, as expected, indicating that the probes have the highest affinity for this material. Chromatographic peaks were very symmetrical, and retention volumes showed no dependence on flow rate or concentration. Except for the relatively low coefficient for carbon tetrachloride in the lipids from horizon C, activity coefficients exhibit a negative relationship with polarizability (i.e. increasing sorption with increasing polarizability). Interestingly, all probes except carbon tetrachloride have higher activity coefficients in (lower affinities for) the lipid material from the deeper horizon, suggesting that the qualitative character of lipids in this sediment changes with depth, along with quantitative changes (note that lipids comprise 3.8% of the organic matter in horizon

B, but only 1.3% in horizon C).

The humic acid fractions show very little affinity for the probes, as indicated by the large activity coefficients obtained. We also observed that peaks were less symmetrical than those obtained with the lipids, and the concentrations needed to achieve infinite dilution were significantly lower. These data and observations indicate that the polar and ionic character of humic acids results in very little tendency for nonpolar solutes to partition into them. A weak surface adsorption process is probably responsible for what little sorption is observed. There does not appear to be any significant change in the sorption properties of humic acids with depth.

Humin showed intermediate affinities for the probes, with sorption of the chlorinated probes being particularly strong. Peak shapes were significantly more symmetrical than those for the humic acids, although some asymmetry was still apparent. As with the lipids, increasing affinity correlates with increasing polarizability, again excepting carbon tetrachloride. In contrast to the lipids, however, there is a very significant increase in sorption of the probes by the lower horizon. This data suggest substantive diagenetic alteration of the humin fraction, resulting in a much less polar, more lipophilic material. Other researchers have observed similar phenomena. Shin et al. (1970) observed that DDT adsorption was greater in more humified soil organic matter. Garbarini and Lion (1986) demonstrated a significant correlation between atomic C/O ratios of various

organic matter samples and the affinity of the organic matter for the hydrophobic solutes toluene and trichloroethylene.

Another explanation for this change may be the inclusion of non-solvent extractable lipids into the humin fraction during diagenesis. In contrast to the studies reported in the previous manuscript (Antworth et al., 1988), only solvent extractable lipids were removed from the organic matrix here. 'Bound' lipids must first be freed by saponification, then removed by solvent extraction. Several workers have noted increases in the amount of bound lipids with depth of burial (Mackenzie et al., 1982 and references cited therein), and it is presumed that diagenetic alteration of sedimentary organic matter results in certain lipids forming ester, amide, ether, etc. linkages with the organic, and possibly inorganic, matrices.

Table 1 also includes activity coefficients for the original, unfractionated organic matter. As with the humin and lipids, sorption increases with increasing solute polarizability. Unlike the humin fraction, however, sorption into the total, unfractionated sedimentary organic matter decreases with increasing horizon depth, in spite of a significantly more lipophilic humin component. This is a reasonable result if we presume that the non-bound, solvent extractable lipid fraction dominates the sorption of nonpolar organic solutes by the intact, unfractionated organic matter, since this lipid fraction comprises only 1.3% of the TOM of horizon C, but 3.8% of the TOM of horizon B.

In order to further illustrate the dominance of the lipid fraction in the sorption process, we have calculated the ratio of the solute activity coefficients of the humic acid, humin and TOM fractions to those in the lipid fractions for the same compound and depth. The results, summarized in Table 2, provide an estimate of the relative affinities of these nonpolar compounds for the various fractions. Again, smaller values in Table 2 reflect affinities more similar to those for the lipid fraction; that is, a more 'lipid-like', or lipophilic, material. The data of Table 2 reinforces the fact that, with increasing depth of burial, the total organic matter contained in the peat sediment becomes slightly less lipophilic, in spite of a substantial increase in the lipophilic character of the humin fraction. This again suggests that the free, solvent-extractable portion of soil and sedimentary lipids dominates the sorption of nonpolar organic solutes.

¹³C NMR Spectroscopy

The zero-delay CP-MAS ¹³C NMR spectra of the total sedimentary organic matter and the humic acid and humin fractions are displayed in Figure 1. Included are spectra from horizon A (12-20 cm) in order to give a broader perspective of the diagenetic processes within this core.

The primary changes observed in the unfractionated organic matter are the relative loss of intensities in resonances arising from alcoholic (54 ppm), carbohydrate (74 ppm) and carboxyl (175 ppm) carbon, with corresponding increases in aliphatic (30 ppm) and aromatic (130,154 ppm) carbon. These changes probably reflect

removal of the more labile carbohydrates, leaving a material enriched in aliphatic and aromatic structures. Orem and Hatcher (1987) observed the same basic trends in whole peats from a sawgrass plain in the Everglades, although that peat appears to contain a significantly greater carbohydrate fraction. Indeed, the spectrum of Orem and Hatcher's whole peat from the 70-90 cm horizon is almost identical to the spectrum we obtained on unfractionated peat from the 151-158 cm horizon.

There appears to be little significant change in the humic acid fraction with depth. Slight decreases in the aliphatic and carboxyl peaks relative to the aromatic peaks are noted, however.

Interpretation of the humin spectra is much less straightforward. First, all of the humin fractions, even that from horizon A, have a significant aliphatic component. These spectra thus resemble those of deeper humin samples (10 cm and below) obtained by Orem and Hatcher. The evolution of our humin, however, appears quite different from that observed by them, where there was a steady loss of carbohydrate, alcoholic and carboxyl carbon in humin from the surface (0-5 cm) through humin in the 55-70 cm horizon. While we observe this same trend in humin evolution on going from the 12-20 cm horizon to the 35-43 cm horizon, both carboxyl and alcoholic peaks reappear in humin from the 151-158 cm horizon. We do not as yet fully understand these observations, but the humin in horizon C may include some incorporated humic acids which are no longer extractable. Alternatively, there may have been some change in the sedimentary

environment which accelerated the production of extractable humic acids in horizon B (or hindered the humic acid evolution in horizon C). These last arguments presume that the hypothesis of Orem and Hatcher that humic acids originate as decomposition products of humin is correct.

As a final word on the NMR spectra of these humin samples, it should be noted that a second set of spectra were obtained in order to ensure that we were not observing some spectral artifact. These spectra were identical to the originals, and we thus believe that we are observing a real phenomenon.

With regard to the present study on the solution properties of organic matter fractions, the most important and consistent difference in humin from horizon B and horizon C appears to be an increase in the relative proportion of aromatic carbon. Furthermore, dipolar dephased NMR spectra (Figure 2) show persistent aromatic resonances after 40 usec, indicating that this aromatic carbon is significantly nonprotonated; that is, highly cross-linked to other carbon moieties. Current efforts are directed at a better understanding of degraded humin structure, and why this structure results in a lipophilic polymeric material when compared to its less altered precursor.

SUMMARY

The sorption of nonpolar, hydrophobic solutes into sedimentary organic matter, and the lipid and humin fractions of the organic matter, is seen to correlate with electronic polarizability of the solutes, implying a non-specific dispersion, or partition, process. As expected, the lipid fraction shows by far the highest affinity for these solutes. Sorption by the total, unfractionated organic matter seems to be dominated by this extractable, non-bound lipid component, even at depth where humin has acquired a significantly lipophilic character.

The results of this physiochemical investigation of sedimentary organic matter and its various components seem to support previous results of Hartley (1960), who described the fats-waxes-resin fraction (i.e. lipids) as the fraction of soil organic matter into which hydrophobic solutes partition, as well as those of Shin et al. (1970) and Garbarini and Lion (1986), both of whom observed increasing hydrophobic solute sorption with increasing maturation of soil and sedimentary organic matter.

ACKNOWLEDGMENTS

This work was supported by the Air Force Office of Scientific Research through a follow-up Mini Grant that is a part of the Faculty and Graduate Student Summer Research Program.

REFERENCES

- Antworth C.P. Cooper W.T. (1987) Applications of inverse chromatography in organic geochemistry. Part 1: Characterization of polar solute - soil organic matter interactions by high performance liquid chromatography. Org. Geochem., submitted.
- Barrer R.M. (1966) Specificity in physical adsorption. J. Colloid Interface Sci., 21, 415-434.
- Briggs G. G. (1973) A simple relationship between soil sorption of organic chemicals and their octanol/water partition coefficient. Proc. 7th Bri. Insecticide Fungicide Conf. 11, pp. 475-478.
- Chiou C. T. (1979) A physical concept of soil-water equilibria for nonionic organic compounds. Science 206, 831-832.
- Conder J.R. McHale S. Jones M.A. (1987) Evaluation of methods for measuring gas-solid chromatographic retention on skewed peaks. Anal. Chem. 58, 2663-2668.
- Conder J.R., Young C.L. (1977) Physicochemical Measurements by Gas Chromatography, J. Wiley and Sons, New York, pp 155-277.
- Garbarini D. R., Lion L. W. (1986) Influence of the nature of soil organics on the sorption of toluene and trichloroethylene. Env. Sci. Technol. 20, 1263-1269.
- Hartley G. S. (1960) In Herbicides in the Soil (edited by Woodford E. F. and Sager G. R.), Blackwell Scientific, pp 63-78.
- Hatcher P.G., Breger I.A., Dennis L.W., Maciel G.E. (1983) Solid-state ^{13}C NMR of sedimentary humic substances. In Aquatic and Terrestrial Humic Material (R.F. Christman and E.T. Gjessing, eds.) Ann Harbor Science, pp. 37-82.
- Karickhoff S. W., Brown D. S. and Scott T. A. (1979) Sorption of hydrophobic pollutants on natural sediments. Water Res. 13, 241-248.
- Mackenzie A.S., Brassell S.C., Eglinton G., Maxwell J.R. (1982) Chemical fossils: The geological fate of steroids. Science 217, 491-504.
- Martire D.E. (1974) Dependence of the solute retention parameters on stationary phase molecular weight in gas-liquid chromatography. Anal. Chem. 46, 626-633.
- Orem W. H. and Hatcher P. G. (1987) Early diagenesis of organic matter in a sawgrass peat from the Everglades, Florida. Int. J. of Coal Geol. 8, 33-54.

Shin Y.O., Chodan J.J., Wolcott A.R. (1970) Adsorption of DDT by soils, soil fractions, and biological materials. J. Agr. Food Chem. **18**, 1129-1133.

Table 1. Molal Activity Coefficients Obtained at 25°C.

Horizon Depth(cm)	Lipids		Humic Acids		Humin		TOM	
	B	C	B	C	B	C	B	C
	35-43	150-158	35-43	150-158	35-43	150-158	35-43	150-158
<u>Solute</u>								
C ₅ H ₁₂	0.036	0.043	>10	>10	5.2	1.5	4.5	5.7
C ₆ H ₁₄	0.013	0.015	9.0	>10	1.3	0.54	2.4	2.3
CCl ₄	0.013	0.004	7.9	7.0	1.6	0.60	1.6	2.0
C ₂ HCl ₃	0.008	0.009	>10	>10	0.45	0.20	0.49	0.54
C ₂ H ₄ Cl ₂	0.003	0.009	8.5	9.8	0.36	0.12	0.55	0.66

Table 2. Relative Activity Coefficients, Normalized to Corresponding Activity Coefficient for Lipid Fraction.

Horizon Depth(cm)	Humic Acid		Humin		TOM	
	B	C	B	C	B	C
	35-43	150-158	35-43	150-158	35-43	150-158
<u>Solute</u>						
C ₅ H ₁₂	278	232	144	34	125	132
C ₆ H ₁₄	692	666	100	36	184	153
CCl ₄	607	1750	123	150	184	500
C ₂ HCl ₃	1250	1111	56	22	61	60
C ₂ H ₄ Cl ₂	2833	3266	120	40	183	220

FIGURE CAPTIONS

Figure 1. CP-MAS ^{13}C NMR spectra of total organic matter, humic acids and humin as a function of depth.

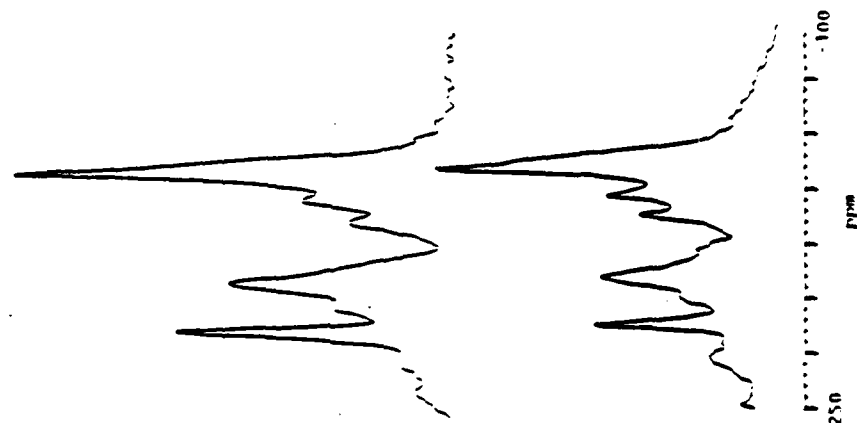
Figure 2. Dipolar dephased CP-MAS ^{13}C NMR spectra (0-40 usec) of humin from 35-43 and 151-158 cm horizons.

MAS - ^{13}C NMR

TOTAL ORGANIC MATTER

HUMIC ACID

HUMIN



DIPOLAR DEPHASING SPECTRAS

HUMIN (151 CM.)

HUMIN (35 CM.)

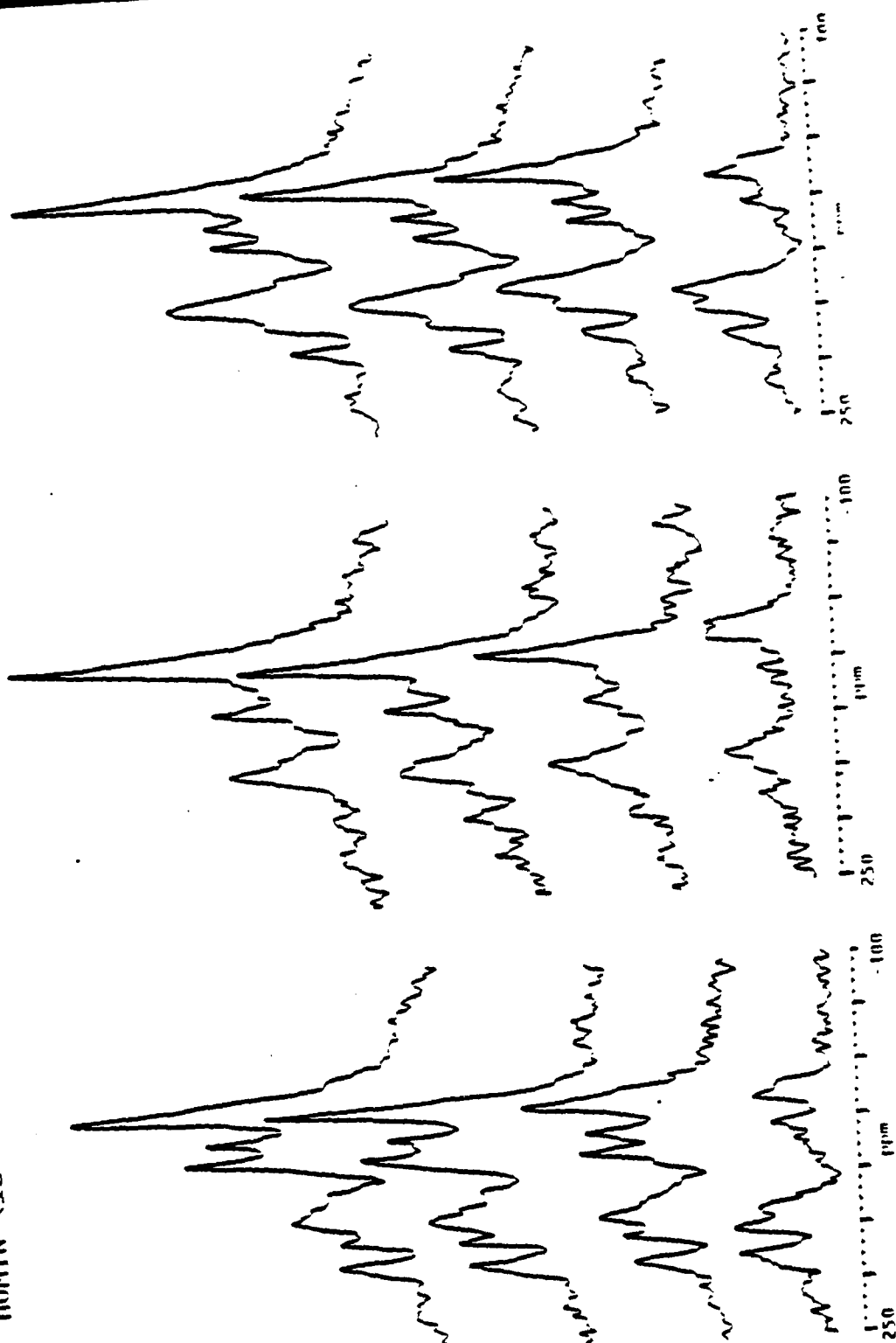
HUMIN (12 CM.)

0 USEC.

10 USEC.

20 USEC.

40 USEC.



FINAL REPORT NUMBER 21
REPORT NOT AVAILABLE AT THIS TIME
Dr. Peter Jeffers
760-7MG-038

1986 USAF-UES RESEARCH INITIATION PROGRAM

Sponsored by the

AIR FORCE OFFICE OF SCIENTIFIC RESEARCH

Conducted by the

UNIVERSAL ENERGY SYSTEMS, INC.

FINAL REPORT

A STUDY OF SEMIHARDENED CONCRETE ARCH STRUCTURE

RESPONSE UNDER PROTECTIVE LAYERS

Prepared by:	Y.S. Kim and R.R. Domingo
Department and	Department of Civil Engineering
University:	Catholic University of America
Research Period:	April 1, 1987 - March 31, 1988
Contract No.:	F49620-85-C-0013/SB5851-0360

ACKNOWLEDGEMENT

The authors would like to thank the Air Force Systems Command, the Air Force Office of Scientific Research and the Universal Energy Systems, Inc. for supporting this research project. In particular, they would like to thank the research engineers in the Facility Systems and Analysis Branch at the Tyndall Air Force Base for suggesting this area of research and for their collaboration.

Also, the authors would like to thank Mr. M. Womack and his staff in the Operations Support Branch at the Tyndall Air Force Base for providing them warm hospitality and excellent working conditions during the stay at Tyndall for the centrifuge model tests.

ABSTRACT

A reinforced concrete arch structure is modeled under a sloping embankment consisting of three different protective layers: compacted soil, concrete slab, and rock cover. The variables taken into account are: bedding condition, embankment slope, embankment soil type, and type of rock cover.

Structural responses are predicted through finite element code, CANDE (Culvert ANALysis and DEsign). The results of CANDE analyses include nonlinear constitutive models for characterizing arch structure and soil, incremental construction and free vertical movement with a symmetric mesh, and allowed the comparison of structural responses for different structural systems modeled.

Also, a preliminary investigation to study the behavior of a buried arch structure using the centrifuge model technique is performed and described in the report.

SECTION I

INTRODUCTION

A. PURPOSE

During the recent years, several research programs were undertaken by the United States Air Force (References 1,2,3,25) to develop the protective antipenetration system for military facilities (e.g., arch-, circular-, and box-type structures) constructed on the ground surface (Figure 1.1). Protective concepts consisting of rock rubble/boulder and burster slab over soils were introduced, and full-scale models were tested to determine the levels of protection against conventional weapons (Figure 1.2). A parametric study on the thickness of rock rubble/boulder layer, ratio of size of rock rubble/boulder to size of the weapons, thickness of burster slab, and density and thickness of sand layer was performed and qualitative results have been obtained from the field model tests. Based on information observed, the system has proven effective to resist the penetration of conventional weapons and it is now being considered for application over military facilities as a hardening protective structure. However, the designers are facing one critical question before the application of the system (Reference 25): Will these military structures be safe under static loadings due to the weight of embankment soil, rock rubble/boulder layers and/or burster slab? The purpose of the research, therefore, is to study the behavior of the buried arch structures subjected to static loadings by using centrifuge and numerical modeling techniques.

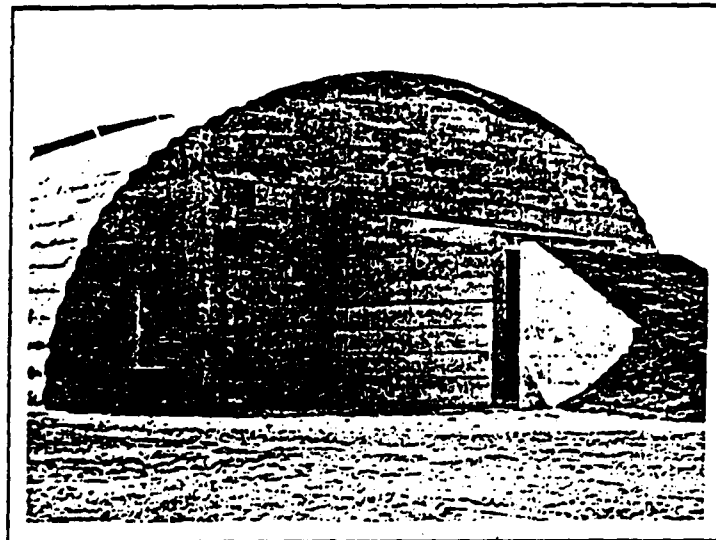
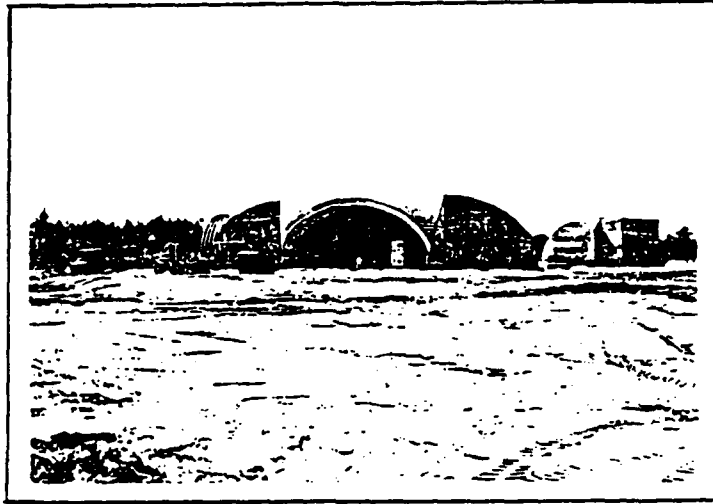
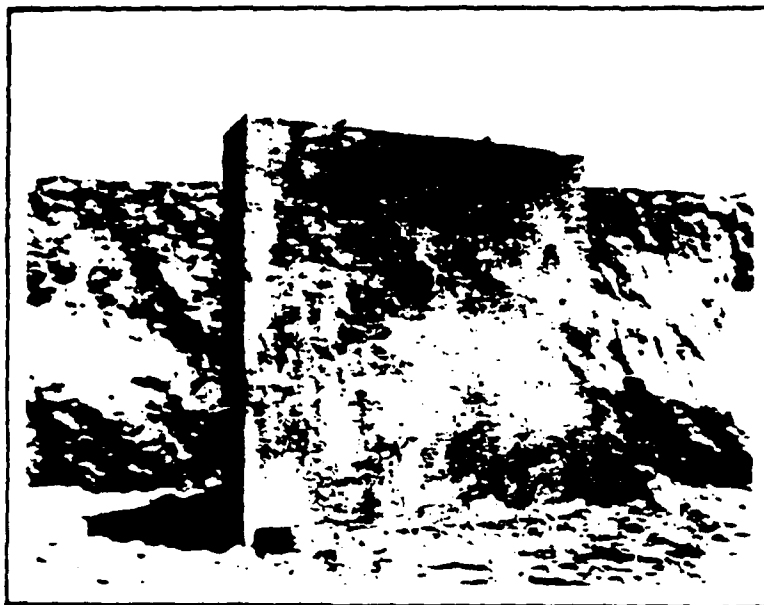
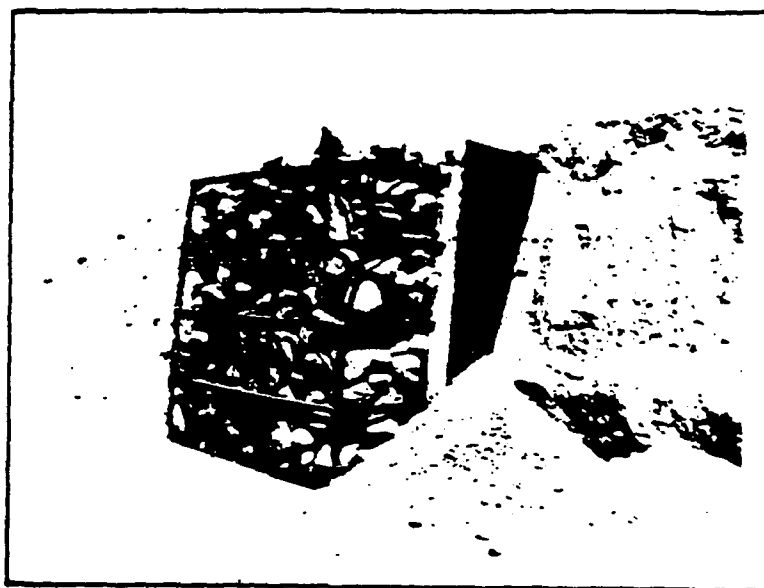


Figure 1.1 Reinforced Concrete Arch Structures



a) Burster Slab



b) Rock/Rubble Protective Layer

Figure 1.2

B. OBJECTIVE

The primary objective of this study is to investigate the soil-structure interaction problems of a buried concrete arch structure subjected to static loadings. More specifically, the objectives of this study are to:

1. Develop an experimental technique to simulate the behavior of a prototype arch structure in a centrifuge.
2. Conduct a preliminary series of centrifuge model experiments on a small capacity centrifuge.
3. Predict the behavior of the arch using finite element analysis.
4. Gain experience necessary for model studies in a large capacity centrifuge.

C. SCOPE

With these objectives in mind, the research is reported in the following sections. They contain a description of the centrifuge facility used for model study; design and fabrication of an accompanying testing apparatus; preliminary model test results, and recommendation for further centrifuge model study; and investigation of the influence of soil types for in-situ bedding and backfill, and slope of the embankment using finite element analysis. Finally, some potential topics for future research in this area are mentioned.

SECTION II

CENTRIFUGE MODEL STUDY

A. FUNDAMENTALS OF CENTRIFUGE MODELING

One of the most ideal approaches for obtaining information on the behavior of prototype structures is full-scale model testing. A full scale model with the necessary instrumentation (i.e., soil stress meters, pore water pressure transducers, settlement gauges and strain gauges, etc.) could give the best results for estimating prototype behavior.

Unfortunately, full-scale model testing has serious major drawbacks: mainly, cost and time of construction and operation. Because of these reasons, small scale model testing is becoming a favorite testing method in geotechnical engineering.

However, use of small scale model tests in the laboratory is severely limited when the gravity body force of the structure itself is the principal load on the system, such as in dams and embankments. This limitation is due to two major factors. One is that soil characteristics are nonlinear and overburden dependent, and the other involves stress magnitudes. The stresses in a small scale model due to its own weight are much smaller in magnitude than those in the corresponding prototype system. To eliminate these deficiencies, the centrifuge modeling technique has been used since 1931. The increase in unit weight is achieved by placing a model in a centrifuge and spinning it to produce an acceleration field that is equivalent to an artificial gravitational field. In this way the state of stress at every point in the model under an artificial

gravitational field is equal to that at the homologous point in the prototype. This technique has been applied to a variety of geotechnical problems (i.e., slope stability, reinforced earth, foundation design, offshore gravity platforms, rockfill dams, tunnels, and buried circular pipes) reported elsewhere (References 5,10,13,14,23,24,28,29 and 30). Table 2.1 summarizes the scaling rules that have been developed for relating the behavior of the centrifuge model and an equivalent full scale geotechnical structure.

B. THE AFESC CENTRIFUGE FACILITY

1. The Centrifuge

The centrifuge installed at Tyndall Air Force Base (AFB) was originally built for testing of electronic and mechanical packages under G-loadings that simulate those experienced in actual flight. It was initially installed at Kirtland AFB, New Mexico. The machine was modified for geotechnical studies in 1981 and moved to the Air Force Engineering and Services Center (AFESC) at Tyndall AFB in 1986. The centrifuge was assembled and housed in a 7-ft. high, 16-ft. diameter, 9-in. thick reinforced concrete retaining structure (Figure 2.1).

The Center's centrifuge is a medium size rotary accelerator designed by Genisco, Inc., of California (Model E-185). The machine is capable of applying controlled centrifugal accelerations up to 100 g's and a limit of 30,000 g-lb. at a nominal radius of 6 ft. The payload of the test package can be as heavy as 500 lb. The machine includes a variable-speed hydraulic drive system, timing belt drive, RPM pick-up, rotating

Table 2.1 Scaling Relations (Reference 29)

Quantity	Full Scale (Prototype)	Centrifugal Model at n g's
Linear Dimension	1	$1/n$
Area	1	$1/n^2$
Volume	1	$1/n^3$
Time		
In Dynamic Terms	1	$1/n$
In Diffusion Cases	1	$1/n^2$
In Viscous Flow Cases	1	1
Velocity (Distance/Time)	1	1
Acceleration (Distance/Time)	1	n
Mass	1	$1/n^3$
Force	1	$1/n^2$
Energy	1	$1/n^3$
Stress (Force/Area)	1	1
Strain (Displacement/Unit Length	1	1
Density	1	1
Energy Density	1	1
Frequency		
In Dynamic Terms	1	n

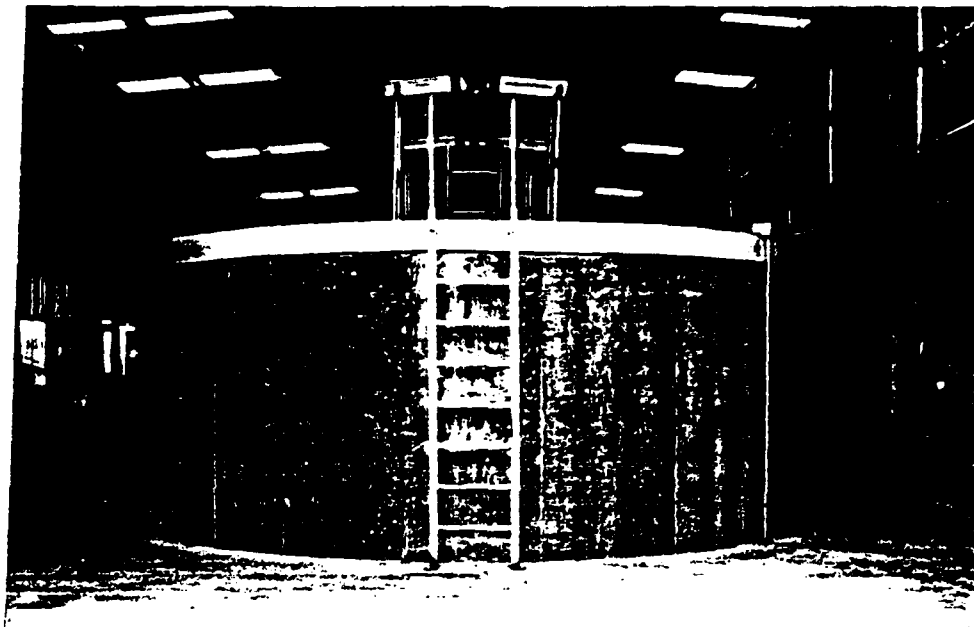


Figure 2.1 A View of the Centrifuge Facility at Tyndall AFB

arm assembly, terminal box for control and test connections.

The hydraulic drive system consists of an electric drive motor coupled to a variable-displacement pump, a constant-displacement fluid motor couple to the rotor drive shaft, and two pressure-relief valves. A 4-way solenoid-operated spring-loaded control valve provides rotational stability, maximum hunting, and constant torque characteristics. The hydraulic power unit is enclosed in the console, and the fluid motor is installed at the bottom of the rotor assembly (Figure 2.2). Maximum pressure of the hydraulic system has been set at approximately 2,200 psi.

The boom consists of two symmetrical cantilever arms, and an adjustable 30-in. square cradle-type mounting platform carried on aircraft-type roller bearings. The platform is held by two arms attached to the spokes by two pivots. It can be locked into horizontal, 45, 90, 135 or 180 degree positions. This permits the soil surface to remain perpendicular to the vector sum of the centrifuge acceleration and the acceleration due to gravity.

One of the unique features of the machine is the automatic dynamic balancing system. Dynamic balance is accomplished automatically by vertical displacement of the two arms of the boom until the center of gravity of the opposing mass lies in the same horizontal plane. It requires approximately 20 seconds for full compensation. If compensation cannot be accomplished within the 12-in. travel limitations, the balance motor is automatically shut down by limit switches. Corrective measures are indicated by the relative attitudes of the mounting

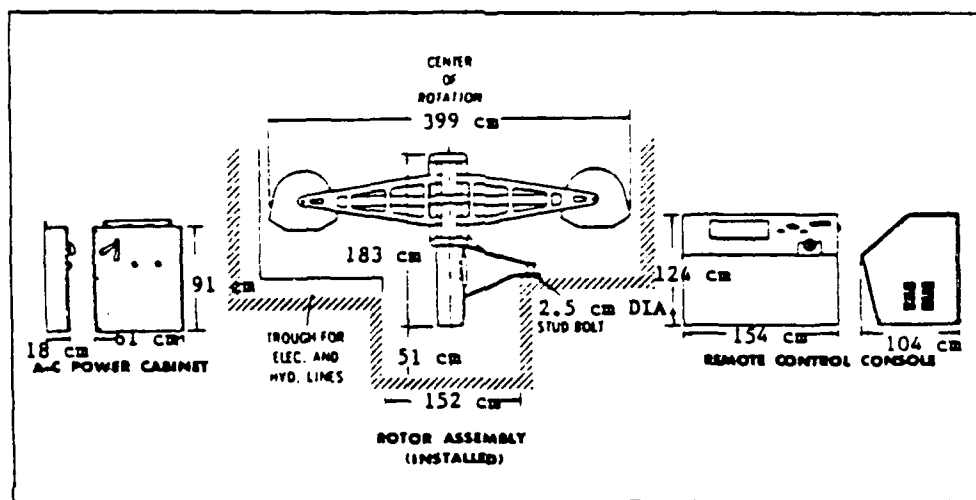


Figure 2.2 Rotary Accelerator (Model E-185) - Outline Drawing

platforms after shut down.

Hydraulic and electrical services are available to the model in flight. The hydraulic lines may be used to conduct compressed air or fluids from the outside control area to the model. Hydraulic services are transmitted through rotary joints. Electrical signals are transmitted to the centrifuge rotor and then to the model in flight through a stack of slip rings. A total of 40 slip rings (electrical channels) are provided in the machine, of which 28 are sending power and receiving signals from transducers which monitor the behavior of the model. These 28 slip rings include 12 instrumentation slip rings (shielded-conductor) designed for 1-amp, low resistance and low noise, and 16 power slip rings (shielded-conductor) of 5-amp current rating. The twelve slip rings not used for test purposes are part of the static and dynamic balancing motor and control circuitry for television. A summary of major specifications is listed in Table 2.2.

Table 2.2 Major Specification

Maximum centrifugal capacity	30,000 g-lb
Maximum acceleration	100 g
Maximum payload	500 lb.
Maximum effective radius	72 in.
Maximum number of rotation	220 rpm
Space of swinging platform	30 in. x 30 in.
Electric Slip Rings	40

2. Video Recording System

Video camera and recording devices are also available as part of the monitoring system. This video camera is mounted near the hub of the centrifuge. This system provides a continuous and instantaneous monitor of the test while in progress, and a permanent, replayable record of model tests.

3. Data Acquisition System

Digital oscilloscopes (Nicolet Model 4094) have been used for collecting sensor signals from model structures for centrifuge model study. The Model 4094 digital oscilloscope with multi-channel plugs is capable of performing acquisition with 12 bit resolution at a rate of 2 million sample/sec (16 bits samples). The system allows zero time to be set anywhere in the displaying area and enables two-channel measurements with each channel set at an independent pre- or post-trigger delay. It displays these two functions as well as a combination of them. Also, the system, a combination of them. A HP plotter interfaced with the oscilloscope has been used to create hard copy records.

C. FABRICATION OF MODEL BOX

A requirement of centrifuge modeling is the fabrication of a model box that contains the small-scale model of the structure together with the soils sample. The dimensions of the model box were made small enough to fit the centrifuge swing bucket platform, and large enough to house the structure model and a sufficient amount of soil sample. The model box has a platform

base of 24 in. x 24 in. and a total height of 17.875 in. It was totally made of 2024-T-35 aluminum plates welded at the sides and the bottom at almost 100% penetration. The model box has a top lid as well a front lid for easy access to the model and cleaning purposes. Both lids are secured by steel screws, the front lid is designed to withstand the internal lateral pressure caused by the soil at increased gravity conditions (100 g's), while the top lid is designed to withstand the pressure generated by the surcharged system (50 psi).

The base of the model box extends 2 in. from every side and has a hole drilled into each corner so as to enable the researchers to bolt down the box onto the centrifuge platform to prevent it from slipping. Although theory states that the box would not slip off the swing bucket while the centrifuge is running, this is merely a safety precaution taken by the researchers. For easy and safe handling of the model box, the top edges of the two opposing sides are extended and holed-out to accomodate crane hooks. A detailed diagram of the model box is illustrated in Figure 2.3

D. ARCH STRUCTURE MODEL AND STRAIN GAUGES

The model semi-circular concrete arch structure was made of a microconcrete mix composed of gypsum molding plaster and silica sand, with gypsum:aggregate:water ratio of 1:2:1 by weight. The structure has an inner diameter of 9 in. and a shell thickness of 0.3 in. The total length was 16 in. The structure model was complete with miniature reinforcement set on both circumferential and longitudinal directions. Reinforcement

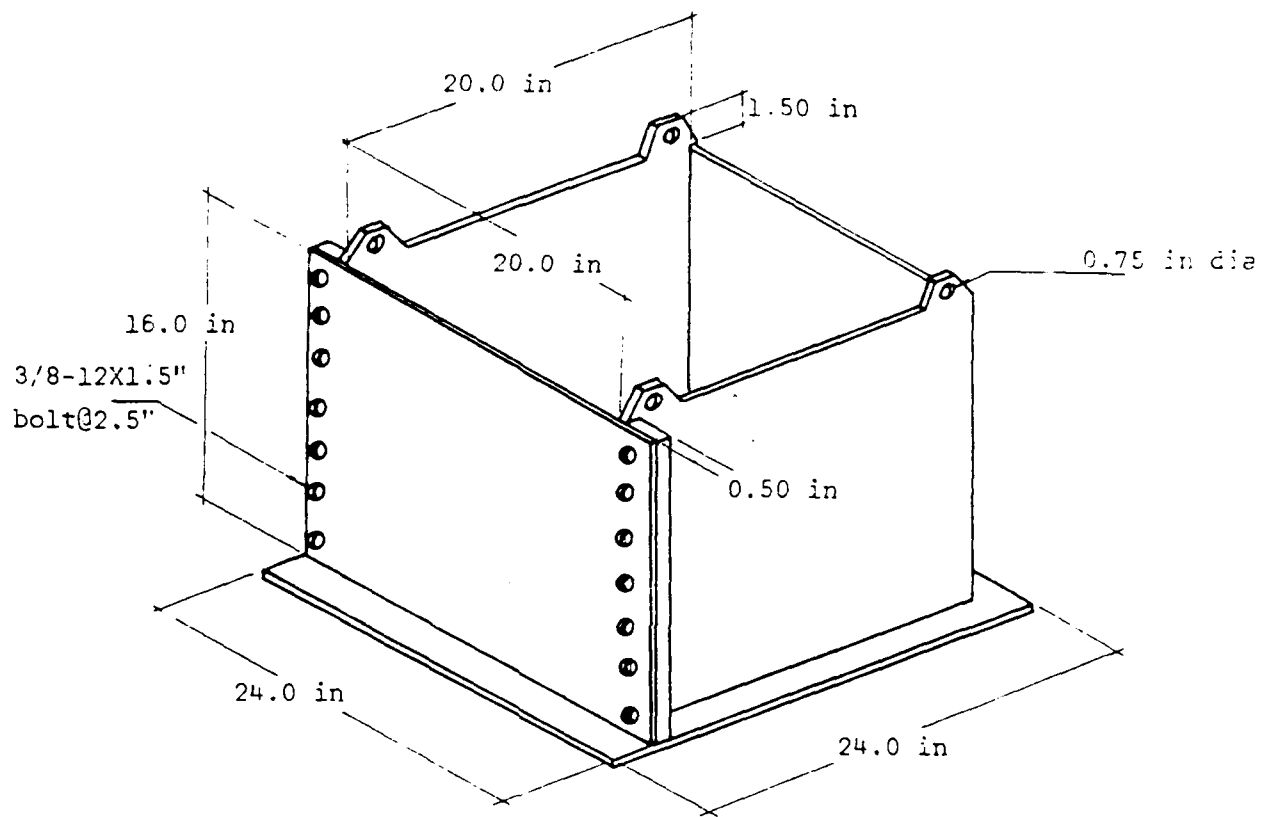


Figure 2.3 The Centrifuge Model Box

bar diameter was 22-gauge. The model arch structure also included a reinforced floor slab made of the same material (see Figure 2.4).

Five pairs of strain gauges (gauge type CEA-13-125UW-120) manufactured by Measurement Group, Inc. were used to measure strain along the circumference of the structure at midspan. Gauges were mounted at 5, 45, 90, 135, 175 degrees and hooked up in a full-bridge fashion. The arch structure with attached strain gauges placed in the model container is shown in Figure 2.5.

E. MODEL PREPARATION

1. Miniaturized Concrete Arch Structure

The structures used in the tests are 1/60th size of the prototype structure. It is made of a microconcrete mix composed of gypsum plaster as cement and silica sand as aggregate. Scaling down the prototype to 1/60th size resulted with a model that requires a membrane thickness of 0.3 inch. Due to this, the consistency of the microconcrete mix had to be very slurry for it to go down the mold. The final mix had a gypsum:aggregate:water ratio of 1:2:1.

The mold is made up of two aluminum tubings, one with an outer diameter equal to the desired inner diameter of the model, the other with an inner diameter equal to the desired outer diameter of the model. The frame work is made of plexiglass which also serves to hold the reinforcement cage in place while letting the mix to cure.

The miniaturized reinforcement used was 22-gauge wires in

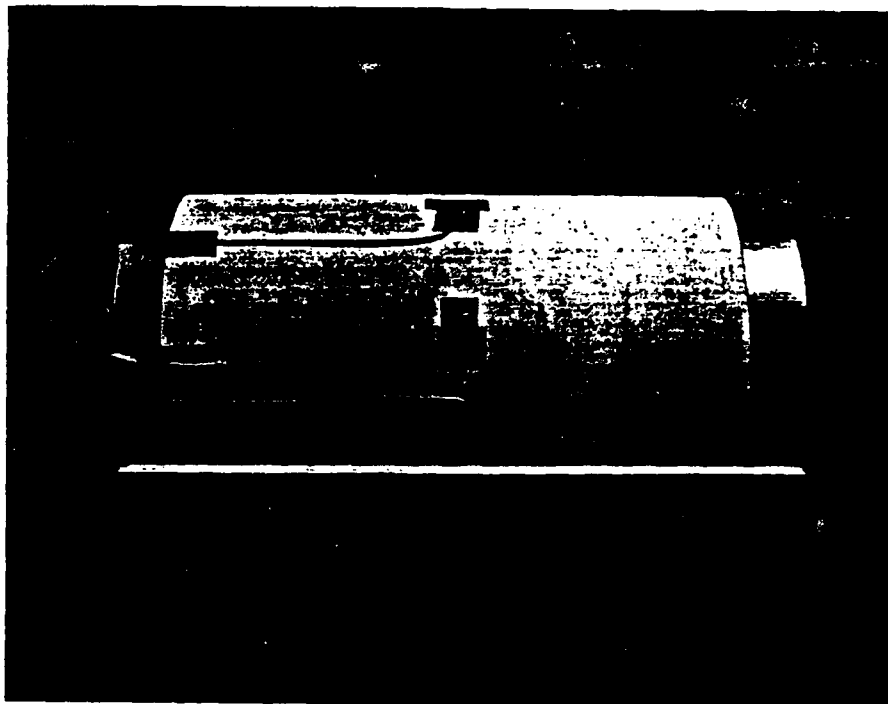
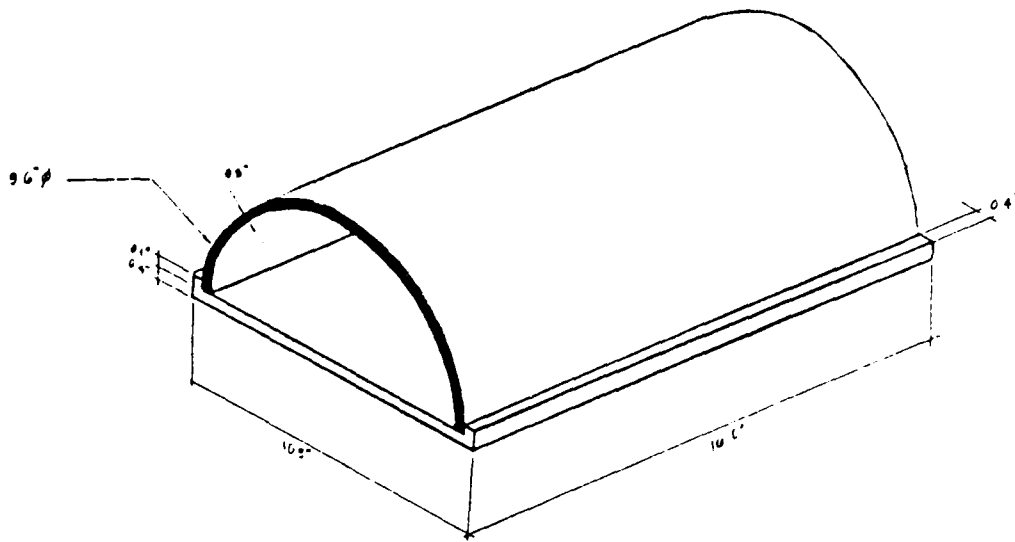


Figure 2.4 The Miniaturized Scale Model with Strain Gauges

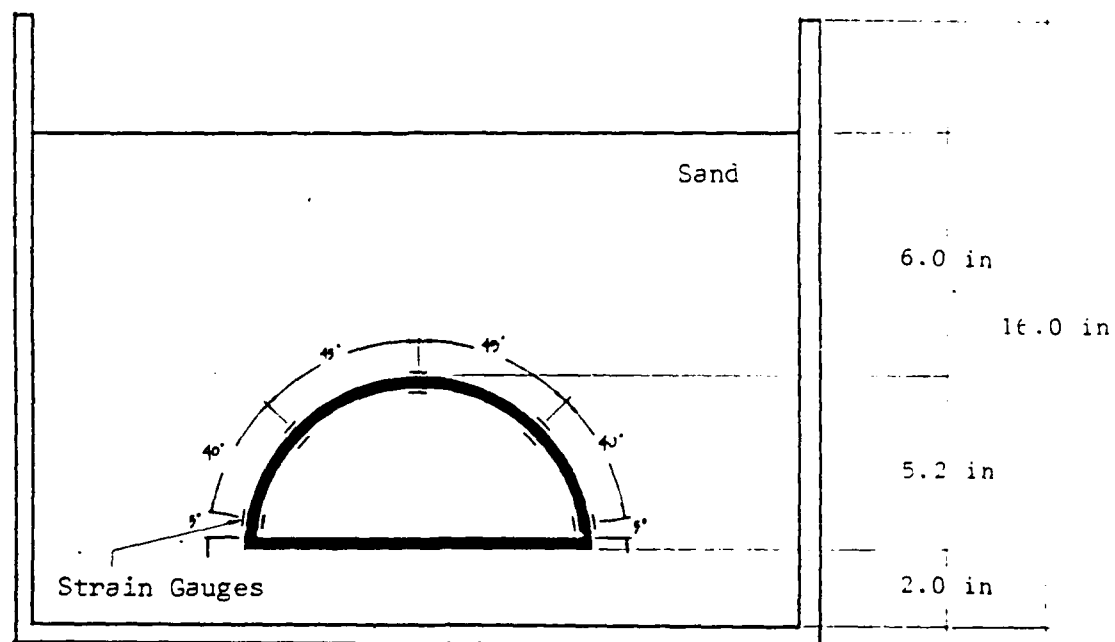


Figure 2.5 The Instrumented Arch Structure in the Model Box

both the longitudinal and circumferential directions. Prior to the installation of the wires, it was necessary to apply a small amount of pretension to remove all bends and coils. Also, it was necessary to roughen up the surface of the wires with very coarse sand paper to assure better bonding to the microconcrete.

The models were left to cure for two days and then were coated with concrete shellac to preserve the water content. Allowing the models to dry for more than the set amount of time produced a very chalky and brittle surface. After application of shellac, the structure was left to cure for at least another two days before testing.

2. Soil Pluviator

To attain reliable data from the tests, most of the variables must be held constant for every test. This includes the soil sample properties. Although grain size and sample height of the soil can easily be produced, it is the reproduction of the soil sample density that is important. For this purpose, the researchers use the sand raining method or, pluviation. This method is commonly used due to its simplicity and for the simple reason that it is the best method of reproducing soil samples. The purpose involves forming a sand mass to a homogeneous condition with a specified density, using a process that can be repeated as many times without the variation of the sand properties other than as chosen by the researchers.

A sand pluviator was designed and built at AFESC/RDCO facility at Tyndall Air Force Base (Figure 2.6). It has a total

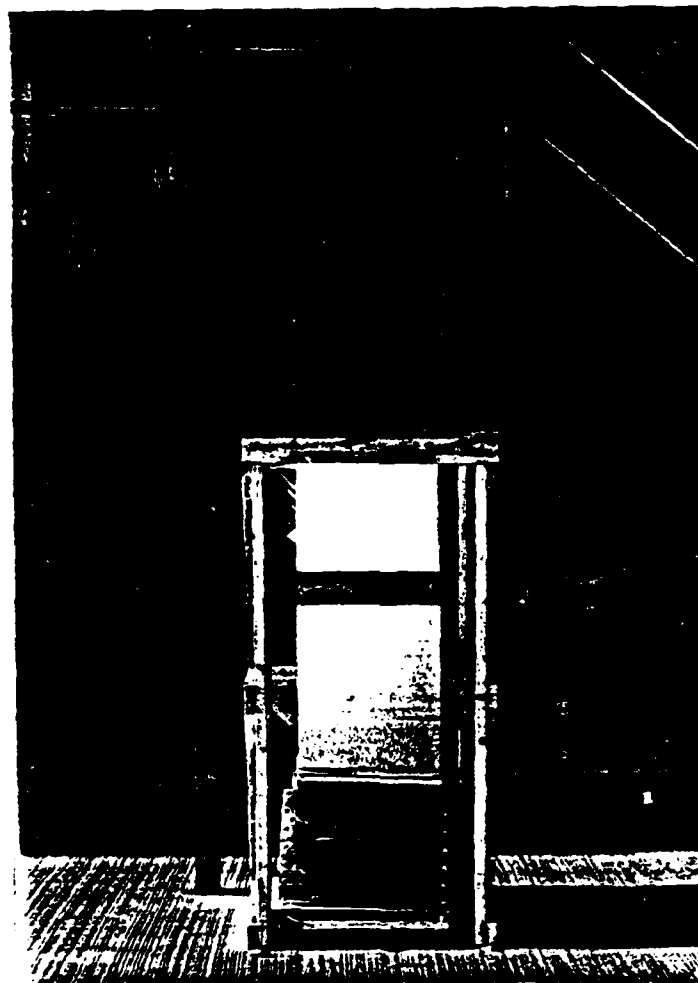


Figure 2.6 The Soil Pluviator

height of approximately 90 inches and covers a minimum area of 12 square feet. The pluviator is capable of producing sand samples of extreme densities. By selecting the proper perforation board, the researcher can control the desired discharge rate resulting to a specific sample density.

The soil strata used as a model consisted of three pluviation steps. The first step was pluviating a shallow sand layer on the bottom of the model box to act as the bedding layer. At the completion of this step, the model box was pulled out from underneath the pluviator and the model was then put in place. The second step was to bury the structure to the desired embankment depth using the same process. Again, the model box is pulled out from underneath the pluviator to set the burster slab model in place. The final layer of sand is then pluviated and the model box is ready to be mounted on the centrifuge swing bucket.

3. Loading Model Box

The first step taken before loading the model box onto the centrifuge swing bucket was to weigh the model box complete with the lid with its contents to determine the amount of counterweight to be used. Since the model box was set on the center of the platform, the counterweight needed was equal to box weight itself (+ 5 lbs). As long as the red indicator light remains off after setting the model box and the counterweight, the system is considered balanced. Note that the weight on either side should not exceed 500 lbs. The model box was then secured onto the centrifuge swing bucket by bolting 't down on

the platform (Figure 2.7).

As soon as the model box is secured onto the swing bucket, all instrumentation is wired up to the slip rings taking note of all channel designations. At the centrifuge control panel, all wires were hooked up to designated ports on the channel switch and onto the strain indicator.

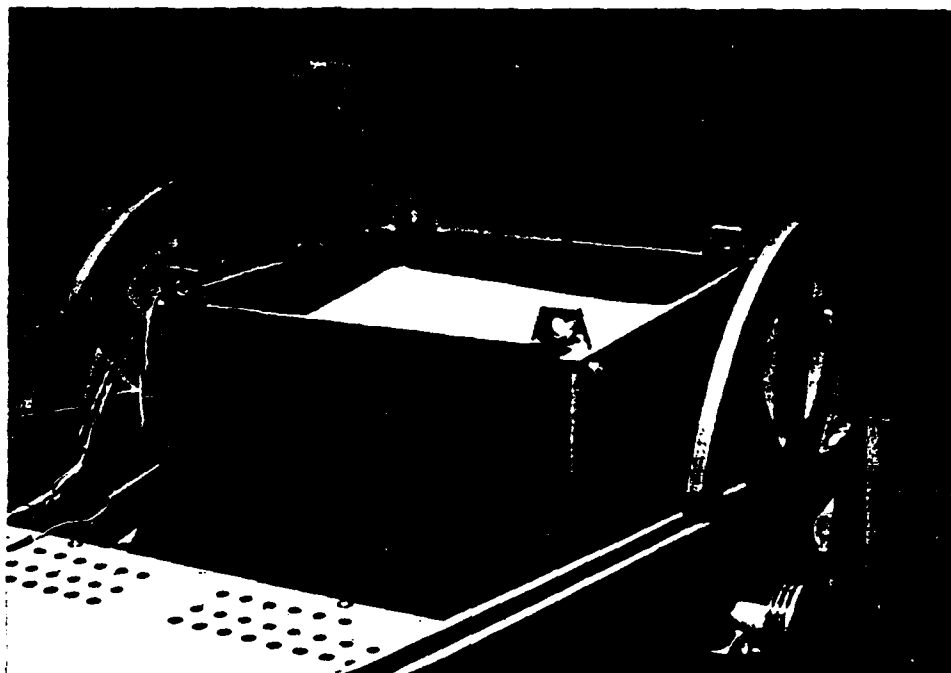


Figure 2.7 The Model Box on the Centrifuge Swing Bucket

SECTION III

FINITE ELEMENT ANALYSIS

A. DESCRIPTION OF THE COMPUTER CODE

The computer code, CANDE (Culvert ANALYSIS and DESign), used in this study was developed by Katona et al. (References 11 and 12). The basic assumptions of the program are: plane strain geometry and loading, small displacement theory, and quasistatic response. The following description summarizes salient features of CANDE used in the analysis.

1. Modeling of Structure

The box culvert was modeled as a series of straight line segments with a one-dimensional beam-column bending element comprising each segment. This bending element employs a plane-strain formulation which neglects shearing deformations. Two nodes with three degrees of freedom per node (horizontal and vertical displacement and a rotation) define each element. At each node, cubic and linear displacement approximations were used in calculations of displacements in the transverse and axial directions, respectively. Figure 3.1 shows the coordinate system of the beam element.

2. Modeling of Soil

Nonconforming quadrilateral and triangular elements were used to represent the soil (see Figure 3.2). The quadrilateral,

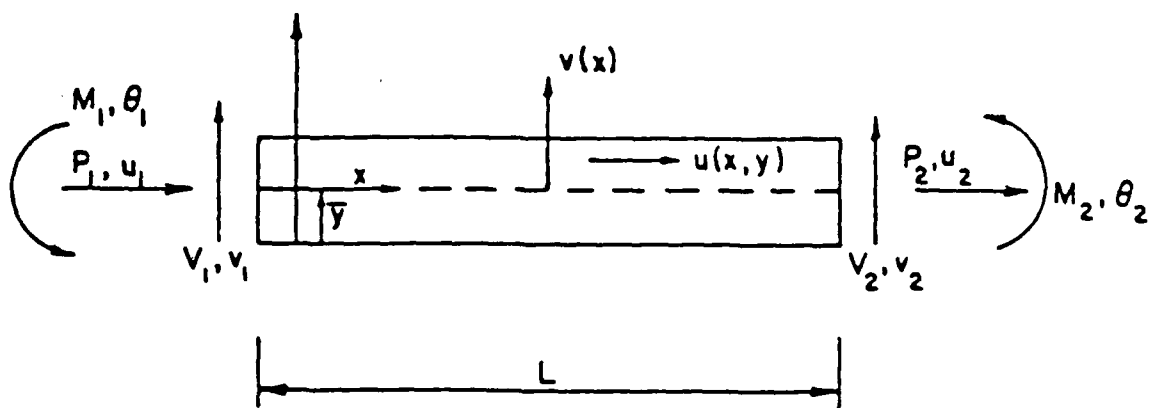


Figure 3.1 The Coordinate System of the Beam Element in CANDE

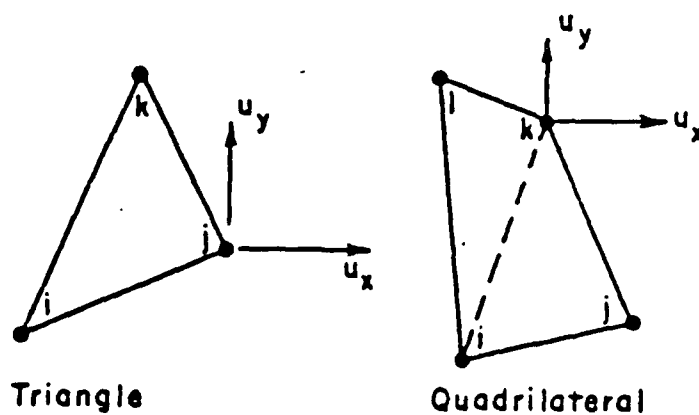


Figure 3.2 The Element Types Used for Soil Model in CANDE

defined by four nodes with two degrees of freedom (horizontal and vertical displacements) per node comprise two triangles with complete, quadratic, interpolation functions specified within each triangle. Application of appropriate constraints and static condensation procedures result in a four-node quadrilateral element (Reference 11).

There are four material characterizations available for the soil properties: linear elastic; incremental elastic (overburden dependent); extended-Hardin; and Duncan's hyperbolic stress-strain relationship, which employs tangent Young's modulus and tangent bulk modulus formulations (References 7, 12, 33).

3. Modeling of Slip

A constrained finite element formulation, which is based on a generalized principle of virtual work, was used to model the relative movement of the soil with respect to the pipe at the soil-structure interface, and relative movement of the soil with respect to the soil-soil interface (i.e., trench). An interface element is defined by a set of paired nodes joining two elements as shown in Figure 3.3. The paired nodes which have two degree of freedom per node (vertical and horizontal displacement), initially take the same position in space before any loading, but are assigned to separate elements. Therefore, each node responds individually under any applied loading. In addition, a third node, which is assigned between the paired nodes, provides normal and shear forces existing between the paired nodes. It should be observed that these interface forces arise only from

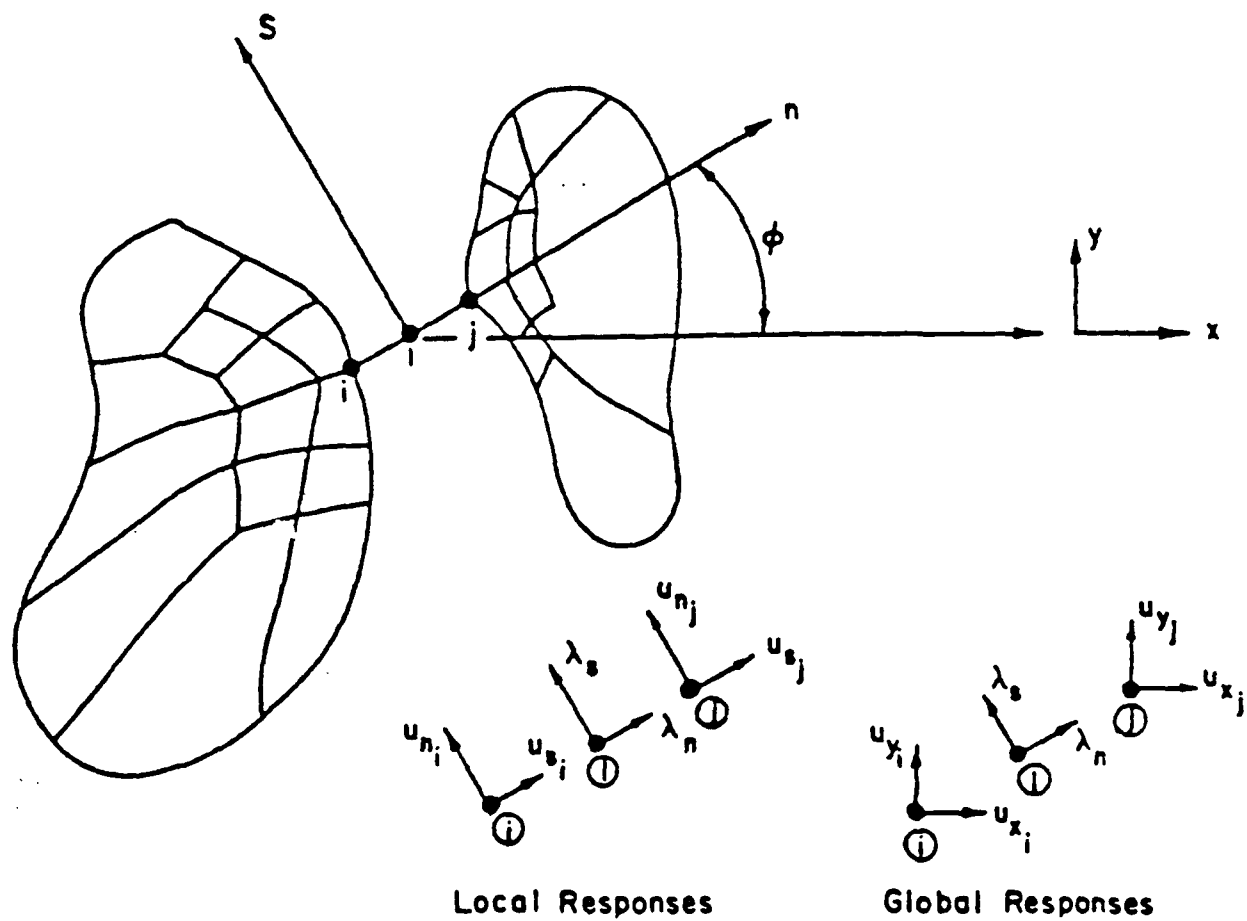


Figure 3.3 Nodes for Constraint Interface Element in CANDE

the adjoining element interaction and applied forces at the paired nodes.

4. Modeling of Incremental Construction

CANDE uses incremental iterative solution techniques to represent the placing of the culvert and embankment in a series of soil layers. The basis of the techniques is superposition of solutions from successive soil layers and a newly added layer. At each increment, iterative calculations determine soil and structure moduli until equilibrium is approximated within an allowable error.

B. FINITE ELEMENT PARAMETERS

1. Finite Element Mesh and Boundary Conditions

The finite element grid with boundard conditions used in this study is shown in Figure. 3.4. Since the model and its loading is symmetric, only half of the mode was analyzed. Boundary conditions on the culvert used in the analysis are show in the figure: a fixed movement conditions in the horizontal direction and free movement condition in the vertical direction. The arch structure was represented by 12 beam-column elements.

2. Soil-Culvert Interface and Incremental Solution

Procedure

A fixed condition was used at the soil-culvert interface. Although it is possible to represent the slip between the continuum (soil) and beam elements, the fixed condition was used

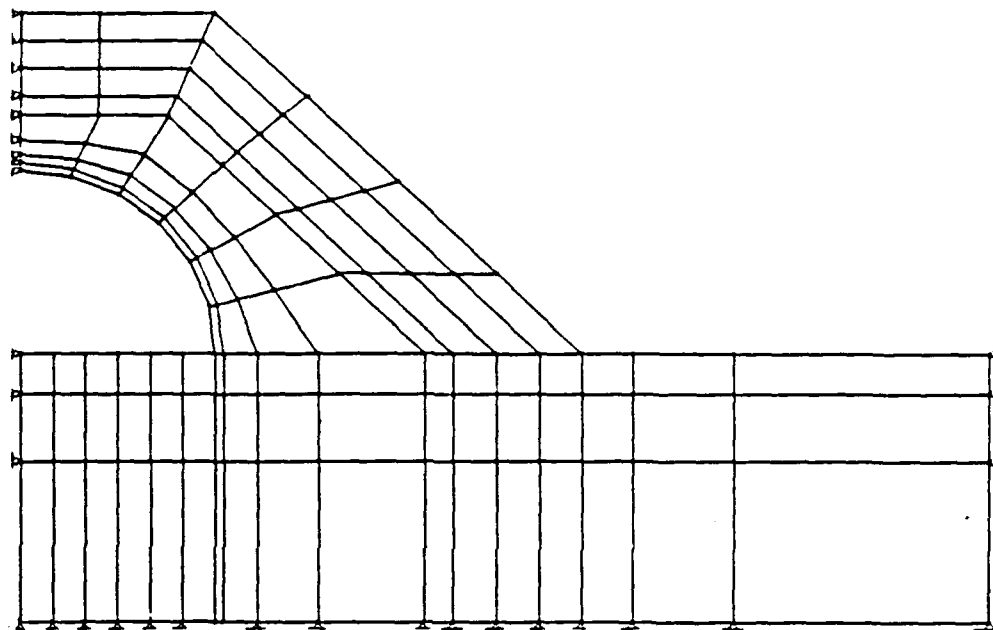


Figure 3.4a. Mesh No. 1: 3 Rock Layers, 45 Degree Slope

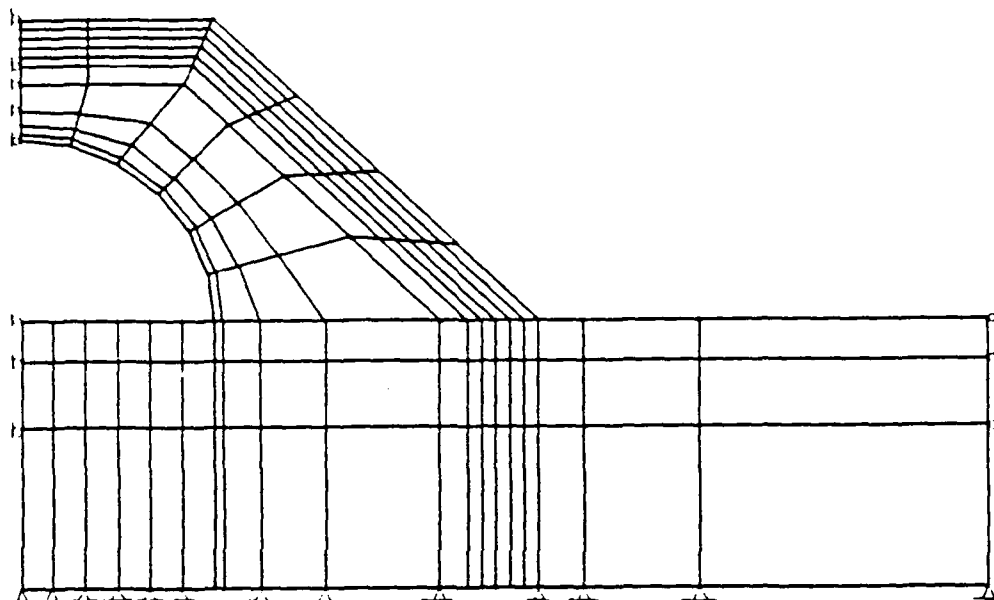


Figure 3.4b Mesh No. 2: 5 Rock Layers, 45 Degree Slope

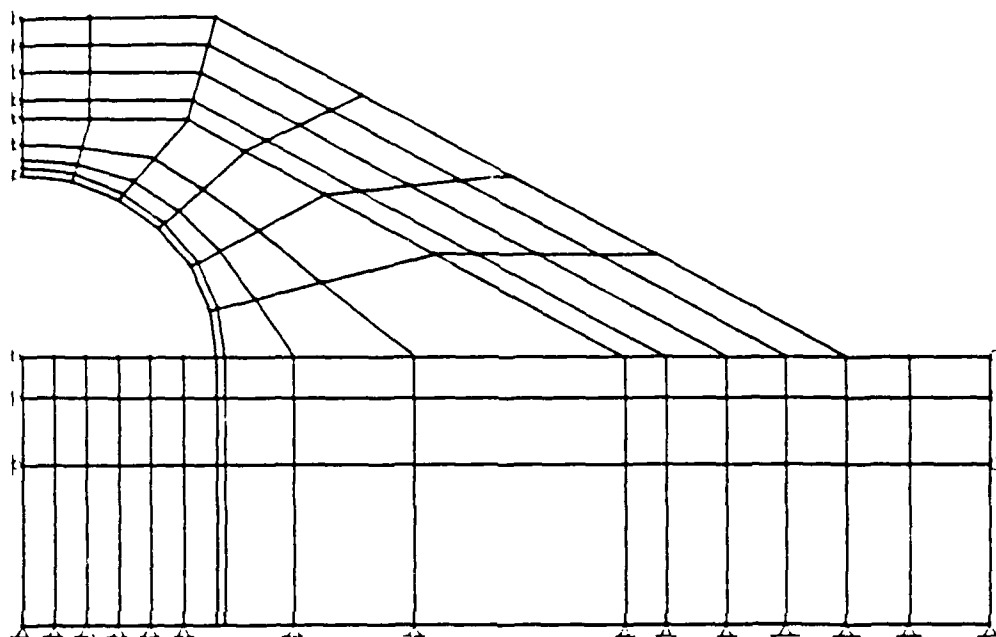


Figure 3.4c Mesh No. 3: 3 Rock Layers, 30 Degree Slope

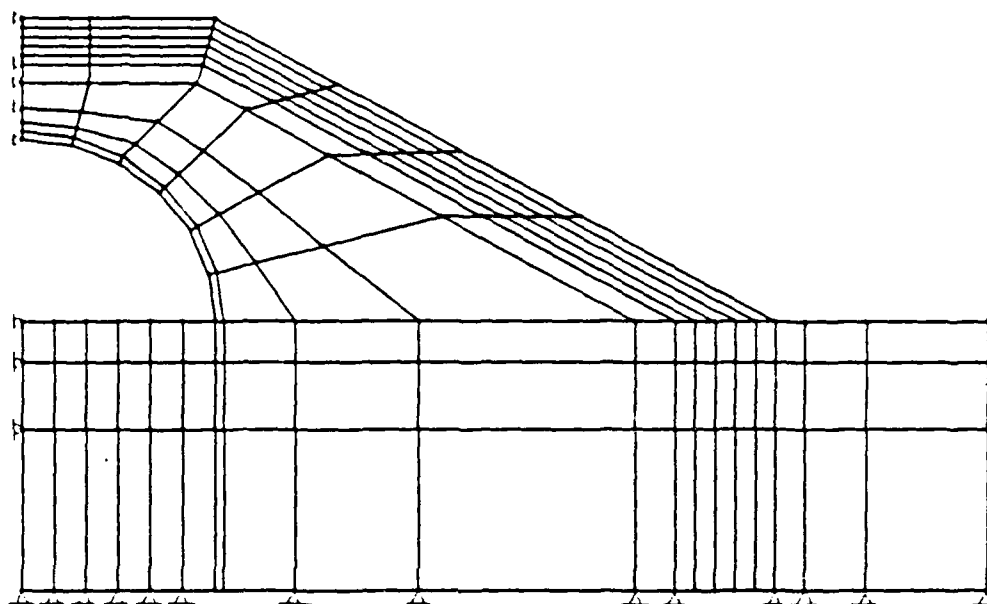


Figure 3.4d Mesh No. 4: 5 Rock Layers, 30 Degree Slope

in this preliminary study due to large amounts of CPU (Central Processing Unit) time, and substantial computational costs when slip was allowed.

The incremental solution procedure for embankment and trench simulated the actual installation process of placing soil layers in a series of lifts. Figure 3.5 shows the construction increment numbers of element groups entering sequentially into a system. The first construction increment included placing all bedding pad, in situ soil, and the arch structural elements. Subsequent increments, numbers 2 through 9, were gravity loaded elements of fill soil.

3. Material Properties

The soil model employed in the study is a characterization proposed by Duncan et al. (References 7 and 12) which has had a substantial history of development and application over the last decade. This soil model characterizes soil behavior with a variable tangent Young's modulus and tangent bulk modulus. Eight parameters are needed to define a particular soil in loading: K , n , R_f , c , ϕ , and $\Delta\phi$ for the tangent Young's modulus; and K_b and m for the tangent bulk modulus. Table 3.1 shows the material properties used for soil, concrete arch, rock, and burster slab in the analysis.

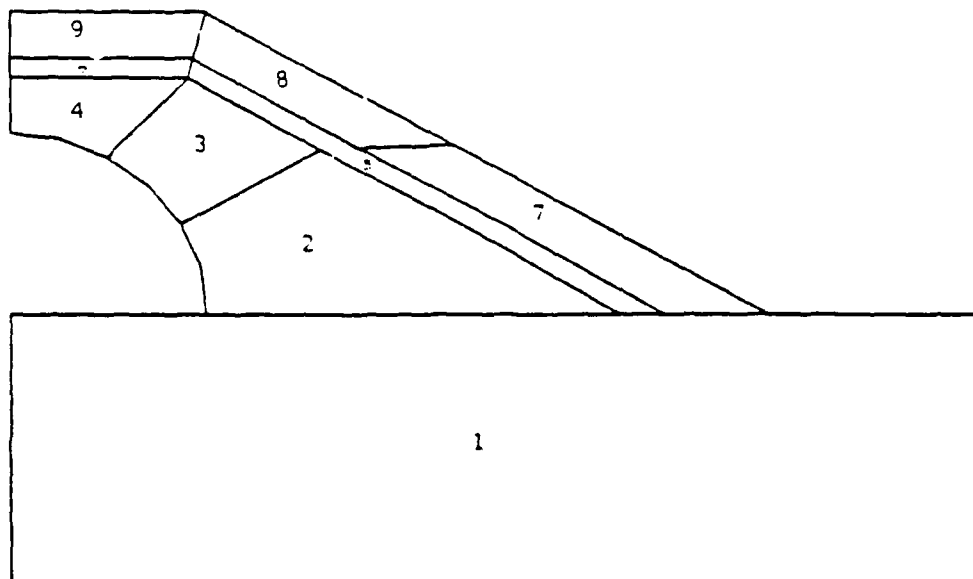


Figure 3.5 Incremental Construction

Unified Soil Classification	RC* Stand. AASHTO	γ_m k/ft ³	ϕ_o deg	$\Delta\phi$ deg	c k/ft ²	K	n	R_f	k_b	m
GW, GP SW, SP Coarse Aggregates	105	0.150	42	9	0	600	0.4	0.7	175	0.2
	100	0.145	39	7	0	450	0.4	0.7	125	0.2
	95	0.140	36	5	0	300	0.4	0.7	75	0.2
	90	0.135	33	3	0	200	0.4	0.7	50	0.2
SM Silty Sand	100	0.135	36	8	0	600	0.25	0.7	450	0.0
	95	0.130	34	6	0	450	0.25	0.7	350	0.0
	90	0.125	32	4	0	300	0.25	0.7	250	0.0
	85	0.120	30	2	0	150	0.25	0.7	150	0.0
SM-SC Silty-Clayey Sand	100	0.135	33	0	0.5	400	0.6	0.7	200	0.5
	95	0.130	33	0	0.4	200	0.6	0.7	100	0.5
	90	0.125	33	0	0.3	150	0.6	0.7	75	0.5
	85	0.120	33	0	0.2	100	0.6	0.7	50	0.5
CL Silty Clay	100	0.135	30	0	0.4	150	0.45	0.7	140	0.2
	95	0.130	30	0	0.3	120	0.45	0.7	110	0.2
	90	0.125	30	0	0.2	90	0.45	0.7	80	0.2
	85	0.120	30	0	0.1	60	0.45	0.7	50	0.2

* RC = relative compaction, in percent

Table 3.1 Duncan's Material Characterization Used for Soil Model

CONCRETE	
Compressive strength, f'_c	5,000 psi
Young's modulus in elastic range, E	4,070,000 psi
Poisson's ratio, ν	0.25
Unit weight, γ	150 pcf
Strain at which tensile cracking occurs	0.0001
Strain at elastic limit in compression	0.0013
Strain at initial compressive strength,	0.0040

REINFORCING STEEL	
Yield stress, f_y	60,000 psi
Young's modulus, E	29,000,000 psi
Poisson's ratio, ν	0.3
Spacing of reinforcement	1.5 in.
Area of inner cage reinforcement	0.31 sq. in./in.
Area of outer cage reinforcement	0.31 sq. in./in.
Thickness of concrete cover to center of inner cage	1.25 in.
Thickness of concrete cover to center of outer cage	1.25 in.

Table 3.2 Concrete and Steel Properties Used for Arch Structure

Type	Young's modulus E	Poisson's ratio ν	Unit weight γ
Rock	1,500,000 psi	0.2	86.94 pcf
Burster slab	4,070,000 psi	0.25	145.0 pcf

Table 3.3 Material Properties used for Rock and Burster Slab

SECTION IV

RESULTS AND DISCUSSIONS

A. CENTRIFUGE MODEL STUDY

Since the authors are the first time-users of the centrifuge facility at Tyndall Air Force Base with a small-scale structure and instrumentation, a series of centrifuge model tests was first performed as a pilot study to check the proper operations of the centrifuge machine and instruments. During this preliminary test, the instruments faced two major difficult problems: (1) a limited number of slip rings available for data transmission, and (2) brush noise caused by dynamic vibration occurred at the centrifuge slip rings. The voltage fluctuations generated by the noise at the slip rings were found to be much greater than the instrument signals themselves. The major centrifuge model tests, therefore, were not able to be performed during the stay at Tyndall Air Force Base due to the limitation and unavailability of testing equipments. Rather, this section discusses the various computer-based data acquisition systems required to overcome these problems for a future centrifuge model study. The description given below is a brief one; readers interested in more detailed information should refer elsewhere (References 8,9,17-22,26,32).

Transmission of Signals:

Direct transmission of signals is used the most in model

studies mainly because of its simplicity and relatively low cost. Also there is no distortion of signals. When used in centrifuge modeling, direct transmission consists of the physical linkage of system components by wire cables. Brush-and-slip ring riggings are a commonly used method of providing a signal path from the centrifuge shaft to the outside. Brush noise is caused by dynamic vibration in the area in which the brush is in contact with the slip ring. This vibration in contact area gives a variation in circuit resistance. An increase in signal level before reaching slip rings, through amplification, can give a desirable increase in the signal-to-noise ratio. Another beneficial technique is to decrease the total brush resistance by providing multiple parallel current paths; noise would be reduced because variations in brush contact for individual brushes would not be as significant when other brushes are in the path. If a large number of slip rings dedicated to signal transmission are available, the direct transmission system should be considered. It has the advantage of simplicity and uninterrupted transmission of signals.

However, for most of the smaller size centrifuges, there are only a limited number of slip rings for data transmission. A multiplexer-demultiplexer unit (indirect method) is therefore used to facilitate the transmission of signals from a relatively large number of sensors. The two most commonly used multiplexer-demultiplexer units are the time division unit and the frequency modulation (FM) frequency division unit. The time

division unit works as a synchronized channel selector as shown in Figure 4.1 where the frequency division unit works as a dedicated frequency carrier along with FM detectors as shown in Figure 4.2. Of the two indirect methods of signal transmission, the time division technique is relatively simple and less costly to install; however, additional control signals are needed to synchronize the functions of the multiplexer and demultiplexer. This additional control and operation time impedes the sampling rate of the system. The frequency division technique, on the other hand, is costly but capable of transmitting signals at much higher rates. Since the FM system is sensitive only to frequency variations and not amplitudes, it is immune to most noises induced along the transmission line.

It should also be mentioned that wireless sensors can be adopted to transmit radio frequency signals thus bypassing the use of connecting wires between sensors and the signal conditioning unit. However, these sensors are very expensive and usually too big in size and too heavy, not readily suitable for geotechnical use. The author does not foresee the need to use wireless sensors in centrifuge modeling in the future.

B. FINITE ELEMENT ANALYSIS

1. The Influence of Installation Type

The first part of this investigation deals with the influence of the type of installation on the relative displacement of the crown of the structure (refer to Figures 4.3 thru 4.6). The comparisons have been made between a system with a 3-layer rock cover versus one with a 5-layer rock cover. All other variables were considered in the comparison to determine

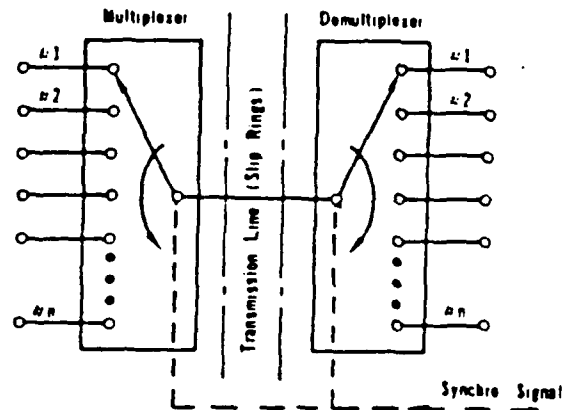


Figure 4.1 A Time Division Multiplexer-Demultiplexer Unit

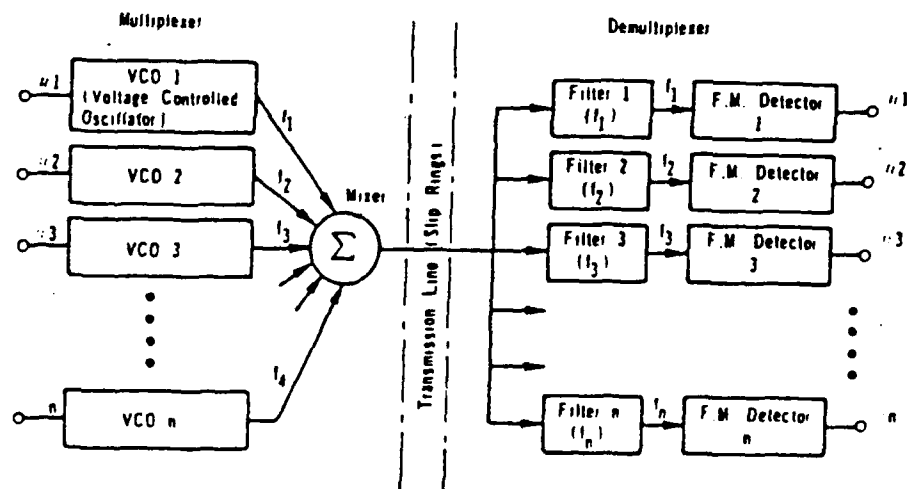


Figure 4.2 A Frequency Division Multiplexer-Demultiplexer Unit

CL85 BEDDING, 30 DEG SLOPE

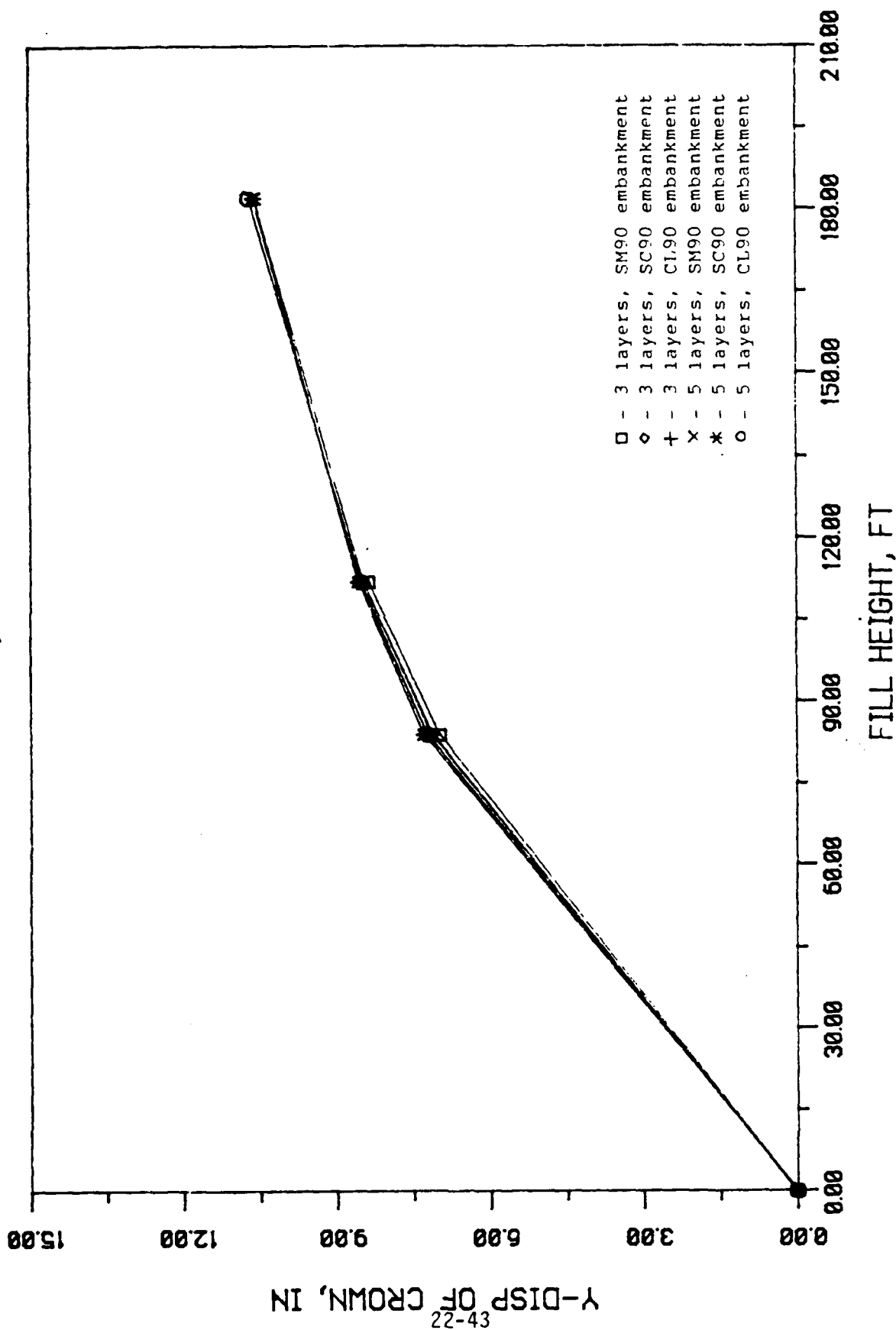


Figure 4.3 Relative Crown Deflection vs. Fill Height for Case 11A

SM85 BEDDING, 30 DEG SLOPE

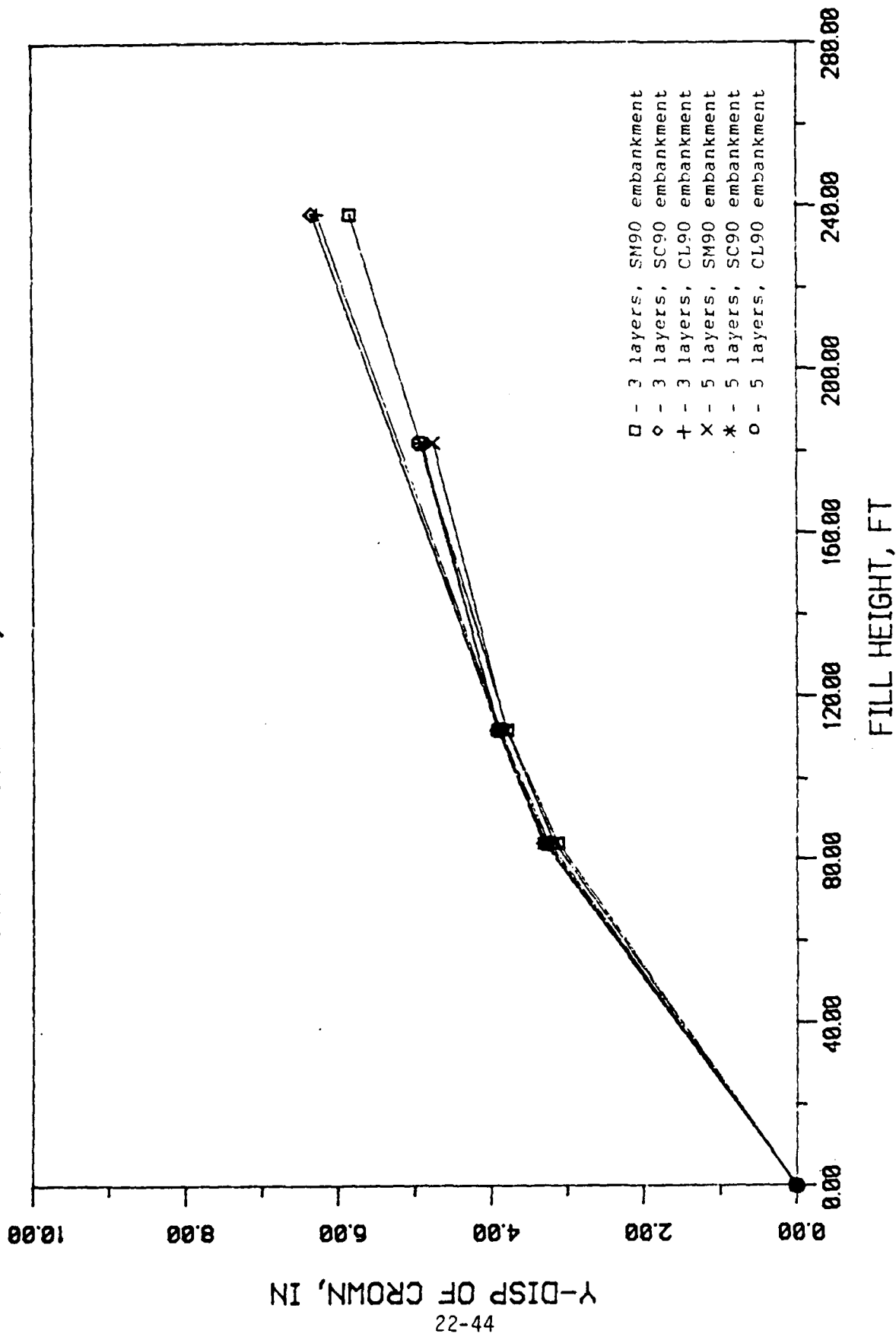


Figure 4.4 Relative Crown Deflection vs. Fill Height for Case 11B

CL85 BEDDING, 45 DEG SLOPE

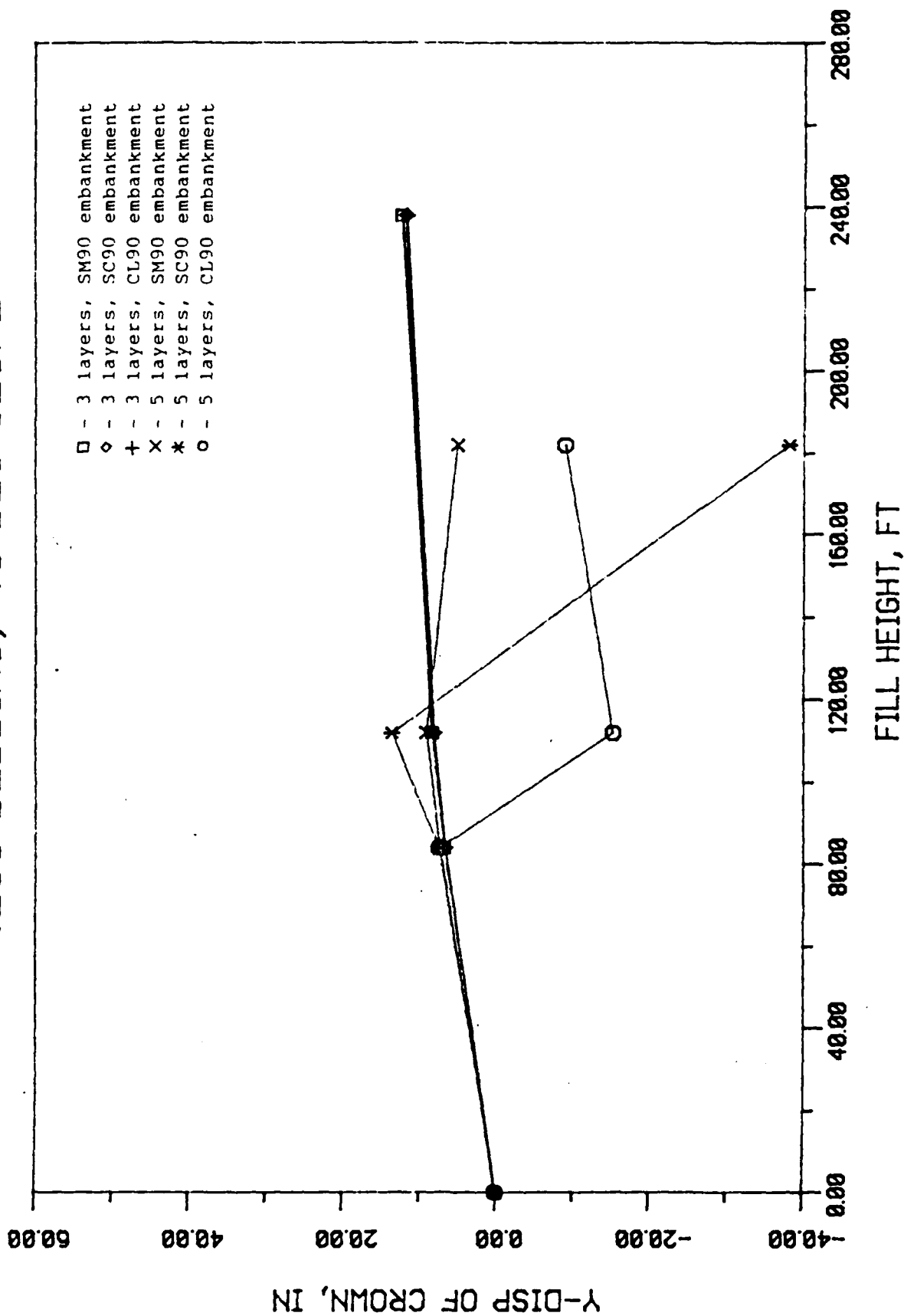


Figure 4.5 Relative Crown Deflection vs. Fill Height for Case 12A

SM85 BEDDING, 45 DEG SLOPE

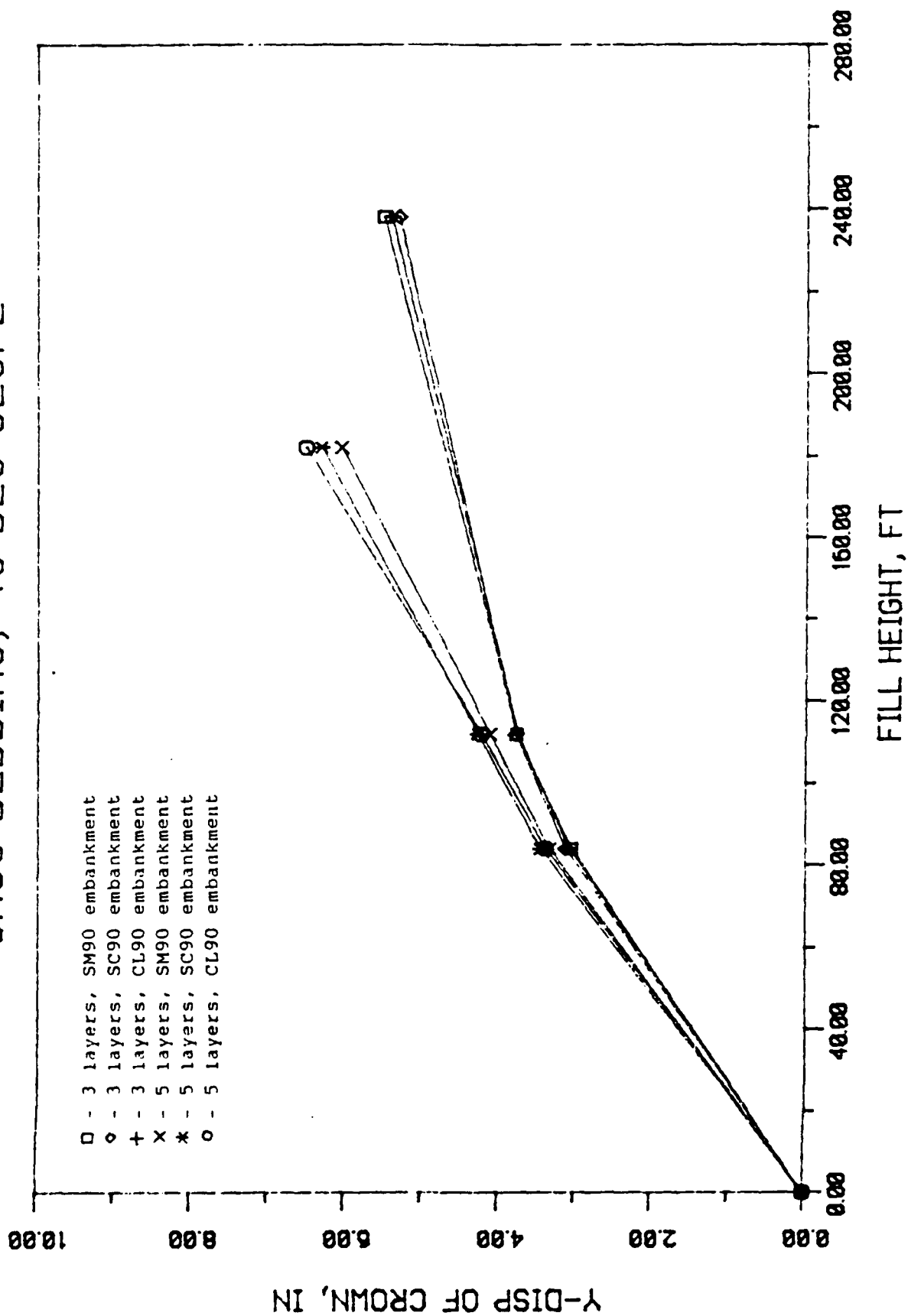


Figure 4.6 Relative Crown Deflection vs. Fill Height for the Case 12B

one with a 5-layer rock cover. All other variables were considered in the comparison to determine the degree of influence of installation type on the displacement of the crown.

For Case 11A where the structure is modeled on CL85 (clay) soil type bedding and 30-degree slope embankment, the finite element analysis predicted a steel safety factor equal to 1.00 at the end of eight construction increments when a 3-layer rock cover is installed, meaning that the steel reinforcement of the structure had failed under these conditions. A 5-layer rock cover proved to be the best alternative in this case.

As for Case 11B where the structure is modeled on SM85 (sand) soil type bedding and 30-degree slope embankment, the influence of the type of rock layer embankment can be seen at fill heights greater than 112 ft. It can clearly be seen that the system under a 5-layer rock embankment caused less crown deflection than the 3-layer type. Minimum relative crown deflection at fill height of 182 ft. is 4.76 inches and occurs when the embankment is of SC90 (sand-clay) type soil.

Case 12A deals with the structure modeled on CL85 soil bedding and 45-degree slope embankment. With the case where the 5-layer rock embankment system was installed, the finite element analysis predicted a steel safety factor and concrete compression safety factor both equal to 1.00 at the end of four construction increments, meaning that the structure had failed under these conditions. In this case, therefore, a 3-layer rock cover would be the best and only solution.

The last installation case examined is Case 12B where the

structure is modeled on SM85 soil type bedding and a 45-degree slope embankment. In this case the influence of the type of rock-layer installed is much more clearly defined. Case I2B shows that the system with a 3-layer rock cover causes less deflection of the crown of the structure. Differences in deflection of the crown is close to the 1.25-inch range. Even at a higher fill height, the system with a 3-layer rock cover causes less deflection than the system with the 5-layer rock cover. Minimum relative crown deflection at a fill height of 182 ft is 5.31 inches and occurs when the embankment soil is of SC90 type and the rock cover is of the 3-layer type.

The second part of the investigation deals with the influence of installation type on the bending moment developed at the crown of the structure depending upon the type of rock cover installed on the system (refer to Figures 4.7 thru 4.10). Similar to the discussion above, the comparison has been made between a system with a 3-layer rock cover versus one with a 5-layer rock cover. In Case I1A, the numerical analysis of the system predicted the failure of the structure under a 3-layer rock cover at the end of eight construction increments. And as for Case I2A, the same situation arised with a structure under a 5-layer rock cover but after the application of only four load increments. Therefore, the comparisons were limited to two cases.

Case I1B showed that at a fill height greater than 182 feet, the system with the 5-layer rock cover produced less bending moment at the crown compared to the one with the 3-layer

CL85 BEDDING, 30 DEG SLOPE

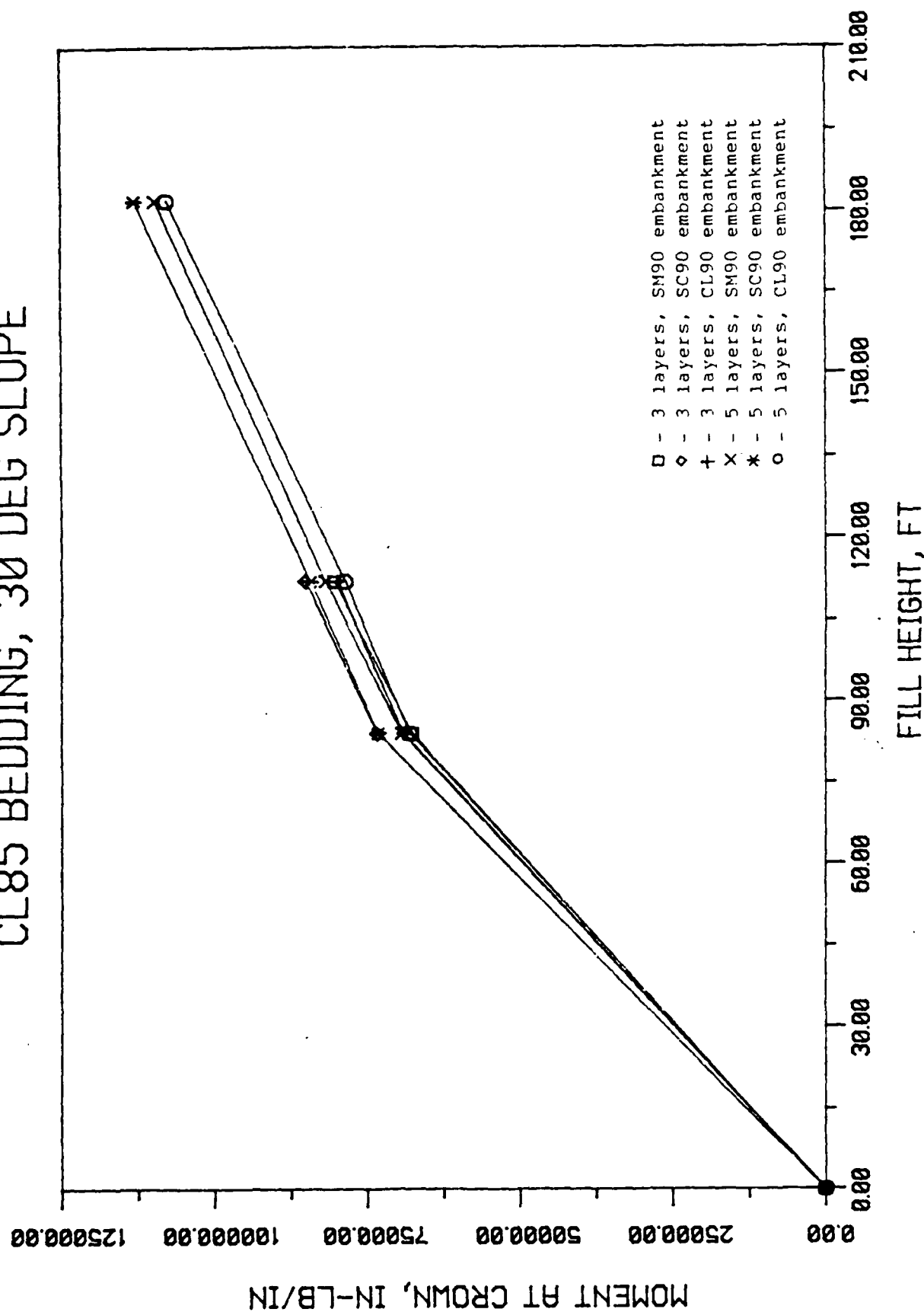


Figure 4.7 Crown Moment vs. Fill Height for Case IIA

SM85 BEDDING, 30 DEG SLOPE

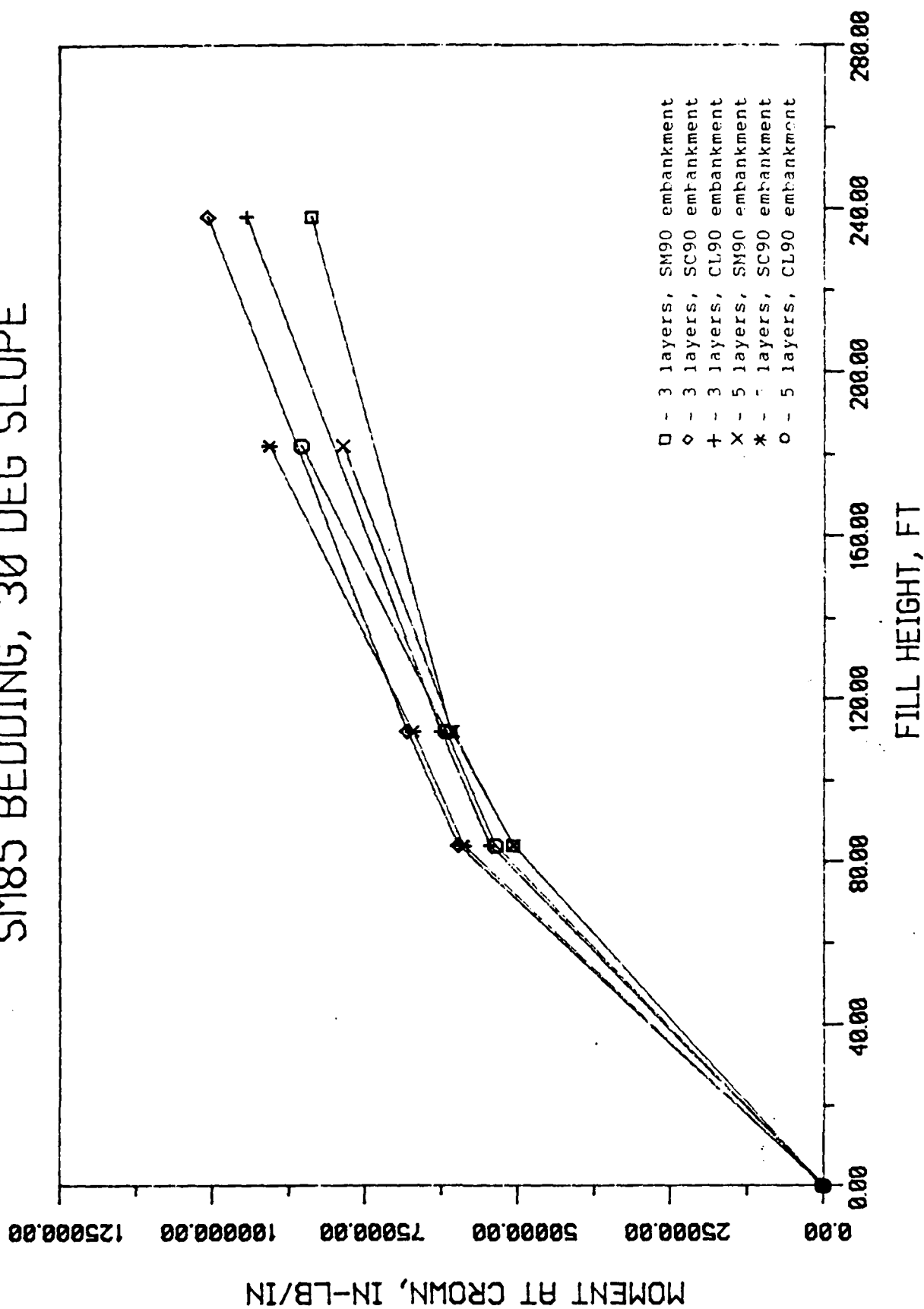


Figure 4.8 Crown Moment vs. Fill Height for Case 11R

CL85 BEDDING, 45 DEG SLOPE

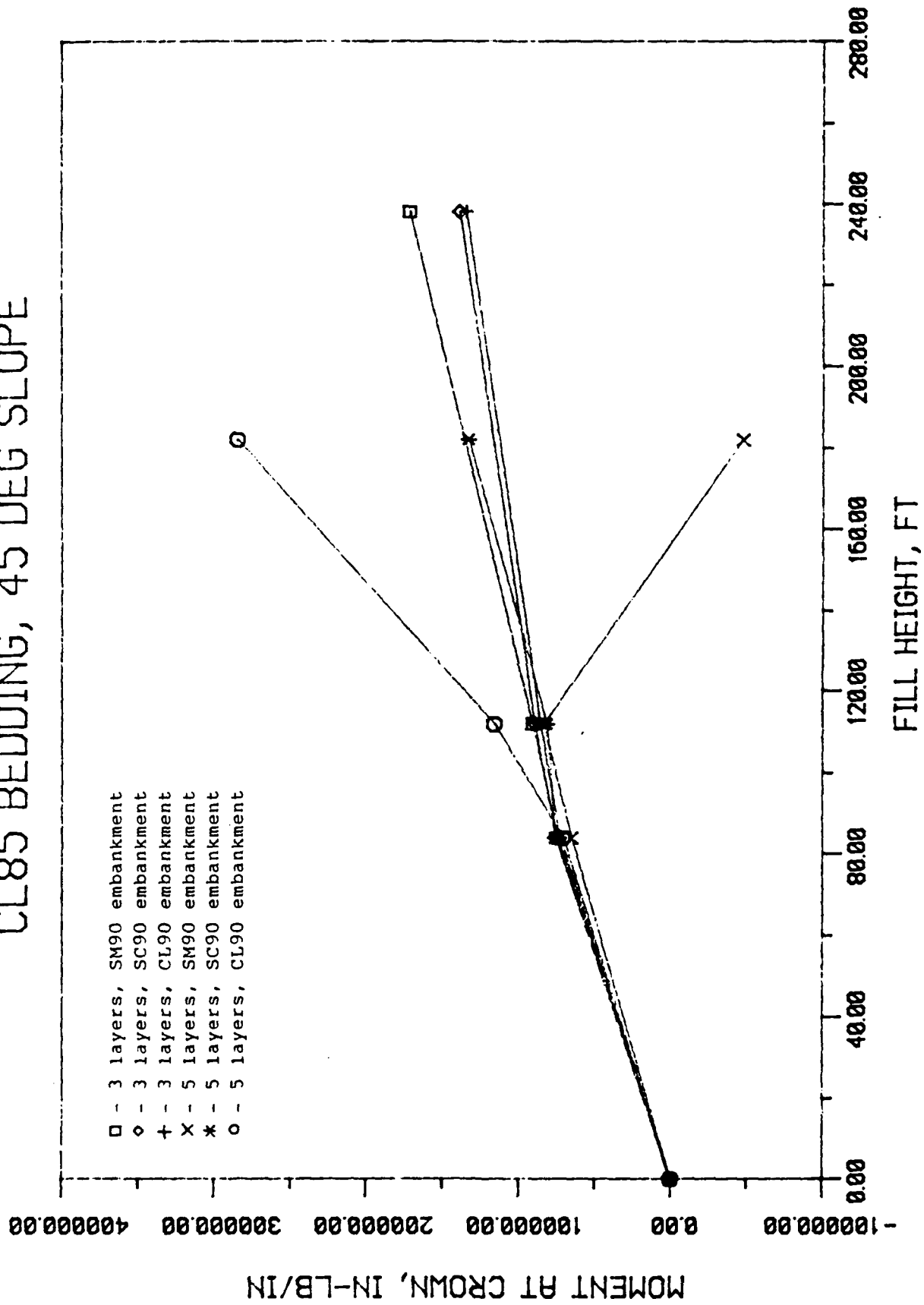


Figure 4.9 Crown Moment vs. Fill Height for Case 12A

SM85 BEDDING, 45 DEG SLOPE

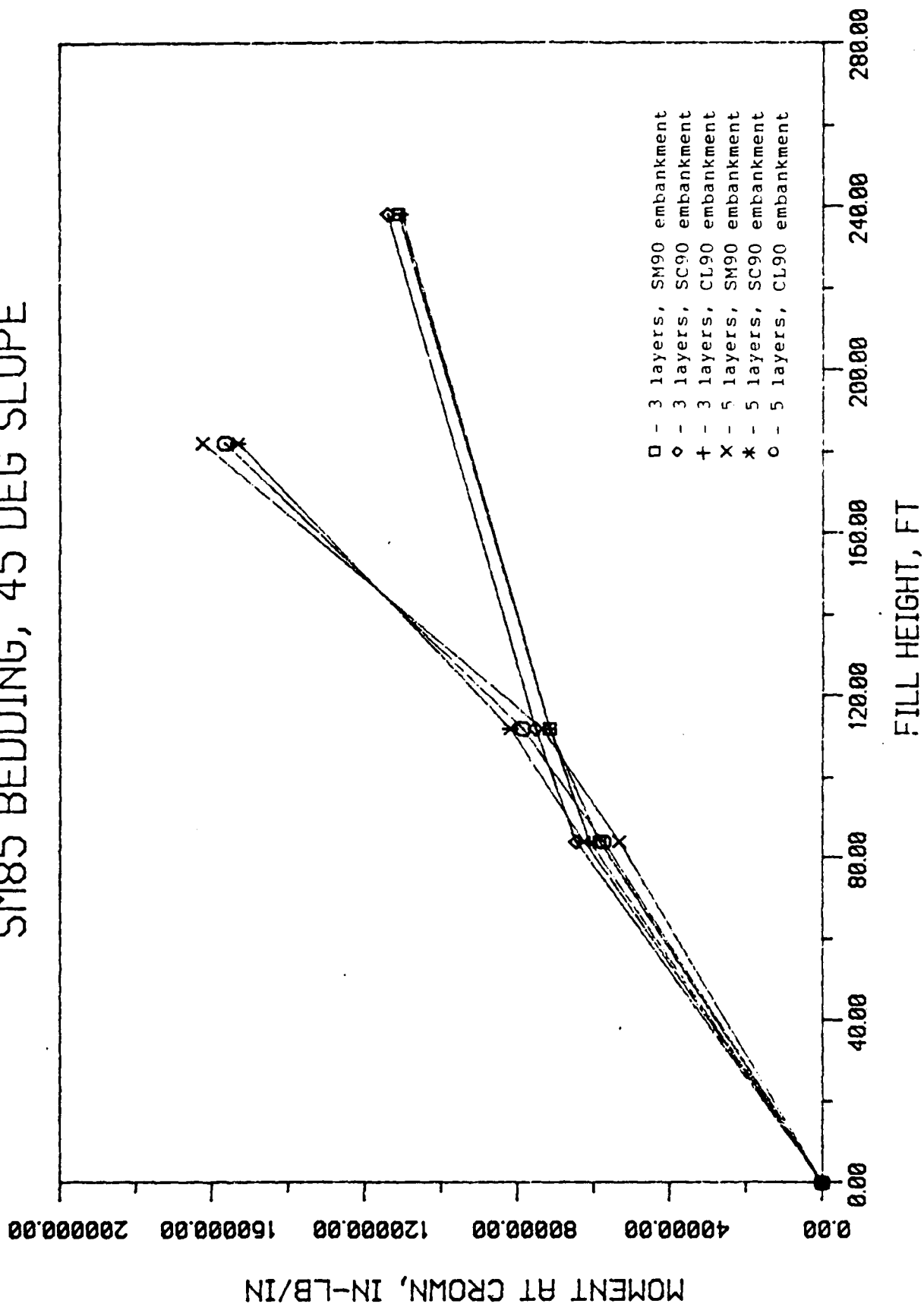


Figure 4.10 Crown Moment vs. Fill Height for Case 12R

rock cover. The difference between the moments occurring at the crown due to the two types of rock cover averaged 7988.667 in-lb/in. Minimum moment developed at the crown of the structure has a magnitude of 78640 in-lb/in and occurs when the embankment is of SM90 type soil.

Case I2B showed that the structure modeled with a 3-layer rock cover produced much less moment at the crown compared to that with a 5-layer rock cover. The average difference of the moment developed at the crown is 45594.0 in-lb/in and minimum moment with a magnitude of 110336.10 in-lb/in. with the use of CL90 soil for the embankment. Although the soil type of the embankment has considerable contribution to this difference, one can still see the dramatic rate of increase in the moment developed at the crown beginning at load increment 7 when the first section of the rock cover is installed. Although the 3-layer type rock cover produces a much higher fill height, the moment developed at the crown of the structure is significantly lower than that generated by the 5-layer type.

Overall, the results discussed in this section are quite consistent. Observing that the moment developed at the structural crown is less when the 3-layer type rock cover is installed at a fill height of 182 ft. But since layer type and embankment height are coupled, the 5-layer type rock cover proves to produce the least amount of bending moment at the crown of the structure at the completion of rock cover installation. The least amount of moment is developed then the 5-layer rock cover is installed in combination with SM90 soil

type for the embankment.

The thrust developed at the crown of the structure is also dependent upon the type of installation that the structure is built under (refer to Figure 4.11 thru 4.14). This section describes thrust in relation to the type of rock cover installed on the system. The comparisons have been made between only two cases wherein the structure withstood the entire loading scheme, these include Case I1B and I2B. The loading scheme for Case I1A with a 3-layer rock embankment and Case I2A caused structural failure after eight and four step load increments, respectively.

Thrust developed at the crown of the structure with a 30-degree slope embankment and SM85 soil type bedding (Case I1B) was minimal with the employment of the 3-layer rock cover. The thrust ranged from 651 lb/in when the embankment is of CL90 type soil to as low as -531 lb/in when the embankment is of SC90 type soil. As for the 5-layer type rock cover, the values of thrust ranged from -1664 lb/in when the embankment is of SC90 type soil to as high as -1810 lb/in when the embankment is of CL90 type soil. Again, even though the fill height generated by the 3-layer rock embankment is much higher than the 5-layer type, it is observed that the final thrust magnitude developed at the crown is less with the 3-layer type rock cover.

Case I2B shows a totally contradicting set of values. At the completion of both types of rock covers, final thrust magnitudes developed at the crown ranged from at least -1413 lb/in when the rock cover type is 5-layer and the embankment is SM90 type soil to as high as 1927 lb/in when the rock cover type

CL85 BEDDING, 30 DEG SLOPE

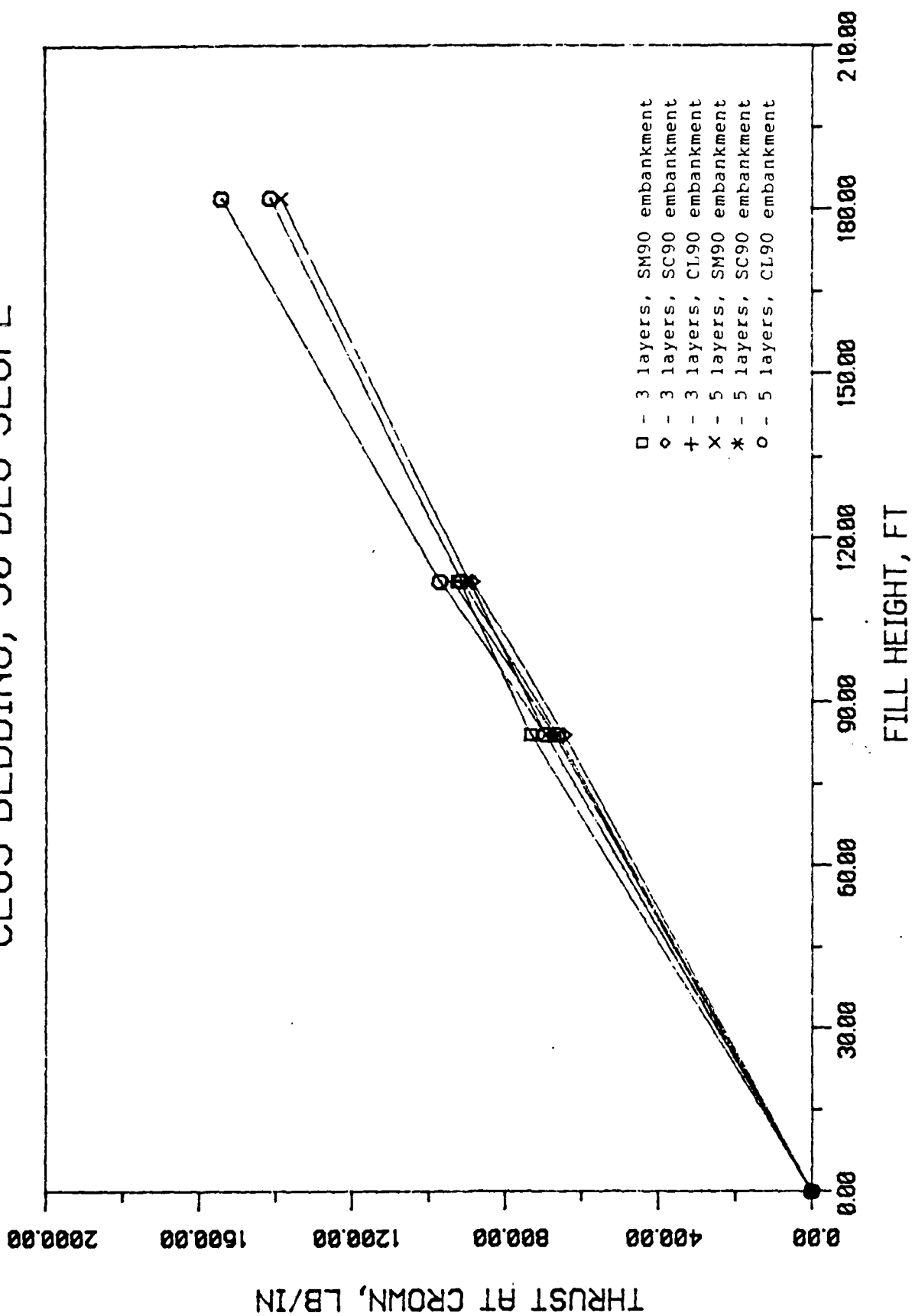


Figure 4.11 Crown Thrust vs. Fill Height for Case 11A

SM85 BEDDING, 30 DEG SLOPE

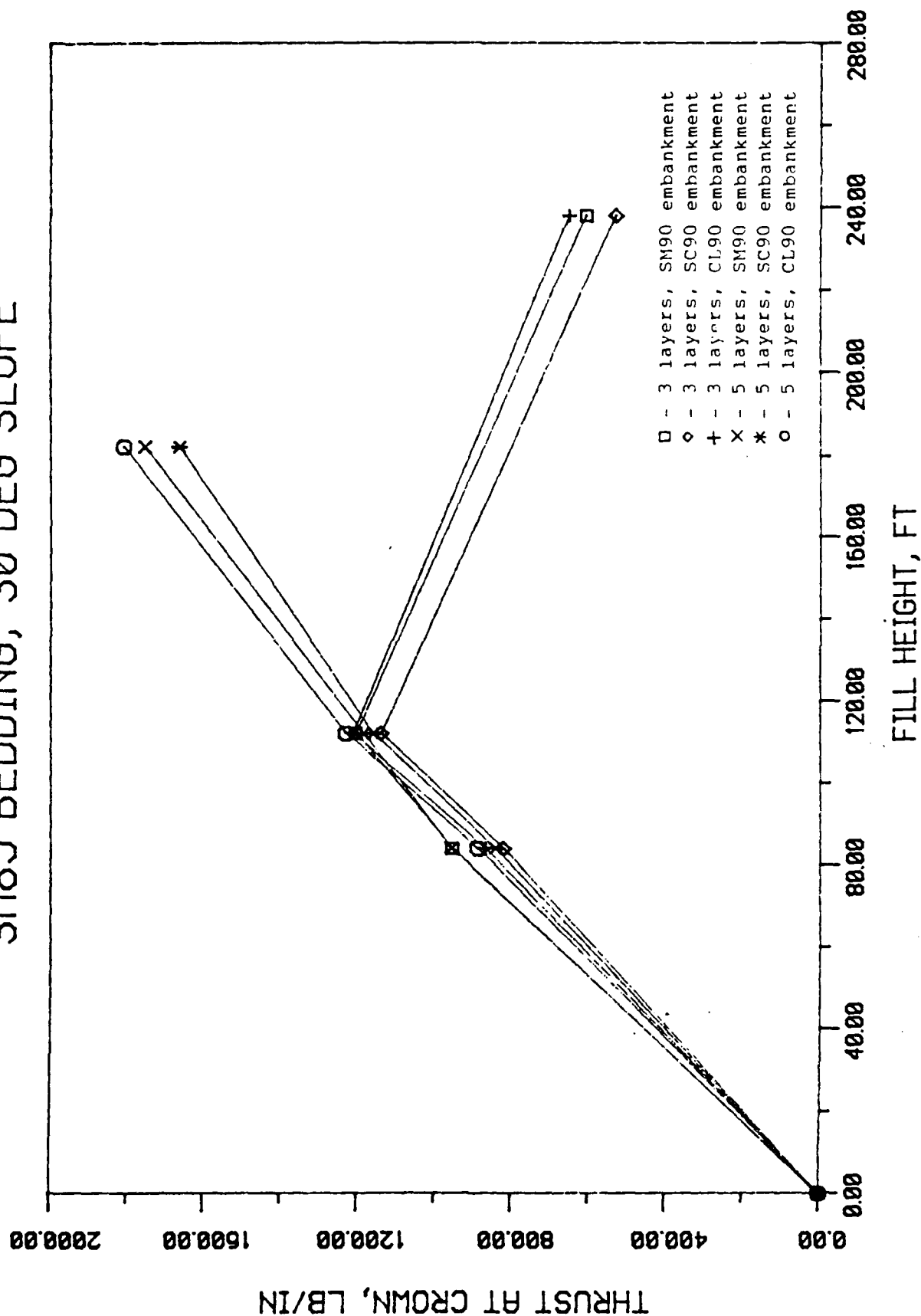


Figure 4.12 Crown Thrust vs. Fill Height for Case 11R

CL85 BEDDING, 45 DEG SLOPE

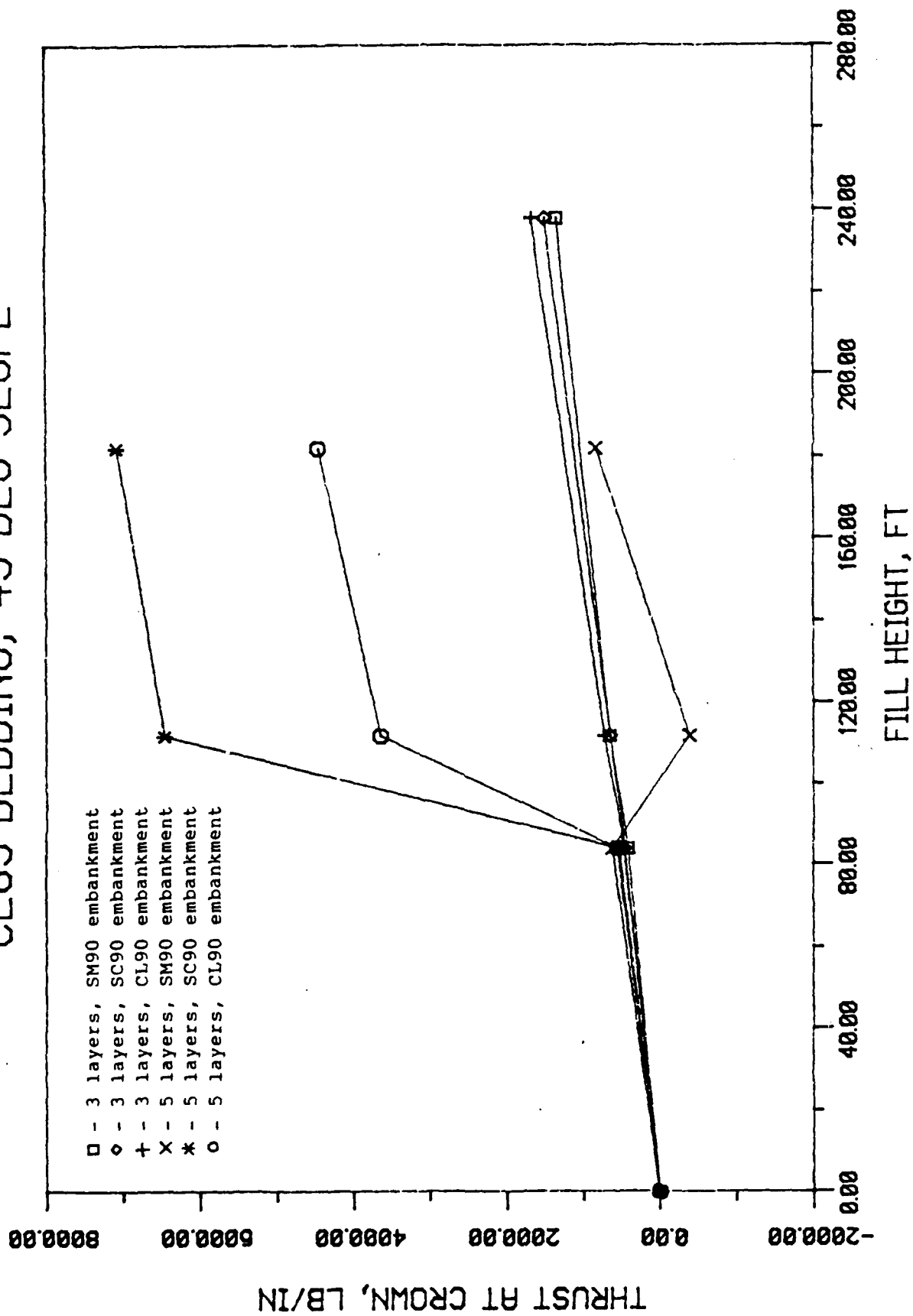


Figure 4.13 Crown Thrust vs. Fill Height for Case 12A

SM85 BEDDING, 45 DEG SLOPE

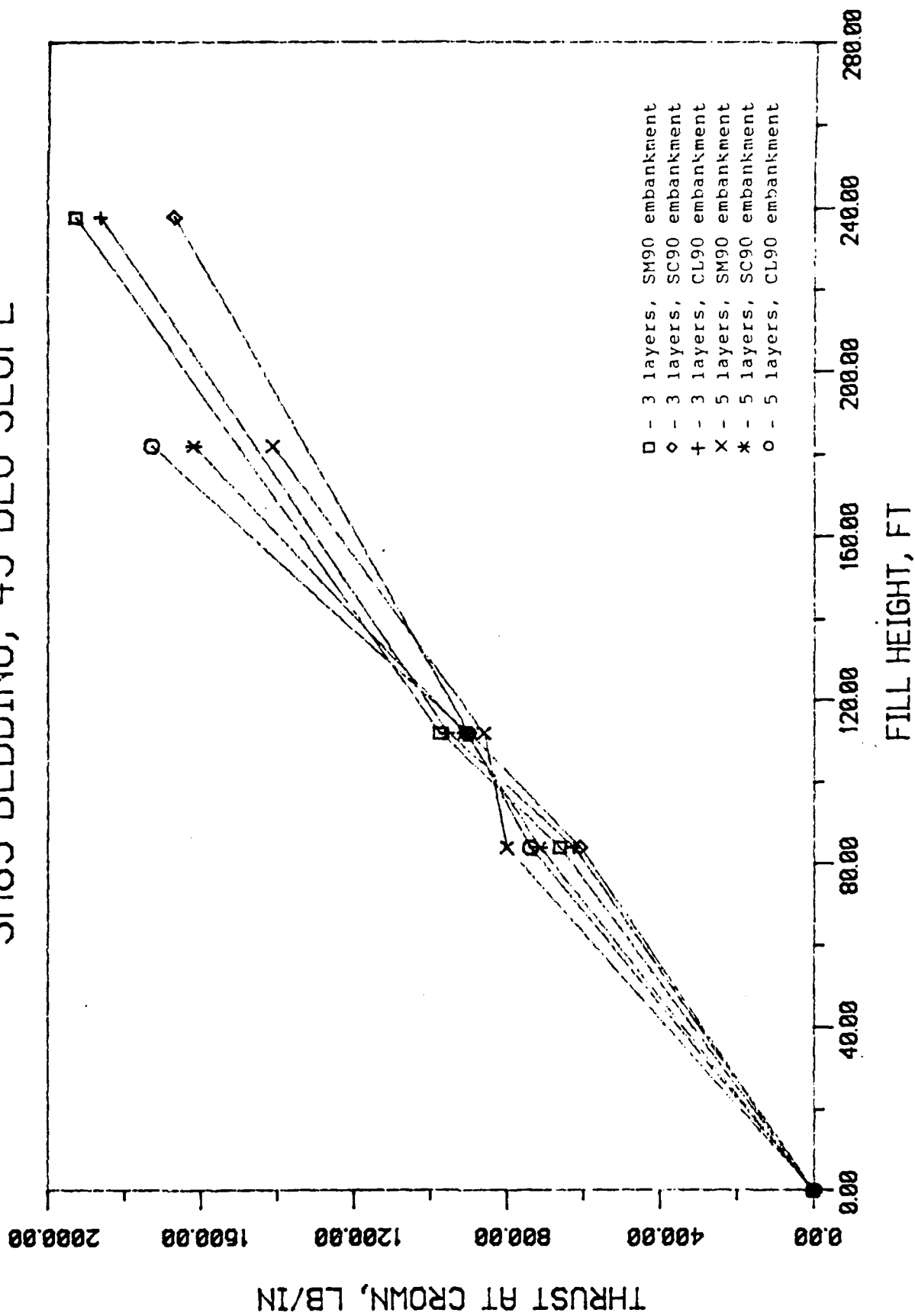


Figure 4.14 Crown Thrust vs. Fill Height for Case 12B

is 3-layer and the embankment is SM90 type soil. The interesting part of this case that when the rock cover is of the 3-layer type, and the embankment is of the SC90 type soil, the final thrust magnitude developed at the crown is 1669 lb/in, the second lowest value for thrust found in this case. It is, therefore, difficult to make any conclusions about the influence of the rock cover type on the thrust for this particular case.

2. The Influence of the Slope of Embankment

To determine the effect of the embankment slope on the deflection of the crown of the structure, certain variables had to be held constant to be able to easily focus on the effect of the slope. The main variable that was held constant in all cases of the analysis is the number of layers used for the rock cover, in this case the 3-layer type, is selected. All other variables such as the bedding and soil embankment conditions were used, but values for crown displacement were compared individually for every case.

The first three cases studied in this discussion is a system with CL85 bedding and combination with SM90, SC90, and CL90 soil type embankments designated as Case IIIA (refer to Figure 4.15). Unfortunately, the structural model failed after eight load increments for all cases with a 30-degree slope embankment. Comparison between the effect of the embankment slope was therefore limited to the values of the crown displacement after installation of step load increment 6, the completion of the concrete slab. In the first case, where the

CL85 BEDDING, 3 LAYERS, SM90 EMBA

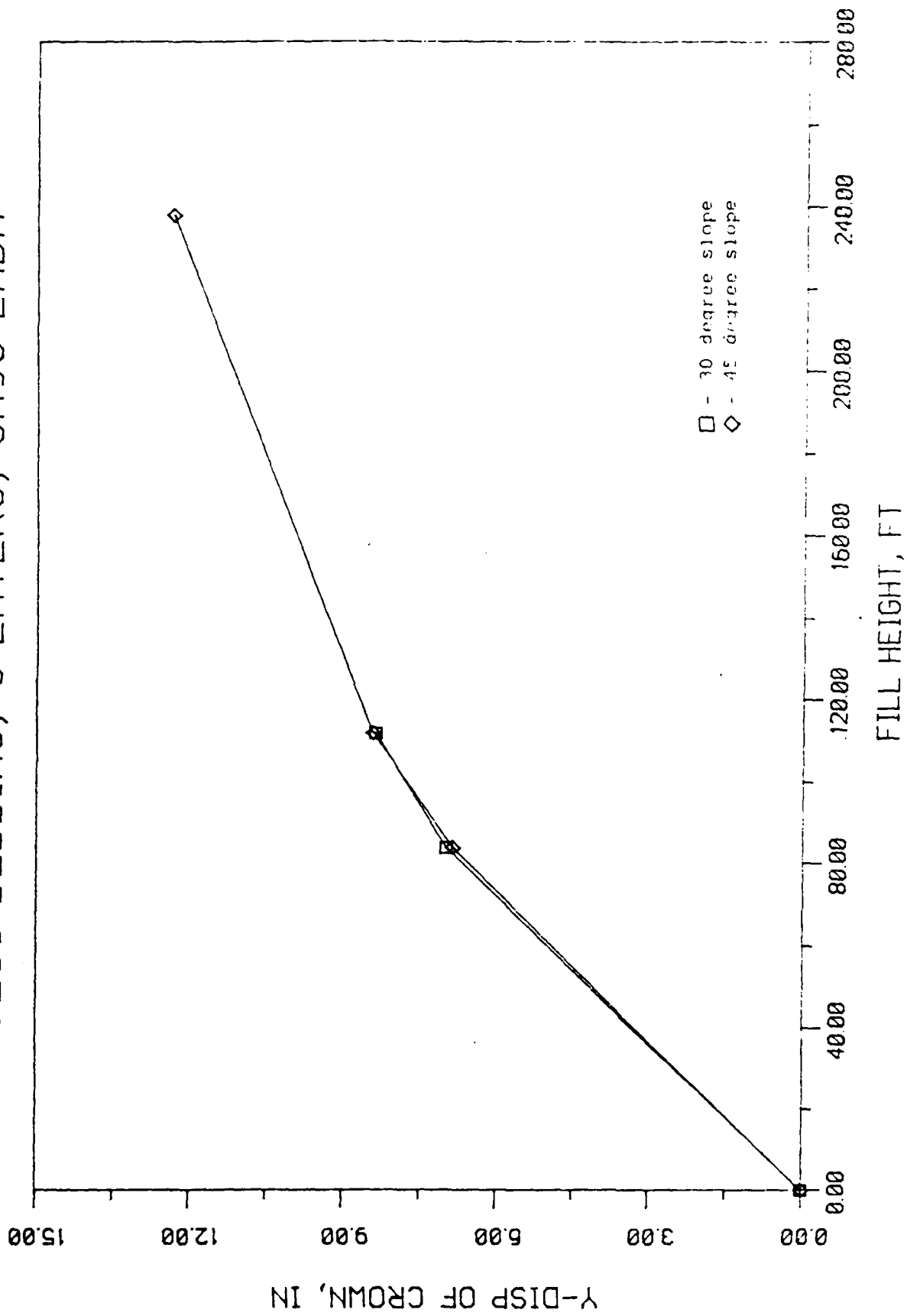


Figure 4.15a Relative Crown Deflection vs. Fill Height for Case 111A

CL85 BEDDING, 3 LAYERS, SC90 EMBA

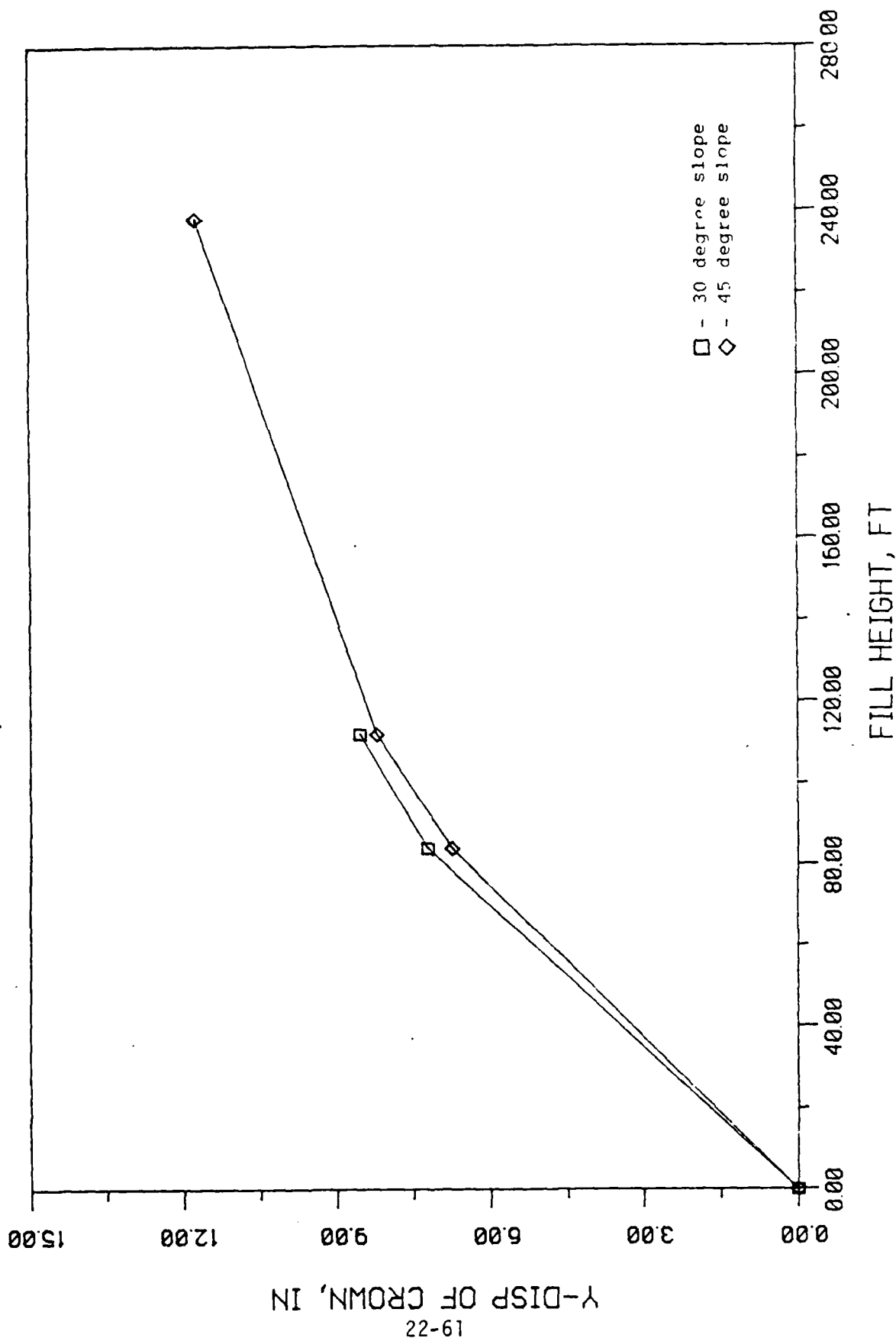


Figure 4.15b Relative Crown Deflection vs. Fill Height for Case IIIA

CL85 BEDDING, 3 LAYERS, CL90 EMBA

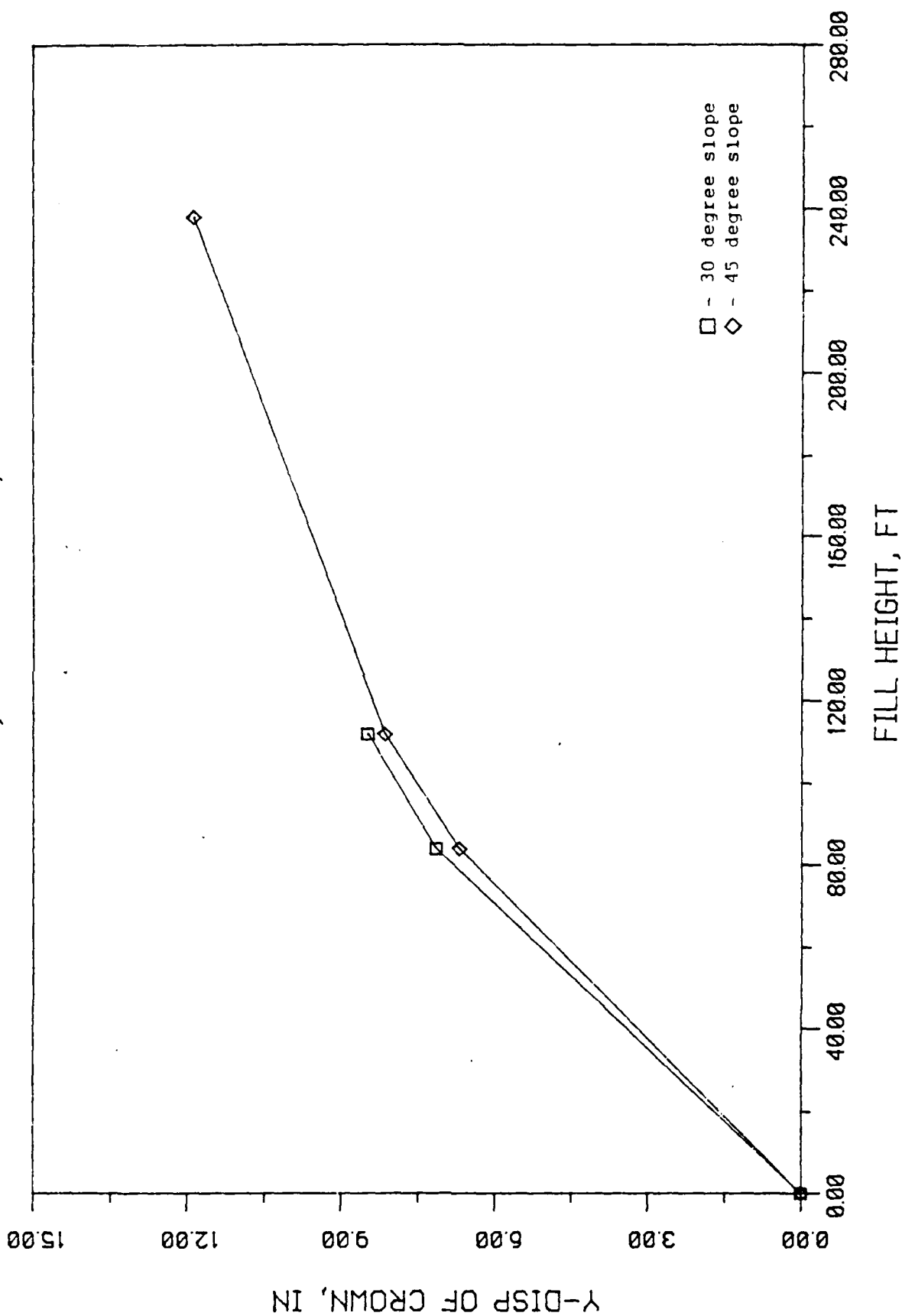


Figure 4.15c Relative Crown Deflection vs. Fill Height for Case IIIA

embankment is made up of SM90 type soil, maximum difference between crown deflection is only 0.13 inch after six load increments. The cases where the embankment is made up of SC90 and CL90 type soil, the influence of the embankment slope is much more apparent. The difference between crown deflection after six load increments was found to be 0.33 inch in both cases.

The next three cases examined in this section is a structure modeled on a bedding condition using SM85 type soil in combination with SM90, SC90, and CL90 type soil for the embankment designated as Case II2B (refer to Figure 4.16). All structural models proved to withstand the entire load scheme for these cases, therefore, producing a complete picture of crown deflection with both the 30 and 45 degree slope embankment. For the model with the SM90 soil embankment, the system with the 30-degree embankment produced greater crown deflection than its counterpart. The difference between the two was 0.33 inch at the end of nine load step increments. For the model with SC90 soil embankment, a better distinction between the crown deflection for both slope conditions. In this case, the 30-degree slope embankment causes a crown deflection of 1.01 inches more than the 45-degree slope embankment at the end of nine step load increments. Finally, for the model with CL90 soil embankment, an embankment slope of 45-degrees produces less crown deflection than the 30-degree embankment slope, the difference being at least 0.86 inch.

SM85 BEDDING, 3 LAYERS, SM90 EMBA

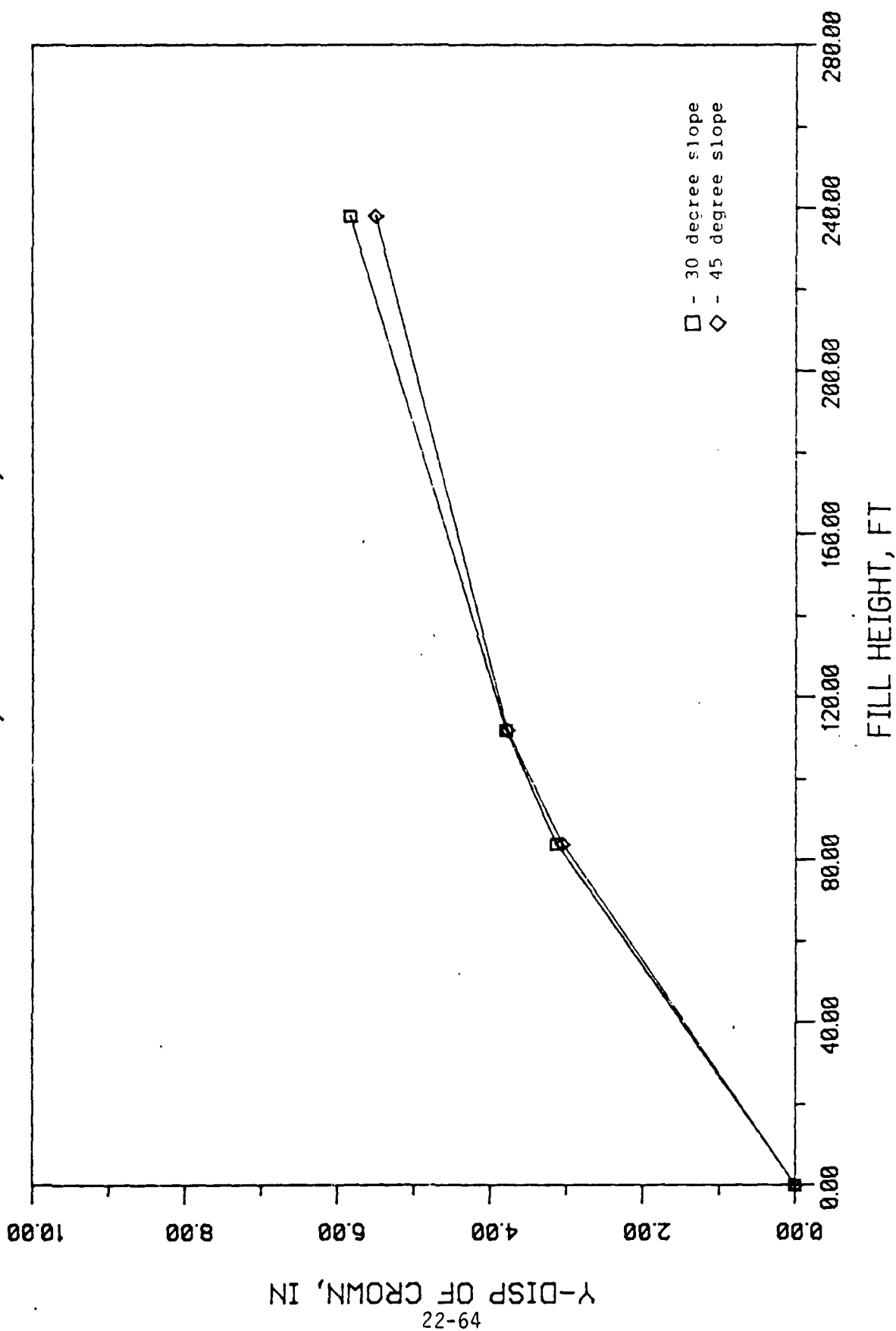


Figure 4.16a Relative Crown Deflection vs. Fill Height for Case 112A

SM85 BEDDING, 3 LAYERS, SC90 EMBA

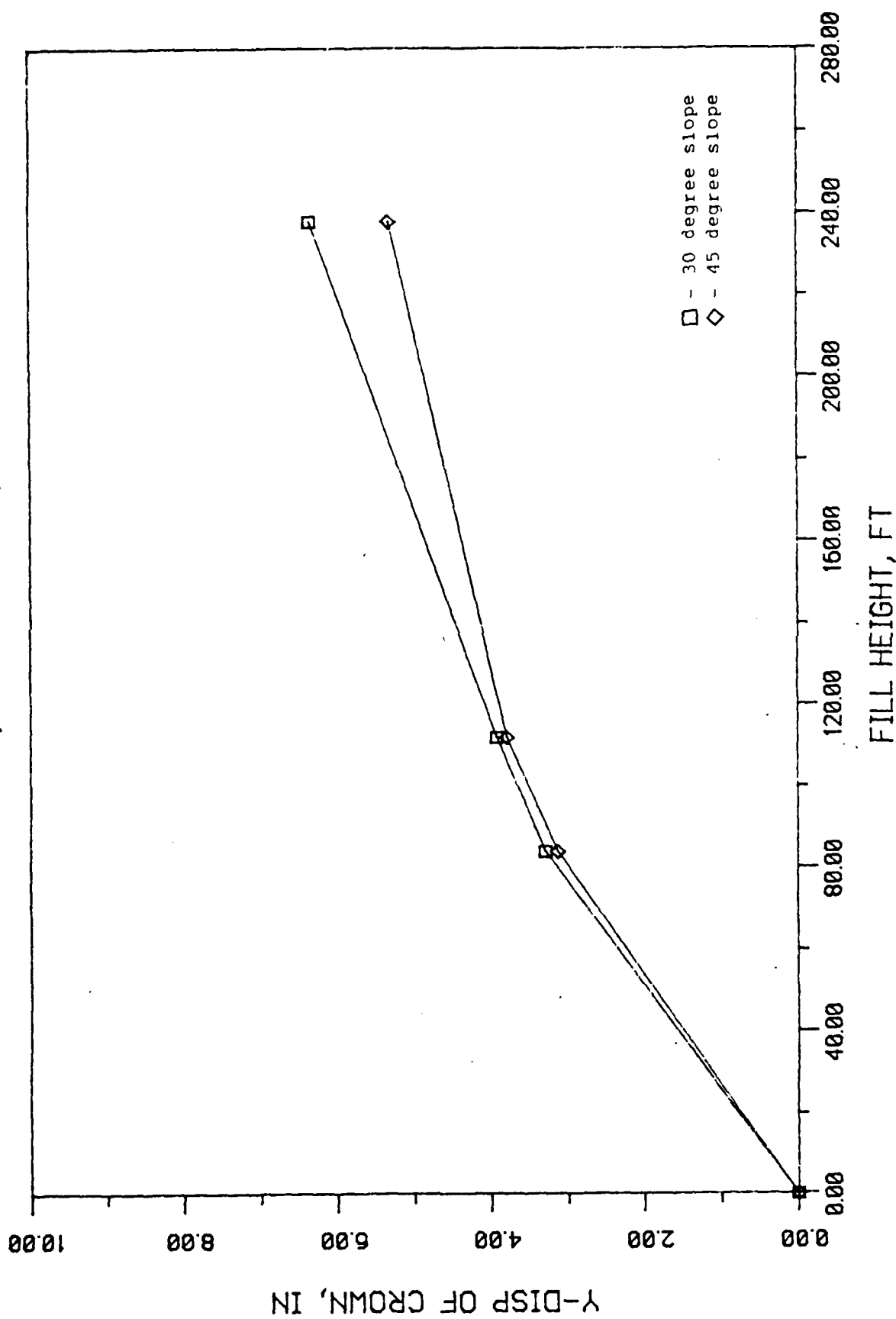


Figure 4.16b Relative Crown Deflection vs. Fill Height for Case 112A

SM85 BEDDING, 3 LAYERS, CL90 EMBA

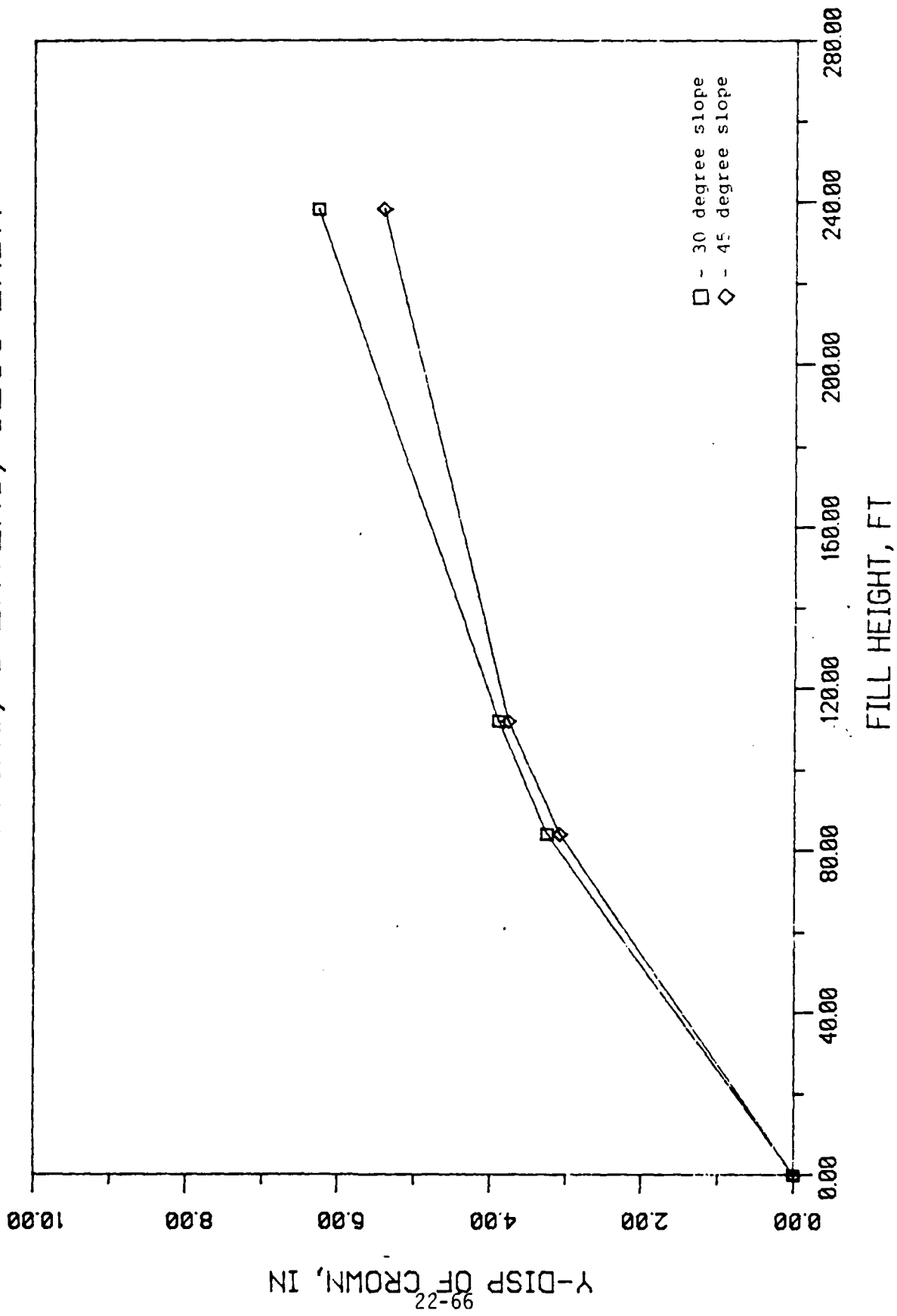


Figure 4.16c Relative Crown Deflection vs. Fill Height for Case 112A

In general, an embankment slope of 45 degrees shall result in less crown deflection for systems with SM85 soil for bedding conditions, and minimal when combined with SC90 soil for the embankment for all cases with a 3-layer rock cover.

A procedure similar to the previous one is used in the analysis of the influence of the embankment slope on the bending moment developed at the crown of the structure. That is, the installation type is held constant, here taken to be the 3-layer type rock cover, to easily focus on the effect of the slope and only the slope on the moment developed at the crown. All other variables are taken into account, though, to assure consistency of the findings. Two bedding conditions, CL85 and SM85, plus three embankment conditions: SM90, SC90, CL90; are included in the analysis.

The first three cases examined is a system with CL85 soil bedding in combination with SM90, SC90, and CL90 soil embankments (refer to Figure 4.17). The structural models failed after the completion eight load increments for all cases with the 30-degree slope embankment. Then again, the comparison between the two slope conditions for the moment developed at the crown is limited to the values of crown moment developed after six load increments. The first case, where the embankment is made up of SM90 type soil, shows that by installing a 30-degree slope embankment, the moment at the crown can be reduced by as much as 10647 in-lb/in, less than that developed with a 45-degree slope embankment at the end of six load increments. The same is true with the next case, where the embankment is

CL85 BEDDING, 3 LAYERS, SM90 EMBA

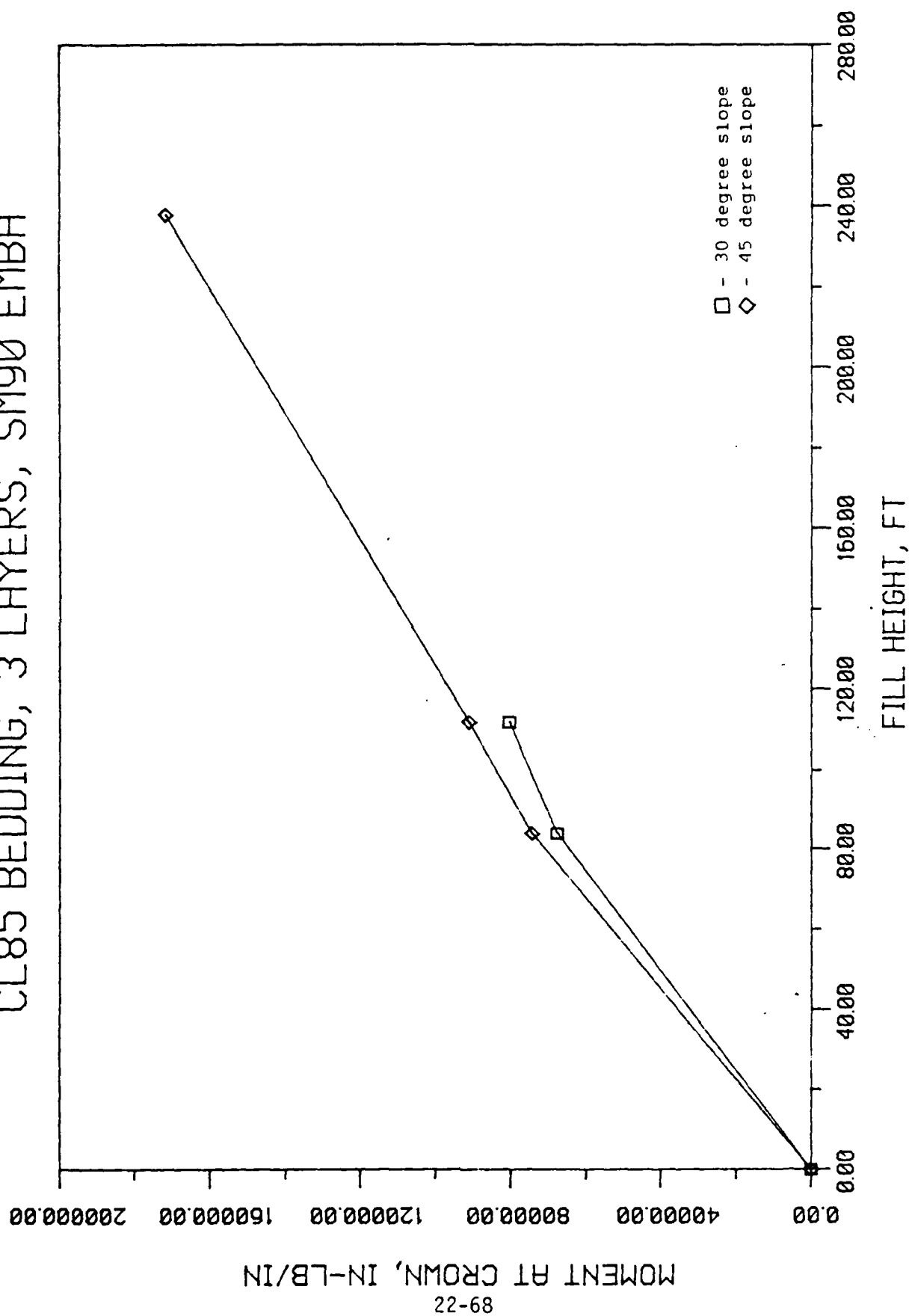


Figure 4.17a Crown Moment vs. Fill Height for Case IIB

CL85 BEDDING, 3 LAYERS, SC90 EMBA

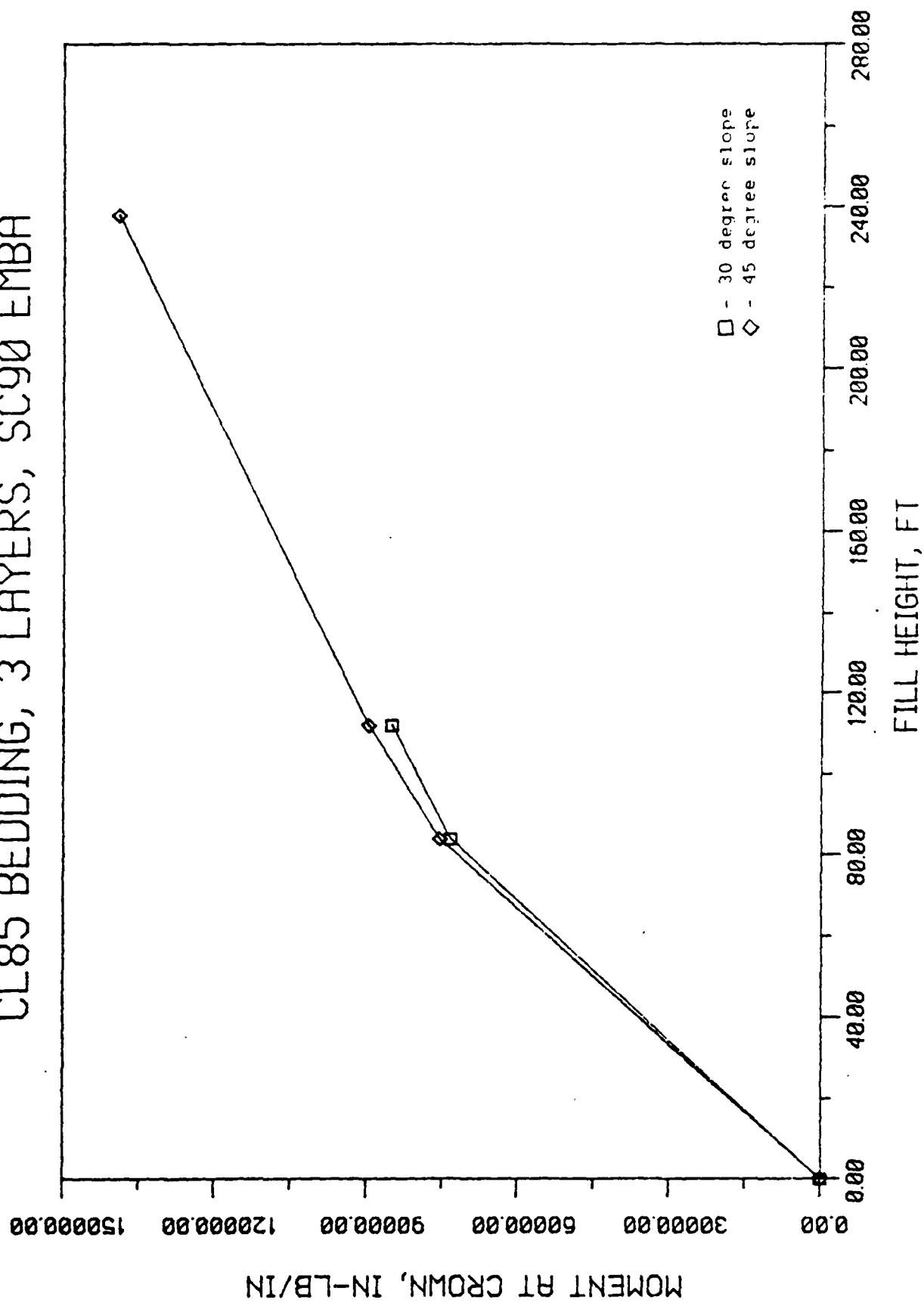


Figure 4.17b Crown Moment vs. Fill Height for Case IIB

CL85 BEDDING, 3 LAYERS, CL90 EMBA

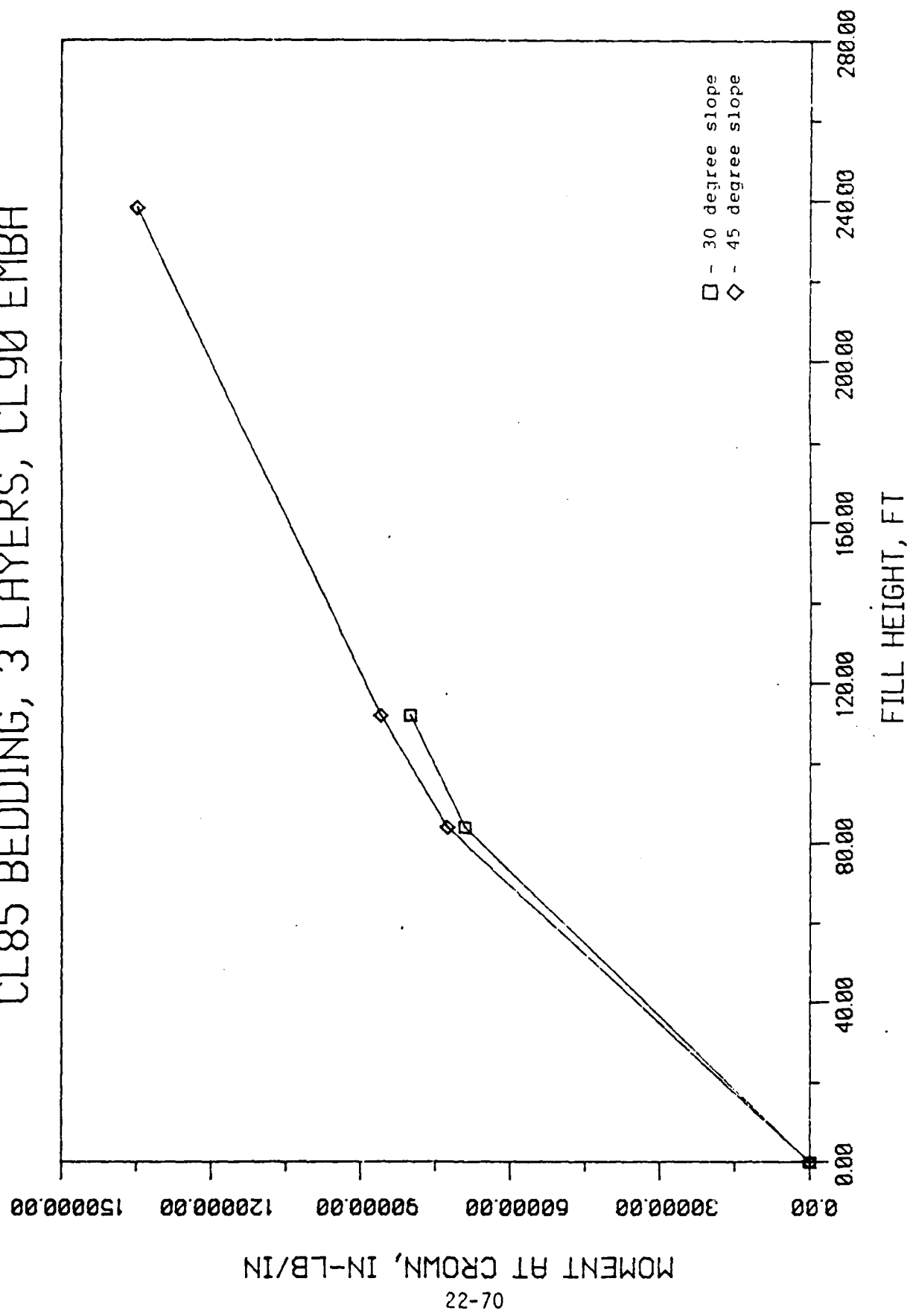


Figure 4.17c Crown Moment vs. Fill Height for Case IIB

made up of SC90 type soil. The moment developed at the crown is 4528 in-lb/in less with a 30-degree slope embankment installed than with a 45-degree slope embankment. Finally with an embankment type soil of CL90 used, a 30-degree slope embankment produces 5939 in-lb/in less moment than a 45-degree slope embankment.

The next three cases examined is a system with SM85 soil bedding in combination with SM90, and CL90 soil embankments (refer to Figure 4.18). For the model with SM90 type soil for the embankment material, the bending moment developed at the crown of the structure was found to be greater when a 45-degree slope embankment is installed. The difference in magnitude being 7705 in-lb/in at the end of four load increments up to 27364 in-lb/in at the completion of nine load increments. Results from the tests using the structure model with SC90 type embankment soil are consistent with the previous one but less the differences in the moment are less dramatic. Results show that again, by using a 30-degree slope embankment, the moment developed at the crown is less than that with a 45-degree embankment. The differences being 4919 in-lb/in at the end of four load increments up to 13344 in-lb/in at the completion of nine load increments. Finally, with the case of the system consisting of an embankment made up of CL90 type soil, it was also found that the embankment with a 30-degree slope produces less moment at the crown. This is the case wherein the influence of the slope on the moment is most apparent. At the end of nine load increments, the crown moment with a 45-degree

SM85 BEDDING, 3 LAYERS, SM90 EMBA

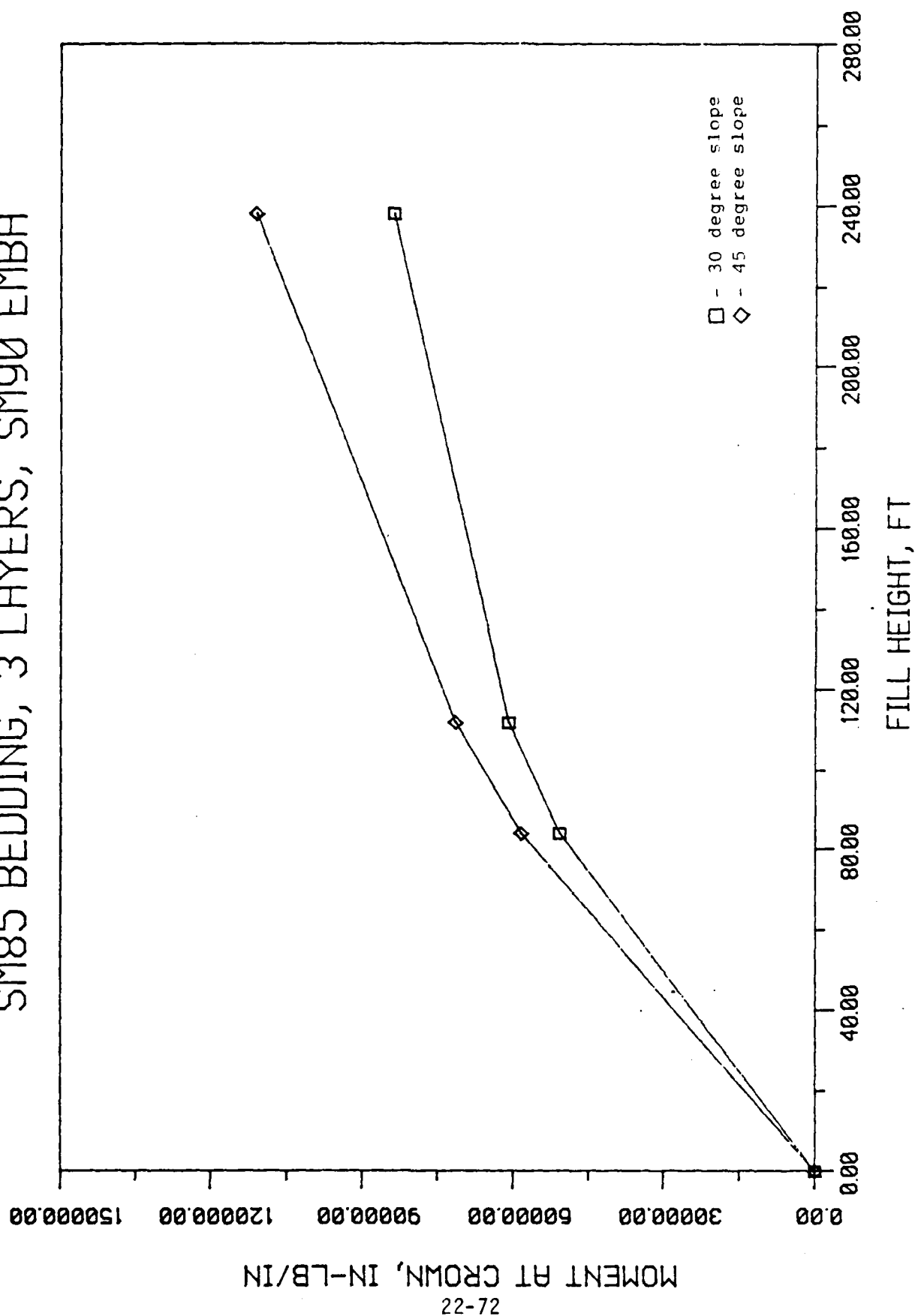


Figure 4.18a Crown Moment vs. Fill Height for Case II2B

SM85 BEDDING, 3 LAYERS, SC90 EMBA

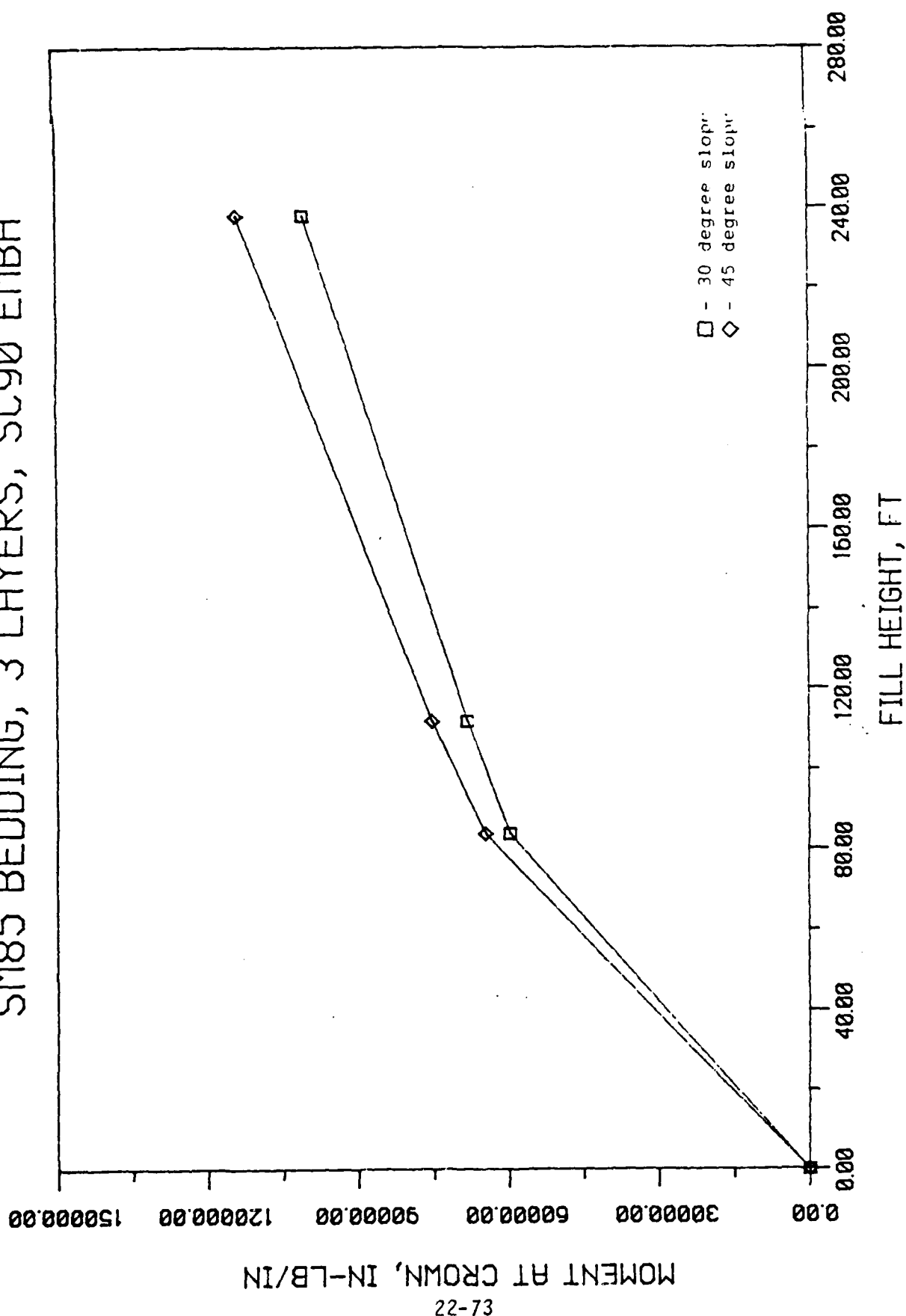


Figure 4.18b Crown Moment vs. Fill Height for Case 112B

SM85 BEDDING, 3 LAYERS, CL90 EMBA

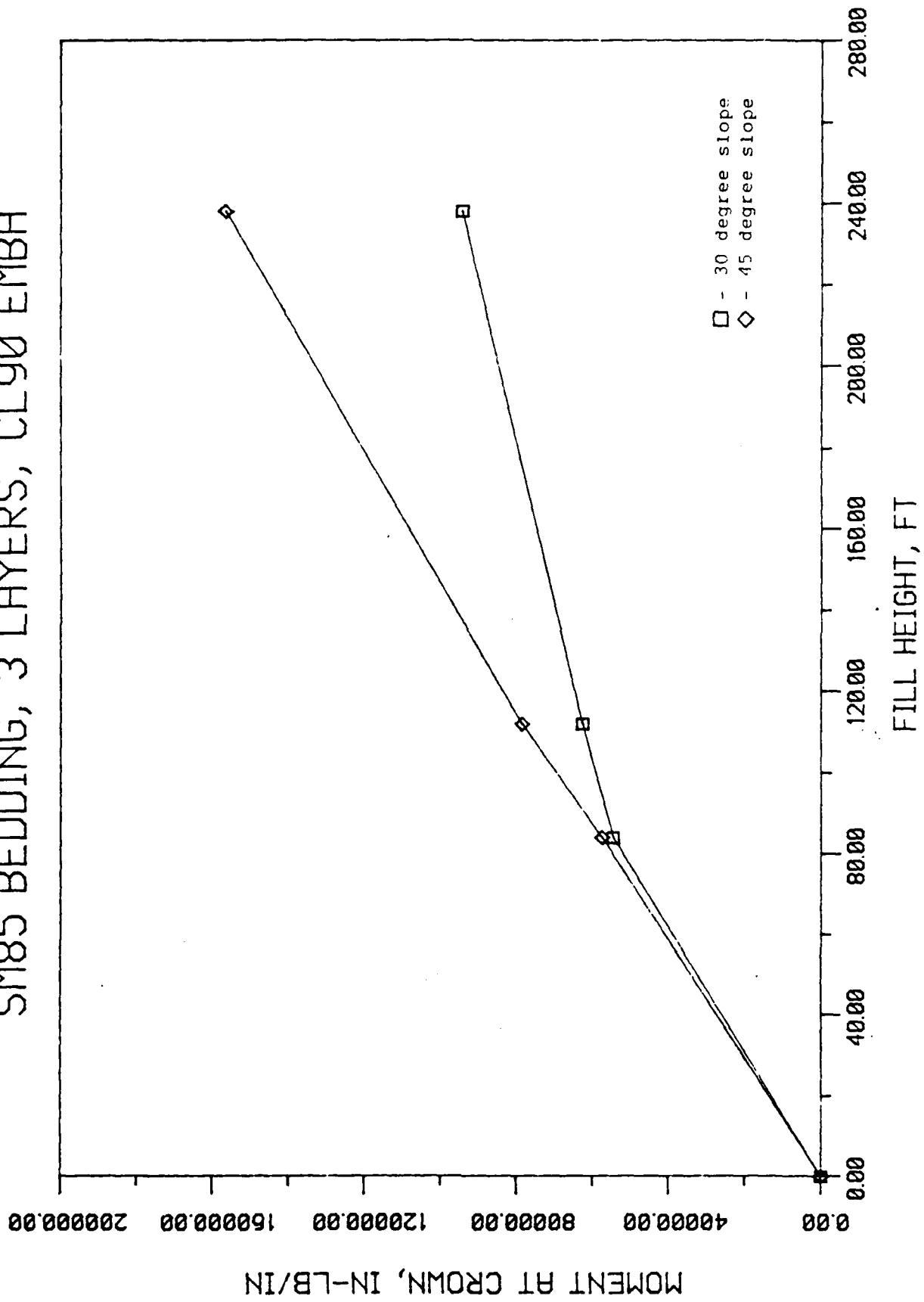


Figure 4.18c Crown Moment vs. Fill Height for Case II2B

slope embankment was found to be 156650 in-lb/in, nearly 665 in-lb/in greater than the moment developed at the crown with a 30-degree slope embankment.

The thrust developed at the crown of the structure is also highly influenced by the slope of the embankment. Again, to make the analysis simpler and to be able to focus on the influence of only the slope, the installation type is held constant for all cases and taken to be the 3-layer type rock cover. The bedding types included in the analysis are SM85 and CL85, and embankment types used are SM90, SC90, and CL90.

The first three cases analyzed are systems in CL85 bedding (refer to Figure 4.19). This condition though, structural models failed after eight load increments for systems with 30-degree slope embankments. Therefore, like the former analyses made in this section the observations will be limited to the crown thrust after six load increments for each case. Even though the 45-degree condition is not feasible in practice, analyses is still performed to determine the consistency of the results. The first case analyzed is the system constructed in a SM90 soil embankment. Here, the results show that an embankment with a 45-degree slope produces less thrust at the crown than an embankment with a 30-degree slope. It was found that at the end of six construction increments, a 45-degree slope produces less thrust at the crown than the 30-degree slope. The difference being 269 lb/in, nearly 42% smaller with a steeper slope. Similarly, the case where the embankment is made of SC90 type soil, the same results occur. An embankment with a 45-degree

CL85 BEDDING, 3 LAYERS, SM90 EMBA

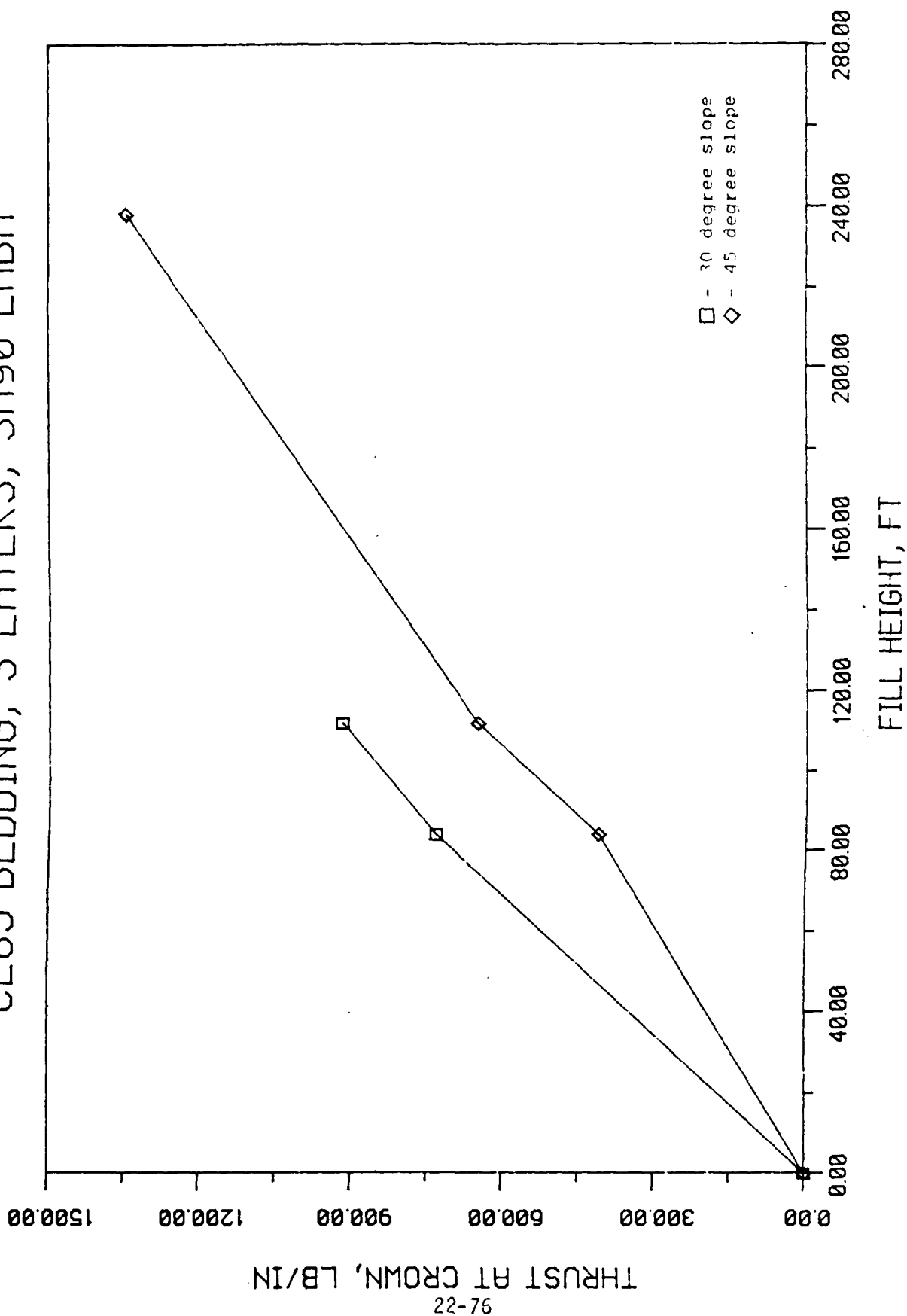


Figure 4.19a Crown Thrust vs. Fill Height for Case IIIc

CL85 BEDDING, 3 LAYERS, SC90 EMBA

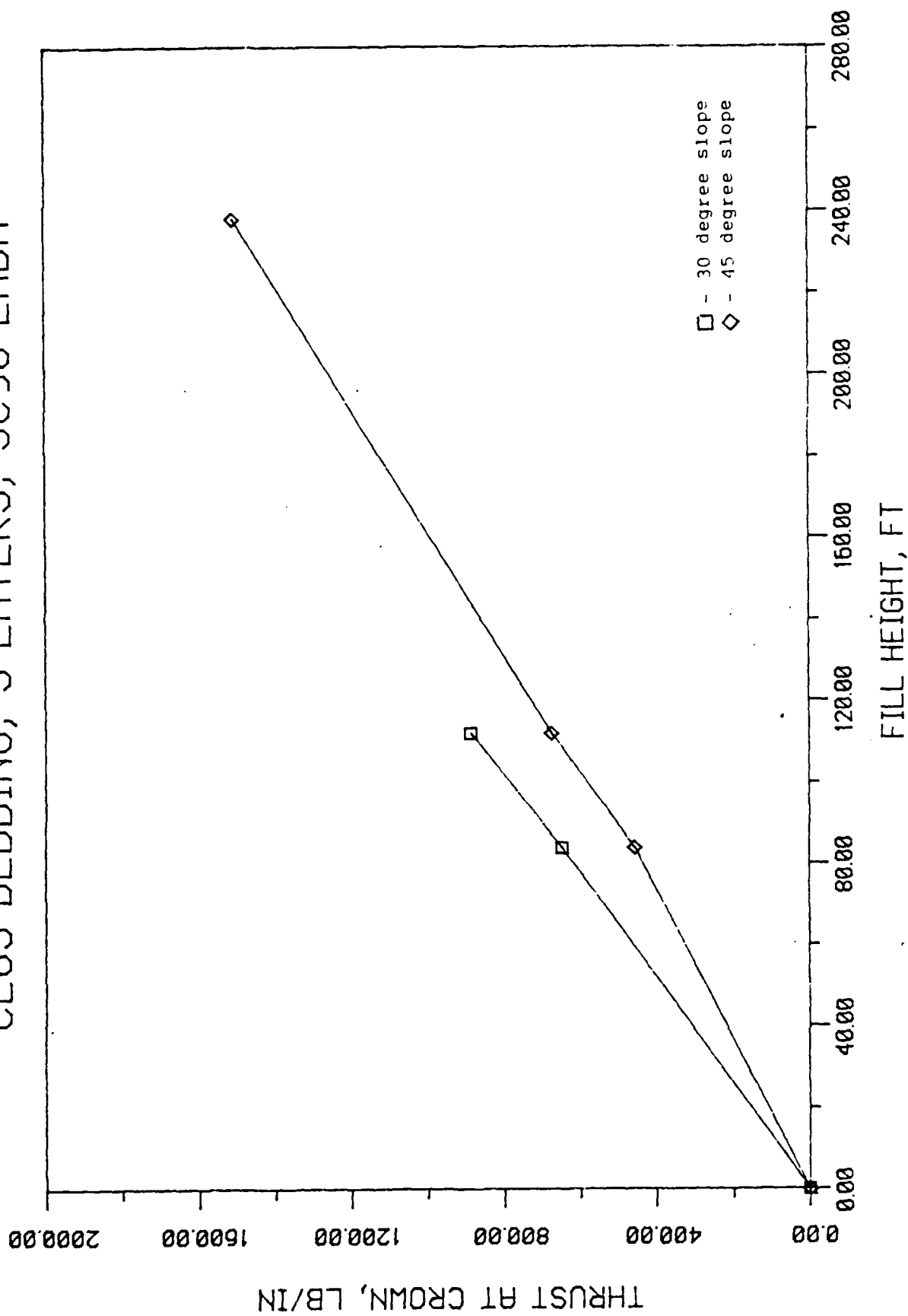


Figure 4.19b Crown Thrust vs. Fill Height for Case IIC

CL85 BEDDING, 3 LAYERS, CL90 EMBA

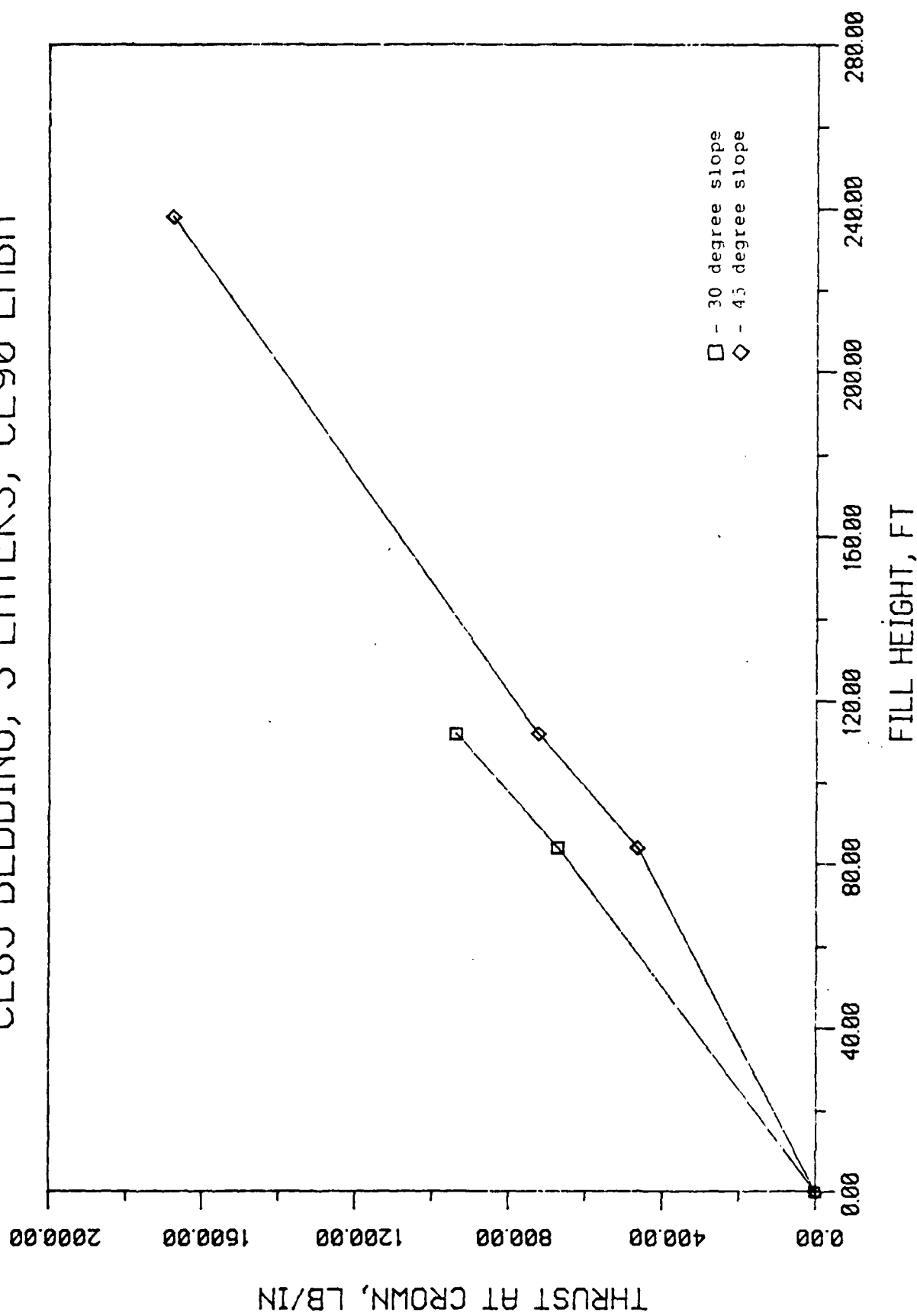


Figure 4.19c Crown Thrust vs. Fill Height for Case IIIc

slope produces nearly 32% less thrust than an embankment with a 30-degree slope. Finally, system with an embankment of CL90 type soil, unsurprisingly yields the same results. An embankment slope of 45-degrees produces nearly 30% less thrust than the embankment with a 30-degree slope. In general, for a system with CL85 soil bedding, an embankment of SM90 type soil installed in a 45-degree slope produces the least thrust at the crown after the completion of all step load increments.

The next three cases examined were systems wherein the structure is modeled on SM85 type soil bedding in combination with SM90, SC90, and CL90 type soil for the embankment (refer to Figure 4.20). In all three cases it was found that at the end of six step load increments, the system with the 30-degree slope embankment produced more thrust at the crown than the 45-degree option, the average difference of the thrust developed at the crown being 242 lb/in. But at the completion of all nine step load increments, it was found that an embankment with a 30-degree slope shall produce a final crown thrust magnitude up to at least 186% to at most 218%. With SM90 soil embankment, the difference of the final thrust magnitude produced at the crown between the 30-degree and 45-degree slope is 1320 lb/in favoring the former. With SC90 soil embankment, the difference was found to be 1212 lb/in. The system producing the least thrust at the end of all step load increments is the one with the SC90 soil for the embankment, with a final crown thrust magnitude of 531 lb/in.

SM85 BEDDING, 3 LAYERS, SM90 EMBA

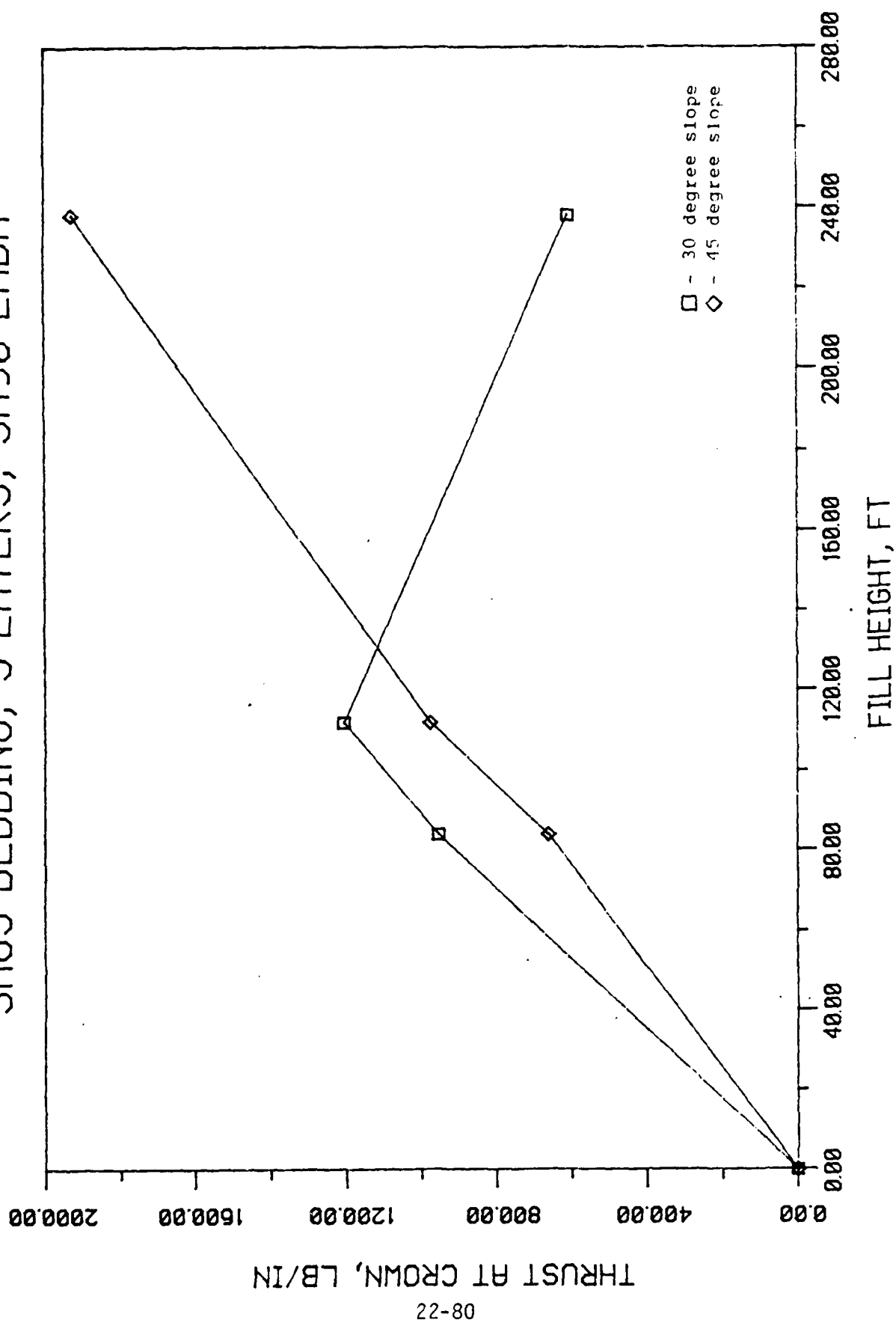


Figure 4.20a Crown Thrust vs. Fill Height for Case 112C

SM85 BEDDING, 3 LAYERS, SC90 EMBA

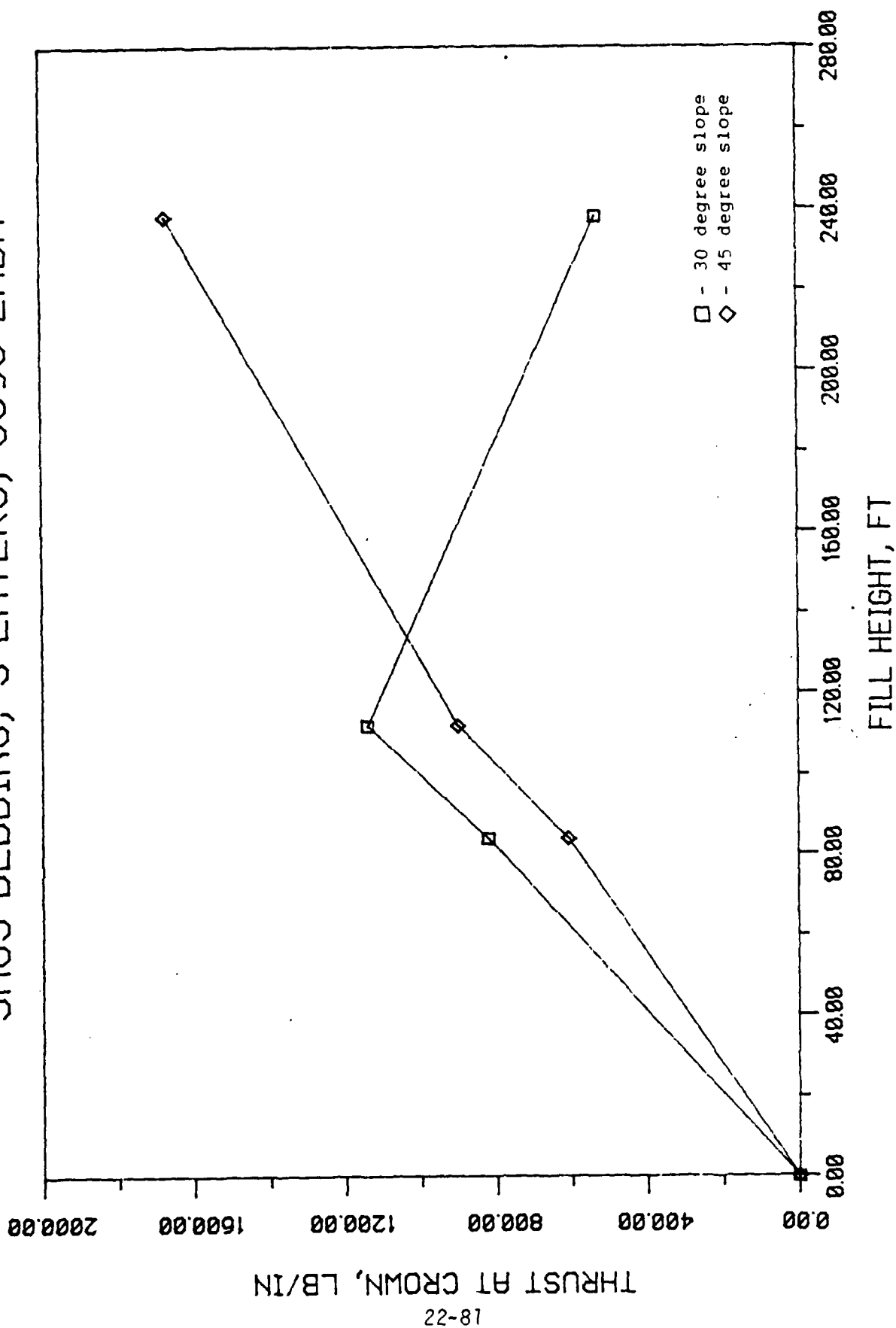


Figure 4.20b Crown Thrust vs. Fill Height for Case II2C

SM85 BEDDING, 3 LAYERS, CL90 EMBA

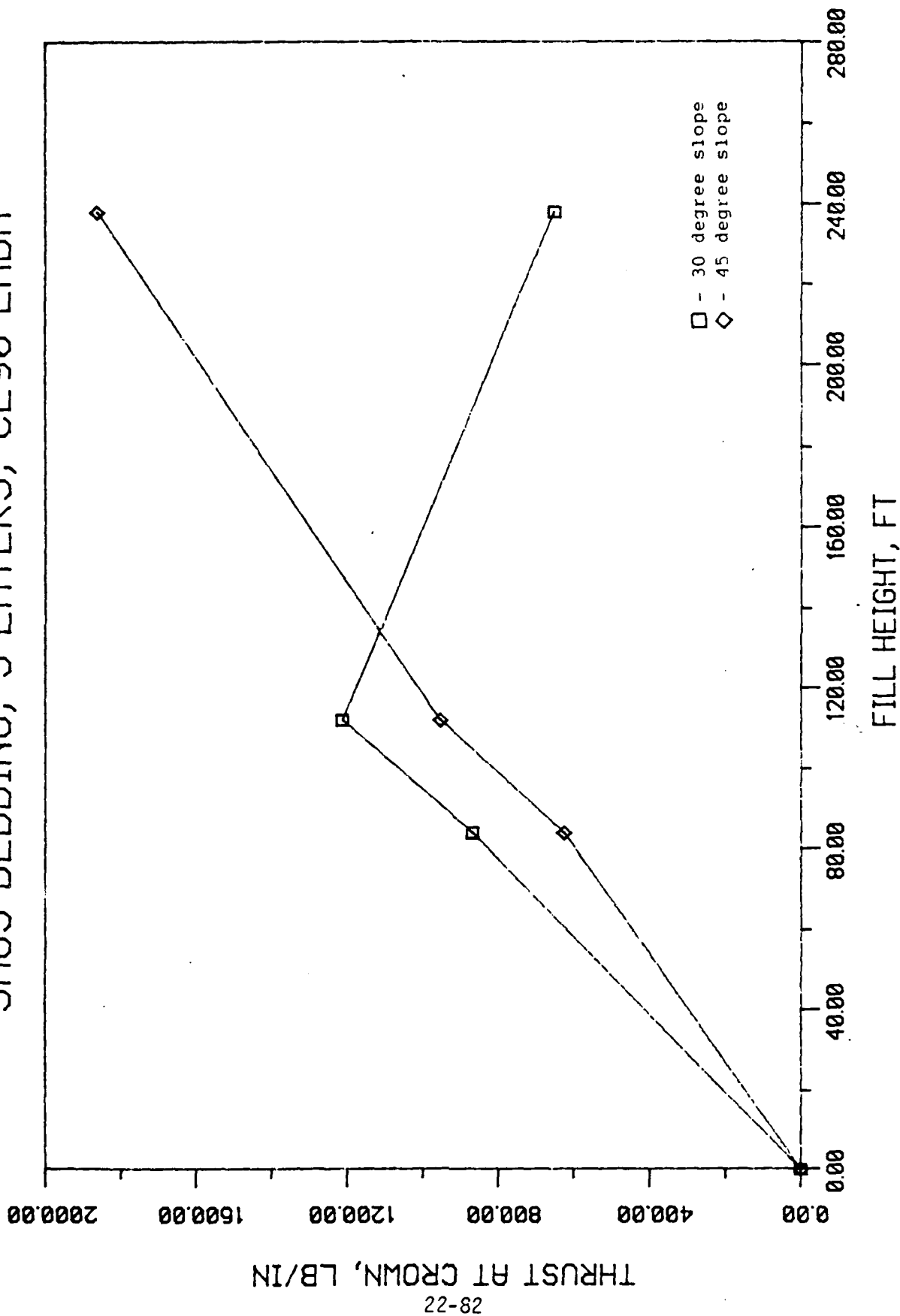


Figure 4.20c Crown Thrust vs. Fill Height for Case II2C

3. The Influence of Soil Type of Embankment

Crown deflection is greatly influenced by soil type, meaning that the physical properties of the soil, not only the density, plays an important part in the determination of load transfer from soil to structure. This section discusses the results found on the influence of soil type on the relative deflection of the crown. To minimize the number of cases to be examined and focus the attention on the influence of only the embankment soil on the structure, the system models were set to have a constant embankment slope, taken to be 30 degrees designated as Case III1. All other variables such as bedding type and the number of layers for the rock cover are taken into account (refer to Figure 4.21).

The first case studied is a system model on CL85 soil bedding with a 3-layer rock cover. Although it was found that at the end of six load increments, crown relative settlement had a standard deviation of 0.07 in. with the minimum of 8.38 in. occurring when the embankment is of SM90 type to maximum of 8.55 in. occurring when the embankment is of SC90 type, the structural models failed. Meaning that these types of embankment soil installed within these conditions is not feasible for practical purposes.

The second case studied is a system similar to the one described above only that this is modeled with a 5-layer rock cover. Relative crown deflection at the completion of all nine load increments had a standard deviation of 0.048 in. with the minimum being 10.58 in. occurring when the embankment is of SM90

CL85 BEDDING, 3 LAYERS, 30 DEG SLOPE

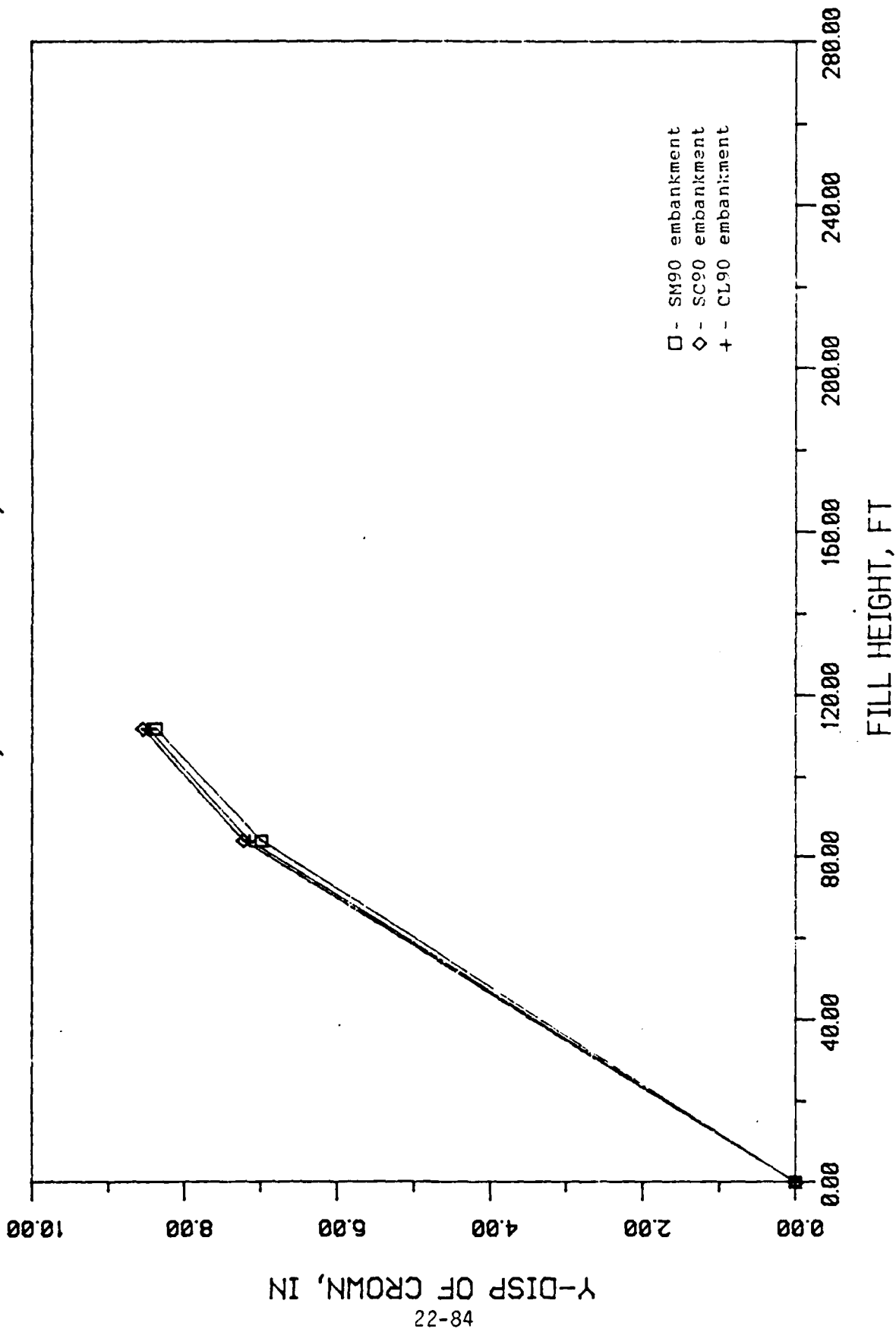


Figure 4.21a Relative Crown Deflection vs. Fill Height for Case III

CL85 BEDDING, 5 LAYERS, 30 DEG SLOPE

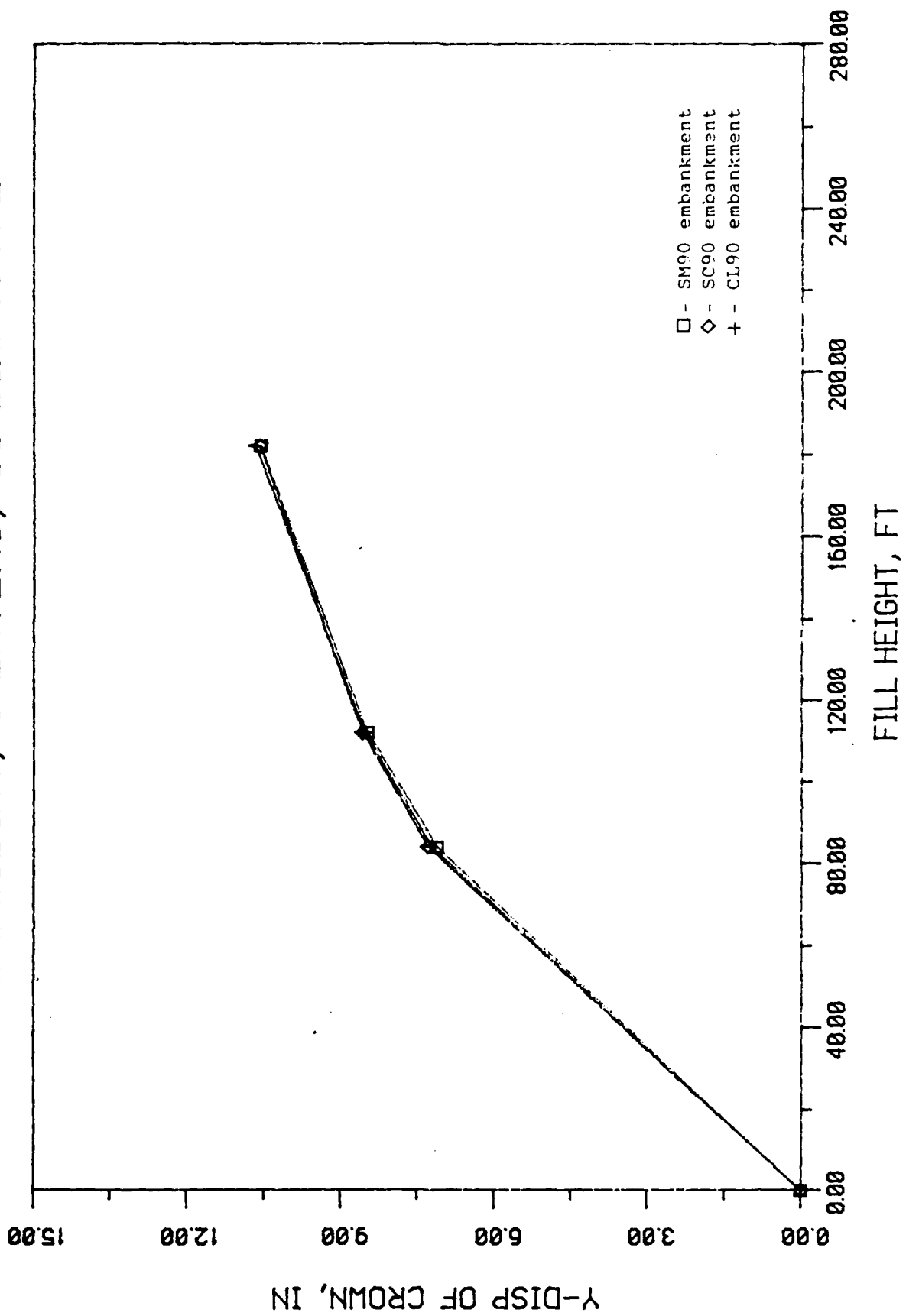


Figure 4.21b Relative Crown Deflection vs. Fill Height for Case III

SM85 BEDDING, 3 LAYERS, 30 DEG SLOPE

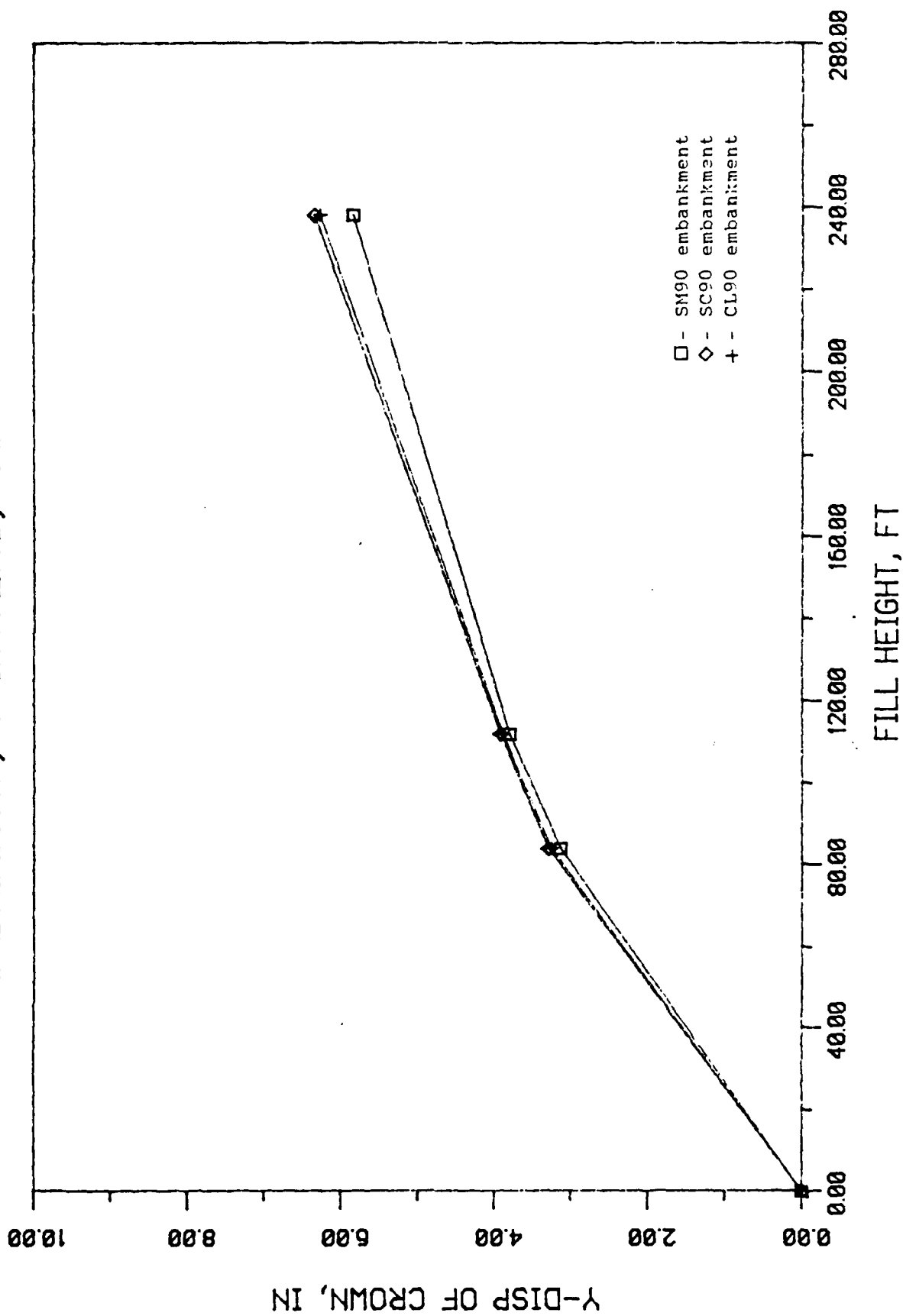


Figure 4.21c Relative Crown Deflection vs. Fill Height for Case III

SM85 BEDDING, 5 LAYERS, 30 DEG SLOPE

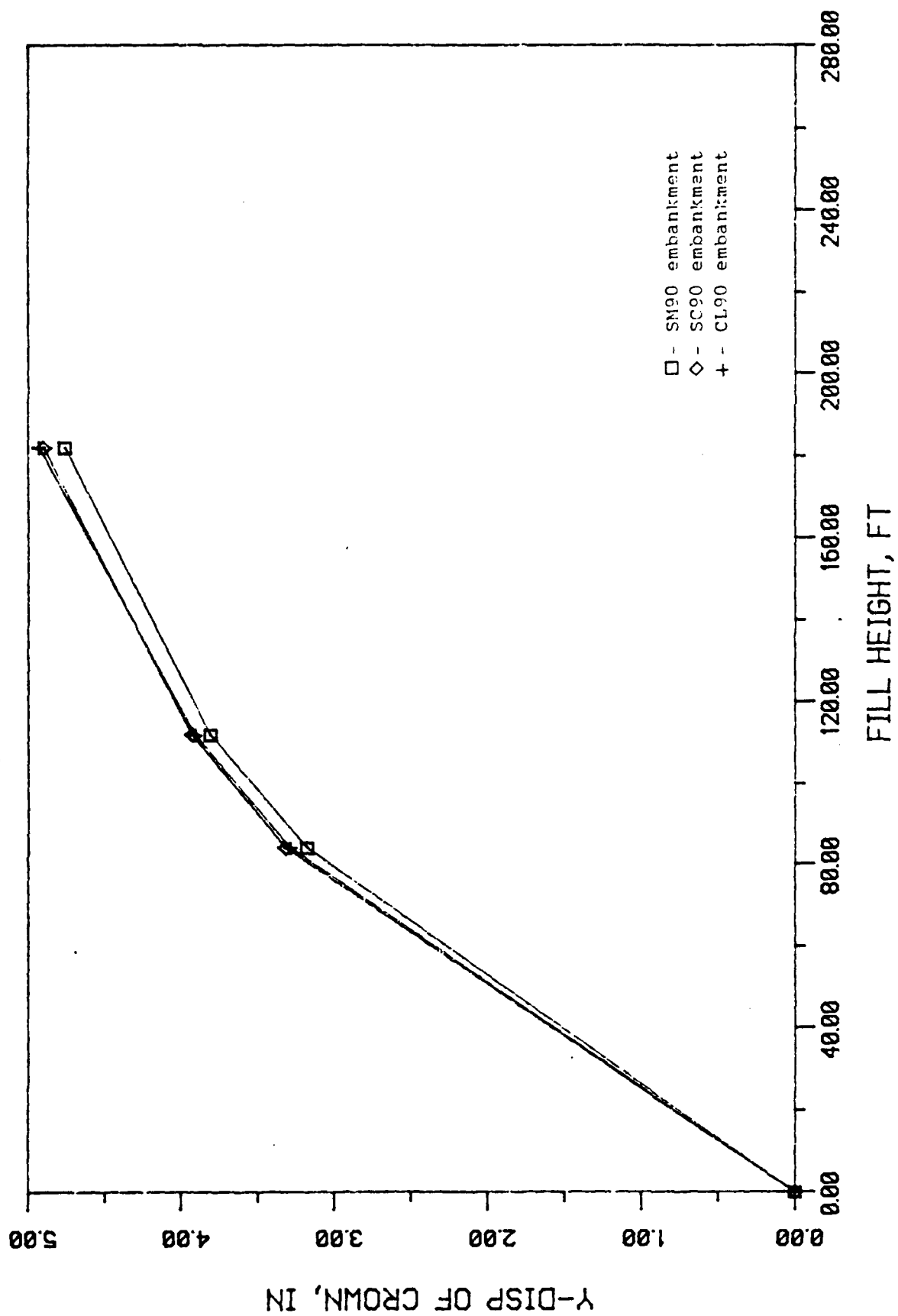


Figure u.2ld Relative Crown Deflection vs. Fill Height for Case III

type to a maximum of 10.69 in. occurring when the embankment is of CL90 type. In this case, it could be said that the soil type for the embankment does not cause extreme difference in the relative deflection of the crown.

The third case is a system modeled on SM85 soil bedding with a 3-layer rock cover installed. In this case, a system model with the SM90 soil embankment caused the least amount of relative crown deflection, being 5.84 in. The installation of SC90 soil for the embankment causes the crown to deflect by 6.34 in., half-inch more than with the previous condition. In this case overall, an SM90 type soil used for the embankment material shall produce the least crown deflection.

The fourth and final case was found to be the most ideal among all the cases studied. The minimum relative crown deflection was found to be 4.76 in. and attained by installing an SM90 soil type embankment under a 5-layer rock-cover over an SM85 soil bedding. The maximum is found to be 4.93 in. with an SC90 soil embankment.

Overall, by examining all the observations mentioned above, it was found that an SM90 type soil used for the embankment causes the least amount of crown relative deflection.

Moments developed at crown are also highly influenced by the soil type of the embankment. In this discussion, similar to the previous one, the system models were set to have a constant embankment slope of 30 degrees for the same reason as to focus the attention on the influence of the embankment soil only. Also, all other variables such as bedding type and the number of

layers for the rock cover are taken into account to visualize the consistency of the results (refer to Figure 4.22).

Case number III2.a involves a system model on CL85 soil bedding with 3 layers of rock as the cover. The moment at the crown of the structure at the completion of six load increments was governed by the CL90 embankment producing a minimum moment magnitude of 80039 in-lb/in. The maximum being 85160 in-lb/in produced by SC90 embankment. This analysis covers crown moment after six load increments only because a system under these conditions failed after eight load increments.

The next case, Case III2.b involves a system modeled in the same manner as the previous one discussed except that a 5-layer rock cover was installed. The structure models withstood the entire load scheme for all nine load increments providing complete data for analysis. The bending moments occurring at the crown had a standard deviation of 2211 in-lb/in with a maximum of 113096 in-lb/in occurring when the embankment is of SC90 soil and a minimum of 17756 in-lb/in occurring when the embankment is of CL90 soil.

The third case, Case III2.c involves a system modeled on an SM85 bedding with a 3-layer rock cover installed. In this case, the embankment made up of SM90 soil produced the least moment magnitude among all three embankment soil types. At the completion of nine load increments, the SM90 type soil produced a crown moment magnitude of 83773 in-lb/in, a magnitude that is 20% less than that produced by SC90 type soil, which in turn produced the greatest crown moment.

CL85 BEDDING, 3 LAYERS, 30 DEG SLOPE

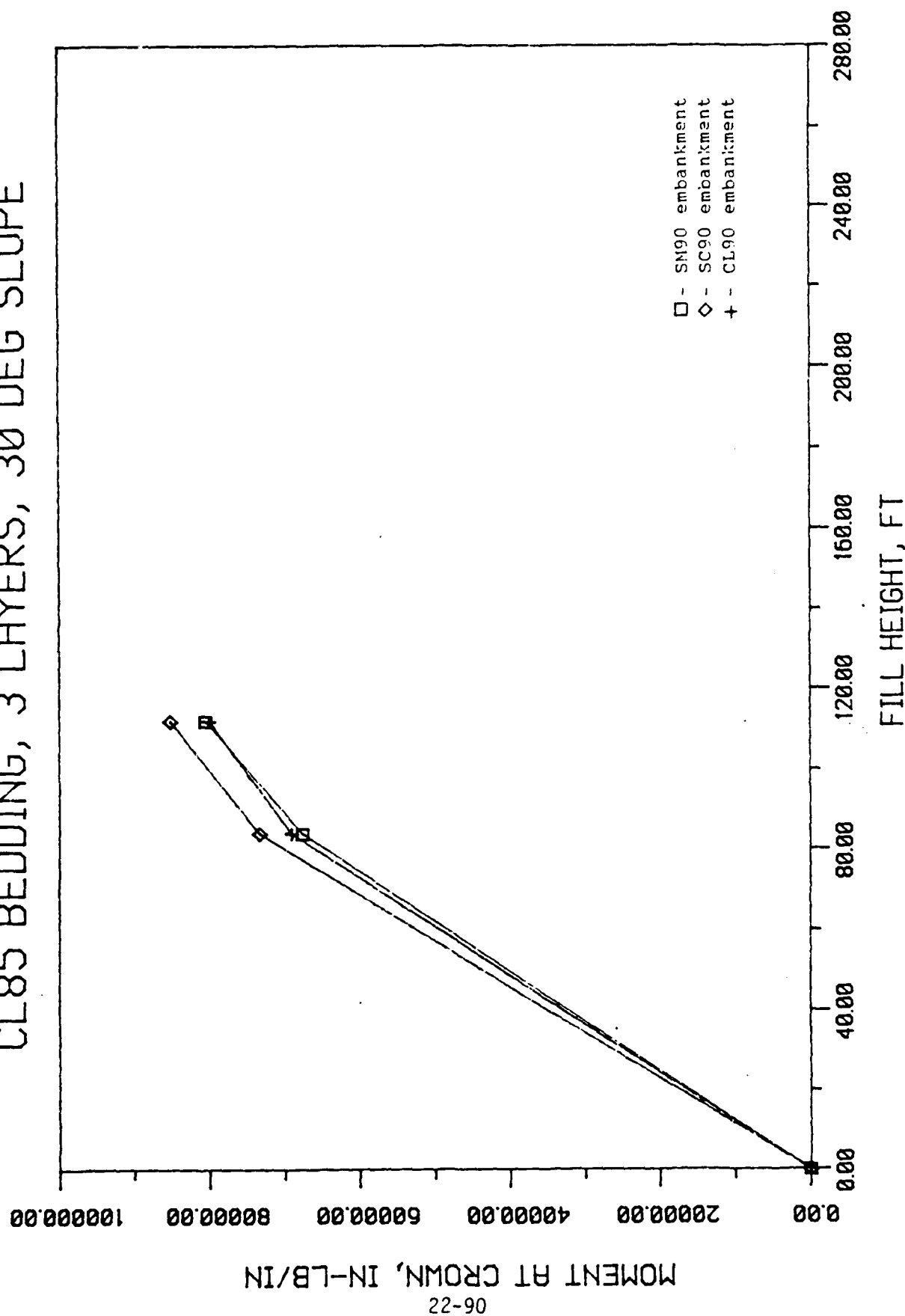


Figure 4.22a Crown Moment vs. Fill Height for Case III2

CL85 BEDDING, 5 LAYERS, 30 DEG SLOPE

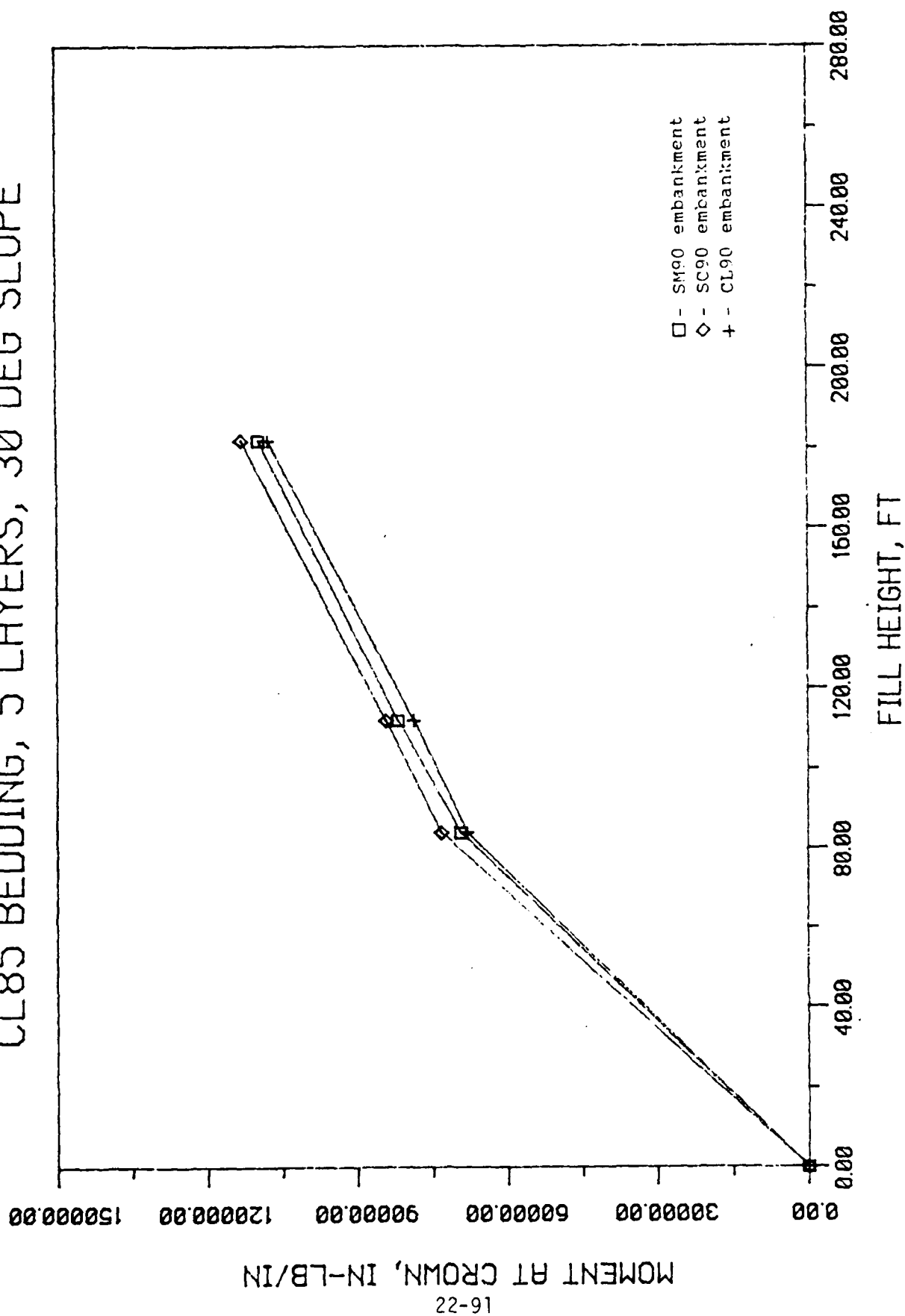


Figure 4.22b Crown Moment vs. Fill Height for Case J112

SM85 BEDDING, 3 LAYERS, 30 DEG SLOPE

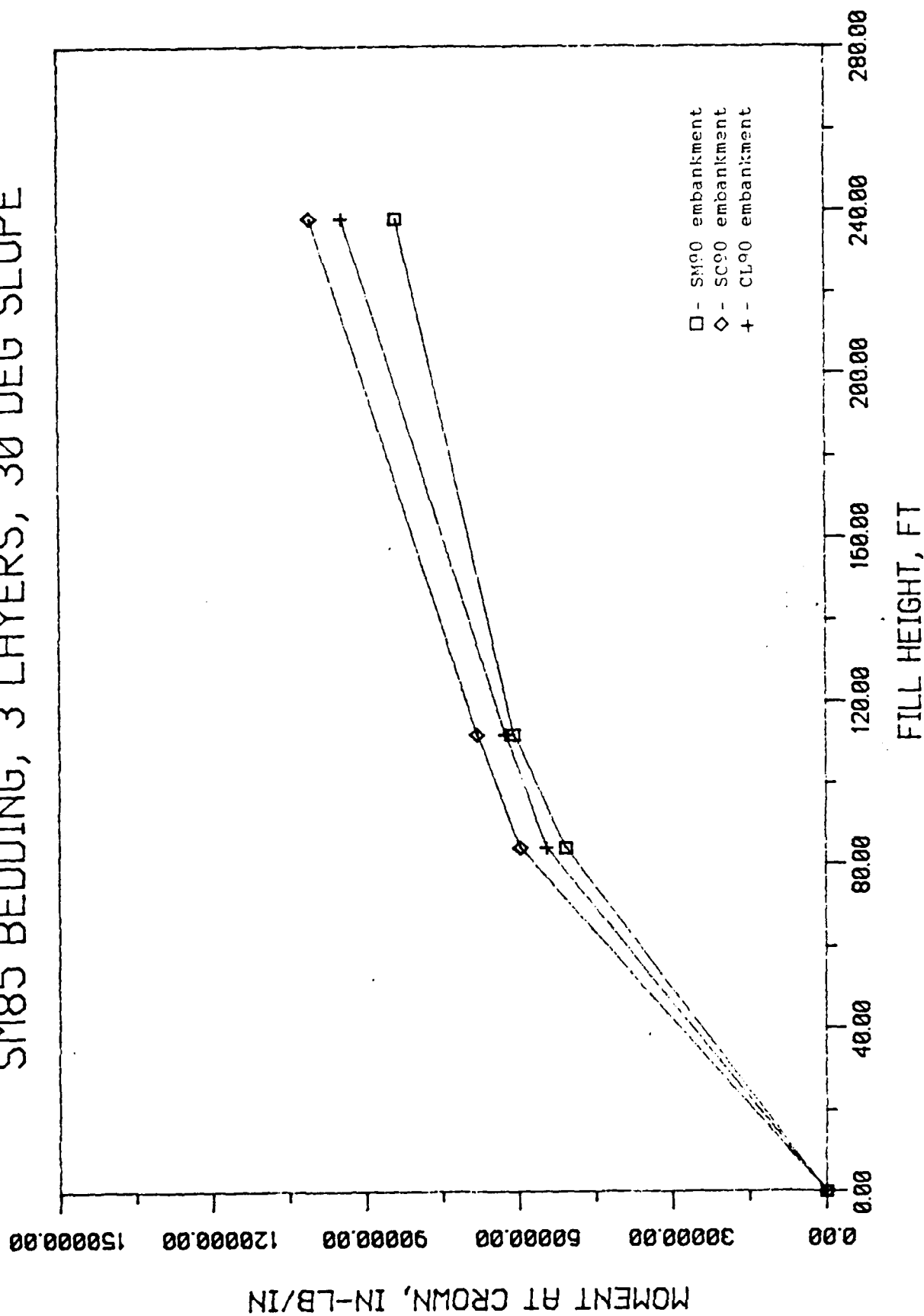


Figure 4.22c Crown Moment vs. Fill Height for Case III?

SM85 BEDDING, 5 LAYERS, 30 DEG SLOPE

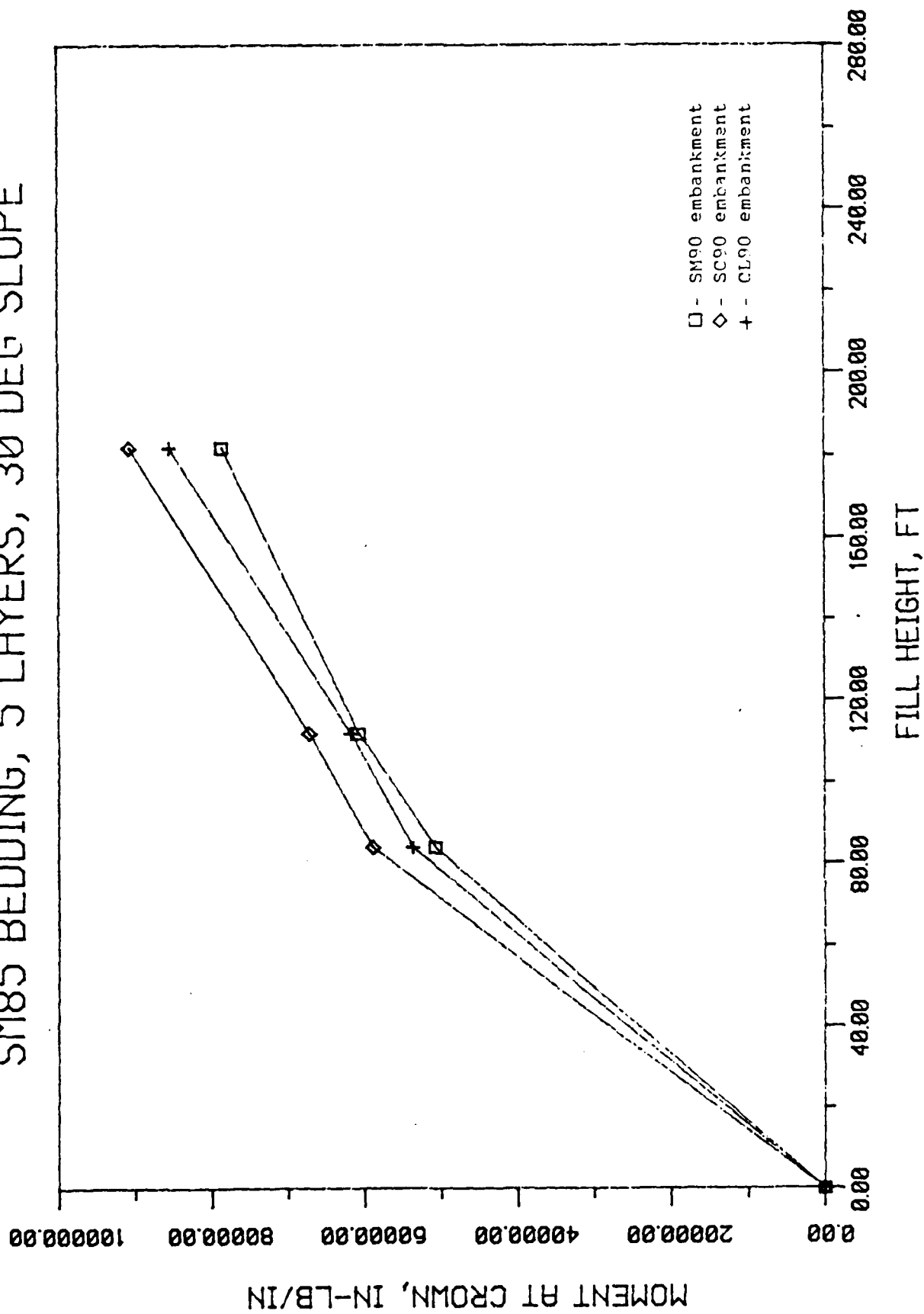


Figure 4.22d Crown Moment vs. Fill Height for Case IJ12

The fourth and final case, Case III2.d is similar to the previous one except that a 5-layer rock cover is installed. And similarly, the SM90 soil produced the least amount of moment at the completion of nine load increments. A standard deviation of 4958.071 in-lb/in with a maximum of 90750 in-lb/in occurring when the embankment is of SC90 type soil, and a minimum of 78640 in-lb/in when the embankment type is SM90.

Thrust developed at the crown, like the other types of structural reactions are also highly dependent on the kind of soil used for the embankment. This discussion shall also be limited to system models with 30-degree slope embankments, taking into account all the other factors such as bedding conditions and the number of layers for the rock cover, designated as Case III3 (refer to Figure 4.23).

The first case to be analyzed is a structure modeled on CL8 under a 3-layer rock cover. Unfortunately, the structural models for this system failed after eight load increments. Therefore, the analysis is limited to the findings after the completion of six load increments. At the end of the fourth load increment, it was found that the CL90 embankment soil produced less crown thrust magnitude than the SM90 type. But at the completion of six load increments, it was found that the SM90 type soil produced less thrust at the crown than the CL90 type, which in turn produced the highest thrust magnitude between all three types. The SC90 type was consistent throughout the entire scheme in producing the least amount of thrust at the crown, the final thrust magnitude after six load

CL85 BEDDING, 3 LAYERS, 30 DEG SLOPE

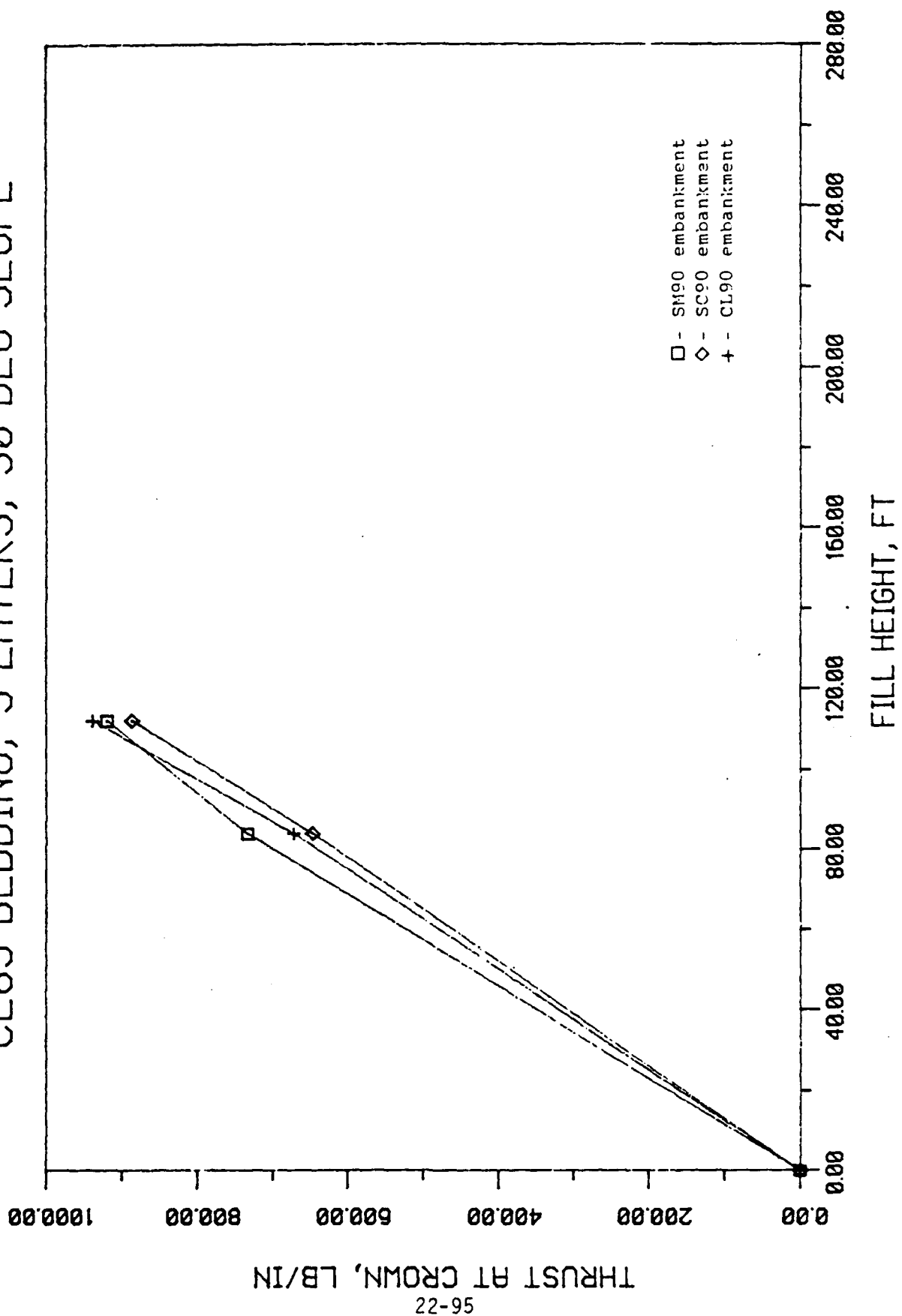


Figure 4.23a Crown Thrust vs. Fill Height for Case III3

CL85 BEDDING, 5 LAYERS, 30 DEG SLOPE

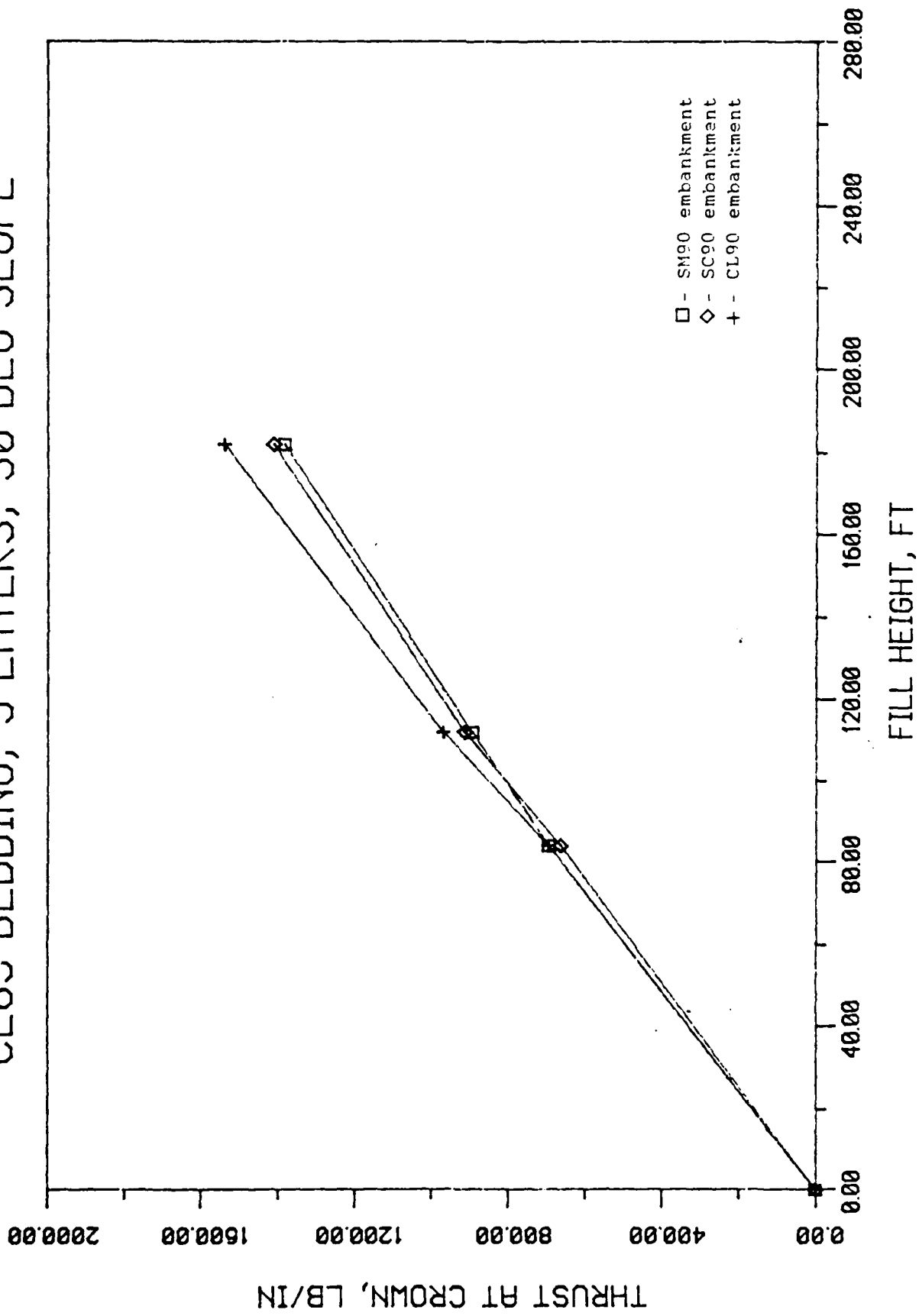


Figure 4.23b Crown Thrust vs. Fill Height for Case III3

SM85 BEDDING, 3 LAYERS, 30 DEG SLOPE

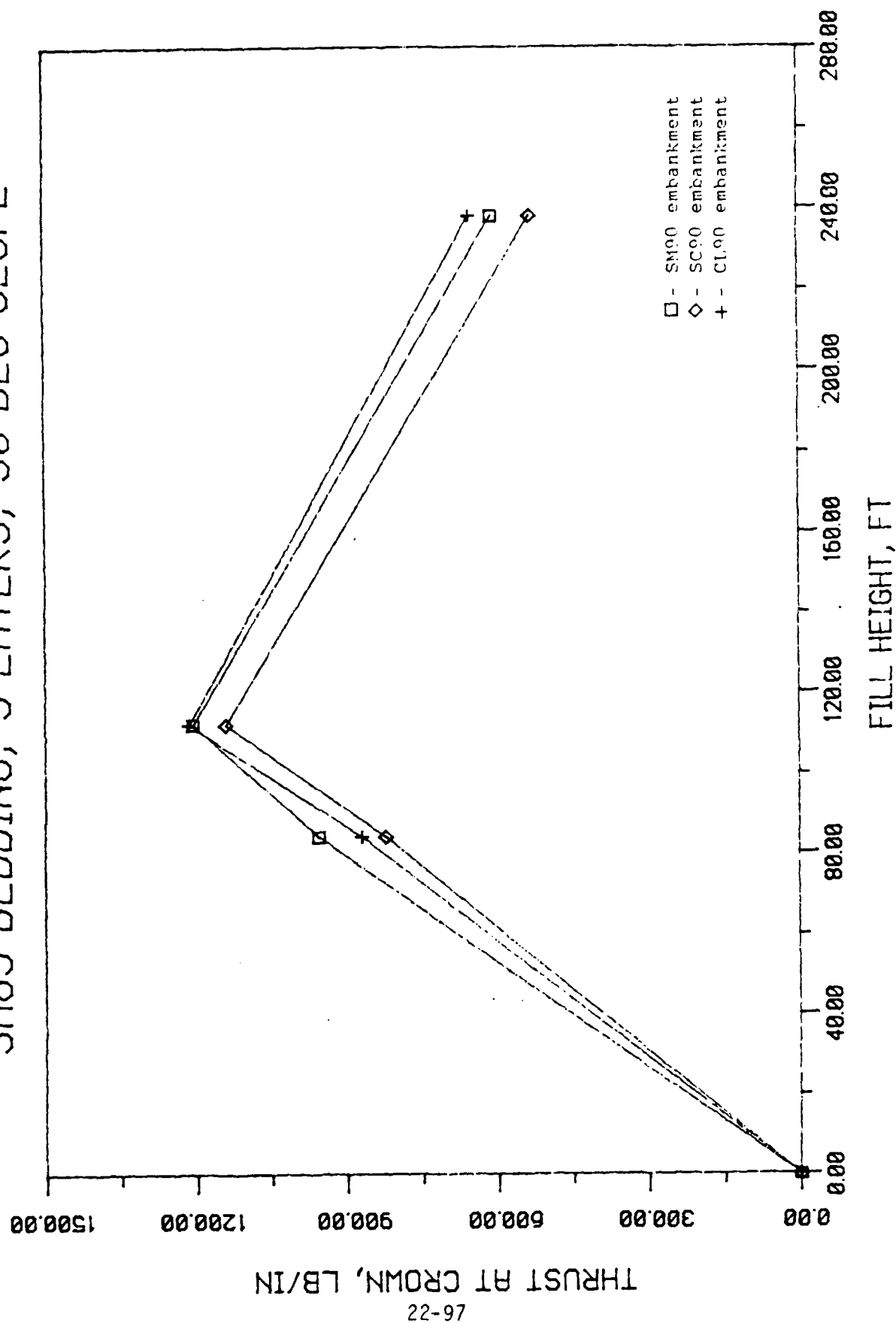


Figure 4.23c Crown Thrust vs. Fill Height for Case III3

SM85 BEDDING, 5 LAYERS, 30 DEG SLOPE

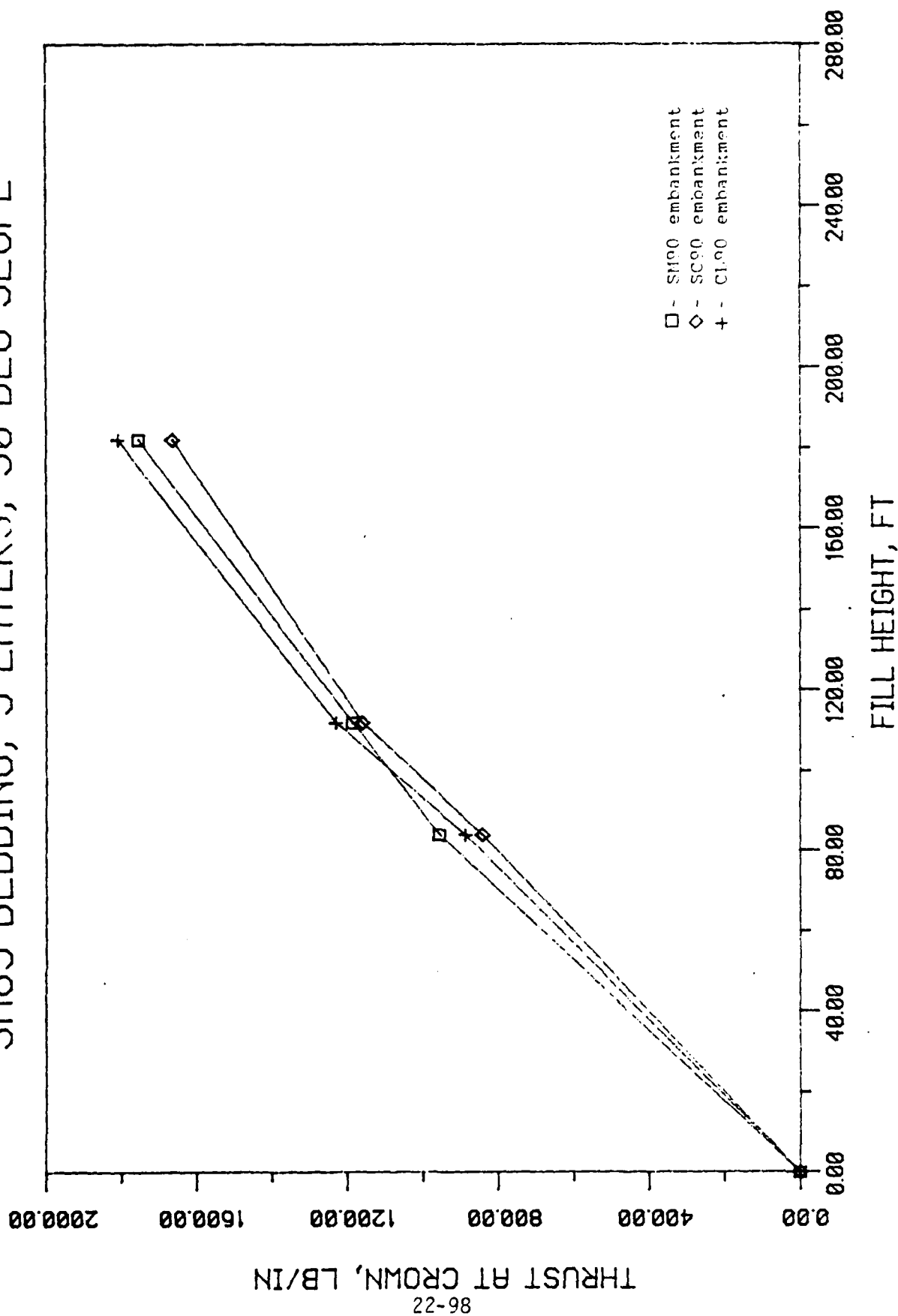


Figure 4.23d Crown Thrust vs. Fill Height for Case IIIa

increments being 887 lb/in.

A different set of results appears when the rock cover of the above case is replaced by the 5-layer type. At the end of four load increments, the SM90 type soil produced greater thrust in magnitude at the crown than the SC90 type. But after six load increments, it was found that the SM90 type soil produced less thrust than the SC90 type. This condition went on until the completion of all nine load increments, making the SM90 type the ideal soil type to use in this case, producing a final crown thrust of 1384 lb/in, 2% less than that produced by the SC90 type. The SC90 type was consistent in producing the largest amount of thrust throughout the entire load increments producing a final crown thrust of 1540 lb/in, 11.3% larger than the minimum.

The most interesting case in this analysis is the case wherein the system is modeled on an SM85 bedding under the 3-layer rock cover. The thrust developed at the crown increased directly proportional to the fill height for all types of embankment soil until the completion of the sixth load increment. The thrust values then decreased even though the fill height continued to increase at the beginning of the seventh load increment. The final thrust developed at the crown per soil type was therefore the least among all the cases studied in this section. The SC90 type produced the least amount of thrust at the crown having a magnitude of 531 lb/in. Followed by embankment soil type SM90 producing a final thrust magnitude of 607 lb/in and then by the CL90 type producing 651

lb./in.

The final case studied in this section is a system modeled on SM85 bedding under a 5-layer rock cover. At the end of fourth load increment, the SM90 soil type produced the greatest amount of thrust at the crown. But after the completion of the sixth load increment, the CL90 soil type produced the highest thrust magnitude among all three embankment types. At the completion of the final load increment, soil type CL90 was found to generate the largest amount of thrust at the crown of the structure, its magnitude being 1810 lb/in. The SC90 type soil was consistent in producing the least amount of thrust on the crown throughout the whole loading scheme, generating a final thrust magnitude after ninth load increment of 1664 lb/in.

SECTION V

SUMMARY, CONCLUSIONS AND RECOMMENDATIONS

A. SUMMARY AND CONCLUSIONS

This report presents an investigation of the behavior of a reinforced concrete arch structure under various embankment and bedding conditions. A finite element analysis of structural responses was performed on system models with varying bedding, embankment slope, embankment soil type, and rock cover type. The findings and conclusions from this investigation are as follows:

1. The results of the finite element model study showed consistency and reliability in predicting soil and structure responses.
2. The structures that were predicted to fail were the ones systemed in the order of:
 - a. Having a CL85 (clay) soil type bedding, with a 3-layer rock cover, and a 30-degree slope embankment. A structure modeled under these conditions was predicted to fail no matter what type of soil was used for the embankment.
 - b. Having a CL85 (clay) soil type bedding, with a 5-layer rock cover, and a 45-degree slope embankment. A structure modeled under these conditions was predicted to fail no matter what type of soil was used for the embankment.
3. Between the two types of bedding materials used in the

tests, it was found that at a relative compaction of 85%, a silty sand type of soil (type SM85) produced less structural settlement than a clayey type soil (CL85).

4. An embankment constructed with a 45-degree slope caused less moments to develop around the structure than an embankment with a 30-degree slope. In addition the former condition also caused structural reaction to develop more in form of axial forces (thrust) rather than bending moments, which is preferable in shell structures.

5. An embankment constructed with a silty sand type (SM85) of soil produces less moment around the structure and encourages structural reaction to develop through axial forces (thrust).

6. A rock-cover composed of a mean boulder diameter of 14 inches and set in five layers causes less magnitude in structural response at the completion of the embankment than a 3-layer rock cover with a mean boulder diameter of 42 inches.

7. Overall, a structure set on an SM85 sand soil type bedding, with SM90 soil embankment, 5-layer type rock cover, and set on a 30-degree slope proves to be the most effective system. The finite element analysis show that an arch structure constructed in this manner will produce the least amount of bending moment, the load transfer onto the structure being concentrated mainly on axial thrust. Figures 4.24 thru 4.26 show the final soil pressure, moment, and thrust distribution for a structure modelled in this manner.

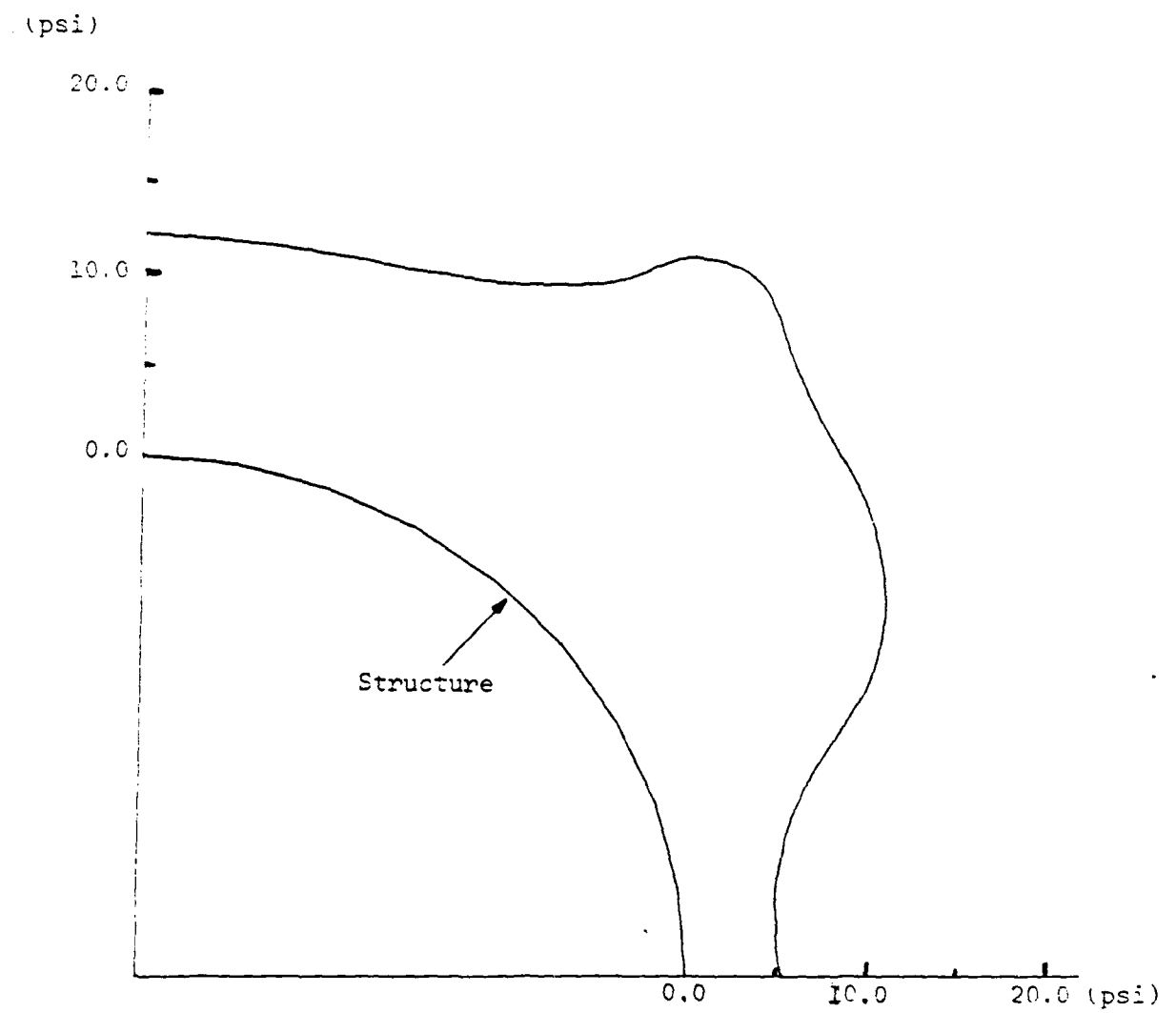


Figure 4.24 Soil Pressure Distribution

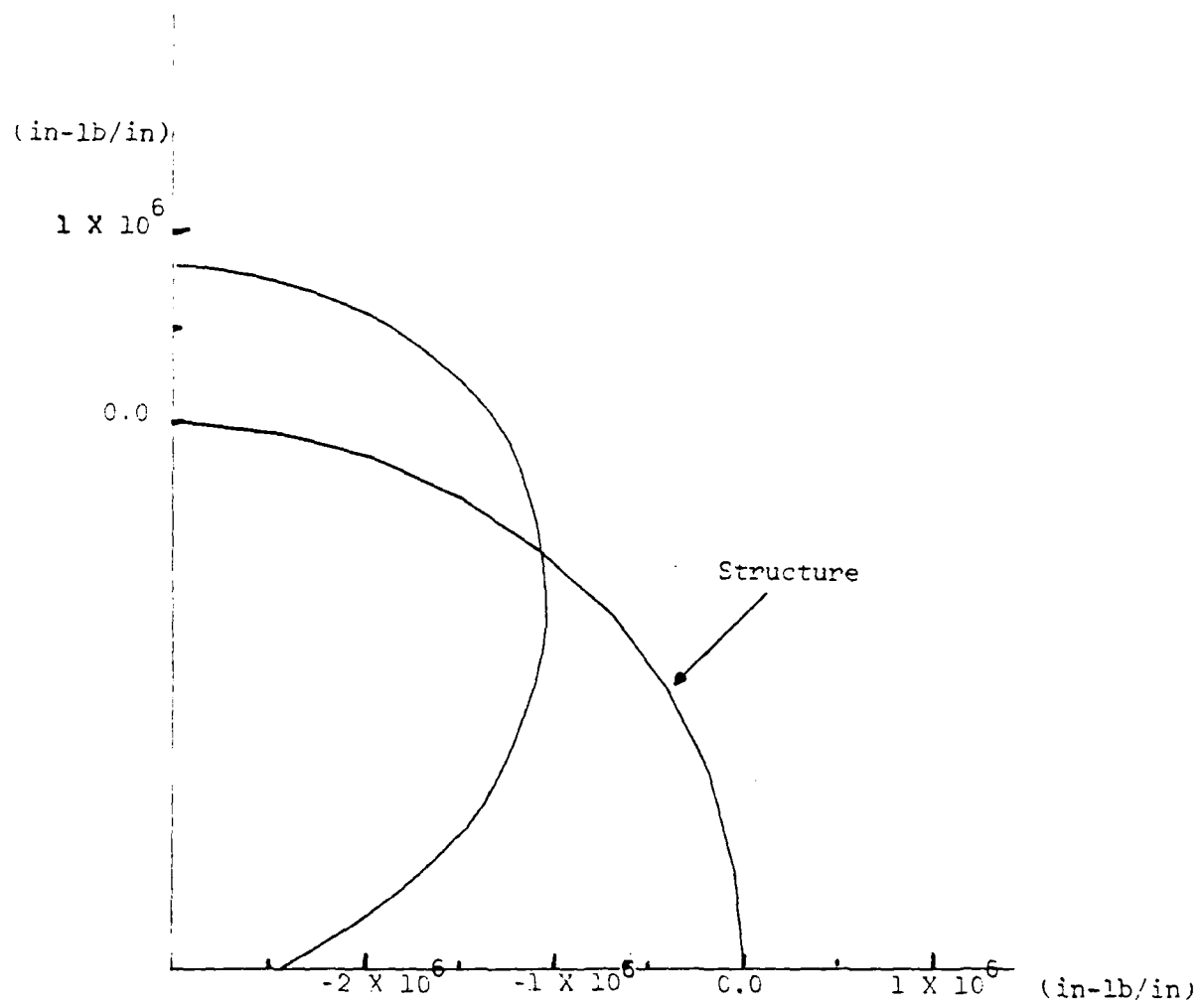


Figure 4.25 Moment Distribution

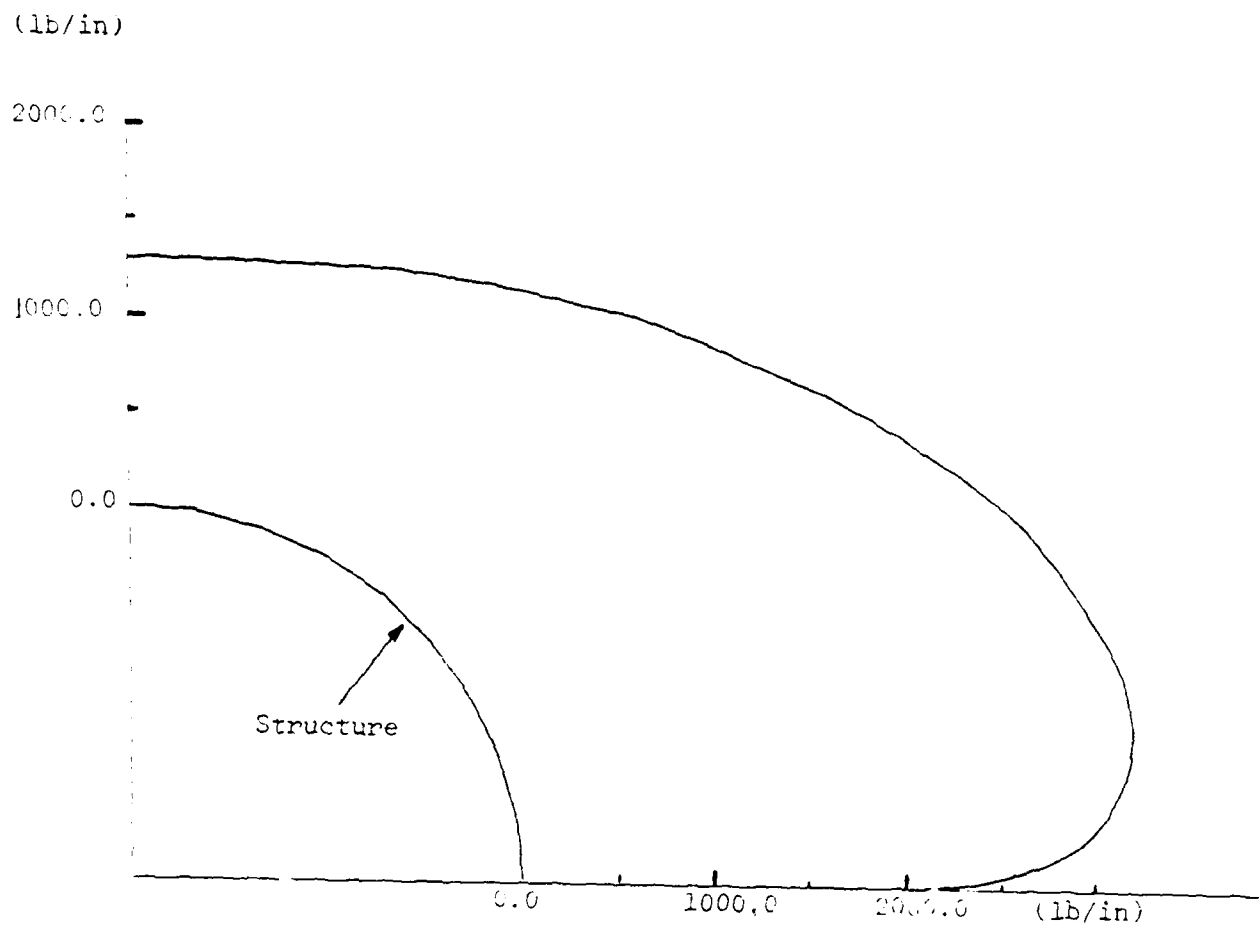


Figure 4.26 Thrust Distribution

B. RECOMMENDATIONS

Recommendations for research based on this study are as follows:

The results of the finite element model study presented in this report are based on the preliminary investigation for the feasibility study of an arch structure in a centrifuge. A more comprehensive (extensive) research including embankments of other sizes and geometries, structural reinforcement, different soil types, compaction for embankments, and bedding parameters is required in order to gain a better understanding of the relationship of the arch structure and the embankment.

In order to achieve a comprehensive model study using the centrifuge model technique, an on-board data acquisition system is required. Past experience of the researchers prove that this is a necessity for acquiring reliable and qualitative data.

A field study is necessary to verify the results of the centrifuge model study and finite element analysis once reasonable information is obtained.

REFERENCES

1. Austin, C.F., Halsey, C.C., Clodt, R.L. and Berry, S.L., "Full Scale Penetration into Semiconfined Diorite Boulders by a Semiarmor-Piercing (SAB) Bomb," Report No. ESL-TR-81-47, Air Force Engineering Services Center, Tyndall AFB, Florida, January 1982, UNCLASSIFIED.
2. Austin, C.F., Halsey, C.C., Clodt, R.L., and Berry, S.L., "Protective Antipenetration Systems Development," Report No. ESL-TR-83-39, Air Force Engineering Services Center, Tyndall AFB, Florida, September, 1983, UNCLASSIFIED.
3. Austin, C.F., Halsey, C.C., Berry, S.L., and Anderson, C.R., "Burster Slab Penetration Test," Report No. ESL-TR-84-49, Air Force Engineering Services Center, Tyndall AFB, Florida, July 1985, UNCLASSIFIED.
4. Bucky, P.B., "Use of Models for the Study of Mining Problems," A.I.M.M.E. Technical Publication No. 425, 1931.
5. Coles, C.K., "Centrifuge Models of a Spile-Reinforced Tunnel," M.S. Thesis, University of California, Davis, June, 1982.
6. Cunningham, C.H., Townsend, F.C., and Fagundo, F.E., "The Development of Micro-Concrete for Scale Model Testing of Buried Structures," Report No. ESL-TR-85-49, Air Force Engineering Services Center, Tyndall AFB, Florida, January 1986.
7. Duncan, J.M., et al., "Strength, Stress-Strain and Bulk Modulus Parameters for Finite Element Analyses of Stresses and Movements in Soil Masses," Report No. UCB/GT/78-02, National Science Foundation, April, 1978.
8. Finkel, J., Computer-Aided Experimentation, John Wiley, New York, 1975.
9. Freeman, R.L. Telecommunication Transmission Handbook, Wiley, New York, 1975.
10. James, R.G., and Larsen, H., "Centrifugal Model tests of Buried Rigid Pipes," Proceedings of the Ninth International Conference on Soil Mechanics and Foundation Engineering, Tokyo, Japan, 1977.
11. Katona, M.G., Smith, J.M., Odello, R.J., and Allgood, J.R., "CANDE-A Modern Approach for the Structural Design and Analysis of Buried Culverts," Report No. FHWA/RD-77/5, Federal Highway Administration, Washington, D.C., October, 1976.

12. Katona, M.G., Vittes, P.D., Lee, C.H., and Ho, H.T., "CANDE-1980: Box Culverts and Soil Models," Report No. FHWA/RD-80/172, Federal Highway Administration, Washington, D.C., May, 1981.
13. Kim, M.M. and Ko, H.Y., "Centrifugal Testing of Soil Slope Models," Transportation Research Record 872, pp. 7-15, 1982.
14. Kim, Y.S., Shen, C.K., and Dang, S., "Centrifuge Model Study of an Oil Storage Tank Foundation on Soft Clay," Proceedings of the 8th European Conference on Soil Mechanics and Foundation Engineering, Helsinki, Finland, May 3-26, 1983.
15. Kim, Y.S., and Davis, R.E., "Proof Testing of A Structural Plate Pipe with Varying Bedding and Backfill Parameters Section VII, Volume 3: Finite Element Analysis," Report No. FHWA/CA/SD-83/04, California Department of Transportation, Sacramento, California, August, 1983.
16. Leonards, G.A., Wu, Tzong-Hsin, and Juang, Charng-Hsein, "Predicting Performance of Buried Conduits," Report No. FHWA/IN/JHRP-81/3, Indiana State Highway Commission, Indianapolis, Indiana, June 1982.
17. Moore, C.A., "Modern Electronics for Geotechnical Engineers, 1. Introduction to Integrated Circuits," Proceedings of the ASTM Geotechnical Testing Journal, Volume 3, Number 2, June, 1980.
18. Moore, C.A., "Modern Electronics for Geotechnical Engineers, 4. Waveform Generators," Proceedings of the ASTM, Geotechnical Testing Journal, Volume 3, Number 2, June, 1980.
19. Moore, C.A., "Modern Electronics for Geotechnical Engineers, 5. Digital Logic Circuits," Proceedings of the ASTM, Geotechnical Testing Journal, Volume 3, Number 3, September, 1980.
20. Moore, C.A., "Modern Electronics for Geotechnical Engineers, 6. Process Control Applications," Proceedings of the ASTM Geotechnical Testing Journal, Volume 3, Number 4, December 1980.
21. Moore, C.A., "Modern Electronics for Geotechnical Engineers, 7. Introduction to Microprocessors," Proceedings of the ASTM Geotechnical Testing Journal, Volume 4, Number 1, March, 1981.

22. Moore, C.A., "Modern Electronics for Geotechnical Engineers 8. Microprocessor Applications," Proceedings of the ASTM, Geotechnical Testing Journal, Volume 4, Number 2, June 1981.
23. Pokrovsky, G.I., and Ryodorov, I.S., "Centrifugal Model Testing in the Mining Industry," Nedra Publishing House, Moscow, 1969.
24. Pokrovsky, G.I., and Ryodorov, I.S., "Centrifugal Model Testing in the Construction Industry," Translation Prepared by Building Establishment Library Translation Service, England, August, 1976.
25. Research Engineers, Personnel Communication, Facility Systems and Analysis Branch, and Operations Support Branch, Air Force Engineering Services Center, Tyndall AFB, Florida, May-August 1986.
26. Roden, M.S., Analog and Digital Communication, Prentice-Hall Englewood Cliffs, NJ, 1979.
27. Rohani, B., "Effectiveness of Rock-Rubble/Boulder Screens for Degrading the Penetration Capability of Kinetic Energy (KE) Projectiles," Report to Office, Chief of Engineers, U.S. Army, Waterways Experiment Station, Vicksburg, Mississippi, December, 1982, UNCLASSIFIED.
28. Schmidt, R.M., and Holsapple, K.A., Journal of Geophysical Research, Vol. 85, No. 1, January, 1980.
29. Scott, R.F., and Morgan, N.R., "Feasibility and Desirability of Constructing a Very Large Centrifuge for Geotechnical Studies," Report 760-170 NSF, California Institute of Technology and JPL, March 1977.
30. Shen, C.K., Kim, Y.S., Bang, S. and Mitchell, J., "Centrifuge Modeling of a Lateral Earth Support," Proceedings of the ASCE, Journal of the Geotechnical Engineering Division, Vol. 108, No. GT9, September, 1982.
31. Shen, C.K., Bang, S., and Kim, Y.S., "Improvement of Oil Storage Tank Foundation on Soft Clay by Fabric-Mesh-Reinforcement," proceedings of the International Symposium on In-Situ-Soil and Rock Reinforcement, Ecole Polytechnique, Ecole Nationale des Ponts et Chaussees, Paris, France, October 9-11, 1984.

32. Shen, C.K., Li, X.S., and Kim, Y.S., "Microcomputer Based Data Acquisition Systems for Centrifuge Modeling," Proceedings of the ASTM, Geotechnical Testing Journal, Volume 7, Number 4, December, 1984.
33. Wong, K.S. and Duncan, J.M., "Hyperbolic Stress-Strain Parameters for Nonlinear Finite Element Analysis of Stresses and Movements in Soil Masses," Report No. TE-74-3, University of California, Berkeley, July, 1974.

FINAL REPORT NUMBER 23
REPORT NOT AVAILABLE AT THIS TIME
Dr. William Schulz
760-7MG-079

1987-1988 RESEARCH INITIATION PROGRAM

Sponsored by the
AIR FORCE OFFICE OF SCIENTIFIC RESEARCH

Conducted by the
UNIVERSAL ENERGY SYSTEMS, INC.

FINAL REPORT

STRESS WAVE PROPAGATION IN
LAYERED MEDIA

Prepared by:	Joseph W. Tedesco
Academic Rank:	Associate Professor
Department and University:	Department of Civil Engineering Auburn University
Date:	August 1988
Contract No.:	F49620-85-C-0013/SB5851-0360
Subcontract No.:	S-760-7MG-034

ABSTRACT

Protective military structures are typically constructed of massive, monolithic concrete slabs. This practice is considered necessary in order to protect personnel and/or vital equipment within the structure from the harmful blast effects of conventional weaponry. A high intensity compressive longitudinal blast wave incident upon a protective shelter propagates through the monolithic concrete shelter wall, and reflects as a tensile wave at the interior face of the wall. The reflected tensile wave can cause extensive spalling of the interior face of the shelter walls, thus posing a potentially dangerous threat to personnel and equipment in the shelter.

A comprehensive numerical analysis is conducted to evaluate the effectiveness of various "layered structures" for enhanced protection against blast effects from conventional weaponry. Of primary concern is the capability of layered systems to mitigate stress wave propagation, and the subsequent elimination of interior spalling.

The finite element method (FEM) is employed to investigate the wave propagation characteristics of three layered systems: 1) concrete-polystyrene-concrete (CPC), 2) sand-polystyrene-concrete (SPC), and 3) sand-polystyrene-concrete-polystyrene-concrete (SPCPC). Both linear and nonlinear material behavior are considered. Stress transmission ratios are determined for each layered system.

The results of the investigation indicate that layered media significantly reduce stress transmission, and that the application of layered media to protective shelters can eliminate interior spalling.

ACKNOWLEDGEMENTS

This research was sponsored by a research grant from the Air Force Office of Scientific Research. Special appreciation is extended to Dr. Allen Ross, Research Fellow, Engineering Research Division, Engineering and Services Laboratory, Tyndall Air Force Base, for his assistance and productive discussions.

I. INTRODUCTION

Motivation

Protective military shelters are typically constructed of massive, monolithic concrete slabs. This practice, which has not changed significantly since the end of the Second World War, is necessary in order to protect personnel and/or vital equipment within the structure from the harmful effects of conventional weaponry. The drastic devaluation of the dollar in the NATO nations during the past several years has made construction costs for these types of structures prohibitive. This fact dramatically underscores the urgency for the development of alternative, cost-effective protective structure designs.

When a typical monolithic concrete protective shelter is subject to an impulse loading (blast wave) from conventional weaponry, a high-intensity stress wave propagates through the shelter wall. The stress wave reflects from the interior face of the shelter wall as a tension wave and can cause extensive spalling of the interior face of the wall. The spalled concrete fragments are hurled away from the wall at high velocities, posing a

potentially dangerous threat to personnel and equipment within the shelter.

Recent experimental studies (5,26) and analytical investigations conducted by Tedesco (20,21), Tedesco et al (23,24), and Landis (14) have indicated that "layered structures" may provide a viable alternative to conventionally hardened structures. The intent of this investigation is to evaluate the effectiveness of various "layered structures" for enhanced protection against impulse loading from conventional weaponry.

Previous Research

Extensive information is available concerning the propagation of stress waves in elastic, isotropic media. Information is also available concerning the propagation of stress waves in inelastic media. The majority of the information, however, deals with stress wave propagation in homogeneous metal wires and bars of uniform cross-section.

Little information is available on the propagation of stress waves through layered media. Even less information exists on the use of layered media in protective shelters to resist high-intensity blast loadings. Recent research, however, indicates that layered structures may provide a viable alternative to conventionally hardened structures.

Analytical investigations conducted by Tedesco (20,21) indicate that layered systems may be utilized to

alter the stress wave propagation characteristics of a protective shelter. The investigations revealed that certain combinations of materials, constructed in layers, significantly reduce the stress transmitted through the shelter walls. It was determined that the combination of materials required to substantially reduce the transmitted stress consists of a low-density, low-strength center layer sandwiched between two high-density, high-strength layers.

Subsequent analytical investigations conducted by Tedesco et al (23,24) examined three layered systems, each consisting of a center absorption layer surrounded by two layers of concrete. The absorption layers examined included air, polystyrene, and soil. The results from these preliminary studies revealed that each layered system significantly reduced the stress transmitted to the interior of the structure.

Analytical investigations conducted by Landis (14) examined layered systems consisting of an absorption layer of polystyrene or soil, sandwiched between two layers of concrete. Both layered systems significantly reduced the stress transmitted through the structure. The polystyrene, however, proved to be a much more effective absorption layer than the soil.

The research conducted in the aforementioned studies investigated only the linear-elastic behavior of the

layered systems. The effect of nonlinear behavior upon stress wave propagation in layered media has not yet been examined.

Objective

The primary objective of this study is to evaluate the effectiveness of layered systems to mitigate stress wave propagation via a comprehensive numerical analysis. The numerical analyses are conducted on several different types of layered systems subject to impulse loading in order to ascertain the characteristics of wave propagation through the various material layers comprising the systems. From the results of the numerical analyses, recommendations for layered systems as an alternative to conventionally hardened protective structures are presented.

Scope of Study

The finite element method (FEM) is utilized in the numerical analyses to investigate the wave propagation characteristics of several layered systems. The layered systems investigated include a concrete-polystyrene-concrete system, a sand-polystyrene-concrete system, and a sand-polystyrene-concrete-polystyrene-concrete system. The dimensions of the concrete and sand layers are constant for each layered system. Polystyrene layers of varying thickness are examined in order to properly assess

the effect of absorption layer thickness upon wave propagation. Both linear and nonlinear material behavior are considered in the wave propagation analysis. The ratio of transmitted stress to incident stress (transmission ratio) is determined for each system investigated.

II. STRESS WAVE PROPAGATION IN SOLIDS

In static analyses, it is assumed that a structure is gradually loaded over an interval of time such that inertial properties have no effect on the response of the structure. The structure is in a state of static equilibrium and time is not a variable in the solution. Dynamic problems, however, occur when loading conditions vary significantly in time to produce inertial forces in the structure. The structure is in a state of dynamic equilibrium, and the response of the structure is time dependent. In general, if the period of the forcing function is less than three times the fundamental period of the structure, then the problem becomes dynamic, and inertial forces must be considered in the structural response (8).

When an elastic body is subjected to dynamic loading, stresses and strains propagate throughout the structure at a finite velocity. In most structural dynamic problems, the rate of application of the load is small in comparison with the velocity of stress/strain propagation. Therefore, the entire structure responds to the loading condition immediately, and wave propagation is not a consideration in the solution. In instances where the

load is applied at a high rate (as in the case of an impact or explosion), however, the propagation of stress/strain waves must be considered in the problem solution.

Basic Stress Wave Theory

A stress wave is defined as a moving part of a medium in a state of stress. Since any stress has associated with it a corresponding strain, stress waves and strain waves are identical. When a force is initially applied to a body, a stress wave is generated at the point of contact. The stress wave propagates away from the point of contact at approximately the seismic velocity of that body. Any point in the body remains unstressed and unaffected by the disturbance until reached by the stress wave. The stress wave propagates through the body, reflects from the boundaries of the body, and interacts with other stress waves to create very complicated stress distributions in the body.

Stress waves are classified as normal or tangential. Normal waves are analagous to the normal component of stress. Mass particles under the influence of a normal wave move parallel to the direction of propagation of the wave. A body subjected to a purely normal wave undergoes a volumetric change due to lengthening or shortening, but does not undergo any rotation. For this reason, normal waves are referred to as longitudinal waves or dilational

waves. Tangential waves are similiar to the shear component of stress. Mass particles under the influence of a tangential wave move perpendicular to the direction of wave propagation. A body subjected to a purely tangential wave undergoes a rotational displacement but does not experience a change in volume. For this reason, tangential waves are referred to as shear waves, rotational waves, or distortional waves.

The general equations governing the propagation of stress waves can be derived by analyzing a differencial volume $\delta x \delta y \delta z$, as shown in Figure 2.1. The residual force F in each direction can be found by summing forces in each direction. Summing forces in the x direction yields

$$F_x = \left(\sigma_x + \frac{\partial \sigma_x}{\partial x} \delta x \right) \delta y \delta z - \sigma_x \delta y \delta z + \left(\tau_{xy} + \frac{\partial \tau_{xy}}{\partial y} \delta y \right) \delta x \delta z - \tau_{xy} \delta x \delta z + \\ + \left(\tau_{xz} + \frac{\partial \tau_{xz}}{\partial z} \delta z \right) \delta x \delta y - \tau_{xz} \delta x \delta y$$

which simplifies to

$$F_x = \left(\frac{\partial \sigma_x}{\partial x} + \frac{\partial \tau_{xy}}{\partial y} + \frac{\partial \tau_{xz}}{\partial z} \right) \delta x \delta y \delta z \quad (2.1)$$

Similiarly,

$$F_y = \left(\frac{\partial \tau_{xy}}{\partial x} + \frac{\partial \sigma_y}{\partial y} + \frac{\partial \tau_{yz}}{\partial z} \right) \delta x \delta y \delta z$$

$$F_z = \left(\frac{\partial \tau_{xz}}{\partial x} + \frac{\partial \tau_{yz}}{\partial y} + \frac{\partial \sigma_z}{\partial z} \right) \delta x \delta y \delta z$$

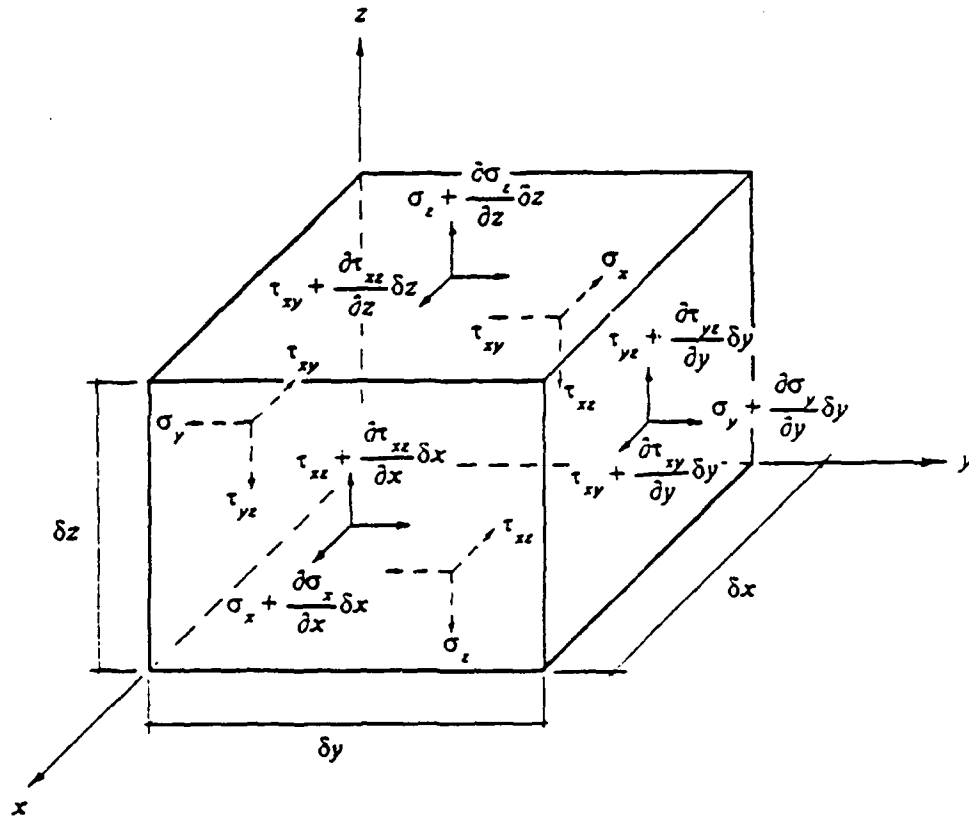


Figure 2.1. Stress Components Acting on a Differential Volume

Applying Newton's 2nd law of motion, $F = ma$, yields

$$F_x = \rho \delta x \delta y \delta z \frac{\partial^2 u}{\partial t^2} \quad (2.2)$$

$$F_y = \rho \delta x \delta y \delta z \frac{\partial^2 v}{\partial t^2}$$

$$F_z = \rho \delta x \delta y \delta z \frac{\partial^2 w}{\partial t^2}$$

Equating equations (2.1) and (2.2) and simplifying yields

$$\rho \frac{\partial^2 u}{\partial t^2} = \frac{\partial \sigma_x}{\partial x} + \frac{\partial \tau_{xy}}{\partial y} + \frac{\partial \tau_{xz}}{\partial z} \quad (2.3)$$

$$\rho \frac{\partial^2 v}{\partial t^2} = \frac{\partial \tau_{xy}}{\partial x} + \frac{\partial \sigma_y}{\partial y} + \frac{\partial \tau_{yz}}{\partial z}$$

$$\rho \frac{\partial^2 w}{\partial t^2} = \frac{\partial \tau_{xz}}{\partial x} + \frac{\partial \tau_{yz}}{\partial y} + \frac{\partial \sigma_z}{\partial z}$$

Equation (2.3) is the governing equation for stress wave propagation in any media, and is valid for any stress-strain relationship. Therefore, the stress wave propagation in any medium is determined by the substitution of the appropriate stress-strain relations into equation (2.3), and the concurrent application of the appropriate boundary conditions.

It has been proven (12,19) that equation (2.3) describes the dilatational and distortional stress wave components. It has also been shown (12,19) that, in any isotropic elastic medium, a stress wave must propagate at a velocity dependent upon the mechanical properties of the medium. A dilatational (longitudinal) wave must travel at a velocity of

$$c_1 = \left[\frac{E(1-\nu)}{(1+\nu)(1-2\nu)\rho} \right]^{\frac{1}{2}} \quad (2.4)$$

and a distortional (rotational) wave must travel at a velocity of

$$c_2 = \sqrt{\frac{G}{\rho}} \quad (2.5)$$

where E is Young's modulus, ν is Poisson's ratio, ρ is the material mass density, and G is the shear modulus (6). Moreover, for an elastic isotropic material, equation

(2.3) can be further simplified to

$$\frac{\partial^2 u}{\partial t^2} = c^2 \nabla^2 u \quad (2.6)$$

$$\frac{\partial^2 v}{\partial t^2} = c^2 \nabla^2 v$$

$$\frac{\partial^2 w}{\partial t^2} = c^2 \nabla^2 w$$

where ∇^2 represents the operation

$$\nabla^2 = \left(\frac{\partial^2}{\partial x^2} + \frac{\partial^2}{\partial y^2} + \frac{\partial^2}{\partial z^2} \right)$$

Plane Stress Wave Propagation

Stress waves are propagated in all directions in a media from the point of a disturbance. At a great enough distance from the disturbance, however, the stress waves are, for all practical purposes, plane waves. In the case of a plane wave, it can be assumed that all mass particles under the influence of the wave are moving either parallel to the direction of wave propagation (dilatational waves) or perpendicular to the direction of wave propagation (distortional waves) (25).

For propagation in the x direction only (refer to Figure 2.2), the deformation becomes a function of x only. Equation (2.6) therefore reduces to

$$\frac{\partial^2 u}{\partial t^2} = c_1^2 \frac{\partial^2 u}{\partial x^2} \quad (2.7)$$

The general solution to this equation is

$$u(x,t) = f_1(x+c_1t) + f_2(x-c_1t) \quad (2.8)$$

where f_1 and f_2 are arbitrary functions depending upon initial conditions and describe the shape of the stress wave. The function f_1 represents a stress wave traveling in the negative x direction with constant velocity c_1 . The function f_2 represents a stress wave traveling in the positive x direction with constant velocity c_1 .

A segment of a plane dilatational wave is illustrated in Figure 2.2. The medium at section A-A in Figure 2.2(a) experiences a normal stress σ_x . After a time interval δt , the segment of the wave initially corresponding to section A-A has traveled a distance δx to section B-B (Figure 2.2(b)). The stress wave has imposed an impulse $\sigma_x \delta t$ on the medium between sections A-A and B-B. Equating this impulse to the change in momentum yields

$$\sigma_x \delta t = \rho V \delta x = \rho V_x c_1 \delta t$$

which reduces to

$$\sigma_x = \rho c_1 V_x \quad \text{or} \quad V_x = \frac{\sigma_x}{\rho c_1} \quad (2.9)$$

where V_x is the particle velocity parallel to the direction of wave propagation. Similarly, for a distortional wave,

$$\tau_{yz} = \rho c_2 V_y \quad \text{or} \quad V_y = \frac{\tau_{yz}}{\rho c_2} \quad (2.10)$$

where V , is the particle velocity perpendicular to the direction of wave propagation. Equations (2.9) and (2.10) indicate that stress and particle velocity are linearly related by the material impedance (acoustic resistance), ρc .

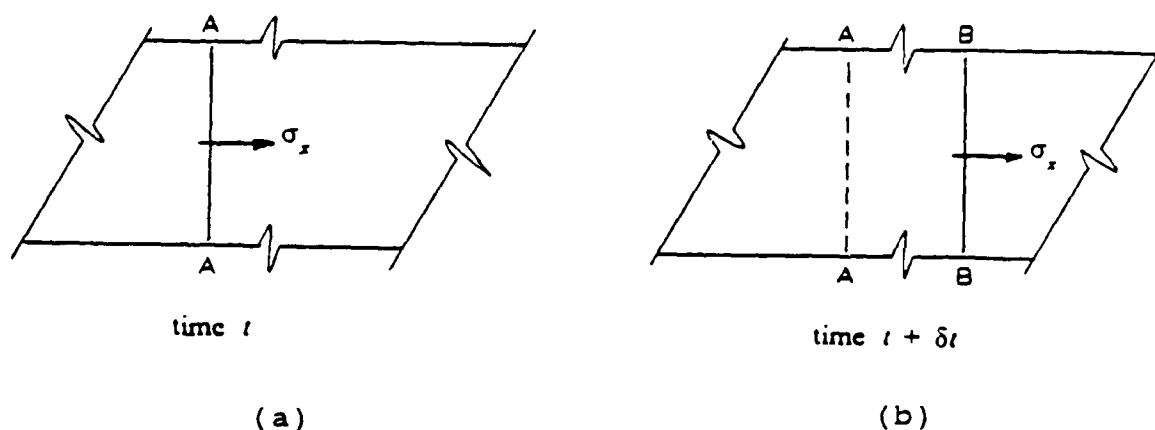


Figure 2.2. Section of Medium Subject to a Transient Stress Wave

The stress wave velocity and the particle velocities must not be construed as the same. The stress wave velocity is the velocity at which the stress wave propagates from one point to another in the medium. For an elastic isotropic medium, this velocity remains constant with both time and position in the medium. The particle velocity is the velocity of the mass particles at some point in the medium. Since the wave propagates through the medium, stressing separate sections of the medium at different times, the particle velocity is not

constant throughout the medium. It should also be noted that the particle velocities for tension and compression waves are opposite in sense. Mass particles subjected to a compressive wave travel in the direction of wave propagation. Mass particles subjected to a tensile wave, however, travel in the direction opposite that of wave propagation.

Stress Wave Propagation in a Uniform Bar

Equation (2.3) describes the motion of a stress wave propagating through an isotropic medium. Theoretically, equation (2.3) can be used to describe the propagation of stress waves in any isotropic solid by solving for the appropriate boundary conditions. However, except for a few simple cases, the solution becomes very complex. Therefore, the propagation of stress waves in a bar of uniform cross section is investigated in order to illustrate the phenomenon.

A differential element of the bar, δx , is shown in Figure 2.3. Assuming plane sections remain plane and the stress is uniformly distributed over the cross section, it follows that

$$\sigma_x = E \frac{\partial u}{\partial x} \quad (2.11)$$

Summing forces in the x direction to obtain the residual

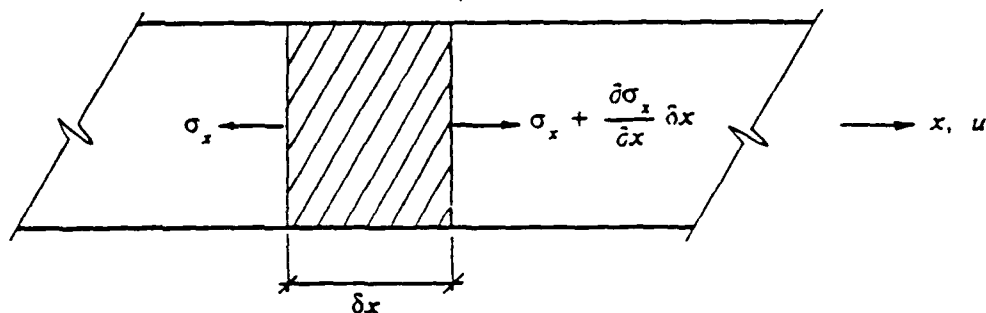


Figure 2.3. Stress Components Acting on a Differential Bar Element

force and applying Newton's second law of motion, $F = ma$, yields

$$A \frac{\partial \sigma_x}{\partial x} \delta x = \rho A \delta x \frac{\partial^2 u}{\partial t^2}$$

Substituting equation (2.11) for σ_x and simplifying yields

$$\frac{\partial^2 u}{\partial t^2} = \frac{E}{\rho} \frac{\partial^2 u}{\partial x^2}$$

or

$$\frac{\partial^2 u}{\partial t^2} = c^2 \frac{\partial^2 u}{\partial x^2} \quad (2.12)$$

where c is the velocity of propagation of longitudinal waves in the bar defined by

$$c = \sqrt{\frac{E}{\rho}} \quad (2.13)$$

Equation (2.12) is identical with equation (2.7), derived for the propagation of a one-dimensional plane wave in a linear isotropic solid. Therefore, the propagation of a plane longitudinal stress wave in a three-dimensional elastic isotropic medium is identical to the propagation of the same stress wave in a bar of uniform cross section. Equation (2.12) is applicable to any elastic isotropic bar of uniform cross section. The relationship between c_l/c and Poisson's ratio ν is illustrated in Figure 2.4. It should be noted that for small Poisson's ratios, the velocity c_l in equation (2.4) approaches the velocity c in equation (2.13). Therefore, the velocity of longitudinal stress wave propagation in a linear isotropic solid of small Poisson ratio is approximately equal to the velocity of propagation in a bar of uniform cross section. In consideration of the above similarities, stress wave propagation in a bar of uniform cross section can be used to model the plane longitudinal stress wave propagation in a linear isotropic medium.

The general solution to equation (2.12) is

$$u(x,t) = f_1(x+ct) + f_2(x-ct) \quad (2.14)$$

where the function f_1 describes a backward moving wave, and the function f_2 describes a forward moving wave. Equating impulse to the change in momentum yields

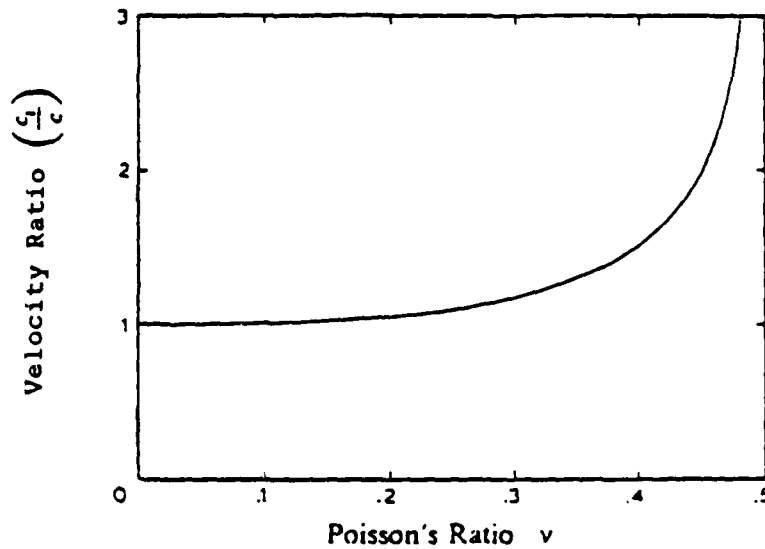


Figure 2.4. Relationship Between Velocity Ratio and Poisson's Ratio

$$\sigma_x = \rho c V \quad \text{or} \quad V = \frac{\sigma_x}{\rho c} \quad (2.15)$$

This is consistent with equation (2.9), and indicates that the particle velocity of the bar is linearly proportional to the stress by the material impedance ρc .

For a forward moving stress wave propagating in the x direction, equation (2.14) reduces to

$$u(x,t) = f_2(x-ct). \quad (2.16)$$

If the stress wave is elastic and plane, then every segment of the stress wave is propagated with the same velocity, and the shape of the stress wave does not change. The solution given by equation (2.16) is depicted graphically in Figure 2.5. Figure 2.5(a) illustrates a forward moving stress wave ab of arbitrary shape at time t_1

propagating in the x direction at constant velocity c . At time $t_1 + \delta t$ (Figure 2.5(b)), the stress wave has traveled a distance $\delta x = c \delta t$ from position ab to position $a'b'$. The shape and amplitude of the stress wave remain unchanged.

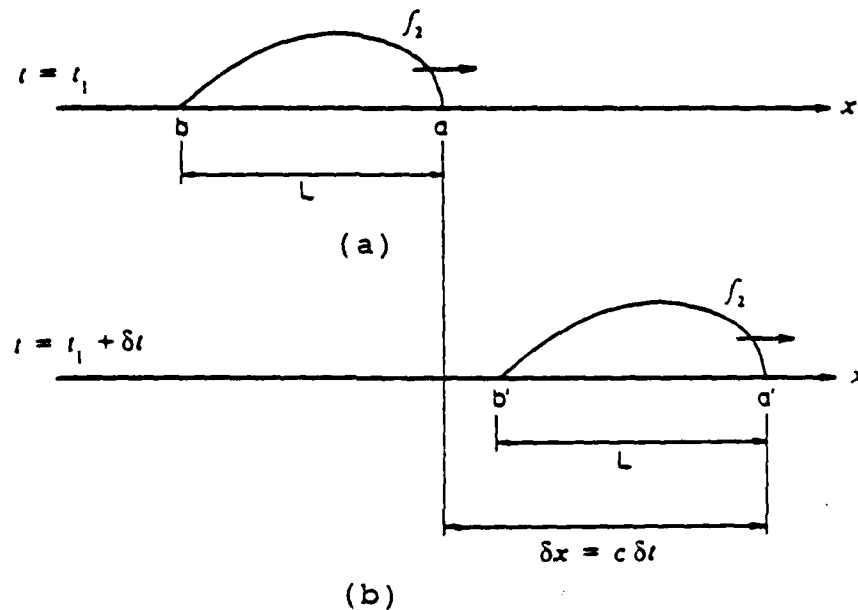


Figure 2.5. Forward Moving Stress Wave Propagating With Velocity c .

Figure 2.5 represents a single stress wave propagating through a uniform bar in the positive x direction. If this stress wave encounters a second stress wave traveling in the negative x direction, the two waves will interfere with one another. The stresses and particle velocities of the two stress waves can be superimposed to obtain the resultant stresses and particle

velocities. The interference of two compression waves traveling in opposite directions is shown in Figure 2.6. The compression waves have the same stress level σ_c , but have particle velocities V_c in opposite directions, as shown in Figure 2.6(a). Figure 2.6(b) reveals the superposition of a portion of the two waves. The stress level is additive in this case, and the compressive stress intensity doubles to $2\sigma_c$. The particle velocities, equal in magnitude but opposite in direction, cancel and become zero.

The interference of a compressive wave and a tensile wave traveling in opposite directions is shown in Figure 2.7. The waves are of equal stress level, σ_c , but of opposite sign. The particle velocities are identical in both magnitude and direction, as shown in Figure 2.7(a). The superposition of the two stress waves is depicted in Figure 2.7(b). In this case, the stresses cancel each other out and the particle velocity doubles to $2V_c$.

Boundary Effects on Stress Wave Propagation

A stress wave will continue to propagate through a linear, isotropic material with no change in shape, intensity, or direction until it encounters a boundary. In general, when an incident longitudinal stress wave reaches a boundary, it is reflected as two separate waves:

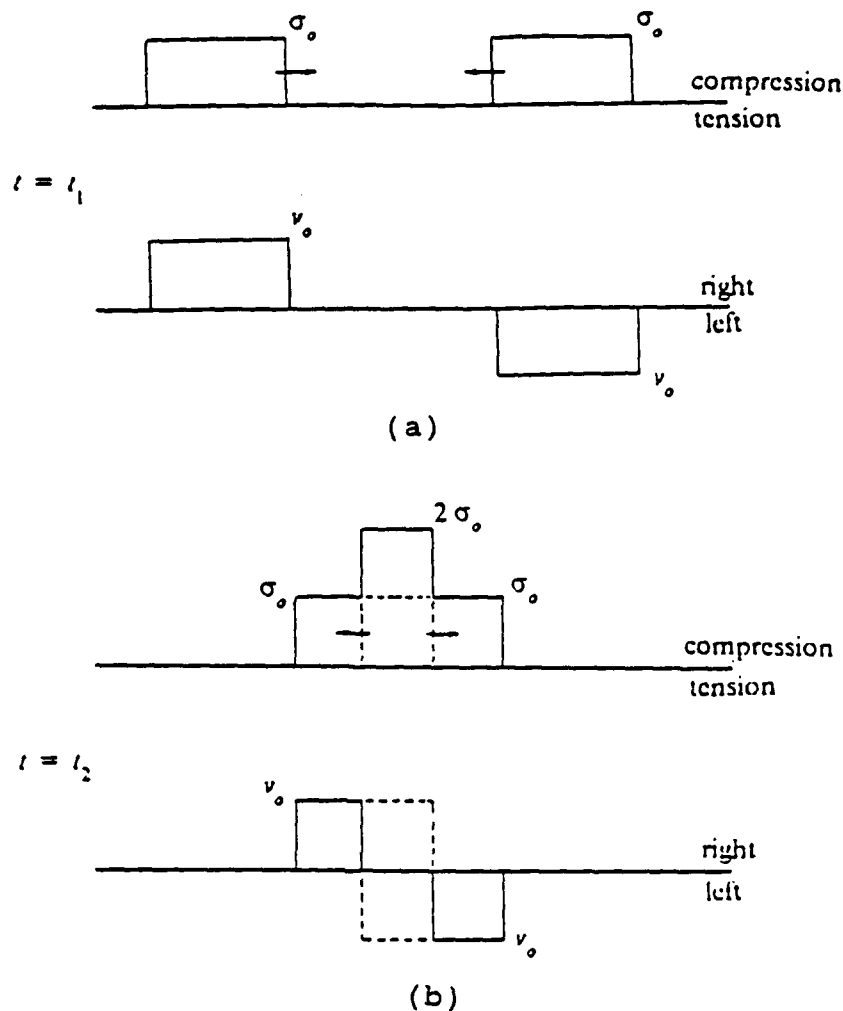
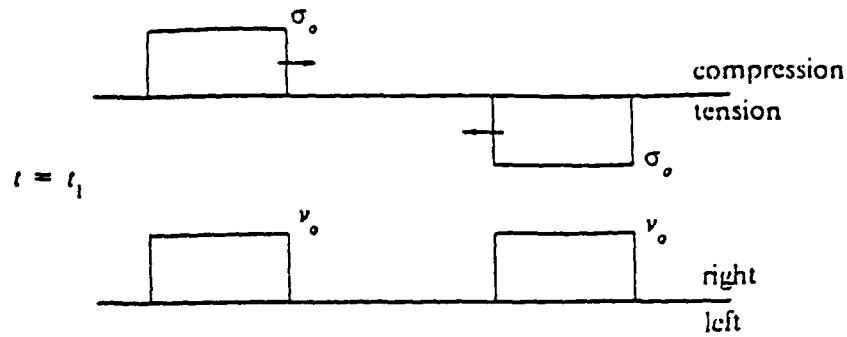


Figure 2.6. Interference and Superposition of Two Compressive Stress Waves.

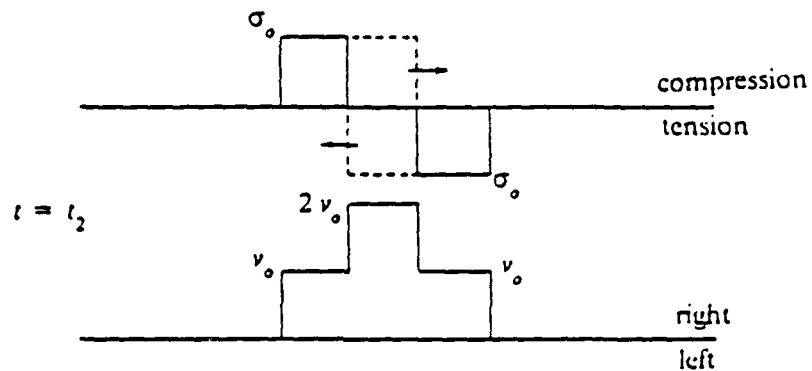
1) a longitudinal wave, and 2) a distortional wave. However, when the incident longitudinal wave is normal to the boundary, the longitudinal wave is reflected as a single longitudinal wave.

Reflection from a Free Surface

A longitudinal wave at normal incidence to a free boundary will be reflected as a longitudinal wave with a



(a)



(b)

Figure 2.7. Interference and Superposition of Compression and Tension Stress Waves.

change in phase. The three boundary conditions governing the reflection from a free surface are: 1) zero stress, 2) nonzero displacement, and 3) nonzero particle velocity at the free surface. An incident longitudinal compression wave will be reflected at full stress level as a longitudinal tension wave. Superposition of the incident and reflected stress waves yields zero stress but a doubling of the particle velocity at the free surface.

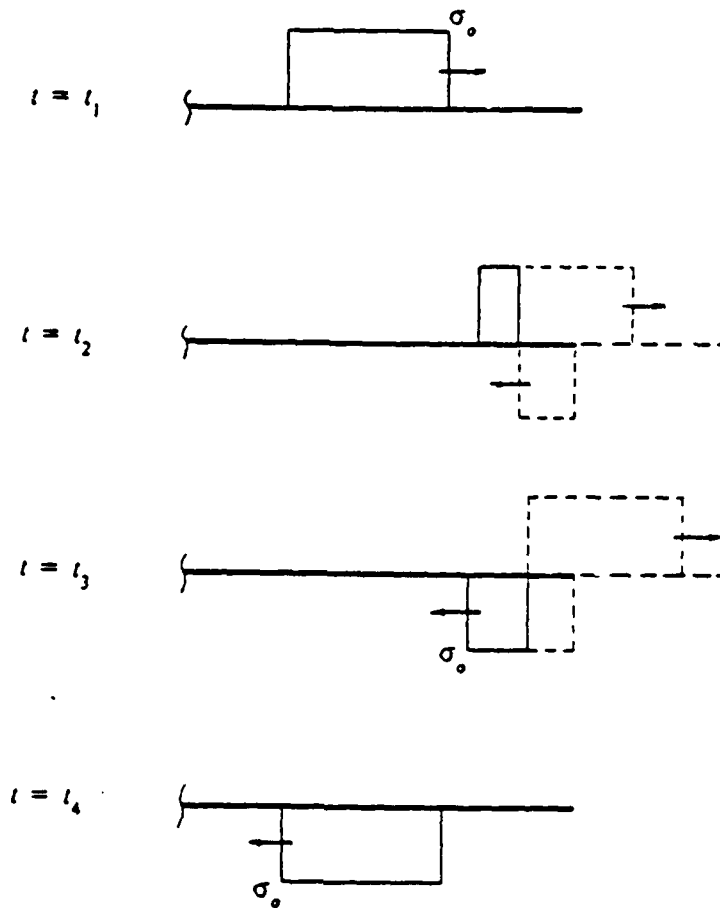


Figure 2.8. Reflection of a Rectangular Wave at a Free Surface.

The reflection of a longitudinal stress wave at normal incidence to a free surface is illustrated in Figures 2.8 and 2.9 for four intervals of time. A rectangular compressive stress wave reflecting from the free end of a bar is shown in Figure 2.8, and a triangular compressive stress wave reflecting from the free end is shown in Figure 2.9. The compression wave is reflected at full intensity as a tensile wave when it reaches the free

surface. It is noted that, upon reflection of the rectangular wave, a segment of the bar adjacent to the free surface remains unstressed. However, upon reflection of the triangular wave, only the free surface remains unstressed. In either case, the maximum stress due to superposition is equal to the maximum incident stress.

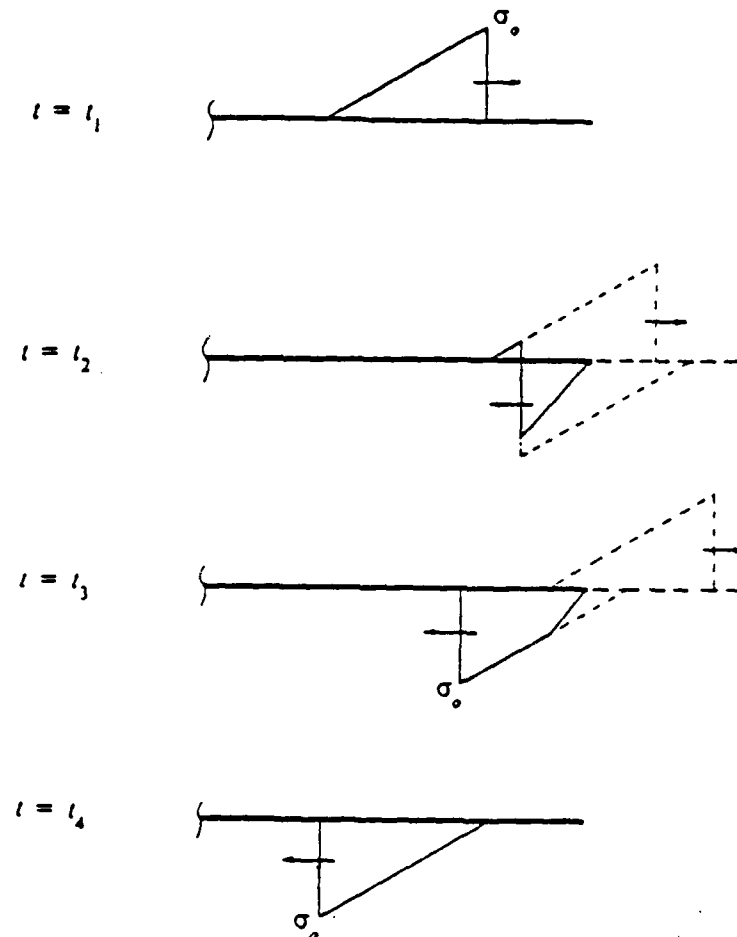


Figure 2.9. Reflection of a Triangular Wave at a Free Surface.

Reflection From a Fixed Boundary

A longitudinal wave at normal incidence to a fixed boundary will be reflected as a longitudinal wave with no change in phase. The three boundary conditions governing the reflection from a fixed surface are: 1) zero displacement, 2) zero particle velocity, and 3) nonzero stress at the fixed surface. An incident longitudinal compression wave will be reflected at full stress level as a compression wave. Superposition of the incident and reflected stress waves yields zero particle velocity, but a doubling of the stress intensity at the fixed surface.

The reflection of a longitudinal stress wave at normal incidence to a fixed surface is illustrated in Figures 2.10 and 2.11 for four intervals of time. A rectangular compressive stress wave reflecting from the fixed end of a bar is shown in Figure 2.10, and a triangular compressive stress wave reflecting from the fixed end is shown in Figure 2.11. The compression wave is reflected at full intensity without a change of phase when it reaches the fixed surface. It is noted that, in the case of an incident triangular wave, a rectangular wave of varying length and intensity is formed as the incident and reflected waves are superimposed. In either case, however, the maximum stress due to superposition is twice that of the maximum stress of the incident wave.

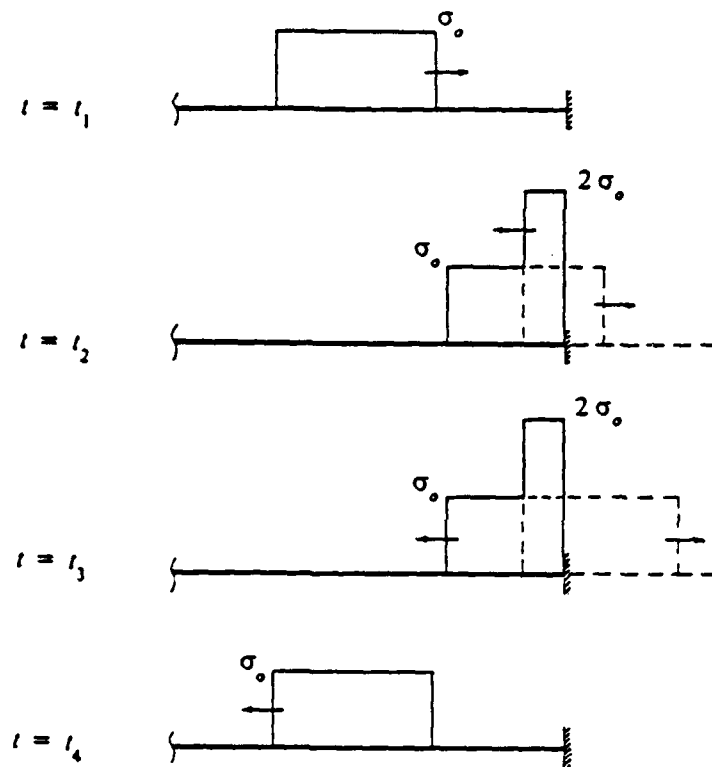


Figure 2.10. Reflection of a Rectangular Wave at a Fixed Surface.

Stress Wave Propagation in Layered Media

The relative strength and density of two dissimilar materials forming a boundary affects stress wave propagation in the media. In general, when an incident longitudinal stress wave reaches a boundary between two dissimilar materials, the wave is reflected and refracted (transmitted) as four separate waves: 1) a reflected longitudinal wave, 2) a reflected distortional wave, 3) a transmitted longitudinal wave, and 4) a transmitted distortional wave. When the incident longitudinal wave is

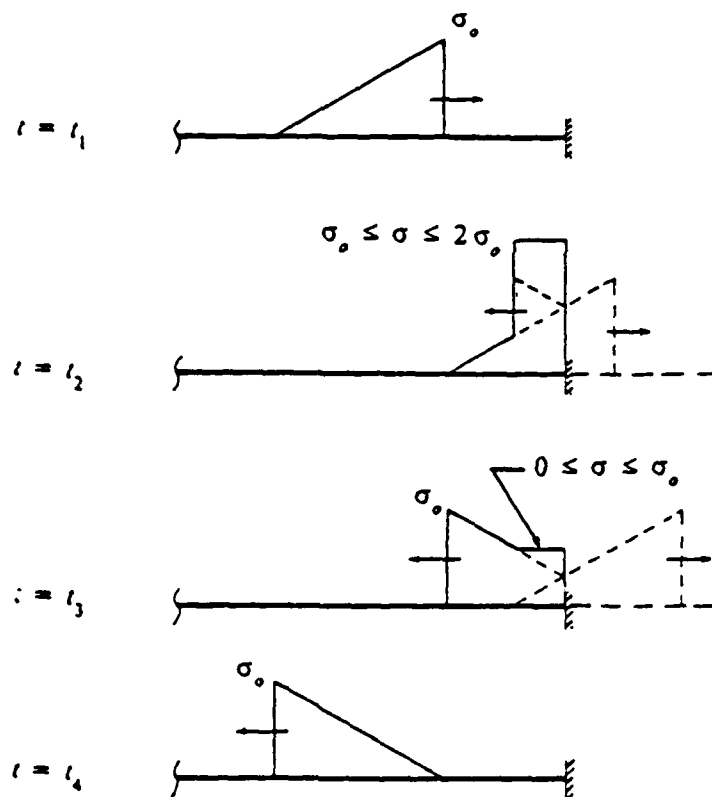


Figure 2.11. Reflection of a Triangular Wave at a Fixed Surface.

normal to the boundary, however, the incident longitudinal wave is reflected and transmitted as a longitudinal wave.

The boundary conditions governing the reflection and refraction at the boundary between two dissimilar materials are defined as the equality of stress and particle velocities in each material at the boundary (assuming the materials remain in constant contact). These conditions are described by the expressions

$$\sigma_I(x,t) + \sigma_R(x,t) = \sigma_T(x,t) \quad (2.17)$$

and

$$V_I(x,t) + V_R(x,t) = V_T(x,t) \quad (2.18)$$

where σ_I , σ_R , σ_T are the incident, reflected, and transmitted stresses, respectively; V_I , V_R , V_T are the respective incident, reflected, and transmitted particle velocities, where

$$V_I = \frac{\sigma_I}{\rho_1 c_1} \quad V_R = -\frac{\sigma_R}{\rho_1 c_1} \quad V_T = \frac{\sigma_T}{\rho_2 c_2}$$

as given by equation (2.15). The subscripts 1 and 2 refer to the first and second materials, respectively. Substituting equation (2.15) for V in equation (2.18) yields

$$\frac{\sigma_I}{\rho_1 c_1} - \frac{\sigma_R}{\rho_1 c_1} = \frac{\sigma_T}{\rho_2 c_2} \quad (2.19)$$

Solving equations (2.17) and (2.19) simultaneously yields

$$\sigma_T = \frac{2 \rho_2 c_2}{\rho_1 c_1 + \rho_2 c_2} \sigma_I \quad (2.20)$$

$$\sigma_R = \frac{\rho_2 c_2 - \rho_1 c_1}{\rho_1 c_1 + \rho_2 c_2} \sigma_I \quad (2.21)$$

Rearranging equations (2.20) and (2.21) yields

$$\frac{\sigma_T}{\sigma_I} = \frac{2 \rho_2 c_2}{\rho_1 c_1 + \rho_2 c_2} \quad (2.22)$$

$$\frac{\sigma_R}{\sigma_I} = \frac{\rho_2 c_2 - \rho_1 c_1}{\rho_1 c_1 + \rho_2 c_2} \quad (2.23)$$

and dividing equation (2.22) by equation (2.23) results in

$$\frac{\sigma_r}{\sigma_i} = \frac{2 \rho_2 c_2}{\rho_2 c_2 - \rho_1 c_1} \quad (2.24)$$

Equations (2.20) through (2.24) also describe the fixed and free boundary conditions previously investigated. When $\rho_2 c_2 = 0$, i.e., a free boundary condition, then $\sigma_r = 0$ and $\frac{\sigma_R}{\sigma_I} = -1$, denoting that an incident compression wave will be reflected at full stress level as a tension wave. When $\rho_2 c_2 = \infty$, describing a fixed boundary condition, $\frac{\sigma_r}{\sigma_i} = 2$ and $\frac{\sigma_R}{\sigma_I} = 1$, indicating that a compression wave reflects at full intensity without a change in phase, and the boundary will experience a stress equal to twice that of the incident stress.

The transmission ratio $\left(\frac{\sigma_r}{\sigma_i}\right)$ and the reflection ratio $\left(\frac{\sigma_R}{\sigma_I}\right)$ are plotted in Figure 2.12 for a stress wave at normal incidence. When $\rho_1 c_1 = \rho_2 c_2$, as in a continuous media, there will be no reflection and the stress wave will be transmitted at full intensity. When $\rho_1 c_1 < \rho_2 c_2$, the reflection ratio is positive, and an incident stress wave will be reflected with no change in phase. When $\rho_1 c_1 > \rho_2 c_2$, the reflection ratio is negative, and an incident stress wave will be reflected with a change in phase. It should be noted, however, that if the boundary between the materials cannot support tension, then an incident tensile

wave will be reflected as if at a free boundary. The lower and upper limits of the transmission ratio are 0 and 2, respectively, representing the extreme cases of free and fixed boundaries. The upper and lower limits of the reflection ratio are -1 and 1, representing the limiting cases of free and fixed boundaries, respectively.

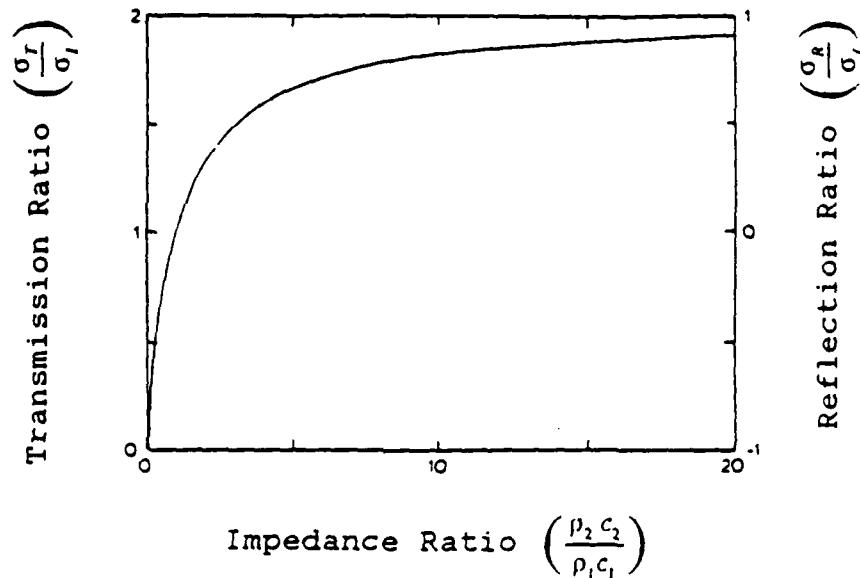


Figure 2.12. Transmission and Reflection Ratios at Normal Incidence vs. the Ratio Between Material Impedances.

The reflection and transmission of a triangular stress wave is illustrated in Figure 2.13 for $\rho_1 c_1 < \rho_2 c_2$. The stress wave is reflected at less than full intensity with no change in phase, and is transmitted at an increased stress level. The length of the stress wave increases in the second material due to the increased wave velocity c_2 of the second material.

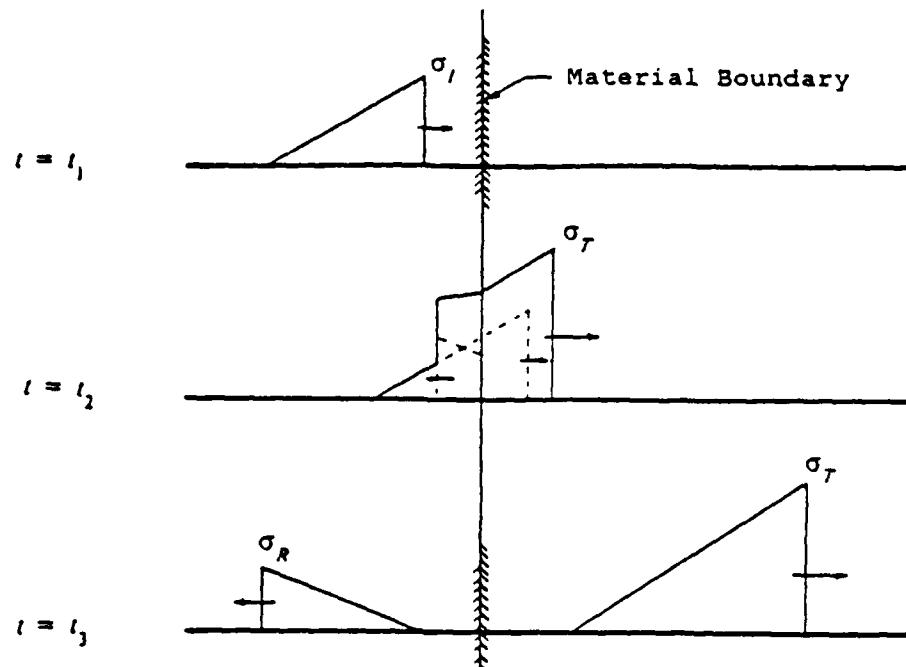


Figure 2.13. Transmission and reflection of a stress wave for $\rho_1 c_1 < \rho_2 c_2$.

The reflection and transmission of a triangular stress wave is illustrated in Figure 2.14 for $\rho_1 c_1 > \rho_2 c_2$. The stress wave is reflected at less than full intensity with a change in phase, and is transmitted at a reduced stress level. The length of the stress wave decreases in the second material due to the reduced wave velocity c_2 of the second material.

Plastic Stress Wave Propagation

The propagation of stress waves in a nonlinear material is a very complex phenomenon. This study will

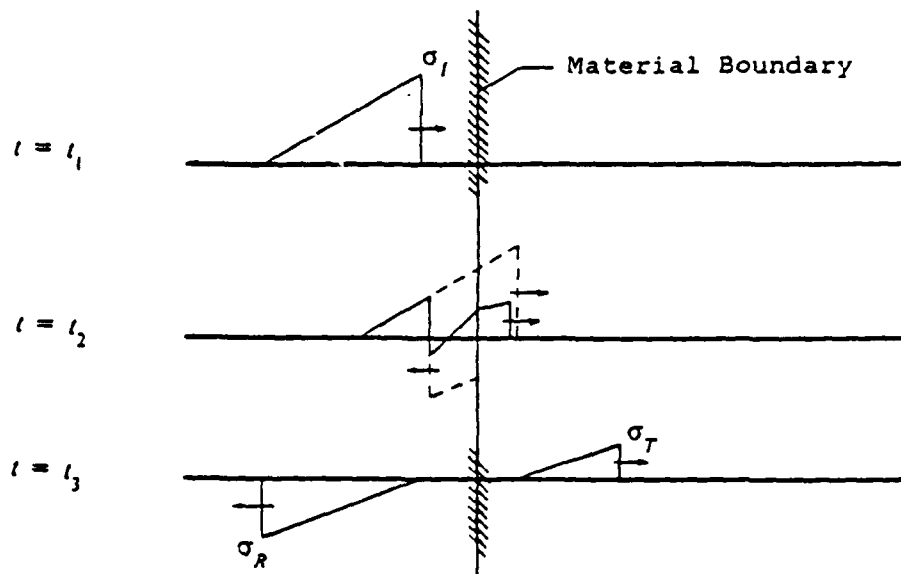


Figure 2.14. Transmission and reflection of a stress wave for $\rho_1 c_1 > \rho_2 c_2$.

address the basic concepts of the subject. For a more detailed investigation, the reader is referred to (10), (12), (17), and (27).

The velocity of stress wave propagation in an elastic medium has been previously defined by equation (2.13) as

$$c = \sqrt{\frac{E}{\rho}}$$

The velocity of a plastic stress wave is a function of the slope of the stress-strain curve and is defined (6) by

$$c_p = \left[\frac{\left(\frac{\partial \sigma}{\partial \epsilon} \right)}{\rho} \right]^{\frac{1}{2}} \quad (2.25)$$

If the material is stressed in the elastic region only,

equation (2.25) simplifies to equation (2.13) by substituting E for $\frac{\partial \sigma}{\partial \epsilon}$ in equation (2.25). A stress-strain curve for a typical elasto-plastic material is shown in Figure 2.15 along with the corresponding stress wave velocity obtained from equation (2.25). It is indicated in Figure 2.15 that, for a typical elasto-plastic material, the plastic stress wave travels at a much lower velocity than the elastic portion of the stress wave. The plastic wave front will therefore lag behind the elastic wave front.

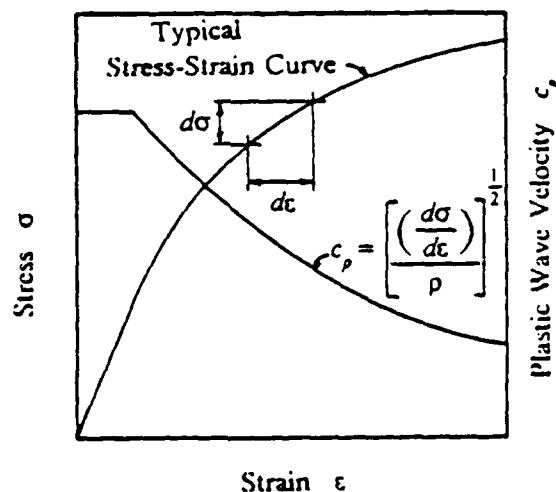


Figure 2.15. Stress-Strain Curve for a Typical Elasto-Plastic Material and Corresponding Wave Velocity.

A representation of a typical stress-strain curve for an elasto-plastic material in compression is shown in

Figure 2.16. If a high intensity shock wave, such as that shown in Figure 2.17, is applied to a material having a constitutive relation similar to that shown in Figure 2.16, the stress wave will propagate through the medium as illustrated in Figure 2.18 (10). The plastic portion of the wave propagates at a velocity less than that of the elastic portion and lags behind the elastic wave front. The wave can be separated into an unstable shock wave, a plastic wave, and an elastic wave. After the wave has traveled a sufficient distance, the unstable shock wave is reduced to a plastic wave. The plastic wave continues to lag behind the elastic wave front until it has been completely reduced to an elastic wave.

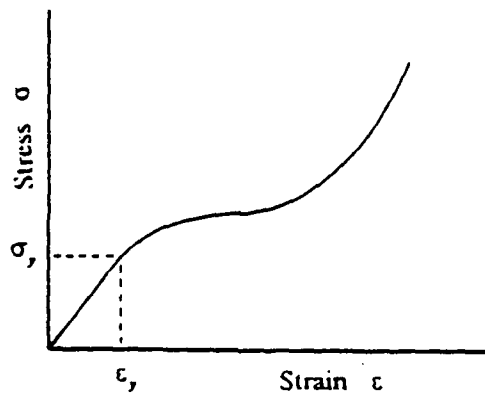


Figure 2.16. Stress-Strain Curve for an Elasto-Plastic Material in Compression.

In general, any high intensity elasto-plastic stress wave will continually change shape until it has been

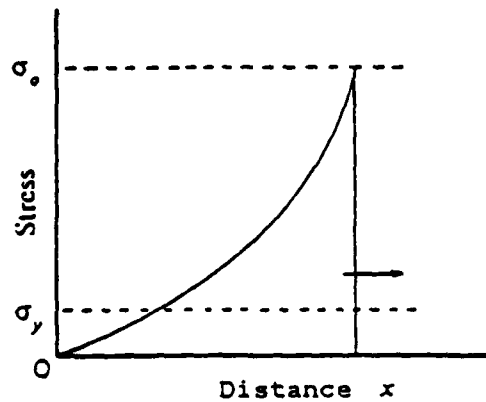


Figure 2.17. Applied High Intensity Shock Wave.

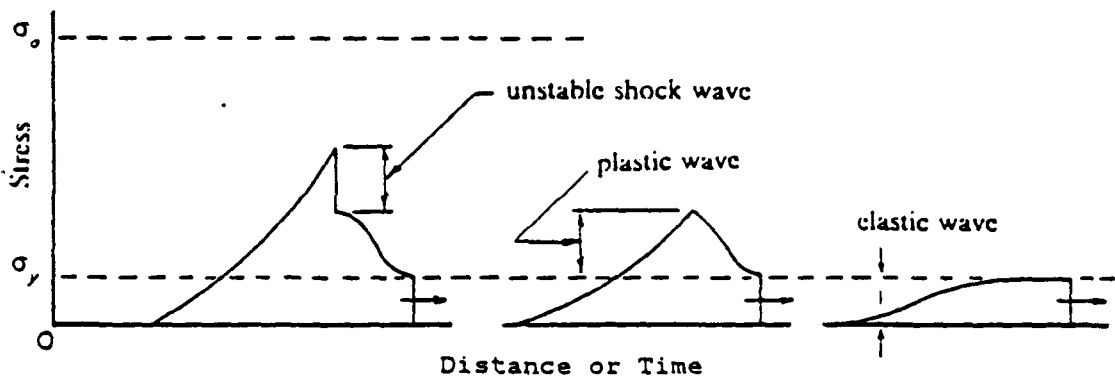


Figure 2.18. Propagation of a High Intensity Stress Wave in an Elasto-Plastic Medium.

completely reduced to an elastic wave. The stress wave is not only reduced in intensity, but is also lengthened, due to the reduced velocity of the plastic portion of the wave.

Stress Wave Propagation and Spalling

Spalling is defined as fracturing caused when a high intensity transient stress wave reflects from a free surface (19). Spalling is a result of the interference of an incident compression wave with its reflected tensile wave at a free surface. The incident triangular compression wave shown in Figure 2.19(a) is reflected as a tensile wave from the free surface as shown in Figure 2.19(b). The superposition of the incident and reflected stress waves results in a net tensile stress near the free surface. The tensile stress increases from zero at the free surface to a maximum value of σ_c some distance from the free surface. The distance from the free surface at which the net tensile stress reaches the maximum value σ_c is a function of the wavelength of the incident stress wave. The maximum possible value of tensile stress due to the superposition of the incident and reflected triangular waves is shown in Figure 2.20. The maximum tensile stress σ_c is reached at a distance of one half the wave length from the free surface.

For a rectangular incident compression wave, as shown in Figure 2.21(a), the reflection from a free surface is illustrated in Figure 2.21(b). The superposition of the incident and reflected stress waves results in an unstressed section of the medium adjacent to the free surface. However, a tensile stress of intensity σ_c

instantaneously develops at some distance from the free surface. The distance from the free surface at which the net tensile stress forms is a function of the wavelength of the incident stress wave. The maximum possible value of tensile stress due to the superposition of the incident and reflected rectangular waves is shown in Figure 2.22. The maximum tensile stress σ_o is attained at a distance of one half the wave length from the free surface. For both the rectangular and triangular wave shapes, the stress at the free surface is always zero.

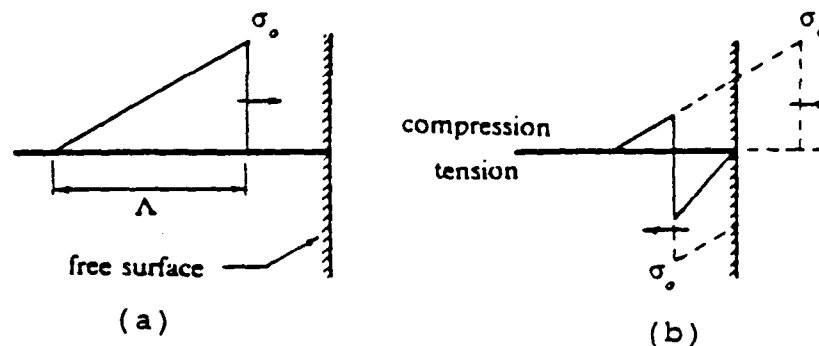


Figure 2.19. Superposition of Stresses During the Reflection of a Triangular Wave from a Free Surface.

For a medium capable of supporting the tensile stress inflicted by wave reflection, the reflected tensile wave will continue to propagate with no change in shape or intensity, and no spalling will occur. If, however, the

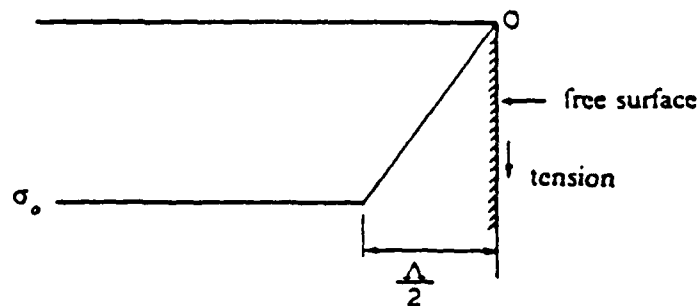


Figure 2.20. Maximum Attainable Tensile Stress During the Reflection of a Triangular Wave from a Free Surface.

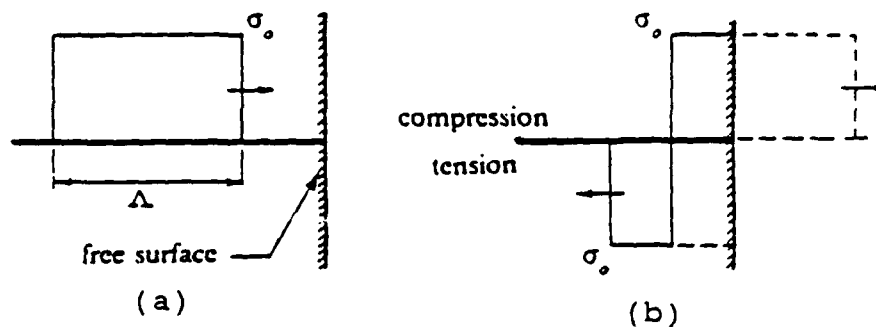


Figure 2.21. Superposition of Stresses During the Reflection of a Rectangular Wave from a Free Surface.

medium is unable to support the tensile stress, spalling will occur and propagation of the reflected stress wave will be altered. The occurrence of spalling and the location of the fractures are dependent upon three factors: 1) the resistance of the material to fracture;

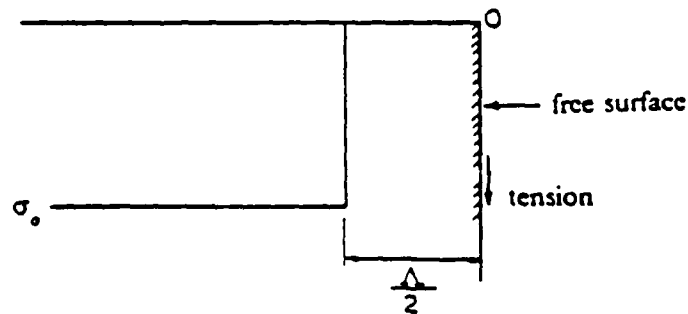


Figure 2.22. Maximum Attainable Tensile Stress During the Reflection of a Rectangular Wave from a Free Surface.

2) the intensity of the tensile stress; and 3) the shape of the stress wave (19).

The stress level at which fracturing occurs in a material is called the critical normal fracture strength. In general, the critical normal fracture strength is considerably higher than the static tensile strength of the material. However, it is difficult to experimentally determine the exact state of stress at the instant of fracture because of the instantaneous stress reversal at the point of fracture (19).

Spalling occurs when the critical normal fracture strength of the material is reached. Multiple spalling is the occurrence of spall in layers parallel to the free surface. Multiple spalling occurs when the stress level is greater than twice the critical normal fracture

strength. The occurrence of a multiple spall caused by an incident compression wave is shown in Figure 2.23. The tensile stress resulting from the superposition of the incident and reflected waves increases until the fracture strength is attained. Once the fracture strength is exceeded, the material spalls, creating a second free surface. If the remaining portion of the incident wave is greater than the fracture strength of the material, then a second spall will occur due to the reflection from the newly created free surface. This process continues until the stress wave no longer exceeds the critical normal fracture strength of the material.

The thickness of the spalled layer is affected by the stress wave profile, as indicated in Figure 2.23. A rectangular stress wave causes thicker spall than a triangular stress wave. This is a result of the shape of the maximum net tensile stress distribution formed by the superposition of the incident and reflected stress waves (refer to Figures 2.20 and 2.22). The net tensile stress resulting from a triangular stress wave builds immediately, thus restricting spall close to the vicinity of the free surface. However, the net tensile stress resulting from a rectangular stress wave remains zero for a distance equal to one half the length of the incident wave before reaching its maximum value, thus causing thicker spall.

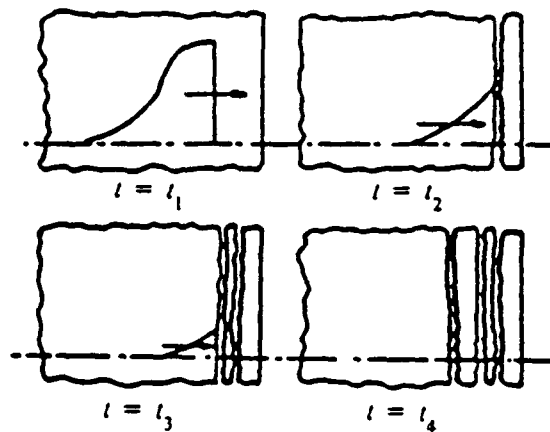


Figure 2.23. Multiple Spalling Caused by a Single Incident Compression Wave.

The particle velocity is linearly related to stress by equation (2.15). Also, the superposition of particle velocities for compression and tension waves traveling in opposite directions is additive. Therefore, the greater the stress level of the incident wave, the greater the velocity at which the spall is propagated away from the free surface. In multiple spalls, caused by a stress wave such as that shown in Figure 2.23, the first spall will have the greatest velocity, and each subsequent spall will have a decreased velocity due to the reduced intensity of the incident stress wave.

III. LAYERED MEDIA FOR PROTECTIVE MILITARY SHELTERS

Protective military shelters are designed to house personnel, vital functions, and equipment of value. As a result, the survivability of the structure is critical and takes precedence over its appearance. The structures are invariably massive, constructed primarily of concrete and soil. Damage to protective shelters from conventional (non-nuclear) weapons occurs as a result of one or more of the following effects: penetration, fragmentation, ground shock, and blast (9). Penetration is a consideration only in the case of a direct hit. Ground shock is a consideration only in the case of a near miss. Fragmentation and blast are considerations in both cases. This study considers only the effects of the blast.

Typical Military Protective Shelters

Typical aboveground and underground protective shelters, designed to survive a near miss of a conventional weapon, are shown in Figures 3.1 and 3.2, respectively. The protective shelter is typically constructed of thick, monolithic concrete walls and roof. This practice is considered necessary in order to resist

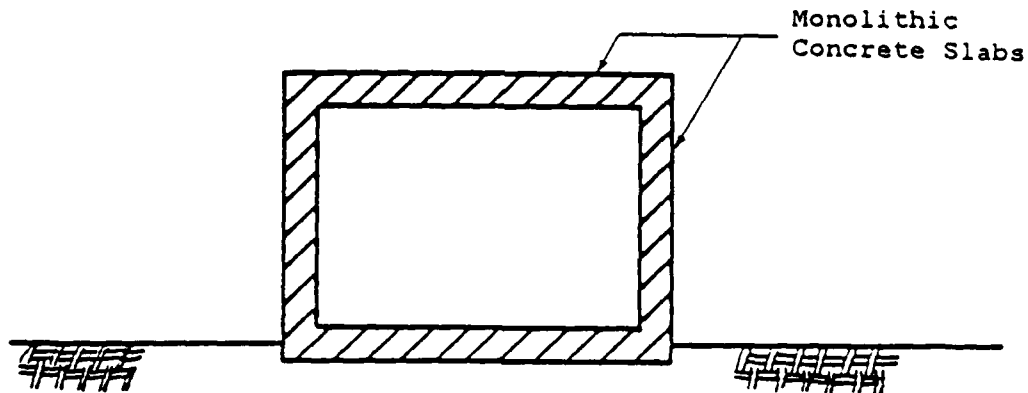


Figure 3.1. Typical Aboveground Protective Shelter.

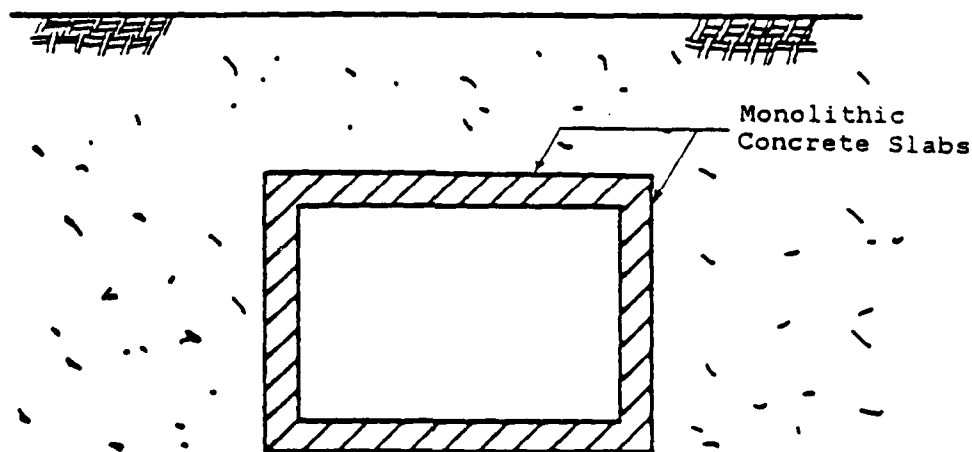


Figure 3.2. Typical Underground Protective Shelter.

the blast pressure and prevent interior spalling of the concrete walls.

A cross section of a typical protective shelter wall is shown in Figure 3.3. When the shelter wall is subject to a blast, the compressive longitudinal blast wave

contacts the exterior surface of the wall and propagates through the monolithic wall with little or no change in shape or intensity. When the compressive stress wave reaches the interior face of the wall, it is reflected at full stress level as a tension wave. The concrete will spall at the interior face of the wall if the intensity of the reflected tension wave is greater than the critical normal fracture strength of the concrete. When the stress wave is intense, the spalled concrete fragments are hurled away from the wall at high velocities, posing a potentially dangerous threat to personnel and equipment within the shelter.

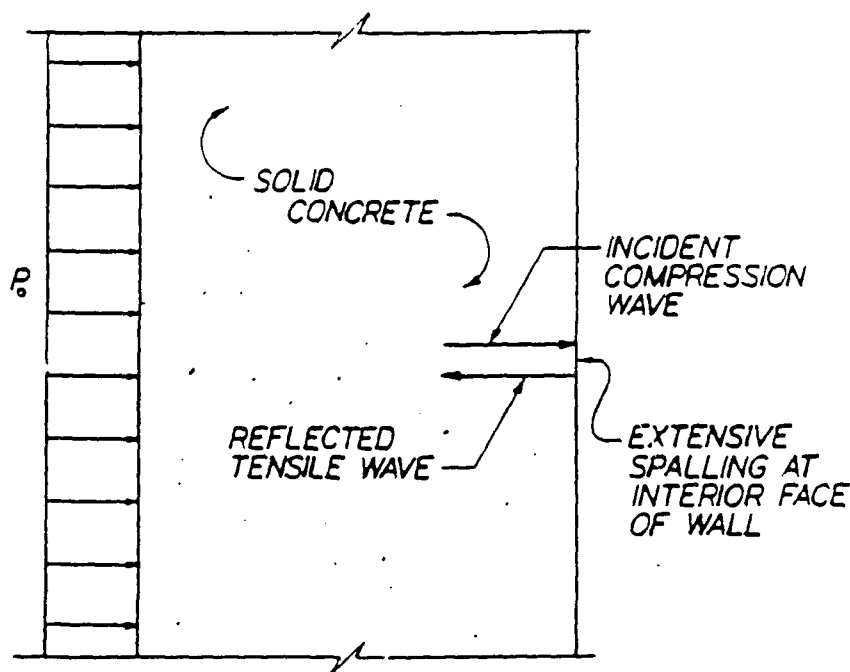


Figure 3.3. Blast Wave Propagation in Monolithic Wall of a Typical Protective Shelter.

Current procedures to reduce or eliminate spall in protective shelters include the construction of earth berms against the exterior face of the shelter walls (Figure 3.4(a)), the installation of steel spall plates on the interior face of the shelter walls (Figure 3.4(b)), and the use of thicker concrete walls (Figure 3.4(c)) (7). Of these methods, earth berms have proven to be the most successful, while the use of thicker walls has been the least successful.

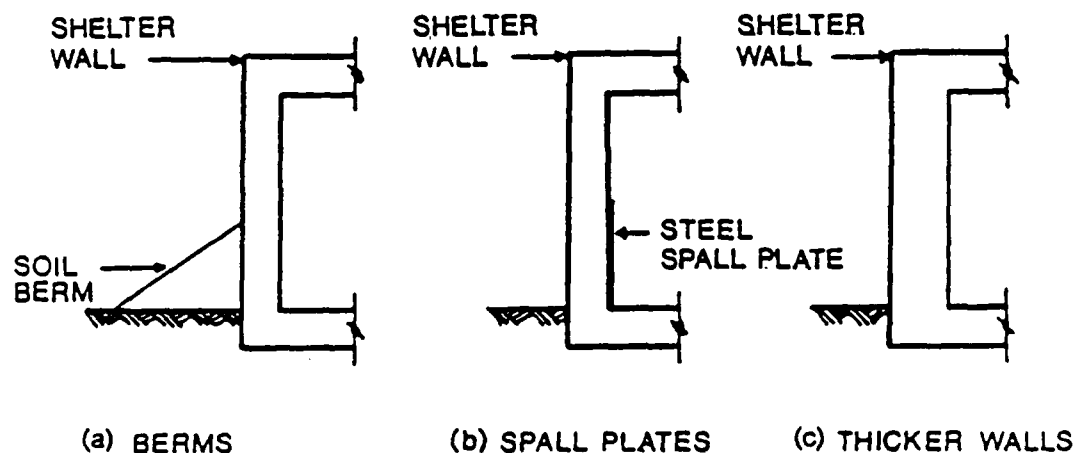


Figure 3.4. Current Procedures to Reduce Spall in Protective Shelters.

Layered Media Applied to Protective Military Shelters

It was shown in Chapter II that the propagation of stress waves in solid media is altered at the boundaries between dissimilar materials. Therefore, it is logical

to assume that layered media can be utilized to alter the stress wave propagation in the walls of a protective structure. The use of layered media to mitigate the incident blast wave, and therefore eliminate spall, in protective shelters is investigated in this study. The layered systems considered consist of an exterior layer of concrete or sand, an absorption layer, and an interior layer of concrete.

The transmission ratio of a three-layered system is determined by two consecutive applications of equation (2.22). Equation (2.22) is first applied to determine the stress wave transmitted from the first layer to the second layer. The stress transmitted to the second layer is the incident stress for the third layer. Equation (2.22) is applied a second time to obtain the stress transmitted to the third layer. Two consecutive applications of equation (2.22) yields

$$\frac{\sigma_T}{\sigma_I} = \left[\frac{2 \rho_2 c_2}{\rho_1 c_1 + \rho_2 c_2} \right] \left[\frac{2 \rho_3 c_3}{\rho_2 c_2 + \rho_3 c_3} \right] \quad (3.1)$$

where the subscripts 1, 2, and 3 refer to the first, second, and third layers, respectively. For a layered system in which the first and third layers consist of the same material (concrete) and the second layer is an absorption layer, equation (3.1) becomes

$$\frac{\sigma_T}{\sigma_I} = \frac{4 (\rho_c c_c) (\rho_a c_a)}{[(\rho_c c_c) + (\rho_a c_a)]^2} \quad (3.2)$$

where the subscripts c and a represent the concrete and absorption layers, respectively. A BASIC computer program was developed to calculate the transmission ratio for layered systems. The program listing and sample output is presented in Appendix A.

Equation (3.2) is depicted graphically in Figure 3.5. The transmission ratio for the system, $\frac{\sigma_r}{\sigma_i}$, is plotted against the ratio of impedances of the concrete and absorption layers, $\frac{\rho_a c_a}{\rho_c c_c}$. If the absorption layer has the same impedance as the concrete layer, then the transmission ratio is equal to one, and no reflection occurs at the boundary between layers. As the impedance ratio diverges from one in either direction, the transmission ratio of the system decreases. An impedance ratio less than one is necessary if the blast wave is to be significantly reduced, as is illustrated in Figure 3.5.

The blast wave propagation through a layered system with an impedance ratio less than one is illustrated in Figure 3.6. The incident compressive longitudinal blast wave propagates through the exterior layer of concrete until the first material boundary is encountered. Upon reaching the boundary between the exterior concrete and the absorption layer, a portion of the blast wave is transmitted to the absorption layer. The remainder of the blast wave is reflected back through the exterior layer of

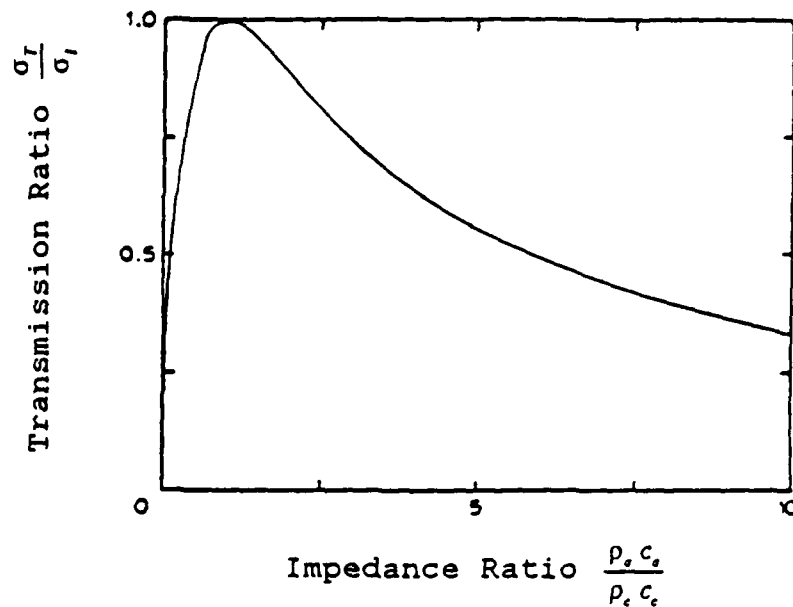


Figure 3.5. Transmission Ratio vs. the Impedance Ratio for the Three Layered System.

concrete as a tensile wave. The transmitted compression wave propagates through the absorption layer until it encounters the interior layer of concrete. At the boundary between the absorption layer and the interior layer of concrete, the compression wave is reflected back through the absorption layer as a compression wave of diminished intensity. Because the compression wave is reflected with no change in phase, the stress wave transmitted to the interior layer of concrete is greater than the reflected wave in the absorption layer. However, the stress wave transmitted to the interior layer of concrete is significantly less than the initial incident blast wave which impinged upon the exterior layer of the

system. If the stress wave transmitted to the interior layer of concrete is less than the critical normal fracture strength of the concrete, then no spalling occurs.

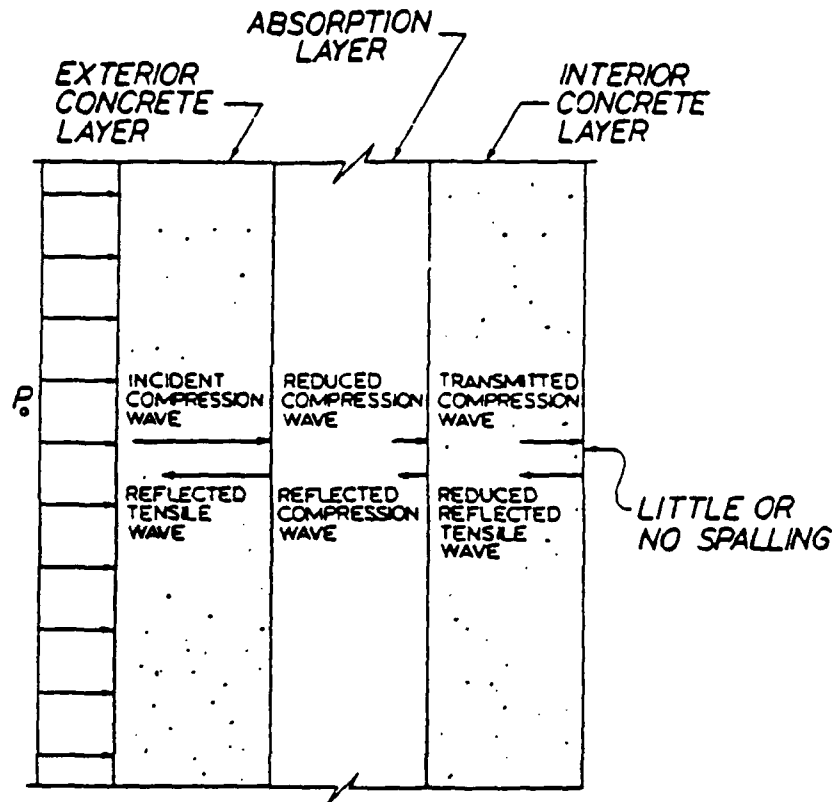


Figure 3.6. Blast Wave Propagation in a Layered System Consisting of an Exterior Concrete Layer, an Absorption Layer, and an Interior Concrete Layer for $(\rho_e c_e) < (\rho_i c_i)$.

Previous research (14,23,24) has shown polystyrene to be extremely effective as an absorption layer. It exhibits very low impedance characteristics and is available in large sheets which afford expedient

construction. For these reasons, polystyrene was selected for the absorption layer in this study.

The layered systems investigated include a concrete-polystyrene-concrete (CPC) system, a sand-polystyrene-concrete (SPC) system, and a sand-polystyrene-concrete-polystyrene-concrete (SPCPC) system. The static, linear properties of the materials are given in Table 3.1. The elastic wave speeds and material impedances for these same materials are listed in Table 3.2.

Table 3.1. Static Linear Material Properties.

	Strength E (psi)	Mass Density ρ (10^{-6}) $\frac{\text{lb} \cdot \text{sec}^2}{\text{in}^4}$	Poisson's Ratio ν
4000 psi Concrete	3605000	217.164	.18
110 pcf Sand	80000	164.745	.25
5.744 pcf Polystyrene	2100	8.604	.15

The intensity of the blast wave is capable of stressing the shelter into the inelastic range. This nonlinearity is addressed to some extent. It is assumed that the concrete behaves linearly at all times. Although this is not the case in the actual structure, the assumption of linearity does not significantly affect the

Table 3.2. Elastic Wave Speeds and Impedances.

	Elastic Wave Speed c in/sec	Impedance ρc $\frac{\text{lb-sec}}{\text{in}^3}$
4000 psi Concrete	128842.4	28.0
110 pcf Sand	22036.3	3.63
5.744 pcf Polystyrene	15622.8	.134

overall behavior of the layered system. Both linear and nonlinear material models are employed for the sand and polystyrene. A linear elastic-perfectly plastic constitutive law, similar to that shown in Figure 3.7, is used to model the nonlinear behavior of the sand and polystyrene. The parameters for the nonlinear sand and polystyrene models are presented in Table 3.3.

The material properties given in Tables 3.1 and 3.3 represent the material behavior under static loading conditions. A protective shelter subjected to a blast loading experiences a high intensity, short duration load at a very rapid rate of application. Materials are often able to tolerate increased stress levels when loaded at a high rate. Laboratory tests performed on concrete specimens under high rates of loading have demonstrated that the dynamic secant modulus, ultimate strength, and tensile strength greatly exceed the corresponding

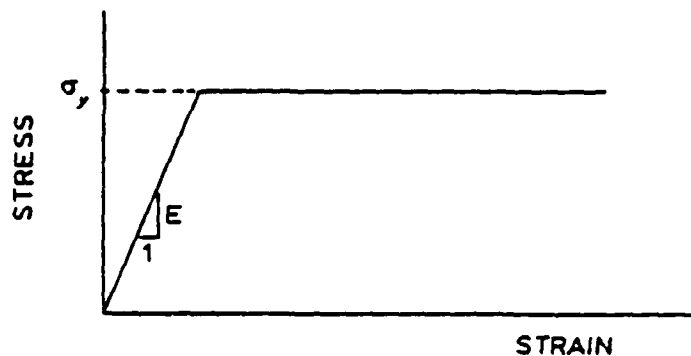


Figure 3.7. Linear Elastic-Perfectly Plastic Constitutive Law Used to Model Nonlinear Behavior.

Table 3.3. Static Nonlinear Material Properties.

	Strength E (psi)	Yield Stress σ_y (psi)	Mass Density ρ (10^{-6}) $\frac{\text{lb} \cdot \text{sec}^2}{\text{in}^4}$	Poisson's Ratio ν
Unconfined Sand	80000	20	164.745	.25
5.744 pcf Polystyrene	2100	55	8.604	.15

strengths determined from static tests (9,15,16,18).

Under dynamic loading, the compressive strength of concrete can increase by as much as a factor of .1.8, and the tensile strength can increase by as much as a factor of 2.2.

Tests on polystyrene at high rates of loading have indicated that the dynamic ultimate strength of polystyrene is much greater than the static strength.

Polystyrene subjected to a dynamic loading can withstand a stress as much as 1.6 times that of the static ultimate strength (11). Soils also exhibit a tendency to withstand higher loads under dynamic loading conditions. The increase in strength is a function of moisture content, porosity, and pre-existing static stress. However, due to the uncertainties involved in accurately assessing the high strain rate effects on material strength, the use of the dynamic material properties in this study is limited.

Concrete-Polystyrene-Concrete System

The concrete-polystyrene-concrete (CPC) system is intended to be used for an aboveground protective shelter. A typical cross section of the CPC system is shown in Figure 3.8. The exterior concrete layer is intended to partially withstand blast effects and to stop any incident fragments. The polystyrene absorption layer causes a significant portion of the blast wave to be reflected back through the exterior concrete layer. The polystyrene layer also traps any concrete fragments spalled from the exterior layer. The interior layer of concrete resists that portion of the stress wave which propagates through the polystyrene layer.

The aboveground CPC system may be constructed by forming the concrete walls against sheets of polystyrene. A possible construction procedure consists of casting the interior concrete wall against polystyrene sheets backed

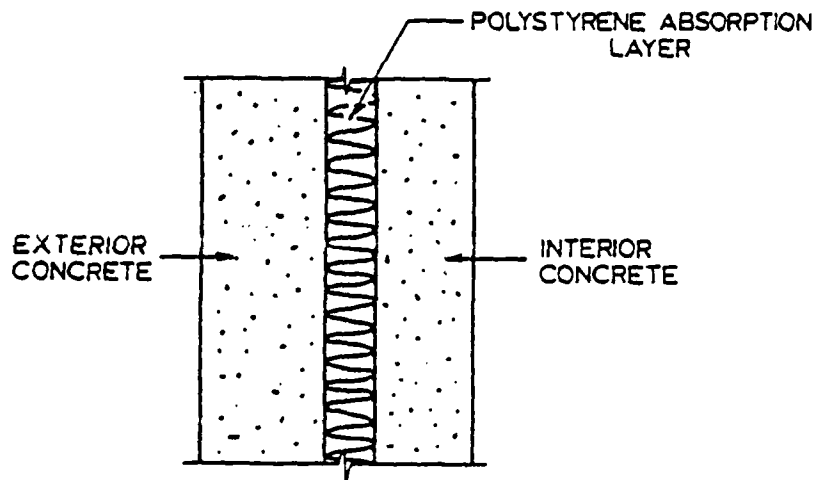


Figure 3.8. Cross Section of the Concrete-Polystyrene-Concrete (CPC) Layered System.

by plywood or metal forms. After the forms are removed, the outside surface of the exterior wall is formed, and the exterior layer of concrete is placed.

Sand-Polystyrene-Concrete System

The sand-polystyrene-concrete (SPC) system is intended to be used for both aboveground and underground protective shelters. A typical cross section of the SPC system is shown in Figure 3.9. The layer of sand is intended to partially withstand the blast effects and to stop any incident fragments. The polystyrene absorption layer reflects a portion of the blast wave back through the sand and reduces the intensity of the blast which wave reaches the interior layer of concrete. The interior layer of concrete resists the remaining portion of the blast.

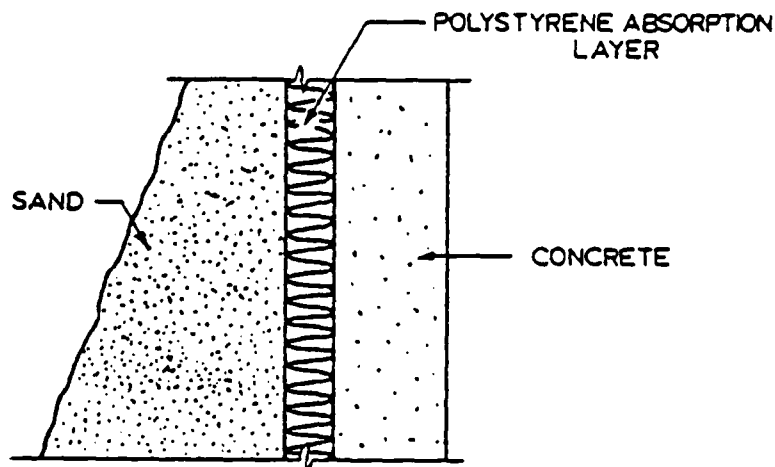


Figure 3.9. Cross Section of the Sand-Polystyrene-Concrete (SPC) Layered System.

Construction of the aboveground SPC system consists of placing sheets of polystyrene against the walls of an existing monolithic concrete shelter. A sand berm is then constructed against the polystyrene sheets to complete the layered system. A typical aboveground SPC system is depicted in Figure 3.10.

Construction of the underground SPC system consists of placing sheets of polystyrene against the walls and roof of a monolithic concrete shelter. The layered system is completed by backfilling against the polystyrene sheets with sand. A typical underground SPC system is illustrated in Figure 3.11.

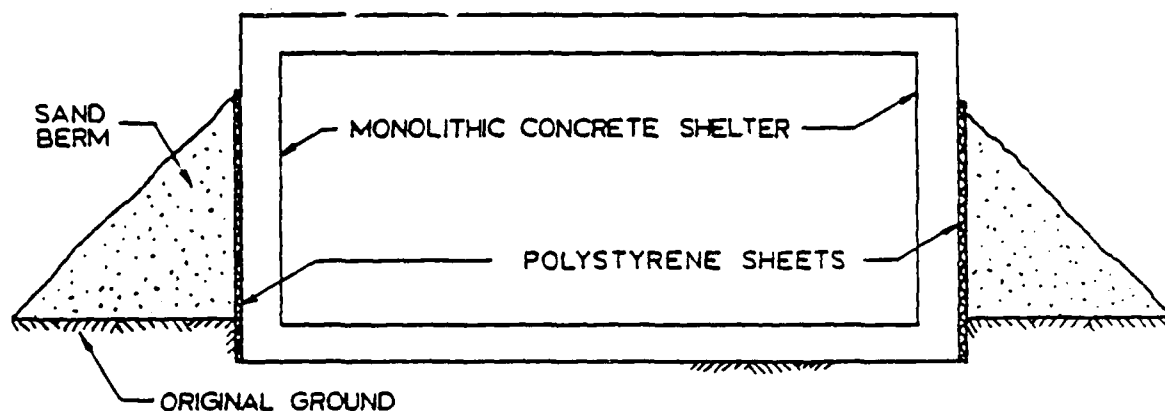


Figure 3.10. Typical Aboveground SPC Layered System.

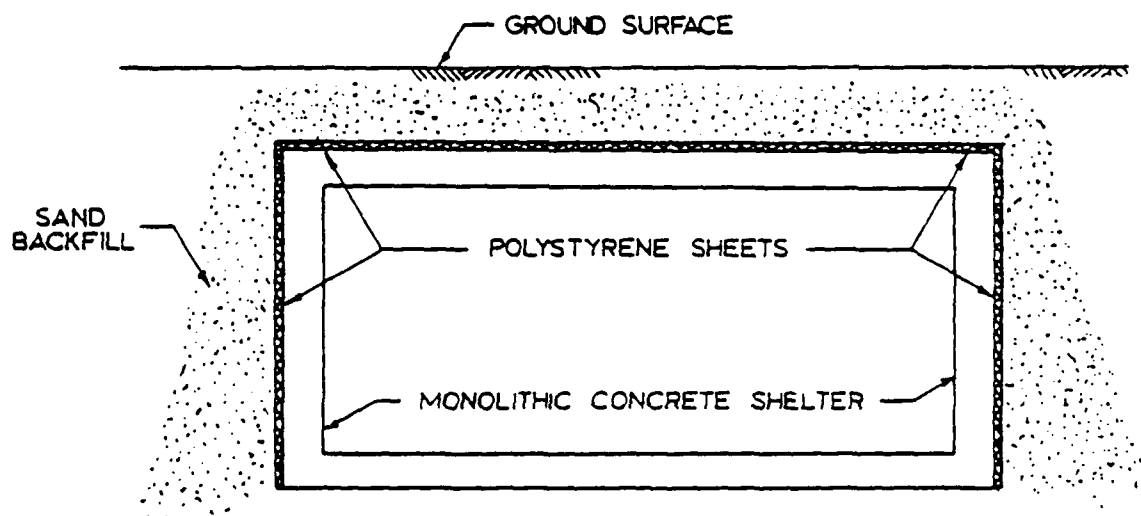


Figure 3.11. Typical Underground SPC Layered System.

Sand-Polystyrene-Concrete-Polystyrene-Concrete System

The sand-polystyrene-concrete-polystyrene-concrete (SPCPC) layered system is intended for use as an aboveground shelter when very high intensity blasts are expected.

A typical cross section of the SPCPC system is shown in Figure 3.12. The sand layer partially withstands the effects of the blast wave and stops any incident fragments. The first polystyrene layer reflects a portion of the blast wave back through the sand, and reduces the blast wave which reaches the exterior layer of concrete. The remaining concrete-polystyrene-concrete layers resist the transmitted blast wave as described in the section on the CPC layered system.

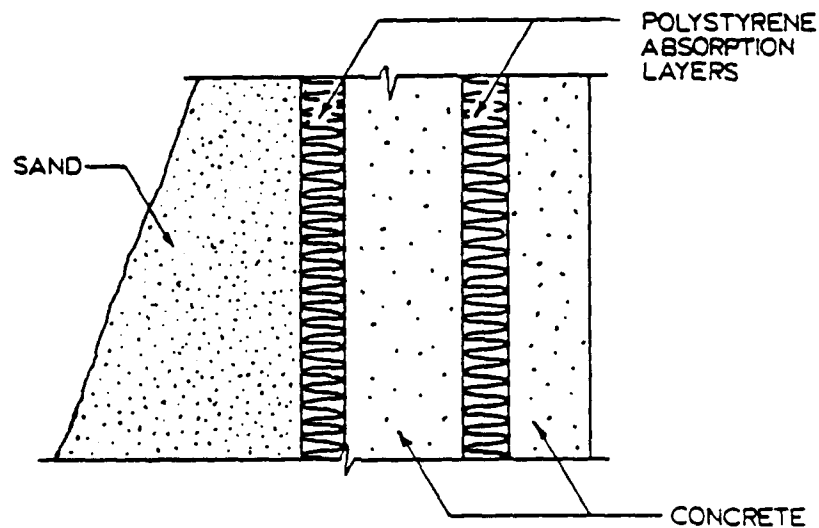


Figure 3.12. Cross Section of the SPCPC Layered System.

Construction of the aboveground SPCPC system consists of adding the exterior polystyrene and soil layers to a CPC system. After the CPC system has been constructed and the exterior forms removed, sheets of polystyrene are placed against the exterior concrete walls. A soil berm

is then constructed against the polystyrene sheets, completing the layered system.

Protective Shelter Loading Condition

An explosion is a violent release of energy from within a confined space. The explosion causes a sudden pressure increase in the surrounding medium, resulting in the formation of a blast wave. The blast wave travels away from the point of detonation at a velocity in excess of the sonic velocity of the surrounding medium. The velocity diminishes with distance, but remains in excess of the sonic velocity. The variation in velocity leads to the rapid formation of a shock front, as illustrated in Figure 3.13 (9). The shock front decays with distance from the point of detonation, as illustrated in Figure 3.14, and eventually drops below atmospheric pressure and becomes negative (9).

The free-field time history of the blast wave at a specified distance from the point of detonation is depicted in Figure 3.15. The shock front arrives at time t_1 with a peak pressure of P_{10} . The pressure then decays to the ambient pressure at time t_2 , thus ending the positive phase of the blast. The pressure then becomes negative, beginning the negative phase of the blast. The negative phase lasts longer than the positive phase, but its

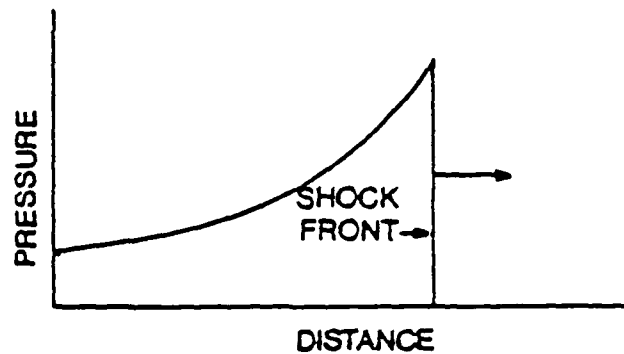


Figure 3.13. Formation of a shock front (9).

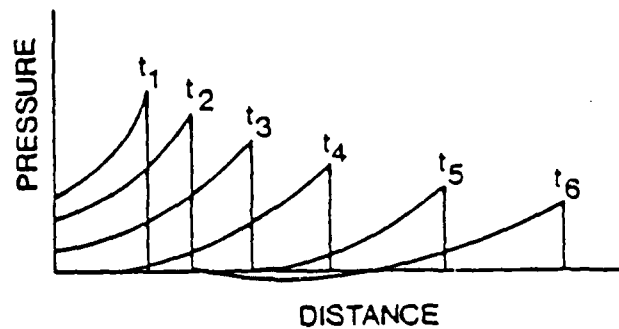


Figure 3.14. Variation of a shock wave with distance at selected times (13).

intensity is small in comparison with the positive phase and is usually neglected.

When the blast wave comes in contact with a rigid surface, such as the wall of a protective shelter, a reflected pressure in excess of the incident pressure is immediately formed. A typical reflected pressure-time

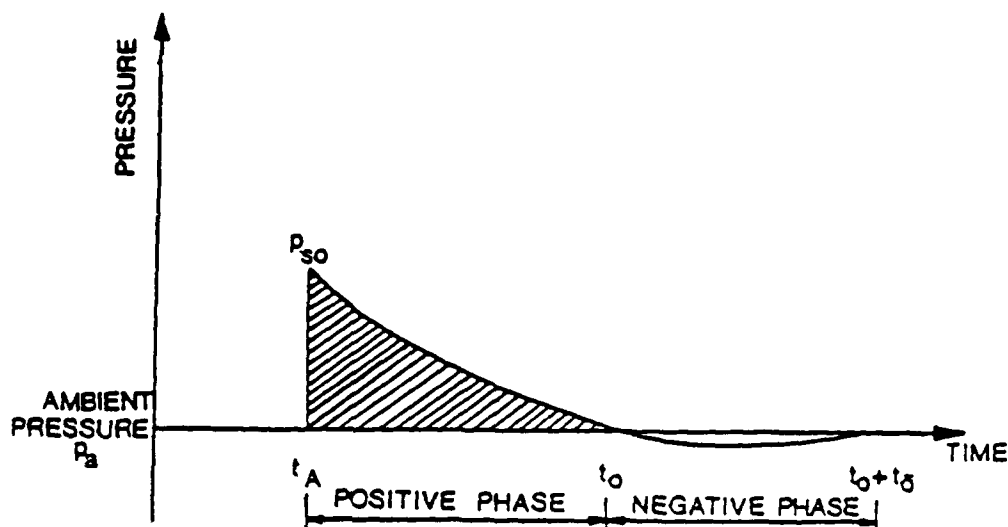


Figure 3.15. Free-field pressure-time history of a given distance from the point of detonation (9).

history is shown in Figure 3.16. The incident pressure P_i causes the reflected pressure P_r to develop. The magnitude of the reflected pressure is a function of the incident pressure and the angle formed between the wave front and the rigid surface.

The magnitude and distribution of the blast pressure on a structure are dependent on the type of explosive, the weight of the explosive, the location of the explosion with respect to the structure, the interaction of the shock front with the ground and surrounding obstructions, and the interaction of the shock front with the structure itself (9). A typical reflected blast pressure-time history measured in half-scale field tests (7) is shown in Figure 3.17. The pressure-time history can be represented by the simple triangular pulse shown in Figure 3.18, thus

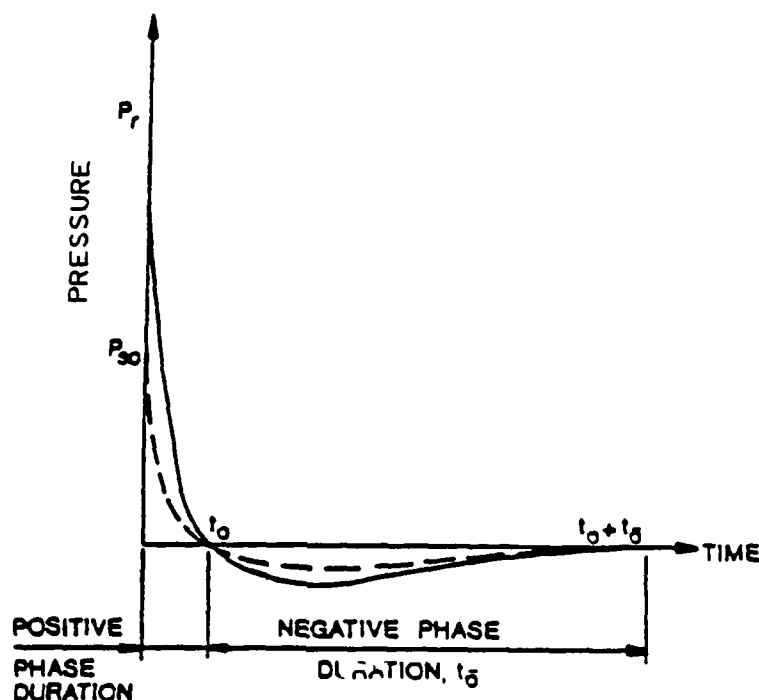


Figure 3.16. Typical reflected pressure-time history (9).

neglecting the short rise time and the negative phase of the blast. The pressure time histories used in this investigation are illustrated in Figures 3.18 through 3.20. A triangular pulse of duration $t_d = 50 \mu \text{ sec}$ is depicted in Figure 3.18 and is used to investigate the response of the layered systems to a short duration blast wave. A rectangular pulse of the same duration, shown in Figure 3.19, is used to model the blast condition in order that the results can be more readily interpreted. A longer triangular pulse of $t_d = 850 \mu \text{ sec}$, illustrated in Figure 3.20, is used to approximate the actual blast durations measured in reference (7).

The magnitude of the blast loading is varied. A peak pressure of 1,000 psi is used in the linear models in

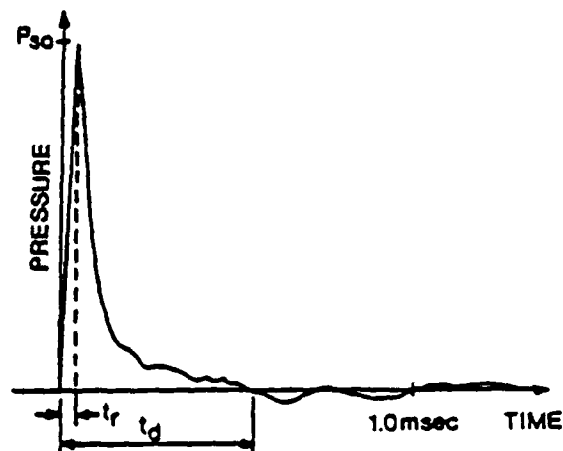


Figure 3.17. Typical reflected pressure-time history measured in tests in reference (7).

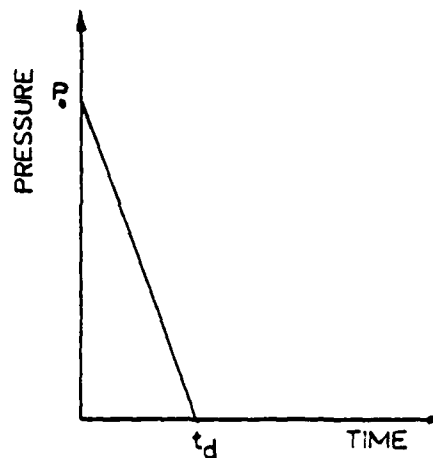


Figure 3.18. Simplified triangular pressure-time history used in the present analysis.

order to facilitate interpretation of the results. In the linear analyses, the resultant stresses can be scaled to any blast load intensity. A peak pressure of 10,000 psi is used in the nonlinear analysis of the layered systems. The 10,000 psi pressure is representative of that induced by currently employed conventional weaponry.

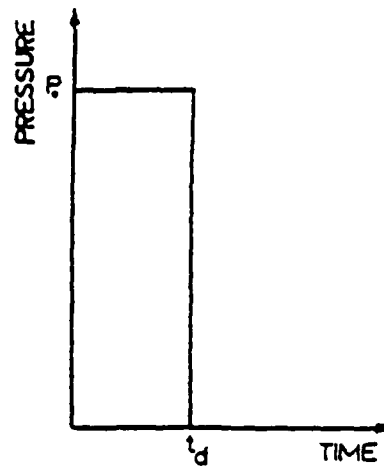


Figure 3.19. Rectangular pressure-time history used in the present analysis.

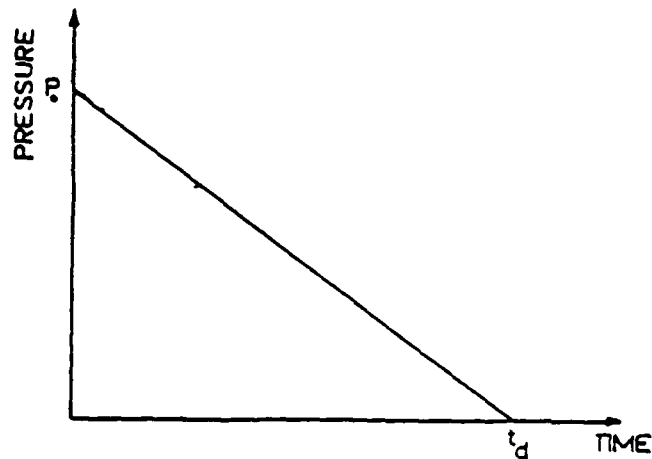


Figure 3.20. Approximation to measured pressure-time history used in the present analysis.

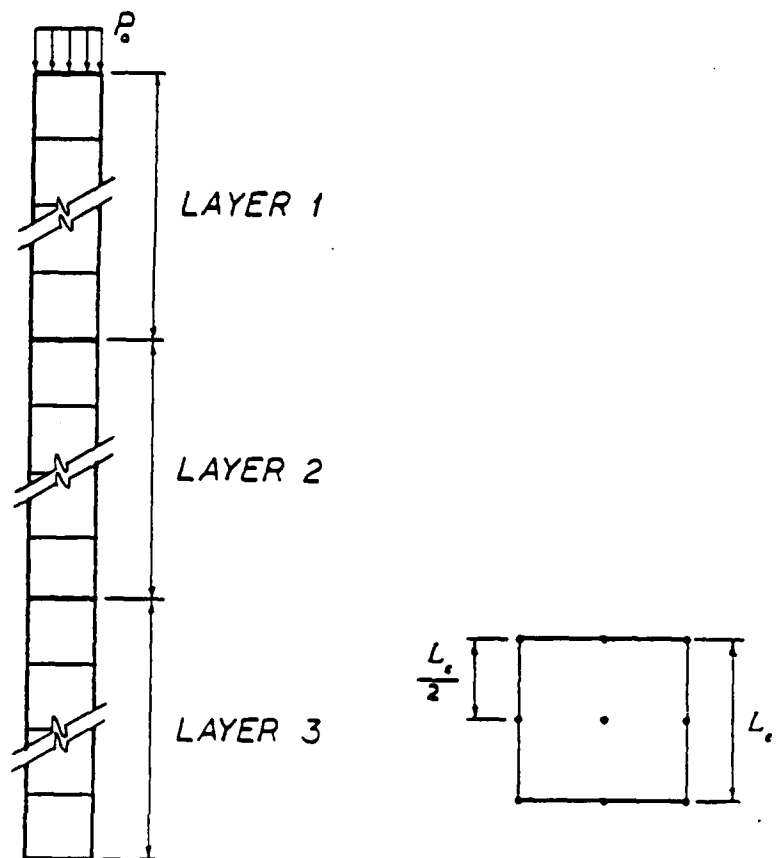
IV. ANALYSIS OF STRESS WAVE PROPAGATION BY THE FINITE ELEMENT METHOD

A comprehensive finite element method (FEM) investigation of stress wave propagation in the layered systems described in Section III was conducted. The FEM study was performed through implementation of the ADINA (1,2,3,4) computer programs. The computer analyses were executed on the Auburn University IBM 3083 academic mainframe and the Alabama Supercomputer Network Cray X-MP/24.

General Description of the Finite Element Models

Any FEM model used in a wave propagation study must consist of a very fine mesh in order to produce accurate results. For this reason, only a very small cross section of each layered system is analyzed. Each FEM model consists of a single column of two-dimensional, nine-node isoparametric finite elements. A typical mesh is illustrated in Figure 4.1(a) and a typical nine-node isoparametric finite element is depicted in Figure 4.1(b).

The major difference between a wave propagation problem and a structural dynamics problem is the number of



(a) Typical FEM Mesh (b) Typical FEM Element

Figure 4.1. Typical Finite Element Mesh Consisting of Nine-Node Isoparametric Elements.

modes that significantly contribute to the response of the structure. In most structural dynamics problems, only a few lower frequencies are excited. Therefore, only these lower modes contribute significantly to the response of the system. In a wave propagation problem, a large number of frequencies are excited. Therefore, a large number of modes significantly contributes to the structural response. For this reason, modal analyses generally do not yield cost effective, accurate results, and a direct

numerical integration procedure must be utilized in the wave propagation analysis.

In the present study, the Newmark method of implicit time integration and a consistent mass matrix formulation are employed. The nonlinear equations are solved with the BFGS matrix update equilibrium iteration method with line searches. A modified Newton equilibrium iteration method is used in several instances to corroborate the results obtained with BFGS method.

The time step selected for temporal integration in a wave propagation problem is critical to the accuracy and stability of the solution. Since the Newmark method is unconditionally stable, selection of the time step can be based entirely upon accuracy considerations. In a wave propagation problem, the maximum time step is related to wave speed in the material and element size. The maximum time step is selected so that the stress wave propagates the distance between element integration points within that time increment. For the nine-noded element depicted in Figure 4.1(b), the maximum time step is defined by

$$(\Delta t)_{\max} = \frac{L_e/2}{c} \quad (4.1)$$

where L_e is the length of an element in the direction of wave propagation, and c is the velocity of wave propagation. It has been determined from previous experience (24) that a time step of

$$\Delta t \leq \frac{1}{3}(\Delta t)_{\max} \quad (4.2)$$

yields accurate results.

The investigation of stress wave propagation in a nonlinear material by the finite element method requires a very fine discretization. Due to the prohibitive computational cost required for the analysis of a completely nonlinear layered system, models consisting only of a single nonlinear material layer are investigated. However, the results of the nonlinear single layer models are used to predict the transmission ratios for the completely nonlinear layered systems, as described in Chapter V.

Linear Concrete Model

A single layer concrete model is investigated to determine the discretization necessary to produce accurate results. The discretization is considered adequate when the incident wave shape is retained as the stress wave propagates through the FEM model. This model is also used as a control to verify that the FEM analysis correctly predicts the stress wave propagation and reflection characteristics of an elastic medium. A typical mesh for the single layer concrete model is illustrated in Figure 4.2. The material properties for the concrete were previously presented in Table 3.1.

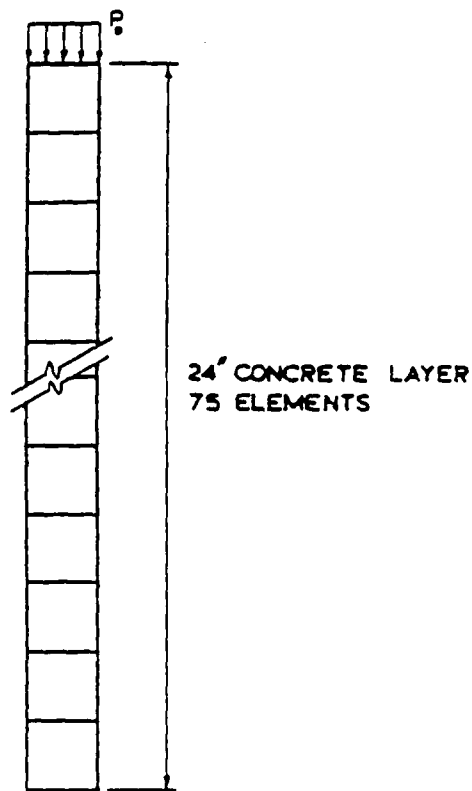


Figure 4.2. Typical Finite Element Mesh for the Linear Concrete Model.

Nonlinear Concrete Model

A nonlinear, single layer concrete FEM model is analyzed to verify that the wave propagation properties of the layered systems are not significantly altered by the assumption of linear behavior of the concrete. A linearly elastic-perfectly plastic constitutive law, such as that illustrated in Figure 3.7, is used to approximate the nonlinearity. The nonlinear model is investigated using both the static and dynamic material properties of concrete. The dynamic strength is taken as 1.6 times the static strength (15,16,18). The static and dynamic nonlinear concrete parameters are presented in Table 4.1.

Table 4.1. Nonlinear Concrete Parameters.

	Strength E (psi)	Yield Stress σ_y (psi)	Mass Density ρ (10^{-6}) $\frac{\text{lb-sec}^2}{\text{in}^4}$	Poisson's Ratio ν
4000 psi Concrete (static)	3605000	4000	217.164	.18
4000 psi Concrete (dynamic)	4560000	6400	217.164	.18

The FEM model considered is a 16" long column comprised of 200 elements (Figure 4.3). Several different wave types are examined in order to ascertain the effects of the nonlinearity upon wave shape and wave duration. The propagation of a 50 μ sec short duration triangular stress wave, an 850 μ sec long duration triangular stress wave, and a 50 μ sec rectangular stress wave are investigated. Stress wave intensities of 7,500 and 10,000 psi are considered.

Nonlinear Polystyrene Model

A nonlinear polystyrene model is investigated in order to examine the effects of the nonlinear absorption layer upon wave propagation. A linearly elastic-perfectly plastic constitutive law, such as that illustrated in Figure 3.7, is used to approximate the nonlinearity. The nonlinear polystyrene parameters were previously presented in Table 3.3.

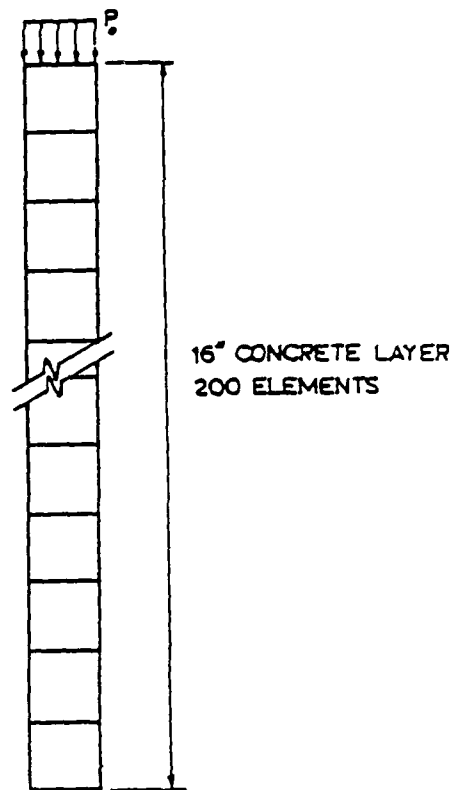


Figure 4.3. Typical Finite Element Mesh for the Nonlinear Concrete Model.

The FEM model considered is a 16" long column comprised of 200 elements (Figure 4.4). Several different wave types are investigated in order to determine the effects of the nonlinearity upon wave shape and wave duration. The propagation of a 50 μ sec short duration triangular stress wave, an 850 μ sec long duration triangular stress wave, and a 50 μ sec rectangular stress wave are investigated. Stress wave intensities of 500 and 1,000 psi are considered.

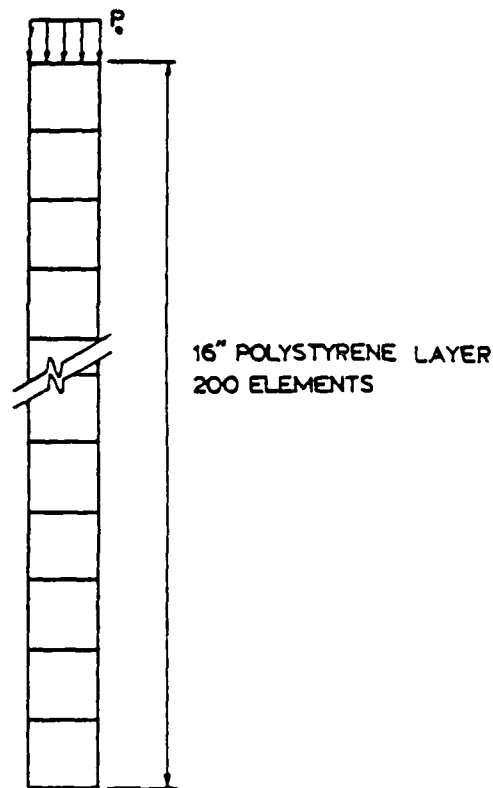


Figure 4.4. Typical Finite Element Mesh for the Nonlinear Polystyrene Model.

Nonlinear Sand Model

A nonlinear FEM sand model is analyzed in order to examine the effect of nonlinearity in the exterior sand layer upon wave propagation. A linearly elastic-perfectly plastic constitutive law, such as that illustrated in Figure 3.7, is used to approximate the nonlinearity. This constitutive law is a very crude representation for the nonlinear response of sand, but does provide some insight to assessing the effects of the nonlinearity upon wave propagation. The nonlinear sand parameters were previously presented in Table 3.3.

The FEM model considered is a 16" long column comprised of 200 elements (Figure 4.5). Several different wave types are investigated in order to determine the effects of nonlinearity upon wave shape and wave duration. The propagation of a 50 μ sec short duration triangular stress wave, an 850 μ sec long duration triangular stress wave, and a 50 μ sec rectangular stress wave are investigated. Stress wave intensities of 5,000 and 10,000 psi are considered.

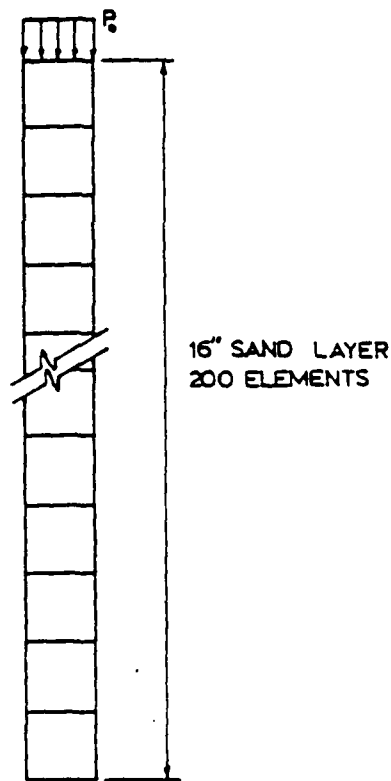


Figure 4.5. Typical Finite Element Mesh for the Nonlinear Sand Model.

Concrete - Polystyrene - Concrete System

Three concrete-polystyrene-concrete (CPC) layered systems are investigated. The length of the polystyrene absorption layer is varied from 2" to 8". The length of the exterior layer of concrete is 10", and the length of the interior layer of concrete is 8". A typical mesh for the CPC system is illustrated in Figure 4.6. The length of the polystyrene layer and the number of elements in each model are given in Table 4.2. Typical ADINA-IN and ADINA-PLOT data files for the CPC-4 FEM models are presented in Appendix B.

The CPC systems are investigated using both linear and nonlinear constitutive laws for the polystyrene absorption layer. The properties for the linear and nonlinear materials were previously presented in Tables 3.1 and 3.3, respectively. An incident stress wave having an intensity of 1,000 psi is applied to the linear systems. A 10,000 psi incident stress wave is applied to the CPC layered systems with the nonlinear polystyrene absorption layer.

Additionally, the nonlinear, single layer analyses of the concrete and polystyrene are utilized to estimate the transmission ratios of the completely nonlinear CPC layered systems. An incident stress wave of 10,000 psi is used in the nonlinear single layer analyses.

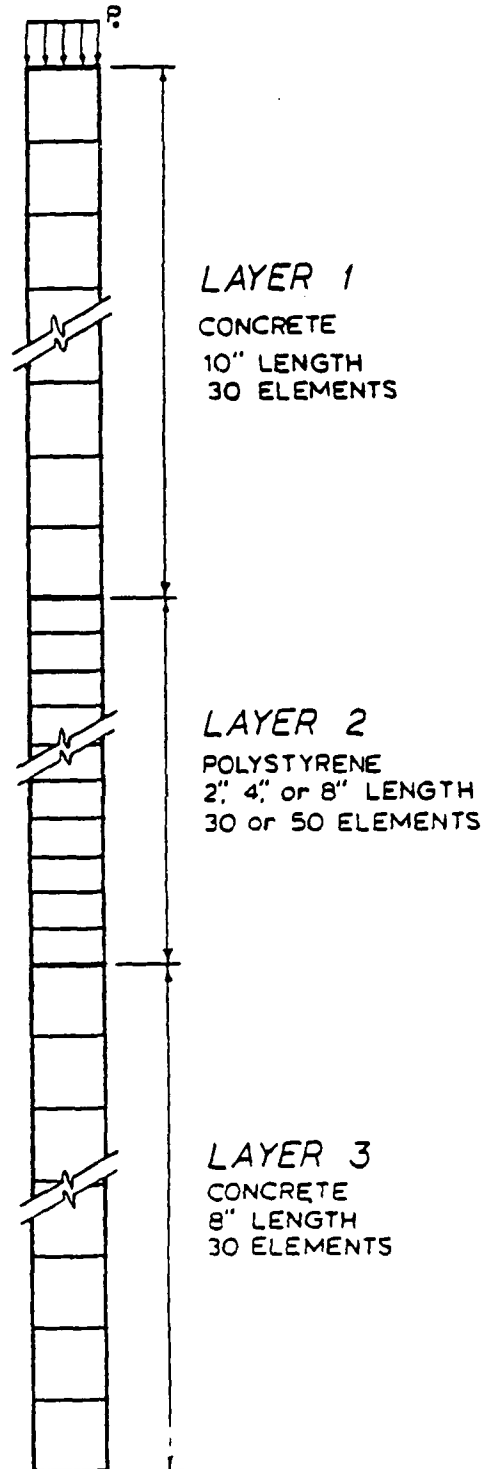


Figure 4.6. Typical Finite Element Mesh for the CPC Layered Systems.

Table 4.2. CPC Model Dimensions and Number of Elements.

Model	Total Length and No. Elements		Exterior Concrete Layer		Polystyrene Absorption Layer		Interior Concrete Layer	
	L	no. el.	L_1	no. el.	L_2	no. el.	L_3	no. el.
CPC-2	20"	90	10"	30	2"	30	8"	30
CPC-4	22"	90	10"	30	4"	30	8"	30
CPC-8	26"	110	10"	30	8"	50	8"	30

Sand - Polystyrene - Concrete System

Three sand-polystyrene-concrete (SPC) layered systems are investigated. The length of the polystyrene absorption layer is varied from 2" to 8". The length of the sand layer is 10", and the length of the concrete layer is 12". A typical mesh for the SPC system is illustrated in Figure 4.7. The length of the polystyrene layer and the number of elements in each model are given in Table 4.3.

The finite element method is utilized only in the investigation of the linear SPC systems. The properties for the linear material models were previously presented in Table 3.1. An incident stress wave of 1,000 psi intensity is used in the linear investigation.

The transmission ratios for the nonlinear SPC systems are estimated using the results of the nonlinear single

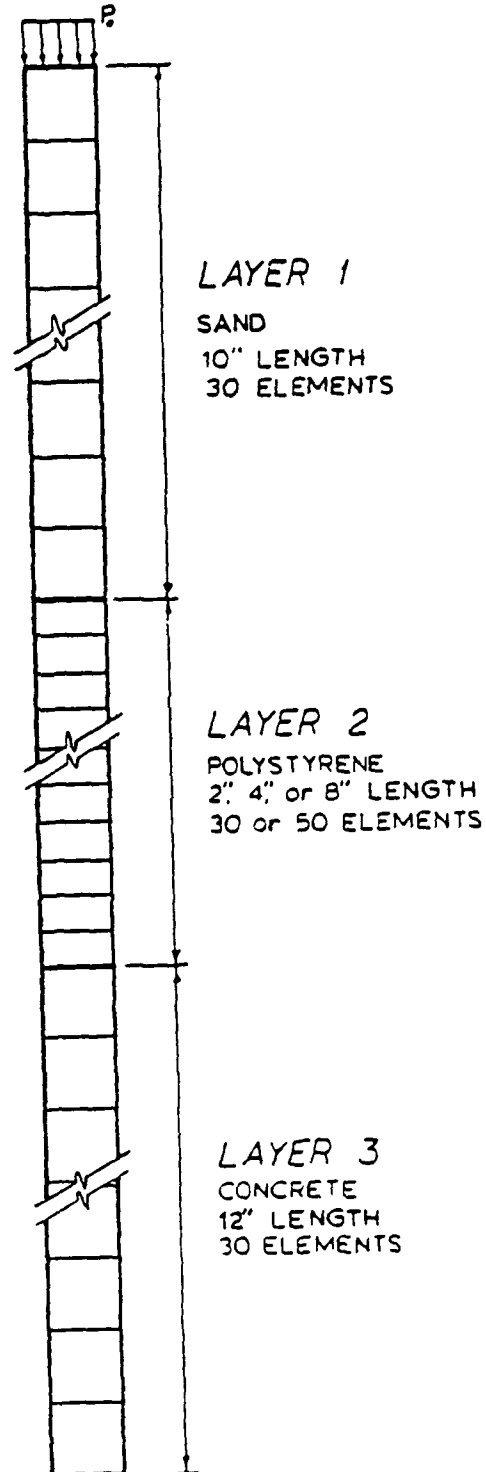


Figure 4.7. Typical Finite Element Mesh for the SPC Layered Systems.

Table 4.3. SPC Model Dimensions and Number of Elements.

Model	Total Length and No. Elements		Exterior Sand Layer		Polystyrene Absorption Layer		Interior Concrete Layer	
	L	no. el.	L_1	no. el.	L_2	no. el.	L_3	no. el.
SPC-2	24"	90	10"	30	2"	30	12"	30
SPC-4	26"	90	10"	30	4"	30	12"	30
SPC-8	30"	110	10"	30	8"	50	12"	30

layer analyses. An incident stress wave of 10,000 psi intensity is used in the nonlinear single layer investigation.

Sand-Polystyrene-Concrete-Polystyrene-Concrete System

Three sand-polystyrene-concrete-polystyrene-concrete (SPCPC) layered systems are investigated. However, an FEM analysis is not conducted for this model due to the prohibitive computational costs. The length of the polystyrene absorption layer is varied from 2" to 8". The length of the sand layer is 10", and the length of each concrete layer is 12". A typical SPCPC system is illustrated in Figure 4.8. The length of the layers for each of the SPCPC models is given in Table 4.4. The properties for the linear and nonlinear materials were previously presented in Tables 3.1 and 3.3.

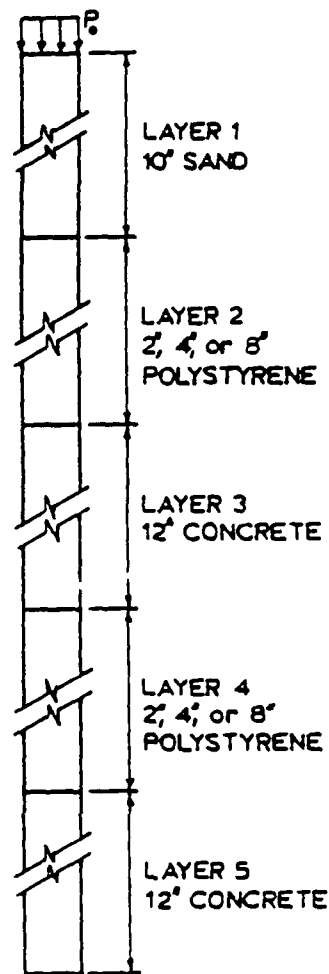


Figure 4.8. Typical SPCPC Layered System.

The transmission ratios of the linear systems is determined by the successive application of equation (2.24). The transmission ratios of the completely nonlinear SPCPC layered systems is estimated from the nonlinear single layer analyses. A 10,000 psi intensity incident stress wave is assumed for the nonlinear investigation.

Table 4.4. SPCPC Layered System Dimensions.

Model	Total Length L	Ext. Sand Layer L_1	Poly. Abs. Layer L_2	Ext. Conc. Layer L_3	Poly. Abs. Layer L_4	Int. Conc. Layer L_5
SPCPC-2	34"	10"	2"	12"	2"	8"
SPCPC-4	38"	10"	4"	12"	4"	8"
SPCPC-8	46"	10"	8"	12"	8"	8"

V. RESULTS OF ANALYSIS

Linear Concrete Model

A typical stress-time history for a point in the linear concrete model, described in Chapter IV, is illustrated in Figure 5.1. The figure depicts an incident rectangular compressive stress wave of intensity 1,000 psi and the corresponding tension wave reflected from the free end. The stress wave is reflected at full intensity. The high frequency oscillations defining the shape of the stress wave are caused by the excitation of high frequency modes in the structure. The theoretical wave propagation and reflection are also shown in Figure 5.1 as a dashed line.

A typical stress trace from wave propagation tests conducted on the Split Hopkinson Pressure Bar (SHPB) (22) is depicted in Figure 5.2. The bar is loaded axially with a high intensity, short duration pressure wave at one end. Each end of the bar is a free surface. An incident compressive wave and two reflected waves are depicted in the figure. The first reflection is caused by the compressive wave reflecting from the unloaded end of the bar as a tension wave. The second reflection is caused when the tensile wave propagates back to the loaded end of

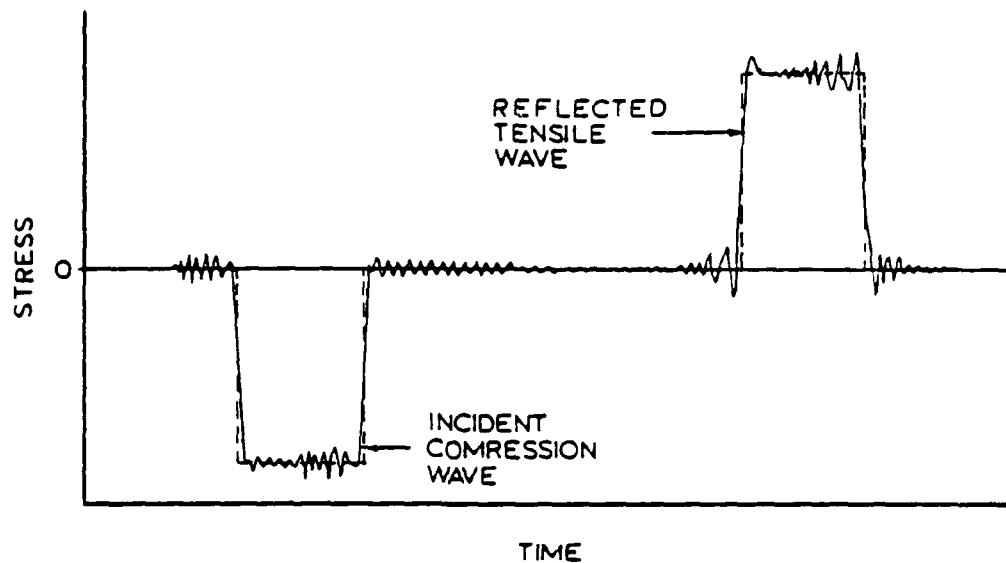


Figure 5.1. Typical Stress-Time History for a Point in the Linear Concrete Model.

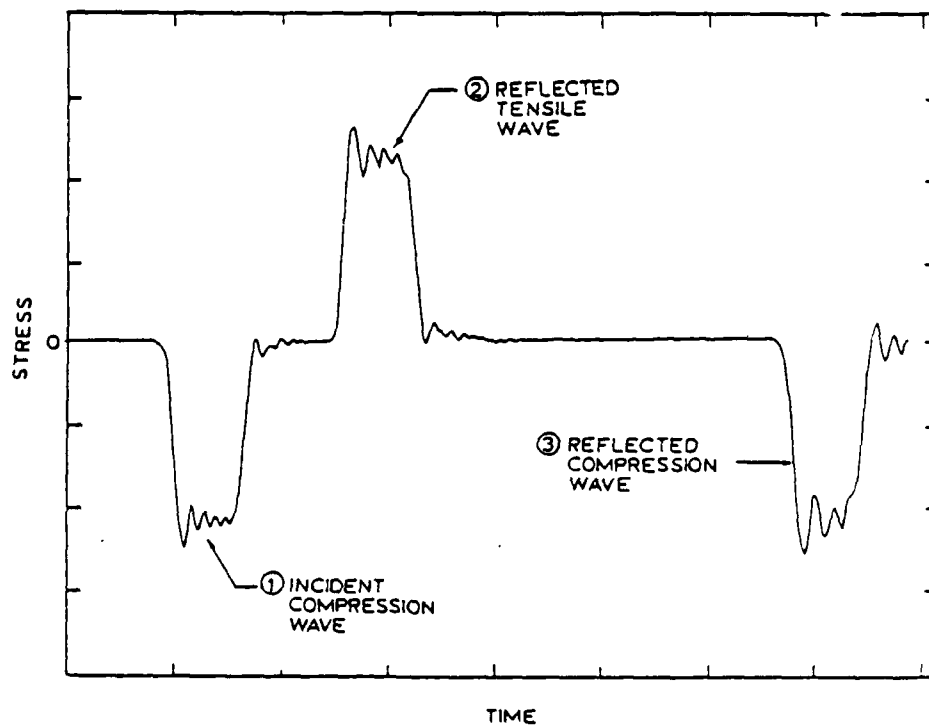


Figure 5.2. Typical Stress-Time History for a Point in the SHPB.

the bar and is reflected as a compression wave. The stress wave is reflected from each free surface at full intensity. It is noted that the stress trace obtained from the SHPB contains the same high frequency oscillations exhibited by the FEM analysis.

Nonlinear Concrete Model

The mitigation of stress waves in the nonlinear concrete model, described in Chapter IV, is illustrated in Figure 5.3. The maximum stress resulting from three types of incident stress waves (1. a short duration triangular wave, 2. a short duration rectangular wave, and 3. a long duration triangular wave) is shown. It is noted that the rate at which the stress wave degenerates is a function of the shape and duration of the incident stress wave. The short duration triangular wave decays very rapidly. However, both the short duration rectangular wave and the long duration triangular wave decay very gradually.

It is observed that the inelastic behavior of the concrete (as modeled by the bilinear constitutive law illustrated in Figure 3.7) does not significantly affect the propagation of either the rectangular or the long duration triangular stress waves. The intensity of the short duration triangular stress wave, however, is drastically reduced in a short distance.

The attenuation of stress waves in the nonlinear concrete model, considering the dynamic strength

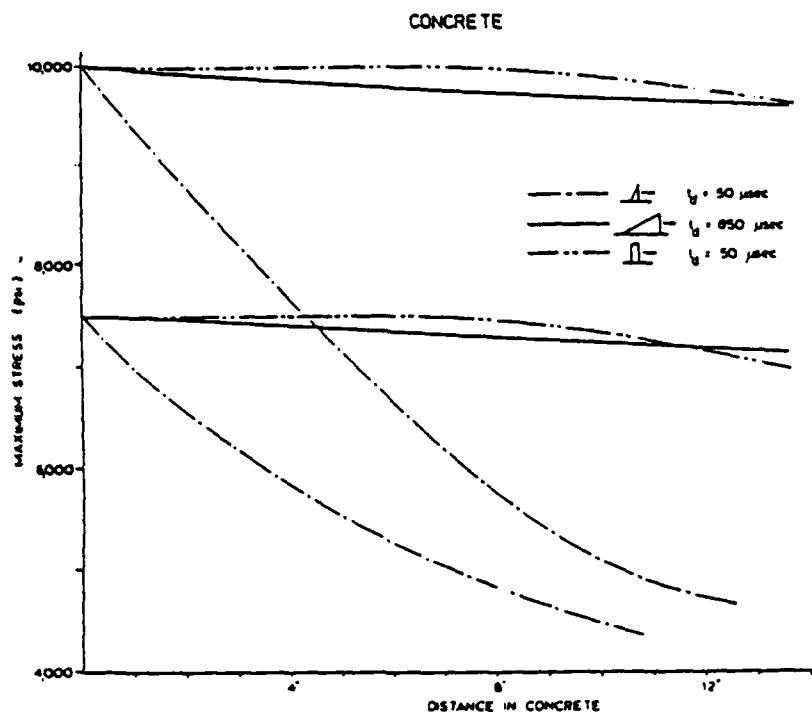


Figure 5.3. Maximum Stress Wave Intensity Versus Distance in Nonlinear Concrete.

characteristics specified in Table 4.1, is represented in Figure 5.4. The nonlinearity of the concrete has a significant effect on the propagation of the short duration triangular wave. However, the rate of decay of the stress wave is lessened. The intensities of the rectangular and long duration triangular waves are not significantly affected.

Nonlinear Polystyrene Model

The propagation of a plastic stress wave in a nonlinear polystyrene medium is illustrated in Figures 5.5 through 5.7. The results are very similiar to the theoretical predictions of plastic wave propagation

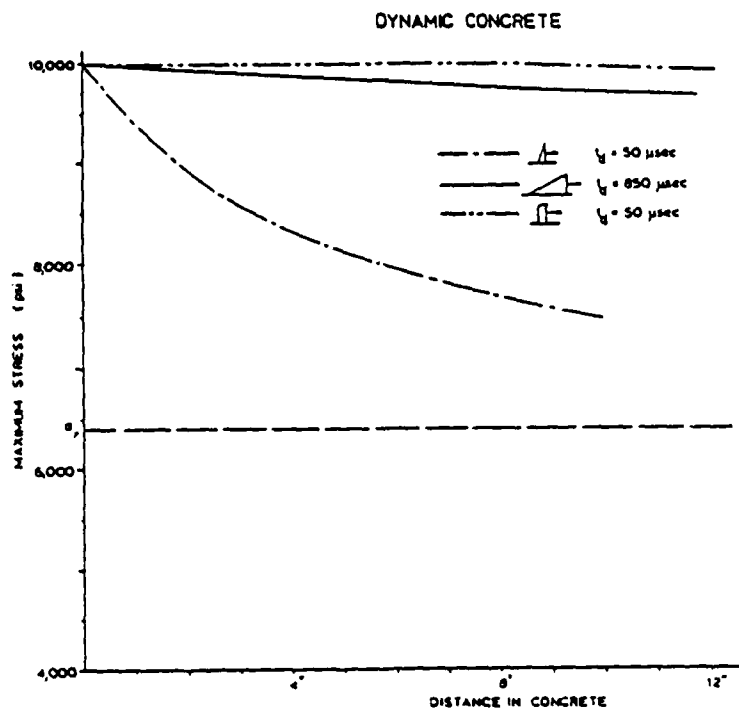


Figure 5.4. Maximum Stress Wave Intensity Versus Distance in Nonlinear Concrete When Dynamic Strength is Considered.

presented in Figure 2.18. In Figure 5.5, the propagation of a short duration triangular stress wave is represented. The plastic portion of the wave propagates at a lower velocity than the elastic portion and lags behind it. As the stress wave propagates through the medium, the wave length increases and the intensity decreases. The entire stress wave becomes elastic after the wave has propagated a sufficient distance.

The propagation of an incident short duration rectangular stress wave is depicted in Figure 5.6. The rectangular stress wave disperses and attenuates with distance. The incident rectangular stress wave becomes

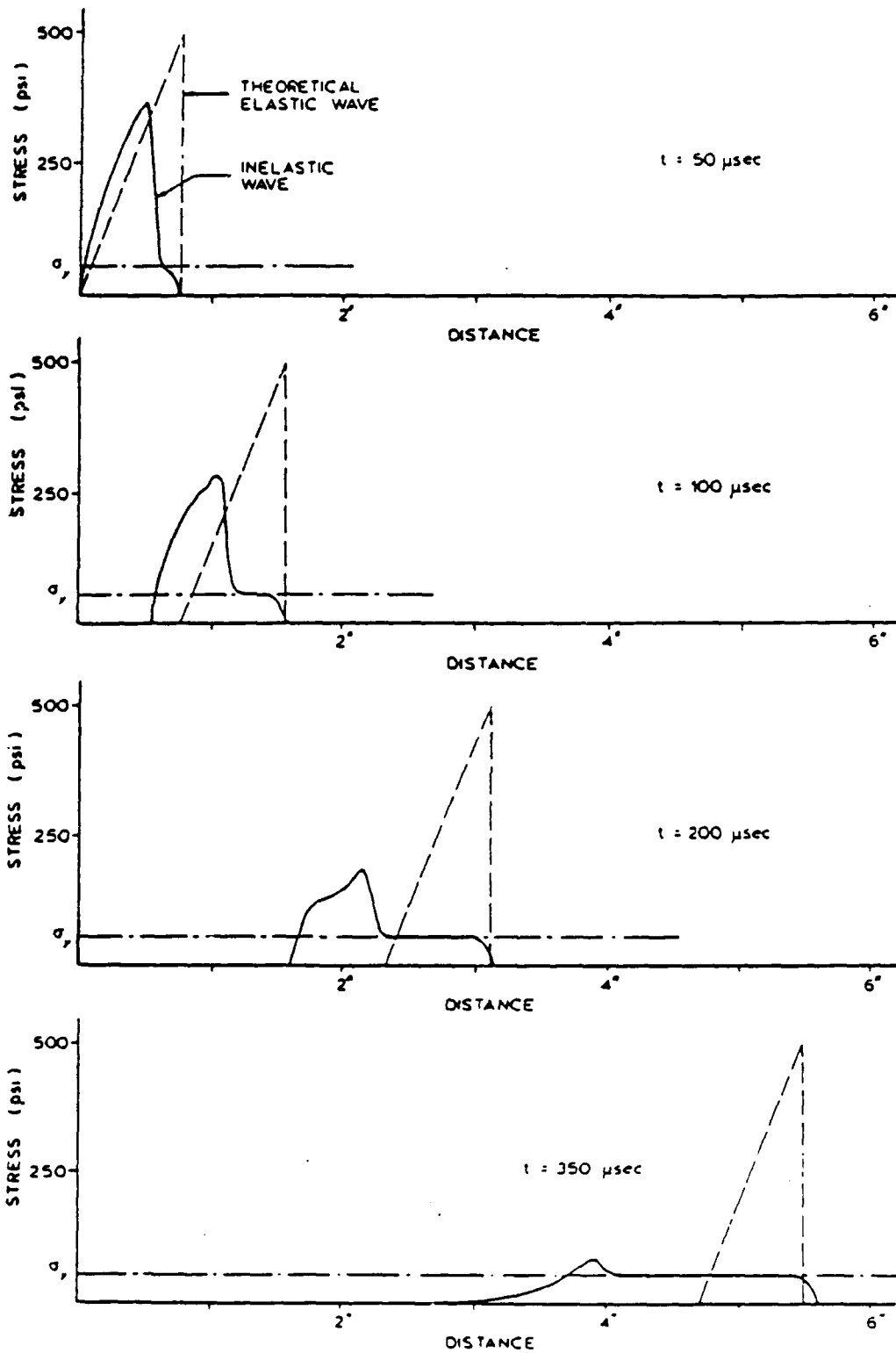


Figure 5.5. Propagation of a Plastic Short Duration Triangular Stress Wave in Polystyrene.

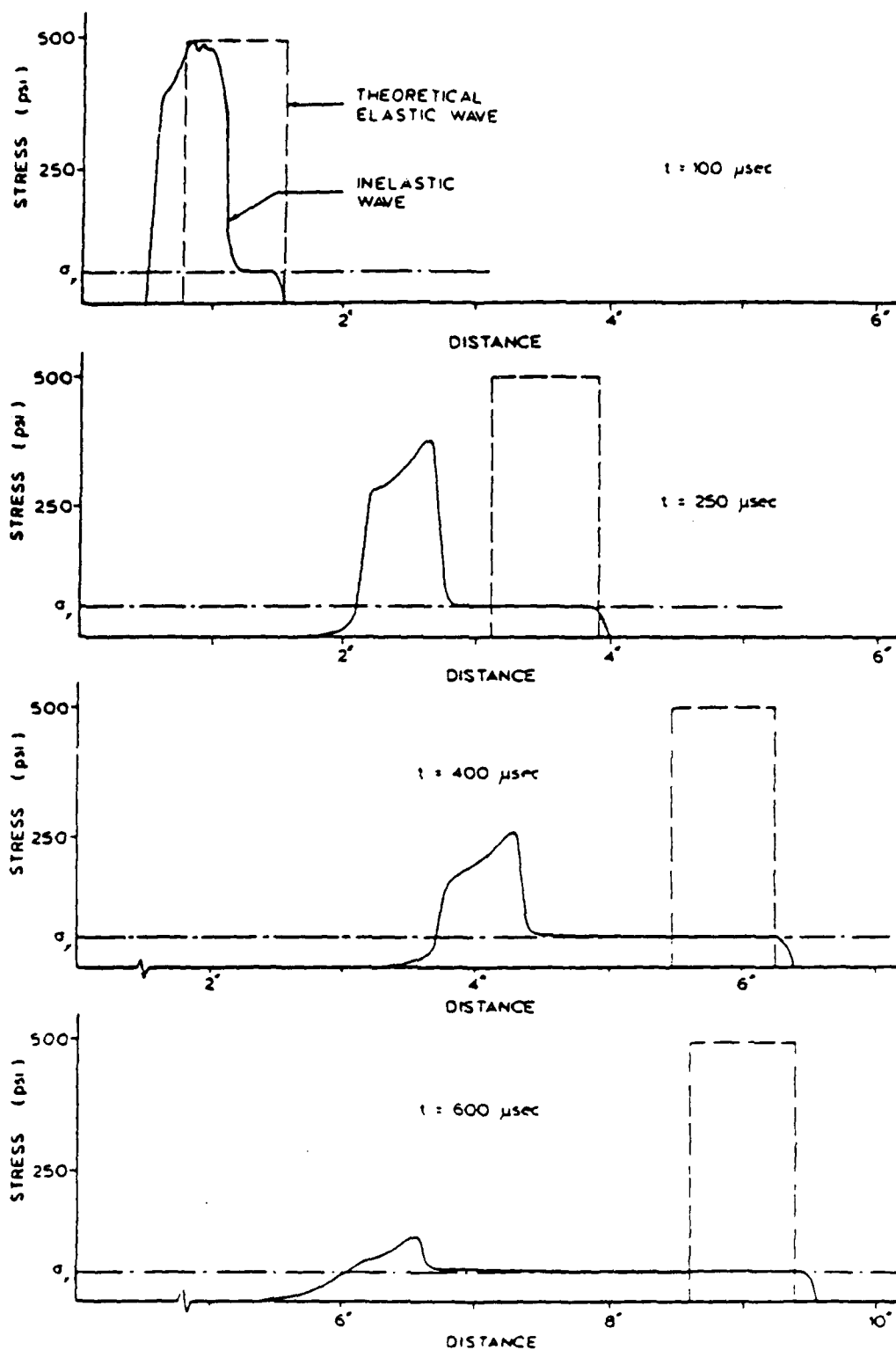


Figure 5.6. Propagation of a Plastic Short Duration Rectangular Stress Wave in Polystyrene.

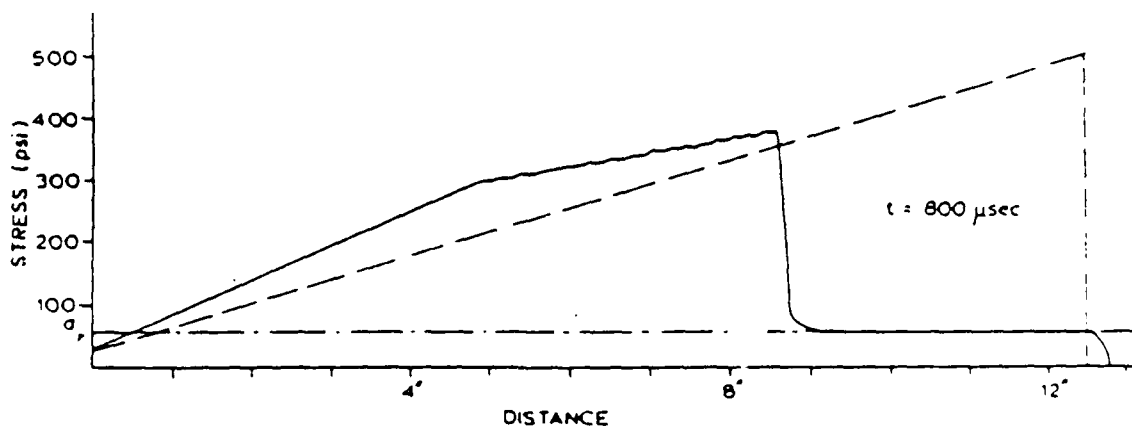
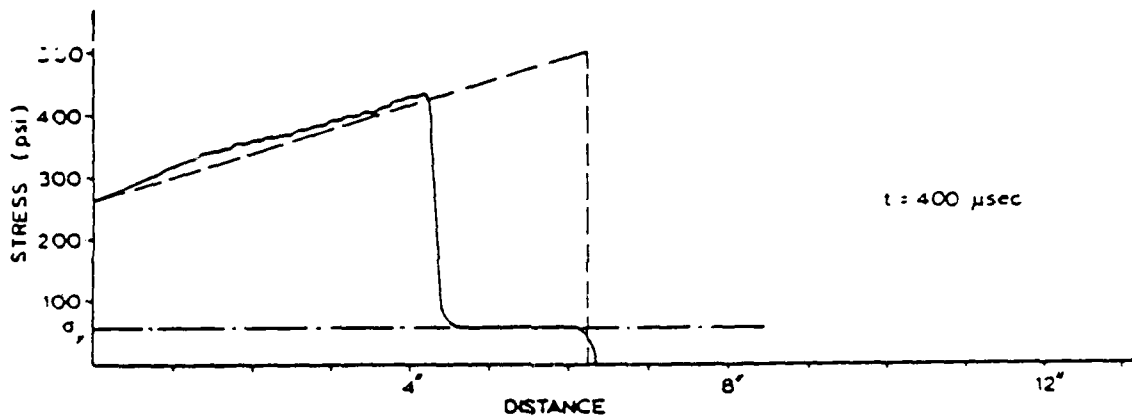
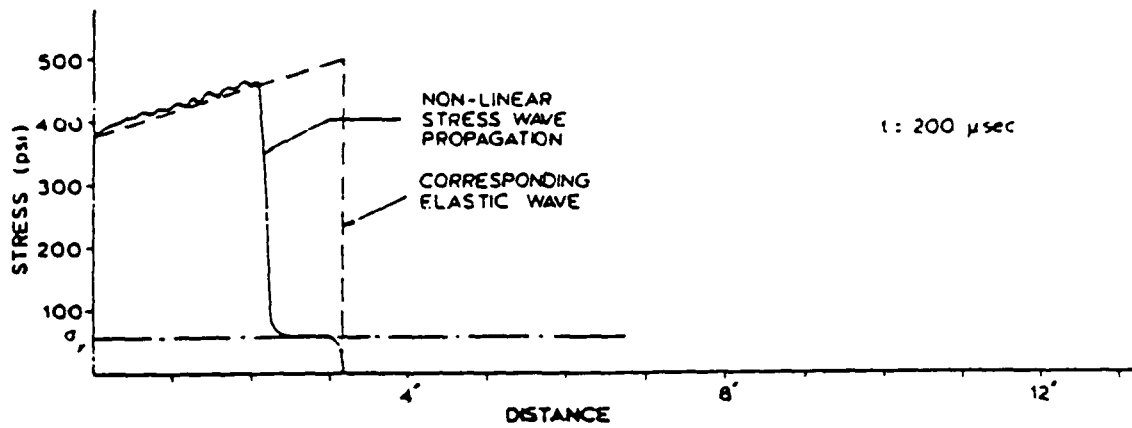


Figure 5.7. Propagation of a Plastic Long Duration Triangular Stress Wave in Polystyrene.

entirely elastic in a greater distance than required for the short duration triangular wave.

The propagation of a long duration triangular stress wave is illustrated in Figure 5.7. The plastic portion of the wave lags behind the elastic portion but exhibits little dispersion. The long duration triangular wave must travel a great distance through the medium before it is fully mitigated to an elastic wave.

The attenuation of several plastic stress waves in nonlinear polystyrene is illustrated in Figure 5.8. It is evident from Figure 5.8 that the degree of attenuation of a plastic stress wave, as it propagates through the polystyrene, is a function of the incident wave shape and initial intensity.

The short duration triangular wave exhibits a high attenuation rate as it propagates through the polystyrene. After a short distance, the intensity of the short duration triangular stress wave is reduced to the yield stress. The rate of attenuation exhibited by the long duration triangular wave, however, is significantly less. A much greater distance is required for the intensity of the long duration triangular stress wave to be reduced to the yield stress of the polystyrene. The attenuation rate of the short duration rectangular wave is less than that of the short duration triangular wave, but is much greater than that of the long duration triangular wave.

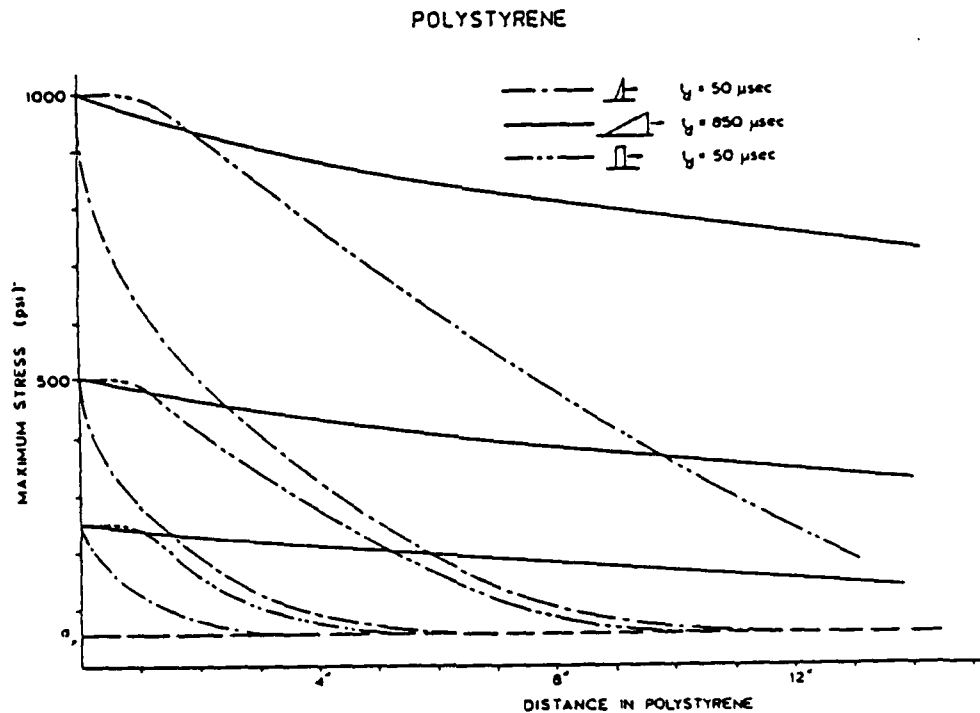


Figure 5.8. Maximum Stress Wave Intensity Versus Position in Polystyrene.

Nonlinear Sand Model

The attenuation of several plastic stress waves in the nonlinear sand model is illustrated in Figure 5.9. Incident stress waves of 500 psi and 1,000 psi intensity are examined. It is evident from Figure 5.9 that the attenuation rate of a plastic stress wave, as it propagates through the sand, is a function of the incident wave shape and initial intensity. The short duration triangular wave exhibits a high rate of attenuation in the nonlinear sand. However, the attenuation rates for the rectangular wave and long duration triangular wave are not as significant.

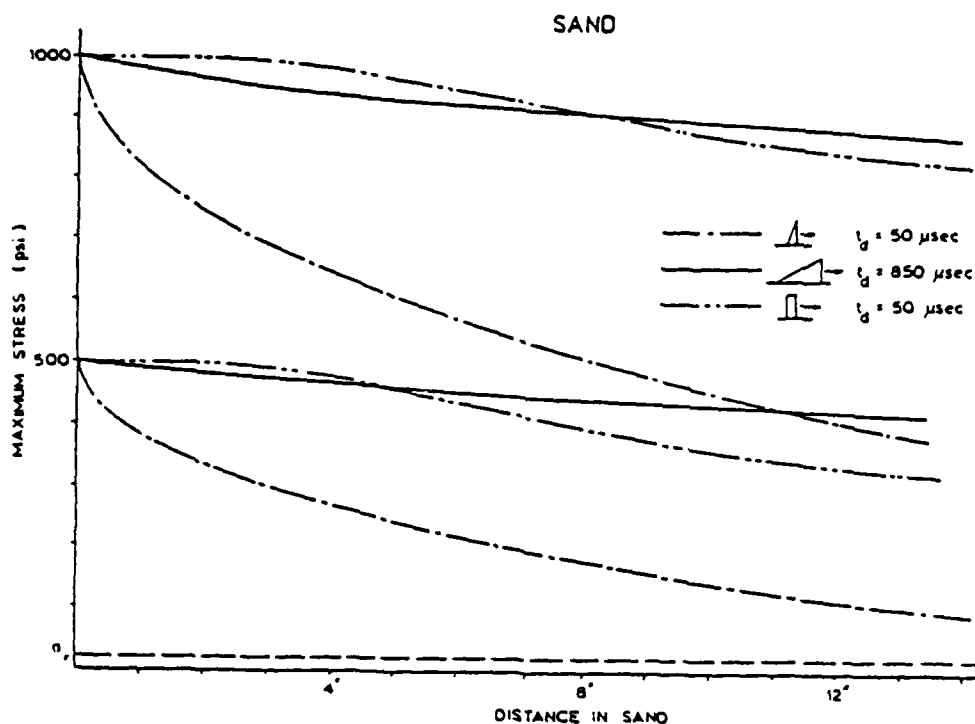


Figure 5.9. Maximum Stress Wave Intensity Versus Position in Sand.

The attenuation of high intensity plastic stress waves in the nonlinear sand is illustrated in Figure 5.10. Incident stress wave intensities ranging from 2,500 psi to 10,000 psi are considered. The attenuation of the short duration triangular wave is significantly affected by the nonlinearity, but the attenuation of the short duration rectangular wave and the long duration triangular wave is not significant.

The influence of Young's modulus, E , and the yield stress, σ_y , upon the attenuation of a short duration triangular wave is illustrated in Figure 5.11. Young's moduli of 20,000 psi and 80,000 psi, and yield stresses of

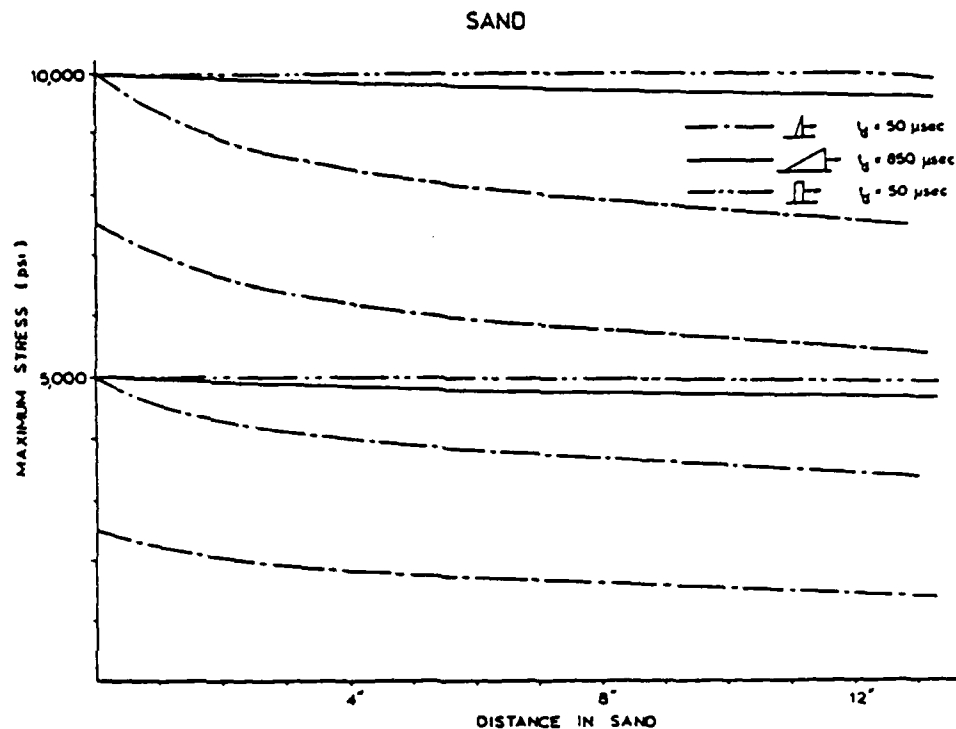


Figure 5.10. Maximum Stress Wave Intensity Versus Position in Sand for Several High-Intensity Incident Stress Waves.

20 psi and 40 psi, are considered. It is noted that as E decreases and/or σ , increases, the rate of attenuation increases.

Concrete - Polystyrene - Concrete System

Typical stress profiles for the CPC system are shown in Figures 5.12 through 5.14. Stress versus position in the model is plotted at selected times. The stress scale is reduced for the polystyrene and interior concrete layers so that observation of the attenuated stress wave can be facilitated. The stress axis for the exterior concrete layer ranges from -10,000 to 10,000 psi. The

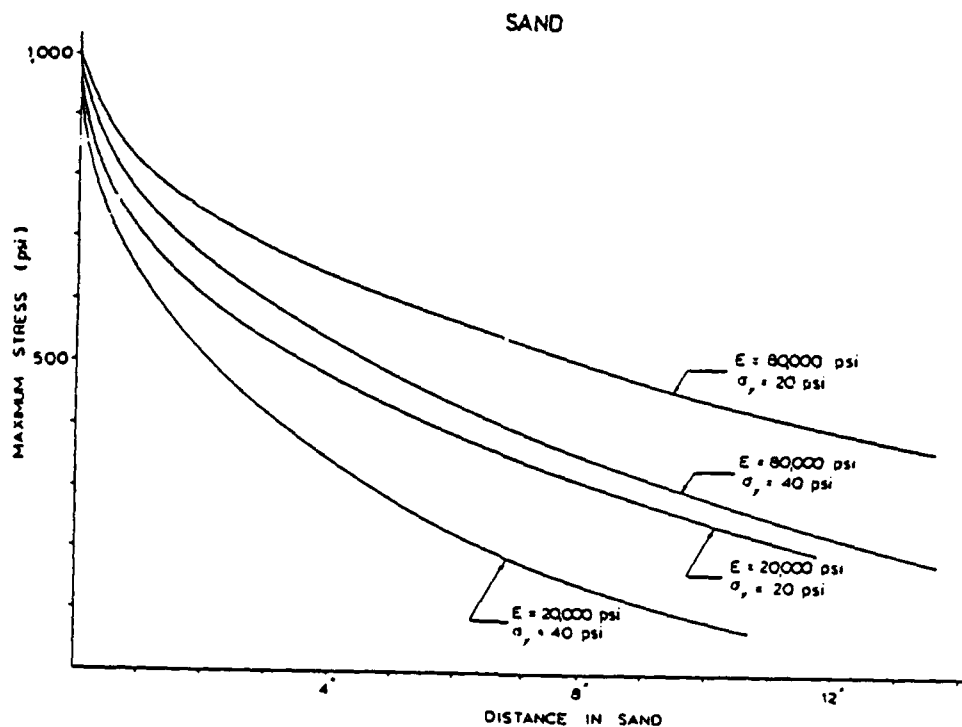


Figure 5.11. Effect of Strength and Yield Stress on Maximum Stress Wave Intensity in Sand.

stress axis for the polystyrene absorption layer and the interior concrete layer ranges from -45 to 45 psi.

The propagation of a short duration rectangular stress wave is illustrated in Figures 5.12 through 5.14. The stress wave profile at a time before the wave encounters the boundary between the exterior concrete layer and the polystyrene absorption layer is depicted in Figure 5.12. The stress profile at a time after the wave encounters the boundary between the exterior concrete layer and the polystyrene absorption layer is presented in Figure 5.13. It is observed that a very small percentage (0.96%) of the stress wave is transmitted to the polystyrene absorption layer, and that the major portion

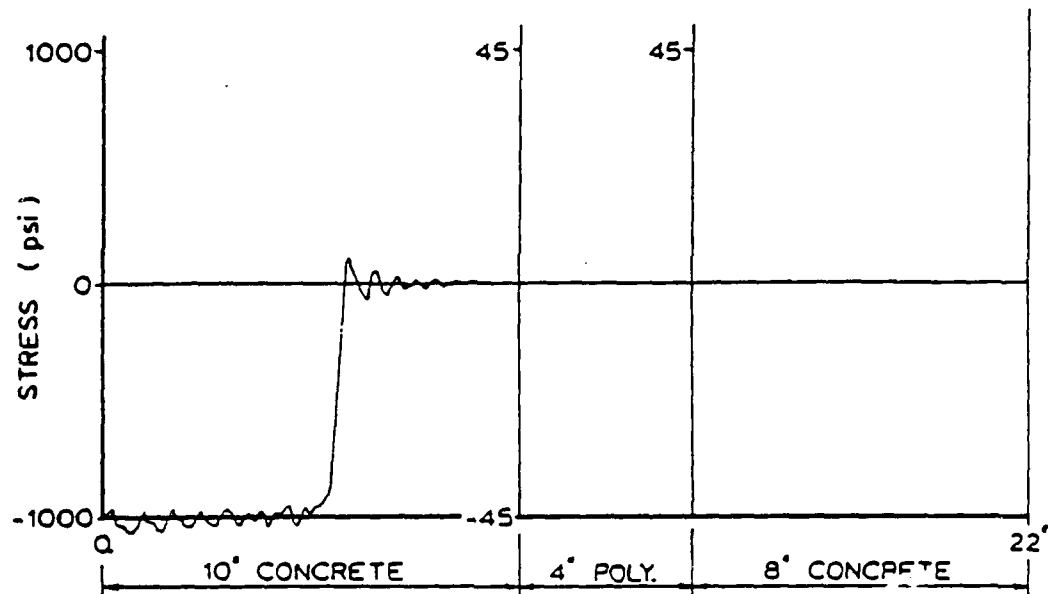


Figure 5.12. Stress Profile of the CPC-4 Layered System Subject to a 1000 psi Short Duration Rectangular Stress Wave. Time = 40.E-6 sec.

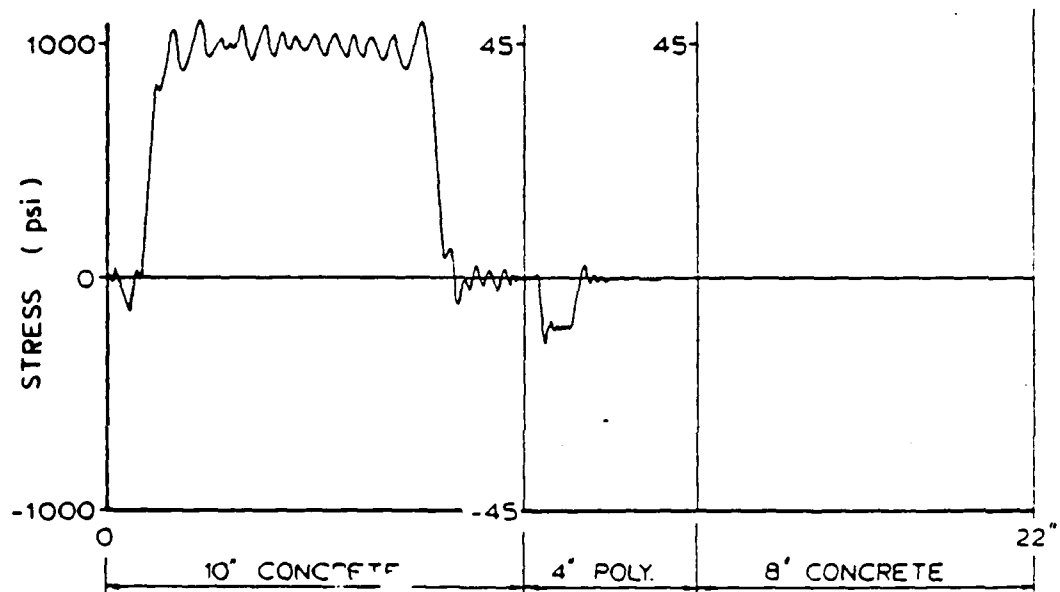


Figure 5.13. Stress Profile of the CPC-4 Layered System Subject to a 1000 psi Short Duration Rectangular Stress Wave. Time = 140.E-6 sec.

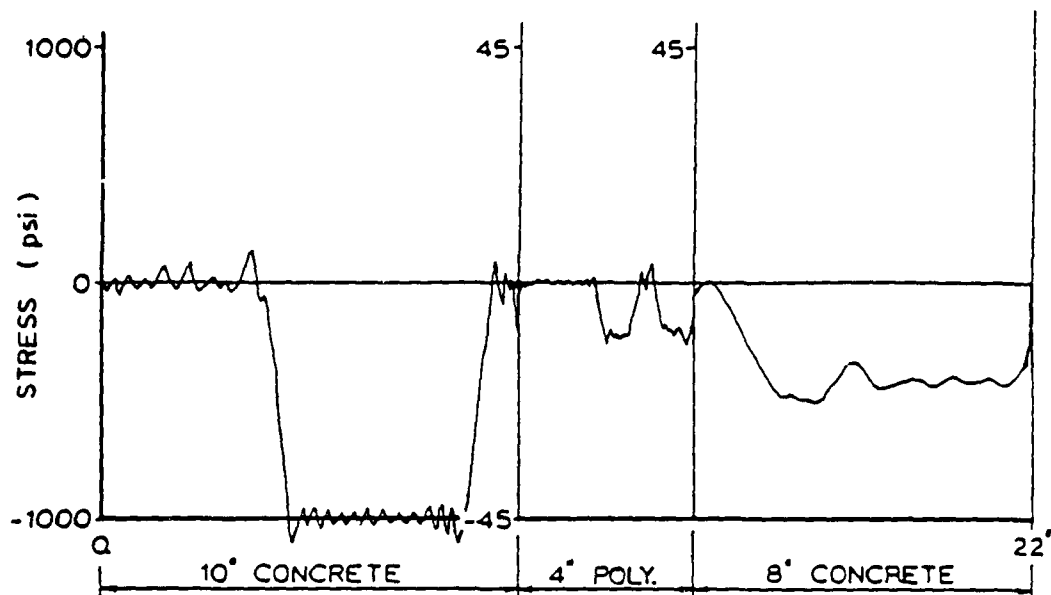


Figure 5.14. Stress Profile of the CPC-4 Layered System Subject to a 1000 psi Short Duration Rectangular Stress Wave. Time = 380.E-6 sec.

of the wave is reflected back through the exterior concrete layer as a tensile wave.

The stress condition in the model at a time after the wave encounters the interior layer of concrete is illustrated in Figure 5.14. The stress wave is transmitted from the polystyrene layer to the interior layer of concrete at an increased intensity. The wave length in the polystyrene is much shorter than in the concrete layers because the wave speed, c_p , in the polystyrene is much less than the wave speed, c_c , in the concrete.

A second stress wave propagating in the polystyrene layer is also shown in Figure 5.14. This wave is caused

by reflections generated in the exterior layer of concrete. These reflections will not occur in the actual structure because the concrete will not withstand the reflected tensile stress. The exterior layer of concrete will spall, thereby diminishing the stress wave until the intensity no longer exceeds the spall threshold of the concrete. Additional stress profiles for the CPC layered systems are presented in Appendix D.

The transmission ratios for the CPC layered system obtained using linear wave transmission and reflection theory are presented in Table 5.1. The theoretical transmission ratios were obtained using the BASIC computer program WAVEPROP.BAS (Appendix A). The program results for the CPC layered system are given in Appendix C. The transmission ratios obtained from the linear FEM analysis are also listed in Table 5.1. The results of the linear FEM analysis exhibit excellent correlation with the predictions of linear stress wave propagation theory.

Transmission ratios for the CPC layered systems, based upon the single layer nonlinear FEM analyses, are given in Table 5.2 for a short duration rectangular incident stress wave. Plastic wave attenuation in each layer is determined directly from the single layer nonlinear analyses described in Chapter IV. The stress transmitted across material boundaries is estimated from linear wave propagation theory.

Table 5.1. Linear Transmission Ratios for the CPC Layered Systems.

Model	Transmission Ratio	
	Linear Theory	Linear FEM Analysis
CPC-2	0.019	0.018
CPC-4	0.019	0.020
CPC-8	0.019	0.019

Table 5.2. Estimated Nonlinear Transmission Ratios for the CPC Layered Systems Subject to a Short Duration Rectangular Incident Stress Wave.

	CPC-2	CPC-4	CPC-8
Incident Upon Ext. Concrete	10,000	10,000	10,000
Intensity at Boundary	9,900	9,900	9,900
Transmitted to Polystyrene	95	95	95
Intensity at Boundary	55	55	55
Transmitted to Int. Concrete	110	110	110
Nonlinear Transmission Ratio	.0110	.0110	.0110

The transmission ratios estimated from the single layer nonlinear FEM analyses are summarized in Table 5.3. The estimated transmission ratio for each CPC layered system is insensitive to wave type since only a very small percentage (0.96%) of each wave is transmitted across the concrete-polystyrene boundary.

Table 5.3. Estimated Nonlinear Transmission Ratios for the CPC Layered Systems Subject to a 10,000 psi Incident Stress Wave.

	Estimated Nonlinear Transmission Ratio		
	CPC-2	CPC-4	CPC-8
Short Duration Triangular Stress Wave	.0098	.0098	.0098
Short Duration Rectangular Stress Wave	.0110	.0110	.0110
Long Duration Triangular Stress Wave	.0110	.0110	.0110

The nonlinear transmission ratios obtained from the FEM analysis of the CPC layered systems, in which only the polystyrene layer is nonlinear, are listed in Table 5.4. For comparison, the transmission ratios estimated from the nonlinear single layer FEM analyses and the transmission ratios obtained from linear wave propagation theory are also presented in Table 5.4. Excellent correlation of the

nonlinear transmission ratios is observed. The significant wave attenuation induced by nonlinear material behavior is clearly demonstrated by the results summarized in Table 5.4.

Table 5.4. Comparison of Linear and Nonlinear Transmission Ratios for the CPC Layered Systems.

Model	Transmission Ratio		
	Nonlinear FEM Analysis	Estimate from Single Layer FEM Analyses	Linear Theory
CPC-2	0.011	0.011	0.019
CPC-4	0.011	0.011	0.019
CPC-8	0.010	0.0098	0.019

Sand - Polystyrene - Concrete System

Typical stress profiles for the SPC system are shown in Figures 5.15 through 5.17. Stress versus position in the model is plotted at selected times. The stress scale is reduced for the polystyrene and interior concrete layers so that observation of the attenuated stress wave can be facilitated. The stress axis for the exterior sand layer ranges from -10,000 to 10,000 psi. The stress axis for the polystyrene absorption layer and the interior concrete layer ranges from -300 to 300 psi.

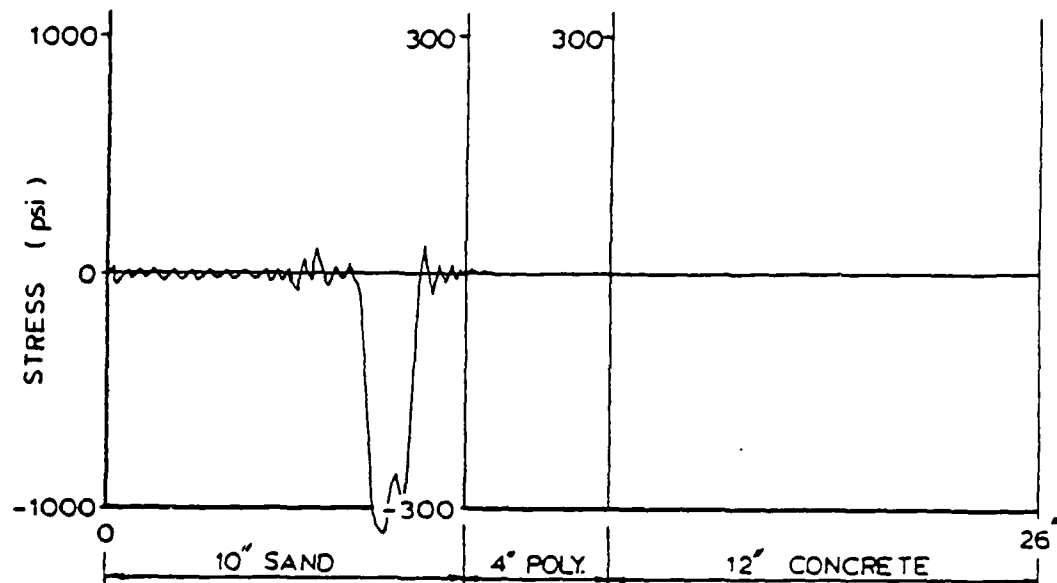


Figure 5.15. Stress Profile of the SPC-4 Layered System Subject to a 1000 psi Short Duration Rectangular Stress Wave. Time = 350.E-6 sec.

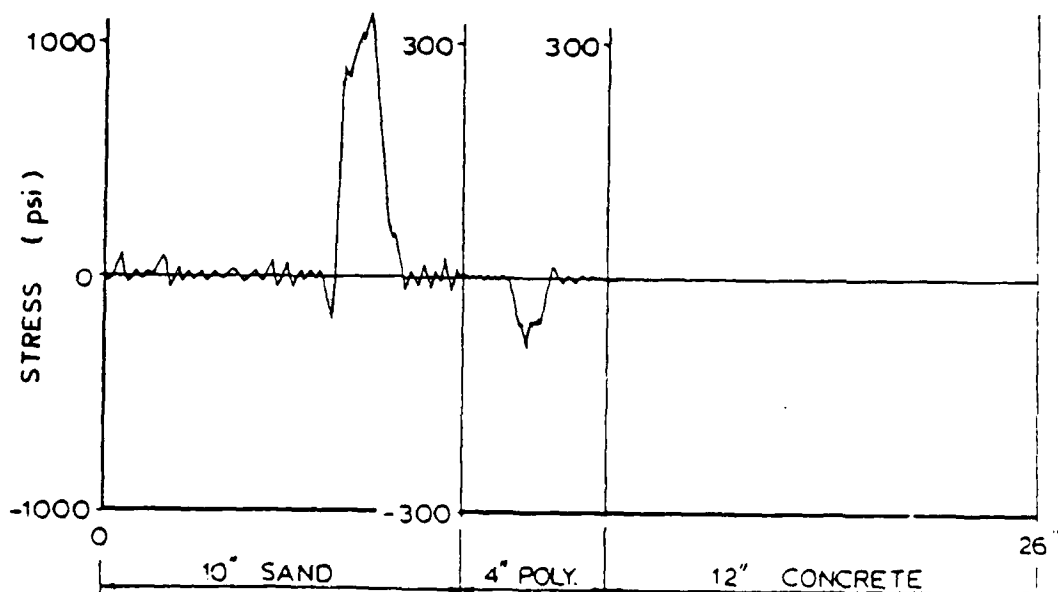


Figure 5.16. Stress Profile of the SPC-4 Layered System Subject to a 1000 psi Short Duration Rectangular Stress Wave. Time = 550.E-6 sec.

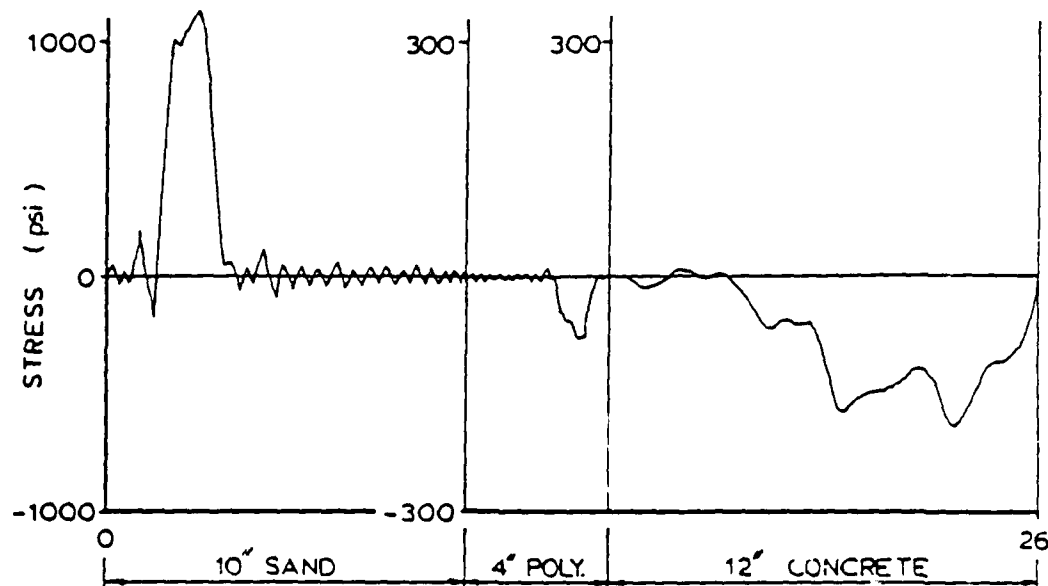


Figure 5.17. Stress Profile of the SPC-4 Layered System Subject to a 1000 psi Short Duration Rectangular Stress Wave. Time = 750.E-6 sec.

The propagation of a short duration rectangular stress wave is illustrated in Figures 5.15 through 5.17. The stress wave profile at a time before it encounters the boundary between the sand and polystyrene layers is depicted in Figure 5.15. The stress profile at a time after the boundary between the exterior sand layer and the polystyrene absorption layer is encountered is represented in Figure 5.16. It is observed that a small percentage (7.14%) of the stress wave is transmitted to the polystyrene absorption layer, and that the major portion of the wave is reflected back through the exterior sand layer as a tensile wave.

The stress condition in the model at a time after the wave encounters the interior layer of concrete is illustrated in Figure 5.17. The stress wave is transmitted from the polystyrene layer to the interior layer of concrete at an increased intensity. Additional stress profiles for the SPC layered systems are presented in Appendix E.

The transmission ratios for the SPC layered systems obtained using linear wave transmission and reflection theory are listed in Table 5.5. The theoretical transmission ratios were obtained using the BASIC computer program WAVEPROP.BAS (Appendix A). The program results for the SPC layered system are given in Appendix C. The transmission ratios obtained from the linear FEM analysis are also listed in Table 5.5. The results of the linear FEM analysis exhibit excellent correlation with the predictions of linear wave propagation theory.

Transmission ratios for the SPC layered systems, based upon the single layer nonlinear FEM analyses, are given in Table 5.6 for a short duration triangular stress wave. Plastic wave attenuation in each layer is determined directly from the single layer nonlinear analyses described in Chapter IV. The stress transmitted across material boundaries is estimated from linear wave propagation theory.

Table 5.5. Linear Transmission Ratios for the SPC Layered Systems.

Model	Transmission Ratio	
	Linear Theory	Linear FEM Analysis
SPC-2	0.142	0.130
SPC-4	0.142	0.150
SPC-8	0.142	0.150

Table 5.6. Estimated Nonlinear Transmission Ratios for the SPC Layered Systems Subject to a Short Duration Triangular Incident Stress Wave.

	SPC-2	SPC-4	SPC-8
Incident Upon Exterior Sand	10,000	10,000	10,000
Intensity at Boundary	8,900	8,900	8,900
Transmitted to Polystyrene	635	635	635
Intensity at Boundary	274	152	55
Transmitted to Int. Concrete	545	303	110
Nonlinear Transmission Ratio	.0545	.0303	.0110

The transmission ratios estimated from the single layer nonlinear FEM analyses are summarized in Table 5.7. The transmission ratio decreases as the thickness of the polystyrene layer is increased. A plot of transmission ratio versus the thickness of the polystyrene absorption layer, for both the linear and nonlinear materials, is shown in Figure 5.18. It is indicated that a thicker polystyrene absorption layer increases the capacity of the layered system to mitigate an incident stress wave, thereby increasing the structures resistance to interior spalling.

Table 5.7. Estimated Nonlinear Transmission Ratios for the SPC Layered Systems Subject to a 10,000 psi Incident Stress Wave.

	Estimated Nonlinear Transmission Ratio		
	SPC-2	SPC-4	SPC-8
Short Duration Triangular Stress Wave	.0545	.0303	.0110
Short Duration Rectangular Stress Wave	.1260	.0967	.0496
Long Duration Triangular Stress Wave	.1304	.1226	.1107

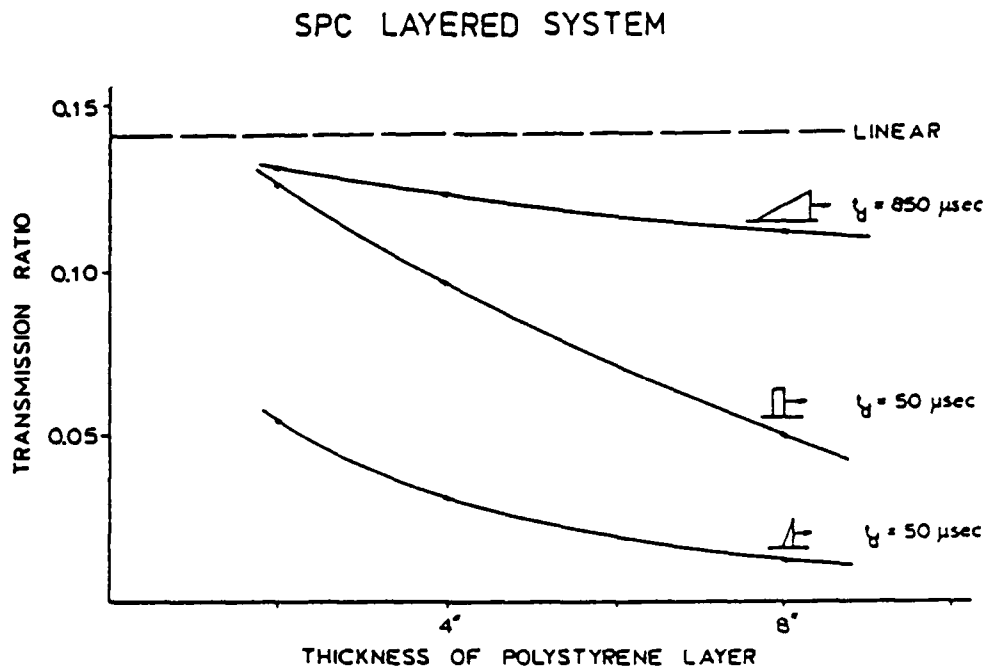


Figure 5.18. Transmission Ratio Versus the Thickness of the Polystyrene Absorption Layer of the SPC Layered System.

Sand-Polystyrene-Concrete-Polystyrene-Concrete System

The transmission ratios for the SPCPC layered systems, based upon the single layer nonlinear FEM analyses, are given in Table 5.8 for a long duration triangular incident stress wave. Plastic wave attenuation in each layer is determined directly from the single layer nonlinear analyses described in Chapter IV. The stress transmitted across material boundaries is estimated from linear wave propagation theory.

The transmission ratios estimated from the single layer nonlinear FEM analyses are summarized in Table 5.9. It is noted that the transmission ratio decreases as the

Table 5.8. Estimated Nonlinear Transmission Ratios for the SPCPC Layered Systems Subject to a 10,000 psi Long Duration Triangular Incident Stress Wave.

	SPCPC-2	SPCPC-4	SPCPC-8
Incident Upon Exterior Sand	10,000	10,000	10,000
Intensity at Boundary	9,900	9,900	9,900
Transmitted to Polystyrene	707	707	707
Intensity at Boundary	655	616	556
Transmitted to Ext. Concrete	1304	1226	1107
Transmitted to Polystyrene	13	12	11
Transmitted to Int. Concrete	26	24	22
Nonlinear Transmission Ratio	.0026	.0024	.0022

thickness of the polystyrene layer is increased. A plot of transmission ratio versus the thickness of the polystyrene absorption layer is shown in Figure 5.19. It is indicated that a thicker polystyrene absorption layer increases the capacity of the layered system to mitigate an incident stress wave, thereby increasing the structures resistance to interior spalling.

Table 5.9. Estimated Nonlinear Transmission Ratios for the SPCPC Layered Systems Subject to a 10,000 psi Incident Stress Wave.

	Estimated Nonlinear Transmission Ratio		
	SPCPC-2	SPCPC-4	SPCPC-8
Short Duration Triangular Stress Wave	.0010	.0006	.0002
Short Duration Rectangular Stress Wave	.0024	.0018	.0010
Long Duration Triangular Stress Wave	.0026	.0024	.0022

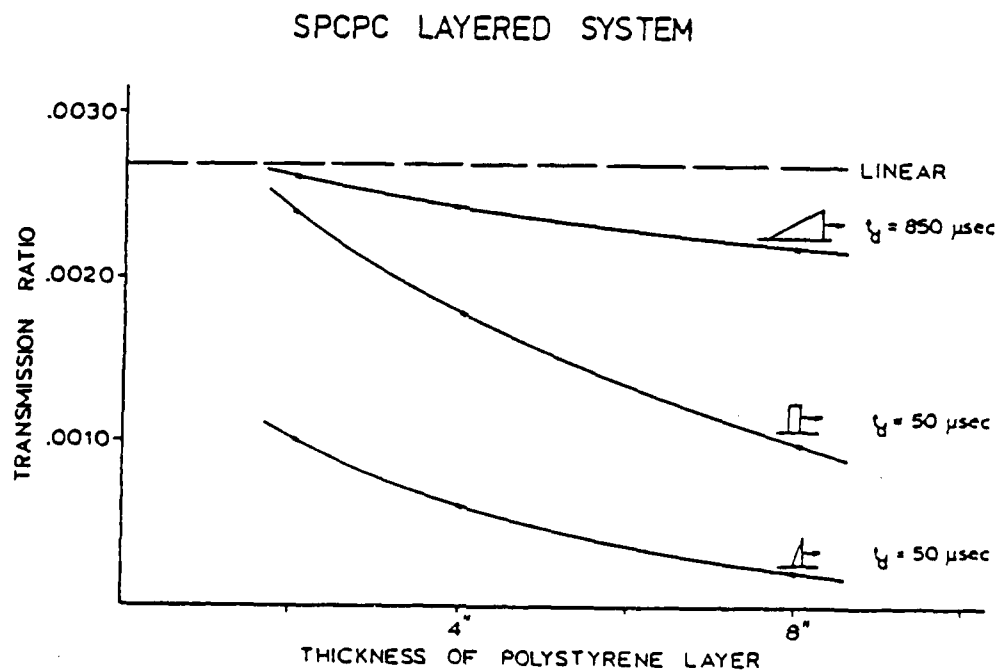


Figure 5.19. Transmission Ratio Versus the Thickness of the Polystyrene Absorption Layer of the SPCPC Layered System.

The thickness of the polystyrene absorption layer has no effect on the transmission ratio of the linear system (see Figure 5.19). The linear transmission ratio for the SPCPC layered systems, obtained from the BASIC computer program WAVEPROP.BAS (Appendix A), is 0.0027. The program results for the SPCPC layered system are given in Appendix C.

VI. CONCLUSIONS AND RECOMMENDATIONS

Conclusions

The finite element method (FEM) has been successfully employed to predict the propagation, reflection, and transmission of stress waves in both homogeneous and layered media. However, very fine discretizations and small integration time steps are required in order for the FEM analyses to yield accurate results. This has resulted in significant computational costs, even for simple FEM models.

It has been shown that layered media significantly alter stress wave propagation characteristics. The proper combination of high impedance and low impedance materials has demonstrated substantial enhancement of stress wave attenuation. This finding suggests that the implementation of layered media in the construction of protective shelters can eliminate blast induced spalling at the interior surface of the shelter walls.

The concrete-polystyrene-concrete (CPC), sand-polystyrene-concrete (SPC), and sand-polystyrene-concrete-polystyrene-concrete (SPCPC) layered systems have been shown to be extremely effective in mitigating an incident stress wave as it propagates through the system. The

transmission ratios for these layered systems, calculated on the assumption of linear material behavior, indicate that their deployment in the construction of protective shelters will eliminate blast induced spalling. The transmission ratios for these systems, calculated on the assumption of inelastic behavior of the media, indicate an even higher degree of attenuation for propagating stress waves, thus lending additional credibility to the layered system concept.

The SPCPC layered system exhibits the highest degree of stress wave attenuation. The linear transmission ratio for this system is calculated to be 0.0027. The nonlinear transmission ratio of the SPCPC-8 layered system is estimated to be as low as 0.0002 for a short duration triangular stress wave, and 0.0022 for a long duration triangular stress wave.

The CPC layered system also exhibits a significant degree of stress wave attenuation. The linear transmission ratio for the CPC systems is 0.019. The nonlinear transmission ratio of the CPC layered system is estimated to be as low as 0.0098 for a short duration triangular stress wave, and 0.0110 for a long duration triangular stress wave.

The SPC layered system is the least effective in terms of stress wave mitigation. The linear transmission ratio for the SPC layered system is 0.142. The nonlinear

transmission ratio of the SPC-8 system is estimated to be 0.011 for a short duration triangular stress wave and 0.1107 for a long duration stress wave. The SPC systems considered were comprised of a 10" thick layer of sand. A structure surrounded by a sand berm, or a buried structure, would be tantamount to a sand layer much thicker than 10". Therefore, the actual nonlinear transmission ratios for the SPC systems would be much less than those determined for the SPC models investigated in this study.

In all the layered systems examined, the thickness of the absorption layer significantly effects the nonlinear transmission ratio. A thicker polystyrene absorption layer results in a reduced nonlinear transmission ratio.

Recommendations

The FEM analyses conducted in this study indicate that the CPC, SPC, and SPCPC layered systems are highly effective in reducing transmitted stresses. However, the transmission ratios were obtained without consideration of the dynamic properties of the concrete, sand, and polystyrene. Also, the nonlinear soil and concrete approximations of linear elastic-perfectly plastic constitutive relations are very crude.

The present study has examined only the wave propagation and attenuation characteristics of the CPC, SPC, and SPCPC layered systems. It is recommended that

additional numerical studies be conducted to investigate the overall structural response of protective shelters employing the layered system concept.

It is recommended that field tests of the CPC, SPC, and SPCPC layered systems be conducted to determine their effectiveness in reducing spall. It is recommended that layered systems consisting of polystyrene layers of 4", 8", and 12" thicknesses be tested.

The SPC layered system is the most cost-effective alternative for retrofitting existing protective shelters. It is recommended that extensive field testing be conducted on the SPC layered systems to determine the optimum thickness of the polystyrene absorption layer.

BIBLIOGRAPHY

1. ADINA - A Finite Element Program For Automatic Dynamic Incremental Nonlinear Analysis, Report AE 84-1, ADINA Engineering, Inc., Watertown, MA, 1984.
2. ADINA-IN - A Program for Generation of Input Data to ADINA, Report AE 84-6, ADINA Engineering, Inc., Watertown, MA, 1984.
3. ADINA-PLOT - A Program for Display and Post-Processing of ADINA Results, Report AE 84-3, ADINA Engineering, Inc., Watertown, MA, 1984.
4. ADINA System Verification Manual, Report AE 84-5, ADINA Engineering, Inc., Watertown, MA, 1984.
5. Balags, P. and Vretblad, B., "Model Tests on Composite Slabs of Light Gauge Metal and Concrete Subjected to Blast Loading," Proceedings of the Second Symposium on the Interaction of Nonnuclear Munitions with Structures, Panama City Beach, FL, 15-18 April, 1985, pp. 143-148.
6. Blake, A., Practical Stress Analysis in Engineering Design, Marcel Dekker, New York, 1982.
7. Colthorp, D.R., Kiger, S.A., Vitayaudom, K.P., and Hilferty, T.J., "Blast Response Tests of Reinforced Concrete Box Structures," Proceedings of the Second Symposium on the Interaction of Nonnuclear Munitions with Structures, Panama City Beach, FL, 15-18 April, 1985, pp. 95-100.
8. Cook, R.D., Concepts and Applications of Finite Element Analysis, 2nd Edition, John Wiley and Sons, New York, 1981.
9. Fundamentals of Protective Design for Conventional Weapons, Department of the Army Waterways Experiment Station, Corps of Engineers, Vicksburg, MS, 1984.
10. Henrych, J., The Dynamics of Explosion and Its Use, Elsevier Scientific Publishing, New York, 1979.

11. Hodge, K.G., and Wasley, R.J., "Dynamic Compressive Behavior of Various Foam Materials," Applied Polymer Symposia, No. 12, pp. 97-109, 1969.
12. Kolsky, H., Stress Waves in Solids, Dover Publications, New York, 1963.
13. Kornhauser, M., Structural Effects of Impact, Spartan Books, Baltimore, MD, 1964.
14. Landis, D.W., Wave Propagation in Layered Structures, Final Report, submitted to AFOSR, Washington, D.C., September, 1987.
15. Malvern, L.E., Jenkins, D.A., Tang, T., and Ross, C.A., "Dynamic Compressive Testing of Concrete," Proceedings of the Second Symposium on the Interaction of Nonnuclear Munitions with Structures, Panama City Beach, FL, 15-18 April, 1985, pp. 194-199.
16. Malvern, L.E., and Ross, C.A., Dynamic Response of Concrete and Concrete Structures, Final Report, submitted to AFOSR, Washington, D.C., May, 1986.
17. Nowacki, W.K., Stress Waves in Non-Elastic Solids, Pergamon Press, New York, 1978.
18. Raphael, J.M., "Tensile Strength of Concrete," ACI Journal, March-April 1984, pp. 158-165.
19. Rhinehart, J.S., Stress Transients in Solids, Hyper Dynamics, Santa Fe, NM, 1975.
20. Tedesco, J.W., Analysis of Layered Structures to Resist Blast Effects of Conventional Weapons, Final Report, submitted to AFOSR, Washington, D.C., April 1987.
21. Tedesco, J.W., Dynamic Stress Analysis of Layered Structures, Final Report, submitted to AFOSR, Washington, D.C., September, 1985.
22. Tedesco, J.W., Pressure Waves in Foam and Foam-Sand Samples, Final Report, submitted to AFOSR, Washington, D.C., September, 1987.

23. Tedesco, J.W., Hayes, J.R., and Landis, D.W., "Dynamic Analysis of Layered Structures," International Symposium on the Interaction of Coventional Munitions with Protective Shelters, Mannheim, West Germany, March 9-13, 1987, Vol. I, pp. 34-43.
24. Tedesco, J.W., Hayes, J.R., and Landis, D.W., "Dynamic Response of Layered Structures Subject to Blast Effects of Nonnuclear Weaponry," Journal of Computers and Structures, Vol. 26, No. 1 of 2, 1987, pp. 79-86.
25. Timoshenko, S.P. and J.N. Goodier, Theory of Elasticity, 3rd Edition, McGraw-Hill Book Company, New York, 1979.
26. Vretblad, B. and Balags, P., "Composite Structures Exposed to Blast Loads," Proceedings of the Third Symposium on the Interaction of Nonnuclear Munitions with Structures, Mannheim, West Germany, March 9-13, 1987, Vol. II, p. 736.
27. Wasley, R.J., Stress Wave Propagation in Solids, Marcel Dekker, New York, 1973.

Appendices can be obtained from
Universal Energy Systems, Inc.

FINAL REPORT NUMBER 25
REPORT NOT AVAILABLE AT THIS TIME
Dr. Dennis Truax
760-7MG-105